

**Experimental and Theoretical Studies of the
Halogen Bond and the Electrophilic
Bromination Reaction**

Linda Jane McAllister

PhD

University of York

Chemistry

May 2014

Abstract

The work presented in this thesis is an investigation into the halogen bond using both experimental and theoretical techniques. These studies have contributed toward the understanding of the interaction during a period when the definition of this interaction was being debated.¹ The interactions investigated have a range of strengths; varying from the very weak interactions with rare gas atoms to the strong interactions with halonium ions acting as halogen-bond donors.

The competition and cooperation between halogen and hydrogen bonds have been investigated including a situation where halogen bonding can be favoured over hydrogen bonding. Small-molecule analogues of orthogonal halogen and hydrogen bonding observed in biological systems have also been produced. The similarity between the two interactions has been highlighted by the fact that the Steiner-Limbach equation can model the bonding in both cases.

New halogen-bonded liquid crystals between dihalogens and alkoxy stilbazoles and alkoxyphenylpyridines have been synthesised and the complexes between elemental iodine and alkoxy stilbazoles unexpectedly showed SmC phases with high stability. Attempts to synthesise equivalent liquid crystals with elemental bromine were unsuccessful, an electrophilic bromination reaction followed by elimination of HBr taking place instead.

In order to understand this reaction further, the intermediates of the electrophilic bromination reaction for different substituted stilbenes was investigated computationally and the results showed that a carbocation intermediate is favoured if an electron-donating substituent is present. In contrast, stilbenes with two electron-withdrawing substituents favoured symmetric bromonium ion intermediates. Such halonium ion intermediates feature a halogen atom that carries a positive charge, which can interact with Lewis bases in a novel category of halogen bonding, which has properties similar to halogen bonding with traditional halogen-bond donors.

Table of Contents

Abstract.....	1
Table of Contents.....	2
List of Figures.....	9
List of Tables.....	29
List of Accompanying Material.....	35
Acknowledgements.....	36
Declaration.....	38
1 Introduction.....	39
1.1 The Halogen Bond.....	39
1.1.1 The σ -hole.....	48
1.1.2 Other σ -hole Interactions.....	50
1.2 Comparison between Hydrogen and Halogen Bonding.....	53
1.2.1 The Hydrogen Bond.....	53
1.3 Competition between Hydrogen and Halogen Bonding.....	56
1.4 Experimental Techniques for Investigating Halogen Bonding.....	58
1.4.1 Single-Crystal X-Ray Diffraction.....	58
1.4.2 NMR Spectroscopy.....	63
1.4.3 Solid-State NMR Spectroscopy.....	66
1.5 Quantum Chemical Methods for Studying Halogen Bonding.....	67
1.5.1 <i>Ab Initio</i> Methods.....	67
1.5.2 Hartree-Fock (HF) Method.....	69
1.5.3 Møller-Plesset (MP) Perturbation Theory.....	71
1.5.4 Coupled-Cluster Approximation.....	73
1.5.5 Basis Sets and Effective Core Potentials (ECPs).....	74
1.5.6 Density Functional Theory (DFT).....	77
1.5.7 Counterpoise (CP) Correction.....	80
1.5.8 Localised Molecular Orbitals (LMOs).....	82
1.5.9 Natural Bond Orbital (NBO) Analysis.....	85
1.5.10 Application of Quantum Chemical Methods to Halogen Bonding.....	88

1.6	Applications of Halogen Bonding	92
1.6.1	Crystal Engineering.....	92
1.6.2	Anion Recognition	97
1.6.3	Catenane and Rotaxane Synthesis.....	102
1.7	Halogen-Bonded Liquid Crystals	106
1.7.1	Introduction to Liquid Crystals	106
1.7.2	Hydrogen-Bonded Liquid Crystals	110
1.7.3	Halogen-Bonded Liquid Crystals.....	117
1.8	Conclusions	119
2	The Halogen Bond Interaction Between Fluorohalides and Isocyanides	121
2.1	Introduction	121
2.1.1	Derivation of the Steiner-Limbach Equation	121
2.1.2	Application of the Steiner-Limbach Equation to Hydrogen-Bonded Complexes	124
2.1.3	Application of the Steiner-Limbach Equation to Halogen-Bonded Complexes	125
2.1.4	A Modified Steiner-Limbach Equation.....	129
2.2	Aim.....	129
2.3	Computational Method.....	130
2.3.1	Geometry Optimisation and Binding Energies	130
2.3.2	Curve-Fitting Procedure.....	131
2.4	Results	132
2.4.1	Geometry Optimisation.....	132
2.4.2	Curve Fitting	138
2.4.3	Hydrogen-Bonded Complexes	148
2.4.4	Curve-Fitting for Hydrogen-Bonded Complexes	166
2.5	Conclusions	178
3	The Attractive, Non-covalent Interactions between Halomethanes and Rare Gases	180
3.1	Introduction	180
3.1.1	Hydrogen Bonding to Rare Gases.....	182
3.1.2	Complexes between Dihalogens and Rare Gases	183

3.1.3	The Dispersion Interaction.....	185
3.1.4	Dispersion Corrected Density Functional Theory	186
3.1.5	Databases for Testing Functional Performance	191
3.1.6	The Performances of Dispersion Corrected Density Functionals.....	192
3.2	Aim.....	194
3.3	Method	195
3.4	Results	197
3.4.1	Geometry Optimisation.....	197
3.4.2	Comparison with Experiment	197
3.4.3	The Performance of <i>Ab Initio</i> and DFT Methods	201
3.4.4	The Significance of the Density of the Integration Grid.....	204
3.4.5	The Effect of Chemical Composition on the Halogen···Rare Gas Interaction.....	212
3.4.6	Localised Molecular Orbitals of Halogen Bond Donor···Rare Gas Complexes	217
3.4.7	Calculations of ^{129}Xe NMR Chemical Shifts.....	223
3.5	Conclusions	234
4	Liquid-Crystalline, Halogen-Bonded Complexes between 4-Alkoxystilbazoles, Alkoxyphenylpyridines and Dihalogens, and the Electrophilic Bromination of Stilbazoles.....	237
4.1	Introduction	237
4.1.1	Halogen-Bonded Liquid Crystals	237
4.1.2	Halogen-Bonded Complexes with Dihalogens	243
4.2	Aim.....	247
4.3	Results	248
4.3.1	Complexes between Iodine and Alkoxystilbazoles	248
4.3.2	Electrophilic Bromination of Alkoxystilbazoles	254
4.3.3	Electrophilic Bromination of Alkylstilbazoles	260
4.3.4	Complexes between Alkoxyphenylpyridines and Dihalogens	264
4.3.5	Liquid Crystal Properties of Complexes with Alkoxyphenylpyridines 278	

4.3.6	Quantum Chemical Calculations of Halogen-Bonded Complexes between Dihalogens and Alkoxyphenylpyridines	280
4.4	Conclusions	285
4.5	Experimental	286
4.5.1	Crystallographic Parameters	286
4.5.2	Materials.....	289
4.5.3	NMR Spectroscopy	290
4.5.4	Single Crystal X-ray Diffraction.....	290
4.5.5	Low-Angle X-ray Diffraction	290
4.5.6	Polarising Optical Microscopy.....	291
4.5.7	Preparation of Iodine Complexes of Alkoxy stilbazoles (1).....	291
4.5.8	Preparation of 2	292
4.5.9	General Procedure for the Preparation of 4-Butyliodobenzene	293
4.5.10	General Procedure for the Preparation of 4-Butylstilbazole.....	294
4.5.11	Preparation of the 1,2-Dibromo Adduct of Butylstilbazole (4)	295
4.5.12	Preparation of 1,2-Dibromo Adduct of Hexyloxystilbazole.....	295
4.5.13	Preparation of Ethanolysis Product of Dodecyloxystilbazole (3).....	296
4.5.14	General Procedure for the Preparation of 4-Alkoxybromobenzene...297	
4.5.15	General Procedure for the Synthesis of 4-Alkoxyphenylpyridines (5-n) 298	
4.5.16	Synthesis of Halogen-Bonded Complexes between 4-Dodecyloxyphenylpyridine and Bromine (6-12).....	300
4.5.17	Synthesis of Halogen-Bonded Complexes between 4-Alkoxyphenylpyridines and Iodine (7-n).....	301
4.5.18	Synthesis of Halogen-Bonded Complexes between Alkoxyphenylpyridines and Iodine Monochloride (8-n)	302
4.5.19	Synthesis of halogen bonded complexes between 4-alkoxyphenylpyridines and iodine monobromide (9-n).....	303
4.5.20	Computational Method	305
5	Electrophilic Bromination of Substituted Stilbenes and Stilbazoles: A Quantum-Chemical Investigation.....	307
5.1	Introduction	307
5.1.1	The Electrophilic Bromination Reaction	308

5.2	Aim.....	311
5.3	Method	311
5.4	Results and Discussion.....	313
5.4.1	Structures of the Intermediates	313
5.4.2	Calculations using DFT	316
5.4.3	Solvent Effects	321
5.4.4	Comparison of Intermediates	322
5.4.5	Correlations with Hammett and Taft Parameters.....	324
5.4.6	Localised Molecular Orbitals.....	328
5.4.7	Structural Correlations and NBO Analyses	330
5.4.8	The Structure of Charge-Transfer Complexes	338
5.5	Conclusions	342
6	Halonium Ions as Halogen Bond Donors	345
6.1	Introduction	345
6.1.1	Stable Halonium Ions of Adamantylidene Adamantane [AdAdX] ⁺ ..	345
6.1.2	Halonium Ions of Ethenes.....	349
6.1.3	Dialkylhalonium Ions.....	350
6.1.4	Diaryliodonium Salts	352
6.1.5	Bis(pyridine)halonium Cations.....	359
6.2	Aim.....	362
6.3	Computational Method.....	364
6.4	Computational Results	368
6.4.1	Geometry Optimisation of Halonium Ion Monomers.....	368
6.4.2	Geometry Optimisation of Complexes with Ammonia	373
6.4.3	Localised Molecular Orbitals.....	377
6.4.4	Complexes with Pyridine	380
6.4.5	NBO Analysis	381
6.4.6	Application of the Steiner-Limbach Equation	392
6.4.7	Directionality of Interactions with Halonium Ions	395
6.4.8	Complexes of Adamantylidene Adamantane Halonium Ions.....	399
6.4.9	Complexes with the Diphenyliodonium Ion	402

6.5	Experimental Results.....	406
6.6	Conclusions	410
6.7	Experimental	413
6.7.1	Crystallographic Parameters	413
6.7.2	Synthesis of Diphenyliodonium Triflate.....	414
7	Competition and Cooperation between Halogen and Hydrogen Bonding	415
7.1	Introduction	415
7.1.1	Halogen and Hydrogen Bonding in Supramolecular Architectures...415	
7.2	Aim.....	421
7.3	Results	422
7.3.1	4-Iodotetrafluorobenzoic Acid (1)	422
7.3.2	Co-crystal between 4-Iodotetrafluorobenzoic Acid and 1,4-Dithiane (2) 423	
7.3.3	Salt/Co-Crystal between 4-Iodotetrafluorobenzoic Acid and Thiomorpholine (3).....	425
7.3.4	1,4-Dithiane-S,S'-dioxide (4)	427
7.3.5	Co-crystal between 4-Bromotetrafluorophenol and 1,4-Dithiane-S,S'- dioxide (5).....	427
7.3.6	Co-crystal between 4-Iodotetrafluorophenol and Thiophene-S-oxide (6)	428
7.3.7	Cooperation between Halogen and Hydrogen Bonding.....	429
7.4	Orthogonal and Non-Orthogonal Halogen and Hydrogen Bonding	434
7.5	Salts of Pentafluorophenol	436
7.5.1	Piperidinium Pentafluorophenate (8)	436
7.5.2	4-(N,N-Dimethylamino)pyridinium Pentafluorophenate • Pentafluorophenol (9) and 4-(Pyrrolidino)pyridinium Pentafluorophenate • Pentafluorophenol (10)	437
7.6	Salts of 4-Iodo-2-3-5-6-tetrafluorophenol.....	438
7.6.1	Piperazine-1,4-dium 4-Iodotetrafluorophenate (11)	438
7.6.2	Imidazolium Iodotetrafluorophenate (12)	439
7.6.3	Dibutylammonium Iodotetrafluorophenate (13)	442
7.6.4	Thiomorpholinium Iodotetrafluorophenate (14)	443

7.6.5	Pyrrolidinium Iodotetrafluorophenate (15).....	444
7.6.6	Morpholinium Iodotetrafluorophenate (16).....	447
7.6.7	4-(N,N-Dimethylamino)pyridinium Iodotetrafluorophenate (17) and 4-(Pyrrolidino)pyridinium Iodotetrafluorophenate (18)	449
7.7	Salts of 4-Bromo-2,3,5,6-tetrafluorophenol	452
7.7.1	Pyrrolidinium Bromotetrafluorophenate (19).....	452
7.7.2	Thiomorpholinium Bromotetrafluorophenate (20).....	453
7.7.3	Piperazine-1,4-dium 4-Bromotetrafluorophenate (21)	455
7.8	Co-crystals of 1,4-Diiidotetrafluorobenzene with Amides	456
7.8.1	Acetamide : 1,4-Diiidotetrafluorobenzene (22)	456
7.8.2	N-Methylbenzamide : 1,4-Diiidotetrafluorobenzene (23)	458
7.9	Discussion	459
7.9.1	Bonding in the Phenate Anions.....	459
7.9.2	Halogen Bonding to Carbonyl Oxygen Atoms.....	467
7.9.3	Bonding Motifs in the Structures and Comparison to Halogen Bonding in Biology	470
7.10	Conclusion.....	477
7.11	Experimental	478
7.11.1	Crystallographic Tables	478
7.11.2	Co-crystal Formation	484
7.11.3	Computational Procedure.....	485
8	Conclusions	486
9	Abbreviations.....	491
10	References	494

List of Figures

Figure 1-1: The molecular structure of the complex between 1,4-dioxane and bromine.	39
Figure 1-2: The molecular structure of the complex between acetone and bromine.	42
Figure 1-3: The relationship between the effective radii of the R–I and I··Y bonds in the structures of trihalide-anions and the charge-transfer complexes investigated by Hassel and co-workers.	43
Figure 1-4: The molecular structures of a) the complex between 1,4-dioxane and sulfuric acid and b) the complex between 1,4-dithiane and iodoform.	43
Figure 1-5: The molecular structure of the complex between bromoform and hexamethylenetetramine.	44
Figure 1-6: The molecular structure of the complex between carbon tetrabromide and <i>p</i> -xylene.	45
Figure 1-7: The molecular structures of a) 2,5-dichloroaniline and b) pentachlorophenol.	45
Figure 1-8: The number of publications in the research topic 'halogen bonding' over the past 15 years.	47
Figure 1-9: Electrostatic potential surfaces calculated at the 0.001 electrons Bohr ⁻³ electronic density isosurface for a) CF ₄ , b) CF ₃ Cl, c) CF ₃ Br and d) CF ₃ I.	49
Figure 1-10: Complexes of fluorinated halobenzenes with acetone investigated to show the substituent effect on the halogen bond.	50
Figure 1-11: a) As··N interactions in the molecular structure of cyanodimethylarsine, b) Se··N interactions in phenylselenyl cyanide, c) P··N interactions in diethyl (8-dimethylamino-1-naphthyl)phosphonate and d) S··N interactions in (Z)-5-(2-pyridylmethylene)-2-thioxoimidazolinone.	51
Figure 1-12: The molecular structure of a fluoride ion encapsulated within an octasilsesquioxane cage.	52
Figure 1-13: The molecular structure of fenobam.	53

Figure 1-14: The electrostatic potentials of a) CF ₃ Br and b) CF ₃ H.....	54
Figure 1-15: The experimentally determined geometries of complexes of formaldehyde with HCl and ClF showing the deviations from linearity, θ	55
Figure 1-16: A 2:1 liquid crystalline complex between stilbazole and 4-iodotetrafluorophenol.....	56
Figure 1-17: The molecular structure of the halogen-bonded complex between 4-iodo-2,3,5,6-tetrafluorophenol and methoxystilbazole.....	56
Figure 1-18: a) 1,2-Bis(4-pyridyl)ethane b) 1,4-diodotetrafluorobenzene and c) hydroquinone.	57
Figure 1-19: a) 1-Methyl-2-pyridin-4-yl-benzimidazole and b) the molecular structure of its complex with 4-iodo-2,3,5,6-tetrafluorooxime.....	58
Figure 1-20: Molecular structures of complexes of DMAP with a) 4-fluoriodobenzene, b) 2,3,4-trifluoriodobenzene and c) pentafluoriodobenzene..	62
Figure 1-21: Molecular structure of the complex of 1-iodoethynyl-4-iodobenzene with 4-phenylpyridine.....	63
Figure 1-22: The halogen-bonded complex between quinuclidine and 1-iodoperfluoropropane investigated by NMR spectroscopy.	64
Figure 1-23: The halogen-bonded complex between a nickel fluoride complex and iodopentafluorobenzene.....	64
Figure 1-24: The formation of the halogen-bonded complex between [Cp ₂ TaH ₃] and iodopentafluorobenzene.....	65
Figure 1-25: The iodoperfluoroarene halogen-bond donors and tributylphosphine oxide halogen-bond acceptor used to investigate substituent effects on complex formation.....	66
Figure 1-26: Molecular structures of complexes a) of 1,4-diodotetrafluorobenzene with tetramethylammonium selenocyanate, b) of decamethonium diiodide with 1,4-diodobenzene and c) 2-bromoanilinium chloride.	67
Figure 1-27: a) The LUMO and b) the LMO corresponding to the lone pair of electrons on nitrogen of the halogen-bonded complex between 1,4-diodotetrafluoriodobenzene.....	84

Figure 1-28: Donor-acceptor interaction between σ and σ^* NBOs.....	86
Figure 1-29: The complex between BrCN and borazine.	88
Figure 1-30: a) Type I and b) type II interaction between two halogen atoms.....	93
Figure 1-31: Halogen-bonded complexes between perfluorocarbon and hydrocarbon compounds. a) Complex between 1,2-diiodotetrafluoroethane and N,N,N',N'-tetramethylethylenediamine and b) complex between 1,2-diiodotetrafluoroethane and K2.2.2.....	93
Figure 1-32: Halogen-bonded complexes of a) 1,4-dibromotetrafluorobenzene and b) 1,3-dibromotetrafluorobenzene with 4,4'-bipyridine.....	94
Figure 1-33: 4,4'-Diiodo-4'',4''-dinitrotetraphnylmethane and the adamantoid structure formed in the crystal structure.....	95
Figure 1-34: The two-dimensional architectures in the halogen-bonded complexes of 1,4-diiodotetrafluorobenzene with a) tetraphenylphosphonium bromide and b) tetraphenylphosphonium iodide.....	96
Figure 1-35: Molecular structure of 1,6-diiodoperfluorohexane with bis(trimethylammonium)dodecane.	97
Figure 1-36: a) The structure of a tridentate receptor and b) the molecular structure of the receptor bound to NaI.	98
Figure 1-37: A tridentate anion receptor based on 2-iodoperfluorobenzoic acid.	98
Figure 1-38: A urea-based receptor with both hydrogen- and halogen-bond donors.	99
Figure 1-39: a) The structure of triazole functionalised zinc(II) porphyrins and b) the molecular structure of an iodotriazole functionalised zinc(II) porphyrin.	100
Figure 1-40: Molecular structures of complexes a) of an <i>anti</i> -bischloroimidazoliophane macrocycle and b) an <i>anti</i> -bisiodoimidazoliophane macrocycle with bromide anions.	101
Figure 1-41: a) The molecular structure and b) space-filling diagram of a <i>syn</i> -bis-bromoimidazoliophane receptor with a bromide anion.	101
Figure 1-42: The pseudorotaxane formed by chloride ion templating of a bromine functionalised imidazolium thread and an isophthalamide macrocycle.	102

Figure 1-43: The molecular structure of the rotaxane formed between a 5-iodo-1,2,3-triazolium thread and an isophthalamide macrocycle.	103
Figure 1-44: Molecular structures of 1,3-dihexyl-2-iodo-4,5-dimethylimidazolium a) chloride and b) iodide and of 4-(4-(t-butyl)phenyl)-3-methyl-1-octyl-5-iodo-1,2,3-triazolium c) chloride and b) iodide.....	104
Figure 1-45: A catenane formed between two bromine functionalised imidazolium macrocycles formed by halogen bonding to a bromide anion.	105
Figure 1-46: Catenane formed by a halogen bond between an iodopyridinium and a pyridine group on two macrocycles.	105
Figure 1-47: Examples of calamitic and discotic liquid crystals.	107
Figure 1-48: Representation of the arrangement of calamitic mesogens of a) nematic (N), b) smectic A (SmA) and c) smectic C (SmC) phases.....	108
Figure 1-49: Schematic diagram of a polarising optical microscope.	109
Figure 1-50: Optical micrographs of a) a N phase and b) a SmA phase.	109
Figure 1-51: Origin of the focal-conic texture observed in SmA phases.	110
Figure 1-52: Hydrogen-bonded liquid crystal between 4-butoxybenzoic acid and <i>trans</i> -4-[(4-ethoxybenzoyl)oxy]-4'-stilbazole.....	111
Figure 1-53: The hydrogen-bonded dimer of 4-butyloxybenzoic acid.....	111
Figure 1-54: Comparison of hydrogen-bonded complex with covalent ester linkage.	112
Figure 1-55: a) 2:1 Hydrogen-bonded complex between 4-methoxybenzoic acid and 4,4'-bipyridine and b) its covalently bonded analogue, 4,4'-biphenyldi(4"-methylbenzoate).	113
Figure 1-56: a) Example of a three-ring, tricatener liquid crystal and b) hydrogen-bonded four-ring, tricatener liquid crystal.	114
Figure 1-57: a) Oxadiazole-based bent-core mesogens and b) their hydrogen-bonded analogues.....	114
Figure 1-58: a) Molecular structure of the hydrogen-bonded complex between octyloxystilbazole and 4-cyanophenol. b) Schematic of the structure of the complexes of alkoxystilbazoles with 3-cyanophenol.	115

Figure 1-59: The hydrogen-bonded liquid crystals of alkoxytilbazoles with nitrophenols.....	116
Figure 1-60: Molecular structure of the complex between octyloxystilbazole and 2,3,5-trifluorophenol.	117
Figure 1-61: The halogen-bonded complex between iodopentafluorobenzene and alkoxytilbazoles.	117
Figure 1-62: The 2:1 halogen-bonded complex between alkoxytilbazoles and 1,4-diiidotetrafluorobenzene.....	118
Figure 1-63: Comparison between a) the halogen bond between an iodobenzene and a pyridine halogen-bond acceptor and b) the covalent bond between two phenyl rings.....	118
Figure 1-64: Comparison between a) the halogen-bonded complex between octyloxystilbazole and 1-[2-(4-octyloxyphenyl)vinyl]-2,3,5,6-tetrafluoro-4-iodobenzene and b) its covalently bonded analogue.....	119
Figure 2-1: Example of a Steiner-Limbach plot for hydrogen-bonded complexes A–H···B.	123
Figure 2-2: 2-Fluorobenzamide and related compounds with intramolecular N–H···F hydrogen bonds modelled using the Steiner-Limbach equation.	125
Figure 2-3: Schematic representation of a) pyrrolo[2,3-b]pyrrole dimers and b) 1,8a-dihydro-1,8-naphthridine dimers. X = H, F, Cl, CH ₃ , CN, CCH, CF ₃ , CCl ₃ , C(CH ₃) ₃ , Si(CH ₃) ₃ , SiF ₃ , SiCl ₃ , NH ₂ , OH or <i>t</i> -Bu.	125
Figure 2-4: The halogen-bond donors and isocyanides acting as halogen-bond acceptors in this investigation.	130
Figure 2-5: Graphs showing the fits of the original Steiner-Limbach equation in its form in Equation 2-1 for complexes with a) and b) FCl, c) and d) FBr and e) and f) FI as the halogen-bond donor.....	142
Figure 2-6: Graphs showing the fit of the original and modified Steiner-Limbach equations for complexes with a) and b) FCl, c) and d) FBr and e) and f) FI as the halogen-bond donor calculated using CP correction.	145
Figure 2-7: Graphs showing the fit of the original and modified Steiner-Limbach equations for complexes with a) and b) FCl, c) and d) FBr and e) and f) FI as the halogen-bond donor calculated without CP correction.	146

Figure 2-8: The hydrogen halides and nitrogen bases in the hydrogen-bonded complexes investigated in this study.....	149
Figure 2-9: Graphs showing the fits of the original Steiner-Limbach equation in its form in Equation 2-1 for complexes with a) and b) HF and c) and d) HCl as the hydrogen-bond donor.....	170
Figure 2-10: Graphs showing the fit of the original and modified Steiner-Limbach equations for complexes with a) and b) HF, c) and d) HCl and e) and f) HBr as the hydrogen-bond donor calculated using CP correction.....	174
Figure 2-11: Graphs showing the fit of the original and modified Steiner-Limbach equations for complexes with a) and b) HF, c) and d) HCl and e) and f) HBr as the hydrogen-bond donor calculated without CP correction.	176
Figure 3-1: The molecular structures of a) cyanuric chloride and b) the formimine-formidoyl chloride model.	180
Figure 3-2: The crystal structure of 2-bromoanilinium chloride	181
Figure 3-3: a) The iodine...xenon separations given as percentages of the sum of the van der Waals radii of iodine and xenon and b) the binding energies of complex 1 , CF ₃ I...Xe, calculated using different methods both with and without CP correction.	202
Figure 3-4: The potential energy curve for complex 3 , CF ₃ Cl...Xe, calculated using the B3LYP-D3 method using the 'Fine' integration grid.	204
Figure 3-5: The potential energy curve of complex 3 , CF ₃ Cl...Xe, calculated at the M06-L-D3 level of theory using the 'Fine' integration grid.....	205
Figure 3-6: The potential energy curve for complex 3 , CF ₃ Cl...Xe, calculated using at the M06-L-D3 level of theory using the 'Fine' and 'UltraFine' pruned integration grids.....	207
Figure 3-7: The potential energy curve for complex 3 , CF ₃ Cl...Xe, calculated at the M06-L-D3 functional using the 'UltraFine' pruned integration grid and an unpruned (99,974) integration grid.	208
Figure 3-8: The potential energy curves for complex 3 , CF ₃ Cl...Xe, calculated at the M06-L-D3 level of theory using the 'UltraFine' pruned integration grid and the (110, 590), (150, 590) and (200, 590) unpruned integration grids.....	209

Figure 3-9: The potential energy curve for complex 1 , $\text{CF}_3\text{I}\cdots\text{Xe}$, calculated at the M06-D3 level of theory using the 'Fine' and 'UltraFine' pruned integration grids and the (200, 590) and (300, 590) unpruned integration grids.	210
Figure 3-10: The potential energy curves of the halogen bonded complex 8 , $\text{CF}_3\text{I}\cdots\text{NH}_3$, calculated at the M06-D3 level of theory using the 'Fine' and 'UltraFine' pruned integration grids.	211
Figure 3-11: The variation of BSSE with I \cdots N separation in complex 8 , $\text{CF}_3\text{I}\cdots\text{NH}_3$, calculated at the M06-D3 level of theory using the 'Fine' and 'UltraFine' integration grids.....	212
Figure 3-12: The halogen atom \cdots xenon separations as percentages of the sum of the van der Waals radii for complexes 1 – 3 calculated using a) different methods and b) the MP2 level of theory with CP correction.....	213
Figure 3-13: The binding energies of complexes 1 – 3 calculated using a) different methods and b) the MP2 level of theory with CP correction.	213
Figure 3-14: The iodine \cdots rare gas atom separations as percentages of the sum of the van der Waals radii for complexes 1, 4 and 5 calculated using a) different methods and b) the MP2 level of theory with CP correction.	214
Figure 3-15: The binding energies of complexes 1, 4 and 5 calculated using a) different methods and b) the MP2 level of theory with CP correction.	215
Figure 3-16: a) The LMO containing a non-bonding electron pair of xenon, directed toward the iodine atom in complex 1 . b) The three LMOs containing the valence lone pairs of electrons on iodine.	217
Figure 3-17: a) The LMO containing a nonbonding electron pair of xenon, directed toward the iodine atom in complex 7 . b) Combined plot of the three LMOs containing valence lone pairs on iodine.	218
Figure 3-18: Combined plots of the LMOs containing valence pairs on the halogen of a) complex 1 , $\text{CF}_3\text{I}\cdots\text{Xe}$, b) complex 2 , $\text{CF}_3\text{Br}\cdots\text{Xe}$, c) complex 3 , $\text{CF}_3\text{Cl}\cdots\text{Xe}$, and d) complex 6 , $\text{CH}_3\text{I}\cdots\text{Xe}$	219
Figure 3-19: The LMO containing a nonbonding electron pair on the rare gas atom of a) complex 1 , $\text{CF}_3\text{I}\cdots\text{Xe}$, b) complex 4 , $\text{CF}_3\text{I}\cdots\text{Kr}$ and c) complex 5 , $\text{CF}_3\text{I}\cdots\text{Ar}$..	220
Figure 3-20: Molecular structure of cryptophane-A	223

Figure 3-21: The crystal structure of xenon encapsulated in β -hydroquinone. a) Top view. b) side view.	224
Figure 3-22: The ^{129}Xe NMR chemical shifts of xenon dissolved in a series of solvents related to the function of the solvent's refractive index, n , given in Equation 3-12.	225
Figure 3-23: The ^{129}Xe chemical shifts of xenon dissolved in a series of n -alkane solvents related to the function of the solvents refractive index given in Equation 3-12.	226
Figure 3-24: The ^{129}Xe NMR chemical shifts of xenon dissolved in a series of solvents and acids related to the function of the refractive index, n , given in Equation 3-12.	227
Figure 3-25: The change in the isotropic shielding tensor of the xenon in complex 7 , $\text{Xe}\cdots\text{ICl}$, compared to free xenon gas as a function of the $\text{I}\cdots\text{Xe}$ separation calculated at the MP2/aug-cc-pVTZ level of theory.	231
Figure 3-26: The variation of the isotropic shielding tensor of xenon in complexes 1 – 3 compared to free xenon gas with $\text{X}\cdots\text{Xe}$ separation calculated at the MP2/aug-cc-pVTZ level of theory.	232
Figure 4-1: Liquid-crystalline, hydrogen-bonded complexes of alkoxytilbazoles with a) 4-nitrophenol, b) 3-nitrophenol, c) 2,4-dinitrophenol and d) 3-cyanophenol.	237
Figure 4-2: Liquid-crystalline, halogen-bonded complexes between alkoxytilbazoles and iodopentafluorobenzene.	238
Figure 4-3: Liquid-crystalline, halogen-bonded complexes between 4-alkoxytilbazoles and α,ω -diiodoperfluoroalkanes.	238
Figure 4-4: Halogen-bonded complexes between alkoxytilbazoles and a) 1,4-dihalotetrafluoriodobenzene ($\text{X} = \text{I}$ or Br) and b) 1,3-diiodotetrafluorobenzene. .	240
Figure 4-5: Halogen-bonded complexes stilbazoles and iodostilbenes with chiral chains.	241
Figure 4-6: Complexes between 4-iodo-2,3,5,6-tetrafluorophenol and alkoxytilbazoles.	241
Figure 4-7: The molecular structure of the 1:1 complex between methoxytilbazole and 4-iodo-2,3,5,6-tetrafluorophenol.	242

Figure 4-8: Selection of halogen-bonded liquid crystals investigated.....	243
Figure 4-9: The molecular structures of the halogen-bonded complexes between a) iodine and 4-picoline and b) bromine and 1,4-dioxane.....	244
Figure 4-10: The molecular structures of a) 4-cyanopyridine and iodine, b) phenazine and iodine, c) 2-(3 <i>H</i>)-(diiodothio)benzoxazole and iodine and d) acridine and iodine, which illustrate the different interaction modes of complexes involving dihalogens.	245
Figure 4-11: The molecular structure of the halogen-bonded complex between a) 4,5-bis(bromomethyl)-1,3-dithiole-2-thione and iodine monochloride and iodine and b) <i>N</i> -methylbenzothiazole-2(3 <i>H</i>)-selone and iodine monobromide.	246
Figure 4-12: Halogen-bonded complexes between iodine and alkoxy stilbazoles..	248
Figure 4-13: The molecular structure of the halogen-bonded complex between iodine and octyloxystilbazole, 1-8	248
Figure 4-14: The 2:2 complex between iodine and octyloxystilbazole (1-8).	249
Figure 4-15: The packing of the structure of the complexes between iodine and octyloxystilbazole (1-8) through the <i>bc</i> -plane.	250
Figure 4-16: a) Optical texture of the SmC phase observed for 1-12 at 123 °C. b) Optical texture of the SmA phase observed for 1-10 at 120 °C.....	251
Figure 4-17: DSC curve of 1-10	252
Figure 4-18: X-ray diffraction patterns in the SmC phase for a) 1-10 at 110 °C and b) 1-12 at 120 °C.....	253
Figure 4-19: Molecular structure of 2	254
Figure 4-20: The Br...O and C–H...Br [−] interactions in the molecular structure of 2	255
Figure 4-21: Stacking of the stilbazolium bromide molecules along the <i>a</i> -axis.....	256
Figure 4-22: The aromatic region of the ¹ H NMR spectrum of 2	256
Figure 4-23: The aromatic region of the ¹ H NMR spectrum of the <i>trans</i> (X) and <i>cis</i> (O) isomers of 2	257

Figure 4-24: a) The NOE spectra observed upon irradiating the singlet of the minor product. b) The NOEs observed upon irradiating the singlet of the major product. c) The ¹ H NMR spectrum of the mixture of <i>trans</i> - 2 and <i>cis</i> - 2	258
Figure 4-25: Proposed mechanism for the formation of 2	259
Figure 4-26: Ethanolysis product of alkoxy stilbazoles (3).	259
Figure 4-27: The ¹ H NMR spectrum of the ethanolysis product of alkoxy stilbazoles (3).	260
Figure 4-28: Synthesis of alkylstilbazoles <i>via</i> a Sandmeyer reaction followed by a Heck cross-coupling reaction.	261
Figure 4-29: The molecular structure of 4	261
Figure 4-30: Ellipsoidal model of 4 showing the disorder in the carbon positions in the 41.3% occupancy model.	262
Figure 4-31: Ellipsoidal model of 4 modelled as a bromonium ion with an unbound bromide anion.	262
Figure 4-32: Herringbone packing in the crystal structure of 4	263
Figure 4-33: Section of the ¹ H NMR spectrum of 4	264
Figure 4-34: Structure of alkoxyphenylpyridines, 5-n	265
Figure 4-35: Synthesis of alkoxyphenylpyridines.	265
Figure 4-36: The interdigitated structures of a) 4'-alkyl-4-cyanobiphenyls and b) <i>N</i> -oxides of 4-(4'-alkoxyphenyl)pyridines.	265
Figure 4-37: The complexes of alkoxyphenylpyridines with dihalogens investigated.	266
Figure 4-38: The molecular structure of hexyloxyphenylpyridinium bromide.	266
Figure 4-39: Propagation of the structure of hexyloxyphenylpyridinium bromide along the <i>b</i> -axis.	267
Figure 4-40: Stacking of the hexyloxyphenylpyridinium bromide.	267
Figure 4-41: The aromatic region of the ¹ H NMR spectrum of a) dodecyloxyphenylpyridine and b) its complex with bromine (6-12).	268

Figure 4-42: The molecular structure of the halogen bonded complex between iodine and butoxyphenylpyridine (7-4).....	269
Figure 4-43: The 2:2 complex between molecular iodine and butoxyphenylpyridine (7-4).....	270
Figure 4-44: The electrostatic potential of the complex between pyridine and iodine mapped onto the 0.03 (e/bohr ³) ^{1/2} electronic density isosurface.....	270
Figure 4-45: The propagation of the structure between iodine and butoxyphenylpyridine (7-4) along the <i>c</i> -axis.....	271
Figure 4-46: The stacking in the crystal structure of the complex between iodine and butoxyphenylpyridine (7-4).	272
Figure 4-47: Molecular structure of the halogen-bonded complex between iodine monochloride and butoxyphenylpyridine (8-4).	273
Figure 4-48: The molecular structures of complexes between ICl and a) DMAP and b) trimethylsilyl-trimethylphosphoranimine.	274
Figure 4-49: The interdigitated structure observed for the halogen-bonded complex of ICl with butoxyphenylpyridine (8-4).....	274
Figure 4-50: The stacking in the crystal structure of the complex between ICl and butoxyphenylpyridine (8-4).	275
Figure 4-51: The molecular structure of the halogen bonded complex between iodine monobromide and butoxyphenylpyridine (9-4).	275
Figure 4-52: The molecular structures of complexes between IBr and a) 2,2'-bipyridine and b) tetra-2-pyridyl-pyrazine.....	276
Figure 4-53: The packing of the complex between IBr and butoxyphenylpyridine (9-4) along the <i>a</i> -axis.....	277
Figure 4-54: The propagation of the structure between IBr and butoxyphenylpyridine (9-4) across the <i>bc</i> -plane.....	278
Figure 4-55: Optical micrographs of the textures observed for the halogen-bonded complex between iodine monochloride and dodecyloxyphenylpyridine (8-12) at a) 162 °C and b) 135 °C.....	279
Figure 5-1: Proposed mechanism for the formation of compound 2.	308

Figure 5-2: The substituted stilbenes and stilbazoles studied in this chapter.	311
Figure 5-3: Definition of the angle θ between the Br–C and central C–C bonds used to classify intermediates.....	313
Figure 5-4: The bond distances used to compare DFT functionals to MP2 results.	316
Figure 5-5: The mean absolute errors of key bond distances and angles calculated using different DFT functionals and the 6-31G(d,p) basis set compared to values calculated at the MP2/6-31G(d,p) level of theory.	319
Figure 5-6: Relationship between the angle θ and (a) the Hammett parameter for para-substituted benzene derivatives σ_p , (b) the Taft parameter for resonance σ_R , (c) the Taft parameter for inductive effects σ_I of substituent X_1 for a series of stilbenes in which $X_2 = \text{NO}_2$	325
Figure 5-7: Relationship between the angle θ and (a) the σ_p parameter of substituent X_2 , (b) the Taft parameter for resonance σ_R , (c) the Taft parameter for inductive effects σ_I for substituent X_2 and for a series of stilbenes with $X_1 = \text{OCH}_3$	327
Figure 5-8: Localised molecular orbitals (LMOs) describing the C–Br bonds in selected intermediates of the electrophilic bromination of stilbenes.....	328
Figure 5-9: Correlation between the overall contribution of the s basis functions on the carbon atoms in the C–Br bonds to the LMOs and the angles θ	329
Figure 5-10: Bond length definitions in the intermediates of the electrophilic bromination of substituted stilbenes.	330
Figure 5-11: Relationships between bond lengths defined in Figure 5-10 and the angle θ for the geometries of the intermediates of the electrophilic bromination of stilbenes 1 – 21 optimised at the MP2/6-31G(d,p) level of theory.....	331
Figure 5-12: The resonance form expected to stabilise the classical carbocation intermediates of stilbenes 1 – 15	332
Figure 5-13: Localised Molecular Orbitals describing the lone pairs of electrons on the O atom of stilbene 3 , $X_1 = \text{OCH}_3$, $X_2 = \text{H}$	333
Figure 5-14: Atom numbering used in the natural population analysis (NPA).	335

Figure 5-15: The relationships between (a) the occupancy of the C-Br σ bonding orbital and (b) the occupancy of the C-Br σ^* antibonding orbital and the angle θ for the intermediates of the electrophilic bromination of stilbenes 1 – 21	337
Figure 5-16: The charge-transfer complex of Br ₂ and stilbene 3 (X ₁ = OCH ₃ , X ₂ = H) optimised at the MP2/6-31G(d,p) level of theory.	338
Figure 5-17: The relationship between the C-Br bond distances in the CTCs and the angle θ in the intermediates.	339
Figure 5-18: Relationship between the binding energy of the CTCs and the sum of the Hammett σ_p parameters of the two substituents of stilbenes 1 – 21	342
Figure 6-1: The molecular structures of a) [AdAdBr] ⁺ Br ₃ ⁻ and b) [AdAdBr] ⁺ OTf ⁻ . ..	346
Figure 6-2: The molecular structure of AdAd iodonium triflate showing the I...O interaction with a crystallisation water.	347
Figure 6-3: The molecular structure of [AdAdCl] ⁺ hexachloroantimonate.	348
Figure 6-4: The pre-reactive complexes of the reaction between ethene and Br ₂ <i>via</i> a) sideways and b) perpendicular attack of bromine.	350
Figure 6-5: Different methods for synthesising dimethyl bromonium cations.	350
Figure 6-6: The molecular structure of a) dimethyl- and b) diethyl-chloronium carborane.	351
Figure 6-7: The crystal structures of bis(trimethylsilyl)halonium cations of a) fluorine, b) chlorine, c) bromine and d) iodine cations.	352
Figure 6-8: a) The general structure of diaryliodonium salts. b) The observed pseudo trigonal bipyramid geometry.	353
Figure 6-9: The molecular structure of diphenylbismuth chloride.	354
Figure 6-10: The molecular structure of diphenyliodonium chloride.	355
Figure 6-11: The molecular structure of diphenyliodonium tetrafluoroborate.	355
Figure 6-12: The molecular structure of [bis(<i>p</i> -methoxyphenyl)](diethylaminocarbamate) iodine(III).	356

Figure 6-13: The molecular structure of phenyl(2-(1-(methoxycarbonyl)ethylaminocarbonyl)phenyl)iodonium trifluoromethanesulfonate.	357
Figure 6-14: The molecular structure of a) diphenyliodonium tetrafluoroborate. 1,10-phenanthroline ³⁸⁰ and b) diphenyliodonium tetrafluoroborate.pyridine.....	358
Figure 6-15: The molecular structure of diphenyliodonium tetraphenylborate.....	359
Figure 6-16: The bromine transfer reaction between bis(<i>sym</i> -collidine)bromonium triflate and AdAd.	360
Figure 6-17: The crystal structures of a) bis(<i>sym</i> -collidine)bromonium perchlorate and b) bis(pyridine)bromonium triflate.	360
Figure 6-18: The mean absolute percentage errors in the $r(X\cdots N)$ separations as a percentage of the sum of the van der Waals radii and the binding energies for complexes of 1 – 3 and 9 with NH ₃ calculated using different density functionals and the aug-cc-pVDZ basis set compared to results obtained at the MP2(Full)/aug-cc-pVDZ level of theory.	366
Figure 6-19: The definition of angles a) θ and b) ϕ	367
Figure 6-20: The localised molecular orbitals of halonium ion 18 (formed from Z-CHF=CHF) corresponding to the C–Br σ -bonding orbitals.	373
Figure 6-21: The relationship between the charge of the halogen atom in the halonium ion and the binding energy of the complex with ammonia calculated at the MP2(Full)/aug-cc-pVDZ level of theory.	376
Figure 6-22: The relationship between the binding energy and the sum of the Hammett parameters of the substituents, σ_p , for complexes 2 and 4 – 15	377
Figure 6-23: The localised molecular orbitals (LMO) for complex 2 ·NH ₃ representing the a) 3-centre-2-electron bond of the bromonium ion of ethene and b) the lone pair of electrons on the nitrogen atom of ammonia.	377
Figure 6-24: The LMOs corresponding to the lone pair of electrons on the bromine atom of the bromonium ion in complex 2 ·NH ₃	378
Figure 6-25: The LMOs corresponding to a) the 3-centre-2-electron bond of the bromonium ion of ethene, b) the lone pair of electrons on bromine at $r(\text{Br}-\pi) = 2.30$ Å and c) the 3-centre-2-electron bond in the bromonium ion of ethene at $r(\text{Br}-\pi) = 4.0$ Å.	379

Figure 6-26: The localised molecular orbitals (LMOs) representing the lone pair of electrons on ammonia for a) complex 1 ·NH ₃ and b) complex 3 ·NH ₃	380
Figure 6-27: The localised molecular orbitals representing a) the Br-N σ-bond in complex 2 ·py, b) the lone pair of electrons on N in complex 4 ·py, c) the C-C π-bond of complex 2 ·py and d) the 3-centre-2-electron bond in complex 4 ·py.....	387
Figure 6-28: The variation of the binding energies of complexes of 1 – 10 with ammonia and pyridine with the WBI of the X··N interaction.....	391
Figure 6-29: a) Steiner-Limbach plot for complexes of 2 and 4 – 15 with NH ₃ and pyridine and b) expansion in the region 0.0 < r ₁ – r ₂ < 0.2.....	393
Figure 6-30: Plot showing the fit of the three-parameter Steiner-Limbach relationship in its r ₂ vs. r ₁ form (Equation 2-7) for complexes of 2 and 4 - 15 with NH ₃ and pyridine.....	395
Figure 6-31: 3D plots showing the variation of binding energy of the complexes a) 22 ·NH ₃ b) 1 ·NH ₃ , c) 23 ·NH ₃ d) 2 ·NH ₃ e) 24 ·NH ₃ and f) 3 ·NH ₃ with angle of approach of the ammonia.....	397
Figure 6-32: The LUMOs of halonium ions a) 1 , b) 2 and c) 3	398
Figure 6-33: The LMOs of complex 25 ·NH ₃ corresponding to the 3-centre-2-electron bond on [AdAdBr] ⁺ and the lone pair of electrons on ammonia..	400
Figure 6-34: The M06-2X/aug-cc-pVDZ optimised geometry of the complex between the diphenyliodonium ion and ammonia.	402
Figure 6-35: The M06-2X/aug-cc-pVDZ optimised geometry of the complex between the diphenyliodonium ion and two ammonia molecules.	403
Figure 6-36: The localised molecular orbitals representing the lone pair of electrons on the nitrogen atom of ammonia and the σ bonding orbital of the C–I bond of the diphenyliodonium ion..	404
Figure 6-37: The LUMO of the diphenyliodonium ion represented as an isosurface at orbital values of ± 0.05 (e/bohr ⁻³) ^{1/2}	405
Figure 6-38: The electrostatic surface potential of the diphenyliodonium ion mapped on the 0.01 (e/bohr ⁻³) ^{1/2} electronic density isosurface.	406
Figure 6-39: The molecular structure of the complex between diphenyliodonium triflate and DMAP.....	407

Figure 6-40: The angles about the square-planar iodine centre in the molecular structure of the complex between diphenyliodonium triflate and DMAP.	408
Figure 6-41: The 2-fold screw axis along the <i>b</i> -axis in the crystal structure of the complex between diphenyliodonium triflate and DMAP.	409
Figure 7-1: The molecular structure of the complex between 4-iodopyridine and 4-nitrobenzoic acid.	416
Figure 7-2: The halogen and hydrogen bonding motifs of the complex between a) 1,4-diiodotetrafluorobenzene and isonicotinamide and b) 4-iodotetrafluorobenzoic acid and 4-iodobenzoic acid and 3-(2-amino-4-methylpyrimidin-6-yl)pyridine.	417
Figure 7-3: The halogen and hydrogen bonding motifs of a) 4-iodotetrafluoroiodobenzoate and 2-aminopyrazinium and b) 4-iodotetrafluorobenzoic acid and 2-amino-3,5,-dibromopyrazine.	418
Figure 7-4: The halogen and hydrogen bonding motifs of a) 4-iodo-2,3,5,6-tetrafluorobenzoic acid, b) 4-iodo-2,3,5,6-tetrafluorophenol, c) 4-iodo-2,3,5,6-tetrafluoroalldoximide and d) 4-bromo-2,3,5,6-alldoximide and 4,4'-azobipyridine.	419
Figure 7-5: The halogen and hydrogen bonding motifs of a) 4-iodo-2,3,5,6-tetrafluoroalldoximide, b) 4-iodo-2,3,5,6-tetrafluorobenzoic acid and c) 4-iodo-2,3,5,6-tetrafluorophenol and 3,3'-azobipyridine.	420
Figure 7-6: Co-crystals formed to investigate cooperativity between halogen and hydrogen bonding.	421
Figure 7-7: Molecular structure of the dimer of 4-iodotetrafluorobenzoic acid (a) seen from above and (b) in an end-on view, (c) space-filling representation of the 4-iodotetrafluorobenzoic acid dimer.	422
Figure 7-8: Packing of 1 in the solid state (a) showing the glide plane and (b) showing the shorter (black line) and longer (red line) I...I separations as two glide planes meet.	423
Figure 7-9: Structure of the polymeric unit of 2	424
Figure 7-10: (a) Structure and packing of complex 2 with the direction of the <i>a</i> -axis shown, (b) 2 showing intermolecular interactions between the carboxylate carbon and neighbouring fluorine atoms.	424
Figure 7-11: Structure and packing of co-crystal 2 in the <i>ab</i> -plane.	425

Figure 7-12: The structure of 3 showing (a) the formula unit and (b) propagation of the formula unit. Note that in (b), the distinction between S and N–H in the neutral thiomorpholine is an artefact of the program (Mercury) used to create the figure. .426	
Figure 7-13: Molecular structure of 4427	
Figure 7-14: Polymeric arrangement in 5 showing the linking hydrogen bonds and Br⋯F interactions.428	
Figure 7-15: Molecular structure of 6 showing the two hydrogen bonds to the oxygen of the thiophene oxide. Atom numbering is from the cif file.429	
Figure 7-16: The crystal structures of a) 18[ane]S ₆ • I ₂ and b) 12[ane]S ₄ • I ₂430	
Figure 7-17: (a) Dibromodotetrafluorobenzene • thiomorpholine co-crystal (b) Axial arrangement of the halogen bond in 3 (disorder removed); (c) axial arrangement of the halogen bond in 7 reported by Cinčić <i>et al.</i>433	
Figure 7-18: The co-crystals studied in this chapter.435	
Figure 7-19: (a) Hydrogen-bonded 2 + 2 dimer of salt 8 (hydrogen bonds drawn in black); (b) Packing motif in 8436	
Figure 7-20: Molecular structure of (a) 9 and (b) 10438	
Figure 7-21: (a) View showing the relative disposition of the two fluorinated rings in (a) 9 and (b) 10438	
Figure 7-22: Two views of the polymeric motif of complex 11 : (a) Side view and (b) top view.439	
Figure 7-23: Crystal packing in 11 . The 4-iodotetrafluorophenol rings are antiparallel.439	
Figure 7-24: The basic polymeric repeat unit in 12440	
Figure 7-25: Illustration of the different hydrogen bonding interactions at O1 and O2 in 12440	
Figure 7-26: (a) The extended polymeric motif in 12 and (b) illustration of the short I⋯F interactions.441	
Figure 7-27: Two views of the hydrogen-bonded unit: (a) viewed looking down the 'axis' of the dibutylammonium chains and (b) at an angle to show the N–H⋯O hydrogen bonds.442	

Figure 7-28: Views of the crystal packing in 13 (a) viewed down the <i>a</i> -axis and (b) viewed down the <i>b</i> -axis.....	442
Figure 7-29: The hydrogen-bonded motif in 14	443
Figure 7-30: Polymeric arrangement in 14 viewed down the <i>b</i> -axis and showing the I··S halogen bonds.....	444
Figure 7-31: (a) The hydrogen-bonded dimer in 15 and (b) side view of the dimer showing the I··O halogen bonds.....	444
Figure 7-32: Two views illustrating the directionality of the I··O halogen bond in 15	445
Figure 7-33: Two views of the crystal packing of 15 looking down the <i>a</i> axis: (a) 'boxes' described by the arrangement of the iodotetrafluorophenate anions and (b) showing the interaction with the pyrrolidinium cations.	446
Figure 7-34: Part of the structure of 15 showing iodotetrafluorophenols not involved in halogen bonding.....	447
Figure 7-35: One of the two chains that occupy the vacancies generated by the grid (shown in green) described by interactions of phenate anions <i>via</i> O··I halogen bonding (a) end-on view and (b) side-on view.....	447
Figure 7-36: Two views on the halogen-bonding interactions into the hydrogen-bonded cation-anion dimers in 16 . The two views relate to one another through a 90° rotation.	448
Figure 7-37: Three views of aspects of the crystal packing of 16 . (a) End-on view of a half-full anion box (b) end-on view of a full anion box and (c) half-full, end-on box from the side.	449
Figure 7-38: (a) View of complex 17 showing the O··H hydrogen bond and I··O halogen bond and (b) the same unit viewed from the side showing its planarity....	450
Figure 7-39: 2D packing in 17	451
Figure 7-40: Partial structure of 18 showing both the hydrogen- and halogen-bonding interaction.	451
Figure 7-41: 2D packing in 18	452
Figure 7-42: Arrangement of the hydrogen-bonded dimer of 19	452

Figure 7-43: Crystal packing in 19 .	453
Figure 7-44: Linear, hydrogen-bonded polymeric arrangement in 20 .	454
Figure 7-45: (a) Side-on view of the extended structure showing the Type I Br...Br interactions and (b) Top view showing only the relative positions of the bromotetrafluorophenate anions.	455
Figure 7-46: View of the polymeric structure of 21 (a) from above and (b) from the side.	456
Figure 7-47: Aspects of the structure of 22 : (a) hydrogen-bonded sheet formed by acetamide; (b) linking of the hydrogen-bonded acetamide sheets by halogen bonding to 1,4-diiidotetrafluorobenzene; (c) 'close-up' showing the hydrogen and halogen bonding at the amide oxygen; (d) packing of 1,4-diiidotetrafluorobenzene viewed down the <i>c</i> -axis.	457
Figure 7-48: Structure of 23 showing (a) the linear, hydrogen-bonded motif of the methylbenzamide linked by 1,4-diiidotetrafluorobenzene and (b) detail of the hydrogen and halogen bonding at the amide carbonyl oxygen.	458
Figure 7-49: Crystal packing in 23 (a) viewed down the <i>b</i> -axis and (b) viewed just off the <i>b</i> -axis (halogen bonds indicated).	459
Figure 7-50: (a) The 'fully' delocalised and (b) the 'partially' delocalised bonding motifs found in the various phenate anions.	460
Figure 7-51: MP2(Full)-optimised geometries: C–C and C–O bond lengths (in Å) of a) pentafluorophenol, b) the pentafluorophenate anion, c) 4-chlorotetrafluorophenol, d) the 4-chlorotetrafluorophenate anion, e) 4-bromotetrafluorophenol f) the 4-bromotetrafluorophenate anion, g) 4-iodotetrafluorophenol and g) the 4-iodotetrafluorophenate anion.	461
Figure 7-52: Electrostatic surface potentials for (a) pentafluorophenol, b) the pentafluorophenate anion, c) 4-chlorotetrafluorophenol, d) the 4-chlorotetrafluorophenate anion, e) 4-bromotetrafluorophenol, f) the 4-bromotetrafluorophenate anions, g) 4-iodotetrafluorophenol and h) the 4-iodotetrafluorophenate anion mapped on the respective 0.03 HF total electronic density isosurfaces.	465
Figure 7-53: The electrostatic surface potentials of a) <i>N</i> -methylacetamide and b) formaldehyde mapped on the 0.03 HF/aug-cc-pVDZ total electronic density isosurface.	466

Figure 7-54: Halogen bonded interactions with ketones. The interaction motif found in (a) acetone : I ₂ and (b) 1,4-diiodotetrafluorobenzene with a bis-4-(<i>N,N</i> -dimethylamino)benzophenone.....	468
Figure 7-55: The crystal structure of 3,6-dibromo-2,5-dimethylterephthaldehyde.	469
Figure 7-56: The crystal structure of 2,5-dihexyloxy-4-bromobenzaldehyde. The.....	469
Figure 7-57: The crystal structure of the bromine substituted, Boc- and <i>N,N</i> -dicyclohexylurea-capped γ -amino acid foldamer..	469
Figure 7-58: Molecular structure of molecular iodine enclosed in cucurbit[6]uril	470
Figure 7-59: a) and b) the LMOs corresponding to the lone electron pairs on O and c) the π orbital on the C=O bond..	472
Figure 7-60: Histogram showing the distribution of X \cdots O-R angles in halogen bonds to oxygen atoms in the PDB.....	473
Figure 7-61: Possible arrangements of hydrogen and halogen bonding at amide oxygens showing (a) both in plane and (b) both out of plane with respect the amide link.	474

List of Tables

Table 1-1: The halogen bond separations and R–X bond lengths of selected complexes studied by Hassel and co-workers.....	41
Table 2-1: The F–Cl (r_1), Cl–C (r_2) and F–C ($r_1 + r_2$) separations and $[r(\text{F–Cl})-r(\text{Cl–C})]$, ($r_1 - r_2$) and binding energies of the MP2(Full)/aug-cc-pVTZ optimised geometries of complexes between FCl and isocyanides CNY.	133
Table 2-2: The F–Br (r_1), Br–C (r_2) and F–C ($r_1 + r_2$) separations and $[r(\text{F–Br})-r(\text{Br–C})]$, ($r_1 - r_2$) and binding energies of the MP2(Full)/aug-cc-pVTZ optimised geometries of complexes between FBr and isocyanides CNY.....	135
Table 2-3: The F–I (r_1), I–C (r_2) and F–C ($r_1 + r_2$) separations and $[r(\text{F–I})-r(\text{I–C})]$, ($r_1 - r_2$) and binding energies of the MP2(Full)/aug-cc-pVTZ (aug-cc-pVTZ-PP on I) optimised geometries of complexes between FI and isocyanides CNY..	137
Table 2-4: The evaluated parameters, r_{01} , r_{02} and b of the three-parameter Steiner-Limbach equation (Equation 2-7) and values of the coefficient of determination, R^2 , maximum absolute residual, e_{max} and the average of the absolute residuals, e_{av} for complexes between fluorohalides and isocyanides, CNY..	139
Table 2-5: The evaluated parameters, r_{01} , r_{02} and b of the original Steiner-Limbach equation in the form with $r_1 + r_2$ correlated with $r_1 - r_2$ (Equation 2-1) and values of the coefficient of determination, R^2 , maximum absolute residual, e_{max} and the average of the absolute residuals, e_{av} for complexes between fluorohalides and isocyanides, CNY.....	141
Table 2-6: The evaluated parameters, r_{01} , r_{02} , b_1 and b_2 of the modified Steiner-Limbach equation (Equation 2-10) and values of the coefficient of determination, R^2 , maximum absolute residual, e_{max} and the average of the absolute residuals, e_{av} for complexes between fluorohalides and isocyanides, CNY..	144
Table 2-7: The MP2/aug-cc-pVDZ (aug-cc-pVDZ-PP on I) optimised F–X and X–C bond distances in the isolated monomers FX and XCN.	147
Table 2-8: The values of parameter b calculated using Equation 2-8 and the values of $r(\text{F–X})$ and $r(\text{X–C})$ given in Table 2-7 for the values of r_{01} and r_{02} respectively. The coefficients of determination for the fit of Steiner-Limbach equations using these calculated parameters on the halogen-bonded complexes FX:CNY are also given.....	148

Table 2-9: The F–H (r_1), H–N (r_2) and F–N ($r_1 + r_2$) separations and $[r(\text{F–H})-r(\text{H–N})]$, ($r_1 - r_2$) and binding energies of the MP2(Full)/aug-cc-pVTZ optimised geometries of complexes between FH and a series of nitrogen bases. ...	150
Table 2-10: The N–H bond length in the protonated nitrogen base monomers.	153
Table 2-11: The Cl–H (r_1), H–N (r_2) and Cl–N ($r_1 + r_2$) separations and $[r(\text{Cl–H})-r(\text{H–N})]$, ($r_1 - r_2$) and binding energies of the MP2(Full)/aug-cc-pVTZ optimised geometries of complexes between ClH and a series of nitrogen bases. Values in parentheses correspond to those calculated without CP correction.....	155
Table 2-12: The Br–H (r_1), H–N (r_2) and Br–N ($r_1 + r_2$) separations and $[r(\text{Br–H})-r(\text{H–N})]$, ($r_1 - r_2$) and binding energies of the MP2(Full)/aug-cc-pVTZ optimised geometries of complexes between BrH and a series of nitrogen bases...	159
Table 2-13: The I–H (r_1), H–N (r_2) and I–N ($r_1 + r_2$) separations and $[r(\text{I–H}) - r(\text{H–N})]$, ($r_1 - r_2$) and binding energies of the MP2(Full)/aug-cc-pVTZ optimised geometries of complexes between IH and a series of nitrogen bases.	163
Table 2-14: Comparison of the theoretical and experimental $r(\text{X}\cdots\text{N})$ distances ($r_1 + r_2$) in complexes between hydrogen halides, XH, and ammonia, NH_3	166
Table 2-15: The evaluated parameters, r_{01} , r_{02} and b of the three-parameter Steiner-Limbach equation (Equation 2-7) and values of the coefficient of determination, R^2 , maximum absolute residual, e_{max} and the average of the absolute residuals, e_{av} for complexes between hydrogen halides XH and nitrogen bases.	167
Table 2-16: The evaluated parameters, r_{01} , r_{02} and b of the original Steiner-Limbach equation (Equation 2-1) and values of the coefficient of determination, R^2 , maximum absolute residual, e_{max} and the average of the absolute residuals, e_{av} for complexes between hydrogen halides XH and nitrogen bases..	169
Table 2-17: The evaluated parameters, r_{01} , r_{02} , b_1 and b_2 of the modified Steiner-Limbach equation (Equation 2-10) and values of the coefficient of determination, R^2 , maximum absolute residual, e_{max} and the average of the absolute residuals, e_{av} for complexes between fluorohalides and isocyanides, CNY.	173
Table 3-1: The complexes included in this investigation.	194
Table 3-2: The halogen atom...rare gas separation, $r(\text{X}\cdots\text{Y})$, expressed as a distance and as a percentage of the sum of the van der Waals radii and the binding energies, ΔE of complexes 1 and 2	198

Table 3-3: The I...Xe separations given as a distance and as a percentage of the sum of the van der Waals radii and the binding energies for complex 7 , Xe...ICl, calculated at different levels of theory.	216
Table 3-4: The C–I bond distances of the CF ₃ I monomer and in complex 1 , CF ₃ I...Xe, and the differences between these distances calculated at different levels of theory.	221
Table 3-5: The C–X bond lengths in the monomers and complexes 1 – 6 calculated at the MP2 level of theory	222
Table 3-6: The ¹²⁹ Xe isotropic shielding tensor of free xenon gas and xenon in complex 7 , the shielding tensor along the <i>z</i> -axis of xenon in complex 7 and the difference in shielding tensors	230
Table 3-7: The optimised coefficients of Equation 3-15 for complex 7	232
Table 3-8: The optimised coefficients of Equation 3-15 for complexes 1 – 3	233
Table 4-1: Thermal properties of halogen bonded complexes 1-n	250
Table 4-2: The temperatures of the Cr – SmA transitions in the complexes of iodine monochloride and iodine monobromide with alkoxyphenylpyridines.	280
Table 4-3: The X...N separation, X–X bond length, binding energy and dipole moment, μ , of the optimised geometries of the halogen-bonded complexes between dihalogens and methoxyphenylpyridine.	282
Table 4-4: The N–O bond length and dipole moment of the <i>N</i> -oxide of methoxyphenylpyridine optimised at the M06-2X and MP2 level of theory using the aug-cc-pVDZ basis set.	283
Table 4-5: The occupancies of the lone pair of electrons on nitrogen, σ^* anti-bonding orbital of the dihalogen and the stabilisation energy for the complexes between dihalogens and methoxyphenylpyridine obtained from NBO analysis at the M06-2X/aug-cc-pVDZ level of theory.	284
Table 4-6: Crystallographic parameters of compounds 1 – 9	287
Table 4-7: Yields and elemental analysis of complexes of iodine with alkoxystilbazoles.	292
Table 4-8: Yields and elemental analysis of alkoxyphenylpyridines (5-n).	300

Table 4-9: Yields and elemental analysis for complexes of iodine with alkoxyphenylpyridines (7-n).....	302
Table 4-10: Yields and elemental analysis for complexes of iodine monochloride with 4-alkoxyphenylpyridines (8-n).	303
Table 4-11: Yields and elemental analysis for complexes of iodine monobromide with 4-alkoxyphenylpyridine (9-n).....	305
Table 5-1: Types of intermediates observed for the electrophilic bromination of stilbenes 1 – 21 according to the magnitude of the angle θ measured for MP2/6-31G(d,p) optimised geometries.....	315
Table 5-2: Types of intermediates observed for the electrophilic bromination of stilbazoles 22 and 23 according to the magnitude of θ measured for MP2/6-31G(d,p) optimised geometries.	316
Table 5-3: Comparison of key bond distances (in Å) and angles (in °) from the optimised geometries of selected stilbenes obtained using MP2 and different DFT methods, all within the 6-31G(d,p) basis.	317
Table 5-4: The type of intermediates observed for the electrophilic bromination of stilbenes 1 – 21 grouped according to the magnitude of the angle θ calculated at the M06-2X/6-31G(d,p) level of theory.	320
Table 5-5: Key bond distances and angles from the MP2/6-31G(d,p) optimised geometries of stilbazoles 22 and 23 carried out in the gas phase and in THF using the PCM method.	321
Table 5-6: Selected bond lengths, angles θ , energies E , activation energies ΔE^\ddagger , Gibbs free energies G and Gibbs free energies of activation ΔG^\ddagger for the bromonium ion transition states (C_2 symmetry) and the carbocation intermediates of stilbenes 1 , 7 , and 12 , optimised at the MP2/6-31G(d,p) level of theory.	323
Table 5-7: Type of intermediate observed for the electrophilic bromination of stilbene 24 according to the magnitude of the angle θ measured for the MP2/6-31G(d,p) optimised geometry.	328
Table 5-8: The π occupancies of the bonds in the intermediates of the electrophilic bromination of substituted stilbenes calculated using NBO analysis at the MP2/6-31G(d,p) level of theory.....	334

Table 5-9: The natural charges of selected atoms in the intermediates of the electrophilic bromination of stilbenes 1 – 21 calculated using natural population analysis (NPA).	336
Table 5-10: The Br···C=C separations and binding energies of CTCs between bromine and substituted stilbenes	340
Table 6-1: The variation of the halogen atom and the substituents of the halonium ions.	362
Table 6-2: The C–X bonds and CCX angles in the MP2(Full)/aug-cc-pVDZ optimised geometries of the halonium ions 1 – 19	369
Table 6-3: Charges on the halogen atoms of the halonium ions included in this study calculated using natural population analysis for geometries optimised at the MP2(Full)/aug-cc-pVDZ level of theory.	371
Table 6-4: The $r(\text{X}\cdots\text{N})$ separations and binding energies of halonium ions 1 – 15 with NH_3 optimised at the MP2(Full)/aug-cc-pVDZ level of theory.	374
Table 6-5: The halogen···nitrogen separations and binding energies of complexes $\text{CF}_3\text{X}\cdots\text{NH}_3$	375
Table 6-6: The $r(\text{X}\cdots\text{N})$ separations, distances between the halogen and the centres of the carbon-carbon bonds, $r(\text{X}\cdots\pi)$, and binding energies for MP2(Full)/aug-cc-pVDZ optimised geometries of complexes of 1 – 10 with pyridine.	381
Table 6-7: Occupancies of the NBOs corresponding to the lone pair of electrons on the nitrogen atom of ammonia and the anti-bonding orbitals of the 3-centre Br-C-C orbital and the stabilisation energy ΔE_{ij} of the interaction between these orbitals for complexes of 1 – 13 with NH_3	382
Table 6-8: The X– π separation in the halonium ions 1 – 13 and in complexes with NH_3	384
Table 6-9: The Occupancies of the NBOs corresponding to the C–C π bond and σ^* anti-bonding orbitals of the Br–N bond in the complexes of 14 and 15 with ammonia.	385
Table 6-10: The occupancies of the NBOs corresponding to the lone pair of electrons on the nitrogen of pyridine and the antibond of the 3-centre XCC bond and stabilisation energies of the interaction between these two orbitals for complexes of 3 – 9 with pyridine.	385

Table 6-11: The occupancies of the C–C π NBO, X–N σ^* NBO and stabilisation energies of the interaction between these two orbitals for complexes of 1 , 2 and 10 with pyridine.	386
Table 6-12: The WBIs of the X \cdots N interaction and C–X bonds in complexes of 1 – 15 with NH ₃ and of 1 – 10 with pyridine.	389
Table 6-13: The WBIs of the X \cdots N interaction in complexes CF ₃ X \cdots NH ₃	390
Table 6-14: The halogen \cdots nitrogen/oxygen separations and binding energies of the M06-2X/aug-cc-pVDZ/cc-pVDZ optimised geometries of complexes of 25 and 26 with NH ₃ and pyridine and 26 ·OH ₂	399
Table 6-15: The occupancies of the NBOs corresponding to the lone pair of electrons on the nitrogen of the base and the anti-bond of the 3-centre X–C–C bond and stabilisation energies for complexes of 25 and 26 with ammonia and pyridine and 26 ·OH ₂	401
Table 6-16: The WBIs of the X \cdots N interaction and C–X bonds of complexes of 25 and 26 with NH ₃ and pyridine and 26 ·OH ₂	401
Table 6-17: The occupancies of the NBO corresponding to the lone pair of electrons on nitrogen and the NBO corresponding to the σ^* C–I anti-bonding orbital and the stabilisation energy of the charge transfer for the complexes between the diphenyliodonium ion and ammonia.	404
Table 7-1: p <i>K</i> _{BI2} and p <i>K</i> _{BHX} values of selected bases.	431
Table 7-2: List of short halogen contacts in 2 and 7	433
Table 7-3: Key phenate bond lengths in complexes studied.	462
Table 7-4: The π -occupancies of the C–C bonds and C–O bond in the phenols and phenate (NBO results).	464
Table 7-5: Crystallographic Properties for the salts and co-crystals studied.	479
Table 7-6: Solvents and Anti-solvents used in the co-crystallisations.	484

List of Accompanying Material

Cartesian coordinates for all optimised geometries and crystallographic information framework (cif) files accompany this thesis on a CD-ROM.

Acknowledgements

I would like to thank my supervisors, Duncan and Peter, for all of their help during my PhD. Your enthusiasm for the research has certainly helped motivate me throughout the project. Thank you for your time and patience and for helping me to develop my research skills.

I would also like to thank the PBK and DWB research groups, including the academics that have visited during my PhD, for the help you have given me and for creating a pleasant working environment. I would particularly like to thank Javier and Alvaro for teaching me a lot about synthetic techniques during the start of my project. Thank you also to Akihiro and James, MChem project students that worked on this project, whose hard work and dedication to the project helped give results that moved the project forward. Also, thank you to the rest of the Advanced Materials and Liquid Research group, who I have shared a lab with in the new E block building for making the transition into a new lab so relaxed.

I would like to thank Heather for training in NMR spectroscopy and for running NOE experiments, Graeme for running elemental analysis on samples and Karl for Mass Spectrometry results. Special thanks go to Adrian, Sam, Natalie and Rob, who carried out X-ray diffraction studies and solved the crystal structures presented in this thesis. Thanks also go to Bertrand Donnio at the Université de Strasbourg who carried out the small angle X-ray diffraction studies. I would also like to thank Abby and Brian in the glassblowing workshop and Chris in the mechanical workshop particularly for making a new Fisher-Porter vessel.

Thank you to Peter O'Brien for his helpful discussions and proposals for the organic mechanism observed for the reaction between bromine and alkoxy stilbazoles. Thank you also to Robin Perutz, whose suggestions during inorganic group meetings

proved to be invaluable, particularly the suggestion to investigate using bromonium ion intermediates as halogen-bond donors.

Thank you to all of the friends that I have made during my PhD, who have made my PhD such an enjoyable experience. Thank you for the memories and friendships that I will take away with me.

Thank you to my family for the support and interest in my project even if you do admit not even understanding the first line of any of the papers I have shown you. Thank you also to Steve for your support during the past three and a half years.

Declaration

I declare that the work presented in this thesis is my own work unless otherwise stated or indicated by references. This work has not been presented for an award at this, or any other, university. Some of the work presented in this thesis has been presented in the following publications:

- L. J. McAllister, D. W. Bruce and P. B. Karadakov, 'Halogen Bonding between Fluorohalides and Isocyanides', *J. Phys. Chem. A*, 2011, **115**, 11079-11086.
- L. J. McAllister, D. W. Bruce and P. B. Karadakov, 'Quantum Chemical Investigation of Attractive Non-Covalent Interactions Between Halomethanes and Rare Gases', *J. Phys. Chem. A*, 2012, **116**, 10621-10628.
- L. J. McAllister, C. Präsang, J. P. W. Wong, R. J. Thatcher, A. C. Whitwood, B. Donnio, P. O'Brien, P. B. Karadakov and D. W. Bruce, 'Halogen-Bonded Liquid Crystals of 4-Alkoxytilbazoles with Molecular Iodine: a Very Short Halogen Bond and Unusual Mesophase Stability', *Chem. Commun.*, 2013, **49**, 3946-3948.
- L. J. McAllister, D. W. Bruce and P. B. Karadakov, 'Electrophilic Bromination of Substituted Stilbenes and Stilbazoles: A Quantum Chemical Investigation', *Phys. Chem. Chem. Phys.*, 2014, **16**, 2576-2587.
- A. Takemura, L. J. McAllister, P. B. Karadakov, N. E. Pridmore, A. C. Whitwood and D. W. Bruce, 'Competition and Cooperation: Hydrogen and Halogen Bonding in Co-crystals Involving 4-Iodotetrafluorobenzoic acid, 4-Iodotetrafluorophenol and 4-Bromotetrafluorophenol', *CrystEngComm*, 2014, **16**, 4254-4264.
- A. Takemura, L. J. McAllister, S. Hart, N. E. Pridmore, P. B. Karadakov, A. C. Whitwood and D. W. Bruce, 'Halogen- and Hydrogen-bonded Salts and Co-crystals Formed from 4-Halo-2,3,5,6-tetrafluorophenol and Cyclic Secondary and Tertiary Amines: Orthogonal and Nonorthogonal Halogen and Hydrogen Bonding, and Synthetic Analogues of Halogen-Bonded Biological Systems', *Chem. Eur. J.*, 2014, **20**, 6721-6732.

1 Introduction

1.1 The Halogen Bond

A halogen bond was first proposed in 1863 by Guthrie in a complex between ammonia and iodine,² although the nature of the interaction was not recognised. Similarly a complex between trimethylamine and bromine was reported by Remsen in 1896.³ Mulliken later proposed the formation of molecular complexes between dihalogens and solvent molecules to explain the fact that iodine forms a brown solution in some solvents and a violet solution in others.⁴ For example, shifts in the UV absorption of solutions of iodine in aromatic solvents suggest the formation of complexes allowing transitions to the excited state that are forbidden in the isolated aromatic molecule.⁴ Attempts were made to propose geometries of the complexes formed, however, these were not properly understood until the structures of many halogen-bonded complexes were determined in the 1950s and 1960s by Hassel and co-workers by single crystal X-ray diffraction. The first complex studied was that between 1,4-dioxane and bromine, which features polymeric chains formed by Br \cdots O interactions (Figure 1-1).⁵

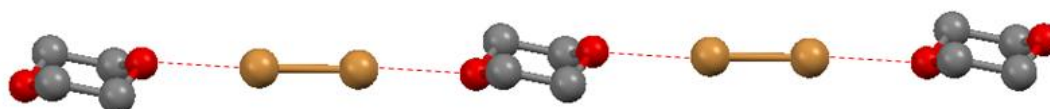


Figure 1-1: The molecular structure of the complex between 1,4-dioxane and bromine.⁵ Hydrogen atoms were not included in the cif file. Br \cdots O interactions are highlighted in red.

Hassel recognised that the Br \cdots O separation, which was found to be 2.71 Å, was longer than the sum of the covalent radii (1.87 Å) but shorter than the sum of the van der Waals radii of bromine and oxygen (3.37 Å). He classified the complexes as charge-transfer in nature with the oxygen atom acting as an electron donor and the bromine acting as an electron acceptor. This was predicated on the observed

lengthening of the Br–Br bond length in the complex (2.31 Å) compared to that in free bromine (2.28 Å) and an assumption that the accepted electron density was to be found in the Br–Br σ^* orbital. The bromine molecule is capable of bridging between two molecules of 1,4-dioxane because the interaction is weak enough not to polarise the bromine molecule too much so that the second bromine atom can still act as a Lewis acid.⁶

Table 1-1 shows bond lengths of selected complexes studied in this period of time. The X...O separations as percentages of the sums of the van der Waals radii in the structures of complexes between 1,4-dioxane and different dihalogens were compared and it was concluded that increasing the size of the halogen led to an increase in the strength of the interaction.⁷ The directionality of the interaction was recognised, with a linear R–X...Y being observed as the preferred arrangement, where R is the group covalently bound to halogen atom X and Y is the electron donating atom.

Similar structures to the 1,4-dioxane complexes were obtained for 1,4-dithiane⁸ and 1,4-diselenane,⁹ however, a polymeric arrangement was not observed because the interaction was stronger and polarised the dihalogen so that the second halogen atom was no longer able to accept electron density. The increase in strength of the complexes as the halogen-bond acceptor changes from O to S and Se can be attributed to Pearson's theory of hard and soft acids and bases (HSAB).¹⁰ Iodine is a soft Lewis acid and the interaction is stronger for softer halogen-bond acceptors.

The complexes of dihalogens with pyridine and trimethylamine have remarkably short I...N separations. This is due to the large halogen-bond basicity of these bases as evidenced by the large pK_{B12} values (2.22 and 3.88, respectively).^{11,12} The pK_{B12} values of nitrogen bases were found to be larger than those for other bases and also reflect the trend observed for the chalcogen bases discussed above.

Table 1-1: The halogen bond separations and R–X bond lengths of selected complexes studied by Hassel and co-workers.

Complex	Halogen Bond	$r(X\cdots Y) / \text{Å}$	% vdW radii	$r(R-X) / \text{Å}$
1,4-Dioxane.Cl ₂ ¹³	Cl \cdots O	2.67	81.7	2.02
1,4-Dioxane.Br ₂ ⁵	Br \cdots O	2.71	80.4	2.31
1,4-Dioxane.I ₂ ¹⁴	I \cdots O	2.81	80.3	2.73
1,4-Dioxane.ICl ¹⁵	I \cdots O	2.60	74.3	2.30
1,4-Dithiane.I ₂ ⁸	I \cdots S	2.87	75.9	2.79
1,4-Diselenane.I ₂ ⁹	I \cdots Se	2.81	72.4	2.83
Acetone.Br ₂ ¹⁶	Br \cdots O	2.82	83.7	2.28
Methanol.Br ₂ ¹⁷	Br \cdots O	2.78	82.5	2.29
4-Picoline.I ₂ ¹⁸	I \cdots N	2.31	65.4	2.83
Pyridine.ICl ¹⁹	I \cdots N	2.26	64.0	2.51
Pyridine.IBr ²⁰	I \cdots N	2.26	64.0	2.66
Pyridine.ICN ²⁰	I \cdots N	2.57	72.8	2.11
N(CH ₃) ₃ .I ₂ ²¹	I \cdots N	2.27	64.3	2.83
N(CH ₃) ₃ .ICl ²²	I \cdots N	2.30	65.2	2.52
Benzyl Sulfide.I ₂ ²³	I \cdots S	2.78	73.5	2.82

The crystal structure obtained for the complex between acetone and bromine revealed that the electron donor can be involved in two interactions if there are two lone pairs of electrons available (Figure 1-2).¹⁶ This leads to a zig-zag polymeric arrangement with bridging bromine molecules between the acetone molecules. If only one lone pair of electrons is available, such as in amines, the electron donor was found to be involved in only one interaction.

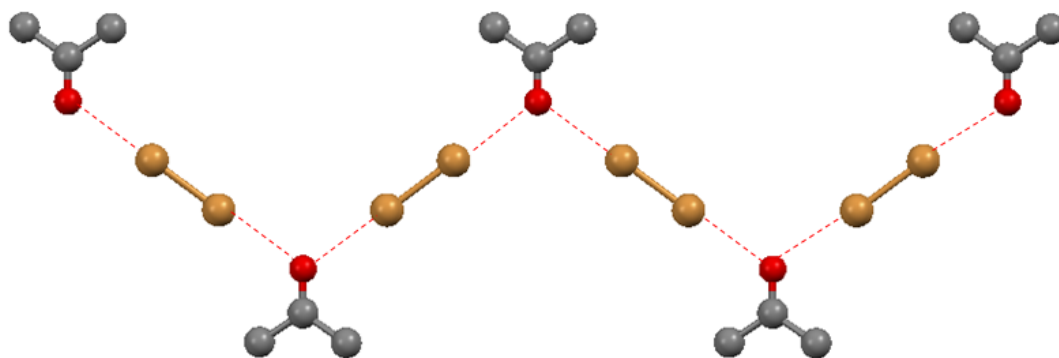


Figure 1-2: The molecular structure of the complex between acetone and bromine.¹⁶ Hydrogen atoms were not included in the cif file. Br...O interactions are highlighted in red.

A similarity between the bonding in trihalide anions and the charge-transfer complexes involving iodine and its monohalides was observed since both feature a shortening of the I...Y bond and a lengthening of the R-I bond.²⁴ Effective radii of the R-I and I...Y bonds, R_1 and R_2 , respectively, were calculated by subtracting the covalent radius of the atom bonded to the iodine atom from the measured intermolecular separation. A linear relationship between R_1 and R_2 was observed (Figure 1-3) confirming the similarity between trihalide anions and charge-transfer complexes.

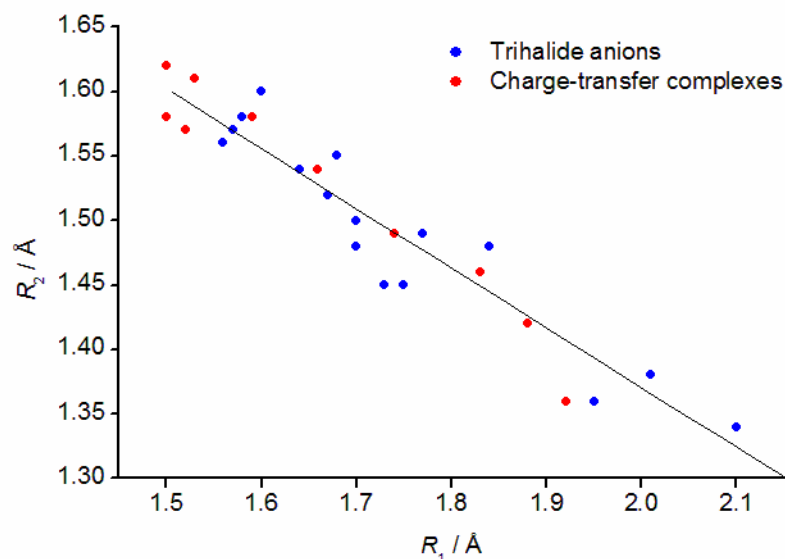


Figure 1-3: The relationship between the effective radii of the R–I and I···Y bonds in the structures of trihalide-anions and the charge-transfer complexes investigated by Hassel and co-workers.²⁴

In his Nobel Prize award lecture,ⁱ Hassel emphasised the similarity between hydrogen and halogen bonding by comparing the crystal structures of the complex between 1,4-dioxane and sulfuric acid and the complex between 1,4-dithiane and iodoform (Figure 1-4).⁷

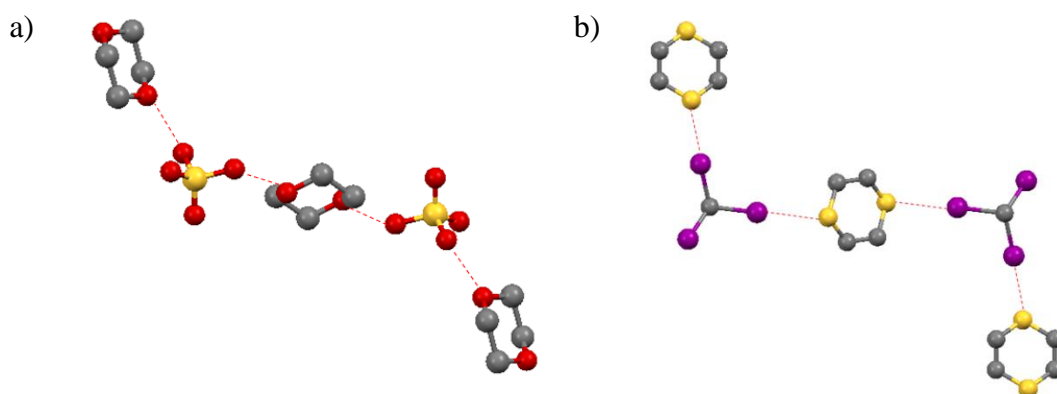


Figure 1-4: The molecular structures of a) the complex between 1,4-dioxane and sulfuric acid²⁵ and b) the complex between 1,4-dithiane and iodoform.²⁶ Hydrogen atoms were not included in the cif file. O–H···O and I···S interactions are highlighted in red.

ⁱ Although it should be noted that Hassel shared the Nobel Prize in Chemistry with Barton in 1969 for developing the concept of conformation.

It was also recognised that hydrogen and halogen bonding can compete. Bromoform can act as either a halogen- or a hydrogen-bond donor and was found to interact with the nitrogen atoms of hexamethylenetetramine through two hydrogen bonds and two halogen bonds (Figure 1-5).²⁷ All of the hydrogen atoms are involved in C–H⋯N interactions, although only one third of the bromine atoms are involved in Br⋯N interactions, suggesting that hydrogen bonds form preferentially over halogen bonds in this structure.

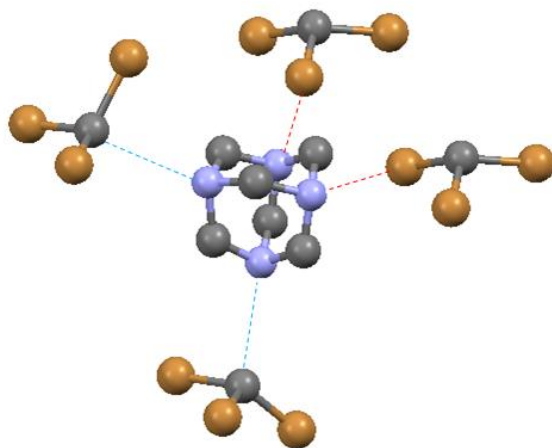


Figure 1-5: The molecular structure of the complex between bromoform and hexamethylenetetramine.²⁷ Hydrogen atoms were not included in the cif file. Br⋯N interactions are shown in red and C–H⋯N hydrogen bonds are shown in blue.

Bent published a comprehensive review of the charge-transfer complexes studied by Hassel and made observations about trends in the strengths of the complexes by comparing series of complexes.²⁸ Amines were found to be the strongest electron donors followed by selenides and sulfides. The hybridisation of the electron donor also affected its strength with sp^3 -hybridised donors being stronger than sp^2 - and sp -hybridised donors. The strength of the interaction increased with the size of the halogen, an observation that was also made by Hassel.⁷ In complexes where the halogen-bond donor was bound covalently to a carbon atom, the hybridisation of that carbon atom also affected the strength of the interaction with halogens bound to sp -

hybridised carbon atoms forming stronger complexes than those bound to sp^2 - or sp^3 -hybridised carbons.

Complexes involving other types of electron donor such as the π -electrons of an aromatic ring (*e.g.* the complex between carbon tetrabromide and *p*-xylene,²⁹ Figure 1-6) and halide anions were included in Bent's review.²⁸

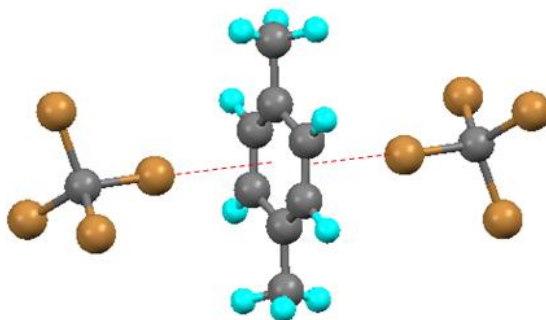


Figure 1-6: The molecular structure of the complex between carbon tetrabromide and *p*-xylene.²⁹ Br \cdots π interactions are highlighted in red. The distance between bromine atom and the centroid of the phenyl ring is 3.339 Å

Bent was also able to identify two types of C–X \cdots X–C interactions; one where both C–X \cdots X angles are similar and approximately 160° (*e.g.* the Cl \cdots Cl interactions in the structure of 2,5-dichloroaniline,³⁰ Figure 1-7a), which would later become known as Type I interactions, and another one where one C–X \cdots X angle is approximately 90° and the other one is 180° (*e.g.* the Cl \cdots Cl interaction in the structure of pentachlorophenol,³¹ Figure 1-7b), which are now referred to as Type II interactions.

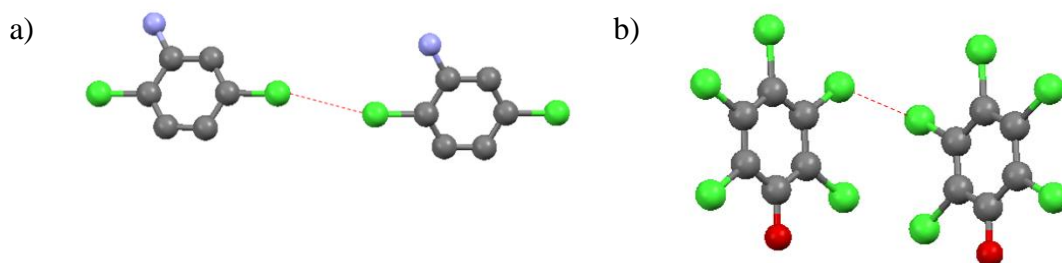


Figure 1-7: The molecular structures of a) 2,5-dichloroaniline³⁰ and b) pentachlorophenol.³¹ Cl \cdots Cl interactions are highlighted in red. Hydrogen atoms have been excluded.

The next significant development in the understanding of the halogen bond was made by Legon, who compared halogen- and hydrogen-bonded complexes in the gas phase using rotational spectroscopy.³² In order to obtain a spectrum for weakly bound complex, a supersonic jet or beam of the gas mixture is expanded through a hole into vacuum. The mixture then undergoes collisionless expansion at which point the complex of interest can be assumed to be frozen in the lowest rotational and vibrational states, and the rotational spectrum can be obtained by a Fourier-transform microwave spectrometer.

The form of the spectrum gives information about the symmetry of the complex and the separations between the atoms can be determined from the rotational constants, which are inversely proportional to the principal moments of inertia. The intermolecular stretching force constant, k_{σ} , which is an indication of the strength of the interaction, can be determined from the centrifugal distortion constants. The nuclear quadrupole coupling constants of the halogen atoms obtained from the hyperfine structure can be used to determine the change in the electric field gradients of each nucleus upon complex formation, which in turn can be used to determine the deviation of the interaction from linearity.

Legon concluded that in complexes between dihalogens and Lewis bases, if the Lewis base has both a non-bonding (n-) and a π -electron pair, then the interaction will form preferentially along the axis of the n-pair. If the Lewis base has only a π -electron pair then the interaction will form along the local symmetry axis of the π -orbital.

Significant progress in the field of halogen bonding was made in the 1990s by Resnati and Metrangolo, who utilised the interaction in crystal engineering and supramolecular chemistry.^{33,34} Their work has helped to promote the interaction and the number of publications in the field has increased dramatically (Figure 1-8).

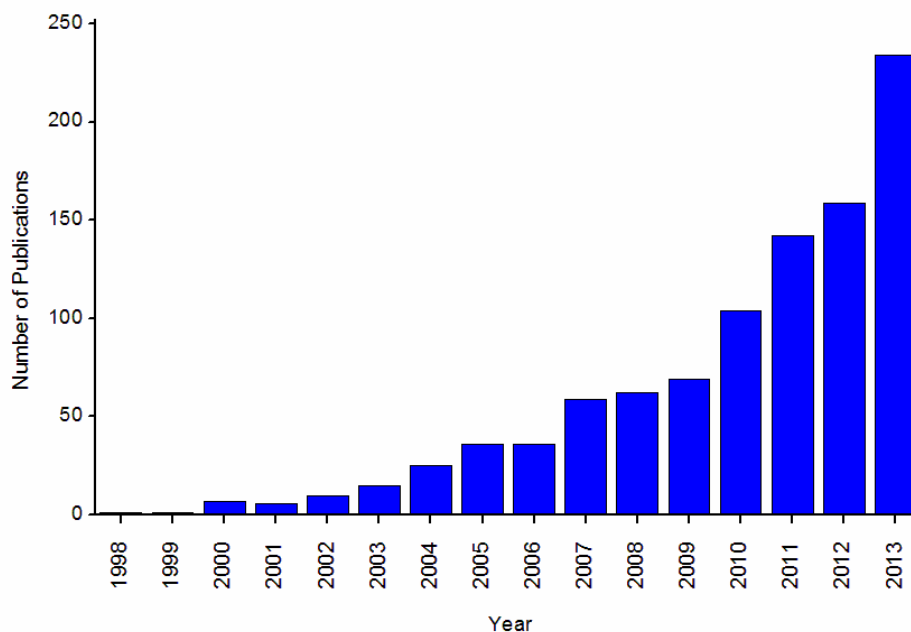


Figure 1-8: The number of publications in the research topic 'halogen bonding' over the past 15 years. The figure is adapted from a search carried out in 2008³⁵ to include recent publications.

Resnati and Metrangolo led the IUPAC task committee which recommended the definition of the halogen bond, shown below.¹

"A halogen bond occurs when there is evidence of a net attractive interaction between an electrophilic region associated with a halogen atom in a molecular entity and a nucleophilic region in another, or the same molecular entity."

The halogen bond is then represented by the three dots in $R-X\cdots Y$. This may be a controversial statement because the whole fragment $R-X\cdots Y$ constitutes the halogen bond; a similar debate was observed in the recent redefinition of the hydrogen bond.³⁶ $R-X$ is defined as the halogen-bond donor and can include dihalogen molecules, haloalkanes, haloarenes and 1-haloalkynes. Y is the halogen-bond acceptor and can include the lone pairs of electrons on an atom, an anion or a region of π -electron density. The definition includes a list of features that encompass many of the observations made by Hassel. This includes the fact that the interatomic separation between X and Y is less than the sum of their van der Waals radii, the

R–X⋯Y angle is close to linear, the R–X bond length increases upon complex formation and the halogen bond increases in strength as the halogen atom becomes more polarisable.

1.1.1 The σ -hole

The ability of a halogen atom, which is typically considered to be electronegative in nature, to form a halogen bond can be rationalised by investigation of the electrostatic potential, $V(r)$ (Equation 1-1), which characterises the ability of a molecule to enter electrostatic interactions. The analytical form of $V(r)$ is given in Equation 1-1:

$$V(r) = \sum_A \frac{Z_A}{|R_A - r|} - \int \frac{\rho(r')dr'}{r' - r} \quad (1-1)$$

where Z_A is the charge on nucleus A and point R_A and $\rho(r)$ is the electron density. The first term in Equation 1-1 corresponds to the contribution of the nuclei and the second term corresponds to the contribution of the electrons.³⁷ It is usual to visualise $V(r)$ by mapping it onto a selected electron density isosurface; the plot obtained in this way is often referred to as the electrostatic potential surface. Clark *et al.*³⁸ calculated the electrostatic potential surfaces of CF_3X , where $\text{X} = \text{F}, \text{Cl}, \text{Br}$ or I . A region of positive electrostatic potential was observed, centred on the extension of the C–X axis for $\text{X} = \text{Cl}, \text{Br}$ and I , which was increasing in size with the increasing polarisability of the halogen, as shown in Figure 1-9. This area was named the σ -hole and it can interact electrostatically with regions of negative $V(r)$ on Lewis bases.

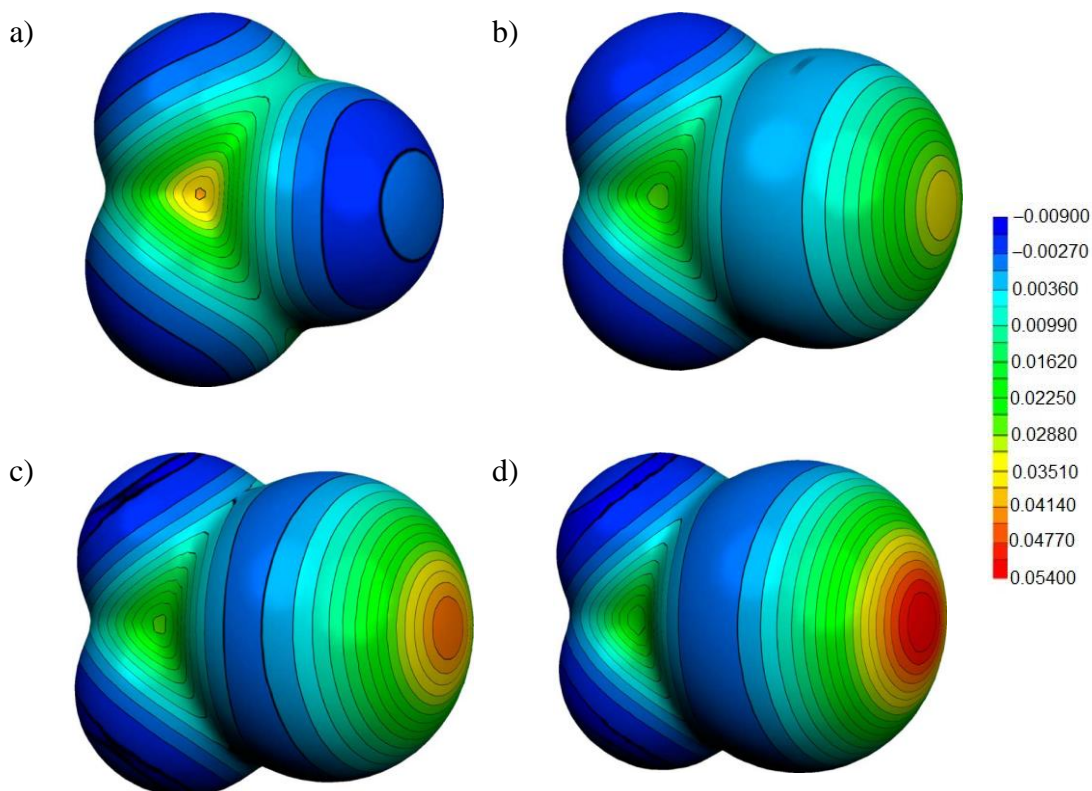


Figure 1-9: Electrostatic potential surfaces calculated at the 0.001 electrons Bohr⁻³ electronic density isosurface for a) CF₄, b) CF₃Cl, c) CF₃Br and d) CF₃I. Electrostatic potentials in Hartrees.³⁸

The origin of the σ -hole was explained using natural bond orbital (NBO) analysis, which reveals that there are three lone pairs of electrons on the halogen atom, of which two are within p -orbitals and one, which lies along the C–X axis, is predominantly s in character due to the p -orbital along this axis contributing to the C–X σ -bonding orbital.³⁸ The two lone pairs of electrons in the p -orbitals lead to the equatorial region of negative potential observed on the halogen atom.³⁹ As the halogen becomes more polarisable or as the group it is bonded to becomes more electronegative, the degree of contribution from the p -orbital into the σ -bonding orbital increases and therefore the degree of s -character in the orbital containing the lone pair of electrons along the C–X axis increases. This causes the σ -hole to increase in size and become more positive leading to stronger halogen-bond interactions.

Therefore the halogen bond is highly tunable by varying the halogen atom and the electron-withdrawing group. It was shown that changing the halogen atom and the fluorine substitution of halobenzenes can affect the size of the σ -hole and the strengths of their complexes with acetone (Figure 1-10).⁴⁰ Similarly introducing electron-donating amine substituents weakens the interaction whereas introducing nitrogen atoms to the ring and carbonyl groups significantly strengthens the interaction.⁴¹

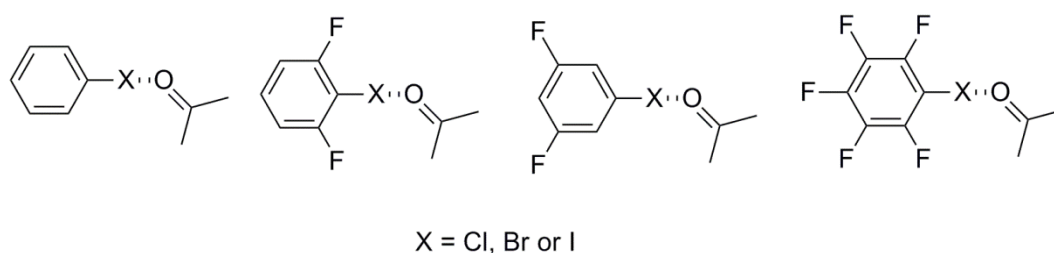


Figure 1-10: Complexes of fluorinated halobenzenes with acetone investigated to show the substituent effect on the halogen bond.

Therefore, it is possible to observe a σ -hole for fluorine if it is bonded to a group that is sufficiently electron-withdrawing such as CN,³⁹ CF₃O⁴² or CF₃SO₂OCO.⁴³ The electrostatic potential surface of F₂ has revealed the presence of a σ -hole that can interact with regions of electron density such as F⁻ to form the trifluoride anion, F₃⁻.

1.1.2 Other σ -hole Interactions

Group 15 and group 16 atoms have been observed to have σ -holes⁴⁴ and can form interactions, known as pnictogen and chalcogen bonds, respectively, similar to halogen bonds. Examples of molecular structures featuring these interactions are shown in Figure 1-11.

These interactions have properties that closely resemble halogen bonds. Pnictogen and chalcogen bonds are directional and more sensitive to angular deviations⁴⁵ from linearity than hydrogen bonds, as would be expected from the σ -holes observed on their electrostatic potential surfaces. Calculations on X–P \cdots P–Y interactions suggest

that these arise from hyperconjugation between the orbital corresponding to the lone pair of electrons on the Lewis base and the anti-bonding orbital of the P–X bond.⁴⁶ This hyperconjugative interaction was found to become more pronounced as the binding energies in a series of chalcogen bonds increases with the introduction of electron-withdrawing substituents.⁴⁷ Comparison of analogous systems shows that halogen bonds involving Lewis bases with nitrogen lone pairs such as ammonia⁴⁸ and trimethylamine⁴⁹ are stronger than chalcogen and pnictogen bonds. Conversely, pnictogen bonds with π -electrons are stronger than the analogous chalcogen and halogen bonds.

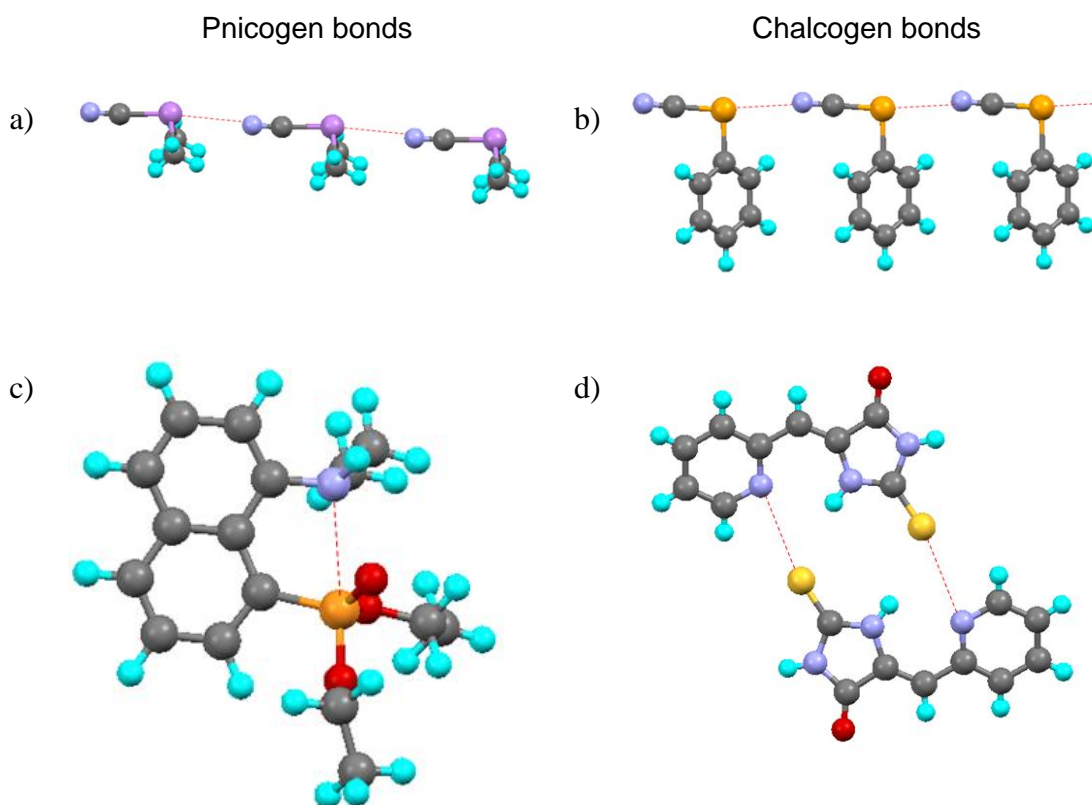


Figure 1-11: a) As...N interactions in the molecular structure of cyano-dimethylarsine,⁵⁰ b) Se...N interactions in phenylselenenyl cyanide,⁵¹ c) P...N interactions in diethyl (8-dimethylamino-1-naphthyl)phosphonate⁵² and d) S...N interactions in (Z)-5-(2-pyridylmethylene)-2-thioxoimidazolinone.⁵³

Group 14 atoms have also been observed to form similar interactions known as tetrel or carbon-bonding. A crystal structure has been obtained with a fluoride ion trapped

within an octasilsesquioxane cage (Figure 1-12).⁵⁴ Calculations of the interaction energies of fluoride ions trapped in $E_8O_{12}(OH)_8$ cages ($E = Si, Ge$ or Sn) reveal that the interaction is large and negative, corresponding to an attractive interaction and, similarly to halogen, chalcogen and pnictogen bonds, the interaction increases in strength as the group 14 atom becomes larger.⁵⁵ Although this disagrees with HSAB theory because the fluoride anion is a hard base, it does coincide with the observation that the σ -hole on the group 14 atom increases in size as it becomes more polarisable.⁴⁴ Silsesquioxanes with iodophenylsubstituents have been observed to form Type II halogen bonds⁵⁶ suggesting that the molecules could be used to investigate the cooperative effects of halogen and tetrel bonding.

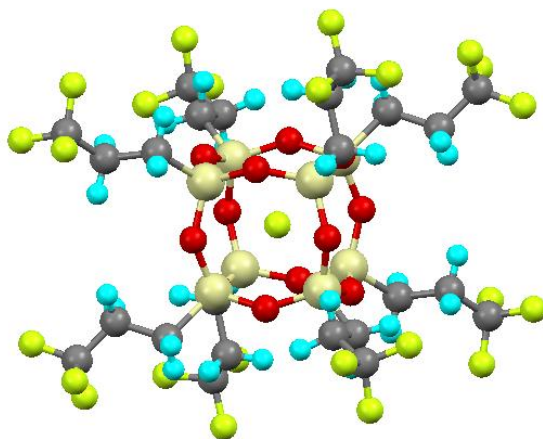


Figure 1-12: The molecular structure of a fluoride ion encapsulated within an octasilsesquioxane cage.⁵⁴

Quantum chemical calculations have also shown that carbon atoms could also form this type of interaction, which lead to the alternative name of 'carbon-bonding'.⁵⁷ Introducing electron-withdrawing substituents to methane makes the carbon atom capable of accepting electron density from Lewis bases such as H_2O , H_2S and NH_3 . This suggests that tetrel bonding could play a role in S_N2 reactions, such as the reaction between CH_3Cl and F^- .⁵⁸ It should, however, be noted that although interactions between a methyl substituent and a Lewis base could be considered as a 'carbon bond', it is more likely that these involve a trifurcated hydrogen-bonded

motif with the methyl hydrogens.⁵⁹ This is the case in the structure of the drug fenobam shown in Figure 1-13, which has a trifurcated C–H···Cl motif rather than a C···Cl 'carbon bond'.⁶⁰

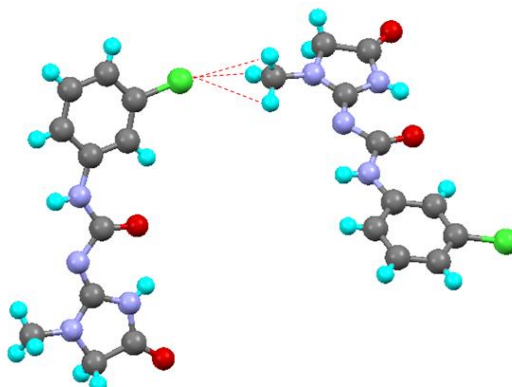


Figure 1-13: The molecular structure of fenobam.⁶⁰ The trifurcated C–H···Cl motif is highlighted in red.

1.2 Comparison between Hydrogen and Halogen Bonding

The observation that halogen bonding is similar to hydrogen bonding has prompted many comparisons between the two interactions.

1.2.1 The Hydrogen Bond

The hydrogen bond is defined as the attractive interaction between a hydrogen atom of molecule or fragment R–H, (where R is more electronegative than H), and a nucleophilic fragment Y–Z.⁶¹ Typically, R is a N, O or F atom, however, this is not always the case since C–H···O and C–H···N hydrogen bonds have been observed. The hydrogen bond arises generally from electrostatic forces, although charge-transfer and dispersion interactions also play a role. The charge-transfer interaction is identified by a lengthening of the R–H bond upon complex formation, which causes a red shift in the infrared R–H stretching frequency. The more electronegative the R group, the stronger the interaction and the shorter the H···Y separation.

The interaction is described as being linear in nature, however, this criterion should be used carefully to identify hydrogen bonds since significant deviations from linearity can be observed, particular for weak interactions. This deviation from linearity is observed more often for hydrogen-bonded complexes than for halogen-bonded complexes, which can be explained by comparing the σ -holes of hydrogen- and halogen-bond donors. The σ -hole observed on halogen-bond donors is focused along the extension of the C–X axis, which indicates that the halogen bond is directional in nature.⁶² This σ -hole is also observed on hydrogen bond donors as demonstrated by the electrostatic potential of CF₃H, which is shown in Figure 1-14, along with the electrostatic potential of CF₃Br for comparison.

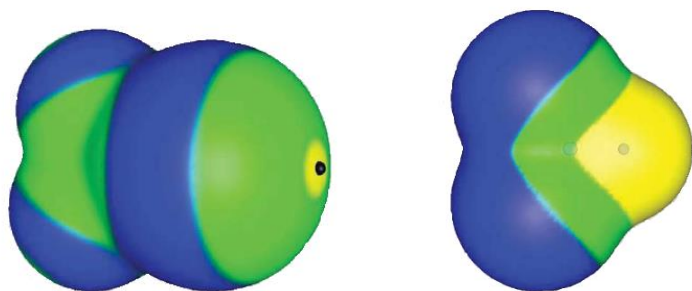


Figure 1-14: The electrostatic potentials of a) CF₃Br and b) CF₃H. Yellow and blue indicate regions of positive and negative electrostatic potentials respectively.⁶²

It can be seen that the whole hydrogen atom of CF₃H has a positive electrostatic potential indicating that hydrogen bonds are less directional than the equivalent halogen bond. The reason for the reduced directionality is because the hydrogen atom does not have lone pairs of electrons within *p*-orbitals, which lead to the equatorial region of negative electrostatic potential observed for halogen-bond donors.

This difference in directionality was also observed experimentally by Legon.³² In the B···HCl complexes studied, the chlorine atom can form a secondary interaction with an electrophilic region on the Lewis base, B. This was not observed in the B···ClF complexes studied. Figure 1-15 shows an example of this difference for the

complexes of formaldehyde with HCl and ClF, where the hydrogen-bonded complex with HCl shows a larger deviation from linearity, measured by the angle θ , than the halogen-bonded complex.

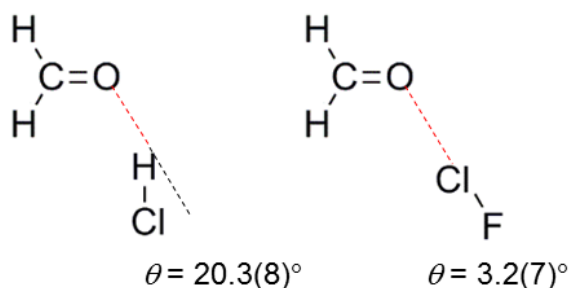


Figure 1-15: The experimentally determined geometries of complexes of formaldehyde with HCl and ClF showing the deviations from linearity, θ .³²

Extensive studies by Legon and co-workers into complexes of the form $B \cdots HX$ and $B \cdots XY$, where B is a Lewis base and X and Y are halogen atoms, have highlighted the similarities of halogen bonding to hydrogen bonding.^{63,64} Pre-reactive species between Lewis bases and compounds HX and XY were isolated by introducing one of the compounds, diluted in argon, using a fast-mixing nozzle⁶⁵ and the rotational spectra of the Mulliken outer complexes were recorded. The halogen-bonded complexes were found to have a structure that was isomorphous with that of their hydrogen-bonded counterparts.³² This observation led to a proposed definition of the halogen bond analogous to that of the hydrogen bond.⁶⁶

Both hydrogen bonds and halogen bonds can form by interacting with a non-bonding n-electron pair or a π -electron pair. The interactions were found to have similar binding strengths and electric charge redistributions.³² This similarity favours the electrostatic σ -hole model for describing the interaction.

1.3 Competition between Hydrogen and Halogen Bonding

Recognising the similarity between hydrogen and halogen bonding introduced the question about the relative strengths of the bonds and which bond would form preferentially. Instinctively it would be expected that hydrogen bonding would be preferred over halogen bonding, which is often found to be a more labile interaction. For example, the liquid-crystalline complex formed from a 2:1 ratio of stilbazole and 4-iodotetrafluorophenol contains both a hydrogen and a halogen bond (Figure 1-16).⁶⁷

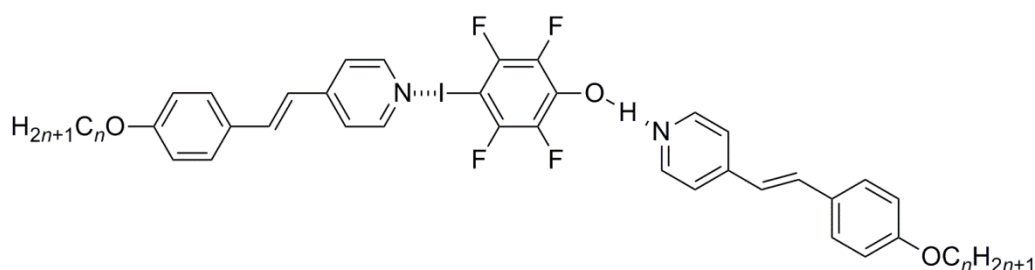


Figure 1-16: A 2:1 liquid crystalline complex between stilbazole and 4-iodotetrafluorophenol. The complex contains both a hydrogen and a halogen bond.⁶⁷

By mixing stilbazole with 4-iodotetrafluorophenol in a 1:1 ratio, it is possible to observe that stilbazole binds preferentially with the hydrogen-bond donor (Figure 1-17). The halogen-bond donor then forms an interaction with the oxygen in the alkoxy group leading to a polymeric arrangement, which is an indication of its highly electrophilic nature.

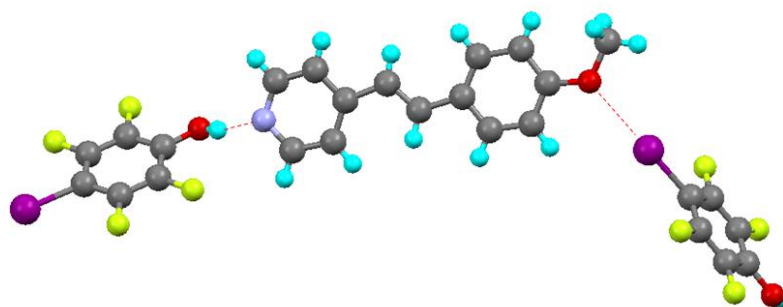


Figure 1-17: The molecular structure of the halogen-bonded complex between 4-iodo-2,3,5,6-tetrafluorophenol and methoxystilbazole.⁶⁷

Corradi *et. al.*⁶⁸ showed that given appropriate conditions, halogen-bonded complexes would form preferentially over their hydrogen-bonded counterparts. An example of a competitive experiment between a halogen-bond and hydrogen-bond donor and a compound that can accept both hydrogen and halogen bonds is shown in Figure 1-18. When 1,2-bis(4-pyridyl)-ethane was in the presence of both hydroquinone (a hydrogen-bond donor) and 1,4-diiodotetrafluorobenzene (a halogen-bond donor), it was the halogen-bonded complex that crystallised. It can be argued that the electron-withdrawing fluorines in 1,4-diiodotetrafluorobenzene will make this molecule a much better acceptor of electron density than hydroquinone.

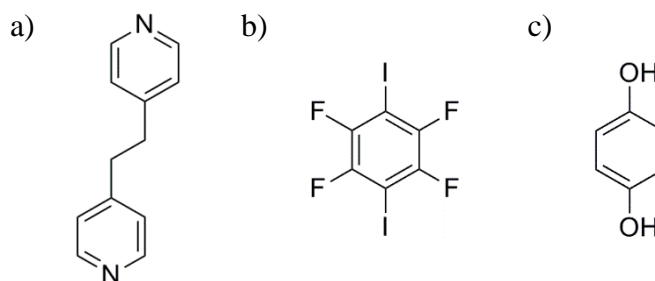


Figure 1-18: a) 1,2-Bis(4-pyridyl)ethane b) 1,4-diiodotetrafluorobenzene and c) hydroquinone.

A more comparable experiment has shown that halogen bonding forms preferentially over hydrogen bonding in a modified form of DNA.⁶⁹ Uracil at a Holliday junction was replaced by 5-bromouracil and the bromine atom was found to be on the inside crossover strand meaning that a Br \cdots O halogen bond had formed as opposed to the equivalent hydrogen bond. Both the halogen- and hydrogen-bond donors are in equivalent environments making this a fair comparison. Exchanging the uracil for a bulkier thymine did not have any stabilising effect on the hydrogen bonding in the junction indicating that the stabilising effect of the 5-bromouracil in the Holliday junction was caused by halogen bonding alone and not by steric effects.⁷⁰

The ability to predict the formation of hydrogen and halogen bonds is beneficial particularly in the field of crystal engineering. Aakeröy and co-workers have conducted extensive studies on systems with both halogen and hydrogen bonding,

which will be described in detail in Chapter 7. It can be predicted that the strongest donor will interact with the strongest acceptor and the second best donor will interact with the second best acceptor, etc.⁷¹ For example, the base 1-methyl-2-pyridin-4-yl-benzimidazole (Figure 1-19a) has two hydrogen/halogen-bond acceptor sites with the benzimidazole site being stronger than the pyridyl site.⁷² When this base is co-crystallised with 4-iodo-2,3,5,6-tetrafluorooxime, the stronger oxime O–H hydrogen-bond donor interacts with the benzimidazole nitrogen and the weaker iodine halogen-bond donor interacts with the pyridyl nitrogen (Figure 1-19b). This concept also explains the observation that in the complex of 4-iodotetrafluorophenol and stilbazole (Figure 1-17) the phenol, which is the stronger donor, interacts with the stronger pyridyl base, and the iodine interacts with the weaker oxygen base.

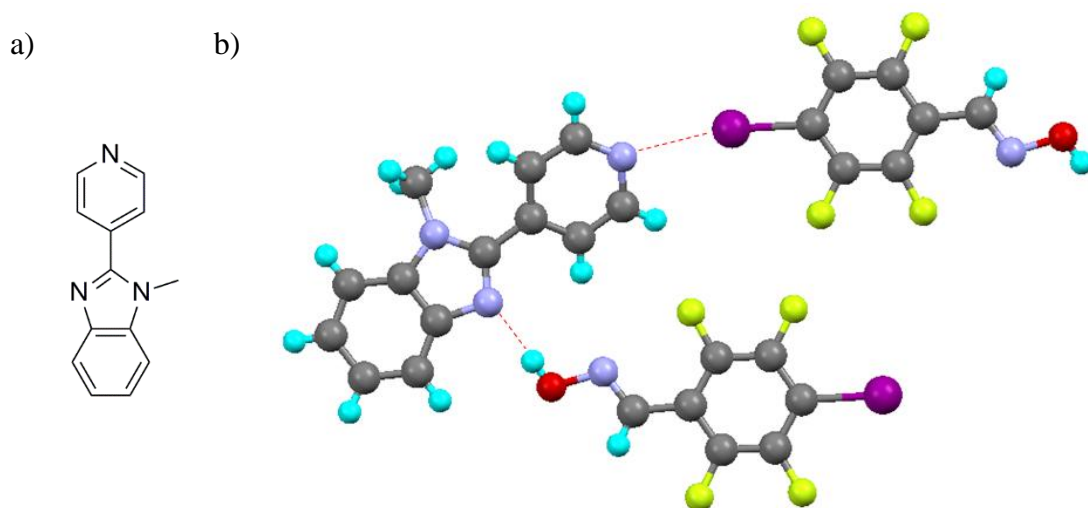


Figure 1-19: a) 1-Methyl-2-pyridin-4-yl-benzimidazole and b) the molecular structure of its complex with 4-iodo-2,3,5,6-tetrafluorooxime.⁷²

1.4 Experimental Techniques for Investigating Halogen Bonding

1.4.1 Single-Crystal X-Ray Diffraction

The most common technique for studying halogen bonding in the solid phase is single-crystal X-ray diffraction, which can determine the positions of the atoms in

the molecular structure and can, therefore, be used to determine the halogen bond length.

In a crystal, the molecules are arranged in a highly ordered structure with molecules related to one another by symmetry leading to an array of repeating structural units. The repeating unit is known as the unit cell and the array of repeating unit cells is known as the lattice.⁷³ The edges of the unit cell are labelled as a , b and c ; the internal angles α , β and γ are chosen so that α is the angle between edges b and c . The unit cell shape is restricted by the rotational and reflectional symmetry elements in the crystal structure and, as a consequence, crystals can be classified into one of seven crystal systems. The presence of specific symmetry elements in the crystal structure defines its space group.

X-Rays have a wavelength that is comparable to the separation between lattice planes in a crystal, as a result of which they are diffracted when they pass through a crystal. This fact was used to develop X-ray crystallography, where the diffraction of the X-rays is measured and used to determine positions of atoms in the crystal. X-Rays are generated by bombarding a metal such as Mo with high-energy electrons.⁷⁴ A monochromatic beam of X-rays is directed at a single crystal and the diffracted beams are detected using a charge-coupled device (CCD) camera. The crystal is rotated so that reflections from all lattice planes can be detected.

The peaks in the diffraction pattern obtained during X-ray crystallography are caused by constructive interference of X-rays reflected off adjacent lattice planes. Bragg's law (Equation 1-2) can be used to calculate the separation between the lattice planes, d , since the angle of approach of the X-ray, θ , is known.

$$n\lambda = 2d\sin\theta \quad (1-2)$$

Here n is the order of the reflection, which is typically absorbed into the value of d , and λ is the wavelength of the X-rays. This equation can be used once the diffraction

pattern has been obtained and indices h , k and l have been assigned to each reflection, to determine the unit cell of the structure.

The scattering factor, f , which accounts for the fact that heavy atoms give stronger scattering than light atoms, is given in Equation 1-3:

$$f = 4\pi \int_0^\infty \rho(r) \frac{\sin(kr)}{kr} r^2 dr, \text{ where } k = \frac{4\pi}{\lambda} \sin\theta \quad (1-3)$$

where $\rho(r)$ is the electron density distribution of the atom at point r . This scattering factor is included in the structure factor, F_{hkl} , which is used in the determination of the detailed structure using the forward Fourier transform given in Equation 1-4:

$$F_{hkl} = \sum_{hkl} f_j e^{i\phi_{hkl}(j)}, \text{ where } \phi_{hkl}(j) = 2\pi (hx_j + ky_j + lz_j) \quad (1-4)$$

where ϕ is the phase of the wave and x_j , y_j and z_j are the fractional coordinates of atom j and h , k and l are the Miller indices of the reflection.

The intensity of the reflection is proportional to the square of the structure factor and can therefore be used to calculate the structure factor, which in turn can be used to calculate the electron density distribution using the reverse Fourier transform shown in Equation 1-5:

$$\rho(r) = \frac{1}{V} \sum_{hkl} F_{hkl} e^{-2\pi i(hx + ky + lz)} \quad (1-5)$$

where V is the volume of the unit cell.

One of the problems that is encountered is the phase problem, where the information about the phase of the X-ray at the peak in the diffraction pattern is lost because the structure factor is obtained by taking the square root of the intensity of the peak. One way to solve this problem is to carry out a Patterson synthesis using Equation 1-6,

which maps the vector separation of the atoms at positions x, y, z and $x + u, y + v, z + w$.

$$P(u, v, w) = \frac{1}{V} \sum_h \sum_k \sum_l |F_{hkl}|^2 e^{-2\pi i(hx + ky + lz)} \quad (1-6)$$

Typically, during a Patterson synthesis, the positions of heavy atoms are determined first because they dominate the scattering pattern and then lighter atoms are determined from their positions relative to a heavy atom.

Modern analyses of crystal structures use direct methods where the probabilities of different phases are analysed in order to select the appropriate phase for the reflections that make the most significant contribution to the electron density map. This method is only possible due to the computational power available to modern crystallographers.

Analysis of a crystal structure by Patterson synthesis or direct methods typically produces only a partial structure so the remainder of the structure needs to be determined. The forward Fourier transform (Equation 1-4) can be used to determine the diffraction pattern that would be expected from the partial structure obtained. The residual factor or R -factor can be calculated using the difference between the calculated structure factors, F_c , and the observed structure factors, F_o (Equation 1-7).

$$R = \frac{\sum ||F_o| - |F_c||}{\sum |F_o|} \quad (1-7)$$

Another residual factor that can be used is the weighted factor, wR_2 (Equation 1-8).

$$wR_2 = \sqrt{\frac{\sum w(F_o^2 - F_c^2)^2}{\sum w(F_o^2)^2}} \quad (1-8)$$

where w is the weight of each reflection. These residual factors can be used to determine the goodness of fit of the calculated structure to the observed diffraction

pattern. The reverse Fourier transform (Equation 1-5) can be applied to the observed amplitudes and the calculated phases to give more information about the structure. A new model for the structure can be obtained and the forward Fourier transform can be carried out again to give new residual factors. This process is repeated until the *R*-factor decreases to a value between 0.02 – 0.07, although it should be noted that this is very dependent on the composition of the crystal and what information is required.

The structure can then be refined by adjusting parameters in the structure determination so as to maximise the fit of the electron density to the observed intensities in the diffraction pattern.

X-Ray crystallography is a particularly useful technique in the investigation of halogen-bonded complexes because the halogen-bond separation can be determined along with any elongation of the R–X covalent bond. For example, the effect of the degree of fluorination of iodobenzenes on the halogen-bond separation of the complexes with DMAP could be determined from the molecular structures obtained by X-ray crystallography (Figure 1-20).⁷⁵ Increasing the number of fluorine atoms caused the N···I separation to decrease indicating an increase in the interaction and a linear correlation was observed with the pK_a values of the related phenols.

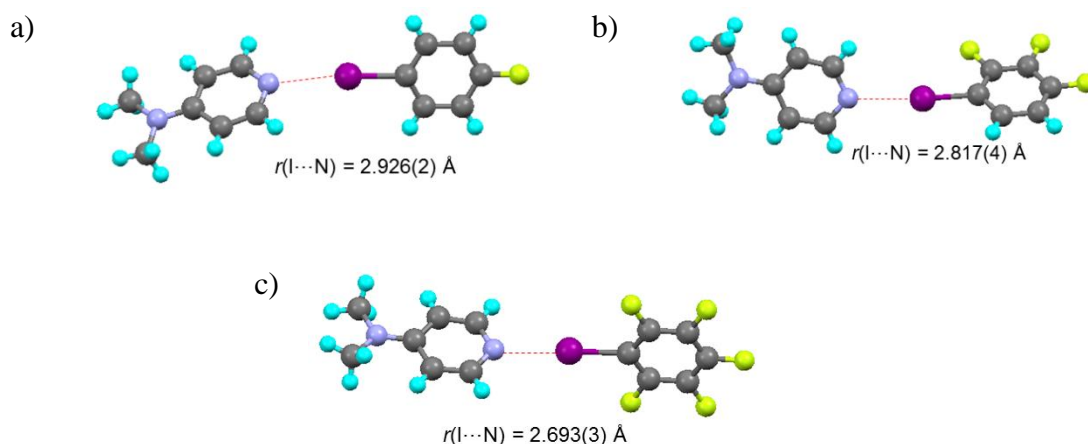


Figure 1-20: Molecular structures of complexes of DMAP with a) 4-fluoroiodobenzene, b) 2,3,4-trifluoroiodobenzene and c) pentafluoroiodobenzene.⁷⁵ I···N separations are highlighted in red.

X-Ray crystallography can also be used to determine the favoured interactions in systems with competing halogen- and hydrogen-bond donors. For example, 1-iodoethynyl-4-iodobenzene, which contains two potential halogen-bond donors, one bound to an sp -hybridised carbon and another one bound to an sp^2 -hybridised carbon, was found to interact with 4-phenylpyridine through the iodoethynyl group (Figure 1-21).⁷⁶ This shows that halogen-bond donors bound to sp -hybridised carbons are preferred over those bound to sp^2 -hybridised carbons, confirming observations made by Hassel in earlier investigations.²⁸

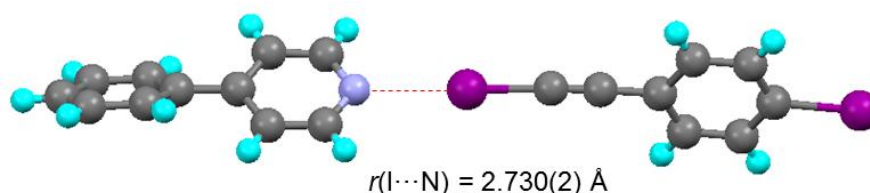


Figure 1-21: Molecular structure of the complex of 1-iodoethynyl-4-iodobenzene with 4-phenylpyridine.⁷⁶

1.4.2 NMR Spectroscopy

NMR spectroscopy has been used to characterise the formation of hydrogen-bonded complexes⁶¹ and can be used to characterise halogen bonding in solution. The formation of a halogen-bonded complex between quinuclidine and 1-iodoperfluoropropane (Figure 1-22) in chloroform caused a change in the ^1H and ^{13}C NMR spectra of quinuclidine.⁷⁷ The interaction could be easily characterised by a 7 ppm upfield shift and significant line broadening in the ^{14}N spectrum of the quinuclidine base. The ^{19}F NMR spectrum of the CF_2I group in the halogen-bond donor was also sensitive to complex formation and a shift of a few ppm was observed. The ratio of the iodide and amine could be varied in order to determine an association constant for the complex.

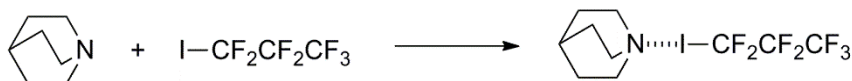


Figure 1-22: The halogen-bonded complex between quinuclidine and 1-iodoperfluoropropane investigated by NMR spectroscopy.⁷⁷

¹⁹F NMR spectroscopy is particularly useful for studying halogen-bonded complexes due to the large ¹⁹F chemical shift range and its high sensitivity. The change in the ¹⁹F chemical shift of the CF₂X fluorine atoms in 1,8-diiodo- and 1,8-dibromoperfluorooctane upon complex formation with basic solvents was found to be sensitive to the strength of the interaction.⁷⁸ In this study, the change in chemical shift was largest for complexes with 1,8-diiodoperfluorooctane as the halogen-bond donor and stronger Lewis bases, such as piperidine and cyclohexylamine, as the halogen-bond acceptor.

NMR spectroscopy is particularly useful in diagnosing halogen-bonded complex formation if the chemical shift examined corresponds to an atom directly involved in the interaction. The formation of a halogen-bonded complex between a nickel fluoride complex and iodopentafluorobenzene (Figure 1-23) was characterised by a downfield shift of 33 ppm of the ¹⁹F chemical shift of the fluoride in the halogen-bond acceptor.⁷⁹ This shift was similar to that observed in the hydrogen-bonded complex between the nickel fluoride complex and indole.

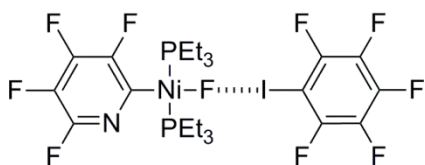


Figure 1-23: The halogen-bonded complex between a nickel fluoride complex and iodopentafluorobenzene.

The enthalpy, ΔH , and entropy, ΔS , of complex formation can be determined by finding association constants at different temperatures and using the van't Hoff equation (Equation 1-9).

$$\frac{d\ln(K_a)}{dT} = \frac{\Delta H^\circ}{RT^2} \quad (1-9)$$

where K_a is the association constant, T is the temperature and R is the ideal gas constant. The changes in the enthalpy and entropy upon formation of the complex between the nickel fluoride complex and iodopentafluorobenzene were found to be negative,⁷⁹ and the values were very sensitive to the solvent, which was thought to be due to competitive $I \cdots \pi$ interactions with aromatic solvents. Thermodynamic parameters can be used to compare the strength of bonding in different complexes. Both the metal and the phosphine ligands affect the enthalpy of formation of the complex.⁸⁰ The enthalpy increases when the metal is changed to palladium and increases further for platinum. PCy_3 ligands are found to give stronger halogen-bonded complexes than PEt_3 and $PiPr_3$ ligands due to its higher σ -donor ability.

Metal hydrides can also act as halogen-bond acceptors making it possible to use 1H NMR spectroscopy to characterise complex formation.⁸¹ A change in chemical shift of 0.39 ppm of the central hydride of $[Cp_2TaH_3]$ was observed upon complex formation with iodopentafluorobenzene (Figure 1-24).

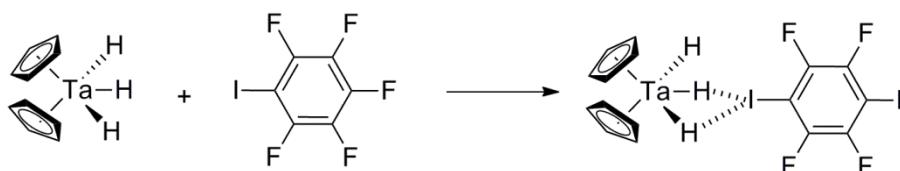


Figure 1-24: The formation of the halogen-bonded complex between $[Cp_2TaH_3]$ and iodopentafluorobenzene.⁸¹

Association constants obtained by ^{19}F NMR spectroscopy have been used to investigate the effect of substituents in the *para* position of iodotetrafluorobenzene on the complex formed with tributylphosphine oxide (Figure 1-25).⁸² The association constant was found to exhibit a linear correlation with the Hammett parameters of the substituents showing that electron-donating substituents weaken the complexes and electron-withdrawing groups increase the strength of the complex.

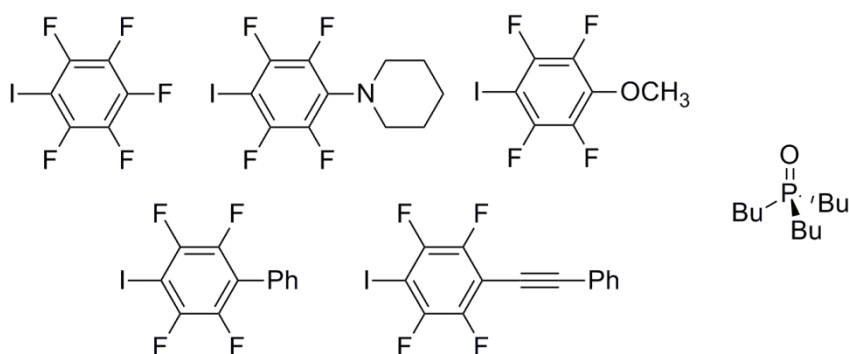


Figure 1-25: The iodoperfluoroarene halogen-bond donors and tributylphosphine oxide halogen-bond acceptor used to investigate substituent effects on complex formation.⁸²

1.4.3 Solid-State NMR Spectroscopy

Solid-state NMR spectroscopy is proving to be a useful technique for studying halogen-bonded complexes particularly when used in conjunction with X-ray crystallography. The ^{13}C NMR chemical shift of the carbon atom bound to the halogen changes in the range of 2.5 – 6 ppm upon complex formation, although it should be noted that this technique has only been used for two types of complexes (complexes of 1,4-diiodotetrafluorobenzene with thiocyanate and selenocyanate bases and complexes of 1,4-diiodobenzene with decamethonium diiodide).⁸³ Significant changes have been observed for the spectra of the halogen-bond acceptor. In complexes of 1,4-diiodotetrafluorobenzene with selenocyanate bases (Figure 1-26a), the ^{77}Se NMR spectra change significantly upon complex formation particularly the component of the chemical shift tensor in the z-direction, δ_{33} .⁸⁴ When complexes of decamethonium diiodide with *para*-dihalogen substituted benzenes were formed (Figure 1-26b) there was a small change of 2 ppm in the ^{15}N NMR chemical shift. The ^{14}N spectra showed a more significant change with a large change in the quadrupolar coupling constant, $C_Q(^{14}\text{N})$.⁸³ For example, $C_Q(^{14}\text{N})$ in the complex of decamethonium diiodide with 1,4-diiodobenzene was 24(2) kHz compared to the value of 85 kHz observed for the decamethonium diiodide monomer. The interactions in haloanilinium halides (Figure 1-26c) were compared using ^{35}Cl , ^{81}Br and ^{127}I spectra, which are challenging to obtain because the nuclides

are all quadrupolar.⁸⁵ The complexes studied were isostructural, so trends in the spectra could be investigated and the change in chemical shift and quadrupolar coupling constant were found to decrease as the interaction strength increases.

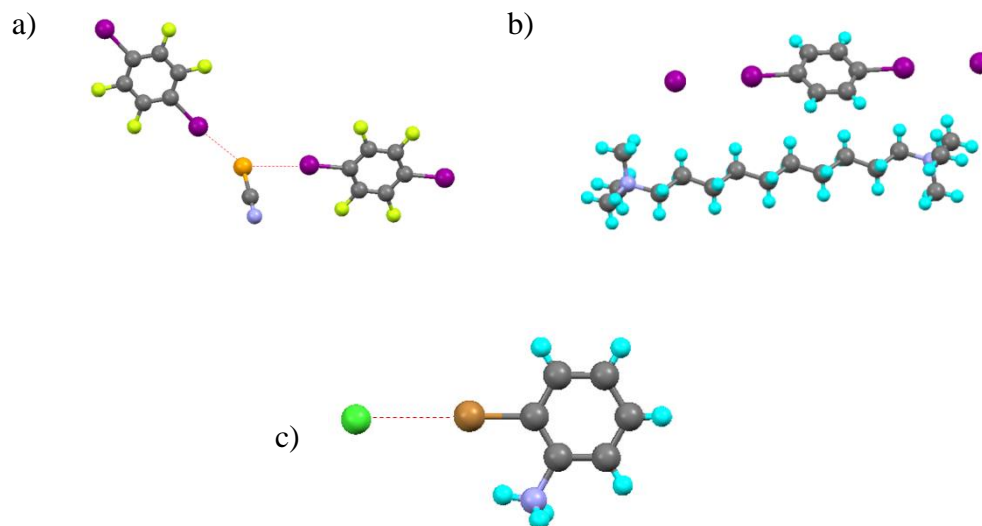


Figure 1-26: Molecular structures of complexes a) of 1,4-diodotetrafluorobenzene with tetramethylammonium selenocyanate (cation omitted),⁸⁴ b) of decamethonium diiodide with 1,4-diiodobenzene⁸³ and c) 2-bromoanilinium chloride.⁸⁵

1.5 Quantum Chemical Methods for Studying Halogen Bonding

Quantum chemical calculations can provide a powerful tool for understanding the nature of halogen bonding and improvements in computational power have made it possible to perform calculations for more complicated systems and at higher levels of theory.

1.5.1 *Ab Initio* Methods

Ab initio means 'from the beginning' and these methods involve solving the Schrödinger equation (Equation 1-10) directly using approximations requiring no experimental data other than the values of fundamental constants.

$$\hat{H}\Psi = E\Psi \quad (1-10)$$

In this equation Ψ is the wavefunction and E is the total energy of the system. \hat{H} is the Hamiltonian operator, which contains terms corresponding to the kinetic and potential energy of the system. For a system with M nuclei and N electrons the Hamiltonian, in atomic units, has the form shown in Equation 1-11. The first two terms correspond to the kinetic energies of the electrons and nuclei, and the remaining three terms correspond to electron-nucleus attraction and electron-electron and nucleus-nucleus repulsions.⁸⁶

$$\hat{H} = -\sum_{i=1}^N \frac{1}{2} \nabla_i^2 - \sum_{I=1}^M \frac{1}{2M_I} \nabla_I^2 - \sum_{i=1}^N \sum_{I=1}^M \frac{z_I}{r_{iI}} + \sum_{i=1}^N \sum_{j>i}^N \frac{1}{r_{ij}} + \sum_{I=1}^M \sum_{J>I}^M \frac{Z_I Z_J}{R_{IJ}} \quad (1-11)$$

\mathbf{r}_i and \mathbf{R}_I stand for the electron and nuclei position vectors, respectively, and Z_I are the nuclear charges. ∇_i^2 is an operator that is given by the sum of the second partial derivatives along the x , y and z axes, see Equation 1-12.

$$\nabla_i^2 = \frac{\partial^2}{\partial x_i^2} + \frac{\partial^2}{\partial y_i^2} + \frac{\partial^2}{\partial z_i^2} \quad (1-12)$$

The Born-Oppenheimer approximation states that since electrons are much lighter than the nuclei and, therefore move much faster, the positions of the nuclei can be considered to be fixed.⁸⁷ Using this approximation the second and last terms in Equation 1-11 can be omitted when dealing with the electrons only, since these terms relate only to the nuclei; this yields the electronic Hamiltonian in the Born-Oppenheimer approximation. Solving the Schrödinger equation involving the electronic Hamiltonian produces the electronic wavefunction, which describes the electrons in the system.

An electron is described by both its position vector, \mathbf{r} , and by its spin coordinate, ω , and the combination of these spatial and spin coordinates can be denoted as \mathbf{x} . Electron spin is not considered in the electronic Hamiltonian so in order to include spin in the electronic wavefunction, it is usual to use Pauli's *ad hoc* approach in

combination with the antisymmetry principle, which states that the electronic wavefunction must be antisymmetric with respect to the exchange of the spatial and spin coordinates of any two electrons (Equation 1-13).

$$\Psi(\mathbf{x}_1, \mathbf{x}_2, \dots, \mathbf{x}_i, \dots, \mathbf{x}_j, \dots, \mathbf{x}_N) = -\Psi(\mathbf{x}_1, \mathbf{x}_2, \dots, \mathbf{x}_j, \dots, \mathbf{x}_i, \dots, \mathbf{x}_N) \quad (1-13)$$

The electronic Hamiltonian can be rewritten in the more concise form shown in Equation 1-14.⁸⁶

$$\hat{H}_{el} = \sum_{i=1}^N h(i) + \sum_{i=1}^N \sum_{j>i}^N g(i, j), \text{ where } h(i) = -\frac{1}{2} \nabla_i^2 - \sum_{l=1}^N \frac{Z_l}{r_{il}}, \text{ and } g(i, j) = \frac{1}{r_{ij}} \quad (1-14)$$

1.5.2 Hartree-Fock (HF) Method

The Schrödinger equation for the electrons would be much easier to solve if electron-electron repulsion, that is, the term involving $g(i, j)$ were neglected. Therefore, the modified Schrödinger equation would take the form shown in Equation 1-15.

$$\left[\sum_{i=1}^N h(i) \right] \Psi = E\Psi \quad (1-15)$$

The solution for Ψ in this equation takes the form of a Hartree product, which is a product of one-electron orbitals, $\psi_i(\mathbf{x}_i)$, and the energy, E , is the sum of the corresponding orbital energies, ϵ_i . One issue with the Hartree product is that it does not obey the antisymmetry principle. Therefore, a more appropriate way of approximating wavefunctions is to use Slater determinants (Equation 1-16).⁸⁸

$$\Psi(\mathbf{x}_1, \mathbf{x}_2, \dots, \mathbf{x}_N) = (N!)^{-1/2} \begin{vmatrix} \psi_1(\mathbf{x}_1) & \psi_1(\mathbf{x}_2) & \cdots & \psi_1(\mathbf{x}_N) \\ \psi_2(\mathbf{x}_1) & \psi_2(\mathbf{x}_2) & \cdots & \psi_2(\mathbf{x}_N) \\ \vdots & \vdots & \ddots & \vdots \\ \psi_N(\mathbf{x}_1) & \psi_N(\mathbf{x}_2) & \cdots & \psi_N(\mathbf{x}_N) \end{vmatrix} \quad (1-16)$$

In the Hartree-Fock (HF) method, the forms of the orbitals in an approximate wavefunction given by a single Slater determinant are varied in order to minimise the energy, E_0 (see Equation 1-17), corresponding to the electronic Hamiltonian in Equation 1-14.

$$E_0 = \langle \Psi_0 | \hat{H} | \Psi_0 \rangle \quad (1-17)$$

The orbitals that minimise this energy are given by the solutions of the Hartree-Fock equations (see Equation 1-18).⁸⁶

$$\hat{F}\varphi_i = \varepsilon_i\varphi_i \quad (1-18)$$

where \hat{F} is the Fock operator, which, for a closed-shell Slater determinant, takes the form shown in Equation 1-19.

$$\hat{F} = \hat{h} + \sum_{j=1}^N (2\hat{J}_j - \hat{K}_j) \quad (1-19)$$

where \hat{J}_j and \hat{K}_j are the so-called Coulomb and exchange operators, which all depend on all orbitals included in the Slater determinant.

The orbitals in Equation 1-18 are usually approximated as a linear combination of atomic orbitals (LCAO), see Equation 1-20:

$$\varphi_i = \sum_{\mu=1}^M \chi_{\mu} c_{\mu i} \quad (1-20)$$

where χ_{μ} are atomic orbital basis functions and $c_{\mu i}$ are coefficients that need to be optimised. The coefficients, $c_{\mu i}$, can be determined using the Hartree-Fock-Roothaan equations (Equation 1-21), which are usually represented in matrix form and solved by numerical methods from linear algebra.⁸⁸

$$\sum_{\mu=1}^M F_{v\mu} c_{\mu i} = \varepsilon_i \sum_{\mu=1}^M S_{v\mu} c_{\mu i}, \text{ where } F_{v\mu} = \langle \chi_v | \hat{F} | \chi_\mu \rangle, \text{ and } S_{v\mu} = \langle \chi_v | \chi_\mu \rangle \quad (1-21)$$

The orbital coefficients can then be used to calculate the one-electron density matrix, $D_{\mu\nu}$ (see Equation 1-22).

$$D_{\mu\nu} = 2 \sum_{j=1}^n c_{\mu j}^* c_{\nu j} \quad (1-22)$$

This density matrix is then used to form a new Fock matrix, which is in turn used to determine new coefficients. A new density matrix is then calculated and compared to the previous density matrix against specified convergence criteria. If these criteria have not been met then this iterative procedure continues. If these criteria are met then the self-consistent field (SCF) procedure is considered to have converged and the total electron energy can be determined using Equation 1-23.

$$E = \frac{1}{2} \sum_{\mu=1}^M \sum_{\nu=1}^M D_{\mu\nu} (h_{\mu\nu} + F_{\mu\nu}) \quad (1-23)$$

The absence of electron correlation in HF theory makes it inappropriate for modelling halogen-bonded complexes because electron correlation plays a significant role in the interaction. It is therefore necessary to use post-HF levels of theory where corrections are made to include electron correlation.

1.5.3 Møller-Plesset (MP) Perturbation Theory

Møller-Plesset perturbation theory is a post-HF method that includes electron correlation. Perturbation theory starts with finding solutions to a simplified Schrödinger equation involving the zeroth-order Hamiltonian, \hat{H}_0 , (see Equation 1-24).

$$\hat{H}_0 \Psi_i^{(0)} = E_i^{(0)} \Psi_i^{(0)} \quad (1-24)$$

The difference between \hat{H}_0 and the Hamiltonian in the actual many-electron Schrödinger equation is known as a perturbation, $\lambda\hat{V}$, to \hat{H}_0 and is given by the expression in Equation 1-25.⁸⁶

$$\hat{H} - \hat{H}_0 = \lambda\hat{V} \quad (1-25)$$

where λ is a small number. Using the zeroth-order Hamiltonian and the perturbation, the original Schrödinger equation, can be re-written as shown in Equation 1-26.

$$(\hat{H}_0 + \lambda\hat{V})\Psi_i = E_i\Psi_i \quad (1-26)$$

The solutions to this equation are given by power series expansions also known as perturbation expansions (Equation 1-27).

$$\Psi_i = \Psi_i^{(0)} + \lambda\Psi_i^{(1)} + \lambda^2\Psi_i^{(2)} + \dots, \text{ and } E_i = E_i^{(0)} + \lambda E_i^{(1)} + \lambda^2 E_i^{(2)} + \dots \quad (1-27)$$

These expansions can be substituted back into the Schrödinger equation and terms with identical powers of λ can be equated to give the terms in the energy series shown in Equation 1-28.⁸⁹

$$E_i^{(0)} = \langle \Psi_i^{(0)} | \hat{H}_0 | \Psi_i^{(0)} \rangle, E_i^{(1)} = \langle \Psi_i^{(0)} | \hat{V} | \Psi_i^{(0)} \rangle \quad (1-28)$$

$$E_i^{(2)} = \langle \Psi_i^{(0)} | \hat{V} | \Psi_i^{(1)} \rangle = \sum_{j \neq i} \frac{|\langle \Psi_i^{(0)} | \hat{V} | \Psi_j^{(0)} \rangle|^2}{E_i^{(0)} - E_j^{(0)}}$$

In Møller-Plesset (MP) perturbation theory the zeroth order Hamiltonian is given by the sum of the Fock operators for all electrons. This means that the zeroth order contribution to the ground-state energy is given by the sum of the orbital energies.

The first-order correction to the energy is given by the expression in Equation 1-29, if λ is set equal to one.

$$E_0^{(1)} = \langle \Psi_0^{(0)} | \hat{V} | \Psi_0^{(0)} \rangle = \langle \Psi_0^{(0)} | \hat{H} - \hat{H}_0 | \Psi_0^{(0)} \rangle = E_{\text{HF}} - \sum_{i=1}^N \varepsilon_i \quad (1-29)$$

The second-order correction to the energy, which is used in the MP2 level of theory, is given in Equation 1-30.

$$E_0^{(2)} = \sum_i \sum_j \sum_p \sum_q \frac{(\langle \psi_p \psi_q | g | \psi_i \psi_j \rangle - \langle \psi_p \psi_q | g | \psi_j \psi_i \rangle)^2}{\varepsilon_i + \varepsilon_j - \varepsilon_p - \varepsilon_q} \quad (1-30)$$

where i, j and p, q are indices of occupied and virtual orbitals, respectively.

Inclusion of this second-order correction means that the MP2 level of theory includes a significant amount of electron correlation energy making it more appropriate for the modelling of halogen-bonded complexes. Indeed it is a popular level of theory for use in computational work in this field.

1.5.4 Coupled-Cluster Approximation

The coupled-cluster approximation involves applying an exponential operator to a simple wavefunction, usually a Slater determinant (see Equation 1-31).⁹⁰

$$\Psi = e^{\hat{T}} \Psi_0, \text{ where } \hat{T} = \sum_i c_i T_i \quad (1-31)$$

Here T_i represent operators generating different excitations. At the CCSD level of theory, single and double excitations are included, and in CCSDT triple excitations are also included. At the CCSD(T) level of theory, the triple excitations are estimated using many-body perturbation theory. Similarly to MP perturbation theory, the coupled-cluster approach accounts for a significant proportion of the electron

correlation energy and it is generally thought of as being superior to MP perturbation theory.

The high accuracy of coupled-cluster methods and their ability to account for electron correlation makes them appropriate for investigating halogen-bonded complexes, although they are computationally expensive making them suitable only for systems with a small number of electrons. Therefore coupled-cluster methods, such as the CCSD(T) level of theory with a large basis set or at the complete basis set limit, are used as a benchmarks when comparing other levels of theory. There is, however, a debate about whether the results obtained with these methods are sufficiently accurate.⁹¹

As the methods of accounting for electron correlation becomes more accurate, the computational cost of the calculation increases. The cost of HF calculations scale approximately by N^3 , MP2 calculations scale by N^5 and CCSD and CCSD(T) calculations scale by N^6 and N^7 , respectively, where N is the number of electrons in the system. Additionally, as the method becomes more accurate, the basis set is required to be large in order to get sufficiently accurate results. Computational cost also increases with increasing basis set size making calculations at the CCSD(T) level of theory often prohibitively expensive.

1.5.5 Basis Sets and Effective Core Potentials (ECPs)

Basis sets are functions, which are or resemble atomic orbitals and are used to form molecular orbitals as linear combinations of atomic orbitals (LCAO). The 1s Slater orbital has the form shown in Equation 1-32 with an exponential factor, ζ , equal to one.⁸⁶

$$\chi_{\text{SO}, 1s} = (\zeta^3 / \pi)^{1/2} e^{-\zeta r} \quad (1-32)$$

Slater orbitals provide a good approximation of atomic orbitals but are not very computationally efficient. It is therefore appropriate to use Gaussian orbitals, which depend on the square of the distance between the electron and the nucleus. The Gaussian orbital corresponding to the 1s orbital of the hydrogen atom has the form shown in Equation 1-33:

$$\chi_{\text{GO}, 1s} = (2\alpha / \pi)^{3/4} e^{-\alpha r^2} \quad (1-33)$$

where α is the exponential factor. Since Gaussian orbitals do not model atomic orbitals accurately, particularly at distances close to and far away from the nucleus, a linear combination of several orbitals can be taken in order to improve performance (Equation 1-34).

$$\varphi_{1s}(r) = \sum_{p=1}^n c_p \chi_{\text{GO}, 1s}(r, \alpha_p) \quad (1-34)$$

where c_p are coefficients that are determined through fitting or optimisation procedure to provide the best approximate atomic orbitals.

Minimal basis sets, such as STO-3G, have just enough functions to describe the core and valence electrons of the constituent atoms and are not sufficiently flexible to allow obtaining accurate computational results.

Double-zeta basis sets have two functions with different exponential factors to describe each atomic orbital. Typically, split-valence basis sets are used where it is only the valence atomic orbitals that are described by a double-zeta basis.

A popular variant of these basis sets are the Pople K-K'K''G split-valence basis sets.⁹² This involves treating the inner shell separately from the valence shell, which, in turn, is split into two parts, each described by a sum of Gaussian functions with different exponents. The most common Pople basis set is 6-31G, which involves 6

Gaussians to describe the inner shell and a valence shell that is split into two parts, described by 3 and 1 Gaussians, respectively.

A Pople basis set can be improved further by adding polarisation functions (denoted by * and **, or p and p,d), which includes adding *d*-type functions to the second row elements and *p*-type functions to the hydrogen atom, respectively. The addition of polarisation functions allows to account for the distortion of the atomic orbitals in the presence of an electric field. The use of polarisation functions is important in the modelling of hydrogen-bonded and halogen-bonded complexes because the interaction leads to a distortion of the electron density of the participating atoms.

Other functions whose inclusion is important in the basis set when modelling hydrogen- and halogen-bonded complexes are diffuse functions (denoted by + or ++), which are Gaussian functions that have very small exponents and can therefore model electron density away from the atomic nuclei.

Another series of basis sets that are popular, particularly in the modelling of hydrogen- and halogen-bonded complexes are Dunning's aug-cc-pVXZ basis sets⁹³⁻⁹⁵ (X = D, T or Q, referring to basis sets of double, triple and quadruple-zeta quality, respectively). Redundant functions have been removed from these basis sets in order to improve computational efficiency. The aug-cc-pVXZ basis sets include polarisation functions and the use of the "aug" prefix leads to the inclusion of diffuse functions.

Relativistic effects need to be accounted for in calculations involving heavy atoms. This can be done using the Douglas-Kroll (DK) Hamiltonian or by the zero-order regular approximation (ZORA), which approximate the four-component Dirac equation.⁹⁶ A more popular method of accounting for relativistic effects is to use effective core potentials (ECPs). They are used to replace the core electrons of the atom and therefore only the valence electrons are included in the quantum chemical calculation. ECPs are generated by partitioning the atomic orbitals into core and

valence orbitals and solving modified Hartree-Fock equations for the valence electrons in an atom, in which the core electrons are accounted for through a potential energy correction, with relativistic effects included for heavier elements.⁹⁷ The solutions are pseudo-orbitals that match the original atomic orbitals in the valence region. These pseudo-orbitals are then used to generate effective potentials, initially in a numerical form, which are later transformed to Gaussian components shown in Equation 1-35 for use in standard quantum chemical packages.

$$U_1(r) = \frac{1}{r^2} \sum_k d_{kl} r^{n_{kl}} e^{-b_{kl} r^2} \quad (1-35)$$

where d_{kl} and b_{kl} are fitting parameters. ECPs are important when modelling halogen-bonded complexes, particularly those involving iodine, because this is a heavier atom where relativistic effects will be significant. The use of ECPs for these atoms also reduces the number of electrons involved in the calculation and therefore decreases computational cost.

1.5.6 Density Functional Theory (DFT)

DFT is based on Hohenberg-Kohn theorem, which states that the ground-state electronic energy can be determined completely by the electronic density, $\rho(r)$, and therefore there is a unique functional that can be used to determine the ground-state energy and the electronic density exactly.^{98,99} This functional cannot be calculated directly, therefore an approximate functional needs to be used,¹⁰⁰ which can result in significant errors in the ground state energy and other computed properties. Despite these potential errors, DFT calculations are popular due to fact that the required computational effort is significantly smaller than that for many advanced *ab initio* methods, as a result of which DFT is often the only option for modelling large systems involving large numbers of electrons.

The total DFT energy is given by Equation 1-36 and represent the sum of kinetic energy of the electrons for a wavefunction in the form of a Slater determinant, $T_s[\rho]$, potential energy due to attraction between electrons and nuclei, $E_{\text{en}}[\rho]$, Coulomb repulsion between electrons, $J[\rho]$, and an exchange-correlation term, $E_{\text{xc}}[\rho]$.¹⁰¹

$$E_{\text{DFT}}[\rho] = T_s[\rho] + E_{\text{en}}[\rho] + J[\rho] + E_{\text{xc}}[\rho] \quad (1-36)$$

The first three terms of Equation 1-36 can be calculated directly using Equations 1-37 – 1-39.

$$T_s[\rho] = \sum_{i=1}^N \left\langle \psi_i \left| -\frac{1}{2} \nabla^2 \right| \psi_i \right\rangle \quad (1-37)$$

$$E_{\text{en}}[\rho] = - \sum_{I=1}^M \int \frac{Z_I \rho(\mathbf{r})}{|\mathbf{R}_I - \mathbf{r}|} d\mathbf{r} \quad (1-38)$$

$$J[\rho] = \frac{1}{2} \iint \frac{\rho(\mathbf{r}_1) \rho(\mathbf{r}_2)}{|\mathbf{r}_1 - \mathbf{r}_2|} d\mathbf{r}_1 d\mathbf{r}_2 \quad (1-39)$$

The exchange-correlation term is a measure of the difference between the true kinetic energy and the kinetic energy calculated using a Slater determinant (Equation 1-37) and the difference between the exact electron-electron interaction energy and the Coulomb repulsion energy (Equation 1-39). The exact form of this exchange-correlation term is impossible to define and many functionals have been developed as attempts to provide reasonable and computationally affordable approximations. These functionals can either be local functionals, which depend only on the electron density, ρ , or gradient-corrected functionals, which depend on both the electron density and its gradient, $\nabla\rho$.

The performances of different DFT functionals have been described to take the form of a Jacob's ladder, where the bottom of the ladder represents Hartree-Fock theory and the top represents chemical accuracy.¹⁰²

The first rung of the ladder corresponds to local density approximation (LDA) functionals (Equation 1-40), such as SVWN. These implement the simplest approach to approximating the exchange-correlation term and assume that the electron density is like that of a uniform electron gas and can be treated as local (*i.e.* close to the nuclei).¹⁰³

$$E_x^{\text{LDA}}[\rho] = -\frac{3}{2} \left(\frac{3}{4\pi} \right)^{1/3} \int \rho^{4/3}(\mathbf{r}) d\mathbf{r} \quad (1-40)$$

The next rung represents generalised gradient approximation (GGA) functionals, such as B88, which are an extension of the LDA functionals with an additional term depending on the gradient of the electron density. An example of a GGA functional is shown in Equation 1-41.

$$E_x^{\text{B88}}[\rho] = E_x^{\text{LDA}}[\rho] - \gamma \int \frac{\rho^{4/3} x^2}{1 + 6 \gamma \sinh^{-1} x} d\mathbf{r}, \text{ where } x = \rho^{-4/3} |\nabla \rho| \quad (1-41)$$

The next rung on the Jacob's ladder features meta-GGA functionals (*e.g.* B95 or TPSS), which are an improvement on GGA functionals and include higher-order terms depending on the electron-density gradient.

Hybrid density functionals, such as the popular B3LYP functional, which are defined as linear combinations of other exchange and correlation GGA functionals and include some exact HF exchange, are on the next rung of the ladder. These functionals involve coefficients that can be adjusted to fit experimental values.

Sometimes considered as the highest rung of the ladder currently achieved corresponds to density functionals that include dispersion interactions such as the

M06 suite of functionals¹⁰⁴ and the DFT-D approach.¹⁰⁵ This classification of functionals will be discussed further in Chapter 3.

1.5.7 Counterpoise (CP) Correction

Basis Set Superposition Error (BSSE) is a common problem in studies of complexes involving non-covalent interactions. It occurs when two (or more) monomers, say A and B, approach one another and monomer A uses basis functions from monomer B to improve its basis set quality and *vice versa*. The inconsistent treatment of the two monomers when they are far apart and close together results in an underestimation of the interaction separation, A...B, and an overestimation of the interaction strength. This error is larger for smaller basis sets because there is a more pronounced improvement when one monomer is utilising the extra basis functions available on the other monomer. The BSSE can be eliminated by performing calculations at the complete basis set limit, however, a far more realistic approach is to use the CP correction.¹⁰⁶

The CP correction involves calculating the energies of the two monomers using the dimer basis and subtracting this from the energy of the dimer calculated using the dimer basis to obtain the interaction energy (Equation 1-42).¹⁰⁷

$$\Delta E_{\text{int}}^{\text{CP}}(AB) = E_{AB}^{AB} - E_A^{AB} - E_B^{AB} \quad (1-42)$$

In order to calculate the energy of monomer A using the dimer basis set, the atoms of monomer B are treated as ghost atoms, which carry the same basis functions, but have no electrons.

There is some debate as to whether the CP method corrects for BSSE accurately because some of the basis set space on monomer B is occupied and are, therefore, not available to the electrons on monomer A due to the Pauli exclusion principle.

Therefore, using the complete dimer basis set to calculate the energy of monomer A could result in an overcorrection for the BSSE.

Schwenke and Truhlar first questioned the use of CP correction when calculating the interaction energy of the HF dimer.¹⁰⁸ These calculations were performed at the HF level of theory so it should be noted that errors could be due to the lack of electron correlation. Similar results were, however, observed in calculations of the interaction energies of He¹⁰⁹ and water dimers,¹¹⁰ the HF trimer¹¹¹ and the FH...NH₃ complex,¹¹² which made use of methods that included electron correlation. One author stated that it was curious to deteriorate a complex's hypersurface to the monomer description in order to improve reliability.¹¹¹ It could, however, be argued that the monomers description needs to be worsened in order for the treatment to be consistent to that of the dimer.

One explanation for the observation of improved results without CP correction in some calculations is that in these cases, the BSSE and basis set incompleteness error (BSIE) cancel each other, resulting in an artificial improvement in the accuracy of the calculation. Results obtained without CP correction, however, do not converge in a systematic manner with the increase of the basis set size, which makes it difficult perform an extrapolation to the complete basis set limit,¹¹³ whereas CP-corrected calculations on hydrogen-bonded complexes have been observed to exhibit the expected systematic convergence with the increase of the basis set size.¹¹⁴

The CP correction has been used successfully to describe the transition states of the Diels-Alder and H-transfer reactions,¹¹⁵ and of complexes between ions and molecules,¹¹⁶ *e.g.* (H₂O)₂H⁺, although care needs to be taken when selecting the fragments involved. In the latter example, a CP correction scheme involving three fragments, where one of the fragments is H⁺, is required. This can explain why the CP correction was found to not improve accuracy in earlier calculations of complexes of this type.¹¹⁰

The CP correction has been shown to improve accuracy at longer separations¹⁰⁹ and when optimising the geometries of hydrogen-bonded dimers on CP corrected potential energy surfaces.¹¹⁷ A systematic study of the use of the CP correction for halogen-bonded complexes revealed that in some cases the corrected values were closer to experimental values although this was not always the case.¹¹⁸

Ideally, the accuracy of calculations would be improved by increasing the basis set size,¹⁰⁹ although this is not always viable due to increases in computational cost. Therefore, the CP correction should be recommended in the calculation of halogen-bonded complexes because the observation of uncorrected values being more accurate is due to the fortuitous cancelling of errors. Since little work has been done to examine the effect of the CP correction on halogen-bonded complexes, the calculations in this work were carried out both with and without the CP correction.

1.5.8 Localised Molecular Orbitals (LMOs)

The molecular orbitals generated from the Hartree-Fock equations are canonical and therefore have orbital energies associated with them. One disadvantage of these orbitals is that they are often delocalised over the whole molecule making them difficult to interpret in terms of bonds and lone pairs. It is, therefore, helpful to calculate localised molecular orbitals (LMOs), which can be achieved by mixing orbitals within a closed-shell Slater determinant, which is possible as the HF energy expectation remains unchanged under a nonsingular linear transformation of the occupied orbitals.

If the Slater determinant has the form shown in Equation 1-43, then the orbitals can be mixed using coefficients, d_{ij} , to give new orbitals φ'_i and the Slater determinant has the form shown in Equation 1-44.

$$\Psi = |\varphi_1\alpha\varphi_1\beta\varphi_2\alpha\varphi_2\beta\dots\varphi_n\alpha\varphi_n\beta| \quad (1-43)$$

$$\Psi' = |\varphi'_1 \alpha \varphi'_1 \beta \varphi'_2 \alpha \varphi'_2 \beta \dots \varphi'_n \alpha \varphi'_n \beta| \quad (1-44)$$

$$\text{where } \varphi'_i = \sum_{j=1}^n d_{ij} \varphi_j, \text{ and } E = \langle \Psi | \hat{H} | \Psi \rangle = \langle \Psi' | \hat{H} | \Psi' \rangle$$

The values of the coefficients d_{ij} can be selected in order to produce localised molecular orbitals (LMOs), which are generally associated with particular bonds or lone pairs of electrons and are, therefore, easier to interpret than canonical orbitals. One method used to choose the coefficients d_{ij} is to use the Edmiston-Ruedenberg localisation procedure.¹¹⁹ This involves maximising the self-repulsion energy given in Equation 1-45.

$$D(\varphi') = \sum_{i=1}^N \langle \varphi'_i \varphi'_i | g | \varphi'_i \varphi'_i \rangle \quad (1-45)$$

Another method is to use the Boys localisation procedure,¹²⁰ which involves maximising the sum of the distances between orbital centroids, defined in Equation 1-46 and Equation 1-47.

$$R_{ia} = \langle \varphi'_i | r_a | \varphi'_i \rangle \quad (1-46)$$

$$\sum_{i>j} \left[(R_{ix} - R_{jx})^2 + (R_{iy} - R_{jy})^2 + (R_{iz} - R_{jz})^2 \right] \quad (1-47)$$

The Edmiston-Ruedenberg method is more expensive computationally and although both methods typically produce similar localised orbitals, there are examples where the Edmiston-Ruedenberg method performs better than the Boys method. For example, the Boys method describes the B–C–B bond in the carborane 1,2-C₂B₄H₆ as a three-centre fractional bond, whereas the Edmiston-Ruedenberg method correctly describes the bond as an open three-centre bond.¹²¹

The use of LMOs to describe the bonding in halogen-bonded complexes can be highlighted by comparing the LUMO and an LMO of the complex between 1,4-diiidotetrafluorobenzene and ammonia (Figure 1-27), which was optimised at the B3LYP/aug-cc-pVDZ (aug-cc-pVDZ-PP on I) level of theory.¹²² The LUMO is delocalised over the entire complex, whereas the LMO is much easier to interpret and clearly shows the lone pair of electrons on the nitrogen directed toward the iodine atom with anti-bonding character in the C–I bond.

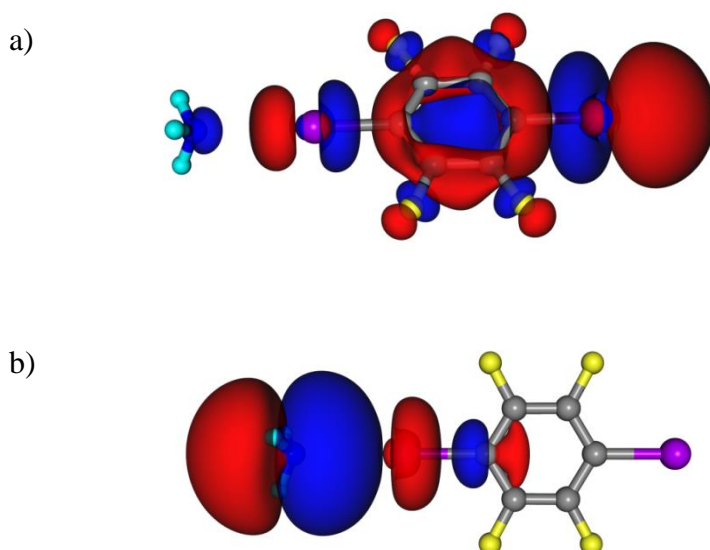


Figure 1-27: a) The LUMO and b) the LMO corresponding to the lone pair of electrons on nitrogen of the halogen-bonded complex between 1,4-diiidotetrafluoriodobenzene.¹²² Orbitals are represented as isosurfaces at orbital value ± 0.02 and ± 0.005 (e/bohr^3)^{-1/2}, respectively.

1.5.9 Natural Bond Orbital (NBO) Analysis

The natural bond orbital (NBO) analysis involves calculating orbitals that have maximum electron density and therefore describes the optimal Lewis structure by using a set of orthonormal orbitals.

The NBO analysis involves transforming the input orbital basis into localised basis sets *via* natural atomic orbitals (NAOs), hybrid orbitals (NHOs), bond orbitals (NBOs) and localised molecular orbitals (NLMOs) in the sequence shown in Equation 1-48.¹²³



The NAOs are constructed *via* an orthogonalisation procedure applied to the input orbitals. The NAOs are required to be orthogonal in order to avoid non-Hermitian terms in the Hamiltonian, which would be unphysical.

The orthonormal NAOs can be used in natural population analysis (NPA) to calculate the charges on the atoms. This is an improvement over the Mulliken population analysis, which uses a specific partitioning of the one-electron density matrix to calculate charges and is very dependent on the basis set chosen. The natural population, $q_i^{(A)}$, of orbital, $\varphi_i^{(A)}$, of atom A is calculated using Equation 1-49. $q_i^{(A)}$ is the diagonal element of the density matrix, T , within the NAO basis set.

$$q_i^{(A)} = \langle \varphi_i^{(A)} | \hat{T} | \varphi_i^{(A)} \rangle \quad (1-49)$$

The charge on atom A, $q^{(A)}$, is the sum of the natural populations of all orbitals (Equation 1-50).

$$q^{(A)} = \sum_i q_i^{(A)} \quad (1-50)$$

The natural Lewis structure of the molecule or complex under investigation can be obtained by searching for core orbitals, lone pairs and bond vectors in the density matrix. The core orbitals are identified as NAOs with occupancies greater than 1.999 e . Lone pairs are identified as vectors centred on one atom with occupancies greater than a preset threshold (typically 1.90). The bond vectors of the natural bond orbitals (NBO) are then identified as vectors over two atoms that exceed the density threshold. If the '3CBOND' keyword is specified, the search can be continued to include bond vectors over three atoms.

The NBOs can be transformed into natural localised molecular orbitals (NLMOs) by partitioning the density matrix into diagonal blocks corresponding to bonding and anti-bonding orbitals, and off-diagonal blocks corresponding to the mixing of filled and unfilled orbitals. Jacobi rotations are applied to the matrix to reduce elements in the off-diagonal blocks to zero giving NLMOs in the diagonal blocks.

NBO analysis can be used to calculate charge-transfer interactions due to hyperconjugative interaction between occupied and unoccupied orbitals. The interaction of these orbitals leads to a second-order lowering of the orbital energy (Figure 1-28). This stabilisation energy, $\Delta E_{\sigma\sigma^*}^{(2)}$, can be calculated using NBO analysis from the relevant element in the Fock matrix.

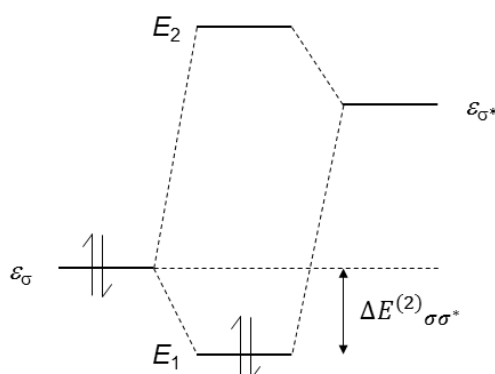


Figure 1-28: Donor-acceptor interaction between σ and σ^* NBOs.

NBO analysis has been used in the study of hydrogen-bonded complexes such as the water dimer¹²⁴ and OC...HF and CO...HF complexes.¹²⁵ In all cases NBO analysis reveals charge transfer from the lone pair of electrons on the Lewis base into the σ^* orbital of the H–O or H–F bond. There is an increase in the occupancy of the σ^* orbital and a decrease in the occupancy of the lone pair compared to the values in the monomers. The fact that the stabilisation energy caused by this charge-transfer of the OC...HF complex is 25.1 kJ mol⁻¹ greater than that of the CO...HF complex can explain why the former isomer is favoured.

NBO analysis has also proven useful in the investigation of halogen-bonded complexes.¹²⁶⁻¹³⁰ The charge on the halogen atom derived from NPA generally reflects its ability to act as a halogen-bond donor and the strength of the complexes it forms with Lewis bases. Similarly to studies with hydrogen-bonded complexes, there is an orbital interaction between the lone pair of electrons on the Lewis base and the σ^* anti-bonding orbital of the R–X bond with a second-order stabilisation energy that correlates with the strength of the complex. The increase in the occupancy of the σ^* orbital, results in a lengthening of the R–X bond in the complex compared to in the monomer, which can explain red-shifting of vibrational frequencies in these complexes.¹³¹ The stabilisation energy of the $n \rightarrow \sigma^*$ hyperconjugative interaction can be compared to the stabilisation energies of other interactions between orbitals in order to classify the interactions present in a complex. For example in the complex between BrCN and borazine (Figure 1-29) the stabilisation energy of the interaction between the lone pair of electrons on the Br atom and the B–N σ^* anti-bonding orbital in the borazine is greater than that of the interaction between the B–N σ^* bonding orbital and the Br–C σ^* anti-bonding orbital indicating that the interaction is a lone pair... π interaction rather than a halogen bond.¹³²

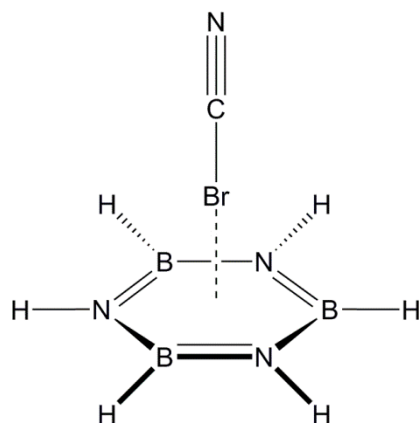


Figure 1-29: The complex between BrCN and borazine.¹³²

NBO analysis has also been used to show that halogen bonding in complexes of F_3C-Cl with Lewis bases, obeys Bent's rule,^{133,134} which states that atoms will maximise the s -character in orbitals directed toward electropositive substituents and the p -character in orbitals directed toward electronegative substituents. Upon complex formation the percentage contribution of the C atom in the C–Cl bond, which is a measure of the polarisation of the bond, increases.¹³⁵

1.5.10 Application of Quantum Chemical Methods to Halogen Bonding

Quantum chemical methods are useful in the investigation of halogen-bonded complexes because they can provide a wealth of information about the nature of the interaction. The results of these calculations agree with experimental observations that the complexes are directional and that they increase in strength as the halogen becomes more polarisable,¹³⁶ with increasing dipole moment of dihalogens¹³⁷ and with the increase of the basicity of the Lewis base. The similarity to hydrogen-bonded complexes has also been recognised¹³⁸ with binding energies falling in a similar range; from the weak complexes between F_2 and ammonia to the complexes of BrF with trimethylamine, which has a binding energy of 83.7 kJ mol^{-1} .¹³⁹ Calculations of spectra have revealed that for complexes of dihalogens, XY, with simple Lewis bases,¹³⁸ or the π electrons of ethene and ethyne,¹³⁷ the IR signal corresponding to the X–Y bond stretch red shifts upon complex formation.

Calculations can also reveal information about the relative contributions to the interaction energy of the halogen-bonded complexes. Similar to the debate on the nature of the hydrogen bond,¹⁴⁰ there is some debate about whether the halogen-bond interaction is due to electrostatics, polarisation, dispersion, charge-transfer or exchange-repulsion. Bent commented on the range of terms that were used to describe the interaction in donor-acceptor complexes in the 1960s²⁸ and expected that all terms were complementary. Although some of these terms are no longer used to describe halogen bonding, a range of phrases are still used to describe the interaction. The definition of the halogen bond states that the interaction is primarily electrostatic in nature but polarisation, charge-transfer and dispersion play important roles.¹ This agrees with observations made in calculations of complexes with chlorine as the halogen-bond donor, which showed that electrostatics dominated, although the contributions of dispersion and charge-transfer were not insignificant.¹⁴¹

It has been argued that this debate is unnecessary since only the total interaction energy is observable experimentally.¹⁴² It has also been argued that an electrostatic interaction includes a degree of polarisation and that charge-transfer is simply an extreme case of polarisation and therefore electrostatics/polarisation and dispersion are sufficient for describing the nature of the halogen bond.¹⁴³ This was highlighted in the symmetry-adapted perturbation theory (SAPT) analysis of the complexes between substituted halobenzenes and acetone previously discussed in Section 1.1.1 (Figure 1-10), which was used to calculate the different contributions to the interaction energy, where electrostatic and dispersion terms were found to dominate the interaction energy.¹⁴⁴ Both terms increase as the strength of the halogen bond increases and the electrostatics term was found to dominate at the optimum separation for all complexes. As the Br...O separation increased, the dispersion term was found to dominate over electrostatics.

SAPT(DFT) analyses were carried out for complexes between Lewis bases and ClF. While electrostatics were found to dominate the binding energy of the complex in

the optimised geometry, the dispersion and polarisation terms played a significant role in the position of the CIF molecule relative to the Lewis base.¹⁴⁵ This contradicts the σ -hole concept, which suggests that the directionality of the halogen bond is an electrostatic phenomenon. It should be noted that the halogen-bond donor in this study is relatively weak and it would be expected that interactions involving iodine or bromine donors would be dominated by electrostatics.

Although electrostatics have been observed to dominate the interaction energy, charge-transfer should not be discounted since calculations of halogen-bonded complexes of dihalogens with ammonia have revealed that charge-transfer increases linearly with the strength of the complex.¹²⁸

A characteristic of the hydrogen bond is that it is cooperative with the presence of additional interactions strengthening the interactions.⁶¹ Calculations can provide information about whether this cooperativity is also observed for halogen-bonded complexes. Cooperativity has been observed for complexes of the type $XY\cdots HNC\cdots XY$ ($X, Y = F, Cl, \text{ and } Br$) where the presence of both hydrogen and halogen bonds increases the strengths of the individual interactions.¹⁴⁶ Halogen bonds have also been observed to be cooperative with lithium bonds, where lithium acts as a Lewis acid,¹⁴⁷ and there are anion $\cdots\pi$ and lone pair $\cdots\pi$ interactions.¹⁴⁸ Another computational study focussed on the cooperativity between halogen bonding and π - π stacking in the complexes of iodofluorobenzenes with pyridine.¹⁴⁹ The relative strengths of the interactions vary with the strengths of the halogen-bond donors with halogen bonding being stronger for strong donors and π - π stacking being stronger for weaker halogen-bond donors, in agreement with observations reported following searches of the CSD.¹⁵⁰ The cooperativity observed increases as the strengths of the individual interactions increase, therefore there is a linear relationship between the Hammett parameter of the substituent on the halogen-bond acceptor and the change in energy due to cooperativity.¹⁵¹

Conversely to the cooperativity observed in other systems, the addition of a second or third halogen-bond in complexes of di- and triiodofluorobenzenes with ammonia led to a lengthening of the N...I separation, although this was a very small effect, with elongations of approximately 1%.¹²²

Calculations have also been used to investigate the effects of different substituents on the halogen-bond donor and acceptors on the interaction. In agreement with experimental results,¹²² the introduction of electron-withdrawing fluorine substituents on halobenzene halogen-bond donors leads to an increase in the strength of the interaction.⁴⁰ Other electron-withdrawing substituents have also been observed to strengthen the interaction, and electron-donating substituents to weaken the interaction. Hammett parameters of the substituents can be correlated with the interaction energies of these complexes.¹⁵² These substituent effects are due predominantly to electrostatics because the substituent changes the size of the σ -hole on the halogen-bond donor.¹⁵³ A linear relationship between the interaction energy, the size of the σ -hole on the halogen-bond donor and the minimum of the electrostatic surface potential of the halogen-bond acceptor has been proposed¹⁵⁴ making it possible to predict the binding energies of complexes. The relationship is empirical in nature, with fitted coefficients, so a test of the accuracy of the predicted interaction energies is required.

Other calculations have revealed that the presence of a lithium substituent on the halogen-bond acceptor can increase interaction strengths,¹⁵⁵ whereas if on the halogen-bond donor, it decreases the interaction strength.¹⁵⁶ Methyl substituents have also been observed to have a significant effect on halogen-bond strength. Introduction of a methyl substituent on the halogen-bond acceptor in the complex $\text{H}_2\text{S}\cdots\text{XF}$ to form $\text{CH}_3(\text{H})\text{S}\cdots\text{XF}$ increases interaction strength so that it becomes stronger than the halogen bond in the complex $\text{H}_2\text{O}\cdots\text{XF}$.¹⁵⁷

1.6 Applications of Halogen Bonding

1.6.1 Crystal Engineering

Crystal engineering is the branch of supramolecular chemistry concerned with the solid state and involves the design of crystal structures by considering the self-assembly of the constituents *via* intermolecular interactions during the crystallisation process.¹⁵⁸ In order to design a crystal structure, a supramolecular retrosynthesis can be carried out in which synthons are determined and the interactions between them are predicted.¹⁵⁹ It can, however, be difficult to predict how these interactions result in a given crystal structure due to the nature of the crystallisation process, during which molecules form clusters which increase in size until a critical nucleus forms, after which crystal growth can occur. Although it may be possible to predict the structure of a small cluster, this does not necessarily relate to the structures of larger clusters or the morphology of the resulting crystal.

The hydrogen bond has proven to be a useful interaction in crystal engineering since it is strong and directional making it easier to predict final structures. The halogen bond is comparable in strength and has greater directionality than its hydrogen bond counterpart, so it is logical that it has been utilised in the area of crystal engineering. As well as being able to predict halogen bonds to Lewis bases, interactions between halogen atoms of the type $C-X\cdots X-C$ are known to form one of two motifs shown in Figure 1-30. Type I interactions are where the halogen atoms approach one another at the same angle. This interaction is a weak interaction driven predominantly by dispersion forces and is not considered as a halogen bond since the σ -hole is not involved in the interaction.¹⁶⁰ Type II interactions are between the σ -hole on one halogen atom and the equatorial region of negative electrostatic potential on the other halogen atom. This interaction is electrostatic in nature and is considered as a halogen bond.¹⁶¹

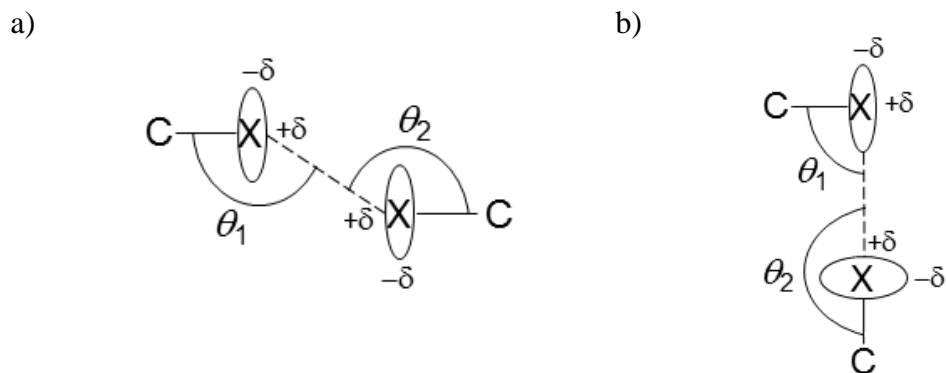


Figure 1-30: a) Type I and b) type II interaction between two halogen atoms.

Many comprehensive reviews about the application of halogen bonding in crystal engineering exist,^{35,161-164} and the Milan group has made the most substantial contribution to this area of halogen bonding research. Initial work by the group focused on structures formed between perfluorocarbon(PFC) and hydrocarbon(HC) compounds (Figure 1-31),¹⁶⁵ where it was noted that the I...N halogen bond was responsible for the stabilisation of a crystal structure between the incompatible perfluorocarbon and hydrocarbon entities.

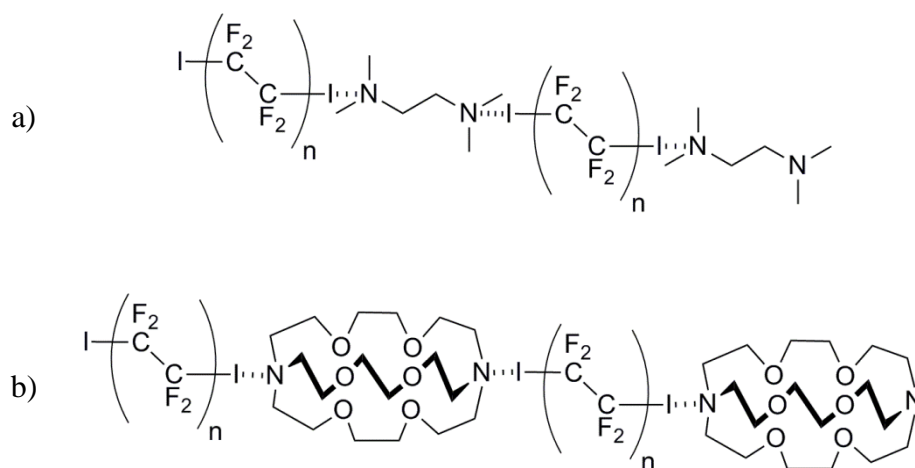


Figure 1-31: Halogen-bonded complexes between perfluorocarbon and hydrocarbon compounds. a) Complex between 1,2-diiodotetrafluoroethane and N,N,N',N'-tetramethylethylenediamine and b) complex between 1,2-diiodotetrafluoroethane and K2.2.2.¹⁶⁵

It is possible to produce infinite chains of halogen-bonded molecules by using bidentate halogen bond donor and acceptor. These can arrange either in a linear fashion or in a herringbone arrangement depending on the angles between the halogen atoms in the halogen-bond donor.¹⁶⁶ For example, the complex of 4,4'-bipyridine with 1,4-dibromotetrafluorobenzene, where the angle between the two bromine atoms is 180° , has a linear arrangement (Figure 1-32a) whereas the complex with 1,3-dibromotetrafluorobenzene, where the angle between the bromine atoms is 120° has a herringbone arrangement (Figure 1-32b).¹⁶⁷

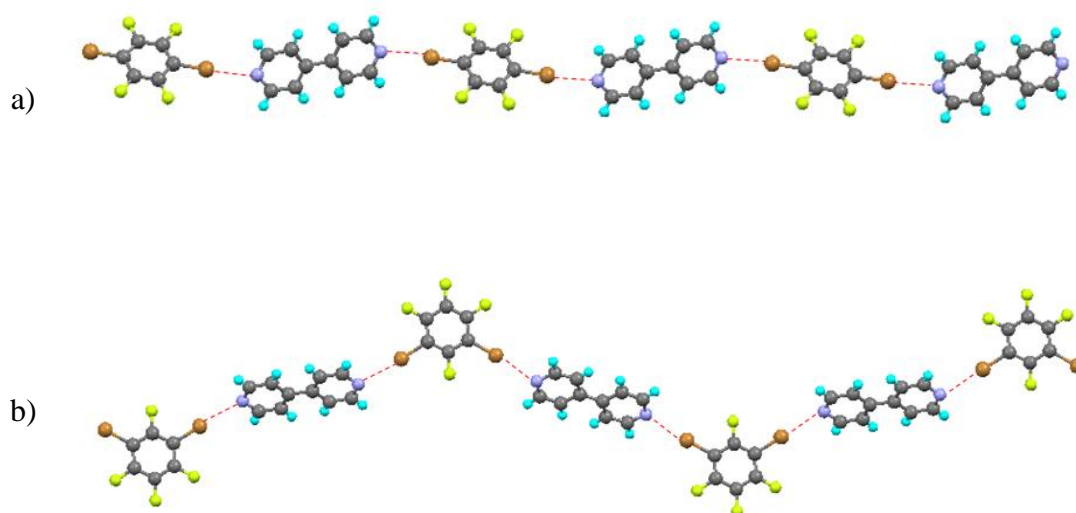


Figure 1-32: Halogen-bonded complexes of a) 1,4-dibromotetrafluorobenzene and b) 1,3-dibromotetrafluorobenzene with 4,4'-bipyridine.¹⁶⁷

An example of a three-dimensional network that can be formed by crystal engineering is an adamantanoid, which can be realised using tetradentate molecules with two halogen-bond donor sites and two halogen-bond acceptor sites (Figure 1-33).¹⁶⁸ These molecules have large spaces in their centres which make them porous and are penetrated by solvent molecules.

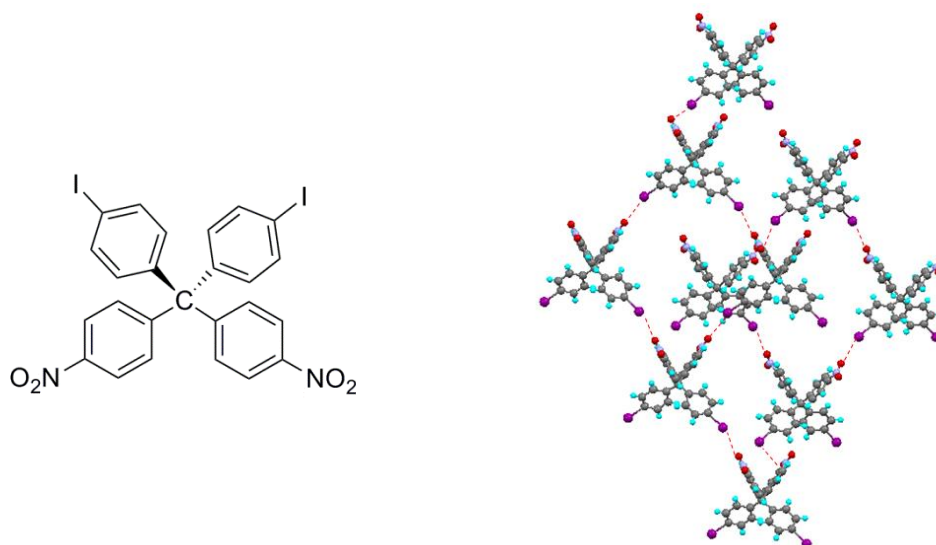


Figure 1-33: 4,4'-Diiodo-4'',4''-dinitrotetraphenylmethane and the adamantoid structure formed in the crystal structure.¹⁶⁸ I...O interactions are highlighted in red.

Halide anions have been shown to be effective halogen-bond acceptors and are capable of halogen bonding with weak halogen-bond donors that are not bound to a significantly electron-withdrawing group.¹⁶⁹ Numerous architectures are possible with halide anions since they have a variety of coordination spheres and geometries, making it possible to form various one-dimensional chains, two-dimensional nets and ribbons and three-dimensional structures. For example, the bromide ion in $\text{Ph}_4\text{P}^+\text{Br}^-$ acts as a tridentate halogen-bond acceptor and its complex with 1,4-diiidotetrafluorobenzene has a honeycomb-like architecture (Figure 1-34a).¹⁷⁰ In the equivalent complex with $\text{Ph}_4\text{P}^+\Gamma^-$, the iodide ion acts as a T-shaped tridentate node. The difference in angle between interactions at the node results in a different architecture and a rectangular array is observed (Figure 1-34b).

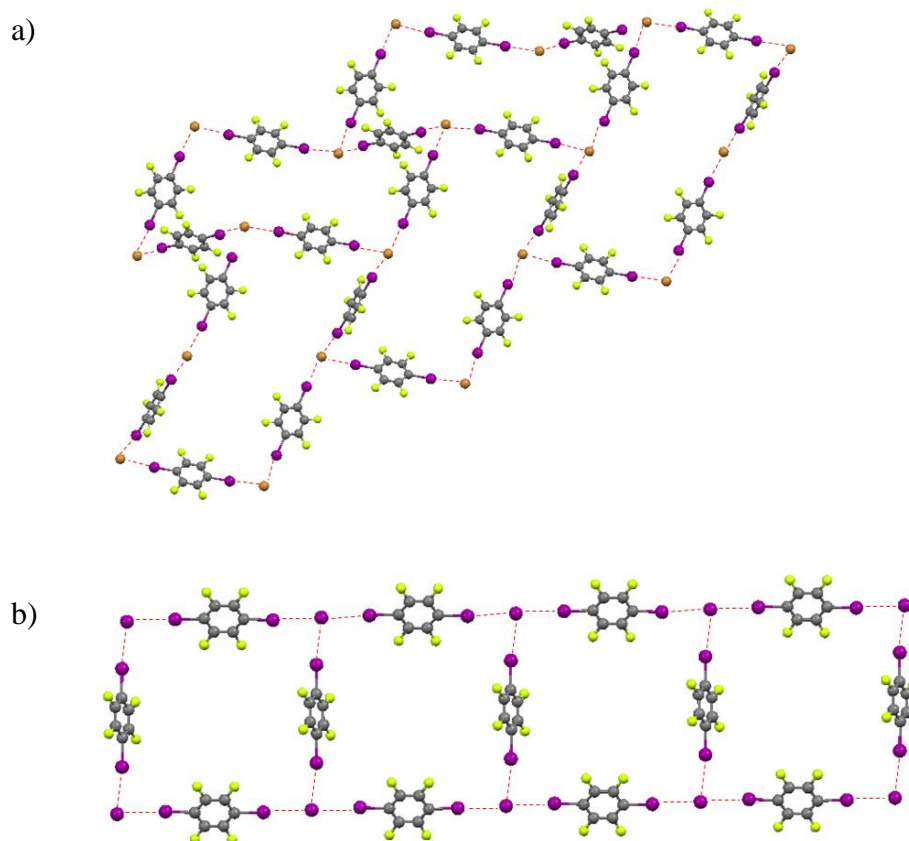


Figure 1-34: The two-dimensional architectures in the halogen-bonded complexes of 1,4-difluorobenzene with a) tetraphenylphosphonium bromide and b) tetraphenylphosphonium iodide.¹⁷⁰ $I\cdots Br^-$ and $I\cdots I^-$ interactions are highlighted in red and cations and solvent molecules have been omitted for clarity.

Application-driven crystal engineering involving halogen bonding is also prevalent. For example, a system that binds selectively to diiodoperfluoroalkanes by size matching has been developed. Crystallising the iodide salt of a bis(trimethylammonium) alkane of a certain chain length with a series of diiodoperfluoroalkanes produces solely the crystal structure in which the length of the diiodoperfluoroalkane halogen bonded to the iodide anions matches the length of the bis(trimethylammonium) alkane cation, such as in the example shown in Figure 1-35.¹⁷¹

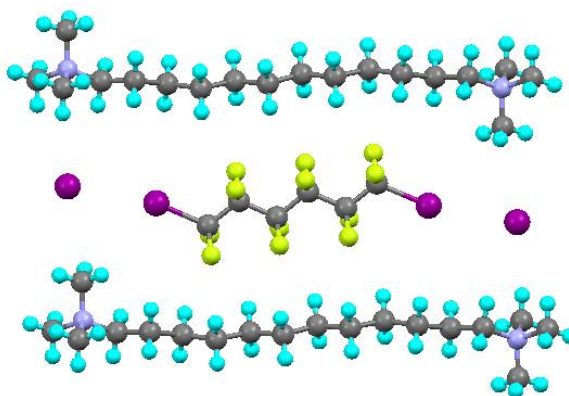


Figure 1-35: Molecular structure of 1,6-diiodoperfluorohexane with bis(trimethylammonium)dodecane.¹⁷¹

1.6.2 Anion Recognition

Since halide ions are good halogen-bond acceptors, it is possible to use halogen bonding in the design of anion receptors. The ability of a receptor to bind particular anions and the selectivity of this binding can be determined from the association constant calculated using NMR titrations.

A tridentate halogen-bond donor, shown in Figure 1-36, was found to preferentially bind Γ^- over Br^- and Cl^- anions,¹⁷² which is an unexpected trend since iodoperfluoroalkanes were found to bind halide anions in the order $\text{Cl}^- > \text{Br}^- > \Gamma^-$.¹⁷³ This is probably due to an improved size-matching with the iodide anion compared to the smaller bromide and chloride anions.

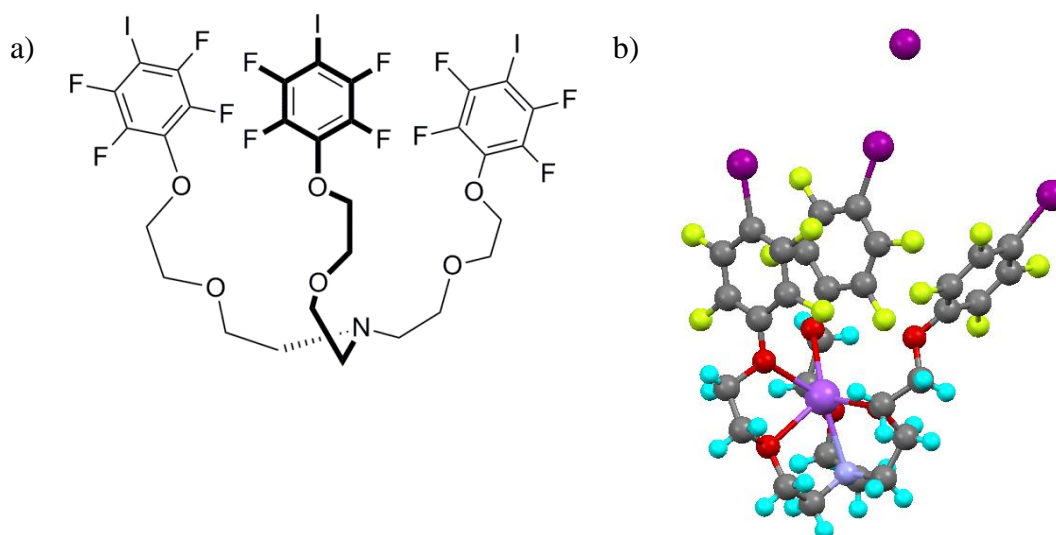


Figure 1-36: a) The structure of a tridentate receptor and b) the molecular structure of the receptor bound to NaI.¹⁷²

Another tridentate receptor that can bind anions *via* halogen bonding is shown in Figure 1-37. Although the receptor with X = I and perfluorinated phenyl rings favoured binding to halide anions over oxoanions, it showed different affinities to the halides with chloride preferred over bromide and iodide anions.¹⁷⁴ Decreasing the number of electron-withdrawing fluorine substituents on the phenyl rings led to a decrease in the binding affinity to chloride anions since the strength of the iodine as a halogen-bond donor decreased. Changing the halogen atom to bromine or chlorine resulted in no binding to chloride anions indicating that a sufficiently strong halogen-bond donor was required.^{175,176}

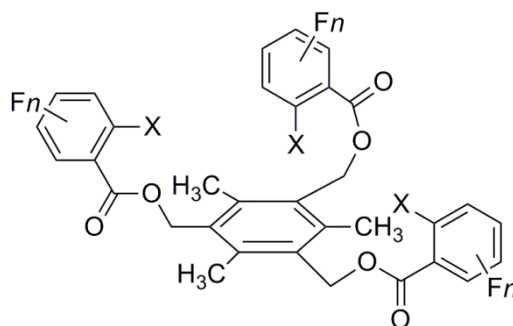


Figure 1-37: A tridentate anion receptor based on 2-iodoperfluorobenzoic acid.¹⁷⁴

A receptor based on urea, which contained both hydrogen and halogen-bond donors was found to have different affinities to anions (Figure 1-38).¹⁷⁷ Benzoate and dihydrogenphosphate oxoanions were found to have high binding affinities with both X = F and X = I. Halide anions were found to bind only to the receptor with an iodine halogen-bond donor with preferences being the same as those for the receptor in Figure 1-37.

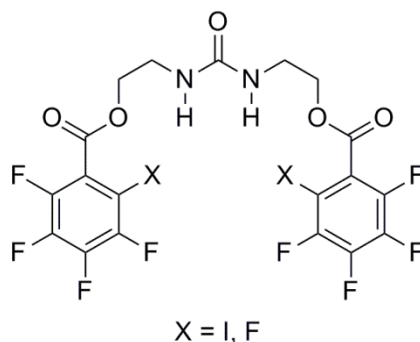


Figure 1-38: A urea-based receptor with both hydrogen- and halogen-bond donors.¹⁷⁷

A similar observation was observed for iodotriazole- and triazole functionalised zinc(II) metalloporphyrins, which favour binding to oxoanions (Figure 1-39). The presence of an iodine halogen-bond donor increases the affinity to halide anions with chloride anions favoured.¹⁷⁸

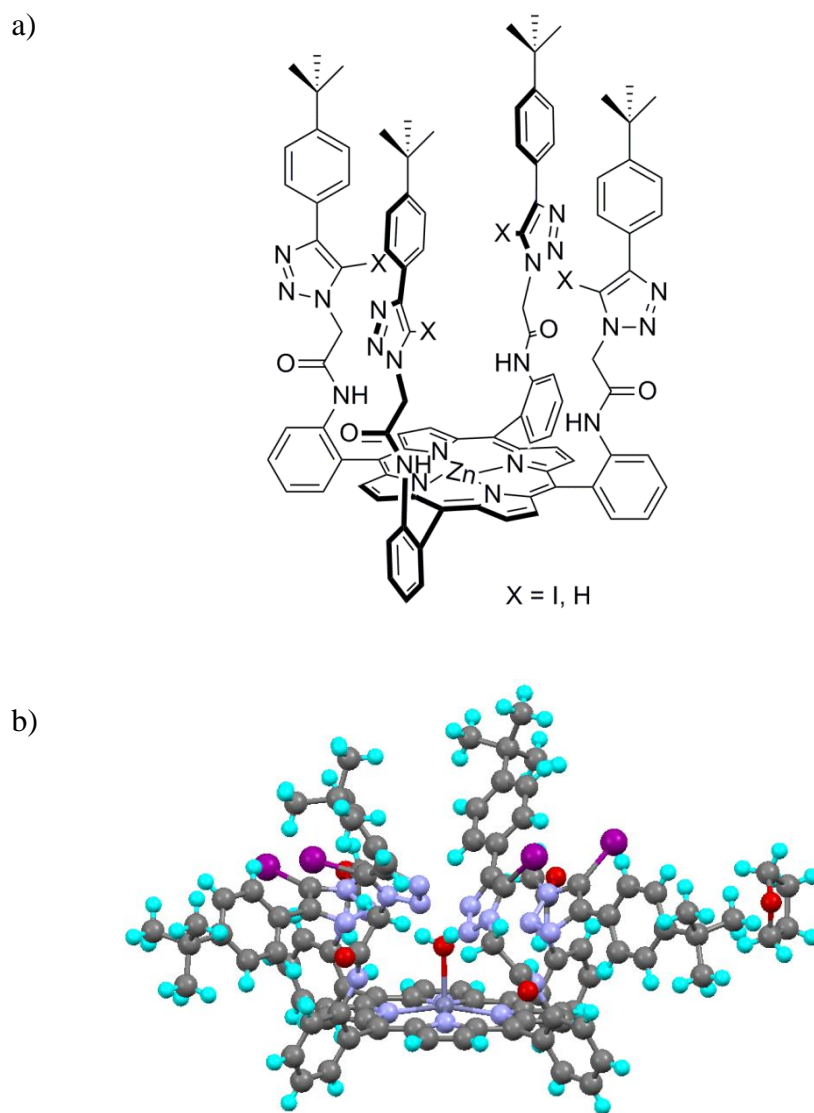


Figure 1-39: a) The structure of triazole functionalised zinc(II) porphyrins and b) the molecular structure of an iodotriazole functionalised zinc(II) porphyrin.¹⁷⁸

Halogen-functionalised imidazolium macrocycles have been observed to be excellent halogen-bond donors forming short halogen bonds to halide anions.¹⁷⁹ Figure 1-40 shows complexes with $\text{Cl}\cdots\text{Br}^-$ and $\text{I}\cdots\text{Br}^-$ separations of 3.236(1) and 2.728(4) Å, respectively, which correspond to 90% and 81% of the sum of the van der Waals radii, respectively.

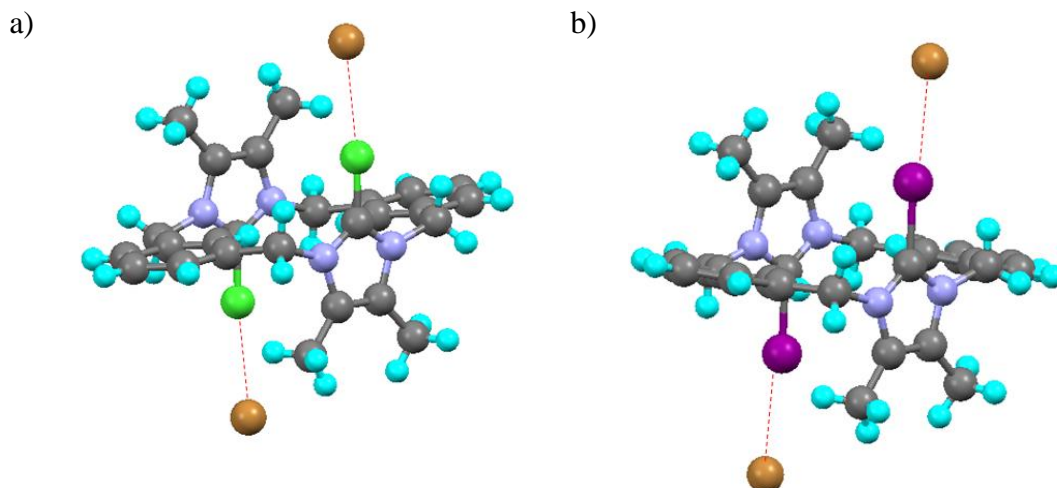


Figure 1-40: Molecular structures of complexes a) of an *anti*- bischloroimidazoliophane macrocycle and b) an *anti*-bisiodoimidazoliophane macrocycle with bromide anions.¹⁷⁹

The *syn*-isomer of a bis-bromoimidazoliophane receptor has been shown to bind bromide ions selectively over other halide anions (Figure 1-41a).¹⁸⁰ Comparison of this halogen bond receptor to its hydrogen bond analogue reveals that this selectivity is increased when the bromine halogen-bond donors are present. The space-filling diagram shown in Figure 1-41b suggests that this selectivity is due to the excellent size compatibility between the receptor and the bromide anion, highlighting that the shape of the receptor can also play a role in its selectivity of anions.

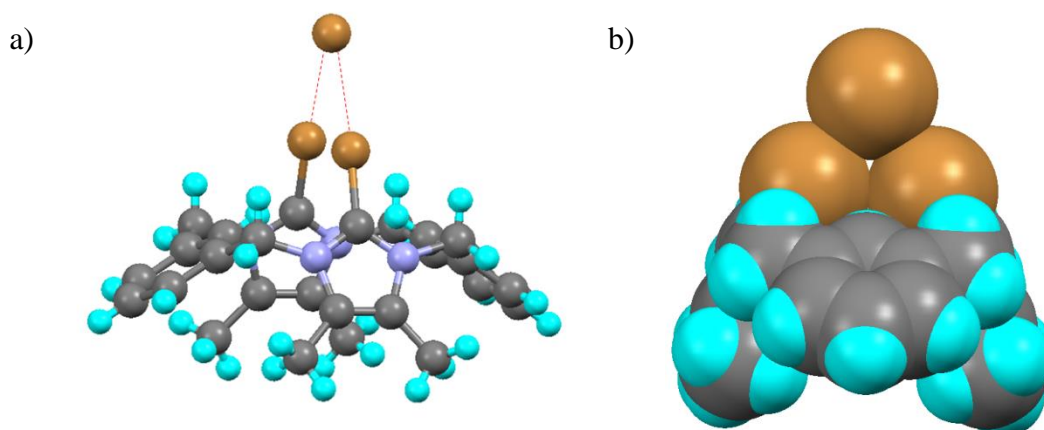


Figure 1-41: a) The molecular structure and b) space-filling diagram of a *syn*-bis-bromoimidazoliophane receptor with a bromide anion.¹⁸⁰ $\text{Br}\cdots\text{Br}^-$ interactions are highlighted in red and solvent molecules have been omitted for clarity.

1.6.3 Catenane and Rotaxane Synthesis

Catenanes, which involve two interlocked rings, and rotaxanes, where a stoppered axle penetrates a macrocycle, have received a lot of attention due to their application in molecular machines.¹⁸¹ Their synthesis typically involves templating using either copper(I) ion, anions or non-covalent interactions, such as hydrogen bonding. Recently, halogen bonding has been observed to be an effective interaction for the synthesis of catenanes and rotaxanes.

A bromine-functionalised imidazolium thread can form a pseudorotaxane with an isophthalamide macrocycle *via* chloride anion templating (Figure 1-42).¹⁸² Both the bromine atom in the thread and amide protons in the macrocycle interact with the chloride anion via halogen and hydrogen bonding, respectively. Comparison of this thread with its hydrogen-bond donor analogue, reveals that the presence of the bromine halogen-bond donor increases the strength of the interaction with the chloride ion template used for the formation of the pseudorotaxane. The stability of the pseudorotaxane can be increased by using an iodine-functionalised imidazolium thread, which can form stronger halogen bonds with the halide anion.¹⁸³

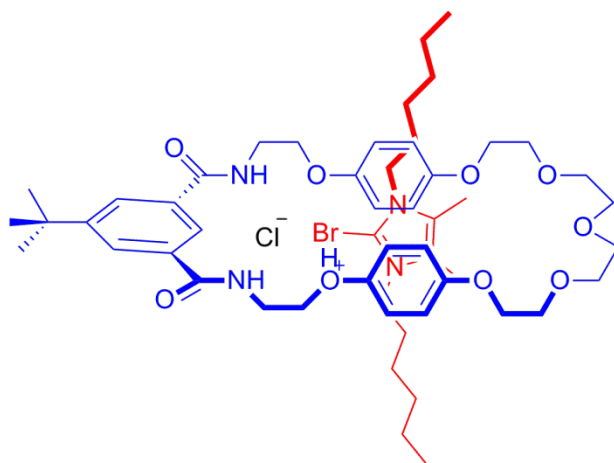


Figure 1-42: The pseudorotaxane formed by chloride ion templating of a bromine functionalised imidazolium thread and an isophthalamide macrocycle.¹⁸²

A rotaxane was formed using a 5-iodo-1,2,3-triazolium thread and the isophthalamide macrocycle used before.¹⁸⁴ Bromide ions were found to yield higher association constants than other halide anions. The molecular structure of the rotaxane (Figure 1-43) confirms that $I\cdots Br^-$ halogen bonds and $N-H\cdots Br^-$ hydrogen bonds are involved in the formation of the rotaxane.

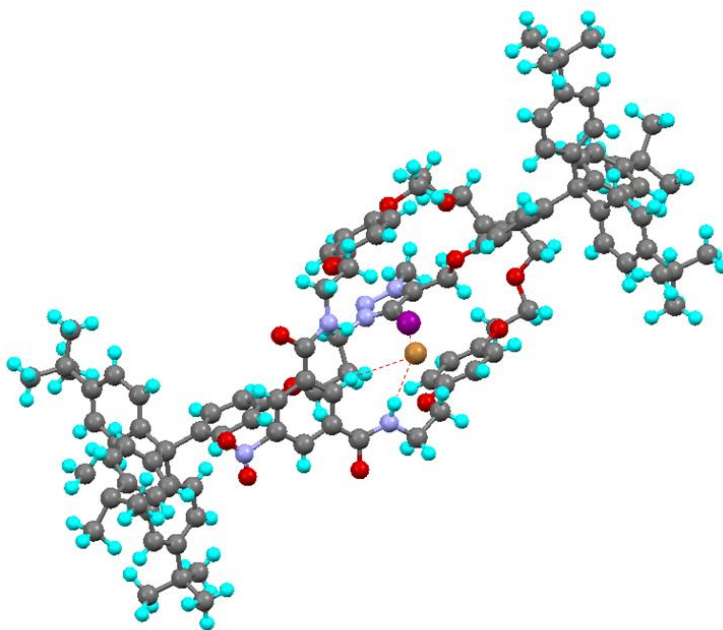


Figure 1-43: The molecular structure of the rotaxane formed between a 5-iodo-1,2,3-triazolium thread and an isophthalamide macrocycle.¹⁸⁴ $I\cdots Br^-$ and $N-H\cdots Br^-$ interactions are highlighted in red.

The association constant of bromide ions with this rotaxane is $1251(10) \text{ mol}^{-1}\text{dm}^3$, which is significantly higher than the association constant of chloride ions with the iodo-imidazolium based pseudorotaxane at $639(105) \text{ mol}^{-1}\text{dm}^3$. This could be due to the 5-iodo-1,2,3-triazolium being more effective at polarising the iodine atom,¹⁸⁵ however, comparison of halogen-bonded complexes of iodo-imidazolium and 5-iodo-1,2,3-triazolium with chloride anions reveals that the $I\cdots Cl^-$ separations are identical (Figure 1-44). A similar observation is made when complexes with iodide anions are compared.

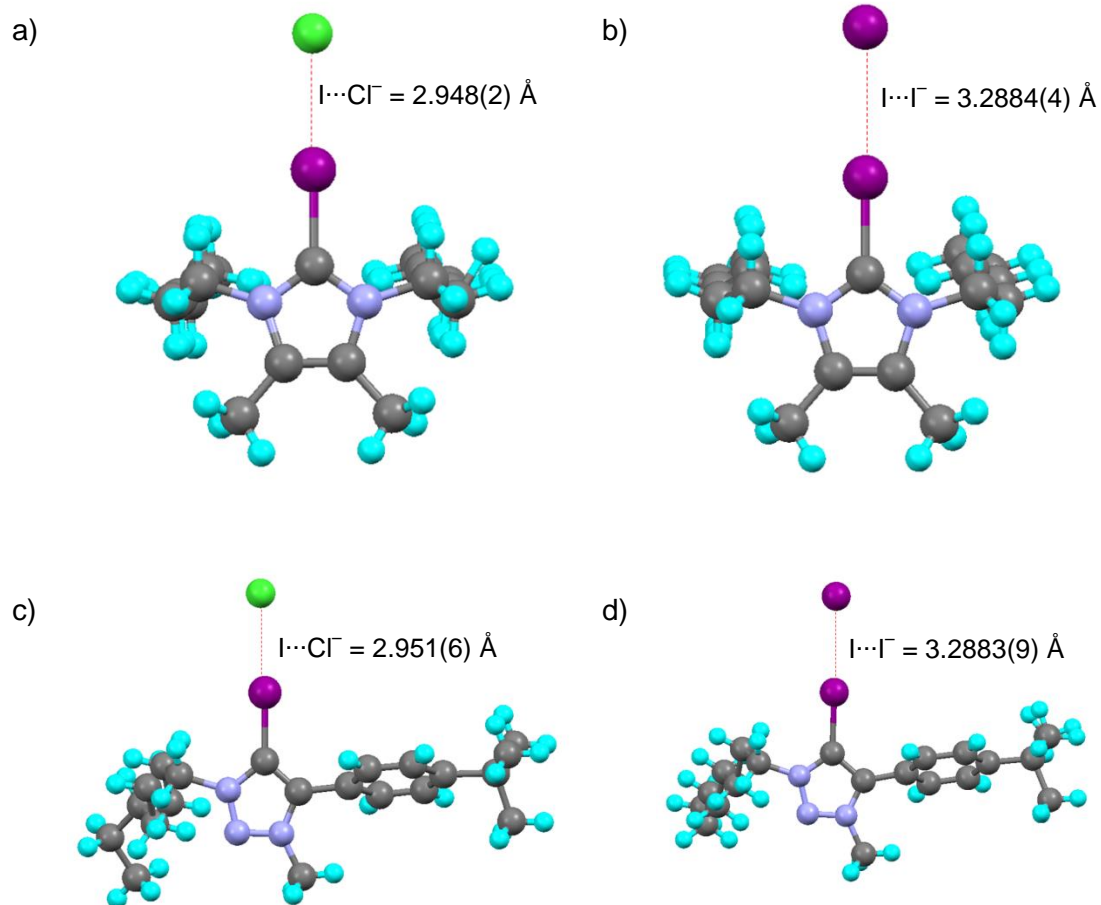


Figure 1-44: Molecular structures of 1,3-dihexyl-2-iodo-4,5-dimethylimidazolium a) chloride and b) iodide¹⁸³ and of 4-(4-(t-butyl)phenyl)-3-methyl-1-octyl-5-iodo-1,2,3-triazolium c) chloride and b) iodide.¹⁸⁴

Bromine-functionalised imidazolium acting as a halogen-bond donor has also been used in the synthesis of catenanes (Figure 1-45).¹⁸⁶ The bromine atoms on two macrocycles form a halogen bond with a bromide anion template and a cyclising reaction leads to the interlocking of the two cycles.

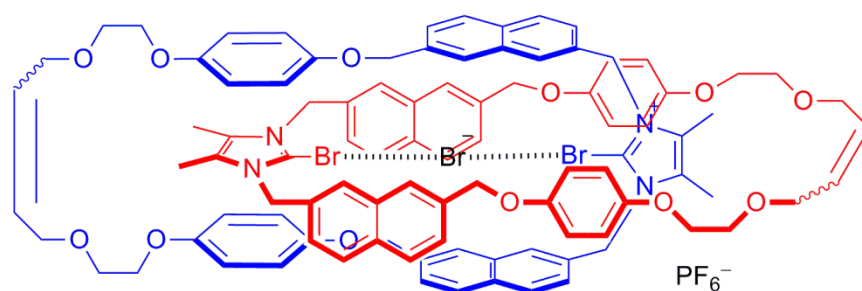


Figure 1-45: A catenane formed between two bromine functionalised imidazolium macrocycles formed by halogen bonding to a bromide anion.¹⁸⁶

A catenane has also been formed using a single halogen bond between an iodine atom in an iodo-pyridinium group on the thread and a pyridine group in the macrocycle (Figure 1-46).¹⁸⁷ The yield of the synthesis of this catenane was low, which could be due to the fact that only one interaction is used to template its synthesis.¹⁸¹ Molecular dynamics (MD) simulations predicted an I...N separation of approximately 3.19 Å, which is 90% of the sum of the van der Waals radii. For an interaction with a pyridine base, this is relatively weak, which could be due to the fact that the iodine atom is not polarised by the presence of electron-withdrawing substituents. Although the MD simulations recognise the presence of a halogen bond in the catenane, they are not sufficiently accurate to give exact values for the I...N separations but can be used to model trends in observations. Therefore, in order to obtain useful information from the MD simulations, other catenanes with different halogen-bond donors should be modelled in order to predict the strongest interaction and therefore the most stable catenane.

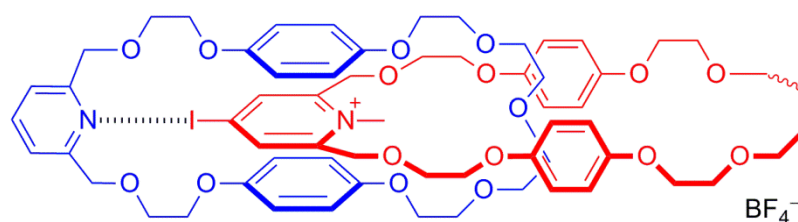


Figure 1-46: Catenane formed by a halogen bond between an iodopyridinium and a pyridine group on two macrocycles.¹⁸⁷

1.7 Halogen-Bonded Liquid Crystals

1.7.1 Introduction to Liquid Crystals

Liquid crystals is the fourth state of matter that occurs during the transition from the crystalline phase to the isotropic liquid phase for some molecules.¹⁸⁸ They can be classified as being either *thermotropic*, where the liquid-crystalline phases are achieved by varying the temperature of the system, or as *lyotropic*, where varying the concentration of the constituents in a solvent leads to the liquid-crystalline phases.¹⁸⁹ They combine the order and optical properties of a crystal and the fluidity of a liquid and it is these properties that make them of interest in applications such as displays,¹⁹⁰ medicine¹⁹¹ and nanostructures.¹⁹²

Molecules that have liquid-crystalline phases are typically anisotropic in nature. Key examples are rod-like, also known as calamitic, and disk-like, also known as discotic, molecules, which have one axis that is very different in dimensions from the other two.¹⁹³ Some examples of calamitic and discotic liquid crystals are shown in Figure 1-47.¹⁹⁴

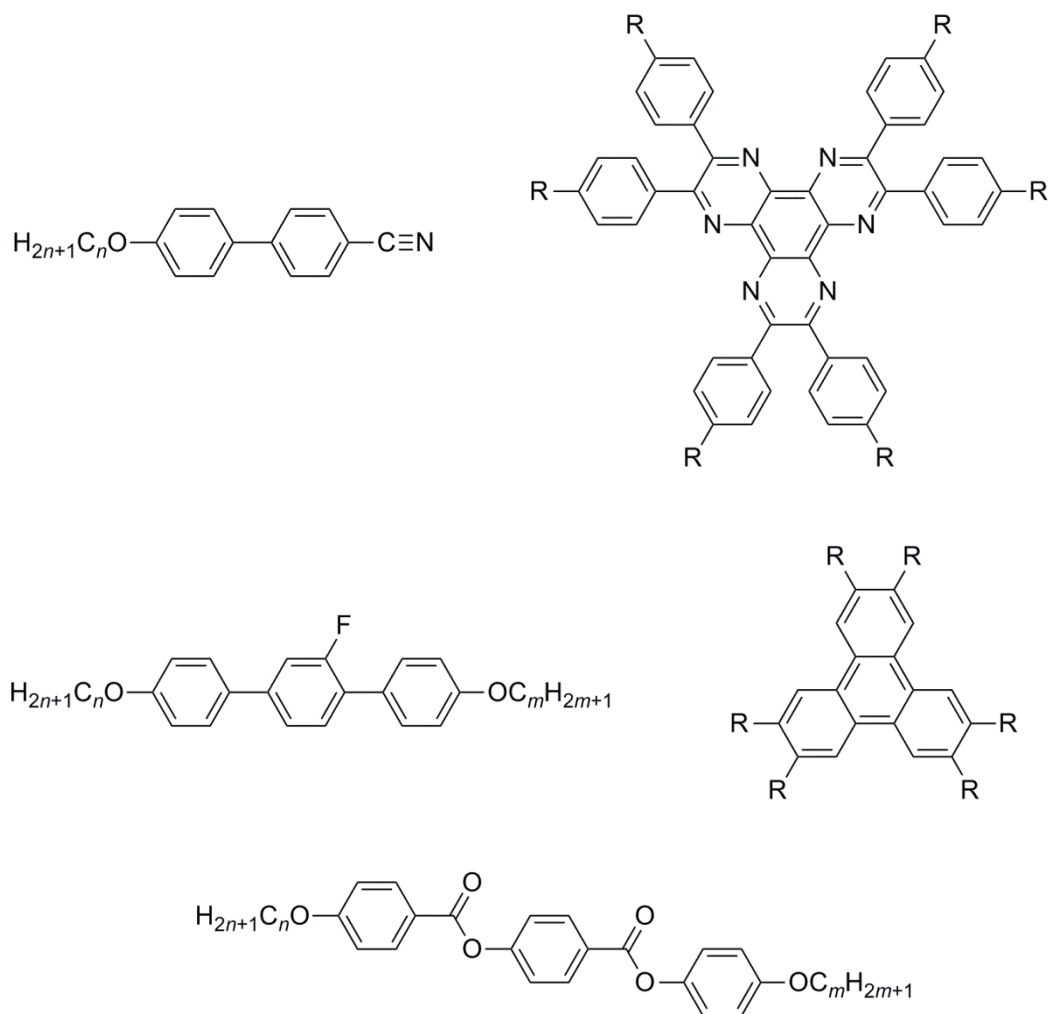


Figure 1-47: Examples of calamitic and discotic liquid crystals.¹⁹⁴

The most common liquid-crystalline phases observed for calamitic liquid crystals are nematic (N) and smectic (Sm) phases (Figure 1-48). In the N phase, the molecules have orientational order but are positionally disordered. The molecules are aligned in one common direction, known as the director, \mathbf{n} . The smectic A (SmA) phase involves molecules loosely arranged in layers with no ordering within the layer; the director of the molecules is orthogonal to the layers. In smectic C (SmC) phases the molecules are tilted with respect to the layers.¹⁹⁵

Discotic liquid crystals typically form columnar phases, where the molecules arrange themselves in columns, which are typically in a hexagonal arrangement. Cubic phases are observed in lyotropic liquid crystals and for block copolymers. These

phases have been observed in liquid crystals involving non-covalent interactions, so will not be discussed further.

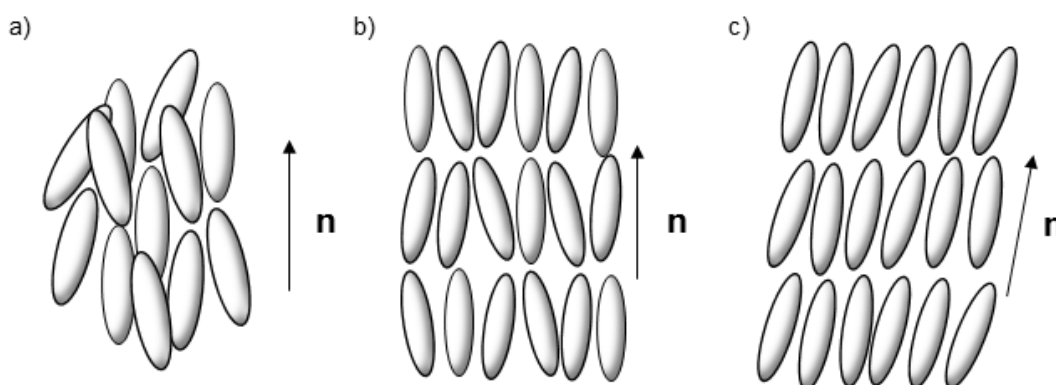


Figure 1-48: Representation of the arrangement of calamitic mesogens of a) nematic (N), b) smectic A (SmA) and c) smectic C (SmC) phases.

Liquid crystals have different refractive indices along different axes and the difference between the indices is known as the birefringence (Δn). This birefringence makes it possible to use polarised optical microscopy to identify the phases formed. The microscope has two polarisers that are crossed such that light would not normally pass through (Figure 1-49). The light passes through the first polariser to produce a plane of polarised light, which forms two refracted rays when it passes through the sample corresponding to the two refractive indices. These two rays interfere with one another and this interference pattern provides an optical texture that is diagnostic of the liquid crystal phase.

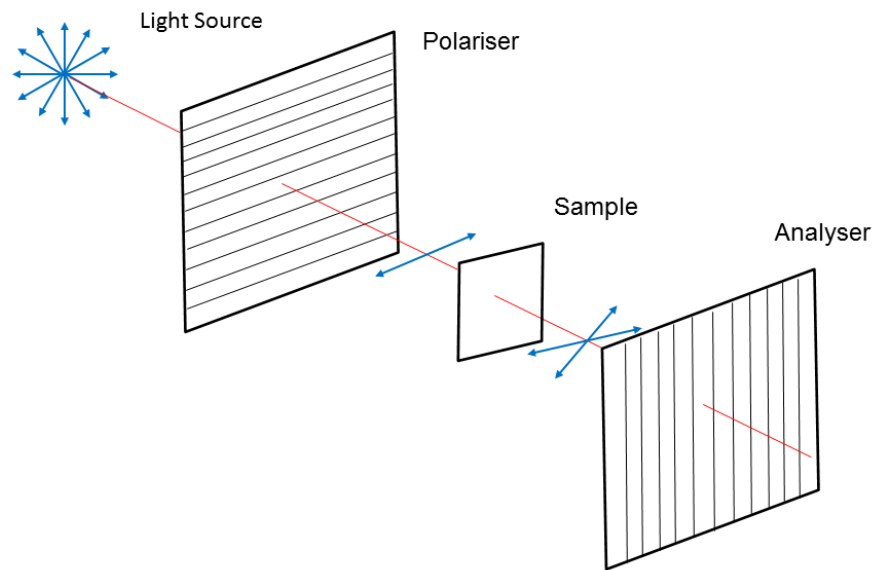


Figure 1-49: Schematic diagram of a polarising optical microscope.

An optical texture that is characteristic of the N phase is the Schlieren texture (Figure 1-50a), where there are black brushes present that correspond to regions where the director in the phase is parallel or perpendicular to the plane of polarised light.¹⁹⁶ The points where the brushes meet are known as point singularities and they can have two or four brushes emanating from them. These singularities originate from defects within the N phase, where the director rotates about this point. The Schlieren texture is also observed for SmC phases, however, there tends to be more point singularities and only four brushes are observed to originate at each point.

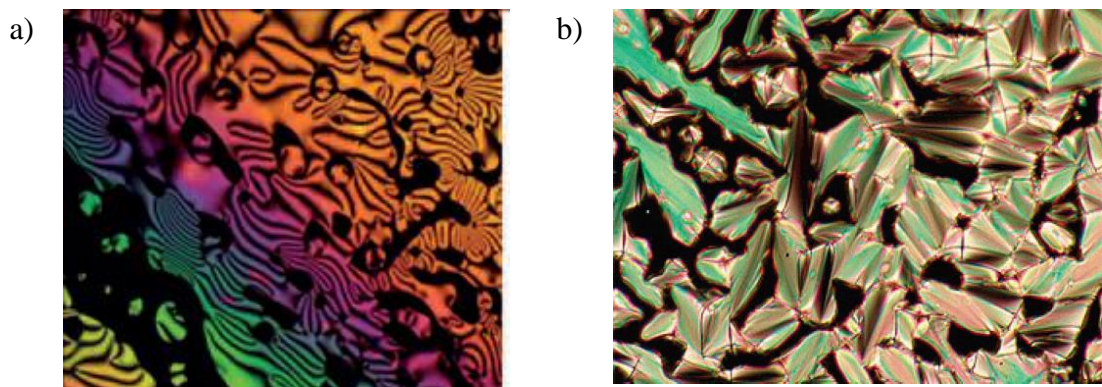


Figure 1-50: Optical micrographs of a) a N phase¹⁹⁷ and b) a SmA phase.¹⁹⁸

The most common texture observed for the SmA is the focal-conic texture (Figure 1-50b), which consists of ellipses and hyperbolae that originate from discontinuities.¹⁹⁹ The origin of this texture can be explained by considering the SmA phase to consist of layers of concentric circles emanating from a central point (Figure 1-51). The overlap between two adjacent circles leads to the formation of a hyperbola and the intersection of the two centres of the circles corresponds to the plane of the ellipse.

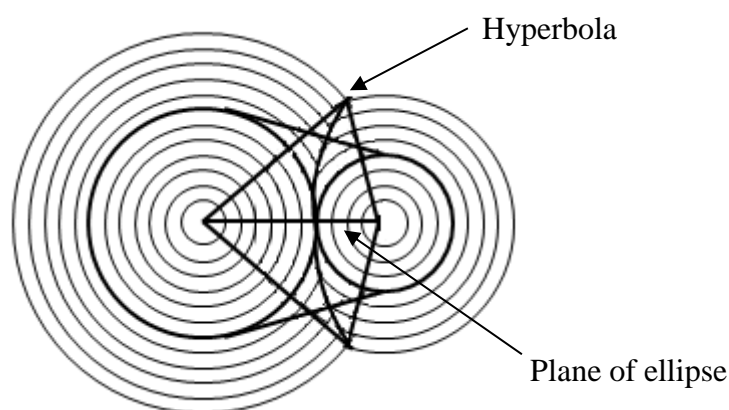


Figure 1-51: Origin of the focal-conic texture observed in SmA phases.¹⁹⁹

This focal-conic texture is only observed if there is planar alignment of the sample, which anchors to the glass slide. If the sample has a homeotropic alignment, where the molecules are perpendicular to the cover slips, the texture has the appearance of an isotropic texture and appears black. Regions of birefringence can be seen due to deformations in the phase.

1.7.2 Hydrogen-Bonded Liquid Crystals

The hydrogen bond has been used to form new thermotropic liquid crystals. The introduction of a hydrogen bond either induces liquid-crystalline properties into materials that are not themselves mesomorphic or causes phase behaviour that is different to that of the constituents. For example, the hydrogen-bonded liquid crystal shown in Figure 1-52 forms a SmA phase from 136 – 160 °C followed by a N phase from 160 – 238 °C.²⁰⁰ This phase behaviour is different to that of the pyridyl

hydrogen-bond acceptor, which shows only a N phase from 165 – 213 °C and the benzoic acid, which as a monomer would not be mesomorphic, although it exists as a N phase from 147 – 160 °C (Figure 1-53).

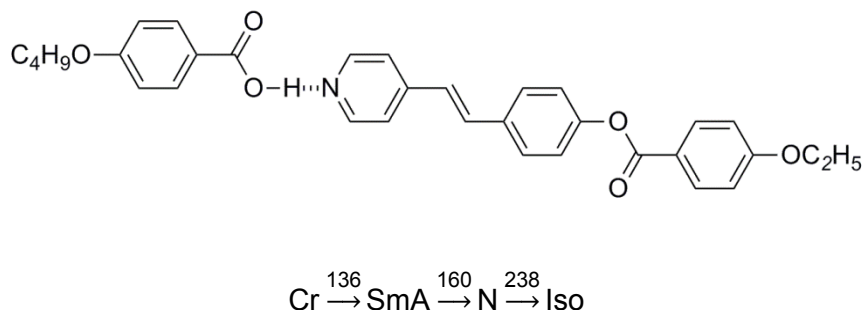


Figure 1-52: Hydrogen-bonded liquid crystal between 4-butoxybenzoic acid and *trans*-4-[(4-ethoxybenzoyl)oxy]-4'-stilbazole.²⁰⁰

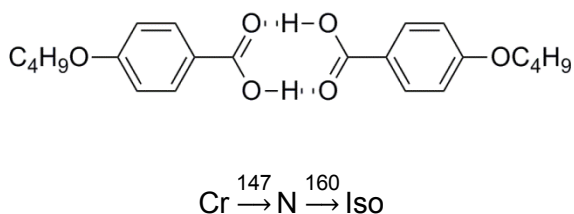


Figure 1-53: The hydrogen-bonded dimer of 4-butoxybenzoic acid.

The high clearing temperature of the hydrogen-bonded complex highlights the stability of the interaction. The strength of this interaction is also shown by the fact that formation of the N···H interaction is favoured over the hydrogen bonds in the benzoic acid dimer. The stability of the hydrogen bond is an important consideration in the study of hydrogen-bonded liquid crystals, particularly in relation to the clearing temperature. There is some debate about whether clearing is driven by cleavage of the hydrogen bond.¹⁹⁴

As well as possible decomposition at the clearing point, the behaviour of the hydrogen-bonded complex as it melts into any mesophases needs to be considered. Some complexes can display biphasic behaviour, where different components melt at different temperature before forming the hydrogen-bonded complex and any mesophases. For example, broad melting was observed for some of the complexes

between alkoxystilbazoles and fluorophenols suggesting that the complex did not form initially.²⁰¹

There is a similarity between the hydrogen bond formed by a benzoic acid with a pyridine base and a covalent ester linkage typically observed in calamitic liquid crystals (Figure 1-54).²⁰² The liquid-crystalline behaviour of a 2:1 hydrogen-bonded complex of 4-methoxybenzoic acid with 4,4'-bipyridine was compared to its covalently bound analogue (Figure 1-55).²⁰³ Both materials have a N phase but the transition temperature into the N phase of the hydrogen-bonded complex is 87 °C lower and the clearing temperature is 227 °C lower than in the covalent molecule. This shows that the mesophases are destabilised by the presence of a hydrogen bond due to its flexibility.

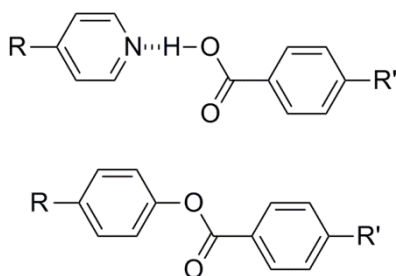


Figure 1-54: Comparison of hydrogen-bonded complex with covalent ester linkage.

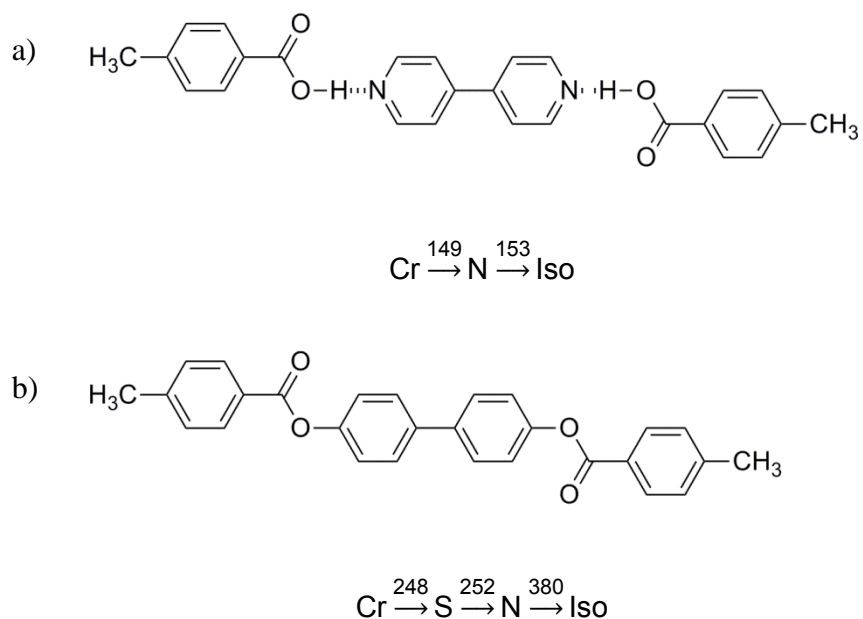


Figure 1-55: a) 2:1 Hydrogen-bonded complex between 4-methoxybenzoic acid and 4,4'-bipyridine and b) its covalently bonded analogue, 4,4'-biphenyldi(4''-methylbenzoate).²⁰³

This reduction in mesophase stability was also observed in the synthesis of hydrogen-bonded analogues of polycatenar mesogens (Figure 1-56a), which consist of a rigid aromatic core with alkoxy chains at both ends giving them properties intermediate between rod-like and disk-like mesogens.²⁰² Initial attempts to synthesise a hydrogen-bonded analogue of a polycatenar mesogen, which had three-aromatic rings in the core were unsuccessful because no mesomorphic behaviour was observed. An additional aromatic ring was required to increase the anisotropy of the material and lead to the formation of N and SmC phases (Figure 1-56b).

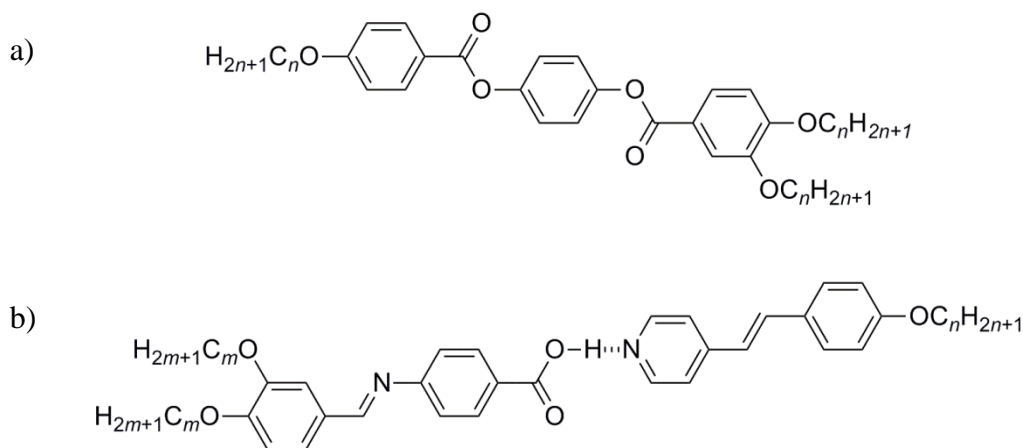


Figure 1-56: a) Example of a three-ring, tricatenaar liquid crystal and b) hydrogen-bonded four-ring, tricatenaar liquid crystal.²⁰²

Attempts to utilise the flexibility of the hydrogen bond in mesomorphic complexes were made in the synthesis of hydrogen-bonded analogues of an oxadiazole, which is a bent core liquid crystal (Figure 1-57).²⁰⁴ The oxadiazole has very high transition temperatures and can slowly degrade in the biaxial nematic phase, N_B , at high temperatures. Hydrogen bonds were, therefore, introduced in order to reduce the transition temperatures and allow investigation of the mesomorphic behaviour without degradation of the material. The central angle of bent-core materials plays an important role in the mesophases that are observed, so by introducing flexibility using hydrogen bonds, this angle was increased and the phases changed from bent-core phases to calamitic SmA phases.

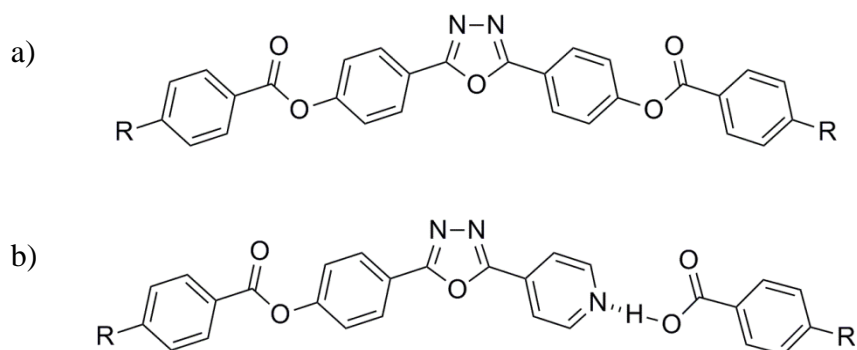


Figure 1-57: a) Oxadiazole-based bent-core mesogens and b) their hydrogen-bonded analogues.²⁰⁴

The majority of hydrogen-bonded liquid crystals involve strong hydrogen-bond donors such as carboxylic acids, however, the hydrogen-bonded complex between 4-cyanophenol and alkoxy stilbazoles were observed to have monotropic SmA and N phases. The crystal structure of the complex with octyloxystilbazole revealed that the geometry of the hydrogen bond led to a bent complex (Figure 1-58a). In order to improve the stability of the mesophases, 3-cyanophenol was used as the hydrogen-bond donor,²⁰⁵ and the linear geometry of this complex (Figure 1-58b) led to the formation of enantiotropic mesophases. Other hydrogen-bonded, liquid-crystalline phases involving phenols have been synthesised including those involving 1,4-hydroquinone and 2,3-dicyanohydroquinone, which have mesophases with enhanced stability due to the greater structural anisotropy of the complexes.

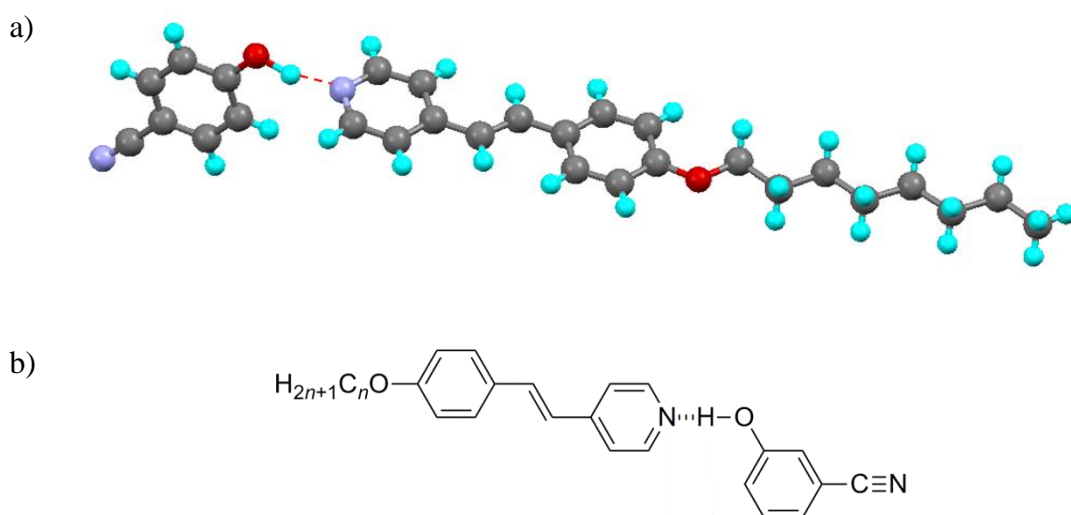


Figure 1-58: a) Molecular structure of the hydrogen-bonded complex between octyloxystilbazole and 4-cyanophenol. The O–H···N hydrogen bond is highlighted in red.²⁰⁵
 b) Schematic of the structure of the complexes of alkoxy stilbazoles with 3-cyanophenol.

Similar complexes of alkoxy stilbazoles with nitrophenols (Figure 1-59) were synthesised and comparisons with the complexes with cyanophenols could be made.²⁰⁶ The mesophases of the complexes with nitrophenols were found to be more thermally stable than the equivalent complexes with cyanophenols. Similar to the complexes with cyanophenols, the mesophases of 3-nitrophenol were more stable than those of 4-nitrophenol due to the former having a more linear geometry. The

effect of an additional nitro substituent was investigated in the complex with 2,4-dinitrophenol, which was found to have more stable mesophases than the mono substituted phenols.

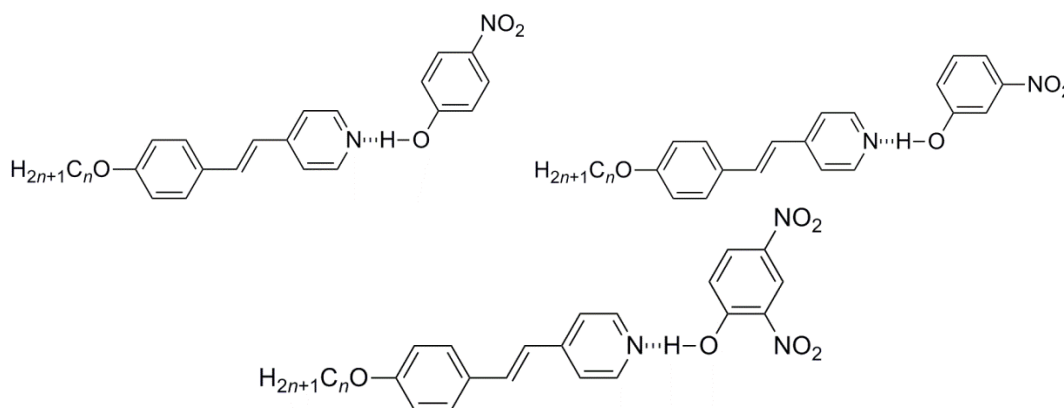


Figure 1-59: The hydrogen-bonded liquid crystals of alkoxy stilbazoles with nitrophenols.

The presence of the electron-withdrawing cyano or nitro substituents in the phenol decreases its pK_a , making it a stronger hydrogen-bond donor. The effect of electron-withdrawing fluorine substituents on phenols and their hydrogen-bonded complexes with stilbazoles was investigated.²⁰¹ It was found that increasing the number of fluorine substituents slightly increased the clearing point of the mesophases observed, however, no correlation between the pK_a of the phenol and the clearing point could be made. The presence of a fluorine substituent *ortho* to the phenol had the most significant effect, which was thought to be due to a secondary $H\cdots F$ interaction between a proton on the pyridyl ring of the stilbazole and this fluorine in the *ortho* position (Figure 1-60). While this secondary interaction was only observed in two crystal structures of the complexes investigated, the consistent stabilisation of the mesophase observed when a fluorine substituent is present in the *ortho* position supports the existence of an intermolecular hydrogen bond in the mesophase.

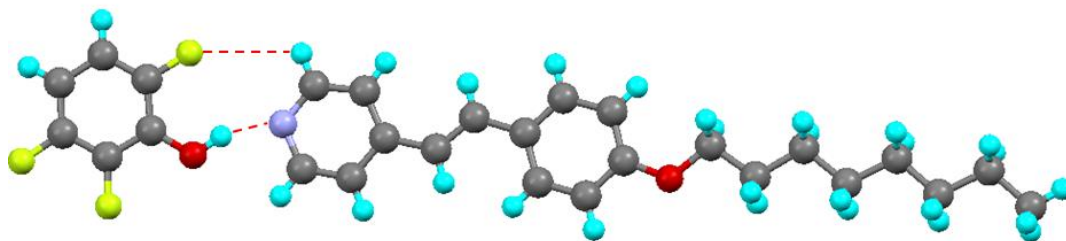


Figure 1-60: Molecular structure of the complex between octyloxystilbazole and 2,3,5-trifluorophenol. O–H···N and H···F interactions are highlighted in red.²⁰¹

1.7.3 Halogen-Bonded Liquid Crystals

Similar to the hydrogen bond, halogen bonds have been observed to induce mesomorphic behaviour in materials that are not themselves mesomorphic. For example, the halogen-bonded complex between iodopentafluorobenzene and alkoxystilbazoles (Figure 1-61) form N and SmA phases, whereas the components do not form any liquid crystal phases themselves.¹⁹⁸

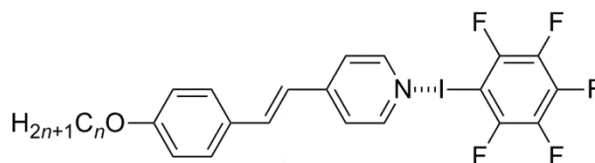


Figure 1-61: The halogen-bonded complex between iodopentafluorobenzene and alkoxystilbazoles.¹⁹⁸

Many of the considerations required for hydrogen-bonded liquid crystals apply in the case of halogen-bonded complexes. Decomposition of the complexes around the clearing temperature can occur due to lability of the halogen bond and, for example, the large enthalpy of clearing of the 2:1 complex between alkoxystilbazoles and 1,4-diodotetrafluoroiodobenzene (Figure 1-62) was ascribed to cleavage of one of the halogen bonds.²⁰⁷



Figure 1-62: The 2:1 halogen-bonded complex between alkoxy-stilbazoles and 1,4-diodotetrafluorobenzene.²⁰⁷

Whereas the hydrogen bond between a benzoic acid and a pyridine acceptor can be compared to a covalent ester linkage, the halogen bond between an iodobenzene and a pyridine acceptor can be compared to a covalent bond between phenyl rings (Figure 1-63).¹⁹⁷



Figure 1-63: Comparison between a) the halogen bond between an iodobenzene and a pyridine halogen-bond acceptor and b) the covalent bond between two phenyl rings.

The liquid crystal behaviour of a halogen-bonded complex between octyloxystilbazole and an iodotetrafluorostilbene (Figure 1-64a) was compared to its covalently bonded analogue (Figure 1-64b) and, similar to hydrogen-bonded complexes, the halogen-bonded complex had a reduced clearing point, this time some 200 °C lower than its covalently bonded analogue. A more detailed review of halogen-bonded liquid crystals can be found in Chapter 4.

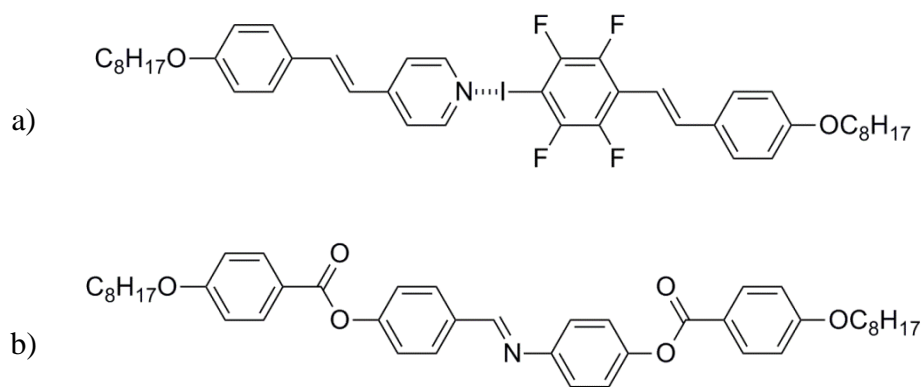


Figure 1-64: Comparison between a) the halogen-bonded complex between octyloxystilbazole and 1-[2-(4-octyloxyphenyl)vinyl]-2,3,5,6-tetrafluoro-4-iodobenzene and b) its covalently bonded analogue.

1.8 Conclusions

Research in the field of halogen bonding is extensive and has helped to improve the understanding of this interaction. The halogen bond, which shows many characteristics of the hydrogen bond, has been observed to originate from a region of positive electrostatic surface potential on the halogen atom, known as the σ -hole,³⁸ which causes the interaction to favour a linear geometry. Due to the σ -hole model, it is generally accepted that halogen bonding arises predominantly from electrostatic interactions, although there is still debate about the relative contributions of charge-transfer, polarisation and dispersion forces in the interaction, and further research is necessary in order to clarify the extents of these contributions.

The binding energies of halogen-bonded complexes investigated ranges from 5 – 180 kJ mol⁻¹¹⁶⁴ and, while this is comparable to hydrogen-bonded complexes, the study of weaker halogen-bonded complexes requires more attention. The definition of the hydrogen bond has recently been revised in order to account for weaker interactions including those to rare gas atoms,¹⁴⁰ therefore it would be beneficial to investigate complexes of this type involving halogen-bond donors in order to establish whether these interactions can be classified as halogen bonds.

The interaction has applications in fields that include crystal engineering,¹⁶⁴ anion recognition,¹⁷³ porous materials²⁰⁸ and liquid crystals.¹⁹⁸ Halogen bonding, like hydrogen bonding, has been observed to induce or change the liquid crystal properties of components upon complex formation. Although a variety of halogen-bonded liquid crystals have been investigated, the range is not as extensive as for hydrogen-bonded liquid crystals. There is also an opportunity to use halogen-bond donors such as dihalogens to synthesise liquid crystals that have different properties to any hydrogen-bonded materials. In molecules capable of forming both halogen and hydrogen bonds, the ability to predict which interactions will be favoured is important, particularly for crystal engineering. Although much research has been carried out in this area, the majority of examples show hydrogen bonding being favoured unless the halogen- and hydrogen-bond donors are not comparable. It would be beneficial to explore new situations where halogen bonding is favoured over hydrogen bonding.

Both experimental and theoretical techniques have proven to be useful in the investigation of the halogen bond and it would be beneficial to combine both aspects in researching the interaction. When considering theoretical approaches, it is important to use methods that include electron correlation. The performance of different *ab initio* and DFT methods needs to be considered carefully and comparisons to benchmark results and experimental data should be made when selecting methods. The use of the CP correction for the BSSE should be included in calculations even though it has been thought to overestimate the interaction. NBO analysis and LMOs can provide useful information about the bonding and orbital interactions in halogen-bonded complexes.

2 The Halogen Bond Interaction Between Fluorohalides and Isocyanides

2.1 Introduction

The geometries of hydrogen-bonded complexes, A–H···B, are dependent on both the strength of the hydrogen-bond donor, AH, and the Lewis base, B, acting as a hydrogen-bond acceptor. Upon formation of a hydrogen bond, the A–H covalent bond lengthens and this lengthening increases as the strength of the hydrogen bond increases and the A···B and H···B distances decrease.²⁰⁹ This variation of the bond lengths in hydrogen-bonded complexes can be modelled accurately using the Steiner-Limbach equation (Equation 2-1), which relates the A–H (r_1) and the H···B (r_2) distances:

$$(r_1 + r_2) = 2r_{02} + (r_1 - r_2) + 2b \ln \left[1 + \exp \left\{ \frac{r_{01} - r_{02} - r_1 + r_2}{b} \right\} \right] \quad (2-1)$$

where r_{01} and r_{02} are parameters that correspond to the A–H and H···B separations in the monomers AH and HB, respectively, and b is a parameter that can be optimised to improve the quality of the fit.

2.1.1 Derivation of the Steiner-Limbach Equation

The Steiner-Limbach equation is derived from the bond valence model, which is used to describe the bonding in inorganic solids.²¹⁰ It originates from Pauling's second principle for determining the structure of complex ionic crystals, which states that the electric charge of an anion in an ionic lattice will compensate the strength of electrostatic valence bonds from the cations. The bond valence model uses bond valences, s , and bond lengths, r , to characterise bonds. The following rules are obeyed (Equations 2-2 and 2-3):

$$\sum_j s_{ij} = V_i \quad (2-2)$$

$$\sum_{\text{loop}} s_{ij} = 0 \quad (2-3)$$

where i and j refer to different atoms and V refers to the atomic valence. The sum of all the bond valences from an atom is equal to its atomic valence and the sum of any bond valences around a loop in the bond network is equal to zero.

The bond length and the bond valence are correlated in Equations 2-4 and 2-5.

$$s_{ij} = \exp\left(\frac{r_{0i} - r_{ij}}{b}\right) \quad (2-4)$$

$$s_{ij} = \left(\frac{r_{ij}}{r_{0i}}\right)^{-N} \quad (2-5)$$

where r_{0i} , b and N are fitted parameters.

Steiner and Saenger applied Equation 2-4 to O–H···O hydrogen bonds.²⁰⁹ Denoting the O–H bond as r_1 and the H···O hydrogen bond as r_2 , and assuming that $s(r_1) + s(r_2) = 1$ (Equation 2-6), Equation 2-7 can be derived.

$$s_1 + s_2 = \exp\left(\frac{r_{01} - r_1}{b}\right) + \exp\left(\frac{r_{02} - r_2}{b}\right) = 1 \quad (2-6)$$

$$r_2 = r_{02} - b \ln\{1 - \exp[(r_{01} - r_1)/b]\} \quad (2-7)$$

Equation 2-7 can then be rearranged to the form shown in Equation 2-1 to give the sum of the bond distances, $r_1 + r_2$, as a function of the difference between the two bond distances, $r_1 - r_2$.

The values of $r_1 + r_2$ can be plotted against values of $r_1 - r_2$ to give a curve similar to that shown in Figure 2-1.²¹¹ The curve shows the pathway of proton transfer from hydrogen-bond donor, A–H to base B. Complexes that fall to the left of the curve and have a negative value of $r_1 - r_2$ are considered hydrogen-bonded complexes. The minimum of the curve corresponds to the point where the hydrogen atom is equidistant from A and B and complexes that are in this region are referred to as proton-shared hydrogen bonds. Complexes that fall in the region to the right of the curve and have a positive value of $r_1 - r_2$ are classified as ion-pair hydrogen bonds.²¹²

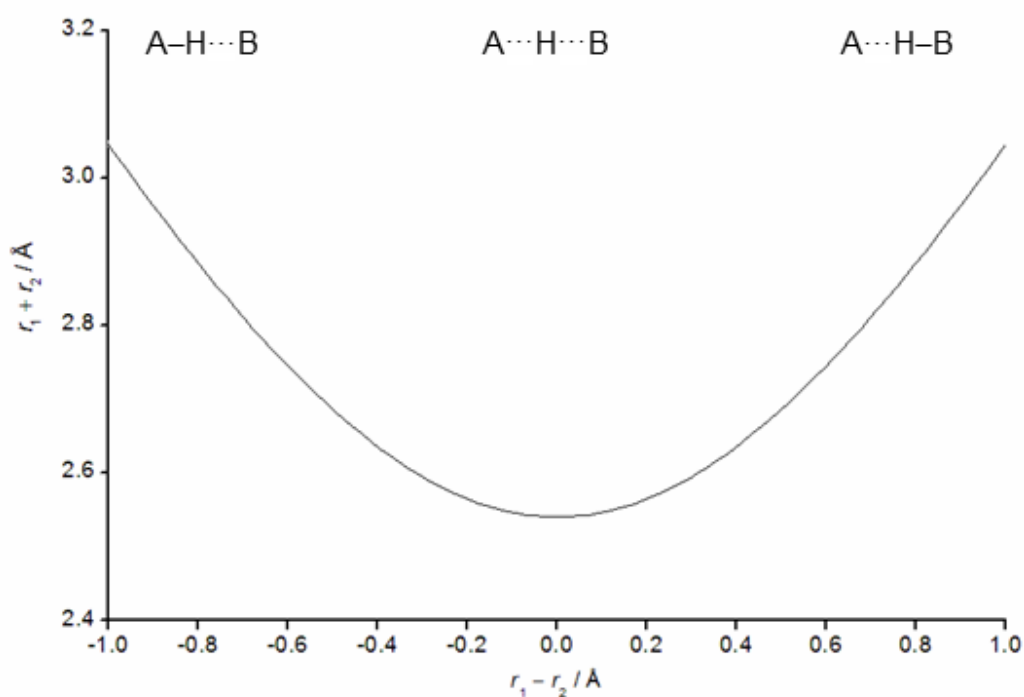


Figure 2-1: Example of a Steiner-Limbach plot for hydrogen-bonded complexes A–H···B.²¹¹

Equation 2-7 was applied to O–H···O hydrogen bond lengths obtained from neutron diffraction experiments data available in the CSD and generally gave a good fit.²⁰⁹ The optimised value of r_{01} was short compared to experimental O–H bond lengths and the curve was too steep for longer hydrogen bonds. The value obtained for symmetrical O···H···O hydrogen bonds was $r_1 = r_2 = 1.201 \text{ \AA}$, which is similar to

experimentally obtained values of 1.195 Å. This shows that the Steiner-Limbach equation is appropriate for modelling interactions of this type.

2.1.2 Application of the Steiner-Limbach Equation to Hydrogen-Bonded Complexes

The Steiner-Limbach equation has been applied to many different systems involving hydrogen bonds and typically produces excellent fits with the coefficient of determination, R^2 , being greater than 0.97 in all cases. The systems include linear and cyclic neutral clusters of HCN and HNC and to the charged clusters formed by protonation or deprotonation of these clusters (*e.g.* $[\text{HNC}\cdots\text{HNCH}\cdots\text{NCH}]^+$ and $[\text{CNH}\cdots\text{CN}\cdots\text{HCN}]^-$)²¹³ and the dimers and trimers of sulfoxide and thioperoxides.²¹⁴

The parameter b can be obtained either by optimisation in order to achieve the best quality of fit or by using Equation 2-8:

$$b = [(r_1 + r_2)_{\min} - (r_{01} + r_{02})]/(2\ln 2) \quad (2-8)$$

where $(r_1 + r_2)_{\min}$ is the minimum distance between A and B in the A-H \cdots B hydrogen bond and r_{01} and r_{02} are the A-H and H-B distances in the monomers AH and HB⁺. This latter method was used in the application of the Steiner-Limbach equation to the unsymmetric hydrogen bonds in complexes between XH (X = F, Cl, Br and NC) and ammonia, where the position of the hydrogen atom was shifted from X to N by varying the surrounding electric field.²¹⁵

The parameters of the Steiner-Limbach equation obtained for the X-H \cdots NH₃ complexes were also used when the equation was applied to data from the optimised geometries of 2-fluorobenzamides and related compounds that feature an intramolecular N-H \cdots F hydrogen bond (Figure 2-2).²¹⁶ The results of this study were particularly interesting because the Steiner-Limbach equation was suitable for modelling not only these intramolecular interactions but a wide range of hydrogen

bonds including the F–H···N interactions between HF and sp - (e.g. F–H···NCH), sp^2 - (e.g. F–H···NC₅H₅) and sp^3 -hybridised (F–H···NH₃) nitrogen bases.

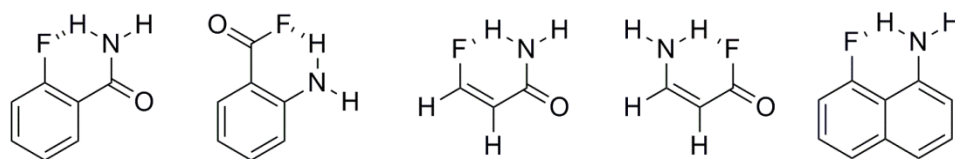


Figure 2-2: 2-Fluorobenzamide and related compounds with intramolecular N–H···F hydrogen bonds modelled using the Steiner-Limbach equation.

The Steiner-Limbach equation has also been applied in a theoretical study of the proton-transfer mechanism in pyrrolo[2,3-*b*]pyrrole dimers (Figure 2-3a) with an excellent fit.²¹⁷ Bond lengths corresponding to the proton transfer in the dimers of 1,8a-dihydro-1,8-naphthridine derivatives (Figure 2-3b) could be added to this data set, since both sets of dimers feature N–H···N hydrogen bonds and maintain the excellent fit to the Steiner-Limbach equation.²¹⁸ The molecules in these dimers are chiral and the study of the hydrogen bonding therein is aimed at the understanding of chiral recognition of small molecules.

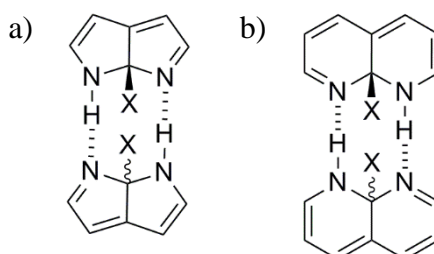


Figure 2-3: Schematic representation of a) pyrrolo[2,3-*b*]pyrrole dimers and b) 1,8a-dihydro-1,8-naphthridine dimers. X = H, F, Cl, CH₃, CN, CCH, CF₃, CCl₃, C(CH₃)₃, Si(CH₃)₃, SiF₃, SiCl₃, NH₂, OH or *t*-Bu.

2.1.3 Application of the Steiner-Limbach Equation to Halogen-Bonded Complexes

The wide range of hydrogen bonds modelled using the Steiner-Limbach equation highlights the usefulness of the equation. The ability of the Steiner-Limbach

equation to model the halogen bond, which has properties similar to the hydrogen bond, can be determined by applying it to a system where the strength of the halogen bond and, therefore, the position of the halogen atom changes. This was achieved by Del Bene *et al.* for complexes between FCl and a series of isocyanides (CNY, Y = CN, NC, NO₂, F, CF₃, Cl, Br, H, CCF, CCH, CH₃, SiH₃, Li and Na).²¹⁹

The geometries of these complexes were optimised using second-order Møller-Plesset perturbation theory (MP2) with the aug'-cc-pVDZ basis set, which corresponds to Dunning's aug-cc-pVDZ basis set applied to all atoms except H and cc-pVDZ basis set for H.²¹⁹ These geometries were analysed in detail and complexes were classified into three categories based on the F–C and F–Cl separations, the difference between the F–Cl and Cl–C separations, $R(\text{F–Cl}) - R(\text{Cl–C})$ and the binding energies, ΔE , of the complexes. These classifications were confirmed by atoms-in-molecules (AIM) analyses; the sign of the Laplacian at the bond critical point (bcp) for the F-Cl bond changed from negative to positive as the interaction changed from a covalent bond to a weak interaction and *vice versa* for the Cl-N bond.

The first category contained complexes with isocyanides that had electron withdrawing groups and were therefore weakly basic (Y = CN, NC, NO₂ and F). These complexes could be considered to have traditional halogen bonds characterised by a low binding energy in the range 23 – 26 kJ mol⁻¹, relatively long F–C separations of approximately 4.1 Å and a negative value for the $[R(\text{F–Cl}) - R(\text{Cl–C})]$ difference.

The second category featured isocyanides that were stronger bases (Y = CF₃, Cl, Br, H, CCF, CCH, CH₃ and SiH₃). The binding energies of these complexes were larger than those of the first category and ranged from 35 to 65 kJ mol⁻¹. The F–C and C–N distances were shorter and the F–Cl distance, resulting in a small positive $[R(\text{F–Cl}) - R(\text{Cl–C})]$ value. The changes in these separations and increase in binding

energy indicated that the chlorine atom was not halfway between the F and isocyanide leading to these complexes being classified as chlorine-shared.

The final category corresponded to complexes with isocyanides that were strongly basic (Y = Li and Na). These complexes had relatively large binding energies of 121 and 140 kJ mol⁻¹ respectively. In these complexes the chlorine atom had transferred from the fluorine to the carbon atom of the isocyanide as indicated by the larger $[R(\text{F}-\text{Cl}) - R(\text{Cl}-\text{C})]$ value. These complexes were referred to as ion-pair complexes.

These results suggest that the halogen bonding in these complexes follows a similar pattern to hydrogen bonding, where variation of the acidity of the proton donor and the basicity of the proton acceptor results in proton transfer to form proton-shared hydrogen bonds and ion-pair complexes.²¹² This makes the system suitable for modelling using the Steiner-Limbach equation and indeed fitting the equation to a plot of $(r_1 + r_2)$ against $(r_1 - r_2)$, where r_1 is the F-Cl distance and r_2 is the Cl...C distance, gave a correlation factor of 0.994.²¹⁹

A similar study was carried out to investigate complexes between FCl and a series of sp, sp² and sp³-hybridised nitrogen bases.²²⁰ Although the binding energies ranged from 3.1 to 99.8 kJ mol⁻¹, there was little variation in the F-N distance and $[R(\text{F}-\text{Cl}) - R(\text{Cl}-\text{N})]$ remained negative for all complexes suggesting that traditional halogen bonding dominated. This observation was rationalised by the fact that the less electronegative C atom forms bases that are better electron donors leading to stronger complexes with FCl.

The geometries of complexes between FCl and a series of sp-hybridised phosphorus bases, PCY (Y = NC, CN, F, H, CCCH, CCCF, CCH₃, Li and Na) were optimised using the same level of theory as that used for complexes with isocyanides.²²¹ The complexes were found to have two configurations; one linear configuration with the chlorine forming a halogen bond with the lone pair on the phosphorus and another

configuration of C_s symmetry, where the chlorine interacts with the π electron density of the P-C triple bond. This latter configuration was previously observed for the protonated PCH molecule, where the most favourable conformation of the cation was with the hydrogen interacting with the P-C π electron density.²²² The complexes FCl:PCY with the linear configuration were optimised and classified in a similar manner to the complexes with isocyanides, although it should be noted that geometries with Y = NC, F, CH₃ and Na gave two imaginary vibrational frequencies and therefore did not correspond to local minima. The majority of halogen bonds were classified as traditional halogen bonds, chlorine-shared halogen bonds were observed for Y = Li and Na and an ion-pair halogen bond was only observed for a complex with the PC⁻ anion.²²¹

The strength of the halogen bond in the complex FCl-CNH can be increased to give an ion-pair halogen bond using cooperativity with other interactions.²²³ The geometries of the complexes FCl-CNH-(CNH)_n, $n = 0 - 4$, were optimised at the MP2/aug-cc-pVTZ level of theory and the effects of additional H...C hydrogen bonds on the halogen bond strengths were investigated. As the number of CNH units and therefore additional hydrogen bonds increased, the binding energy of the halogen bond increased, however, the halogen bond remained chlorine-shared. Introducing an alkali metal to the complexes to give FCl-CNH-CNLi and FCl-CNH-CNNa increased the strength of the halogen bond further to produce an ion pair halogen bond. This is not surprising since the introduction of an alkali metal will lead to proton transfer in the hydrogen-bonded segment of the complex and CN⁻ has been observed to have an ion pair complex with FCl.²¹⁹ Cooperativity could be used to create an ion pair halogen bond by using the fluorine of FCl as a hydrogen-bond acceptor. The complex FH-FCl-CNH was found to have a binding energy for the halogen bond that is 186.56 kJ mol⁻¹ greater than that of the original FCl-CNH complex.²²³

2.1.4 A Modified Steiner-Limbach Equation

The derivation of the Steiner-Limbach equation shows that the parameter b is specific for a particular bond, as can be observed in Equation 2-4. In hydrogen- and halogen-bonded complexes, the covalent and non-covalent bonds should differ in nature significantly suggesting that different parameters b_i should be used. If this is applied to the sum of the bond valences of the covalent and non-covalent bonds, then Equation 2-6 is transformed into Equation 2-9.

$$s_1 + s_2 = \exp\left(\frac{r_{01} - r_1}{b_1}\right) + \exp\left(\frac{r_{02} - r_2}{b_2}\right) = 1 \quad (2-9)$$

Equation 2-9 can then be rearranged to give the modified Steiner-Limbach equation, Equation 2-10.

$$r_2 = r_{02} - b_2 \ln\{1 - \exp[(r_{01} - r_1)/b_1]\} \quad (2-10)$$

It is not possible to rearrange Equation 2-10 into a form equivalent to the original Steiner-Limbach equation given in Equation 2-1 because of the different b_i parameters.

2.2 Aim

The aim of the work reported in this chapter is to investigate whether the halogen-shared and ion-pair interactions observed for complexes between FCl and isocyanides (**4** – **17** in Figure 2-4) are also observed for stronger halogen-bond donors, FBr and FI. The optimised geometries of these complexes will then be tested against the original Steiner-Limbach equation, Equation 2-1, to investigate whether this relationship is appropriate for these complexes. The modified 4-parameter Steiner-Limbach equation, Equation 2-10, will be fitted to all data sets and the goodness-of-fit will be compared to that for the 3-parameter Steiner-Limbach equation, Equation 2-7, in order to determine whether introducing a new parameter

to the equation is necessary. This modified Steiner-Limbach equation will then be applied to hydrogen-bonded complexes in order to identify whether this improves the goodness-of-fit.

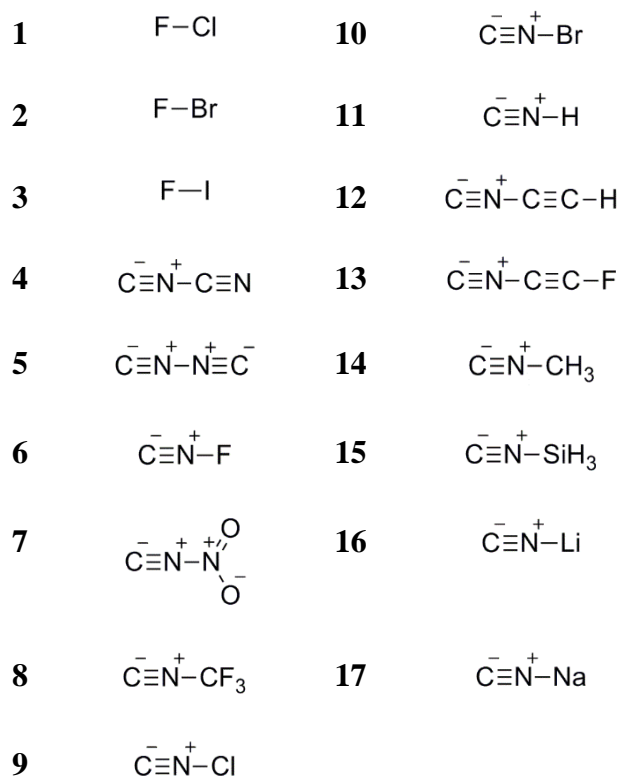


Figure 2-4: The halogen-bond donors and isocyanides acting as halogen-bond acceptors in this investigation.

2.3 Computational Method

2.3.1 Geometry Optimisation and Binding Energies

The geometries of all complexes and monomers were optimised at the MP2(Full) level of theory using the aug-cc-pVTZ basis set for all atoms except iodine, where the aug-cc-pVTZ-PP basis set was used with an effective core potential (ECP), replacing the 28 inner core electrons with pseudopotentials, in order to account for relativistic effects. There has been debate about whether the use of counterpoise (CP) correction overcompensates for the basis set superposition error (BSSE) and its

utility has been questioned.^{109,111,224} Therefore the calculations were carried out both with and without CP correction of the BSSE in order to investigate its effect.

Calculations were carried out using the 'VeryTight' convergence criteria to ensure high accuracy. Vibrational frequency calculations were carried out to ensure that the optimised geometries corresponded to global minima of the potential energy surface. The results of the calculations were checked to ensure that the expected point group for the complex was achieved. If this was not the case, the geometry was adjusted as required and the optimisation procedure was repeated using the 'symmetry' keyword with the appropriate point group applied. If convergence of the geometry optimisation was difficult to achieve, then the 'CalcFC' keyword, which requests calculation of the force constants (equivalent to the second derivatives of the energy, collected in the Hessian matrix) at the start of the geometry optimisation or the 'CalcAll' keyword, which ensures calculation of the force constants at each iteration, were specified.

The binding energy was calculated as the difference between the energy of the optimised geometry of the complex and the sum of the energies of the optimised geometries of the monomers. All calculations were carried out in Gaussian03²²⁵ and Gaussian09.²²⁶ Optimised geometries were visualised using Molden²²⁷ and Molekel.²²⁸

2.3.2 Curve-Fitting Procedure

The fluorine-halogen and halogen-carbon separations in the optimised geometries were fitted to the original and modified Steiner-Limbach equations using the "NonLinearModel" tool in Mathematica.²²⁹ The non-linear model was written in the format of the original or modified Steiner-Limbach equations with parameters r_{01} , r_{02} , b_1 and b_2 with suitable initial guesses specified. These parameters were then evaluated by Mathematica in order to obtain the best fit to the data. Initially the "Rsquared" tool was used to calculate the coefficient of determination, R^2 , in order to

establish the goodness-of-fit of data to the Steiner-Limbach equation. This tool gave large values of R^2 that appeared to overstate the goodness-of-fit when compared to a plot of the data with the evaluated Steiner-Limbach equation. Therefore, the coefficient of determination, R^2 , was calculated directly using the definition in Equation 2-11. The maximum absolute value of a single residual, e_{\max} and the average of the residuals, e_{av} , were also used to determine the goodness of fit.

$$R^2 = 1 - \frac{RSS}{TSS} \quad (2-11)$$

where RSS is the sum of the squares of the residuals and TSS is the total sum of the squares of the deviations of the data from the mean value.

Occasionally it was noted that the values of the parameters were affected by the choice of initial guesses. In these cases, calculations with different initial guesses were run in order to maximise the value of R^2 that could be obtained.

2.4 Results

2.4.1 Geometry Optimisation

The geometries of all of the complexes were optimised successfully at the MP2(Full)/aug-cc-pVTZ (aug-cc-pVTZ-PP on I) level of theory. The majority of complexes have $C_{\infty v}$ symmetry, with the exception of complexes with isocyanides CNCF₃, CNCH₃ and CNSiH₃, which have C_{3v} symmetry and complexes with CNNO₂, which have C_{2v} symmetry. Table 2-1 shows the key separations r_1 and r_2 , and the binding energies for the complexes with FCl as the halogen-bond donor.

Table 2-1: The F–Cl (r_1), Cl–C (r_2) and F–C ($r_1 + r_2$) separations and $[r(\text{F–Cl})-r(\text{Cl–C})]$, ($r_1 - r_2$) and binding energies of the MP2(Full)/aug-cc-pVTZ optimised geometries of complexes between FCl and isocyanides CNY. Values in parentheses correspond to those calculated without CP correction. The complexes are ordered with increasing binding energy of the CP corrected results.

	Complex	$r_1 / \text{\AA}$	$r_2 / \text{\AA}$	$r_1 + r_2 / \text{\AA}$	$r_1 - r_2 / \text{\AA}$	$\Delta E / \text{kJ mol}^{-1}$
1.4	FCl:CNCN	1.6577 (1.6718)	2.5301 (2.3561)	4.1878 (4.0279)	-0.8724 (-0.6843)	19.55 (29.68)
1.5	FCl:CNNC	1.6603 (1.6756)	2.5089 (2.3346)	4.1692 (4.0102)	-0.8486 (-0.6590)	21.16 (31.76)
1.6	FCl:CNF	1.6631 (1.6739)	2.5004 (2.3753)	4.1635 (4.0492)	-0.8373 (-0.7014)	23.02 (31.50)
1.7	FCl:CNNO ₂	1.8779 (1.8639)	1.7411 (1.6903)	3.6190 (3.5542)	0.1368 (0.1736)	23.39 (44.48)
1.8	FCl:CNCF ₃	1.8468 (1.6762)	1.7192 (1.8630)	3.5660 (3.5392)	0.1276 (-0.1868)	24.29 (48.01)
1.9	FCl:CNCI	1.6850 (1.8598)	2.3307 (1.7172)	4.0157 (3.5770)	-0.6457 (0.1426)	28.64 (51.28)
1.10	FCl:CNBr	1.8445 (1.8705)	1.7672 (1.7043)	3.6117 (3.5748)	0.0773 (0.1662)	34.40 (60.67)
1.11	FCl:CNH	1.8556 (1.8756)	1.7393 (1.6912)	3.5949 (3.5668)	0.1163 (0.1844)	36.16 (56.90)
1.12	FCl:CNCCH	1.8616 (1.8760)	1.7131 (1.6760)	3.5747 (3.5520)	0.1485 (0.2000)	38.57 (63.51)
1.13	FCl:CNCCF	1.8614 (1.8772)	1.7198 (1.6804)	3.5812 (3.5576)	0.1416 (0.1968)	38.72 (64.18)
1.14	FCl:CNCH ₃	1.8671 (1.8890)	1.7522 (1.7034)	3.6193 (3.5924)	0.1149 (0.1856)	49.50 (71.49)
1.15	FCl:CNSiH ₃	1.8853 (1.8995)	1.7032 (1.6687)	3.5885 (3.5682)	0.1821 (0.2308)	53.53 (78.68)
1.16	FCl:CNLi	1.9547 (1.9693)	1.6995 (1.6719)	3.6542 (3.6412)	0.2552 (0.2974)	108.61 (132.38)
1.17	FCl:CNNa	1.9787 (1.9935)	1.6990 (1.6715)	3.6777 (3.6650)	0.2797 (0.3220)	125.59 (152.99)

The results obtained from these calculations are similar to those in the literature.²¹⁹

The values are not exactly identical because a slightly different basis set was used for

the H atoms. These calculations were carried out at the MP2(Full) level of theory, which includes correlation effects for all electrons, whereas results reported by Del Bene *et al.* were calculated using a frozen core where only the correlation effects of the valence electrons are included.

The complexes can be classified into three groups: Those corresponding to complexes with traditional halogen bonds, chlorine-shared complexes and ion-pair complexes. The complexes in the first group are characterised by a smaller binding energy, a larger F–C separation and a negative value for $[r(\text{F–Cl}) - r(\text{Cl–C})]$.

As the isocyanide becomes a stronger base, chlorine-shared complexes are formed, characterised by a shorter the F–C distance, a small positive value of $[r(\text{F–Cl}) - r(\text{Cl–C})]$ and a larger binding energy. The ion-pair complexes, FCl:CNLi and FCl:CNNa, are characterised by a F–C distance that is slightly longer than in the chlorine-shared complexes, a larger positive value of $[r(\text{F–Cl}) - r(\text{Cl–C})]$ and a larger binding energy.

Comparing the results for geometries optimised both with and without CP correction shows that the BSSE is significant for these complexes despite the large basis set used. This indicates that the calculations are below the complete basis set limit. The results without CP correction lead to a stronger binding energy, a longer F–Cl separation and a shorter Cl–C separation. Although it has been suggested that CP correction overcompensates for the BSSE resulting in an underestimation of the interaction energy,^{108,110,111} it will be assumed that for these complexes the CP corrected results are more accurate, which has been the case for calculations on other, similar complexes in the literature.^{115,116,230} Table 2-2 shows the results of the geometry optimisation of the complexes between fluorobromide and isocyanides CNY at the MP2(Full)/aug-cc-pVTZ level of theory.

Table 2-2: The F–Br (r_1), Br–C (r_2) and F–C ($r_1 + r_2$) separations and $[r(\text{F–Br})-r(\text{Br–C})]$, ($r_1 - r_2$) and binding energies of the MP2(Full)/aug-cc-pVTZ optimised geometries of complexes between FBr and isocyanides CNY. Values in parentheses correspond to those calculated without CP correction. The complexes are ordered with increasing binding energy of the CP corrected results.

	Complex	$r_1 / \text{Å}$	$r_2 / \text{Å}$	$r_1 + r_2 / \text{Å}$	$r_1 - r_2 / \text{Å}$	$\Delta E / \text{kJ mol}^{-1}$
2.5	FBr:CNNC	1.8150 (1.8715)	2.2280 (1.9635)	4.0430 (3.8350)	-0.4130 (-0.0920)	36.72 (67.23)
2.6	FBr:CNF	1.8025 (1.8309)	2.3360 (2.1567)	4.1385 (3.9876)	-0.5335 (-0.3258)	37.69 (59.54)
2.4	FBr:CNCN	1.8678 (1.8956)	1.9762 (1.8761)	3.8440 (3.7717)	-0.1084 (0.0195)	38.22 (72.88)
2.7	FBr:CNNO ₂	1.8459 (1.8884)	2.0959 (1.9318)	3.9418 (3.8202)	-0.2500 (-0.0434)	38.93 (69.30)
2.8	FBr:CNCF ₃	1.8486 (1.8914)	2.0813 (1.9194)	3.9299 (3.8108)	-0.2327 (-0.0280)	41.42 (72.43)
2.9	FBr:CNCI	1.8455 (1.8837)	2.1288 (1.9765)	3.9743 (3.8602)	-0.2833 (-0.0928)	49.18 (77.92)
2.10	FBr:CNBr	1.8586 (1.8951)	2.0858 (1.9499)	3.9444 (3.8450)	-0.2272 (-0.0548)	53.19 (85.76)
2.11	FBr:CNH	1.8579 (1.8935)	2.0863 (1.9541)	3.9442 (3.8476)	-0.2284 (-0.0606)	53.19 (79.30)
2.12	FBr:CNCCH	1.8809 (1.9083)	1.9913 (1.8974)	3.8722 (3.8057)	-0.1104 (0.0109)	54.39 (88.83)
2.13	FBr:CNCCF	1.8791 (1.9077)	2.0031 (1.9050)	3.8822 (3.8127)	-0.1240 (0.0027)	54.91 (89.57)
2.15	FBr:CNSiH ₃	1.8946 (1.9205)	1.9862 (1.9009)	3.8808 (3.8214)	-0.0916 (0.0196)	65.42 (98.31)
2.14	FBr:CNCH ₃	1.8776 (1.9058)	2.0530 (1.9058)	3.9306 (3.8116)	-0.1754 (0.0000)	66.08 (95.78)
2.16	FBr:CNLi	1.9560 (1.8974)	1.9490 (1.9696)	3.9050 (3.8670)	0.0070 (-0.0722)	114.23 (145.56)
2.17	FBr:CNNa	1.9504 (1.8966)	1.9663 (1.9859)	3.9167 (3.8825)	-0.0159 (-0.0893)	129.49 (164.27)

In these complexes, the F–C separation varies very little with the increase in basicity of the isocyanide and the value of $[r(\text{F–Br}) - r(\text{Br–C})]$ is, with the exception of the complex with CNLi, always negative. This suggests that the interaction in these complexes should be classified as a traditional halogen bond. Exceptions are the F...Br...C interactions in the complexes with CNLi and CNNa, which are intermediate between traditional halogen bonds and bromine-shared interactions, since the differences between the F–Br and Br–C distances are very small and the binding energies are large. The interaction energies are larger than the equivalent complexes with fluorochloride as would be expected since bromine is a stronger halogen-bond donor.

Similar to the results in Table 2-1, the CP correction makes a significant difference to the optimised bond separations and binding energies of the complexes. In some cases this leads to a different classification of the type of interaction, for example, for the complexes with CNCH₃, CNSiH₃ and CNCCH, which have an interaction intermediate between traditional halogen bonds and bromine-shared interactions when the results without CP correction are considered. This highlights the importance of using the CP correction in these calculations.

Table 2-3 shows the results of the geometry optimisation of complexes between fluoroiodides and isocyanides CNY at the MP2(Full)/aug-cc-pVTZ (aug-cc-pVTZ-PP on I) level of theory.

Table 2-3: The F–I (r_1), I–C (r_2) and F–C ($r_1 + r_2$) separations and $[r(\text{F–I})-r(\text{I–C})]$, ($r_1 - r_2$) and binding energies of the MP2(Full)/aug-cc-pVTZ (aug-cc-pVTZ-PP on I) optimised geometries of complexes between FI and isocyanides CNY. Values in parentheses correspond to those calculated without CP correction. The complexes are ordered with increasing binding energy of the CP corrected results.

	Complex	$r_1 / \text{\AA}$	$r_2 / \text{\AA}$	$r_1 + r_2 / \text{\AA}$	$r_1 - r_2 / \text{\AA}$	$\Delta E / \text{kJ mol}^{-1}$
3.8	FI:CNCF ₃	1.9852	2.2853	4.2705	-0.3001	48.89
		(2.0004)	(2.1807)	(4.1811)	(-0.1803)	(80.43)
3.6	FI:CNF	1.9681	2.4072	4.3753	-0.4391	52.21
		(1.9774)	(2.3176)	(4.2950)	(-0.3402)	(70.33)
3.5	FI:CNNC	1.9778	2.3067	4.2068	-0.2250	53.36
		(1.9932)	(2.1937)	(4.1280)	(-0.1170)	(77.79)
3.4	FI:CNCN	1.9909	2.2159	4.2845	-0.3289	55.24
		(2.0055)	(2.1225)	(4.1869)	(-0.2005)	(81.83)
3.7	FI:CNNO ₂	1.9849	2.2864	4.2713	-0.3015	55.25
		(1.9995)	(2.1835)	(4.1830)	(-0.1840)	(77.97)
3.9	FI:CNCI	1.9880	2.3069	4.2949	-0.3189	65.40
		(2.0003)	(2.2194)	(4.2197)	(-0.2191)	(87.50)
3.11	FI:CNH	1.9906	2.3020	4.2926	-0.3114	68.48
		(2.0023)	(2.2198)	(4.2221)	(-0.2175)	(87.37)
3.10	FI:CNBr	1.9929	2.2902	4.2831	-0.2973	69.13
		(2.0059)	(2.2021)	(4.2080)	(-0.1962)	(93.99)
3.12	FI:CNCCH	2.0011	2.2307	4.2318	-0.2296	70.72
		(2.0147)	(2.1459)	(4.1606)	(-0.1312)	(96.81)
3.13	FI:CNCCF	2.0006	2.2394	4.2400	-0.2388	71.24
		(2.0140)	(2.1540)	(4.1680)	(-0.1400)	(97.65)
3.15	FI:CNSiH ₃	2.0068	2.2452	4.2520	-0.2384	79.37
		(2.0192)	(2.1682)	(4.1874)	(-0.1490)	(103.41)
3.14	FI:CNCH ₃	2.0022	2.2812	4.2834	-0.2790	81.42
		(2.0134)	(2.2067)	(4.2201)	(-0.1933)	(103.20)
3.16	FI:CNLi	2.0434	2.2184	4.2618	-0.1750	124.78
		(2.0530)	(2.1671)	(4.2201)	(-0.1141)	(146.83)
3.17	FI:CNNa	2.0553	2.2115	4.2668	-0.1562	139.12
		(2.0658)	(2.1598)	(4.2256)	(-0.0940)	(169.59)

The F–C separations in these complexes vary very little with the basicity of the isocyanide. The I···C distance is always longer than the F–I separation leading to a negative value of $[r(\text{F–I}) - r(\text{I–C})]$, which suggests that the interactions in all of the complexes should be classified as traditional halogen bonds. The binding energies of these complexes are larger than the equivalent complexes with fluorobromide and fluorochloride due to iodine being the stronger halogen-bond donor.

2.4.2 Curve Fitting

The parameters of the three- and four-parameter Steiner-Limbach equations were evaluated for each data set and the coefficient of determination, R^2 was calculated using Equation 2-11. The maximum absolute residual, e_{max} , and the average of the absolute residuals, e_{av} , were also calculated to estimate the quality of the fit. Table 2-4 shows these values for the three-parameter Steiner-Limbach equation (Equation 2-7).

Comparing the values for the data sets obtained for calculations with and without CP correction shows that there is a significant difference with a better quality of fit observed for the data with the CP correction as seen in the larger R^2 values and smaller values of e_{max} and e_{av} . This improvement in the quality of fit suggests that the use of CP correction for these calculations does improve the accuracy of the optimised geometries.

The value of R^2 decreases as the halogen-bond donor becomes more polarisable. The fact that all the interactions with FBr and FI as the halogen-bond donor are classified as traditional halogen bonds means that the values of r_1 and r_2 cover a much narrower range when compared with the values for complexes with FCl as the halogen-bond donor. This leads to a greater spread of results for complexes with these halogen-bond donors.

Table 2-4: The evaluated parameters, r_{01} , r_{02} and b of the three-parameter Steiner-Limbach equation (Equation 2-7) and values of the coefficient of determination, R^2 , maximum absolute residual, e_{\max} and the average of the absolute residuals, e_{av} for complexes between fluorohalides and isocyanides, CNY. Results for calculations without CP correction are given in parentheses.

Halogen-Bond Donor	$r_{01} / \text{\AA}$	$r_{02} / \text{\AA}$	b	R^2	e_{\max}	e_{av}
1, FCI	1.6318	1.39994	0.413033	0.989	0.0656	0.0297
	(1.67058)	(1.64464)	(0.153136)	(0.870)	(0.2906)	(0.0522)
2, FBr	1.78831	1.83946	0.189969	0.938	0.0671	0.0200
	(1.82259)	(1.84765)	(0.115799)	(0.828)	(0.0596)	(0.0223)
3, FI	1.9648	2.19011	0.0702668	0.804	0.0566	0.0155
	(1.9765)	(2.15121)	(0.0429418)	(0.698)	(0.0593)	(0.0185)

The values of the parameters obtained by fitting the three-parameter Steiner-Limbach equation in the form given in Equation 2-7 for complexes with FCI as the halogen-bond donor are different from those obtained by Del Bene *et al.*, who obtained values for r_{01} and r_{02} of 1.666 and 1.651 Å, respectively, compared to the values of 1.6318 and 1.3994 Å, respectively, obtained in this study (Table 2-4).²¹⁹ The coefficient of determination given was 0.994, which is an improvement on the value of 0.989 given in Table 2-4.

Although the computational methods used differ (*vide supra*) this does not account for the significant differences here. The parameters obtained by Del Bene *et al.* were fitted to the original Steiner-Limbach equation given in Equation 2-1, (which correlates $r_1 + r_2$ with $r_1 - r_2$ rather than r_2 against r_1 (Equation 2-7)), which was the form used to calculate the parameters given in Table 2-4. This would account for the difference in the values particularly since the form of the Steiner-Limbach equation given in Equation 2-1 can eliminate outliers, which leads to an improvement in the goodness-of-fit.

The parameters were recalculated for all sets of halogen-bonded complexes using the form of the Steiner-Limbach equation given in Equation 2-1 and are shown in Table 2-5.

Table 2-5: The evaluated parameters, r_{01} , r_{02} and b of the original Steiner-Limbach equation in the form with $r_1 + r_2$ correlated with $r_1 - r_2$ (Equation 2-1) and values of the coefficient of determination, R^2 , maximum absolute residual, e_{\max} and the average of the absolute residuals, e_{av} for complexes between fluorohalides and isocyanides, CNY. Results for calculations without CP correction are given in parentheses.

Halogen-Bond Donor	$r_{01} / \text{\AA}$	$r_{02} / \text{\AA}$	b	R^2	e_{\max}	e_{av}
1, FCl	1.66213	1.63547	0.206962	0.993	0.0307	0.0186
	(1.66997)	(1.66390)	(0.122862)	(0.989)	(0.0367)	(0.0156)
2, FBr	1.79938	1.86209	0.163859	0.931	0.0478	0.0153
	(1.80008)	(1.67823)	(0.236725)	(0.782)	(0.0488)	(0.0178)
3, FI	1.97576	2.19346	0.0533009	0.844	0.0366	0.0118
	(1.98508)	(2.12767)	(0.0498164)	(0.610)	(0.0571)	(0.0194)

The values of the parameters for the complexes with FCl as the halogen-bond donor are more similar to those obtained by Del Bene *et al.*. Graphs showing the fit of the Steiner-Limbach equation in the form in Equation 2-1 to the data are given in Figure 2-5.

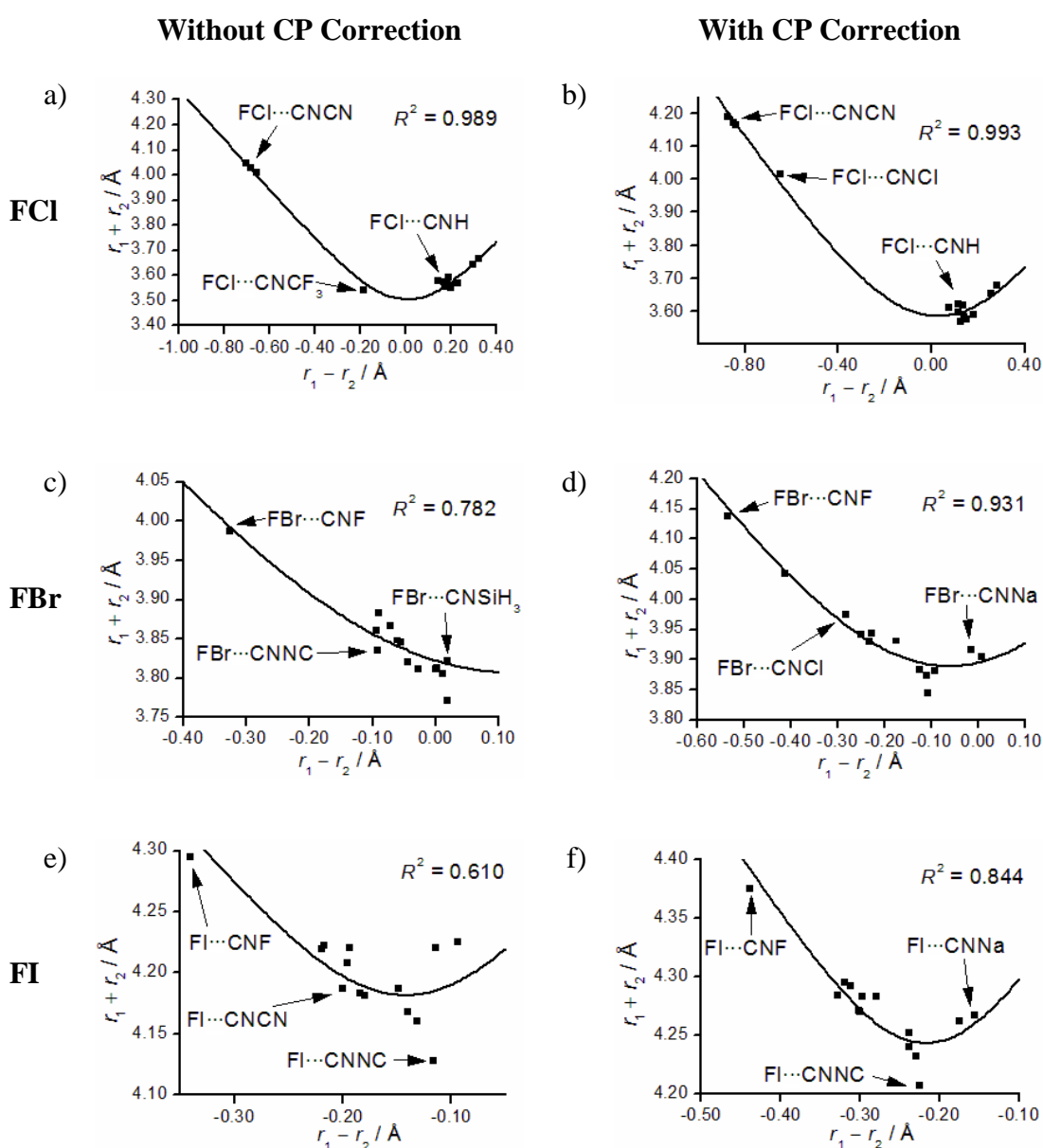


Figure 2-5: Graphs showing the fits of the original Steiner-Limbach equation in its form in Equation 2-1 for complexes with a) and b) FCl, c) and d) FBr and e) and f) FI as the halogen-bond donor. Figures in the left hand column correspond to results of calculations without CP correction and figures in the right hand column correspond to results with CP correction of the BSSE.

The results are similar to those using the Steiner-Limbach equation in the form in Equation 2-7; the use of counterpoise correction in the calculation results in an improvement in the goodness-of-fit and the values of R^2 decrease as the halogen becomes more polarisable.

A benefit of using the Steiner-Limbach equation in the form given in Equation 2-1 rather than the form in Equation 2-7 is that having an addition within the logarithm rather than a subtraction avoids having negative values within the logarithm making it easier to optimise the parameters.

The parameters of the four-parameter Steiner-Limbach equation (Equation 2-10) and the measures of the goodness of fit are given in Table 2-6. There are significant differences between the values of b_1 and b_2 , particularly for complexes with FCI as the halogen-bond donor. This highlights the need for the introduction of a new parameter in the Steiner-Limbach equation and that the two bonds that these parameters describe are significantly different.

Table 2-6: The evaluated parameters, r_{01} , r_{02} , b_1 and b_2 of the modified Steiner-Limbach equation (Equation 2-10) and values of the coefficient of determination, R^2 , maximum absolute residual, e_{\max} and the average of the absolute residuals, e_{av} for complexes between fluorohalides and isocyanides, CNY. Results for calculations without CP correction are given in parentheses.

Halogen-Bond Donor	$r_{01} / \text{\AA}$	$r_{02} / \text{\AA}$	b_1	b_2	R^2	e_{\max}	e_{av}
1, FCl	1.44176	1.65694	0.0864868	10.3601	0.997	0.0340	0.0179
	(1.65964)	(1.68683)	(0.00935658)	(2.30372)	(0.883)	(0.2506)	(0.0551)
2, FBr	1.70194	1.93062	0.0517989	2.59899	0.945	0.0624	0.0186
	(1.75563)	(1.88552)	(0.0393223)	(1.69762)	(0.829)	(0.0584)	(0.0223)
3, FI	1.96510	2.18388	0.0843672	0.0664381	0.804	0.0566	0.0155
	(1.95469)	(2.16091)	(0.0139925)	(0.710074)	(0.701)	(0.0575)	(0.0185)

Graphs showing the fit of the three and four parameter Steiner-Limbach equations to the data calculated with and without CP correction are given in Figures 2-6 and 2-7, respectively, in order to compare the performances of the two equations.

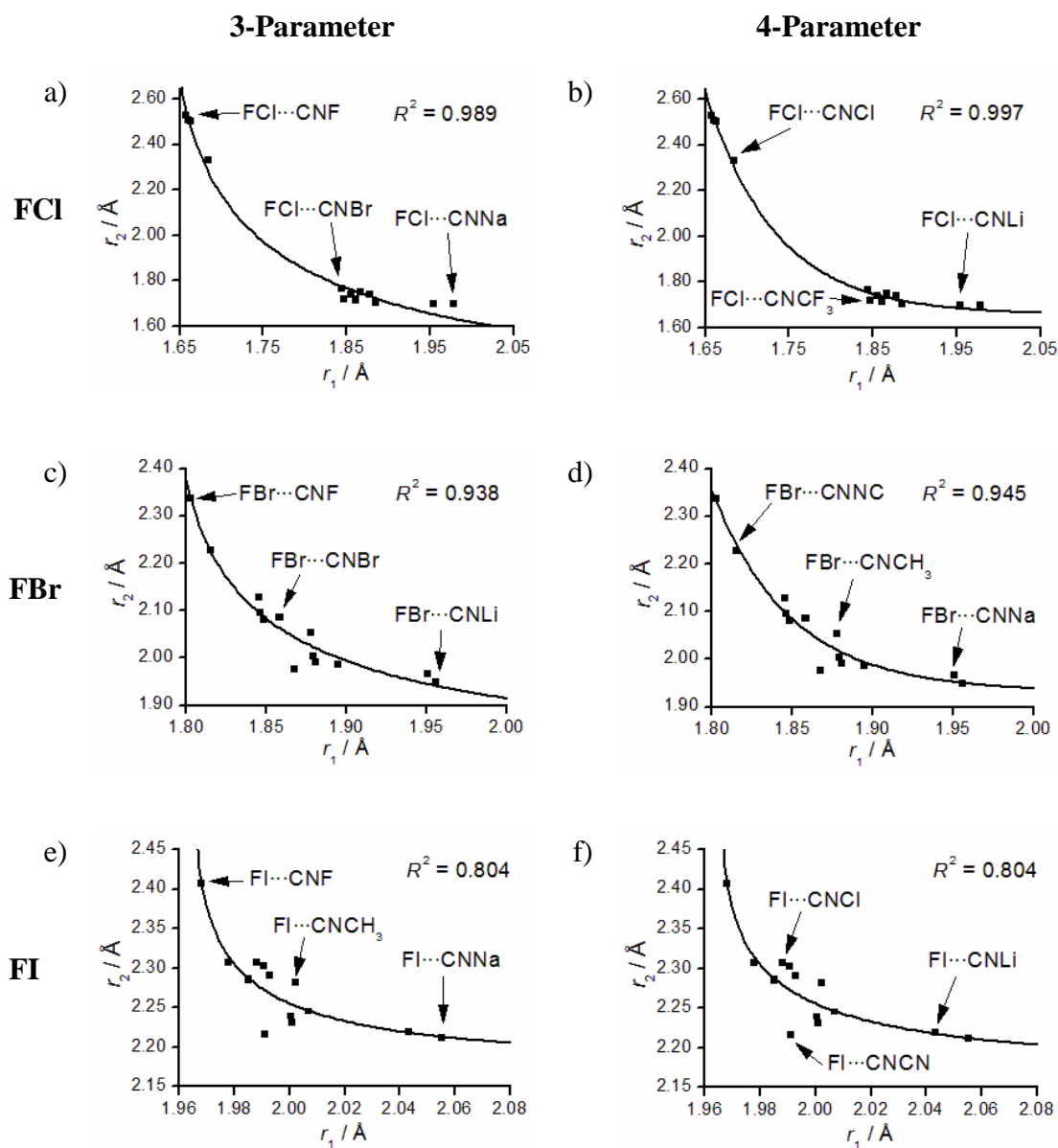


Figure 2-6: Graphs showing the fit of the original and modified Steiner-Limbach equations for complexes with a) and b) FCl, c) and d) FBr and e) and f) FI as the halogen-bond donor calculated using CP correction. Graphs in the left hand column have been fitted with the three-parameter Steiner-Limbach equation (Equation 2-7) and graphs in the right hand column have been fitted with the four-parameter Steiner-Limbach equation (Equation 2-10).

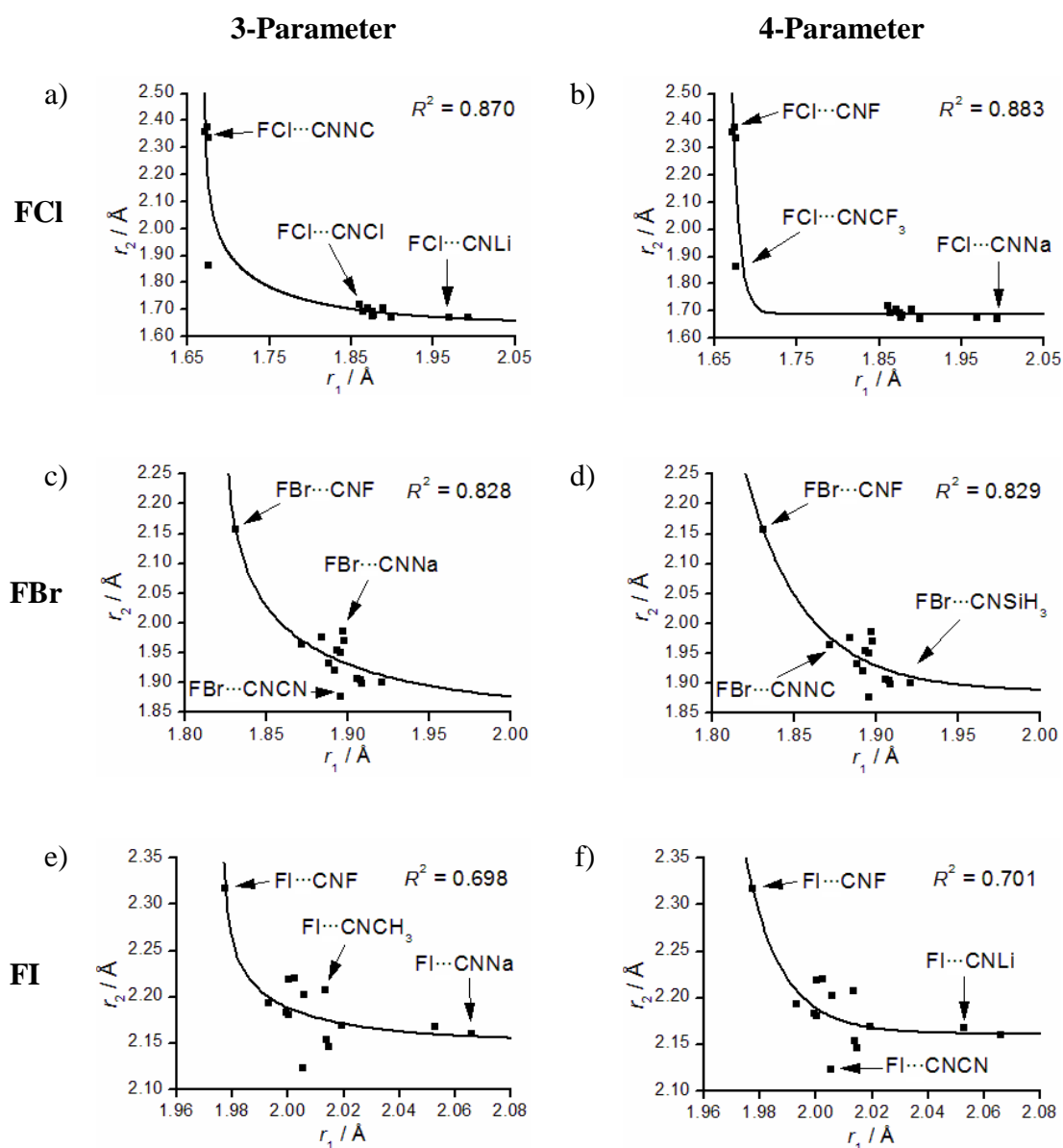


Figure 2-7: Graphs showing the fit of the original and modified Steiner-Limbach equations for complexes with a) and b) FCl, c) and d) FBr and e) and f) FI as the halogen-bond donor calculated without CP correction. Graphs in the left hand column have been fitted with the three-parameter Steiner-Limbach equation (Equation 2-7) and graphs in the right hand column have been fitted with the four-parameter Steiner-Limbach equation (Equation 2-10).

It can be seen that for complexes with FCl as the halogen-bond donor there is an improvement on the goodness of fit when using the four-parameter Steiner-Limbach equation compared to the three-parameter equation. The four-parameter equation particularly improves the fit for the two points corresponding to ion-pair complexes

(FCl:CNLi and FCl:CNNa), where the value of r_1 is much longer than r_2 . As the halogen becomes more polarisable there is little difference in the performances of the three and four-parameter equations. The data for these halogen-bond donors is more spread out and the introduction of a new parameter is unable to improve the fit.

The parameters r_{01} and r_{02} in all forms of the Steiner-Limbach equation correspond to the reference F–X and X–C bond distances in the FX and XCN monomers. These monomers were optimised at the MP2/aug-cc-pVDZ (aug-cc-pVDZ-PP on I) level of theory and the optimised F–X and X–C bond lengths are given in Table 2-7.

Table 2-7: The MP2/aug-cc-pVDZ (aug-cc-pVDZ-PP on I) optimised F–X and X–C bond distances in the isolated monomers FX and XCN.

Molecule 1	Molecule 2	$r(\text{F-X}) / \text{Å}$	$r(\text{X-C}) / \text{Å}$
1, FCl	ClCN	1.6346	1.6251
2, FBr	BrCN	1.7511	1.7697
3, FI	ICN	1.9148	1.9765

There is a reasonable agreement between the values of $r(\text{F-X})$ and $r(\text{X-C})$ given in Table 2-7 and the values of r_{01} and r_{02} given in Tables 2-4, 2-5 and 2-6, although there are some deviations particularly for complexes with more polarisable halogens. The deviations are similar for all three forms of the Steiner-Limbach equation.

The value of parameter b has been calculated using Equation 2-8 when the Steiner-Limbach equation was applied to a series of hydrogen-bonded complexes. This equation was used to calculate the value of b for the halogen-bonded complexes in this study using the values of $r(\text{F-X})$ and $r(\text{X-C})$ in Table 2-7 for r_{01} and r_{02} , respectively, (Table 2-8). The coefficients of determination for the fits of the Steiner-Limbach equations in both forms (Equation 2-1 and Equation 2-7) on the halogen-bonded complexes in this study are also given in Table 2-8.

Table 2-8: The values of parameter b calculated using Equation 2-8 and the values of $r(\text{F-X})$ and $r(\text{X-C})$ given in Table 2-7 for the values of r_{01} and r_{02} respectively. The coefficients of determination for the fit of Steiner-Limbach equations using these calculated parameters on the halogen-bonded complexes FX:CNY are also given. Coefficients for equations applied to data calculated without CP correction are given in parentheses.

Halogen-bond donor	b_{calc}	R^2 (Eq 2-1)	R^2 (Eq 2-7)
1, FCl	0.220949	0.620	0.977
		(0.658)	(0.946)
2, FBr	0.233140	0.336	0.549
		(0.780)	(0.557)
3, FI	0.227585	0.434	0.559
		(-0.202)	(0.0907)

The values of b_{calc} in Table 2-8 differ significantly from the values of b in Tables 2-4 and 2-5 obtained by maximising the fit. The coefficients of determination are significantly lower than the optimised values particularly when these calculated parameters are used in the Steiner-Limbach equation in the form in Equation 2-7. This suggests that although calculating the parameter b using Equation 2-8 is appropriate for hydrogen-bonded complexes it is not appropriate for the halogen-bonded complexes in this study.

2.4.3 Hydrogen-Bonded Complexes

It has been established that the introduction of a new parameter to the Steiner-Limbach equation has improved the fit for halogen-bonded complexes particularly with Cl as the halogen-bond donor. The Steiner-Limbach equation was originally developed for hydrogen-bonded complexes²⁰⁹ so it would be of interest to examine the performance of the modified equation on a series of hydrogen-bonded complexes.

18	F-H	28	N≡C-Cl
19	Cl-H	29	N≡C-C≡C-H
20	Br-H	30	N≡C-H
21	I-H	31	N≡C-C≡C-F
22	N≡N	32	$\begin{array}{c} \text{F} \\ \\ \text{N}=\text{C}-\text{F} \\ \\ \text{H} \end{array}$
23	$\text{N}\equiv\text{C}-\overset{\oplus}{\text{N}}\begin{array}{l} \text{O} \\ // \\ \text{O} \end{array}$	33	N≡C-CH ₃
24	N≡C-C≡N	34	$\begin{array}{c} \text{H} \\ \\ \text{N}=\text{C}-\text{H} \\ \\ \text{H} \end{array}$
25	N≡C-N ⁺ ≡C ⁻	35	NH ₃
26	N≡C-CF ₃	36	$\begin{array}{c} \text{H} \\ \\ \text{N}=\text{C}-\text{H} \\ \\ \text{CH}_3 \end{array}$
27	N≡C-F	37	N≡C-Li

Figure 2-8: The hydrogen halides and nitrogen bases in the hydrogen-bonded complexes investigated in this study.

The geometries of hydrogen-bonded complexes between acids XH, where X = F, Cl, Br or I and a series of nitrogen bases (shown in Figure 2-8) were optimised at the MP2/aug-cc-pVTZ level of theory.ⁱⁱ Many of the nitrogen bases chosen have been used previously in an investigation of halogen-bonded complexes with FCl,²²⁰ with some additional, common nitrogen bases added. The X-H and H···N distances (r_1 and r_2 respectively) have been obtained and are given in Table 2-9 and Tables 2-11 – 2-13 along with $r_1 + r_2$, $r_1 - r_2$ and the binding energies for these complexes.

ⁱⁱ The geometry optimisations of complexes with nitrogen bases **24**, **30** and **32 – 36** were carried out by Akihiro Takemura as part of his MChem final year project, which I co-supervised.

Table 2-9: The F–H (r_1), H–N (r_2) and F–N ($r_1 + r_2$) separations and [$r(\text{F–H})-r(\text{H–N})$], ($r_1 - r_2$) and binding energies of the MP2(Full)/aug-cc-pVTZ optimised geometries of complexes between FH and a series of nitrogen bases. Values in parentheses correspond to those calculated without CP correction. The complexes are ordered with increasing binding energy of the CP corrected results.

Complex	$r_1 / \text{Å}$	$r_2 / \text{Å}$	$r_1 + r_2 / \text{Å}$	$r_1 - r_2 / \text{Å}$	$\Delta E / \text{kJ mol}^{-1}$
18.22					
FH:N ₂	0.9234 (0.9324)	2.0932 (2.0240)	3.0165 (2.9474)	-1.1698 (-1.1005)	9.47 (14.52)
18.23					
FH:NCNO ₂	0.9281 (0.9285)	1.9327 (1.8781)	2.8609 (2.8066)	-1.1005 (-0.9496)	20.10 (27.40)
18.24					
FH:NCCN	0.9287 (0.9290)	1.9203 (1.8698)	2.8490 (2.7988)	-0.9916 (-0.9408)	21.29 (29.45)
18.25					
FH:NCNC	0.9295 (0.9301)	1.9018 (1.8469)	2.8313 (2.7771)	-0.9723 (-0.9168)	23.37 (31.50)
18.26					
FH:NCCF ₃	0.9295 (0.9299)	1.9045 (1.8570)	2.8341 (2.7870)	-0.9750 (-0.9271)	23.39 (30.69)
18.27					
FH:NCF	0.9317 (0.9318)	1.8681 (1.8249)	2.7993 (2.7568)	-0.9368 (-0.8931)	28.12 (36.20)

Table 2-9: (Continued)

Complex	$r_1 / \text{\AA}$	$r_2 / \text{\AA}$	$r_1 + r_2 / \text{\AA}$	$r_1 - r_2 / \text{\AA}$	$\Delta E / \text{kJ mol}^{-1}$
18.28	0.9326 (0.9333)	1.8527 (1.8060)	2.7853 (2.7393)	-0.9201 (-0.8727)	30.26 (39.32)
18.29	0.9329 (0.9332)	1.8517 (1.8112)	2.7845 (2.7444)	-0.9188 (-0.8780)	30.65 (37.91)
18.30	0.9328 (0.9333)	1.8517 (1.8121)	2.7845 (2.7454)	-0.9189 (-0.8787)	30.89 (37.72)
18.31	0.9333 (0.9335)	1.8447 (1.8075)	2.7780 (2.7410)	-0.9114 (-0.8739)	31.54 (39.18)
18.32	0.9385 (0.9399)	1.7961 (1.7563)	2.7346 (2.6961)	-0.8575 (-0.8164)	34.35 (39.75)
18.33	0.9361 (0.9365)	1.8082 (1.7766)	2.7443 (2.7131)	-0.8721 (-0.8401)	37.38 (44.57)
18.34	0.9509 (0.9524)	1.7013 (1.6739)	2.6521 (2.6263)	-0.7504 (-0.7215)	49.06 (53.98)

Table 2-9: (Continued)

Complex	$r_1 / \text{\AA}$	$r_2 / \text{\AA}$	$r_1 + r_2 / \text{\AA}$	$r_1 - r_2 / \text{\AA}$	$\Delta E / \text{kJ mol}^{-1}$
18.35 FH:NH ₃	0.9538 (0.9550)	1.6991 (1.6756)	2.6527 (2.6306)	-0.7456 (-0.7206)	51.24 (55.99)
18.36 FH:N(CH ₃)CH ₂	0.9556 (0.9579)	1.6788 (1.6465)	2.6344 (2.6044)	-0.7232 (-0.6886)	51.97 (58.35)
18.37 FH:NCLi	0.9473 (0.9497)	1.7183 (1.6741)	2.6656 (2.6238)	-0.7710 (-0.7244)	56.41 (66.58)

Table 2-9 shows that all of the hydrogen bonds between HF and the series of nitrogen bases studied are traditional hydrogen bonds since the value of $r_1 - r_2$ is always negative. The value of r_1 is slightly elongated when compared to the length of the H–F bond in the monomer, which is 0.9201 Å. The value of r_2 is considerably longer than the length of the N–H bond in the protonated nitrogen base monomers, Table 2-10.

Table 2-10: The N–H bond length in the protonated nitrogen base monomers.

Base	Protonated base	$r(\text{N–H}^+) / \text{Å}$
22	$[\text{HN}_2]^+$	1.0328
23	$[\text{HNCNO}_2]^+$	1.0149
24	$[\text{HNCCN}]^+$	1.0147
25	$[\text{HNCNC}]^+$	1.0123
26	$[\text{HNCCF}_3]^+$	1.0141
27	$[\text{HNCF}]^+$	1.0119
28	$[\text{HNCCI}]^+$	1.0091
29	$[\text{HNCCCH}]^+$	1.0090
30	$[\text{HNCH}]^+$	1.0133
31	$[\text{HNCCCF}]^+$	1.0081
32	$[\text{HN(H)CF}_2]^+$	1.0131
33	$[\text{HNCCH}_3]^+$	1.0086
34	$[\text{HN(H)CH}_2]^+$	1.0143
35	$[\text{HNH}_3]^+$	1.0201
36	$[\text{HN(CH}_3\text{)CH}_2]^+$	1.0165
37	$[\text{HNCLi}]^+$	1.0035

As the nitrogen bases become more basic, the hydrogen bond in the complex becomes stronger as indicated by the increase in binding energy, decrease in r_2 and

lengthening of r_1 . Although the hydrogen bonds become stronger, a proton-shared hydrogen bond is not observed.

Similar to the case with halogen-bonded complexes, counterpoise correction is important in these calculations. There is a significant difference in bond distances and the binding energies when comparing those calculated with and without counterpoise correction with the latter leading to an overestimation of the hydrogen bond strength.

Table 2-11 shows the results for complexes with HCl as the hydrogen-bond donor. The results are similar to those in Table 2-9 with all the hydrogen bonds being classified as traditional hydrogen bonds with a large value of r_2 and a negative value for $r_1 - r_2$. The values of r_1 show a slight lengthening when compared to the H-Cl bond length in the HCl monomer, which is 1.2710 Å.

Table 2-11: The Cl–H (r_1), H–N (r_2) and Cl–N ($r_1 + r_2$) separations and $[r(\text{Cl–H})-r(\text{H–N})]$, ($r_1 - r_2$) and binding energies of the MP2(Full)/aug-cc-pVTZ optimised geometries of complexes between ClH and a series of nitrogen bases. Values in parentheses correspond to those calculated without CP correction. The complexes are ordered with increasing binding energy of the CP corrected results.

	Complex	$r_1 / \text{Å}$	$r_2 / \text{Å}$	$r_1 + r_2 / \text{Å}$	$r_1 - r_2 / \text{Å}$	$\Delta E / \text{kJ mol}^{-1}$
19.22	ClH:N ₂	1.2731	2.3594	3.6325	-1.0864	6.06
		(1.2732)	(2.1988)	(3.4720)	(-0.9255)	(12.20)
19.23	ClH:NCNO ₂	1.2773	2.1594	3.4367	-0.8820	13.05
		(1.2786)	(2.0312)	(3.3098)	(-0.7527)	(21.62)
19.24	ClH:NCCN	1.2780	2.1408	3.4188	-0.8763	13.91
		(1.2794)	(2.0117)	(3.2911)	(-0.7322)	(23.80)
19.26	ClH:NCCF ₃	1.2788	2.1244	3.4032	-0.8456	15.16
		(1.2802)	(2.0040)	(3.2842)	(-0.7238)	(24.12)
19.25	ClH:NCNC	1.2790	2.1133	3.3923	-0.8343	15.41
		(1.2808)	(1.9879)	(3.2686)	(-0.7071)	(25.13)
19.27	ClH:NCF	1.2810	2.0676	3.3486	-0.7866	18.63
		(1.2825)	(1.9668)	(3.2493)	(-0.6844)	(28.35)

Table 2-11: (Continued).

	Complex	$r_1 / \text{\AA}$	$r_2 / \text{\AA}$	$r_1 + r_2 / \text{\AA}$	$r_1 - r_2 / \text{\AA}$	$\Delta E / \text{kJ mol}^{-1}$
19.28	ClH:NCCI	1.2826	2.0427	3.3253	-0.7601	20.32
		(1.2845)	(1.9393)	(3.2238)	(-0.6549)	(31.28)
19.30	ClH:NCH	1.2826	2.0493	3.3319	-0.7667	20.38
		(1.2846)	(1.9501)	(3.2346)	(-0.6655)	(28.92)
19.29	ClH:NCCCH	1.2829	2.0403	3.3232	-0.7574	20.63
		(1.2852)	(1.9330)	(3.2182)	(-0.6479)	(29.80)
19.31	ClH:NCCCF	1.2835	2.0309	3.3144	-0.7475	21.24
		(1.2857)	(1.9252)	(3.2109)	(-0.6395)	(31.02)
19.32	ClH:N(H)CF ₂	1.2893	1.9714	3.2607	-0.6822	22.50
		(1.2926)	(1.8810)	(3.1736)	(-0.5884)	(30.22)
19.33	ClH:NCCH ₃	1.2870	1.9810	3.2680	-0.6939	25.35
		(1.2892)	(1.8944)	(3.1836)	(-0.6053)	(35.04)
19.35	ClH:NH ₃	1.3168	1.7868	3.1035	-0.4699	35.24
		(1.3234)	(1.7204)	(3.0438)	(-0.3970)	(43.27)

Table 2-11: (Continued).

Complex	$r_1 / \text{\AA}$	$r_2 / \text{\AA}$	$r_1 + r_2 / \text{\AA}$	$r_1 - r_2 / \text{\AA}$	$\Delta E / \text{kJ mol}^{-1}$
19.34 ClH:N(H)CH ₂	1.3140 (1.3201)	1.7724 (1.7065)	3.0864 (3.0650)	-0.4585 (-0.3864)	35.33 (43.51)
19.36 ClH:N(CH ₃)CH ₂	1.3298 (1.3404)	1.7007 (1.6266)	3.0305 (2.9670)	-0.3709 (-0.2862)	39.27 (5010)
19.37 ClH:NCLi	1.3063 (1.3119)	1.8166 (1.7392)	3.1228 (3.0512)	-0.5103 (-0.4273)	41.12 (54.03)

The fact that all the complexes are classified as traditional hydrogen bonds and not ion-pair complexes, indicating that proton transfer has not occurred in any complex, could be surprising considering the acidity of HCl and the strengths of some of the bases investigated. There has been some debate about whether ammonia and HCl interact via an ion-pair Mulliken inner complex, $\text{H}_3\text{NH}^+\cdots\text{Cl}^-$, or via a hydrogen-bonded outer complex, $\text{H}_3\text{N}\cdots\text{ClH}$.²³¹ Experiments carried out using rotational spectroscopy in the gas phase revealed that the interaction was via the latter hydrogen-bond interaction.²³² This observation was explained as being to the Coulombic interaction in the ion-pair interaction being too small to compensate for the energy required for proton transfer.²³³ Hydrogen bond interactions were also observed for complexes between ammonia and HBr ²³⁴ and HI ²³³, indicating that increasing the acidity of the hydrogen-bond donor was insufficient to cause proton transfer. Proton transfer was observed in clusters $(\text{NH}_3,\text{HCl})_n$, when $n = 2$,²³⁵ because the increase in the Coulombic interaction is sufficient to overcome the proton transfer energy. Proton transfer is also observed if trimethylammonia, $(\text{CH}_3)_3\text{N}$,²³⁶⁻²³⁸ is the base because the basicity increases. The bases included in this study are not sufficiently basic to cause proton transfer.

Table 2-12: The Br–H (r_1), H–N (r_2) and Br–N ($r_1 + r_2$) separations and [$r(\text{Br–H}) - r(\text{H–N})$], ($r_1 - r_2$) and binding energies of the MP2(Full)/aug-cc-pVTZ optimised geometries of complexes between BrH and a series of nitrogen bases. Values in parentheses correspond to those calculated without CP correction. The complexes are ordered with increasing binding energy of the CP corrected results.

Complex	$r_1 / \text{Å}$	$r_2 / \text{Å}$	$r_1 + r_2 / \text{Å}$	$r_1 - r_2 / \text{Å}$	$\Delta E / \text{kJ mol}^{-1}$
20.22 BrH:N ₂	1.4005 (1.4017)	2.4514 (2.2304)	3.8519 (3.6320)	-1.0509 (-0.8287)	5.25 (13.78)
20.23 BrH:NCNO ₂	1.4040 (1.4069)	2.2390 (2.0558)	3.6430 (3.4627)	-0.8350 (-0.6489)	11.22 (23.03)
20.24 BrH:NCCN	1.4046 (1.4078)	2.2200 (2.0336)	3.6246 (3.4414)	-0.8154 (-0.6258)	11.98 (25.50)
20.26 BrH:NCCF ₃	1.4053 (1.4087)	2.2040 (2.0277)	3.6092 (3.4364)	-0.7987 (-0.6190)	12.97 (25.44)
20.25 BrH:NCNC	1.4055 (1.4093)	2.1899 (2.0096)	3.5954 (3.4189)	-0.7844 (-0.6003)	13.27 (26.61)
20.27 BrH:NCF	1.4073 (1.4109)	2.1402 (1.9917)	3.5474 (3.4026)	-0.7329 (-0.5808)	16.01 (28.88)

Table 2-12: (Continued).

Complex	$r_1 / \text{\AA}$	$r_2 / \text{\AA}$	$r_1 + r_2 / \text{\AA}$	$r_1 - r_2 / \text{\AA}$	$\Delta E / \text{kJ mol}^{-1}$
20.30 BrH:NCH	1.4087 (1.4131)	2.1216 (1.9741)	3.5303 (3.3871)	-0.7129 (-0.5610)	17.47 (29.29)
20.28 BrH:NCCI	1.4088 (1.4132)	2.1114 (1.9565)	3.5202 (3.3697)	-0.7027 (-0.5433)	17.57 (32.00)
20.29 BrH:NCCCH	1.4091 (1.4140)	2.1086 (1.9474)	3.5177 (3.3614)	-0.6996 (-0.5334)	17.86 (31.34)
20.31 BrH:NCCCF	1.4095 (1.4146)	2.0985 (1.9385)	3.5080 (3.3531)	-0.6889 (-0.5238)	18.39 (32.44)
20.32 BrH:N(H)CF ₂	1.4149 (1.4230)	2.0365 (1.8762)	3.4514 (3.2991)	-0.6216 (-0.4532)	19.28 (31.18)
20.33 BrH:NCCCH ₃	1.4129 (1.4187)	2.0438 (1.9047)	3.4567 (3.3234)	-0.6309 (-0.4860)	21.91 (35.97)

Table 2-12: (Continued).

Complex	$r_1 / \text{\AA}$	$r_2 / \text{\AA}$	$r_1 + r_2 / \text{\AA}$	$r_1 - r_2 / \text{\AA}$	$\Delta E / \text{kJ mol}^{-1}$
20.35 BrH:NH ₃	1.4464 (1.4694)	1.8074 (1.6600)	3.2539 (3.1294)	-0.3610 (-0.1906)	30.85 (44.21)
20.34 BrH:N(H)CH ₂	1.4441 (1.4680)	1.7857 (1.6268)	3.2299 (3.0948)	-0.3416 (-0.1587)	31.68 (46.15)
20.36 BrH:N(CH ₃)CH ₂	1.4716 (1.7127)	1.6668 (1.2023)	3.1385 (2.9146)	-0.1952 (0.5099)	36.26 (57.75)
20.37 BrH:NCLi	1.4337 (1.4485)	1.8460 (1.7101)	3.2797 (3.1585)	-0.4123 (-0.2616)	36.71 (55.00)

Table 2-12 shows the results for complexes with HBr as the hydrogen-bond donor. The results are similar to those found for HF and HCl as the hydrogen-bond donor, since the majority of hydrogen bonds are classified as traditional hydrogen bonds. The exception to this is the complex $\text{BrH:N(CH}_3\text{)CH}_2$ optimised without counterpoise correction, which can be classified as an ion-pair hydrogen bond. In this complex the value of r_1 is considerably longer than the H-Br bond length in the HBr monomer, 1.3990 Å. The values of $r_1 - r_2$ is positive and the value of r_2 is much shorter than for complexes with traditional hydrogen bonds and approaches the value of the H-N bond length in the protonated monomer. The optimised geometry of this complex calculated with counterpoise correction gives a very different result with the complex showing characteristics of a traditional hydrogen bond.

Table 2-13: The I–H (r_1), H–N (r_2) and I–N ($r_1 + r_2$) separations and [$r(\text{I–H}) - r(\text{H–N})$], ($r_1 - r_2$) and binding energies of the MP2(Full)/aug-cc-pVTZ optimised geometries of complexes between IH and a series of nitrogen bases. Values in parentheses correspond to those calculated without CP correction. The complexes are ordered with increasing binding energy of the CP corrected results.

	Complex	$r_1 / \text{Å}$	$r_2 / \text{Å}$	$r_1 + r_2 / \text{Å}$	$r_1 - r_2 / \text{Å}$	$\Delta E / \text{kJ mol}^{-1}$
21.22	IH:N ₂	1.5972	2.5960	4.1932	-0.9989	4.09
		(1.5965)	(2.3978)	(3.9943)	(-0.8013)	(10.13)
21.23	IH:NCNO ₂	1.5997	2.3709	3.9706	-0.7713	8.66
		(1.5998)	(2.2100)	(3.8098)	(-0.6102)	(17.35)
21.24	IH:NCCN	1.6002	2.3500	3.9501	-0.7498	9.28
		(1.6004)	(2.1856)	(3.7859)	(-0.5852)	(19.35)
21.26	IH:NCCF ₃	1.6006	2.3355	3.9361	-0.7349	9.92
		(1.6009)	(2.1855)	(3.7864)	(-0.5845)	(19.04)
21.25	IH:NCNC	1.6009	2.3162	3.9172	-0.7153	10.27
		(1.6013)	(2.1712)	(3.7725)	(-0.5699)	(19.74)
21.27	IH:NCF	1.6023	2.2616	3.8639	-0.6593	12.28
		(1.6032)	(2.1289)	(3.7321)	(-0.5258)	(22.10)

Table 2-13: (Continued).

Complex	$r_1 / \text{\AA}$	$r_2 / \text{\AA}$	$r_1 + r_2 / \text{\AA}$	$r_1 - r_2 / \text{\AA}$	$\Delta E / \text{kJ mol}^{-1}$
21.30 IH:NCH	1.6034 (1.6048)	2.2438 (2.1183)	3.8472 (3.7231)	-0.6404 (-0.5135)	13.33 (21.77)
21.28 IH:NCCI	1.6036 (1.6053)	2.2276 (2.0811)	3.8313 (3.6864)	-0.6240 (-0.4757)	13.60 (24.83)
21.29 IH:NCCCH	1.6039 (1.6058)	2.2243 (2.0770)	3.8282 (3.6827)	-0.6205 (-0.4712)	13.87 (23.18)
21.31 IH:NCCCF	1.6043 (1.6064)	2.2133 (2.0623)	3.8176 (3.6687)	-0.6091 (-0.4559)	14.27 (24.22)
21.32 IH:N(H)CF ₂	1.6088 (1.6123)	2.1525 (2.0298)	3.7612 (3.6421)	-0.5437 (-0.4176)	14.68 (22.55)
21.33 IH:NCCCH ₃	1.6072 (1.6097)	2.1523 (2.0269)	3.7596 (3.6366)	-0.5451 (-0.4172)	16.95 (27.17)

Table 2-13: (Continued).

Complex	$r_1 / \text{\AA}$	$r_2 / \text{\AA}$	$r_1 + r_2 / \text{\AA}$	$r_1 - r_2 / \text{\AA}$	$\Delta E / \text{kJ mol}^{-1}$
21.35 IH:NH ₃	1.6504	1.8231	3.4735	-0.1728	24.32
	(1.9839)	(1.1701)	(3.1540)	(0.8139)	(38.02)
21.34 IH:N(H)CH ₂	1.6491	1.7887	3.4378	-0.1397	26.26
	(1.9978)	(1.1544)	(3.1522)	(0.8434)	(40.69)
21.37 IH:NCLi	1.6308	1.8944	3.5251	-0.2636	29.89
	(1.6463)	(1.7514)	(3.3978)	(-0.1051)	(44.51)
21.36 IH:N(CH ₃)CH ₂	2.0133	1.1527	3.1660	0.8605	41.79
	(2.0137)	(1.1345)	(3.1482)	(0.8792)	(61.90)

Table 2-13 shows the results with HI as the hydrogen-bond donor. The majority of the hydrogen bonds present are traditional hydrogen bonds as observed with the other hydrogen-bond donors. There are a few more examples of ion-pair hydrogen bonds, as would be expected due to the acidity of HI being greater than that of other hydrogen halides.

The results obtained for complexes with base **35**, NH₃, can be compared to experimental results obtained by rotational spectroscopy in the gas phase (Table 2-14). There is excellent agreement between the experimental and theoretical values showing that the level of theory used in this investigation is appropriate for modelling these complexes.

Table 2-14: Comparison of the theoretical and experimental $r(X\cdots N)$ distances ($r_1 + r_2$) in complexes between hydrogen halides, XH, and ammonia, NH₃.

Complex	$r_1 + r_2 / \text{\AA}$		
	Experimental	Theory	% Difference
18.35 FH:NH ₃	2.71 ²³⁸	2.6527	2.11
19.35 ClH:NH ₃	3.136 ²³²	3.1035	1.04
20.35 BrH:NH ₃	3.255 ²³⁴	3.2539	0.03
21.35 IH:NH ₃	3.584 ²³⁸	3.4735	3.08

2.4.4 Curve-Fitting for Hydrogen-Bonded Complexes

The parameters of the three-parameter Steiner-Limbach equation in the form given in Equation 2-7 were optimised to give the best goodness of fit for the values of r_1 and r_2 for the hydrogen-bonded complexes with nitrogen bases (Table 2-15).

Table 2-15: The evaluated parameters, r_{01} , r_{02} and b of the three-parameter Steiner-Limbach equation (Equation 2-7) and values of the coefficient of determination, R^2 , maximum absolute residual, e_{\max} and the average of the absolute residuals, e_{av} for complexes between hydrogen halides XH and nitrogen bases. Results for calculations without CP correction are given in parentheses.

Hydrogen-Bond Donor	$r_{01} / \text{\AA}$	$r_{02} / \text{\AA}$	b	R^2	e_{\max}	e_{av}
18, HF	0.9204	1.3886	0.1731	0.998	0.00883	0.00285
	(0.9200)	(1.3986)	(0.1617)	(0.994)	(0.0131)	(0.00380)
19, HCl	1.2699	1.3877	0.2261	0.996	0.0201	0.00614
	(1.2683)	(1.3782)	(0.2150)	(0.992)	(0.0223)	(0.00793)
20, HBr	1.3978	1.3804	0.2370	0.995	0.0276	0.00838
	(1.3872)	(1.0630)	(0.3465)	(0.989)	(0.0586)	(0.0201)
21, HI	1.5951	1.0856	0.3497	0.798	0.284	0.142
	(1.5872)	(1.0223)	(0.3586)	(0.997)	(0.0622)	(0.0212)

With the exception of the complexes with HI as the hydrogen-bond donor, the goodness of fit of the Steiner-Limbach equation on data calculated with counterpoise is better than that for data calculated without counterpoise correction as indicated by the R^2 values closer to 1 and the smaller values of e_{\max} and e_{av} . This is similar to the results observed for halogen-bonded complexes, although the differences here are not as large.

The coefficient of determination, R^2 , is particularly low for the complexes with HI as the hydrogen-bond donor because the residuals for complexes with smaller values of r_1 and larger values of r_2 . The curve produced by the three-parameter equation is too steep in this region and fails to model complexes with weaker bases accurately. This highlights the advantage of using the original Steiner-Limbach equation in the form with $r_1 + r_2$ given as a function of $r_1 - r_2$.

The values for parameter r_{01} are similar to the H–X bond distance in the HX monomer. The values of r_{02} for the complexes with HI as the hydrogen-bond donor and HBr as the hydrogen-bond donor when calculated without CP correction are only marginally longer than the length of the N–H bond in the protonated nitrogen monomers. The value of r_{02} for the other data sets is much longer. This could be due to the fact that these data sets contain only complexes with traditional hydrogen bonds so the optimised parameters do not allow for proton-shared or ion-pair hydrogen bonds.

The parameters of the Steiner-Limbach equation in its original form with $r_1 + r_2$ correlated with $r_1 - r_2$ (Equation 2-1) were evaluated for the hydrogen-bonded complexes between hydrogen halides and nitrogen bases (Table 2-16).

Table 2-16: The evaluated parameters, r_{01} , r_{02} and b of the original Steiner-Limbach equation (Equation 2-1) and values of the coefficient of determination, R^2 , maximum absolute residual, e_{\max} and the average of the absolute residuals, e_{av} for complexes between hydrogen halides XH and nitrogen bases. Results for calculations without CP correction are given in parentheses.

Hydrogen-Bond Donor	$r_{01} / \text{\AA}$	$r_{02} / \text{\AA}$	b	R^2	e_{\max}	e_{av}
18, HF	0.9203	1.3848	0.1745	0.999	0.00285	0.000644
	(0.9191)	(1.3733)	(0.1725)	(0.999)	(0.00511)	(0.00102)
19, HCl	1.2669	1.2954	0.2651	0.999	0.00786	0.00149
	(1.2622)	(1.2545)	(0.2735)	(0.999)	(0.0103)	(0.00212)
20, HBr	1.3932	1.2322	0.3000	0.999	0.0095	0.00187
	(1.3754)	(0.9570)	(0.4170)	(0.999)	(0.0139)	(0.00334)
21, HI	1.5826	0.9578	0.4285	0.999	0.0117	0.00324
	(1.5787)	(0.9683)	(0.4116)	(0.999)	(0.0125)	(0.00359)

The goodness of fit of the Steiner-Limbach equation is better for all complexes in this form compared to the form in Equation 2-7 due to the fact that this form can eliminate any outliers.

The values of the parameters are similar irrespective of the form of the Steiner-Limbach equation with a slightly larger difference for the complexes with HI as the hydrogen-bond donor.

Figure 2-9 shows the fit of the original Steiner-Limbach equation with the parameters given in Table 2-16 for hydrogen-bonded complexes between hydrogen halides and nitrogen bases.

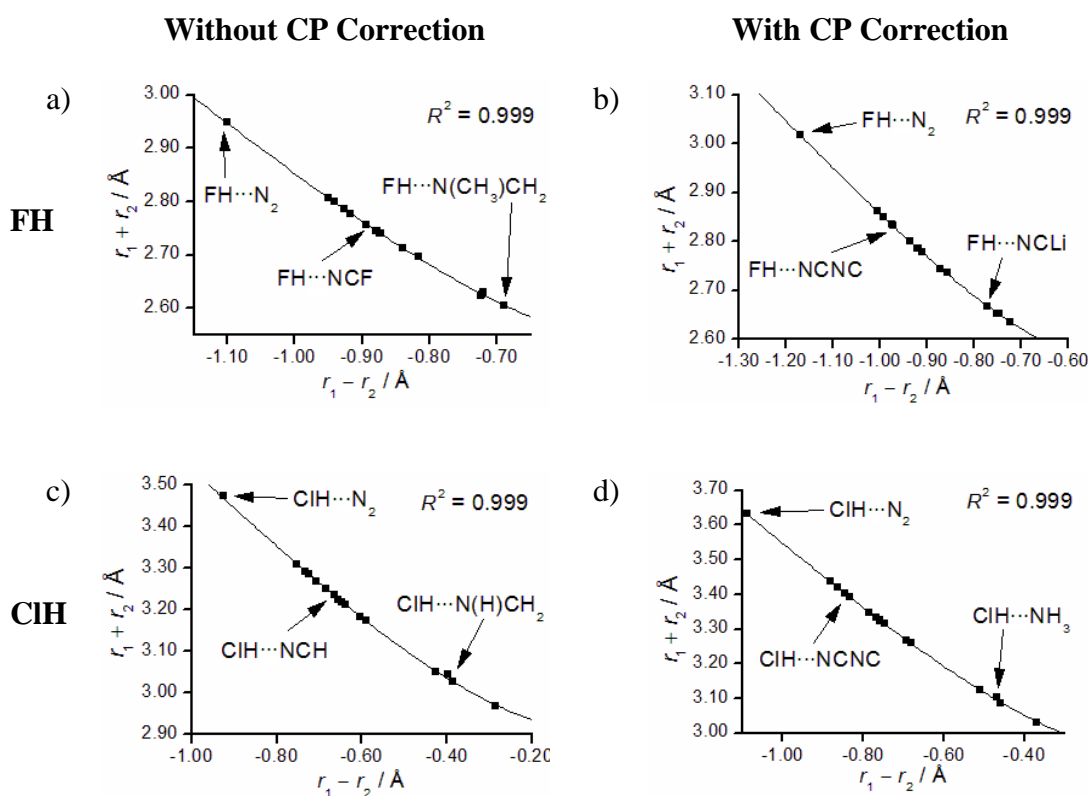


Figure 2-9: Graphs showing the fits of the original Steiner-Limbach equation in its form in Equation 2-1 for complexes with a) and b) HF and c) and d) HCl as the hydrogen-bond donor. Figures in the left hand column correspond to results of calculations without CP correction and figures in the right hand column correspond to results with CP correction of the BSSE.

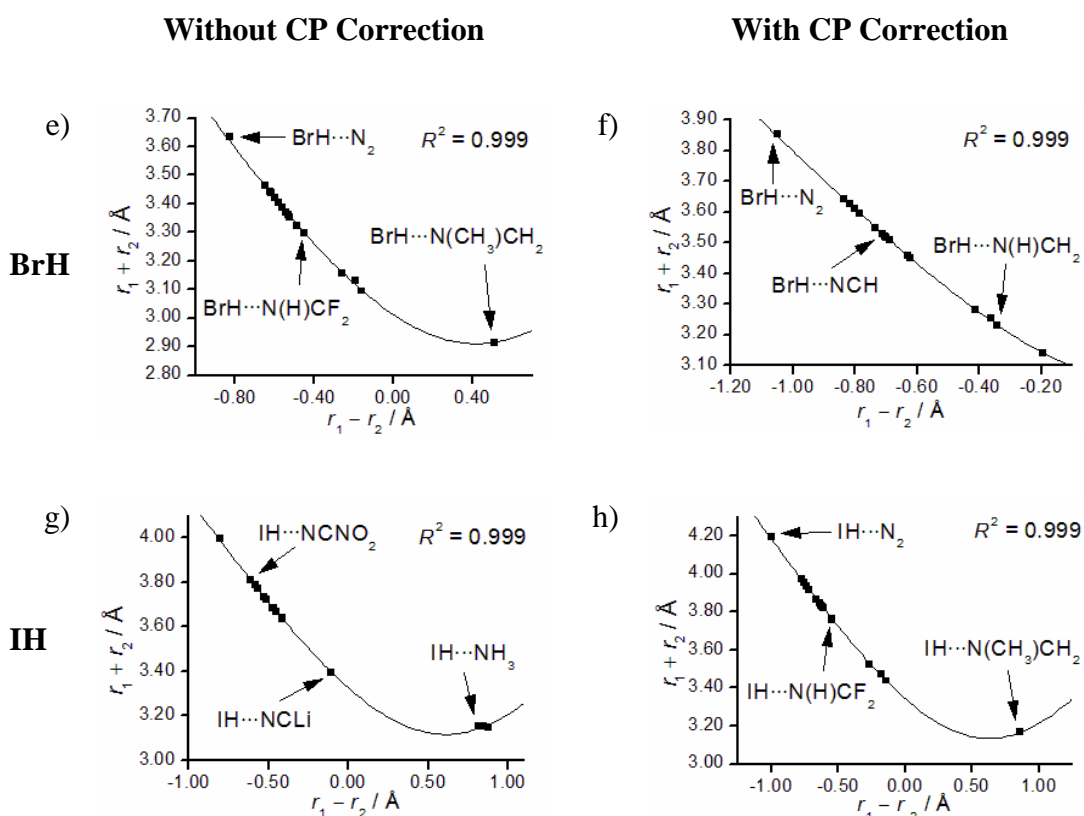


Figure 2-9: (Continued). Graphs showing the fits of the original Steiner-Limbach equation in its form in Equation 2-1 for complexes with e) and f) HBr and g) and h) HI as the hydrogen-bond donor. Figures in the left hand column correspond to results of calculations without CP correction and figures in the right hand column correspond to results with CP correction of the BSSE.

The goodness of fit observed for both forms of the Steiner-Limbach equation are considerably better for these hydrogen-bonded complexes than for the halogen-bonded complexes discussed previously.

The parameters of the four-parameter Steiner-Limbach equation (Equation 2-10) were evaluated for these hydrogen-bonded complexes to investigate whether the introduction of a new parameter can improve the goodness of fit. The parameters for the data sets with HF as the hydrogen-bond donor could be evaluated successfully but difficulties were encountered for complexes with the other hydrogen-bond donors.

Mathematica gave an error when evaluating the parameters to optimise the goodness of fit for the equation stating that the non-linear model fit used failed to converge. Attempts to evaluate the parameters manually revealed that decreasing the value of r_{02} led to an increase in the value of b_1 with very little change to the goodness of fit. It was therefore decided to set the value of r_{02} to 1.0135 Å, the average value of the N–H bond length in the protonated nitrogen monomers given in Table 2-10 and evaluate the remaining three parameters. Table 2-17 shows these evaluated parameters. This suggests that the flexibility of the equation created by the introduction of an additional parameter is lost because the value of one parameter is set to a given value. This could also suggest that having four adjustable parameters in the equation is unnecessary because three parameters are sufficient for describing the bonding in these complexes.

In order to compare the performances of the three and four-parameter Steiner-Limbach equations, graphs showing the fit to the data are given in Figures 2-10 and 2-11.

Table 2-17: The evaluated parameters, r_{01} , r_{02} , b_1 and b_2 of the modified Steiner-Limbach equation (Equation 2-10) and values of the coefficient of determination, R^2 , maximum absolute residual, e_{\max} and the average of the absolute residuals, e_{av} for complexes between fluorohalides and isocyanides, CNY. Results for calculations without CP correction are given in parentheses.

Hydrogen-Bond Donor	r_{01} /Å	r_{02} /Å	b_1	b_2	R^2	e_{\max}	e_{av}
18, HF	0.9203	1.4374	0.1200	0.1789	0.998	0.00849	0.00283
	(0.9203)	(1.1775)	(0.8464)	(0.1510)	(0.994)	(0.0134)	(0.00367)
19, HCl	1.2702	1.0135	1.5917	0.2123	0.996	0.0198	0.00572
	(1.2689)	(1.0135)	(1.7505)	(0.1965)	(0.993)	(0.0219)	(0.00741)
20, HBr	1.3981	1.0135	1.4889	0.2228	0.995	0.0265	0.00765
	(1.3915)	(1.0135)	(0.5367)	(0.2963)	(0.992)	(0.0535)	(0.0184)
21, HI	1.5935	1.0135	0.6604	0.2943	0.988	0.0827	0.0281
	(1.5882)	(1.0135)	(0.4018)	(0.3415)	(0.996)	(0.0547)	(0.0215)

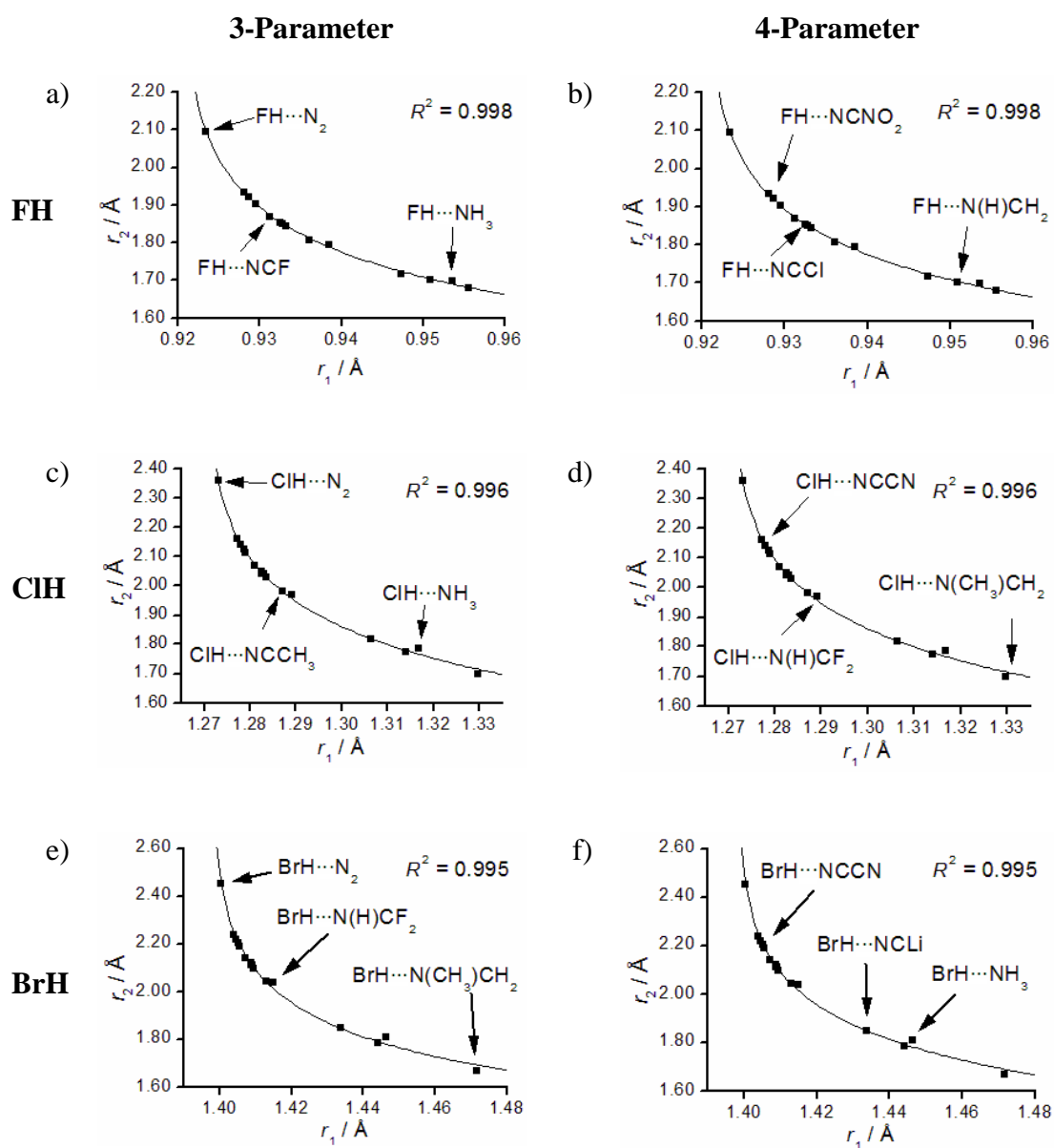


Figure 2-10: Graphs showing the fit of the original and modified Steiner-Limbach equations for complexes with a) and b) HF, c) and d) HCl and e) and f) HBr as the hydrogen-bond donor calculated using CP correction. Graphs in the left hand column have been fitted with the three-parameter Steiner-Limbach equation (Equation 2-7) and graphs in the right hand column have been fitted with the four-parameter Steiner-Limbach equation (Equation 2-10).

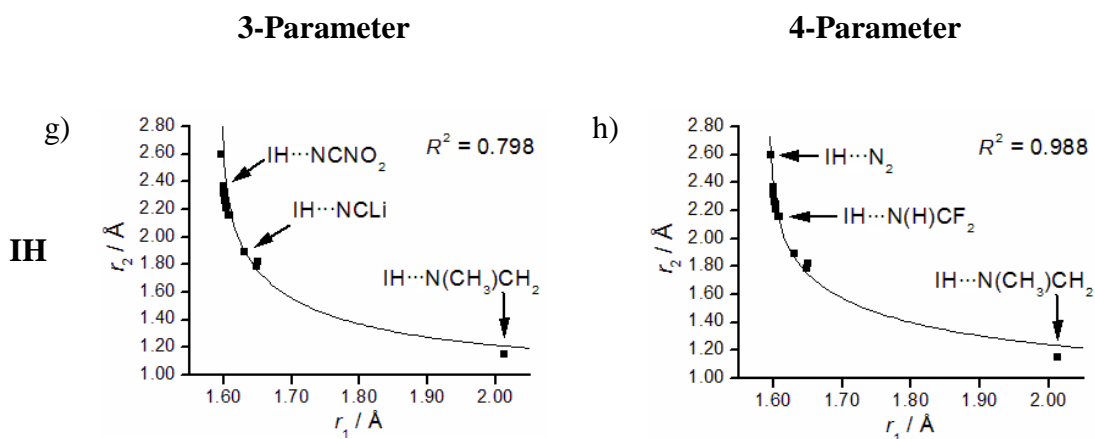


Figure 2-10: (Continued). Graphs showing the fit of the original and modified Steiner-Limbach equations for complexes with g) and h) HI as the hydrogen-bond donor calculated using CP correction. Graphs in the left hand column have been fitted with the three-parameter Steiner-Limbach equation (Equation 2-7) and graphs in the right hand column have been fitted with the four-parameter Steiner-Limbach equation (Equation 2-10).

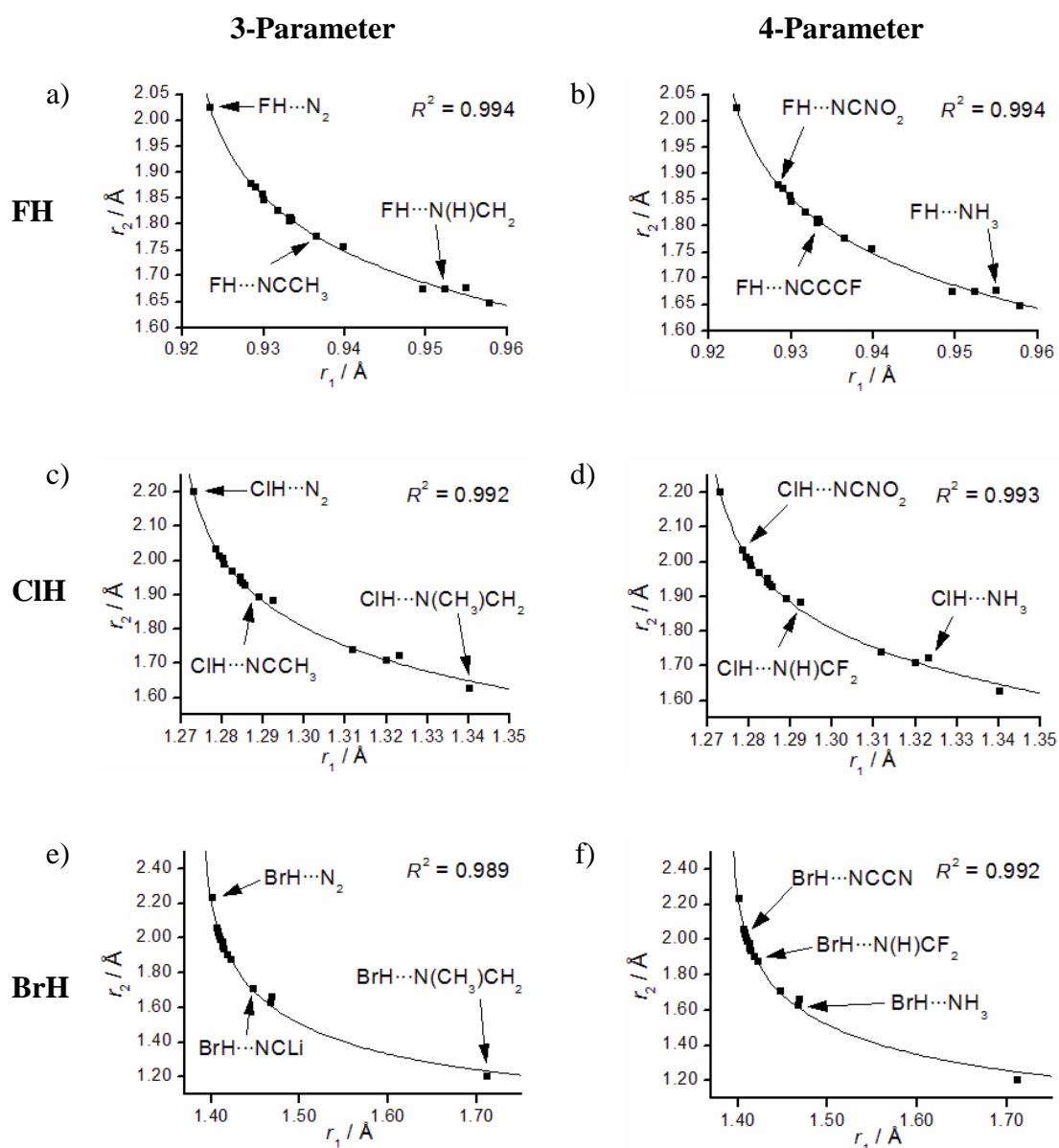


Figure 2-11: Graphs showing the fit of the original and modified Steiner-Limbach equations for complexes with a) and b) HF, c) and d) HCl and e) and f) HBr as the hydrogen-bond donor calculated without CP correction. Graphs in the left hand column have been fitted with the three-parameter Steiner-Limbach equation (Equation 2-7) and graphs in the right hand column have been fitted with the four-parameter Steiner-Limbach equation (Equation 2-10).

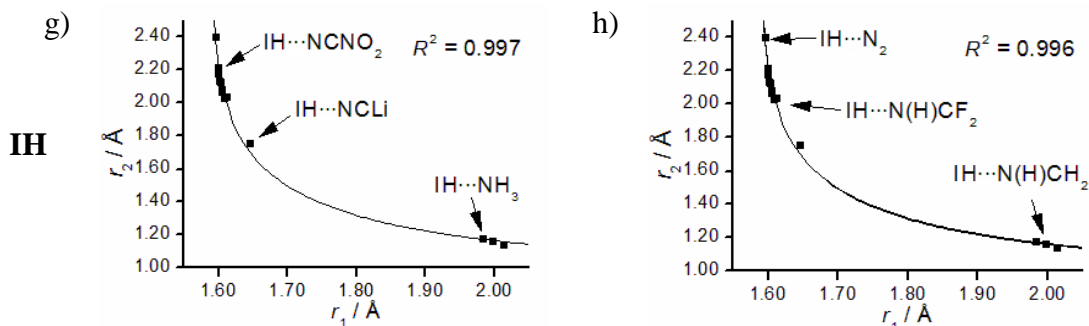


Figure 2-11: (Continued). Graphs showing the fit of the original and modified Steiner-Limbach equations for complexes with g) and h) HI as the hydrogen-bond donor calculated without CP correction. Graphs in the left hand column have been fitted with the three-parameter Steiner-Limbach equation (Equation 2-7) and graphs in the right hand column have been fitted with the four-parameter Steiner-Limbach equation (Equation 2-10).

Figures 2-10 and 2-11 show that there is very little difference in the performance of the three- and four-parameter Steiner-Limbach equations. The only improvement in performance is observed for complexes with HI as the hydrogen-bond donor with counterpoise correction. It is not surprising that the introduction of a new parameter to the Steiner-Limbach equation doesn't lead to an improvement of performance because the three-parameter Steiner-Limbach equation performs very well. This shows that three parameters are sufficient at modelling the bonding in these hydrogen-bonded complexes and the introduction of a new parameter is unnecessary. This is highlighted by the fact that during the optimisation of the four-parameter equation, one of the parameters was redundant and a set value was used.

2.5 Conclusions

The geometries of halogen-bonded complexes between fluorohalides, FX (X = Cl, Br and I), and isocyanides, CNY (Y = CN, NC, NO₂, F, CF₃, Cl, Br, H, CCF, CCH, CH₃, SiH₃, Li and Na) were optimised at the MP2/aug-cc-pVTZ (aug-cc-pVTZ-PP on I) level of theory. Calculations were carried out both with and without CP correction of the BSSE, which led to significant differences in the results. The importance of the use of the CP correction in geometry optimisations was highlighted by the improved quality of the fits to the Steiner-Limbach equations using CP corrected geometries.

In agreement with previous studies,²¹⁹ complexes with FCl were found to change geometry from a traditional halogen bond, to a chlorine-shared halogen bond and finally to an ion-pair halogen bond as the basicity of the isocyanide increased. In contrast, complexes with FBr only had bromine-shared halogen bonds for the complexes with the strongest bases, CNLi and CNNa and complexes with fluoriodide were found to have only a traditional halogen bond for all isocyanides.

The Steiner-Limbach equation, Equation 2-1, an equation developed from the bond valence model that can be used to model the bond lengths in hydrogen-bonded complexes, was fitted to the bond distances observed in the halogen-bonded complexes. The goodness-of-fit was found to decrease as the halogen in the fluorohalide became more polarisable.

A new parameter was introduced to the Steiner-Limbach equation to take into account the difference between the covalent and non-covalent bond in the halogen bond F–X···C. The goodness-of-fit using this four-parameter version of the Steiner-Limbach equation was improved compared to the original three-parameter equation particularly for complexes with FCl. The improvement for complexes with FBr and FI was not as pronounced due to outlying points.

Since the Steiner-Limbach equation was originally designed for hydrogen-bonded complexes, the performance of the four-parameter Steiner-Limbach equation was tested on the MP2/aug-cc-pVTZ optimised geometries of complexes between XH, X = F, Cl, Br and I, and a series of nitrogen bases. The original three-parameter relationship was found to perform very well leaving little room for improvement for the four-parameter relationship, which performed equally well, showing minor improvements in a limited number of cases.

This study has confirmed that the Steiner-Limbach equation is very suitable for modelling the bonding in hydrogen-bonded complexes, but in order to model halogen-bonded complexes, where there is a greater difference between the covalent and non-covalent bonds in the interaction, a new parameter can be introduced to improve the model.

3 The Attractive, Non-covalent Interactions between Halomethanes and Rare Gases

3.1 Introduction

Halogen bonds have strengths that range from 5 kJ mol^{-1} to 180 kJ mol^{-1} .¹⁶⁴ The strength of the halogen bond depends on numerous factors including the choice of halogen, the presence of electron withdrawing groups in the halogen-bond donor and the nature of the base acting as a halogen-bond acceptor. These factors make halogen bonding a tuneable interaction, which makes it useful in crystal engineering and supramolecular chemistry.

One of the weakest known halogen-bond interactions is the $\text{N}\cdots\text{Cl}$ interaction in azaaromatic chlorides, Figure 3-1a.

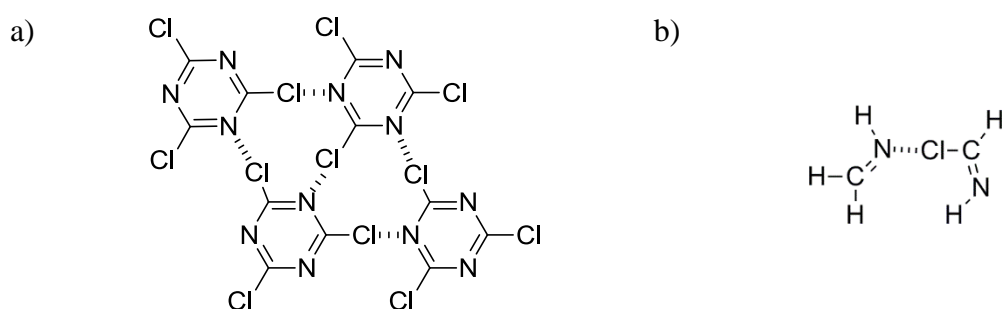


Figure 3-1: The molecular structures of a) cyanuric chloride and b) the formimine-formidoyl chloride model.²³⁹

The $\text{N}\cdots\text{Cl}$ separations are approximately 3.10 \AA , 94% of the sum of the van der Waals radii. *Ab initio* calculations of a formimine-formidoyl chloride model complex, Figure 3-1b, suggested an interaction strength of approximately 5.1 kJ mol^{-1} .

Weak halogen bonding has also been observed in haloanilinium halides (Figure 3-2)²⁴⁰ which have $\text{X}\cdots\text{Y}^-$ separations ranging between 88% and 103% of the sum of

the van der Waals radii, the strongest of these complexes being those of iodoanilinium salts.⁸⁵

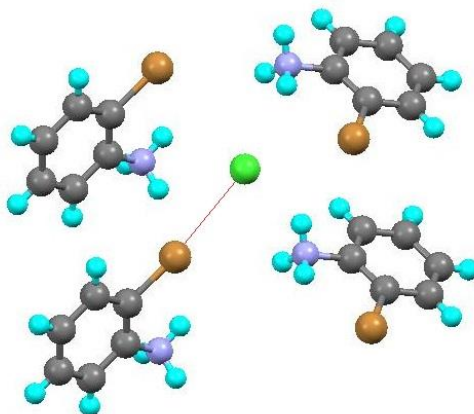


Figure 3-2: The crystal structure of 2-bromoanilinium chloride with the Br...Cl⁻ contact highlighted in red.

In these examples of weak halogen bonds, it is the halogen-bond donor that causes the interaction to be weak because it involves either smaller, less polarisable halogens, *e.g.* Cl, or there are no functional groups that are sufficiently electron withdrawing to activate the halogen atom. In this study, the aim is to investigate complexes where the halogen-bond acceptor is weak and is therefore responsible for the weakness of the interaction.

The effect of the halogen-bond acceptor on the strength of the interactions has been investigated in the gas phase by comparing a series of complexes B...XY, where X, Y = Cl, Br or I and B is a Lewis base. Comparing values of the force constant, k_{σ} , for these complexes reveals that the strength of the interactions in these complexes, for a given XY, are in the order $N_2 < OC < HCCH \sim H_2CCH_2 \sim HCN < H_2O \sim PH_3 < H_2S < NH_3$.³² This trend follows the nucleophilicities of the bases. It would be anticipated that rare gas atoms would have a nucleophilicity that is lower than that of N_2 , and so to explore the limits of weak interactions involving halogens, rare gas atoms can be selected as the halogen-bond acceptor.

Interactions involving rare gas atoms, particularly xenon, are of interest because of their ability to act as anaesthetics.²⁴¹ The mechanism responsible for this was relatively unknown until a study in 1998²⁴² found that rather than enhance the activity of inhibitory γ -aminobutyric acid type A receptors, as is the case for most anaesthetics, xenon inhibits *N*-methyl-D-aspartate (NMDA) receptors, a mechanism known to be adopted by nitrous oxide. Molecular Dynamics (MD) simulations have been used to identify the mechanism of interaction between xenon and NMDA receptors.²⁴³ Despite the fact that developments have been made to understand how xenon causes anaesthesia, an understanding of its interactions at a more fundamental level will help to develop progress further.

3.1.1 Hydrogen Bonding to Rare Gases

There is some debate about whether the interaction within complexes between rare gas atoms and acids can be classified as hydrogen bonds or van der Waals interactions.²¹² Molecular beam scattering experiments and *ab initio* calculations of complexes between water and rare gas atoms, Rg, reveal that for the lighter rare gases (He and Ne), the depth and the position of the potential energy well of these complexes is similar to those observed for oxygen-rare gas complexes, suggesting that both complexes are driven by van der Waals interactions.²⁴⁴ *Ab initio* calculations corroborate this observation revealing that for these complexes, the O–H \cdots Rg interaction deviates significantly from linearity and the binding energy is small. For heavier rare gases, there is an increase in binding energy (2.79 kJ mol⁻¹ for the H₂O \cdots Kr complex) and the rare gas atom is found to be aligned along the direction of the O–H bond, suggesting that the interaction can be classified as a hydrogen bond. Similarly, calculations on the H₂SO₄ \cdots Xe complex, where the O–H \cdots Xe angle is found to be approximately linear, and the observation of a red-shift in the value of $\nu(\text{OH})$ of H₂O in H₂SO₄ trapped in a Xe matrix compared to

H₂SO₄ trapped in an Ar matrix, confirm that interactions with heavier rare gas atoms are not through van der Waals interactions only.²⁴⁵

The proposal that interactions with heavier rare gas atoms can be classified as hydrogen bonding is also supported by Atoms in Molecules (AIM) analysis of the MP2/6-311++G(d,p) optimised geometry of the complex between formic acid and krypton.²⁴⁶ The electron density at the O–H···Kr bond critical point (bcp) has a value of $7.20 \times 10^{-3} \text{ e/bohr}^3$, which is close to the typical value for hydrogen bonds and is considerably larger than that for the O–H···Ar interaction. Calculations of the formic acid-xenon complex have shown that it has an interaction energy similar to the complex with krypton.²⁴⁷ Symmetry-adapted perturbation theory (SAPT) analysis of these complexes reveals that the interaction is predominantly dispersion in nature with an increase in the induction energy term as the rare gas atom becomes more polarisable.²⁴⁸ The shift in the O–H stretching band of the FTIR spectrum obtained for carboxylic acids in a xenon matrix can be used to estimate the interaction energy, which were found to be in the range of 1 – 2 kJ mol⁻¹ and compared well with theoretically obtained values. The interaction energies were found to increase with the strength of the acid with trichloroacetic acid forming the strongest complex.²⁴⁹

The change from van der Waals complexes for He, Ne and Ar to hydrogen-bonded complexes for Kr and Xe has also been observed through the change in the A–H stretching vibration for complexes between rare gas atoms and a series of acids, AH (A = F, Cl, Br, NC, CN, HO, FO, ClO and BrO), optimised at the MP2(FC)/def2-TZVPP²⁵⁰ and at the CCSD(T)/def2-TZVPPD²⁵¹ levels of theory. The stabilisation energies of these complexes were found to increase as the difference between the proton affinities of the acid and the rare gas decreased.

3.1.2 Complexes between Dihalogens and Rare Gases

There have been extensive studies of complexes between rare gases and dihalogens utilising both theoretical and experimental methods. The calculated potential energy

surfaces of these complexes suggest two minima corresponding to a linear and to a T-shaped configuration.²⁵² The relative depths of these minima depend on factors including the strength of the van der Waals interaction and exchange repulsion.²⁵³ The linear isomer is typically found to have a deeper potential well for complexes with both homonuclear and heteronuclear dihalogens, with the dipole moment of the dihalogen playing a role in the latter. The linear isomer also tends to have a higher zero point energy than the T-shaped conformer due to the potential energy surface being anharmonic and the presence of an additional degree of freedom.²⁵⁴ This can lead to the T-shaped isomer being observed experimentally despite the linear isomer being the more stable thermodynamically. The experimental technique used to analyse these complexes can affect the isomer observed; rovibronic spectroscopy favours the T-shaped isomer, whereas microwave techniques favour the linear isomer.

Much of the systematic work that helped define the halogen bond was carried out in the gas phase using rotational spectroscopic techniques including molecular beam resonance spectroscopy and Fourier-transform microwave spectroscopy.³² In the course of some of these studies, complexes between argon and dihalogens were observed. The complexes $\text{Ar}\cdots\text{BrCl}$ ²⁵⁵ and $\text{Ar}\cdots\text{ICl}$ ²⁵⁶ were compared to $\text{Ar}\cdots\text{ClF}$ ²⁵⁷ and were found to have linear geometries. The values of $r(\text{Ar}\cdots\text{X})$ ($\text{X} = \text{Br}, \text{I}, \text{Cl}$) were found to be 93%, 88% and 90% of the sum of the van der Waals radii, respectively. This agrees with the observation that the strength of the dihalogens as halogen bond donors follows the same trend as the electric dipole moment, μ : $\text{ICl} > \text{ClF} > \text{BrCl}$.³²

The halogen-bonded complex formed between CF_3I and krypton has been recently studied by rotational spectroscopy²⁵⁸ and the spectrum obtained could be analysed to obtain a value of $r(\text{I}\cdots\text{Kr}) = 3.830(1) \text{ \AA}$. This distance represents 96% of the sum of the van der Waals radii of iodine and krypton and indicates the presence of a weak interaction. The nature of the interaction was confirmed by the value of the harmonic

force constant for the I...Kr stretching, $k_{\sigma} = 2.80 \text{ N m}^{-1}$. This force constant is comparable to those obtained for the Ar...BrCl and Ar...ICl complexes, where $k_{\sigma} = 2.79$ and 3.20 N m^{-1} respectively.^{255,256} The force constant is considerably weaker than those observed for complexes between dihalogens Br₂, BrCl, ClF and ICl with typical Lewis bases (CO, HCN, H₂O, H₂S, PH₃ and NH₃) where k_{σ} ranges from 5.1 to 34.3 N m^{-1} .³²

Rare gas atoms are isoelectronic with halide anions, which have been utilised as halogen-bond acceptors in previous studies.^{169,259-262} The strength of the I...X⁻ halogen bonds has been found to decrease in the order $\text{I}^{-} > \text{Br}^{-} > \text{Cl}^{-} > \text{F}^{-}$,¹⁶⁴ which is an indication that the strongest halogen bonds are those involving more polarisable halide anions. It is, therefore, predicted that halogen bonds to heavier rare gases, which are more polarisable, will be stronger. One of the aims of the current study is to lend support to this prediction.

Halogen bonding has been studied extensively in the solid phase in view of its application in crystal engineering and some of this research has focused on the use of iodoperfluoroalkanes,^{77,162,165,263} since the polarisability of the iodine atom and the electron-withdrawing effect of the fluorine groups combine to yield a strong halogen bond donor. In the gas phase, trifluoromethyl iodide (CF₃I) is, therefore, an appropriate molecule to substitute for iodoperfluoroalkanes. Yet, despite the good electron-withdrawing ability of the CF₃ group, chlorine is even better in this respect, which suggests that iodine monochloride, ICl, should also be a strong halogen-bond donor. Indeed, complexes of ICl with Lewis bases have been found to give the largest halogen bond harmonic force constants k_{σ} when compared with other dihalogens.³² For these reasons, ICl is included in this study.

3.1.3 The Dispersion Interaction

Complexes involving rare gas atoms are dominated by van der Waals forces or the dispersion interaction. The dispersion force arises from the fluctuations in the charge

density of a species that can lead to an instantaneous dipole, which induces a dipole in a neighbouring species leading to an attractive interaction.²⁶⁴ The energy of the dispersion interaction follows the relationship shown in Equation 3-1.

$$E_{\text{disp}} = -\frac{C_6}{R^6} \quad (3-1)$$

where C_6 is a constant and R is the separation between the two interacting atoms.

The fluctuation in the charge distribution is related to the polarisability of the species meaning that the dispersion interaction is related to the polarisabilities of the molecules involved in the interaction. The London formula, Equation 3-2, which is derived from second-order perturbation theory with approximations, shows this dependency.

$$E_{\text{disp}} = -\frac{3}{2} \left(\frac{I_A I_B}{I_A + I_B} \right) \left(\frac{\alpha_A \alpha_B}{R^6} \right) \quad (3-2)$$

Here I_A and I_B are the ionisation potentials of atoms A and B respectively, α_A and α_B are the polarisabilities of atoms A and B, respectively, and R is the separation between atoms A and B.

A more rigorous expression for C_6 , which makes it possible to calculate the coefficient from the polarisabilities, has been derived and is given in Equation 3-3.²⁶⁵

$$C_6 = \frac{3}{\pi} \int_0^\infty \alpha_A(i\omega) \alpha_B(i\omega) d\omega \quad (3-3)$$

Here ω is a frequency variable chosen at random to evaluate the integral.

3.1.4 Dispersion Corrected Density Functional Theory

The fact that the attraction between a rare gas atom and a halogen atom is due predominantly to dispersion interactions can cause problems when using density

functional theory (DFT), which often underestimates weak interactions.²⁶⁶ This is due to an approximation made by design within most exchange-correlation functionals, namely that the exchange-correlation energy is calculated from the local properties of electron density at a given point on a grid, making the exchange-correlation energy local, whereas dispersion energy requires a non-local description.²⁶⁷

Specific functionals have been formulated with the aim of achieving more accurate descriptions of complexes with dispersion interactions, including the generalised gradient approximation (GGA)-type functional with dispersion correction, B97-D,²⁶⁸ the M06 suite of hybrid meta-exchange functionals,¹⁰⁴ the X3LYP hybrid functional²⁶⁹ and the dispersion-corrected functional SSB-D,²⁶⁶ which combines the PBE and OPBE functionals to maximise performance for modelling π - π stacking, hydrogen bonding, spin states and S_N2 reaction barriers.²⁷⁰

The B97-D functional involves adding a semi-empirical dispersion correction to the B97 functional.²⁷¹ The form of this dispersion correction is shown in Equation 3-4:

$$E_{\text{disp}} = -s_6 \sum_{i=1}^{N_{\text{at}}-1} \sum_{j=i+1}^{N_{\text{at}}} \frac{C_6^{ij}}{R_{ij}^6} f_{\text{dmp}}(R_{ij}) \quad (3-4)$$

where s_6 is a scaling factor unique to the density functional, which is optimised by a least-squares fitting approach on a training set, N_{at} is the number of atoms in the system under investigation, C_6^{ij} is the dispersion correction coefficient for atoms i and j , R_{ij} is the interatomic distance between atoms i and j , and f_{dmp} is a damping function. The damping function is required in order to avoid singularities when R is small and takes the form shown in Equation 3-5.

$$f_{\text{dmp}}(R_{ij}) = \frac{1}{1 + \exp(-d(R_{ij}/r_w - 1))} \quad (3-5)$$

Here r_w is the sum of the van der Waals radii of atoms i and j and d is a parameter fitted using a training set of systems using a least-squares optimisation.

The C_6 coefficients for each atom in the periodic table up to and including Xe, were determined using Equation 3-6.

$$C_6^i = 0.05NI_p^i \alpha^i \quad (3-6)$$

In this equation I_p^i is the ionisation potential of the atom, α is the static dipole polarisability and $N = 2, 10, 18, 36$ and 54 for atoms in periods 1 – 5 of the periodic table, respectively. The C_6 coefficients of the two interacting atoms are combined by taking the square root of the product of the C_6 coefficients of each atom.

The DFT-D3 approach was developed similar to the DFT-D method described above.¹⁰⁵ The equation for the dispersion energy includes higher-order terms, in addition to the R^{-6} term, see Equation 3-7.

$$E_{\text{disp}} = \sum_{ij} \sum_{n=6,8,10,\dots} s_n \frac{C_n^{ij}}{R_{ij}^n} f_{d,n}(R_{ij}) \quad (3-7)$$

The damping function for DFT-D3 methods was also improved because the original function, see Equation 3-5, overemphasised the range of the dispersion correction. The modified form of the damping function is given in Equation 3-8.

$$f_{d,n}(R_{ij}) = \frac{1}{1 + 6(R_{ij}/s_{r,n}R_0^{ij})^{-\alpha_n}} \quad (3-8)$$

Here $s_{r,n}$, is a scaling factor for the cut-off radii R_0^{ij} . The DFT-D3 method also improves on the DFT-D method because important parameters are determined from first principles rather than by a least-squares fitting.

The C_6 coefficients can also be calculated using the exchange-hole dipole moment (XDM) method, which involves a model of the instantaneous dipole moment between the hole produced by the movement of an electron in a system and a neighbouring system.²⁶⁵ This method can reduce the computational cost of calculating the coefficients using the polarisabilities of the interacting atoms.

The M06 suite of functionals (with the exception of M06-L) are hybrid functionals that combine both Hartree-Fock(HF) and DFT exchange terms, see Equation 3-9.¹⁰⁴

$$E_{XC}^{hyb} = \frac{X}{100} E_X^{HF} + \left(1 - \frac{X}{100}\right) E_X^{DFT} + E_C^{DFT} \quad (3-9)$$

The DFT exchange term is based on the PBE functional and the correlation term is based on the τ HCTH and BMK functionals. These functionals are highly parameterised; in addition to the parameter X in Equation 3-9, there are six parameters within the exchange and correlation functions. The M06 functional has been designed to be accurate for transition metal elements, main group thermochemistry, transition states and complexes with non-covalent interactions; the training set used to optimise the parameters includes complexes with these features. The M06-2X functional is designed to be accurate for only main group chemistry and therefore transition metal complexes are not included in the training set.

The M06-L functional is a local density functional that incorporates both the PBE and VSXC functionals.²⁷² As with the M06 functional, the M06-L functional has been designed to be accurate for transition metal complexes, main group thermochemistry, transition states and non-covalent interactions. A local density functional with accuracy for these properties has been designed to reduce the computational cost as compared to hybrid functionals.

The M06-HF functional is similar to the M06-L functional, but has full Hartree-Fock exchange and has the form shown in Equation 3-10.²⁷³

$$E_{XC}^{M06-HF} = E_{XC}^{M06} + E_X^{HF} \quad (3-10)$$

This functional is not appropriate for transition metal complexes and so this functional was optimised to be accurate for main group thermochemistry, transition states and non-covalent interactions.

The X3LYP functional has a form that is similar to B3LYP but has been extended to improve the performance of modelling dispersion interactions and has been designed for investigating ligand binding to proteins.²⁶⁹ It involves mixing the B88 and PW91 exchange functionals with the mixing parameters optimised for complexes involving non-covalent interactions. The mixed exchange energy is combined with the LYP correlation energy, a portion of exact exchange and Slater local exchange to give the X3LYP functional.

Another method for correcting for dispersion interactions in DFT calculations is the use of dispersion correcting potentials (DCPs),²⁷⁴ which can be viewed as analogous to ECPs and consist of a sum of Gaussian type functions with the form shown in Equation 3-11:

$$U_1(r) = r^{-2} \sum_{i=1}^{N_1} c_{li} r^{n_{li}} e^{-\zeta_{li} r^2} \quad (3-11)$$

where N_1 is the number of Gaussian functions, n_{li} is a parameter, typically given the value of 2 and c_{li} and ζ_{li} are adjustable parameters. These parameters are fitted so that results for a dataset including complexes with non-covalent interactions are comparable to those calculated at the CCSD(T)/CBS limit. This method can, therefore, be used without CP correction because correction of the BSSE included is not necessary due to the fitting to CBS results. These DCPs have been derived for use with the PBE, PW91, B971 and B3LYP²⁷⁵ functionals; they were developed originally for modelling the carbon atoms in hydrocarbon dimers,²⁷⁶ but have

recently been used effectively for hydrogen-bonded complexes.²⁷⁷ One of the benefits of this method is that it can be used with any computational program with the capabilities of reading ECPs and it does not add any computational cost. Its drawback is that it is heavily parameterised.

3.1.5 Databases for Testing Functional Performance

In order to assess the performance of dispersion-corrected density functionals, databases containing complexes where the dispersion interaction is significant need to be developed. The geometries of these complexes are optimised at the CCSD(T)/CBS level of theory so that the data are an accurate benchmark for comparing results. The JSCH-2005 database contains more than 100 DNA base pairs and amino acid pairs, making it relevant to biological applications.²⁶⁷ The S22 dataset is one of the most commonly used when assessing the ability of density functionals to model dispersion interactions. It features seven hydrogen bonded complexes, eight complexes where the interaction is predominantly dispersion and seven complexes with a mixture of interactions. There are issues with the S22 dataset because there are questions over the accuracy of the data, some of which are extrapolated to the CCSD(T)/CSD limit. The dataset is also not balanced, with aromatic systems dominating over aliphatic systems.²⁷⁸ The S66 database is an extension of the S22 database that was developed in order to eliminate these issues. It has a good balance between aromatic and aliphatic systems, and between electrostatic and dispersion forces making it suitable for assessing the performance of functionals.²⁷⁹ One of the disadvantages of this database is that only the atoms C, N, O and H are represented, so it is questionable whether functionals that perform well for this dataset will perform well for complexes between rare gas atoms and halogen-bond donors.

A more extensive database is the GMTKN30 database, which consists of 1218 single-point calculations and covers a range of properties such as atomisation

energies, electron affinities and ionisation potentials, reaction energies and non-covalent interactions.²⁷¹ This database is more appropriate when testing the general performance of functionals.

3.1.6 The Performances of Dispersion-Corrected Density Functionals

The addition of the semi-empirical dispersion correction to density functionals has been found to improve significantly their performance when comparing results for the S22 database.²⁶⁷ The B97-D functional has been recommended for modelling non-covalent interactions based on its performance on the S22 dataset.

The performances of density functionals at modelling the hydrogen-bond interaction in the water dimer were assessed, and X3LYP and B2PLYP-D were found to perform well.²⁸⁰ The results were, however, compared to values calculated at the MP2 level of theory, which will have errors associated with it. Comparing the DFT results to experimentally determined values, X3LYP performs best for binding energies but the M05 and B3LYP functionals predict the O...O separation better.

A more appropriate assessment of the performances of density functionals at modelling hydrogen bonding compared optimised geometries of water hexamers.²⁶⁶ DFT-D functionals, BLYP-D, B3LYP-D, B2PLYP-D and revSSB-D, a revised version of the SSB-D functional, were found to exhibit good performance; the binding energies and the relative order of the different conformers were similar to those calculated at the CCSD(T)/aug'-cc-pVTZ level of theory. The semi-empirical dispersion correction is also found to be important for the modelling of noble gas dimers where B3LYP-D and PBE-D and B97-D perform well. Good performance has been also observed for the PBE functional without this dispersion correction and for the M05-2X functional.²⁶⁶

Initial tests of the performance of the M06 suite of functional at modelling non-covalent interactions were carried out using databases containing hydrogen-bonded

dimers (*e.g.* NH₃⋯H₂O), charge-transfer complexes (*e.g.* NH₃⋯ClF), complexes with dipole interactions (*e.g.* HCl⋯H₂S), weakly interacting species (*e.g.* Ne₂) and π - π stacking interactions.²⁸¹ The M06 functionals performed better than all of the other functionals tested, with the M06-2X and the M05-2X functionals performing better than the M06 functional, followed by M06-HF, the M05 and finally the M06-L functional.¹⁰⁴ The other functionals tested are a mixture of local functionals, GGA and meta-GGA functionals and hybrid functionals that are popular in the literature. None of these functionals was developed specifically to account for dispersion interactions so it is not surprising that the M06 suite of functionals perform best.

The ability of the M06-2X functional to model the S22 dataset was compared to the TPSS-D functional, which is an accurate DFT-D method.²⁶⁷ Although the M06-2X functional performed better for hydrogen-bonded complexes, it was not as accurate for dispersion-bonded complexes. The M06-2X functional had characteristics similar to pure density functionals and it underestimated the binding energies of hydrogen-bonded complexes.

The performances of a large number of DFT-D3 methods have been analysed in a recent extensive benchmarking study using the GMTKN30 database.²⁷¹ DFT-D3 was found to outperform functionals that do not include the dispersion correction and was comparable to other methods accounting for dispersion effects (the van der Waals density functional vdW-DF2 and the Vydrov-van Voorhis functional VV10).²⁸²

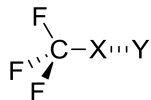
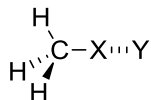
The performance of DFT functionals has been analysed for a series of halogen-bonded complexes by comparing the calculated energies of interaction with the Gibbs free energies obtained experimentally.²⁸³ The GGA functionals B97-1, B97-2 and B98 were found to perform well, with high correlation between the experimental and calculated thermodynamic properties. The M06 suite of functionals and the DFT-D dispersion corrected functionals performed poorly despite their ability to account for dispersion interactions. The calculations were carried out using the

Gaussian²²⁶ default 'Fine' pruned integration grid, which could be one of the reasons for these unexpected results.

3.2 Aim

The aim of the work presented in this chapter is to undertake a computational investigation of complexes formed between halogen bond donors and rare gas atoms; those included in the investigation are given in Table 3-1.

Table 3-1: The complexes included in this investigation.

	X	Y	
	I	Xe	1
	Br	Xe	2
	Cl	Xe	3
	I	Kr	4
	I	Ar	5
	I	Xe	6
Cl—X...Y	I	Xe	7

The complexes were selected so that the effect of the halogen (complexes **1 – 3**), the rare gas atom (complexes **1, 4** and **5**) and electron-withdrawing fluorine atoms (complexes **1** and **6**) can be investigated. Complex **7** has also been included because iodine monochloride has been shown to be a stronger halogen bond donor.³²

Although dispersion-corrected density functionals have been assessed for complexes involving rare gas atoms²⁶⁶ and halogen-bonded systems,²⁸³ the results of the latter were unexpected because dispersion-corrected methods performed poorly and

complexes involving a combination of halogen atoms and rare gases have not been assessed, making it necessary to test different density functionals for the complexes investigated in this study. Therefore, the performances of popular density functionals such as B3LYP and PBE at modelling these complexes will be compared to functionals parameterised for dispersion corrections, namely the M06 suite of functionals and functionals with semi-empirical dispersion corrections, B97-D, B3LYP-D3, M06-L-D3 and X3LYP.

The bonding in these complexes will be investigated using localised molecular orbitals (LMOs), which will help to analyse the nature of the interactions present.

One aim of the calculations is to determine whether the interaction between the halogen bond donors and rare gas atoms can be classified as halogen bonding or a van der Waals interaction.

3.3 Method

The monomer and complex geometries were optimised at the MP2, CCSD, B3LYP, M06, M06-L, M06-2X, M06-HF, X3LYP, PBE and B97-D levels of theory using Gaussian 09²²⁶ and 'VeryTight' convergence criteria. Calculations were carried out using the aug-cc-pVTZ basis set for all atoms excluding I and Xe, where the aug-cc-pVTZ-PP basis set was used, which includes an effective core potential (ECP) in order to take relativistic effects into account. The calculations of the complexes were carried out both with and without counterpoise (CP) correction of the basis set superposition error (BSSE). The 'Full' keyword was used for CCSD and MP2 calculations to ensure that all electrons were correlated. Vibrational frequency calculations were carried out to show that the optimised geometries corresponded to global minima on the potential energy surface. DFT calculations were initially carried out using the 'Fine' pruned integration grid but as this produced irregular potential energy curves with varying X...Y distance (*vide infra*), the 'UltraFine'

pruned integration grid was employed instead. Binding energies for the complexes were calculated as the difference between the sum of the energies of the monomers and the energy of the complex calculated with and without CP correction.

The DFT-D3 corrections were applied to the B3LYP and M06-L optimised geometries calculated with CP correction. For each complex, the X...Y distance was varied whilst keeping the remaining atoms fixed. The D3 corrections at each point along this potential energy curve were added to the B3LYP and M06-L energies to produce a new DFT-D3 potential energy curve. The minima of these new potential energy curves were located using an interpolating function within Mathematica.²²⁹ The D3 corrections were calculated using the code of Grimme *et al.*^{105,284} The D3 corrections of the B3LYP energies were calculated using the Becke-Johnson (BJ) damping,²⁸⁵ whereas the D3 corrections of the M06-L energies were calculated with zero damping.

The Hartree-Fock (HF) orbitals of the complexes were localised using the Edmiston-Ruedenberg localisation procedure implemented in GAMESS-US.²⁸⁶ The orbitals were visualised using Molekel.²²⁸

Calculations of the isotropic shielding tensor of Xe were carried out using the gauge-including atomic orbital (GIAO) method at the MP2/aug-cc-pVTZ level of theory using Gaussian 09 and at the CCSD/aug-cc-pVTZ level of theory using CFOUR. Curves showing the change in isotropic shielding tensor with X...Xe separation were produced by calculating the isotropic shielding tensor for each given X...Xe separation, without re-optimisation of the other geometrical parameters for each separation.

3.4 Results

3.4.1 Geometry Optimisation

Table 3-2 shows for complexes **1** – **6**, the halogen...rare gas separations given both as a distance and as a percentage of the sum of the van der Waals radii and the binding energies. For all complexes the X...Y separation is less than the sum of the van der Waals radii and the binding energy is positive showing that there is an attractive interaction between the rare gas atom and the halogen.

3.4.2 Comparison with Experiment

Complex **4** has been studied experimentally and can be compared to the results shown in Table 3-2.²⁵⁸ The experimentally determined I...Kr separation in complex **4** is 3.830 Å. This is longer than most I...Kr distances calculated without the use of CP correction but is only slightly shorter than those calculated with CP correction. The values obtained using CP-corrected MP2 and B3LYP-D3 methods give excellent agreement with this experimental value with differences of only ca. 0.03 Å and 0.04 Å, respectively. This close agreement shows that the methods employed are very good at describing the weak interaction present in these complexes and also allows comparison with other levels of theory.

Table 3-2: The halogen atom...rare gas separation, $r(X\cdots Y)$, expressed as a distance and as a percentage of the sum of the van der Waals radii and the binding energies, ΔE of complexes **1** and **2**. Results obtained without CP correction are given in parentheses.

Complex	Method	$r(X\cdots Y) / \text{\AA}$	$\frac{r(X\cdots Y)}{r_w(X) + r_w(Y)} / \%$	$\Delta E / \text{kJ mol}^{-1}$
1, CF₃I...Xe	CCSD	4.155 (3.903)	100.4 (94.3)	2.84 (6.95)
	MP2	3.972 (3.765)	95.9 (90.9)	4.98 (10.23)
	M06	3.858 (3.848)	93.2 (92.9)	3.12 (3.50)
	M06-L	3.900 (3.885)	94.2 (93.8)	2.64 (3.48)
	M06-2X	3.857 (3.857)	93.2 (93.2)	3.62 (3.78)
	M06-HF	4.728 (3.976)	114.2 (96.0)	1.04 (1.50)
	B3LYP	4.768 (4.625)	115.2 (111.7)	-0.31 (-0.21)
	B97-D	4.087 (4.082)	98.7 (98.6)	6.22 (6.42)
	PBE	4.070 (4.053)	98.3 (97.9)	2.08 (2.23)
	X3LYP	4.320 (4.299)	104.4 (103.8)	0.50 (0.61)
	B3LYP-D3	3.980	96.1	5.84
	M06-L-D3	3.899	94.2	2.78
2, CF₃Br...Xe	CCSD	4.084 (3.825)	101.8 (95.4)	2.20 (6.46)
	MP2	3.899 (3.686)	97.2 (91.9)	3.84 (9.12)
	M06	4.289 (4.286)	107.0 (106.9)	0.85 (1.00)
	M06-L	4.308 (4.286)	107.4 (106.9)	1.06 (1.56)
	M06-2X	3.802 (3.804)	94.8 (94.9)	2.04 (2.23)
	M06-HF	4.305 (4.284)	107.4 (106.8)	0.88 (1.21)
	B3LYP	9.479 (9.392)	236.4 (234.2)	0.00 (0.00)
	B97-D	4.009 (4.006)	100.0 (99.9)	4.27 (4.44)
	B3LYP-D3	3.918	97.7	4.22
	M06-L-D3	4.306	107.4	1.20

Table 3-2: (Continued)

3, CF₃Cl...Xe	CCSD	4.047 (3.829)	103.5 (97.9)	2.00 (4.95)
	MP2	3.866 (3.689)	98.9 (94.3)	3.08 (6.64)
	M06	4.307 (4.305)	110.2 (110.1)	0.65 (0.80)
	M06-L	4.315 (4.298)	110.4 (109.9)	0.93 (1.34)
	M06-2X	3.809 (3.804)	97.4 (97.3)	1.29 (1.50)
	M06-HF	4.277 (4.272)	109.4 (109.2)	0.82 (1.08)
	B3LYP	9.564 (9.336)	244.6 (238.8)	0.00 (0.00)
	B97-D	4.007 (4.003)	102.5 (102.4)	2.80 (2.93)
	B3LYP-D3	3.879	99.2	3.13
	M06-L-D3	4.313	110.3	1.09
4, CF₃I...Kr	CCSD	4.018 (3.729)	100.5 (93.2)	2.23 (7.18)
	MP2	3.857 (3.616)	96.4 (90.4)	3.72 (9.77)
	M06	3.777 (3.770)	94.4 (94.2)	1.46 (1.91)
	M06-L	4.130 (3.741)	103.2 (93.5)	1.39 (2.24)
	M06-2X	3.704 (3.694)	92.6 (92.4)	2.59 (2.94)
	M06-HF	4.117 (4.079)	102.9 (102.0)	1.01 (1.63)
	B3LYP	8.791 (8.785)	219.8 (219.6)	0.00 (0.00)
	B97-D	3.996 (3.986)	99.9 (99.6)	4.34 (4.61)
	B3LYP-D3	3.872	96.8	4.17
	M06-L-D3	4.127	103.2	1.48

Table 3-2: (Continued)

5, CF₃I ···Ar	CCSD	3.918 (3.690)	101.5 (95.6)	1.78 (4.17)
	MP2	3.776 (3.583)	97.8 (92.8)	2.84 (5.76)
	M06	3.990 (3.984)	103.4 (103.2)	1.08 (1.45)
	M06-L	4.326 (4.007)	112.08 (103.81)	1.45 (1.93)
	M06-2X	3.602 (3.588)	93.3 (93.0)	1.98 (2.27)
	M06-HF	3.991 (3.970)	103.4 (102.9)	0.98 (1.42)
	B3LYP	8.956 (7.480)	232.0 (193.8)	0.00 (0.00)
	B97-D	3.944 (3.931)	102.2 (101.8)	2.90 (3.08)
	B3LYP-D3	3.918	101.5	3.00
	M06-L-D3	4.325	112.04	1.52
6, CH₃I ···Xe	CCSD	4.257 (3.998)	102.8 (96.6)	2.38 (5.78)
	MP2	4.047 (3.836)	97.8 (92.6)	4.48 (9.00)
	M06	3.963 (3.953)	95.7 (95.5)	2.31 (2.59)
	M06-L	4.032 (3.991)	97.4 (96.4)	1.76 (2.45)
	M06-2X	3.945 (3.942)	95.3 (95.2)	2.77 (2.88)
	M06-HF	4.930 (4.225)	119.1 (102.1)	0.92 (0.92)
	B3LYP	9.887 (8.267)	238.8 (199.7)	0.00 (0.00)
	B97-D	4.148 (4.145)	100.2 (100.1)	5.33 (5.48)
	B3LYP-D3	4.088	98.7	4.80
	M06-L-D3	4.027	97.3	1.89

3.4.3 The Performance of *Ab Initio* and DFT Methods

In order to determine the most appropriate level of theory for investigating these complexes, the geometry for complex **1** was optimised using a range of *ab initio* and DFT methods. The results of these calculations are shown in Figure 3-3.

It has been shown (*vide supra*) that the CP-corrected MP2 and B3LYP-D3 levels of theory are capable of reproducing experimentally determined geometries for these complexes. The remaining methods studied will be compared to these methods in order to determine their accuracy at modelling these complexes.

While it would be assumed that the results obtained at the highest *ab initio* level of theory, CCSD, would be the most accurate, it has been observed that CCSD underestimates the interaction strengths for these weakly bound complexes. Ideally, results calculated at the CCSD(T) level of theory extrapolated to the complete basis set limit would be used as a benchmark for the other levels of theory, however, these calculations were not carried out because of their prohibitive computational costs.

The B3LYP functional was included in this investigation due to its popularity. The results in Figure 3-3 show, however, that this functional severely underestimates the interaction strength and predicts an I \cdots Xe separation that is longer than the sum of the van der Waals radii and a negative binding energy, incorrectly implying a repulsive interaction. The B3LYP functional is therefore inappropriate for the study of such complexes since it is incapable of modelling dispersion interactions.

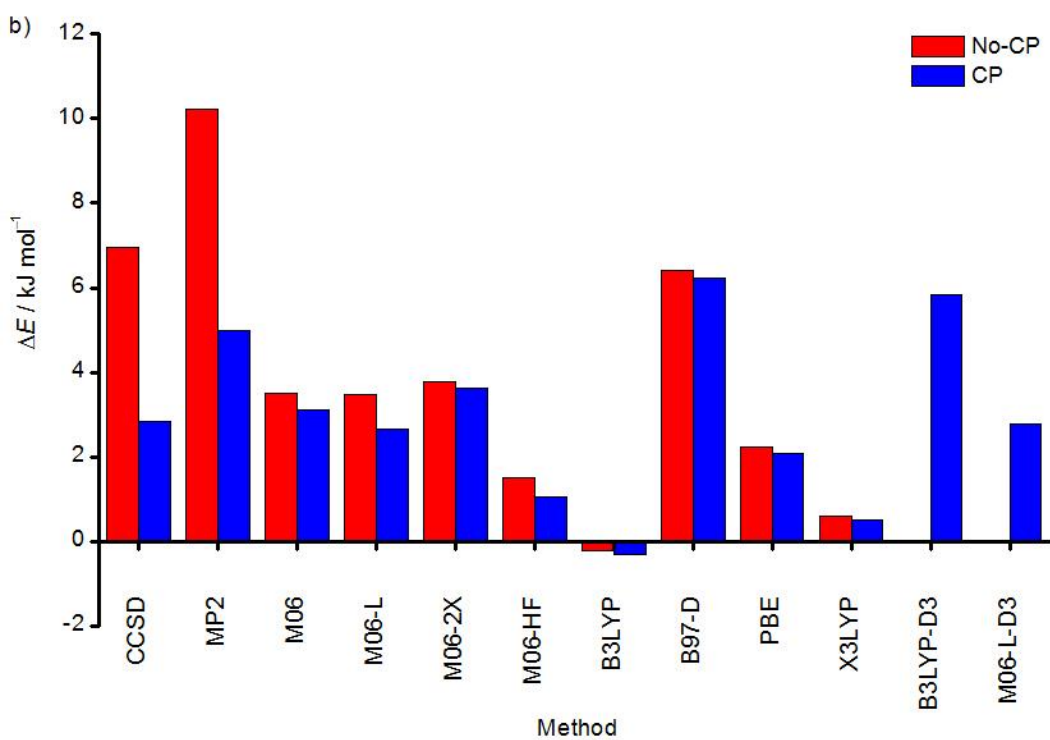
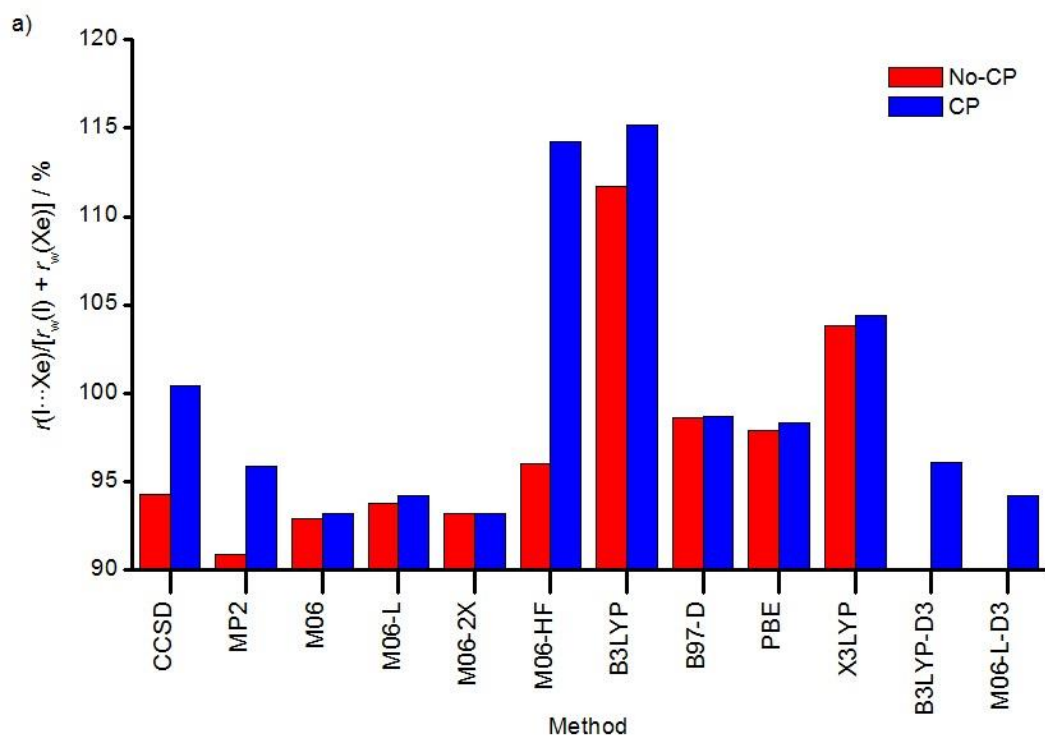


Figure 3-3: a) The iodine...xenon separations given as percentages of the sum of the van der Waals radii of iodine and xenon and b) the binding energies of complex **1**, $\text{CF}_3\text{I}\cdots\text{Xe}$, calculated using different methods both with and without CP correction.

The M06 suite of functionals, chosen for this study because they are parameterised with dispersion interactions included, perform much better than B3LYP, yielding interatomic distances shorter than the sums of the van der Waals radii and binding energies comparable to those calculated with the CCSD method using CP correction. It should be noted, however, that the M06-HF functional with CP correction produces an anomalous result for the I \cdots Xe separation, which could be due to the oscillations observed in the potential energy surface for the M06 suite of functionals (*vide infra*).

The B97-D functional, which includes a semi-empirical dispersion correction, was included in this study and was found to perform well with I \cdots Xe separations and binding energies that fall approximately in between the CCSD and MP2 results using CP correction. The results obtained using this functional are likely to be similar to those expected using the CCSD(T) method at the complete basis set limit as it was designed to replicate these results.²⁶⁸

The PBE functional is a simple generalised gradient approximation (GGA) functional that has been included because it has been observed to perform well for the hydrogen-bonding between DNA base pairs²⁸⁷ and can be compared with functionals that do include dispersion corrections.²⁸⁸ Surprisingly, this functional performs well with an I \cdots Xe separation similar to that obtained with the B97-D functional, although the binding energies are slightly underestimated.

The X3LYP functional was selected as it was developed in order to improve accuracy for hydrogen-bonded and van der Waals complexes,²⁶⁹ but it performed poorly and underestimated the interaction strength. This is likely to be due to the fact that the functional contains a local description of the correlation term and for an accurate description of dispersion interactions, both the exchange and correlation terms are required to be non-local.²⁶⁷

Applying the D3 correction to the B3LYP functional leads to a marked improvement in the performance and the I...Xe separations and binding energies become comparable to those calculated at the MP2 level of theory using CP correction.

The M06-L-D3 results are very similar to those calculated using the M06-L functional without the D3 correction, as the D3 correction was very small due to the M06-L functional already accounting for dispersion interactions.

3.4.4 The Significance of the Density of the Integration Gridⁱⁱⁱ

In order to apply the D3 correction to the B3LYP and M06-L functionals, a potential energy curve along the X...Y separation was produced and the minimum was determined using an interpolating function. An example of this potential energy curve is shown in Figure 3-4.

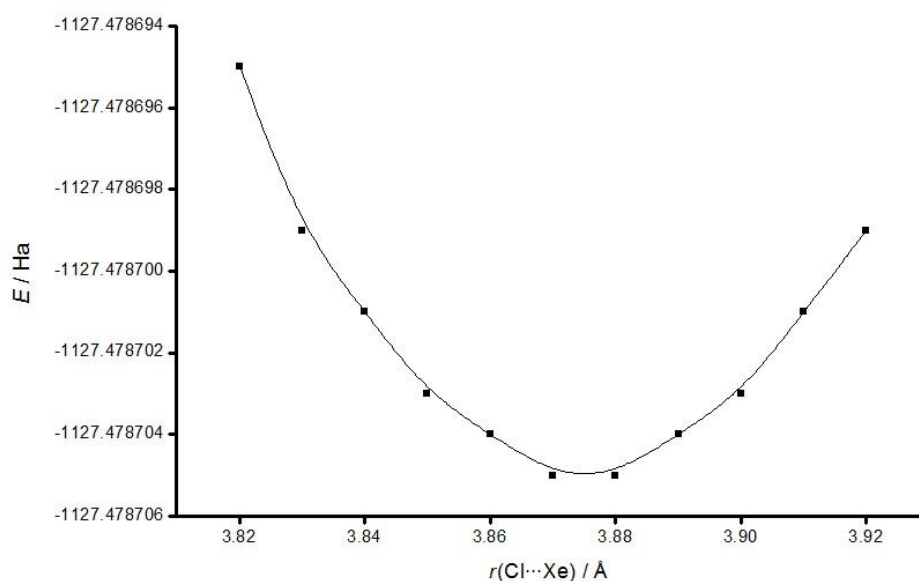


Figure 3-4: The potential energy curve for complex **3**, $\text{CF}_3\text{Cl}\cdots\text{Xe}$, calculated using the B3LYP-D3 method using the 'Fine' integration grid.

ⁱⁱⁱ Calculations of the potential energy curves of complex **3** using the M06-L-D3 functional and the 'UltraFine' and denser integration grids were carried out by Dr Peter Karadakov.

Initially calculations were carried out using the 'Fine' pruned integration grid, which is the default setting in Gaussian 09. The potential energy curve for complex **3** calculated using M06-L-D3 is shown in Figure 3-5.

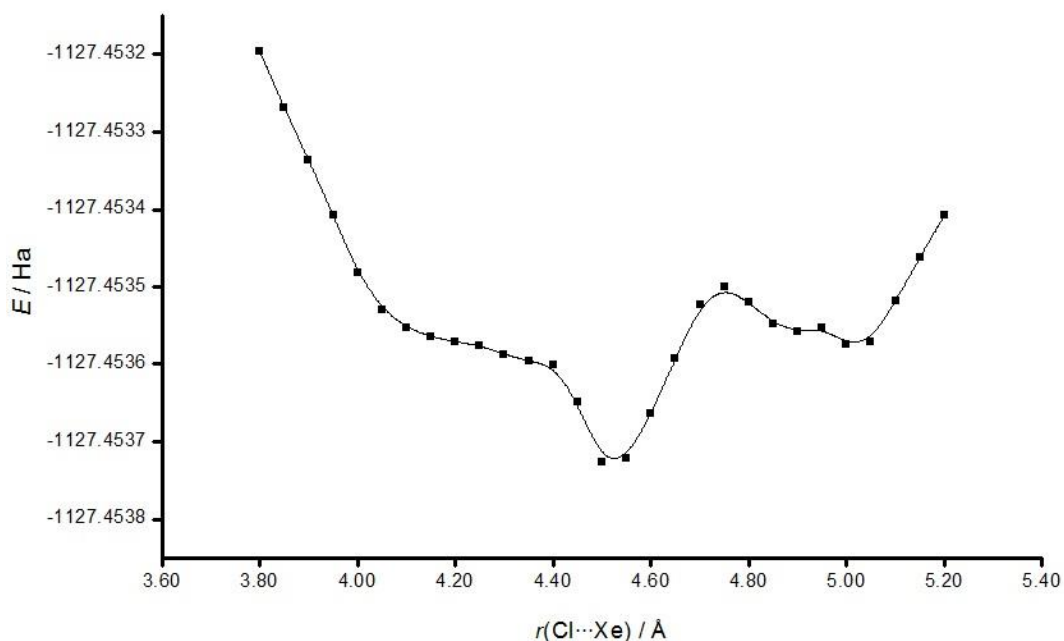


Figure 3-5: The potential energy curve of complex **3**, $\text{CF}_3\text{Cl}\cdots\text{Xe}$, calculated at the M06-L-D3 level of theory using the 'Fine' integration grid.

The shape of the potential energy curve shown in Figure 3-5 is unexpected for these complexes because it is not a smooth, continuous function like that observed in Figure 3-4. This phenomenon has been observed previously in calculations of the argon dimer using the VSXC functional, where oscillations of the potential energy surface were observed for less dense integration grids.²⁸⁹ The VSXC functional is a precursor of the M06 suite of functionals¹⁰⁴ and so it is not entirely surprising that this phenomenon is observed here.

The potential energy curve of the argon dimer was also calculated using the M06 suite of functionals²⁹⁰ and oscillations in the potential energy surface were observed for all functionals using the default 'Fine' grid. An 'UltraFine' grid was found to produce smooth potential energy curves for the M06-2X functional, whereas a more

dense integration grid, (250, 590), was required for M06, M06-L and M06-HF functionals. The dependence of the integration grid on calculations using the M06 suite of functionals was also observed in a benchmarking study,²⁷¹ with the dependence being particularly large for the M06-HF functional, affecting results for alkane conformers and sugar conformers the most.

The influence of the integration grid on calculations has been observed for calculations of 34 organic reactions using the M06 suite functionals.²⁹¹ Significant errors were observed for the SG-1 grid, which is the default grid in Q-Chem. This grid consists of 50 radial points and 194 angular points per shell, which is less dense than the 'Fine' integration grid in Gaussian. Although significant errors were not observed for the 'Fine' integration grid, it should be noted that the potential energy curves for the organic compounds investigated will be significantly deeper than the potential energy curves for the rare gas complexes in this study. The origin of these errors was investigated and that due to the exchange energy was significantly greater than that from electron correlation. Another study has concluded that these errors originate from the correction of self-interaction within the correlation term,²⁹² suggesting that there is some debate about the origin of these errors.

Increasing the density of the integration grid from a 'Fine' to an 'UltraFine' pruned grid for calculation of the potential energy surface of **3** resulted in a smoother curve, yet this was still far from ideal.

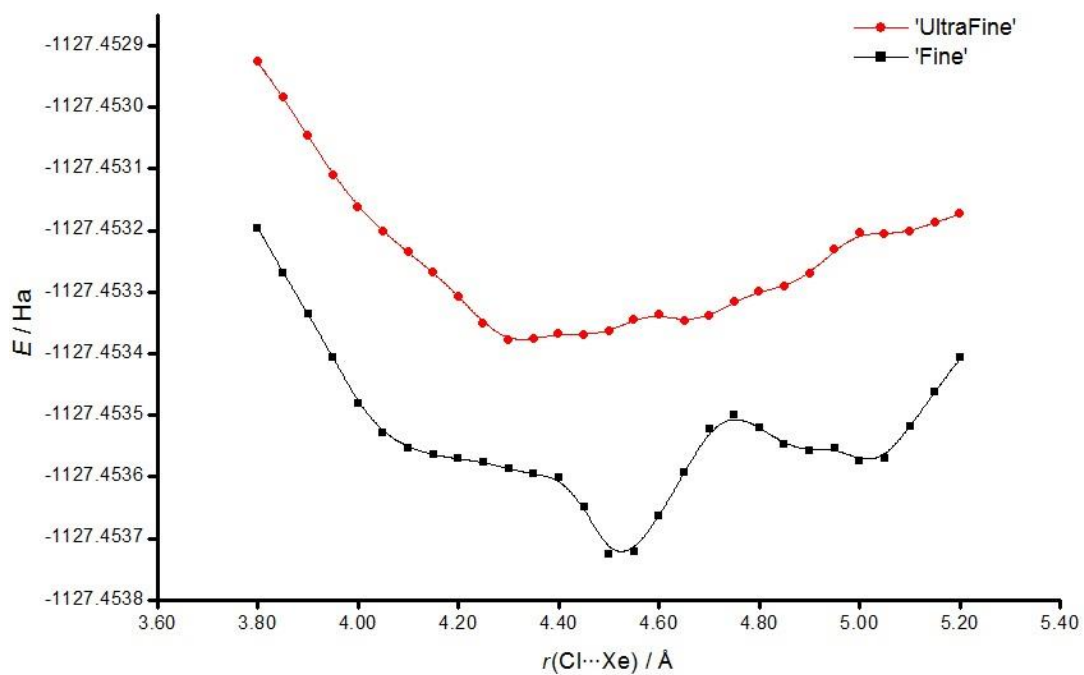


Figure 3-6: The potential energy curve for complex **3**, $\text{CF}_3\text{Cl}\cdots\text{Xe}$, calculated using at the M06-L-D3 level of theory using the 'Fine' and 'UltraFine' pruned integration grids.

The potential energy curve was also created using even denser integration grids in order to see if a further improvement on the shape of the potential energy curve could be achieved.

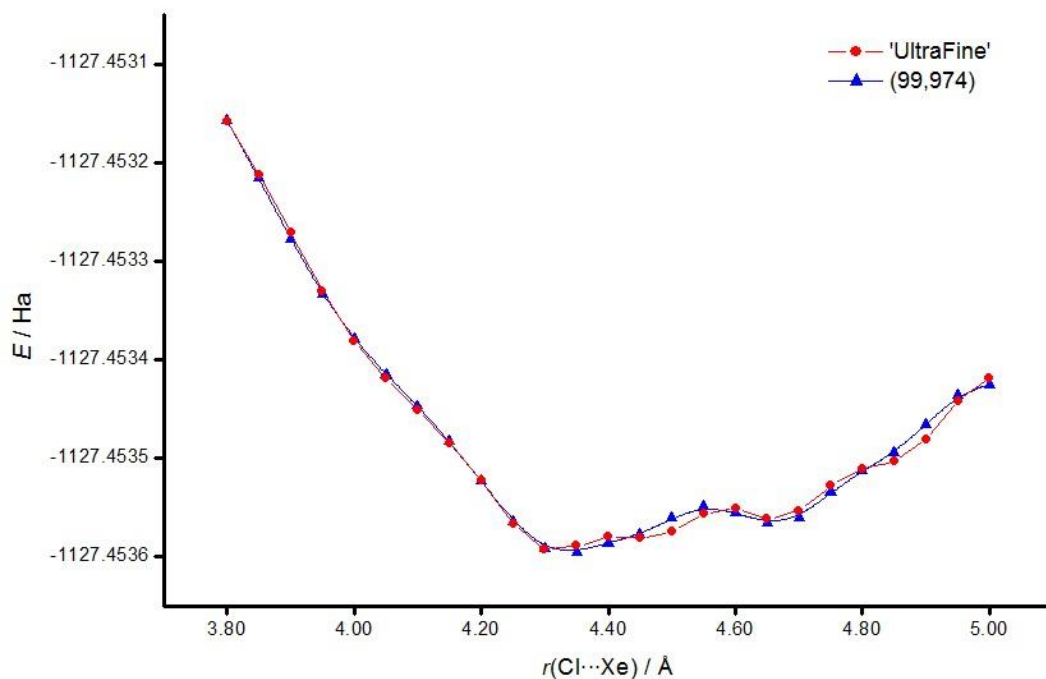


Figure 3-7: The potential energy curve for complex **3**, $\text{CF}_3\text{Cl}\cdots\text{Xe}$, calculated at the M06-L-D3 functional using the 'UltraFine' pruned integration grid and an unpruned (99,974) integration grid.

The 'UltraFine' grid is a pruned grid that consists of 99 radial shells and 590 angular points on each shell. Figure 3-7 shows the effect of increasing the number of angular points per shell to 974 using the unpruned (99, 974) integration grid. It can be seen that there is very little difference between the two potential energy curves. The effect of increasing the number of radial shells was therefore investigated.

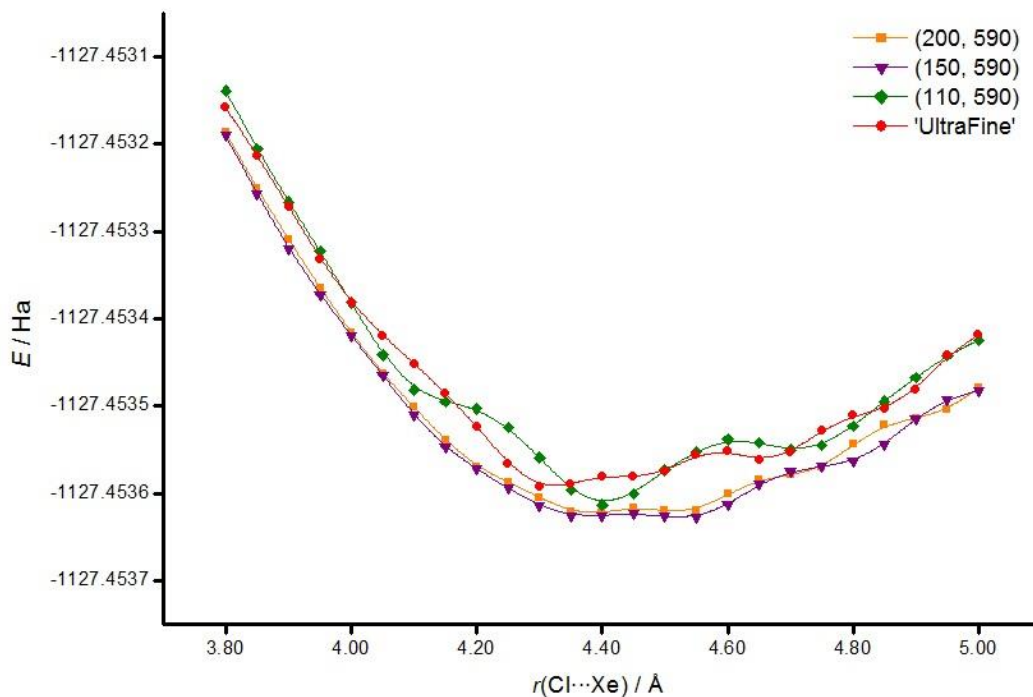


Figure 3-8: The potential energy curves for complex **3**, $\text{CF}_3\text{Cl}\cdots\text{Xe}$, calculated at the M06-L-D3 level of theory using the 'UltraFine' pruned integration grid and the (110, 590), (150, 590) and (200, 590) unpruned integration grids.

Figure 3-8 shows that as the number of radial shells in the integration grid increases, the potential energy curve becomes smoother. It should be noted that even for the integration grid with 200 radial shells, the curve is not perfect. The choice of integration grid for these calculations is clearly important because for the curves shown in Figures 3-7 and 3-9, the position of the minimum is affected by the density of the grid, with differences of up to 0.2 \AA . This dependence on integration grid density could account for some of the anomalous results observed for the optimised geometries of the complexes using the M06 suite of functionals.

This phenomenon was observed for the entire M06 suite of functionals and was particularly pronounced for the weaker complexes, such as complex **3**, in the examples above.

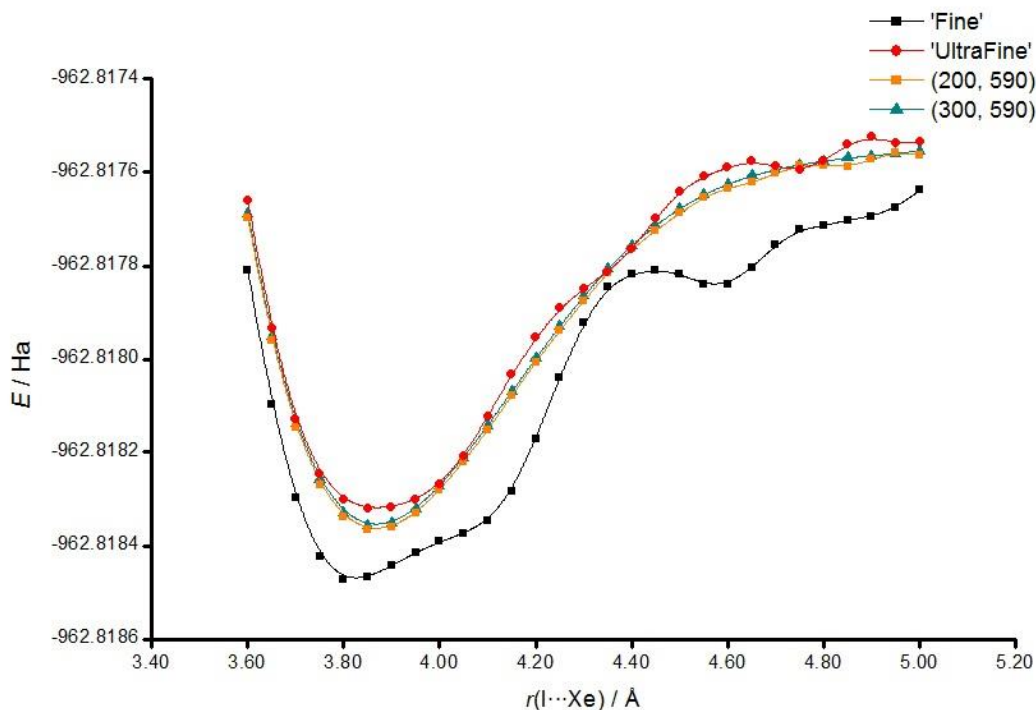


Figure 3-9: The potential energy curve for complex **1**, $\text{CF}_3\text{I}\cdots\text{Xe}$, calculated at the M06-D3 level of theory using the 'Fine' and 'UltraFine' pruned integration grids and the (200, 590) and (300, 590) unpruned integration grids.

Figure 3-9 shows the potential energy curves for complex **1** calculated using the M06-D3 level of theory and a range of integration grids. The same phenomenon is also observed for this functional but the curves are not as irregular because **1** is a stronger complex than **3** and excluding the results using the 'Fine' integration grid, the positions of the minima are the same.

Concerned that this issue could affect all calculations of halogen-bonded complexes using the M06 suite of functionals, calculations were carried out on the complex between trifluoromethyl iodide and ammonia, complex **8**, which features a halogen bond of typical strength.

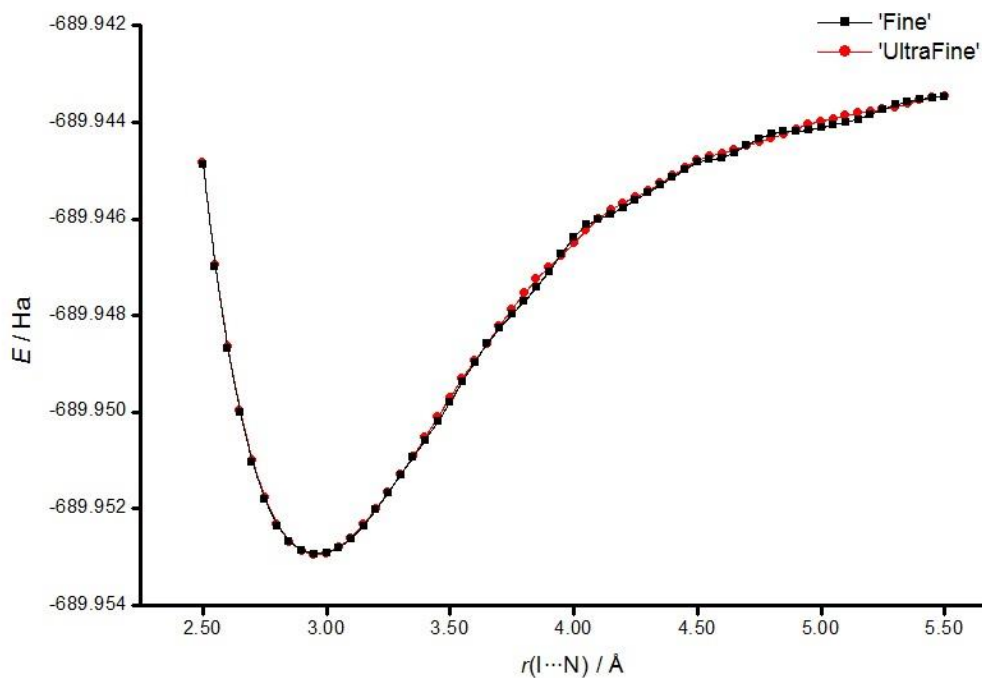


Figure 3-10: The potential energy curves of the halogen bonded complex **8**, $\text{CF}_3\text{I}\cdots\text{NH}_3$, calculated at the M06-D3 level of theory using the 'Fine' and 'UltraFine' pruned integration grids.

Figure 3-10 shows that the potential energy curves for complex **8** are approximately identical using both the 'Fine' and 'UltraFine' integration grids, and that they are relatively smooth and have a defined minimum. This shows that although the density of the integration grid needs to be considered when investigating weakly bound complexes, it plays a less important role for typical halogen-bonded complexes. It should be noted, however, that plotting the BSSE against the I...N separation for complex **8** shows an oscillation for values calculated using the 'Fine' integration grid (Figure 3-11). Values calculated using the 'UltraFine' integration grid display a typical smooth curve.

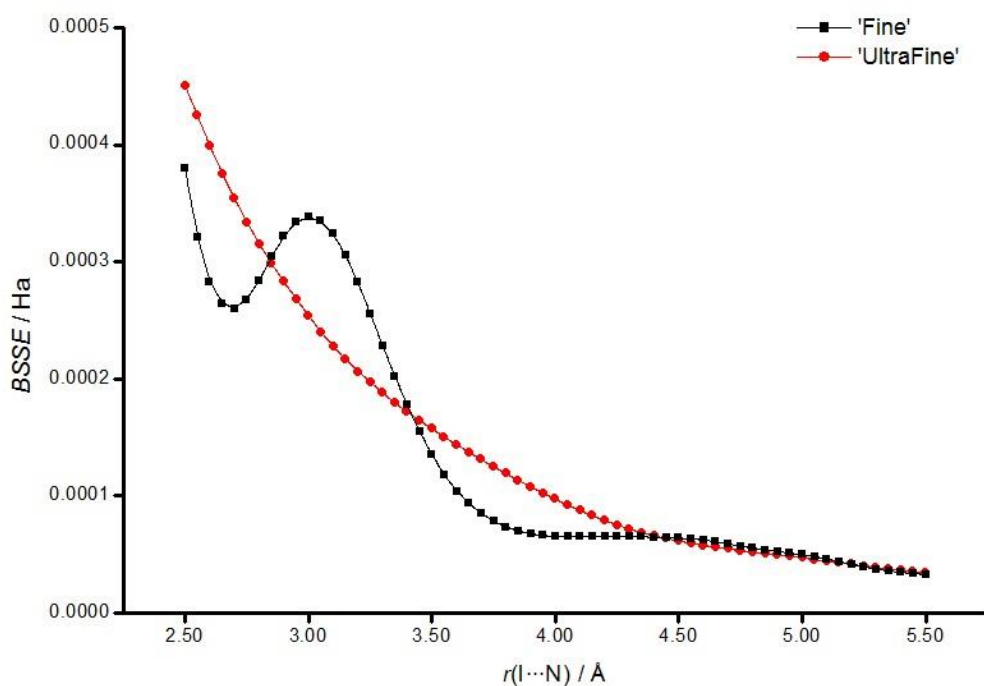


Figure 3-11: The variation of BSSE with I...N separation in complex **8**, $\text{CF}_3\text{I}\cdots\text{NH}_3$, calculated at the M06-D3 level of theory using the 'Fine' and 'UltraFine' integration grids.

As the density of the integration grid increases, the computational expense of the calculation increases and for the densest integration grids, the benefit usually observed for DFT methods is lost since the computational expense becomes similar to some *ab initio* methods. It was decided that the 'UltraFine' integration grid should be used for all DFT calculations since this produces a reasonable potential energy curve without being too computationally expensive.

3.4.5 The Effect of Chemical Composition on the Halogen...Rare Gas Interaction

Complexes **1** – **3** can be compared in order to investigate the effect of changing the halogen-bond donor on the interaction strength of the complex. Figure 3-12 shows the halogen...xenon separations for complexes **1** – **3** as a percentage of the sum of the van der Waals radii. Values calculated using most of the levels of theory are shown in Figure 3-12a, while those calculated at the MP2 level of theory, which was

observed to be the most accurate, are shown in Figure 3-12b in order to clarify the trends observed. Figure 3-13 shows similar graphs for the binding energies of complexes **1** – **3**.

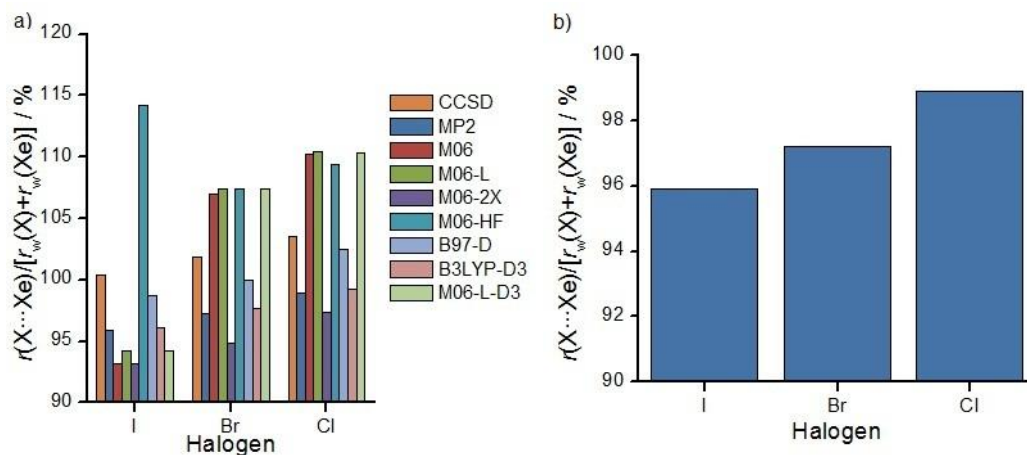


Figure 3-12: The halogen atom...xenon separations as percentages of the sum of the van der Waals radii for complexes **1** – **3** calculated using a) different methods and b) the MP2 level of theory with CP correction.

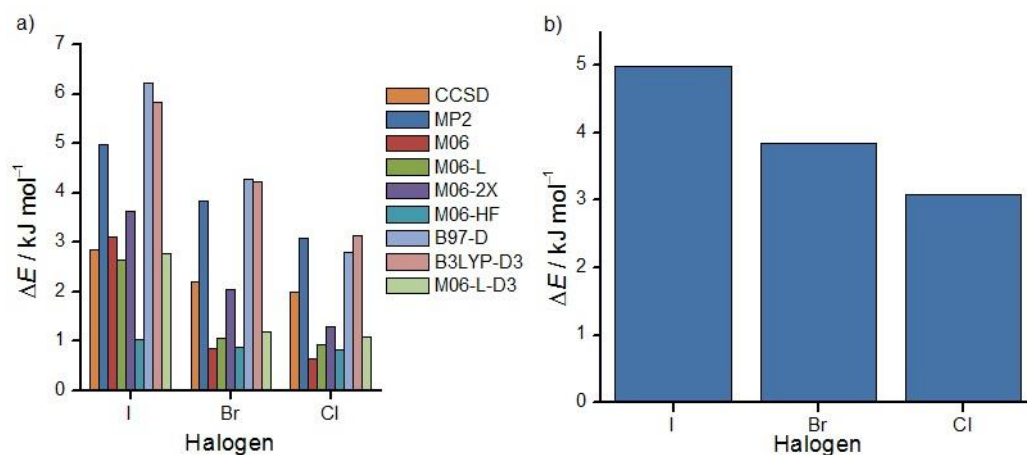


Figure 3-13: The binding energies of complexes **1** – **3** calculated using a) different methods and b) the MP2 level of theory with CP correction.

Figure 3-12 shows that as the halogen becomes more polarisable, the halogen...xenon separation decreases accompanied by an increase in binding energy (Figure 3-13). This indicates that the interaction becomes stronger as the halogen becomes more polarisable, which is consistent with trends observed in halogen bonding and the fact that the σ -hole becomes larger and more positive for more

polarisable halogens.³⁸ This trend is observed for the majority of the levels of theory but the anomalous result for complex **1** using the M06-HF functional means that the trend is not observed in this case.

The effect of the rare gas atom on the interaction strengths of the complexes can be investigated by comparing complexes **1**, **4** and **5**. Figure 3-14 shows the iodine···rare gas separation as a percentage of the sum of the van der Waals radii for complexes **1**, **4** and **5**. Figure 3-14a shows the values calculated using most level of theory and Figure 3-14b shows the values calculated at the MP2 level of theory in order to clarify the trends observed. Figure 3-15 shows similar graphs for the binding energies of complexes **1**, **4** and **5**.

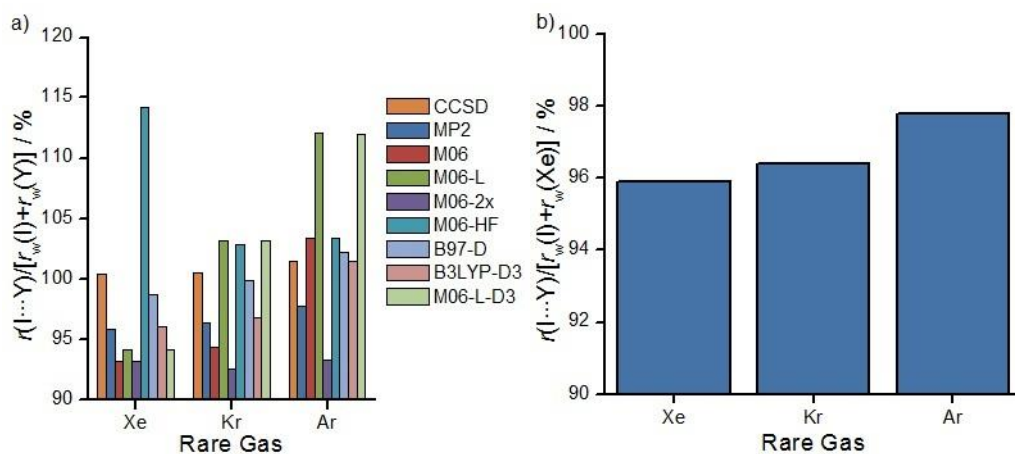


Figure 3-14: The iodine···rare gas atom separations as percentages of the sum of the van der Waals radii for complexes **1**, **4** and **5** calculated using a) different methods and b) the MP2 level of theory with CP correction.

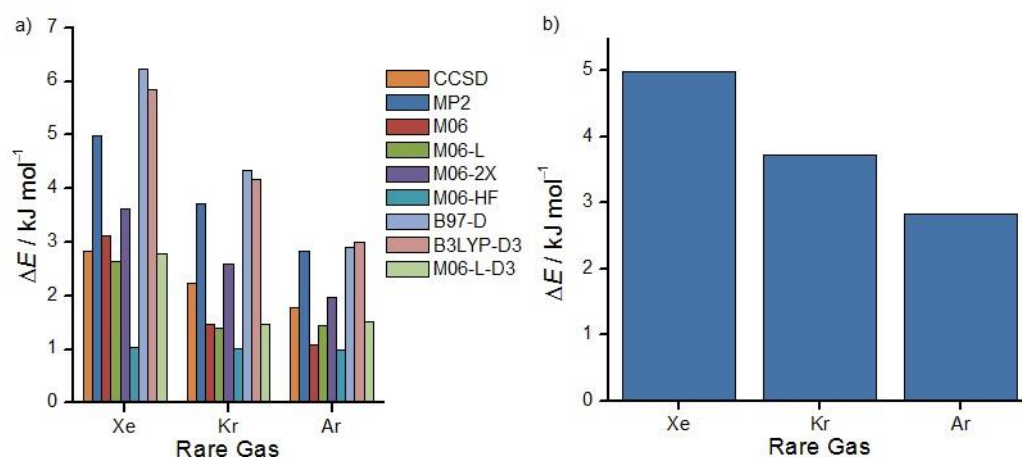


Figure 3-15: The binding energies of complexes **1**, **4** and **5** calculated using a) different methods and b) the MP2 level of theory with CP correction.

Figures 3-14 and 3-15 show that as the rare gas atom becomes more polarisable, the I \cdots Rg separation decreases and the binding energy increases. Rare gas atoms are isoelectronic with halide anions and this trend is similar to that observed for halide anions acting as halogen bond acceptors.²⁶²

The effect of the electron-withdrawing trifluoromethyl group on the interaction strength was investigated by comparing complexes **1** and **6**. In the majority of cases, the I \cdots Xe separation was shorter and the binding energy was larger for complex **1** than for complex **6**, consistent with observations that the presence of an electron-withdrawing trifluoromethyl group leads to a stronger σ -hole.^{293,294} It is interesting to note that even without an electron-withdrawing group, the I \cdots Xe separation is close to or slightly lower than the sum of the van der Waals radii and that the binding energy is positive, suggesting an attractive interaction.

Iodine monochloride has been observed to be a particularly strong halogen bond donor,³² and so Xe \cdots ICl (**7**) was investigated to observe the effect of a significantly stronger halogen-bond donor on these complexes.

Table 3-3, shows the I \cdots Xe separations and binding energies for complex **7** calculated using different levels of theory. Comparing these values to those for complex **1** (Table 3-2) shows that the binding energies are larger and the I \cdots Xe

separations are shorter for complex **7**, consistent with ICl being the stronger halogen-bond donor. It is worth noting that the I...Xe separations for **7** are significantly shorter than the sum of the van der Waals radii and that the binding energies are within the realm of those defined for traditional halogen bonds (5 – 180 kJ mol⁻¹).¹⁶⁴ This shows that with a significantly strong halogen-bond donor, rare gas atoms ought to be able to act as halogen-bond acceptors producing a significant interaction.

Table 3-3: The I...Xe separations given as a distance and as a percentage of the sum of the van der Waals radii and the binding energies for complex **7**, Xe...ICl, calculated at different levels of theory. Calculations carried out without CP correction are given in parentheses.

Complex	Method	$r(\text{I}\cdots\text{Xe}) / \text{\AA}$	$\frac{r(X\cdots Y)}{r_w(X) + r_w(Y)} / \%$	$\Delta E / \text{kJ mol}^{-1}$
7 , Xe...ICl	CCSD	3.888 (3.676)	93.9 (88.8)	4.41 (9.96)
	MP2	3.685 (3.524)	89.0 (85.1)	8.18 (15.43)
	M06	3.590 (3.581)	86.7 (86.5)	11.51 (11.92)
	M06-L	3.590 (3.578)	86.7 (86.4)	15.26 (15.90)
	M06-2X	3.626 (3.626)	87.6 (87.6)	9.95 (10.03)
	M06-HF	3.593 (3.573)	86.8 (86.3)	7.11 (8.05)
	B3LYP	3.802 (3.798)	91.8 (91.7)	4.76 (4.82)
	B97-D	3.924 (3.921)	94.8 (94.7)	13.44 (13.52)
	B3LYP-D3	3.660	88.5	9.74
	M06-L-D3	3.559	86.0	8.48

3.4.6 Localised Molecular Orbitals of Halogen Bond Donor...Rare Gas Complexes

In order to gain insight into the nature of the interaction in these complexes, the molecular orbitals of complexes **1** and **7** were localised using the Edmiston-Ruedenberg method and are shown in Figures 3-16 and 3-17.

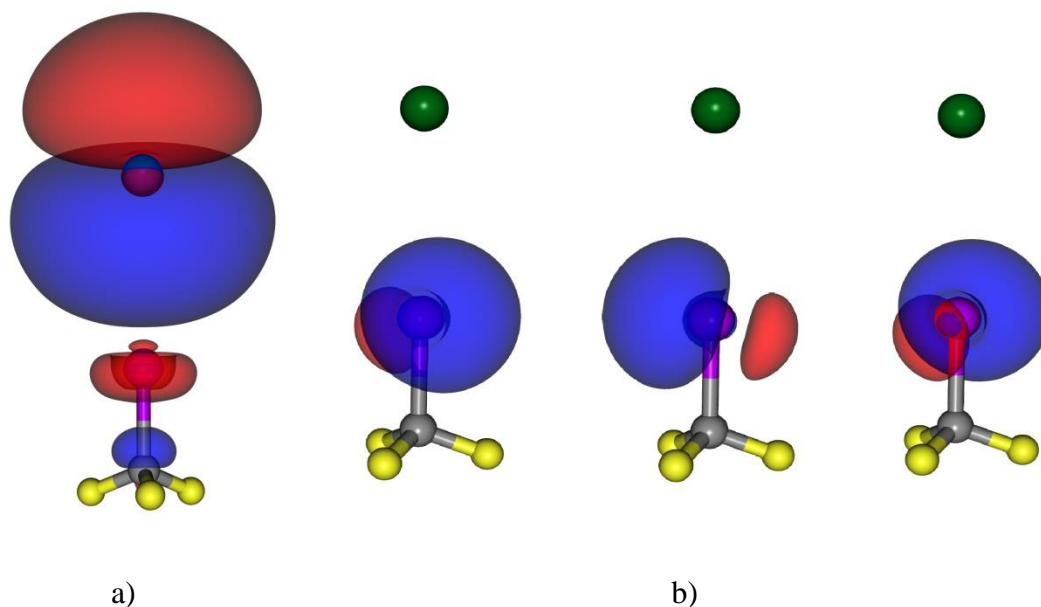


Figure 3-16: a) The LMO containing a non-bonding electron pair of xenon, directed toward the iodine atom in complex **1**. b) The three LMOs containing the valence lone pairs of electrons on iodine. The orbitals are represented as isosurfaces at orbital values of a) ± 0.0025 (e/bohr^3)^{1/2} and b) ± 0.05 (e/bohr^3)^{1/2}. The atoms are coloured as follows: xenon, green; iodine, purple; carbon, grey; fluorine, yellow.

Figure 3-16a shows a p-like LMO on the xenon atom of complex **1**, which contains a non-bonding electron pair. This LMO is directed towards the iodine atom of CF₃I and is antibonding over the C–I bond. A similar LMO is also observed for complex **7** (Figure 3-17a). This is similar to the LMO observed for the lone pair of electrons on the nitrogen of ammonia in its complex with 1,4-diiodotetrafluorobenzene.¹²² This illustrates that despite the differing strengths of the interactions in complex **1** and the 1,4-diiodotetrafluorobenzene...ammonia complex, the nature of the interaction is similar.

The other LMOs are sp^3 -like and correspond to lone pairs of electrons on the iodine atom (Figure 3-16b). For complex **7** these three LMOs have been combined to give Figure 3-17b.

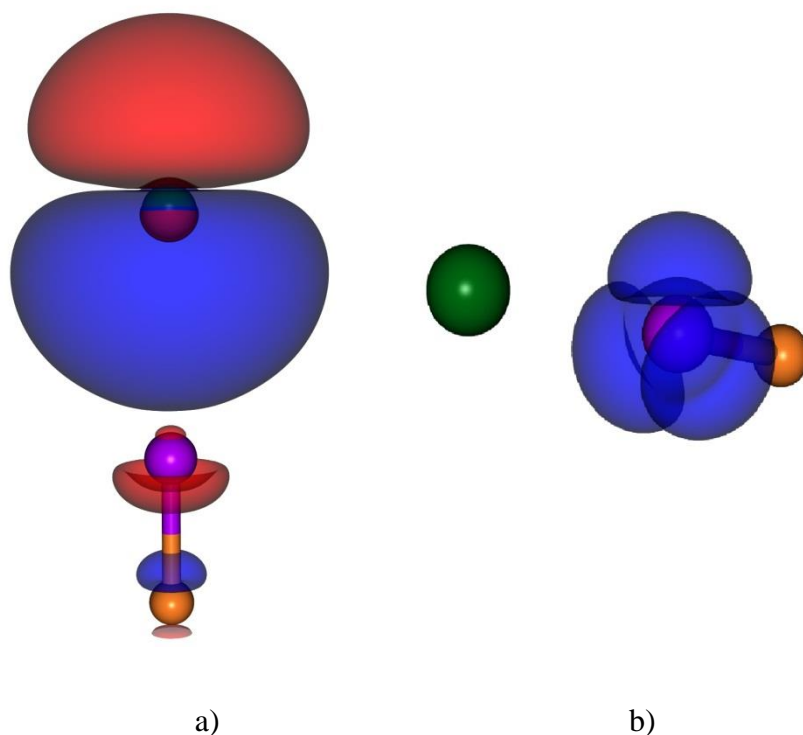


Figure 3-17: a) The LMO containing a nonbonding electron pair of xenon, directed toward the iodine atom in complex **7**. b) Combined plot of the three LMOs containing valence lone pairs on iodine. The orbitals are represented as isosurfaces at orbital values of a) ± 0.005 (e/bohr^3)^{1/2} and b) ± 0.15 (e/bohr^3)^{1/2}. The atoms are coloured as follows: xenon, green; iodine, purple; chlorine, orange.

The combination of the three LMOs corresponding to the valence lone pairs on iodine highlights a region with depleted electron density, which corresponds to the σ -hole on the iodine atom and provides a novel explanation of the σ -hole.

The LMOs on the halogen atom in complexes **1 – 3** and **6** can be compared to show the variation of their shapes with the strength of the halogen bond donor, see Figure 3-18.

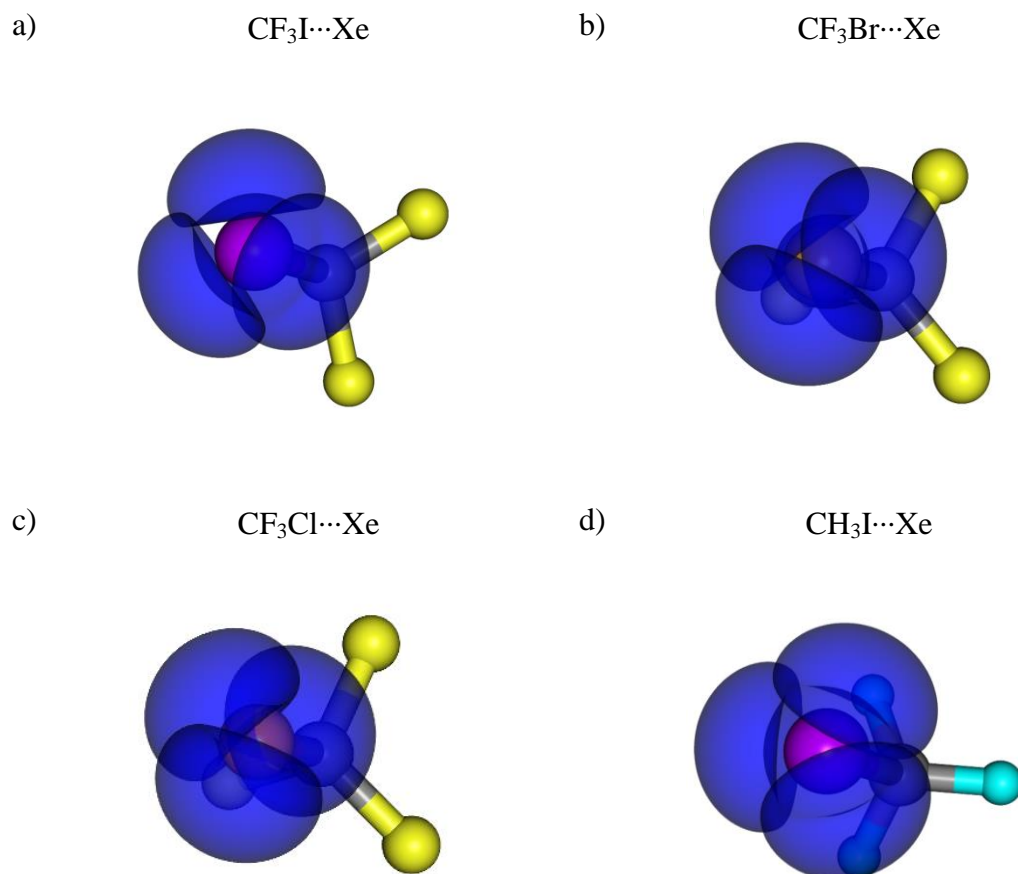


Figure 3-18: Combined plots of the LMOs containing valence pairs on the halogen of a) complex **1**, $\text{CF}_3\text{I}\cdots\text{Xe}$, b) complex **2**, $\text{CF}_3\text{Br}\cdots\text{Xe}$, c) complex **3**, $\text{CF}_3\text{Cl}\cdots\text{Xe}$, and d) complex **6**, $\text{CH}_3\text{I}\cdots\text{Xe}$. The orbitals are represented as isosurfaces at orbital values of ± 0.15 $(e/\text{bohr}^3)^{1/2}$. The atoms are coloured as follows: xenon, green; carbon, grey; fluorine, yellow; hydrogen, blue; iodine, purple; bromine, brown; chlorine, orange.

Figure 3-18 shows that as the halogen becomes more polarisable, the region of depleted electron density between the LMOs on the halogen becomes smaller, which is similar to the trend observed for electrostatic surface potential diagrams often used to describe the σ -hole.³⁸ Comparing complexes **1** and **6** shows that the electron-withdrawing fluorine atoms have very little effect on the LMOs on the halogen atom.

The LMOs on the rare gas atoms of complexes **1**, **4** and **5** can be compared to examine how the rare gas atom affects the antibonding character in the C–I bond (Figure 3-19). It is observed that as the rare gas atom becomes more polarisable,

despite the fact that the LMO on the rare gas atom does not change appearance, the degree of antibonding induced in the C–I bond increases.

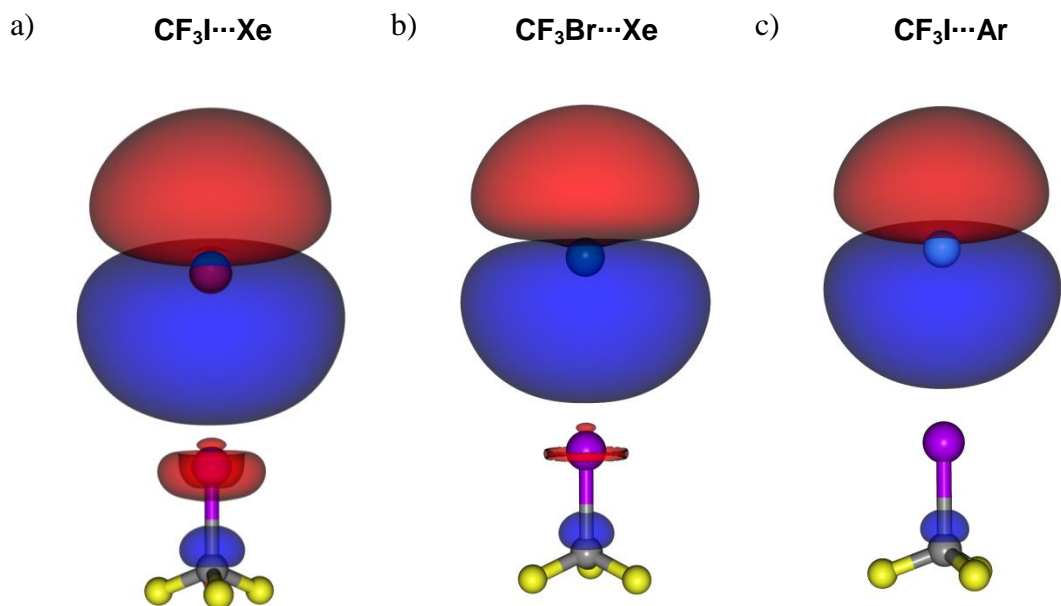


Figure 3-19: The LMO containing a nonbonding electron pair on the rare gas atom of a) complex **1**, CF₃I···Xe, b) complex **4**, CF₃I···Kr and c) complex **5**, CF₃I···Ar. The orbitals are represented as isosurfaces at orbital values of ± 0.0025 (e/bohr³)^{1/2}. The atoms are coloured as follows: xenon, green; carbon, grey; fluorine, yellow; iodine, purple; krypton, turquoise; argon, blue.

The antibonding character observed over the C–I bond in Figures 3-16a, 3-17a and 3-19 suggests that there should be elongation of the C–I bond in the complex compared to the unbound monomer. The C–I bond lengths of CF₃I calculated at different levels of theory are given in Table 3-4 with the C–I bond length in complex **1**; the difference between the two C–I bond lengths, $\Delta r(\text{C–I})$, is reported as a distance and as a percentage change.

Table 3-4: The C–I bond distances of the CF₃I monomer and in complex **1**, CF₃I⋯Xe, and the differences between these distances calculated at different levels of theory. Values obtained from calculations carried out without CP correction are given in parentheses.

Method	$r(\text{C-I})$ monomer / Å	$r(\text{C-I})$ complex / Å	$10^3 \Delta r(\text{C-I})$ / Å	$\Delta r(\text{C-I})$ / %
CCSD	2.1305	2.1307 (2.1304)	0.2 (–0.1)	0.01 (0.00)
MP2	2.1255	2.1265 (2.1264)	1.0 (0.9)	0.05 (0.04)
M06	2.1636	2.1659 (2.1659)	2.3 (2.3)	0.11 (0.11)
M06-L	2.1778	2.1802 (2.1802)	2.4 (2.4)	0.11 (0.11)
M06-2X	2.1459	2.1473 (2.1472)	1.4 (1.3)	0.07 (0.06)
M06-HF	2.1157	2.1159 (2.1161)	0.2 (0.4)	0.01 (0.02)
B3LYP	2.1738	2.1738 (2.1738)	0 (0)	0 (0)
B97-D	2.2138	2.2135 (2.2134)	–0.3 (–0.4)	–0.01 (–0.02)

Table 3-4 shows that for the majority of the levels of theory there is a small elongation of the C–I bond in complex **1** compared to the monomer, but the differences are very small because the complex is weak. Indeed it could be argued that the C–I bond distances are the same in the complex and monomer once errors are accounted for. It should be noted that the orbital value selected for the isosurface of the LMO shown in Figure 3-16a is very small, which could explain why the anti-bonding character is observed even though the C–I bond elongation is very small.

The C–X and I–Cl bond lengths in the monomers and the complexes **1** – **7** are shown in Table 3-5. These values were calculated using the MP2 level of theory, which was found to be the most reliable theoretical approach.

Table 3-5: The C–X bond lengths in the monomers and complexes **1** – **6** calculated at the MP2 level of theory. Calculations carried out without CP correction are given in parentheses.

Complex	$r(\text{C-X})$ monomer / Å	$r(\text{C-X})$ complex / Å	$10^3 \Delta r(\text{C-X}) / \text{Å}$	$\Delta r(\text{C-X}) / \%$
1 , CF ₃ I⋯Xe	2.1255	2.1265 (2.1264)	1.0 (0.9)	0.05 (0.04)
2 , CF ₃ Br⋯Xe	1.9020	1.9028 (1.9033)	0.8 (1.3)	0.04 (0.07)
3 , CF ₃ Cl⋯Xe	1.7440	1.7446 (1.7444)	0.6 (0.4)	0.03 (0.02)
4 , CF ₃ I⋯Kr	2.1255	2.1259 (2.1252)	0.4 (–0.3)	0.02 (–0.01)
5 , CF ₃ I⋯Ar	2.1255	2.1256 (2.1250)	0.1 (–0.5)	0.00 (–0.02)
6 , CH ₃ I⋯Xe	2.1168	2.1179 (2.1180)	1.1 (1.2)	0.05 (0.06)
7 , Xe⋯ICl	2.3181	2.3239 (2.3265)	5.8 (8.4)	0.25 (0.36)

Similar to the data in Table 3-4, the results in Table 3-5 show that while some elongation of the C–X bond on complexation can be observed in **1** to **6**, the change is small enough to be considered within the error limits of the calculation. For complex **7**, however, the elongation of the I–Cl bond is significant and beyond the error in the calculation, corroborating with the fact that the anti-bonding character in the LMO shown in Figure 3-17a is observed at an isosurface at a much higher orbital value than that for complex **1**.

The shapes of the LMOs observed in Figures 3-16 and 3-17 are similar to the electronic density isosurface calculated for the H₂O⋯CF₄ complex, which is believed to be a typical van der Waals complex.²⁹⁵ The H₂O⋯CCl₄ complex is a much stronger complex with charge transfer playing a significant role in the interaction, and its electronic density isosurface differs from those in Figures 3-16 and 3-17 because the lobe of the interacting chlorine atom crosses the isodensity boundary of the water oxygen giving it a flattened appearance. This suggests that the complexes in this study are similar to van der Waals complexes and that charge transfer does not play an important role in the interaction.

3.4.7 Calculations of ^{129}Xe NMR Chemical Shifts

It would be desirable to observe the formation of these complexes experimentally, and one method that could be employed for this purpose is ^{129}Xe NMR spectroscopy, which is very sensitive to the environment of the xenon atom. This sensitivity is illustrated in the change in the ^{129}Xe NMR chemical shift when encapsulated in cryptophane A, shown in Figure 3-20, where a shift of 160 ppm is observed compared to free xenon.²⁹⁶ The shift in chemical shift was also sensitive to deuteration of functional groups in the cryptophane A²⁹⁷ and to the cryptophane A binding to a protein.²⁹⁸ The size of the cryptophane and the substituents bound to its aromatic rings can also affect the change in the chemical shift.²⁹⁹

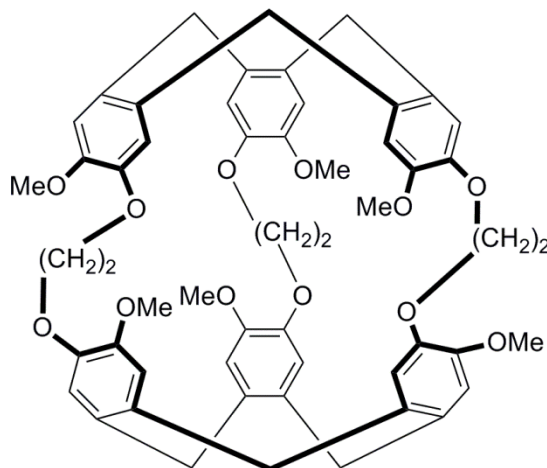


Figure 3-20: Molecular structure of cryptophane-A

Xenon encapsulated in fullerene is reported to have a chemical shift change of 8.89 ppm compared to xenon dissolved in benzene and of 179.24 ppm compared to free xenon gas.³⁰⁰ The interactions responsible for this change in chemical shift are dispersion and Xe $\cdots\pi$ interactions. The fact that the chemical shift change is similar to that of xenon encapsulated in cryptophaneA suggests that in the latter, these types of interactions dominate.

^{129}Xe NMR spectroscopy has also been used to investigate hydrogen bonds involving xenon. The crystal structure of xenon encapsulated within a β -

hydroquinone host is shown in Figure 3-21.³⁰¹ The ^{129}Xe NMR spectrum of this complex reveals a chemical shift change of 160 ppm upon complex formation, which is similar to that observed for cryptophaneA. The authors claim that O–H \cdots Xe and O \cdots Xe interactions are present in the structure and are responsible for the change in the chemical shift, however, the O–H \cdots Xe angles are 93.40° and $103.24(6)^\circ$, which is a significant deviation from linearity. Also, the O \cdots Xe separations are 3.809(1) and 3.8185(9) Å, which is longer than the sum of the van der Waals radii. The side view of the crystal structure, Figure 3-21b, clearly shows that the xenon atom does not lie in the plane of the hydrogen bonds within the β -hydroquinone. Therefore, the interactions with xenon cannot be classified as hydrogen-bonds and the change in chemical shift is likely to be due to dispersion or π interactions, which accounts for the fact that the chemical shift change is similar to that observed in cryptophaneA.

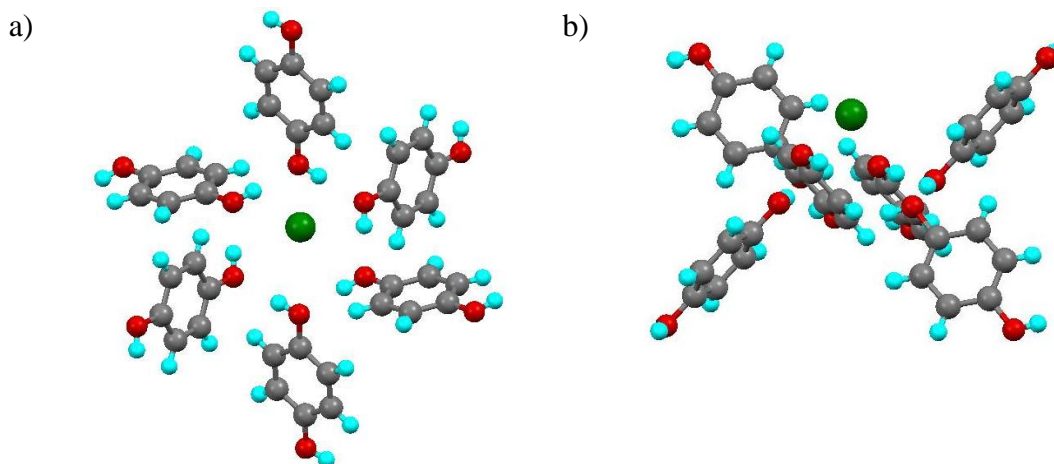


Figure 3-21: The crystal structure of xenon encapsulated in β -hydroquinone. a) Top view.
b) side view.

The ^{129}Xe NMR chemical shifts of xenon gas dissolved in a series of solvents have been measured,³⁰² referenced to the shift of pure xenon gas extrapolated to zero pressure. These chemical shifts were plotted against a function of the refractive index, Equation 3-12, which was derived from the Frank-Condon absorption of light by solute molecules in terms of the dielectric constant $K = n^2$,³⁰³ to give a linear relationship as shown in Figure 3-22.

$$f(n^2) = \left[\frac{n^2 - 1}{2n^2 + 1} \right]^2 \quad (3-12)$$

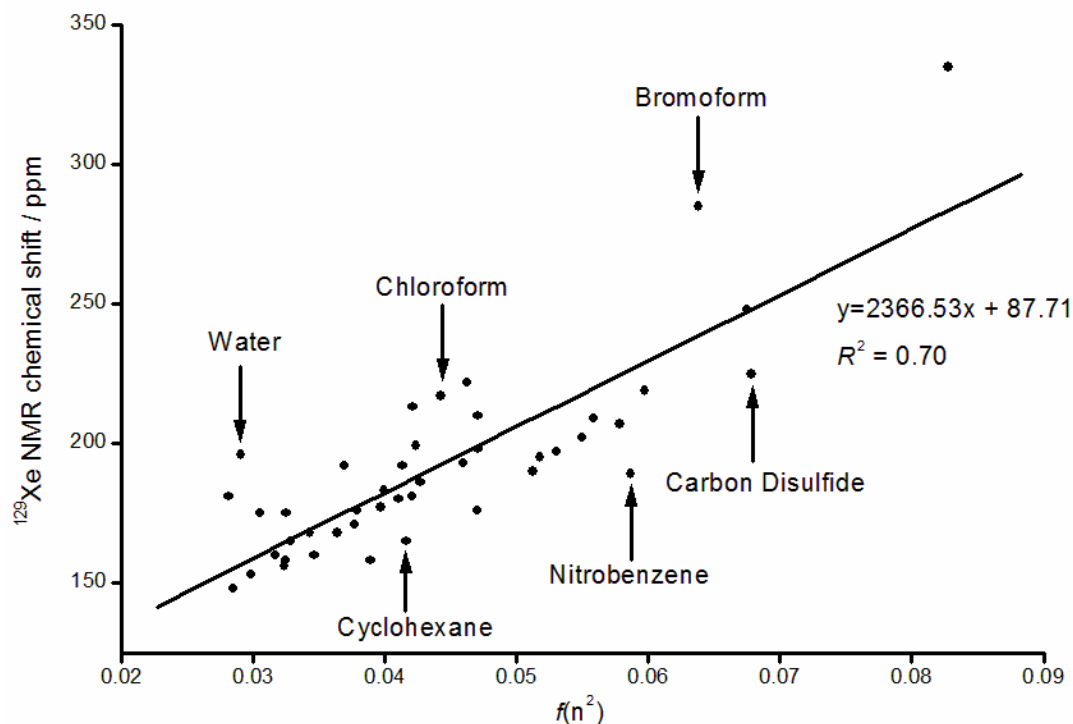


Figure 3-22: The ^{129}Xe NMR chemical shifts of xenon dissolved in a series of solvents related to the function of the solvent's refractive index, n , given in Equation 3-12.

The relationship in Figure 3-22 does not have a particularly strong linear correlation because a wide range of solvents was employed, including n -alkanes, n -alcohols, halogenated solvents and aromatic solvents. If only one category is considered, then the linear correlation can be improved as shown for the case of n -alkanes in Figure 3-23.

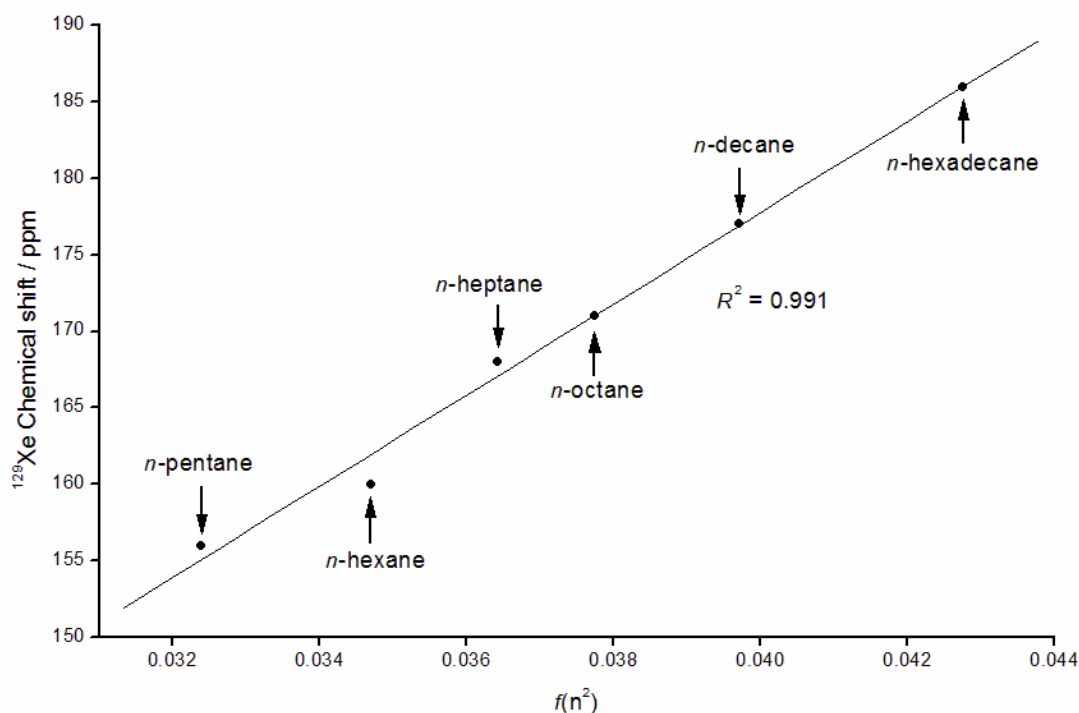


Figure 3-23: The ^{129}Xe chemical shifts of xenon dissolved in a series of n -alkane solvents related to the function of the solvents refractive index given in Equation 3-12.

The refractive index of a solvent is related to its polarisability, Equation 3-13:²⁶⁴

$$n \approx 1 + \frac{2\pi N_A \alpha \rho}{M} \quad (3-13)$$

where N_A is Avogadro's constant, ρ is the density of the medium and M is the molar mass. The polarisability is then related to the dispersion force between two molecules, Section 3.1.3, which suggests that dispersion interactions between the xenon atom and the solvent molecules is responsible for the ^{129}Xe chemical shift change reported in these studies.^{302,303}

The chemical shift of xenon dissolved in a series of strong acids was compared to the chemical shift of xenon dissolved in the equivalent methyl ester,³⁰⁴ and the data for the strong acids were found to deviate significantly from the linear relationship with $f(n^2)$, Figure 3-24.

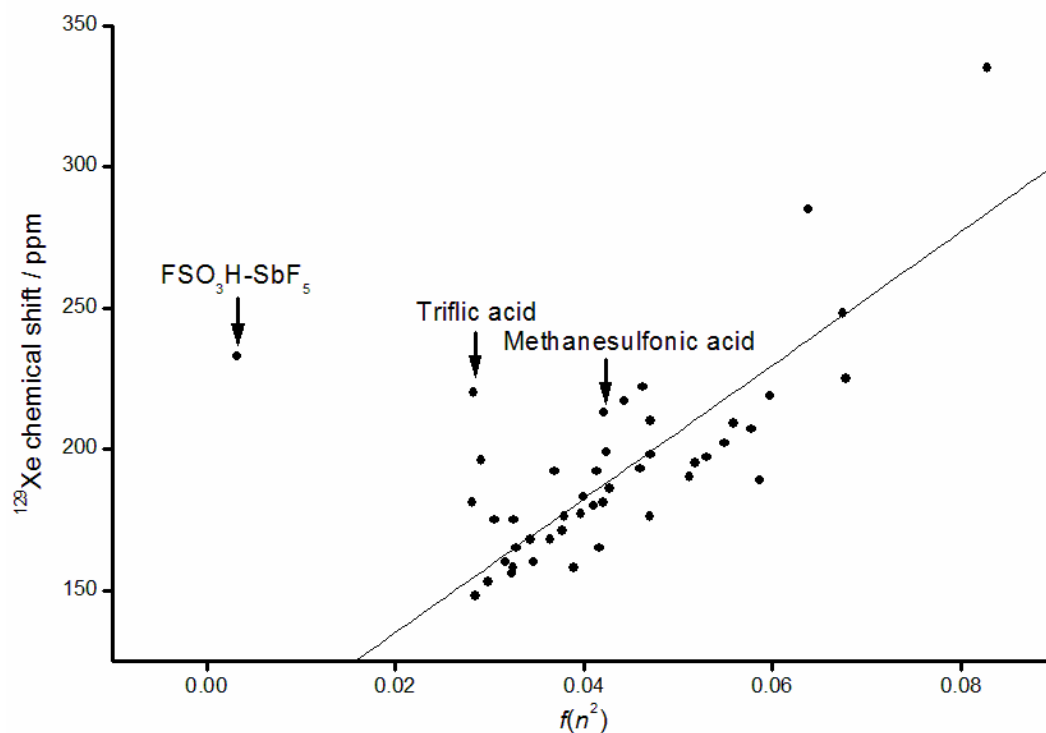


Figure 3-24: The ^{129}Xe NMR chemical shifts of xenon dissolved in a series of solvents and acids related to the function of the refractive index, n , given in Equation 3-12. The linear fit shown does not include the outlying data for acids and is identical to that in Figure 3-22.

This relationship between ^{129}Xe NMR chemical shifts and $f(n^2)$ is not ideal because it rarely passes through the origin and requires solvents to be collected in related groups in order to achieve a good correlation. Therefore, an alternative correlation was devised which relates the ^{129}Xe NMR chemical shift of xenon dissolved in a particular solvent with the ^{13}C chemical shift of $^{13}\text{CH}_4$ dissolved in the same solvent.³⁰⁵ These values are similar because van der Waals interactions are responsible for the chemical shifts in both cases and methane has a similar polarisability to xenon.

In order to understand the origin of the relationship observed in Figures 3-23 and 3-24, the overall shielding constant can be separated into the sum of four terms corresponding to contributions from the magnetic susceptibility, van der Waals interactions, anisotropy of molecular susceptibilities of the solvent and electrostatic interactions with permanent electric moments. In the case of xenon dissolved in n -

alkanes, the last two are very small and can be assumed to be zero and the contribution from van der Waals interactions is found to dominate. For a series of *n*-alkanes, this van der Waals contribution has a non-linear relationship with the number of carbon atoms in the alkyl chain but a linear relationship when the percentage of methylene groups is considered.³⁰⁶ This suggests that interactions with methylene groups have a greater effect on the change in chemical shift when compared to interactions with methyl groups. This has, however, been contradicted by a study showing that the deshielding effect due to methyl groups is greater than that of methylene groups,³⁰⁷ corroborated by calculation of the dispersion interaction energies suggesting that this is the correct order of contributions from these groups. Molecular dynamics (MD) simulations of xenon dissolved in alkanes showed that methyl groups contribute more than methylene groups.³⁰⁸ This observation was rationalised by the fact that methyl groups have a larger number of hydrogen atoms that can affect the chemical shift. The authors claim that previous observations involving relationships with the number of carbon atoms did not compare solvents in the same thermodynamic state; the solvents were not at the same reduced temperature.

A similar analysis of the relative contributions of methyl, methylene and halogen groups to the change in chemical shift of xenon dissolved in 1-haloalkanes was carried out,³⁰⁹ and the contribution of the halogens was found to increase as they became more polarisable due to an increase in the interaction strength.

It is possible to use quantum chemical calculations to predict the change in ¹²⁹Xe NMR chemical shift of xenon in different environments, which was undertaken for xenon in hydrogen-bonded complexes with the simple acids: FH, ClH, BrH, NCH, CNH, HOH, FOH, ClOH and BrOH. The isotropic chemical shift was found to be in the range 54 – 85 ppm,²⁵⁰ and was observed to decrease initially with increasing proton affinity of the acid and then increase for proton affinities above 1480 kJ mol⁻¹.

The isotropic xenon chemical shift of xenon in the rare gas dimers, Xe–Xe, Xe–Kr, Xe–Ar and Xe–Ne was calculated as a function of the Xe⋯Rg separation using the B3LYP functional,³¹⁰ which was shown to produce results similar to CCSD(T) for the Ne–Ne dimer.³¹¹ The difference in the isotropic chemical shift compared to free Xe gas decreases as the Xe⋯Rg separation decreases and this change can be described using the function shown in Equation 3-14.

$$\sigma_{iso}(R) - \sigma(\infty) = C_6R^{-6} + C_8R^{-8} + \dots \quad (3-14)$$

The intermolecular shielding was found to depend predominantly on orbital overlap and exchange rather than electron correlation, which could explain why the B3LYP functional can reproduce CCSD(T) results despite its poor performance in describing dispersion interactions.

Shielding surfaces for the interactions between Xe and CO₂, CO, N₂, CH₄ and CF₄ were calculated at the HF and B3LYP levels of theory and compared to experimental data.³¹² These surfaces were found to take a similar form to those for the rare gas dimers. Potential functions were also calculated which can be used in molecular dynamics (MD) calculations of the xenon chemical shift of xenon dissolved in a solvent.

Xenon dissolved in a solvent was modelled initially as xenon in a molecular cage of solvent molecules.³¹³ For many cases, experimental chemical shift were reproduced reasonably well by the MD calculations, particularly for xenon dissolved in water. The MD calculations show that the chemical shift of xenon dissolved in perfluorinated alkanes is lower than their non-fluorinated counterparts, which contradicts the idea that dispersion interactions cause the change in chemical shift. The chemical shift caused by the xenon interacting with the face of the CF₄ molecule is lower to that of the CH₄ molecule because the xenon-CF₄ separation is greater.

MD simulations, where the solvent molecules are allowed to undergo conformational changes, show that this flexibility has a significant effect on the Xe chemical shift.³⁰⁸

The isotropic shielding tensors of ^{129}Xe in the free gas and in complex **7** were calculated at the MP2/aug-cc-pVTZ and CCSD/aug-cc-pVTZ levels of theory. The shielding tensor of ^{129}Xe in complex **7** along the z -axis, the principal axis of the complex, was also calculated.

Table 3-6: The ^{129}Xe isotropic shielding tensor of free xenon gas and xenon in complex **7**, the shielding tensor along the z -axis of xenon in complex **7** and the difference in shielding tensors. Calculations were carried out within the aug-cc-pVTZ basis set.

Method	σ_{iso} Free Xe / ppm	σ_{iso} complex 7 / ppm	σ_{zz} complex 7 / ppm	$\Delta\sigma_{\text{iso}}$ / ppm	$\sigma_{zz} - \sigma_{\text{iso}}$ / ppm
MP2	514.54	514.06	517.45	-0.48	2.91
CCSD	514.60	522.50	517.51	7.91	2.92

Table 3-6 shows that at both levels of theory the change in the calculated isotropic shielding tensors is negligible. This result was unexpected because it was anticipated that the significant interaction present in this complex would lead to more substantial change in the ^{129}Xe chemical shift. This is particularly unexpected as large changes in xenon chemical shifts have been observed simply upon dissolving it in different solvents, which involves a much weaker interaction.³⁰²

The isotropic shielding tensor was therefore calculated for a range of I...Xe separations, see Figure 3-25.

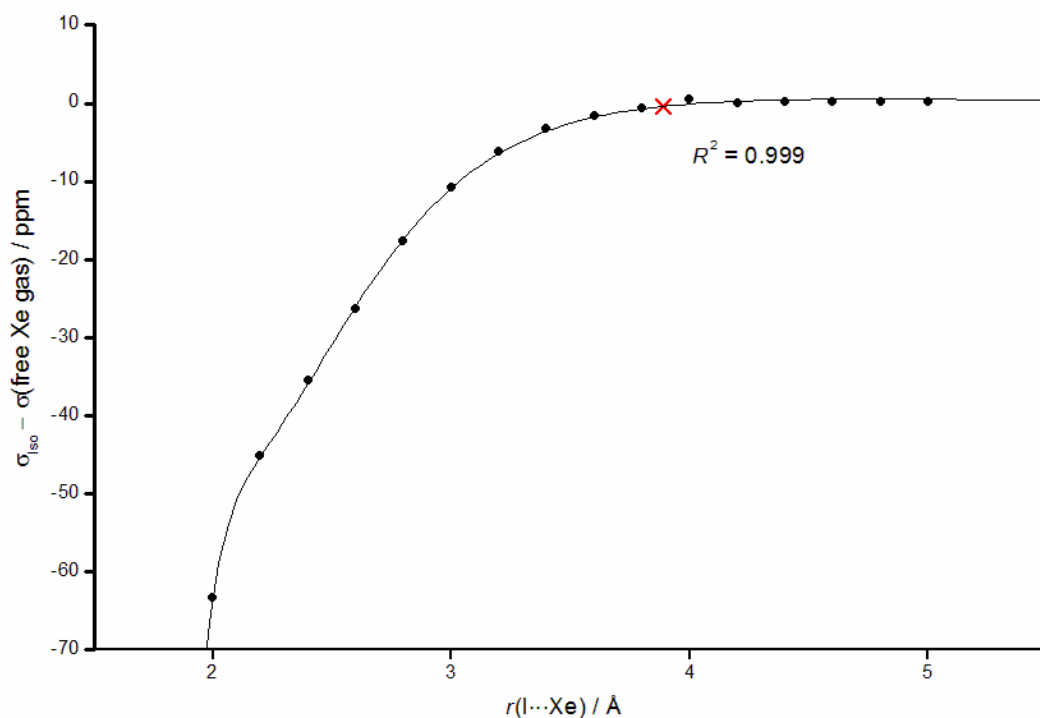


Figure 3-25: The change in the isotropic shielding tensor of the xenon in complex **7**, Xe...ICl, compared to free xenon gas as a function of the I...Xe separation calculated at the MP2/aug-cc-pVTZ level of theory. The data point highlighted in red corresponds to the optimised I...Xe separation. The curve corresponds to Equation 3-15 with optimised parameters C_p given in Table 3-7.

Figure 3-25 shows that although the change in the isotropic shielding tensor is negligible for the optimised geometry, it increases significantly as the I...Xe separation decreases. This curve is similar to that found for rare gas dimers³¹⁰ and xenon interacting with CF₄ and CH₄.³¹² The data can be fitted to the formula shown in Equation 3-15.

$$\sigma_{\text{iso}} - \sigma(\infty) = \sum_{p=6, \text{even}}^{14} C_p R^{-p} \quad (3-15)$$

The coefficients, C_p , were optimised to fit the data using Mathematica²²⁹ and are given in Table 3-7.

Table 3-7: The optimised coefficients of Equation 3-15 for complex **7**.

Coefficient	Value / \AA^{-6}
C_6	3.382×10^4
C_8	-8.637×10^5
C_{10}	6.050×10^6
C_{12}	-1.660×10^7
C_{14}	1.520×10^7

Similar isotropic shielding curves were calculated for complexes **1** – **3** between trifluoromethylhalides and xenon, Figure 3-26.

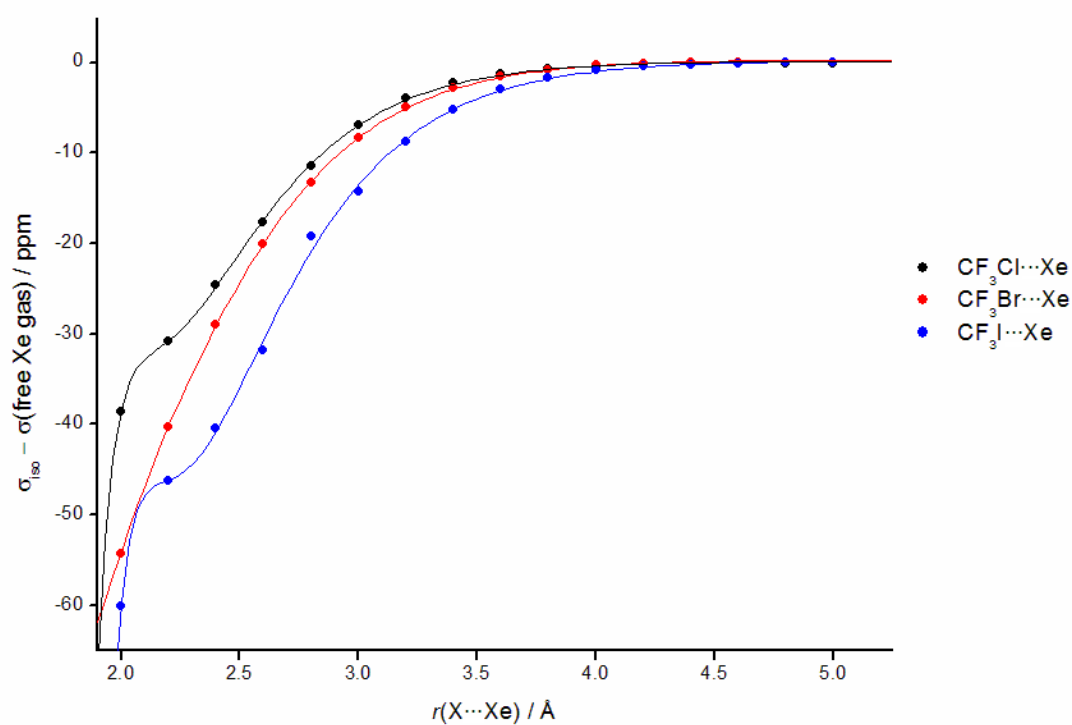


Figure 3-26: The variation of the isotropic shielding tensor of xenon in complexes **1** – **3** compared to free xenon gas with X...Xe separation calculated at the MP2/aug-cc-pVTZ level of theory.

Similar to complex **7**, the isotropic shielding curves were calculated by optimising the coefficients in Equation 3-15 and their values are given in Table 3-8.

The curves in Figure 3-26 can be compared to investigate the effect of the halogen-bond donor on the isotropic shielding tensor. It can be seen that, at a given X...Xe separation, the change in the isotropic shielding tensor compared to free xenon gas is largest in complex **1** and decreases as the halogen becomes smaller and less polarisable. This shows that the strongest halogen-bond donor, which forms a stronger complex with the xenon atom, has the most pronounced effect on the isotropic shielding tensor of the xenon atom.

Table 3-8: The optimised coefficients of Equation 3-15 for complexes **1** – **3**.

Coefficient	Value / Å ⁻⁶		
	1 , CF ₃ I...Xe	2 , CF ₃ Br...Xe	3 , CF ₃ Cl...Xe
C ₆	1.841 × 10 ⁴	1.984 × 10 ⁴	9.202 × 10 ³
C ₈	-5.162 × 10 ⁵	-5.470 × 10 ⁵	-2.218 × 10 ⁵
C ₁₀	2.655 × 10 ⁶	4.011 × 10 ⁶	7.468 × 10 ⁵
C ₁₂	-1.791 × 10 ⁶	-1.214 × 10 ⁷	1.699 × 10 ⁶
C ₁₄	-7.980 × 10 ⁶	1.342 × 10 ⁷	-7.540 × 10 ⁶

Comparing the optimised coefficients of Equation 3-15 in Tables 3-7 and 3-8 shows that, with the exception of C₁₂ and C₁₄, which only make a small contribution to the overall curve, the isotropic shielding curves are similar for complexes **1** – **3** and **7**. The coefficients for complex **3** are smaller than for complexes **1** and **2** due to the gradient of the curve being shallower, indicating that this weaker halogen-bond donor has a smaller effect on the isotropic shielding tensor of xenon. The coefficients

for complex **7** are the largest due to it being the strongest complex and having the largest effect of the isotropic shielding tensor of Xe.

The shielding tensor functions for complex **7** and for complexes **1** – **3** could be used in MD simulations to calculate the chemical shifts of xenon dissolved in ICl or trifluoromethylhalides.

3.5 Conclusions

The geometries of complexes between trifluoromethyl halides, iodomethane and iodine monochloride with rare gas atoms have been optimised and the properties of these complexes investigated using a range of theoretical approaches.

The geometry optimisations revealed that in the majority of complexes, the halogen···rare gas separation is less than the sum of the van der Waals radii and the binding energy is positive, indicating that the interaction is attractive. These interactions should be classified as weak halogen bonds even though the interaction is predominantly dispersive in nature and the binding energies are more typical of van der Waals complexes because they have characteristics similar to halogen-bonded complexes. The interaction was found to arise from a region of positive electrostatic surface potential on the halogen-bond donor interacting with electron density in the rare gas atom. This was observed from the localised molecular orbitals corresponding to valence pairs of electrons on the halogen bond donor can be combined to reveal a region of depleted electron density, and can be considered as an alternative depiction of the σ -hole. As the halogen becomes more polarisable this region of depleted electron density increases in size corroborating with the observation that as the halogen atom in the complexes became more polarisable, the binding energy increased and the halogen···xenon separation, as a percentage of the van der Waals radii, decreased suggesting that the interaction became stronger.

The lone pair of electrons on the rare gas atoms donating into the C–X/I–Cl antibonding orbital, as observed from the localised molecular orbitals, is similar to that observed for traditional halogen-bonded complexes. This induces antibonding character along the C–X (I–Cl for complex **7**) bond. This antibonding character is also apparent from the slight elongation of the C–X/I–Cl bond.

As the rare gas atom becomes more polarisable the interaction becomes stronger. This result was anticipated because rare gas atoms are isoelectronic with halide anions, which become stronger halogen-bond acceptors with increasing polarisability.¹⁶⁴ Complex **7**, involving iodine monochloride, was found to have a significantly stronger interaction, as expected for a stronger halogen-bond donor.³²

The performances of different *ab initio* and DFT methods compared to experimental results, have shown that the MP2 and B3LYP-D3 levels of theory are the most accurate at modelling these complexes, with the B3LYP-D3 functional performing well mainly because it involves an empirical dispersion correction. Similarly, the B97-D functional also gave binding energies and halogen⋯rare gas separations close to the MP2 results.

The M06 suite of functionals, parameterised to account for dispersion interactions, also performed well but were found to be dependent on the density of the integration grid. If the default 'Fine' integration grid was used, the potential energy curve along the halogen⋯rare gas separation was found to have an irregular shape. The effect is significant for these complexes due to the potential energy curve being shallow and was not observed for a complex involving a traditional, stronger halogen bond. Increasing the density of the integration grid improves the shape of the potential energy curve but also increases the computational cost of the calculation. These functionals are therefore not recommended for use on very weakly interacting complexes similar to those studied.

The B3LYP and X3LYP functionals were found to perform poorly and they underestimated the interaction. Indeed the B3LYP functional gave a halogen...rare gas separation that was longer than the sum of the van der Waals radii and suggested a repulsive interaction.

The change in the ^{129}Xe shielding tensor for complex **7** was calculated and found to be very small. The shielding tensor for this complex and complexes **1** – **3** were calculated for different X...Xe separations and shielding tensor functions were determined using these data. These functions could be used in molecular dynamics calculations to determine the chemical shifts of xenon dissolved in iodine monochloride or trifluoromethylhalides. Comparison of complexes **1** – **3** showed that stronger halogen-bond donors caused a greater change in the isotropic shielding tensor of the xenon gas.

4 Liquid-Crystalline, Halogen-Bonded Complexes between 4-Alkoxy stilbazoles, Alkoxyphenylpyridines and Dihalogens, and the Electrophilic Bromination of Stilbazoles

4.1 Introduction

4.1.1 Halogen-Bonded Liquid Crystals

As discussed in the Introduction (Chapter 1), it has been observed that the hydrogen bond can be a useful tool to induce mesomorphism in compounds that are themselves non-mesomorphic.³¹⁴ Investigations into halogen-bonded compounds have shown that this interaction can be equally as useful to induce mesomorphism.

Alkoxy stilbazoles were found to be useful compounds that, when hydrogen-bonded to nitrophenols²⁰⁶ or cyanophenols,²⁰⁵ formed liquid-crystalline complexes (Figure 4-1) even though both components were themselves not liquid-crystalline. The interaction was sufficiently strong for the mesophases to form.

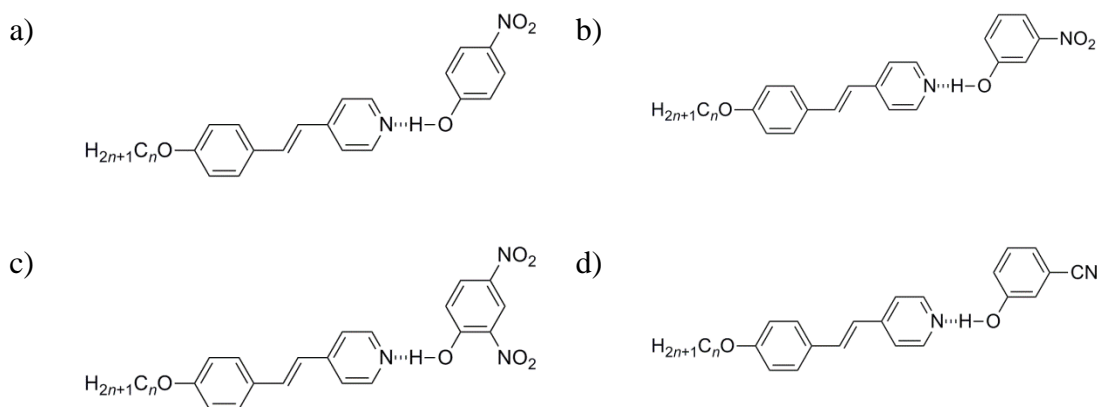


Figure 4-1: Liquid-crystalline, hydrogen-bonded complexes of alkoxy stilbazoles with a) 4-nitrophenol, b) 3-nitrophenol, c) 2,4-dinitrophenol²⁰⁶ and d) 3-cyanophenol.²⁰⁵

Alkoxy stilbazoles were, therefore, a useful starting material for investigations into halogen-bonded liquid crystals, the first example being a complex between an alkoxy stilbazole and iodopentafluorobenzene, Figure 4-2.¹⁹⁸

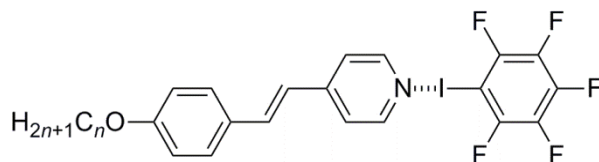


Figure 4-2: Liquid-crystalline, halogen-bonded complexes between alkoxy stilbazoles and iodopentafluorobenzene.

Alkoxy stilbazoles with a short alkoxy chains ($n = 4$ or 6) showed monotropic nematic (N) and smectic A (SmA) phases, whereas enantiotropic SmA phases were observed for stilbazoles with longer alkyl chains ($n = 8 - 12$). The mesophases and therefore the halogen bonds in these complexes were found to be stable up to $84\text{ }^{\circ}\text{C}$, which was comparable to that of the hydrogen-bonded complex between dodecyloxystilbazole and pentafluorophenol.¹⁹⁸ This shows that the halogen bonds in complexes of stilbazoles with iodopentafluorophenol are similar in strength to the hydrogen bonds in analogous complexes, highlighting that the halogen bond is sufficiently strong for mesophases to form.

Changing the halogen-bond donor to an α,ω -diiodoperfluoroalkane allowed the formation of a halogen-bonded complex containing three components, Figure 4-3.²⁶³

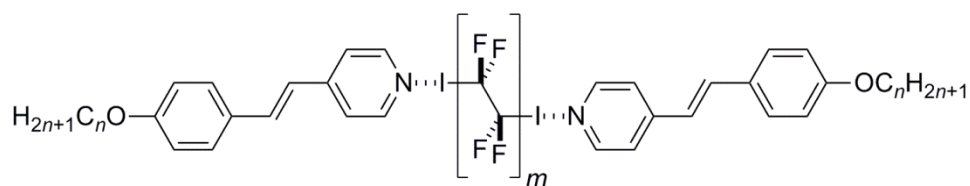


Figure 4-3: Liquid-crystalline, halogen-bonded complexes between 4-alkoxy stilbazoles and α,ω -diiodoperfluoroalkanes.²⁶³

It might have been expected that the liquid-crystalline character of these complexes would be dominated by the microphase segregation between the perfluorocarbon and hydrocarbon moieties leading to a dominance in lamellar phases. The complexes

were, however, observed to have nematic phases as characterised by polarising optical microscopy and it was believed that this was due to the presence of the flexible N...I interaction. These complexes of alkoxystilbazoles with α,ω -diiodoperfluoroalkanes were found to have a greater thermal stability compared to complexes with iodopentafluorobenzene with mesophases present up to 103.5 °C.

Further studies into complexes of this nature have included complexes of alkoxystilbazoles with 1,4-dihalotetrafluorobenzenes (Figure 4-4a),²⁰⁷ which formed liquid crystals in the case of complexes with 1,4-diiodotetrafluorobenzene, whereas complexes with 1,4-dibromotetrafluorobenzene were not liquid crystalline. This shows that using a weaker halogen-bond donor leads to an interaction that is not sufficiently strong for mesophases to form.

Complexes of alkoxystilbazoles with 1,3-diiodotetrafluorobenzene were also investigated and were found to form a bent-core liquid crystal with a chiral nematic (N*) phase (Figure 4-4b).³¹⁵ In this phase the molecules are arranged such that the director rotates in a helical manner through the material. This complex was of particular interest since upon cooling, the complex was observed to undergo an Iso – N – N* transition sequence. It is believed that upon heating, one of the N...I interactions ruptures leaving the 1:1 complex, which has a non-chiral nematic phase. Cooling causes a re-formation of the other N...I halogen bond giving the 2:1 complex which has a chiral nematic phase. The formation of chiral mesophases by achiral molecules has previously been observed for bent-core mesogens, although typically in tilted smectic phases.³¹⁶ This chirality arises from the combination of tilt (lowering of symmetry) and the bent (low-symmetry C_{2v}) geometry of the constituent molecules.

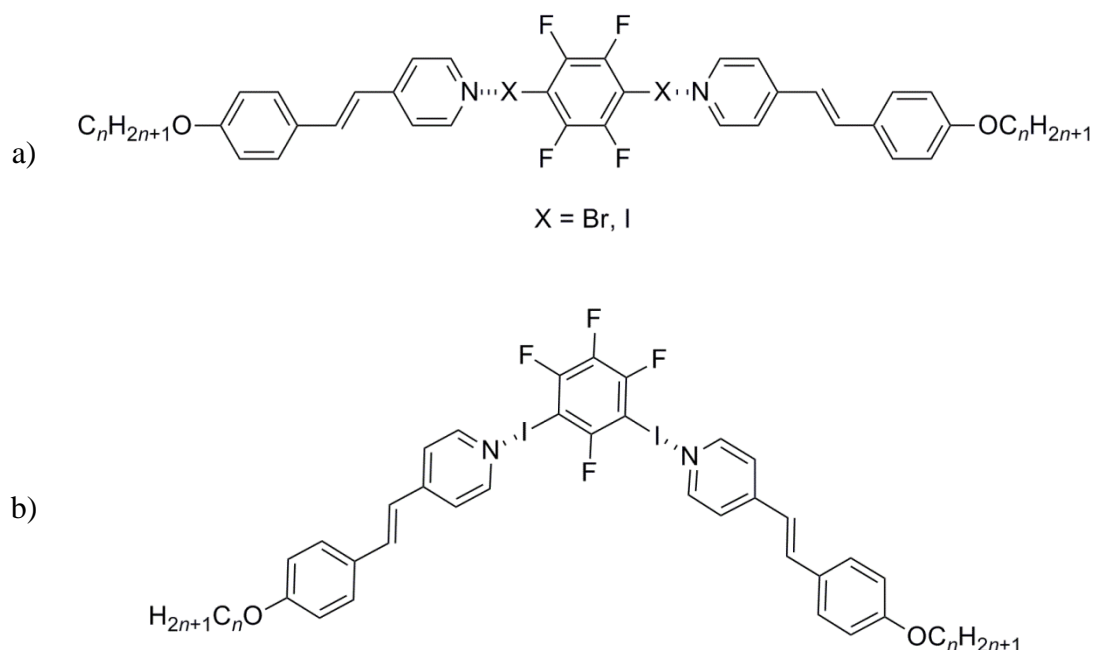


Figure 4-4: Halogen-bonded complexes between alkoxy-stilbazoles and a) 1,4-dihalotetrafluoriodobenzene ($X = \text{I or Br}$)²⁰⁷ and b) 1,3-diiidotetrafluorobenzene.³¹⁵

Chiral liquid-crystal phases have also been formed for the complexes between stilbazoles and iodostilbenes with chiral citronellyl chains (Figure 4-5).¹⁹⁷ The presence of a chiral chain on the stilbazole lead to the formation of conventional N^* phases with similar transition temperatures found for the *R* and *S* isomers. There was no distinction in phase behaviour dependence on which moiety the citronellyl substituent is found, however, when there was a dodecyloxy chain on the stilbazole and citronellyl on the iodostilbene, a smectic A phase was found, implying that the nature of the alkoxy-stilbazole dominates mesophases.

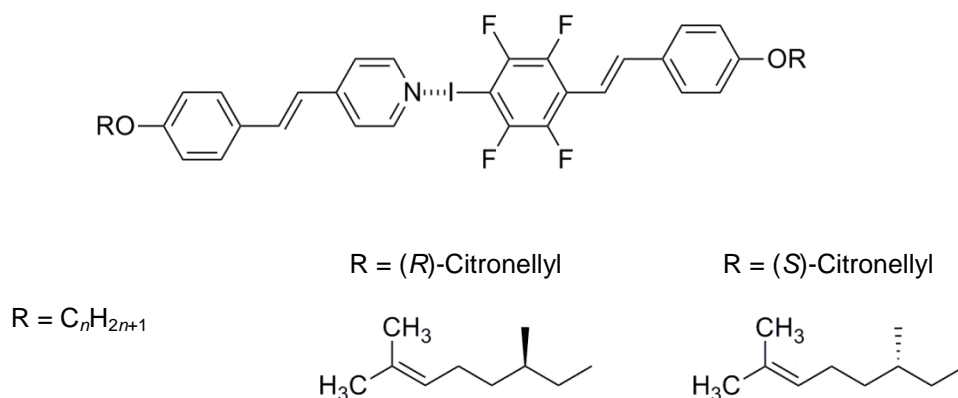


Figure 4-5: Halogen-bonded complexes stilbazoles and iodostilbenes with chiral chains.¹⁹⁷

4-Iodo-2,3,5,6-tetrafluorophenol can act as both a halogen- and a hydrogen-bond donor and forms complexes with alkoxystilbazoles, Figure 4-6.⁶⁷

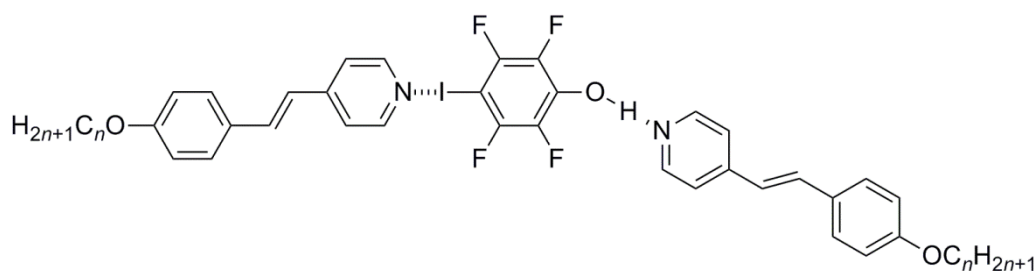


Figure 4-6: Complexes between 4-iodo-2,3,5,6-tetrafluorophenol and alkoxystilbazoles.⁶⁷

The complex with the shortest alkyl chain ($n = 4$) was found to have a monotropic N phase, whereas complexes with longer chains ($n = 6, 8$ and 10) have enantiotropic N phases and a SmA phase was observed for $n = 12$. Mixing the alkoxystilbazole and 4-iodo-2,3,5,6-tetrafluorophenol in a 1:1 ratio gave the hydrogen-bonded complex (Figure 4-7). While, the pyridyl nitrogen favours the formation of a hydrogen bond, the iodine atom forms an I...O interaction with the oxygen atom in the methoxy group. The thermal properties of the 1:1 complexes were compared to those for the 2:1 complexes. No mesophases were observed for $n = 4$ and 6 , a monotropic N phase was observed for $n = 8$ and enantiotropic SmA phases were observed for $n = 10$ and 12 . The difference in the thermal properties highlights the significance of the halogen bond interaction in these complexes.

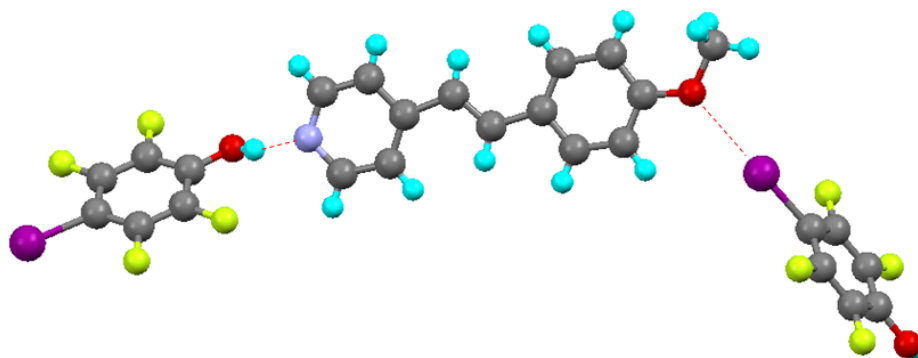


Figure 4-7: The molecular structure of the 1:1 complex between methoxystilbazole and 4-iodo-2,3,5,6-tetrafluorophenol.⁶⁷

An extensive study of halogen-bonded liquid crystals was carried out to investigate the structural effects on the properties.¹⁹⁷ This included comparing complexes with three and four aromatic rings, and alkene and ester linkages in the halogen-bond donor; a selection of these complexes is shown in Figure 4-8. The complexes with three aromatic rings were found to have lower clearing temperatures than those with four aromatic rings. Complexes with three aromatic rings with an alkyl or alkoxy pyridine as the halogen-bond acceptor showed mesophases that were more thermally stable than whereas complexes with stilbazoles as the halogen-bond acceptor, highlighting the ability of stilbazoles to stabilise mesophases. This is emphasised by the observation that the memorphic properties observed are more strongly dependent on the length of the alkoxy chain on the stilbazole rather than the chain on the halogen-bond donor. These complexes differ from those discussed previously because the phases are predominantly enantiotropic, which is due to the crystal phase in these complexes being destabilised and the liquid crystal phases being stabilised.

It was observed that for these halogen-bonded complexes, although the presence of a halogen bond destabilises the clearing point when compared to analogous covalent liquid crystals, the complexes were otherwise insensitive to the interaction. The clearing temperature was found to have an almost linear relationship with the total

number of carbon chain atoms, showing that whether the chains were positioned on the halogen-bond donor or acceptor had no effect.

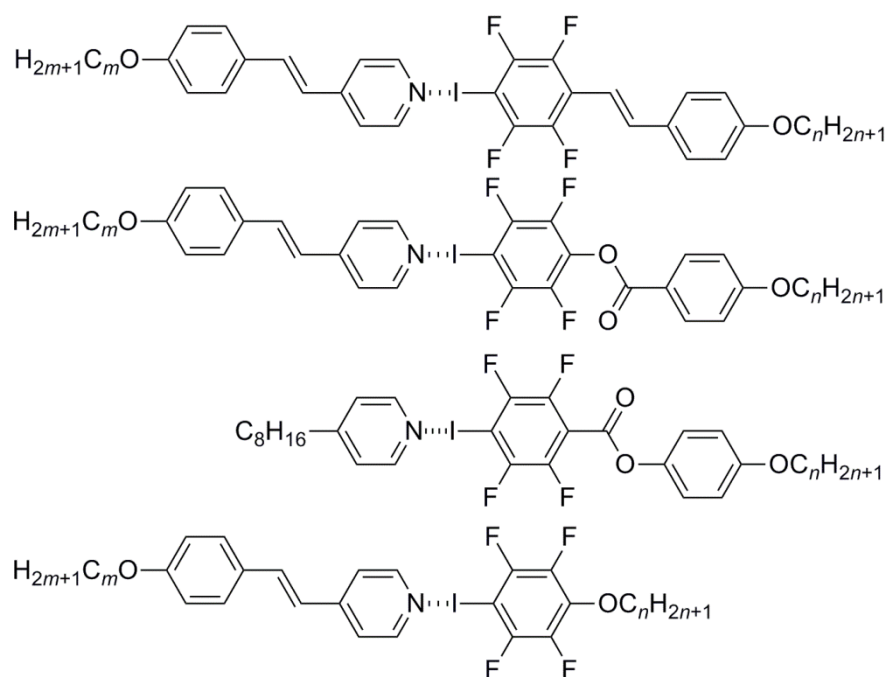


Figure 4-8: Selection of halogen-bonded liquid crystals investigated.¹⁹⁷

4.1.2 Halogen-Bonded Complexes with Dihalogens

Dihalogens can act as halogen-bond donors and have been observed to have a σ -hole.⁶⁶ Unlike in other halogen-bond donors where the halogen atom is covalently bonded to electron-withdrawing groups, homonuclear dihalogens have no electric dipole moment. The σ -hole arises from the electric quadrupole moment, which leads to an anisotropic charge distribution around the halogen atoms.³²

Hassel demonstrated some of the first examples of dihalogens acting as halogen-bond donors, forming crystal structures of complexes between iodine and 4-picoline,¹⁸ and bromine with 1,4-dioxane (Figure 4-9).⁵ In the former, the I \cdots N separation was found to be 2.31 Å, which is 65% of the sum of the van der Waals radii indicating a strong interaction. The I–I bond was also found to lengthen by 0.17 Å indicating a degree of occupancy of the I–I anti-bonding orbital. The shape of the

4-picoline ring in the molecular structure is unusual and shows significant distortions from a hexagonal geometry, which is a reflection of the poor refinement of the structure of this ring along the projection of the *b*-axis due to overlapping pairs of carbon atoms.¹⁸ The *R*-factor of the structure is consequently, relatively large at 0.12. The positions of the iodine atoms are relatively accurate in comparison because they are heavy atoms that can be determined by a Patterson synthesis.

The Br...O separation in the complex between bromine and 1,4-dioxane was 2.72 Å, which is 81% of the sum of the van der Waals radii. Although not as strong as the complex between iodine and 4-picoline, the interaction is relatively strong considering bromine is not as strong a halogen-bond donor.

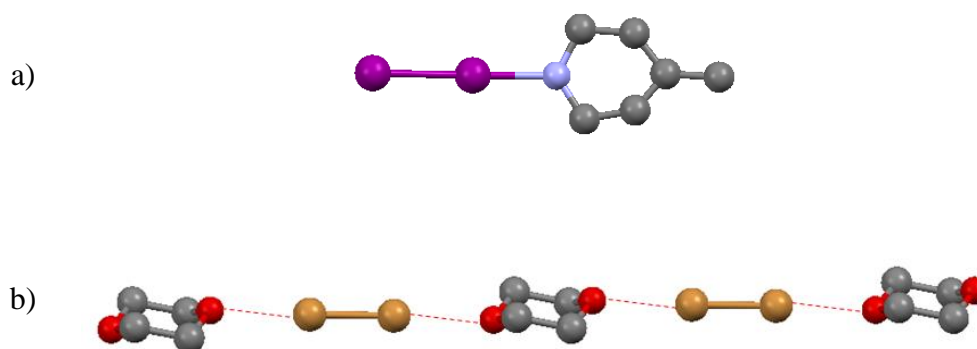


Figure 4-9: The molecular structures of the halogen-bonded complexes between a) iodine and 4-picoline¹⁸ and b) bromine and 1,4-dioxane.⁵ Br...O interactions are highlighted in red and hydrogen atoms have not been included.

The structures of complexes between iodine and Lewis bases fall into one of three categories.⁶ First is as a simple adduct, where only one end of the iodine molecule interacts with the Lewis base, as in the molecular structure of the complex between iodine and 4-picoline (Figure 4-9a), is often observed. Another example of this is in the molecular structure of the halogen-bonded complex between 4-cyanopyridine and iodine (Figure 4-10a).³¹⁷ Weaker Lewis bases can interact with both ends of the iodine molecule leading to a bridged adduct,³¹⁸ similar to that observed in the complex between bromine and 1,4-dioxane (Figure 4-9b) and in the complex of

phenazine with iodine (Figure 4-10b).³¹⁹ In the presence of a strong Lewis base, the iodine molecule polarises, making it possible for the second iodine atom to interact with a further molecule of iodine *via* a Type 2 interaction, with an I...I-I angle close to 90°. Since the iodine can act as both an acceptor and donor of electron density, these are known as amphoteric adducts³²⁰ and an example is shown in the complex between 2-(3*H*)-(diiodothio)benzoxazole and iodine (Figure 4-10c).³²¹ A bridged amphoteric adduct, such as that in the complex between acridine and iodine (Figure 4-10d) can be formed if the second iodine molecule bridges two iodine molecules that are interacting with a Lewis base.³²⁰

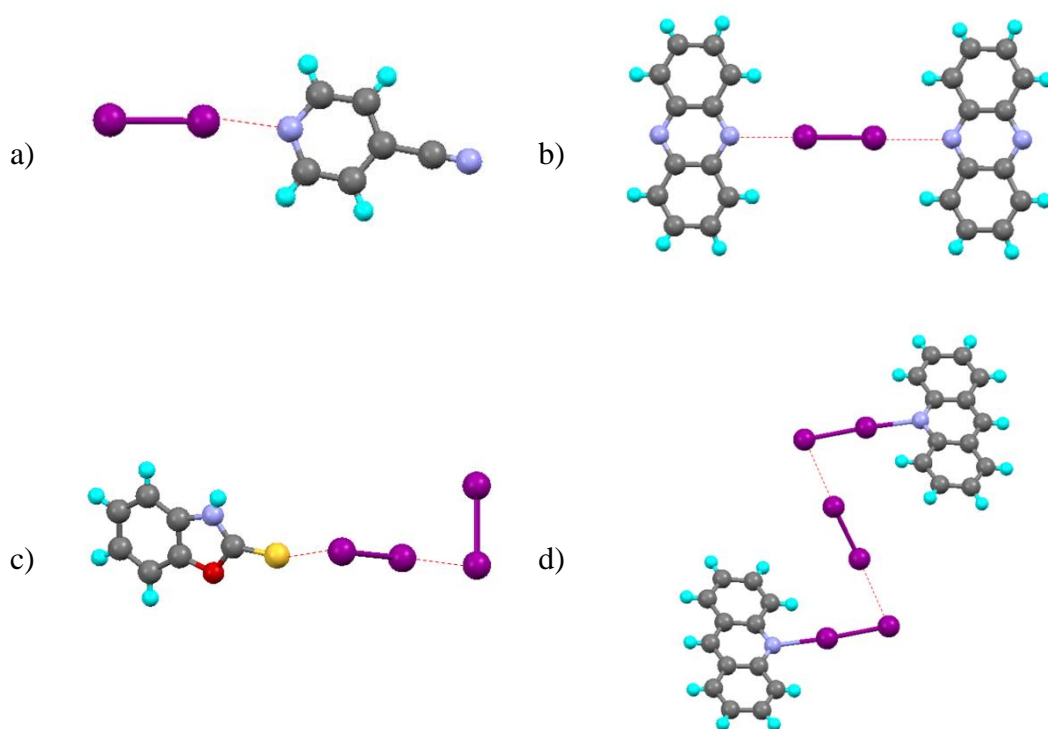


Figure 4-10: The molecular structures of a) 4-cyanopyridine and iodine,³¹⁷ b) phenazine and iodine,³¹⁹ c) 2-(3*H*)-(diiodothio)benzoxazole and iodine³²¹ and d) acridine and iodine,³²⁰ which illustrate the different interaction modes of complexes involving dihalogens.

Bromine has been found to form both the simple and bridged adducts, but due to its lower polarisability the halogen bonds involved are weaker in strength. This lower polarisability also accounts for why amphoteric adducts are not observed for complexes with bromine because the bromine molecule is not polarised sufficiently

for the second bromine atom to act as a halogen-bond acceptor. Complexes of iodine monochloride and iodine monobromide typically form simple adducts with the iodine atom forming a halogen bond with the Lewis base. Exceptions to this are the complexes between bis(bromomethyl)-1,3-dithiole-2-thione and iodine monochloride (Figure 4-11a),³²² and between *N*-methylbenzothiazole-2(3*H*)-selone and iodine monobromide (Figure 4-11b),³²³ which have been shown to both form amphoteric adducts.⁶ In the former example, there is a molecule of iodine that acts as a bridge between the chlorine atoms of two molecules of iodine monochloride so the bonding mode is not quite the same as the bridged amphoteric adducts of complexes involving only molecular iodine. In the latter example, the I–Br bond is lengthened to 3.129(2) Å and the bonding could be described as an ionic interaction between an iodide anion and [IBr₂][–].

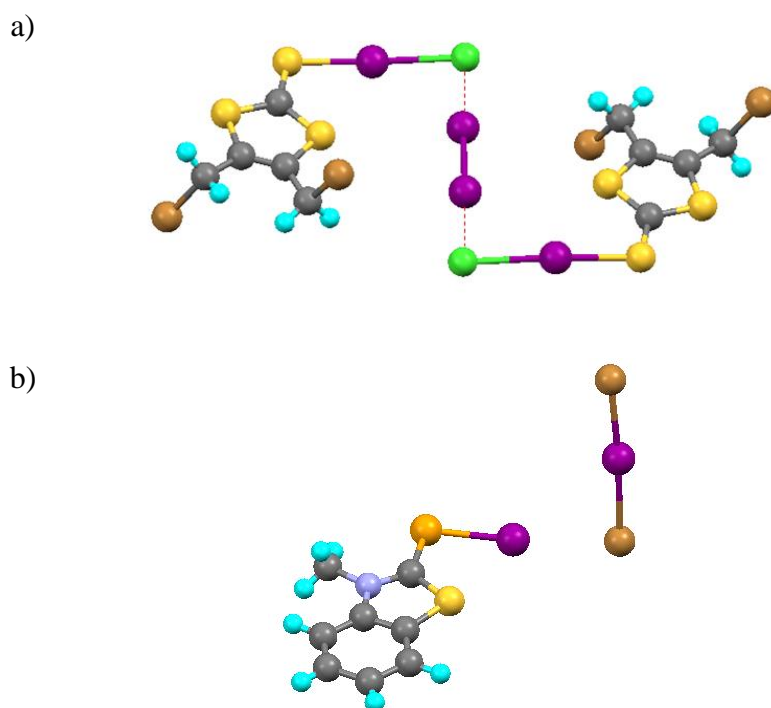


Figure 4-11: The molecular structure of the halogen-bonded complex between a) 4,5-bis(bromomethyl)-1,3-dithiole-2-thione and iodine monochloride and iodine³²² and b) *N*-methylbenzothiazole-2(3*H*)-selone and iodine monobromide.³²³

The crystal structures of halogen-bonded complexes between pyridine and ICl and IBr were determined by X-ray crystallography at 110 K and 298 K.³²⁴ The complexes were found to form simple adducts with strong interactions characterised by the short I...N separations and X-I...N angles close to 180°. As the complex is cooled, the I-X bond length increases and the I...N separation decreases slightly suggesting a strengthening of the interaction. A neutron powder diffraction structure of the complex with IBr reveals weak C-H...Br interactions, which weaken as the temperature increases and leads to thermal expansion along the crystallographic *b*-axis and colossal thermal expansion within the *ac*-plane. These studies show the balance between hydrogen and halogen bonding in crystal structures because as the temperature increases, the I...N halogen bond weakens leading to a decrease in the I-Br bond length, which causes a decrease in the partial negative charge on the bromine atom resulting in a weakening of the C-H...Br hydrogen bonds.

The halogen-bonded complexes between dihalogens and simple Lewis bases have been investigated experimentally using rotational spectroscopy in the gas phase and the relative strengths of the complexes can be determined from the force constant.³² For any Lewis base, the order of the dihalogens in terms of the strengths of the complex formed is $F_2 < Cl_2 < Br_2 < BrCl < ClF < ICl$. The dihalogens are stronger halogen-bond donors as the halogen becomes more polarisable and as the difference in electronegativities of the two halogens increases. Iodine was not included in this study but it would be expected to have a strength between ClF and ICl. An identical order of dihalogens was observed when comparing interaction energies of complexes between dihalogens and ammonia calculated at the CCSD(T), MP2, B3LYP and BH&HLYP levels of theory using the aug-cc-pVTZ basis set.¹³⁹

4.2 Aim

The aim of the work presented in this chapter is to synthesise new halogen-bonded, liquid-crystalline materials between alkoxy stilbazoles and dihalogens. It has been

shown that forming a halogen bond with an alkoxy stilbazole can induce mesomorphism and, since dihalogens have been observed to form strong halogen-bond interactions, the halogen bond in complexes of alkoxy stilbazoles with dihalogens should be sufficiently strong for mesophases to form.

4.3 Results

4.3.1 Complexes between Iodine and Alkoxy stilbazoles

Halogen-bonded complexes between molecular iodine and alkoxy stilbazoles, **1-*n***, Figure 4-12, were synthesised by the addition of a solution of iodine in hexane to a solution of the alkoxy stilbazole in chloroform. The resulting orange precipitate was found to be the 1:1 complex based on elemental analysis.

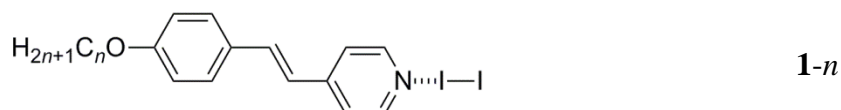


Figure 4-12: Halogen-bonded complexes between iodine and alkoxy stilbazoles.

A single crystal of the halogen-bonded complex between iodine and octyloxystilbazole, **1-8**, suitable for X-ray diffraction (XRD) was grown from toluene and the structure is shown in Figure 4-13.^{iv}

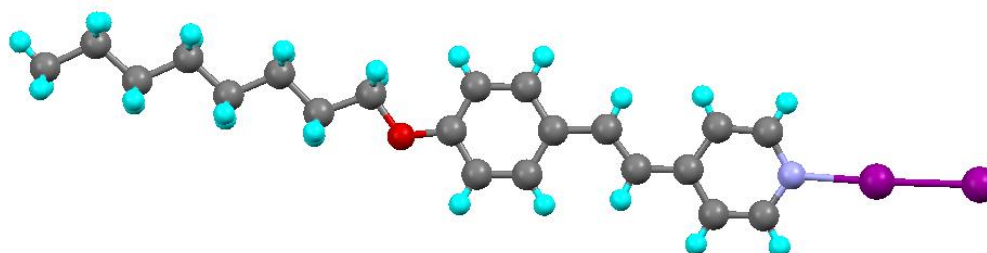


Figure 4-13: The molecular structure of the halogen-bonded complex between iodine and octyloxystilbazole, **1-8**.

^{iv} Single crystal obtained by Carsten Präsang.

The complex crystallised in space group $P\bar{1}$ with two 1:1 halogen bonded complexes between iodine and octyloxystilbazole in the unit cell. The I...N separation is 2.353(5) Å, which is 67% of the sum of the van der Waals radii. This is one of the shortest separations observed for halogen-bonded complexes involving molecular iodine. The I–I bond length is 2.8298(7) Å, which is 0.115 Å longer than that observed in the iodine monomer, while the N...I–I angle is 176.4(2)°, which is almost linear consistent with a strong halogen bond. The phenyl and the pyridyl rings deviate only slightly from planarity with a torsion angle between the two rings of 11.0(7)°.

The iodine atom not involved in the halogen bond forms a weak interaction with a neighbouring iodine of an adjacent complex leading to a 2:2 complex (Figure 4-14). The I...I separation is 3.8891(7) Å, which is 98% of twice the van der Waals radius of iodine and the I–I...I angles are 164.41°, indicating a type I interaction; this bonding mode is different to those previously observed in halogen-bonded complexes involving dihalogens.⁶ Amphoteric adducts, where the iodine atom not involved in the halogen-bond with the Lewis base acts as a halogen-bond acceptor, involve type II iodine interactions, where the I–I...I angle approaches 90°.

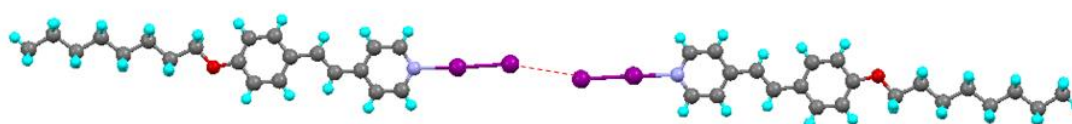


Figure 4-14: The 2:2 complex between iodine and octyloxystilbazole (1-8). The I...I interaction is highlighted in red.

The structure propagates through the *bc*-plane through weak C–H... π interactions between the alkoxychain on the stilbazole and the pyridine ring of a neighbouring stilbazole (Figure 4-15).

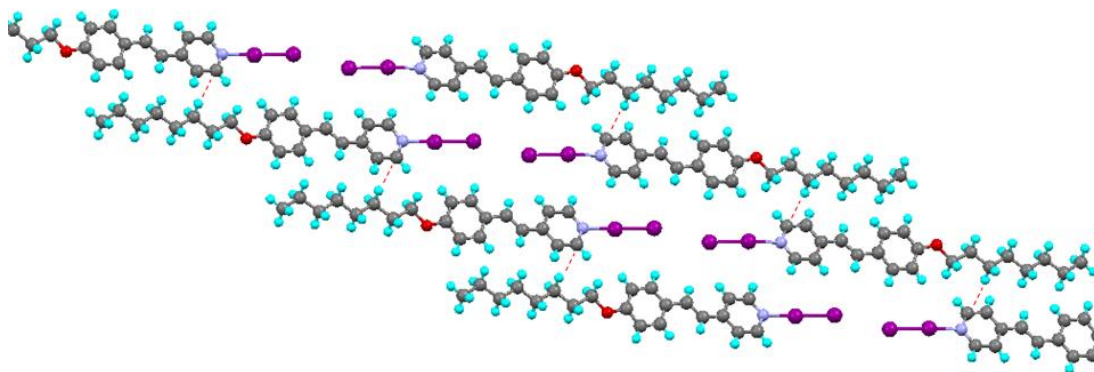


Figure 4-15: The packing of the structure of the complexes between iodine and octyloxystilbazole (**1-8**) through the *bc*-plane. C–H··· π interactions are highlighted in red.

The liquid crystal properties of the halogen-bonded complexes **1-*n*** were investigated using polarising optical microscopy (POM). The mesophases observed and transition temperatures are shown in Table 4-1.

Table 4-1: Thermal properties of halogen bonded complexes **1-*n***.

Complex	Transition	$T / ^\circ\text{C}$
1-4	Cr–Cr + Iso	145
	Cr + Iso–Iso	217
	(Iso–SmA)	(214)
1-6	Cr–Cr + Iso	155
	Cr + Iso–Iso	213
	(Iso–SmA)	(204.5)
1-8	Cr–SmA	146.7
	SmA–Iso	207
1-10	Cr–SmC	108.5
	SmC–SmA	117.0
	SmA–Iso	230
1-12	Cr–SmC	112.0
	SmC–SmA	139.5
	SmA–Iso	208

The complexes with the longest alkyl chains, **1-10** and **1-12**, showed enantiotropic SmC phases that transformed into a SmA phase upon heating. These phases were characterised by their textures (Figure 4-16).

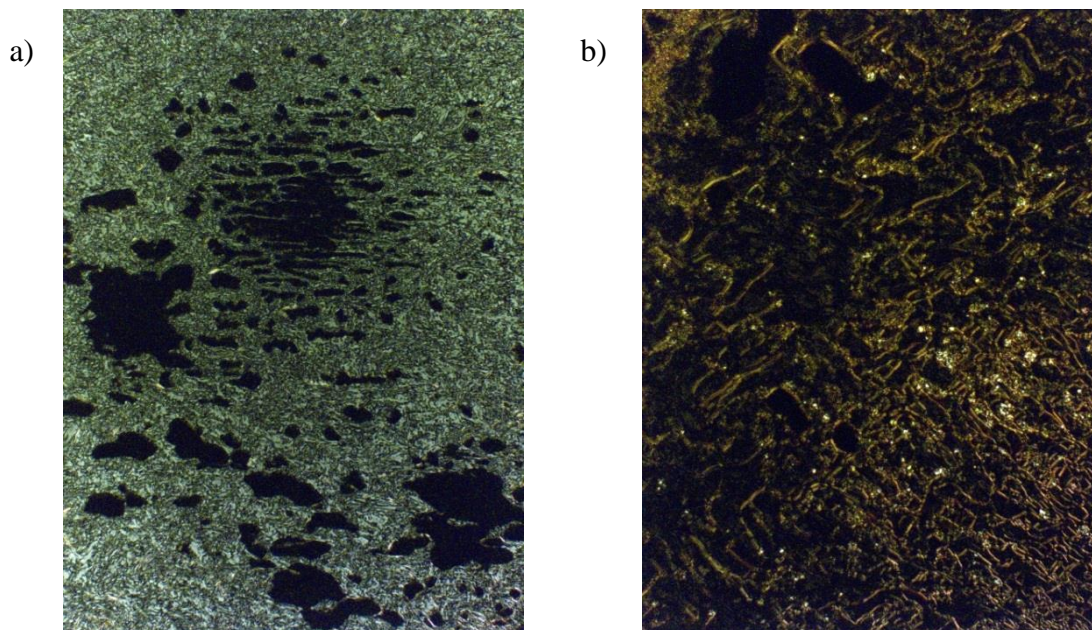


Figure 4-16: a) Optical texture of the SmC phase observed for **1-12** at 123 °C. b) Optical texture of the SmA phase observed for **1-10** at 120 °C.

Both phases have a streaky texture that is characteristic of lamellar phases. In the SmA phase, the background is extinct due to regions of homeotropic alignment. The SmC phase has a silver background due to the tilt of the molecules with respect to the layers. Differential scanning calorimetry (DSC) was used to investigate these transitions and showed that the SmC–SmA phase transition was second order (Figure 4-17).

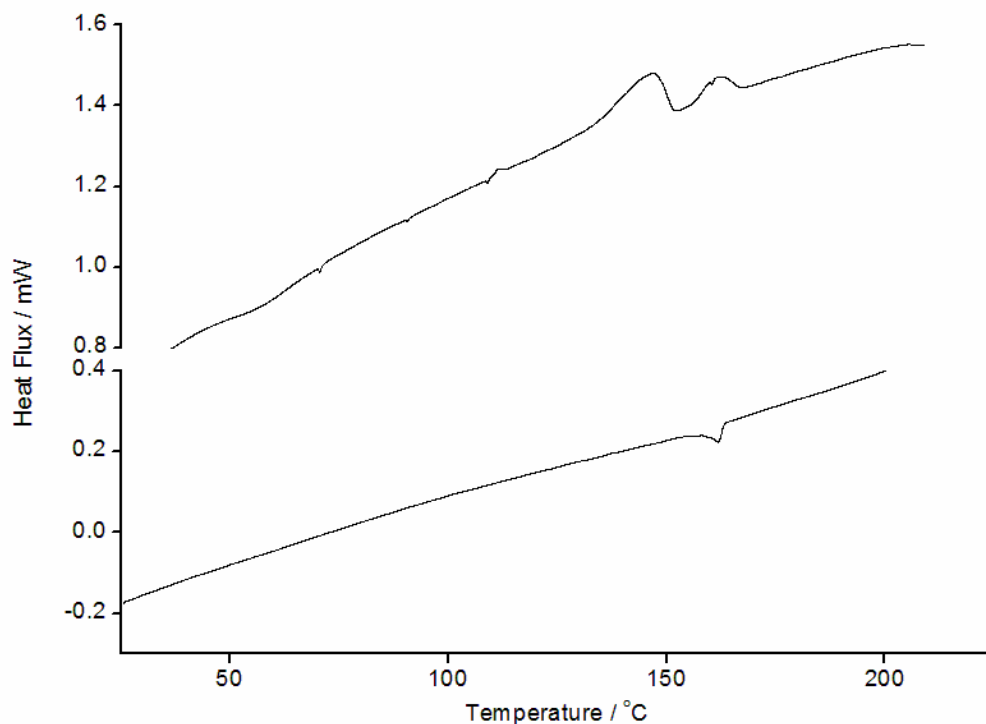


Figure 4-17: DSC curve of 1-10.

Complex **1-8** melted from the crystalline solid to a SmA phase at 146.7 °C. If the sample was slowly heated after this temperature, the mesophase crystallised at 157 °C and re-melted to the SmA phase at 177.5 °C. If the heating was fast after 146.7 °C, then this crystallisation was not observed and the SmA phase existed until clearing at 207 °C.

Complexes **1-4** and **1-6** showed no liquid crystalline properties. As the complex was heated the sample melted to give a mixture of an isotropic liquid and a crystalline solid. This was accompanied by a darkening suggesting extrusion of iodine. This was confirmed by thermogravimetric analysis (TGA), the reduction in mass of the sample upon heating corresponded to loss of one equivalent of iodine. This removal of one iodine molecule would suggest the formation of a 2:1 complex.

The SmC phase observed for complexes **1-10** and **1-12** was unexpected since it has not previously been observed for simple dipolar complexes. Therefore, the complexes were investigated by X-ray diffraction at a temperature just above the

Cr–SmC transition,^v the temperature being chosen since the complex was found to be unstable at higher temperatures and in the X-ray beam. One small-angle reflection, $d(001)$ was observed for both complexes, Figure 4-18.

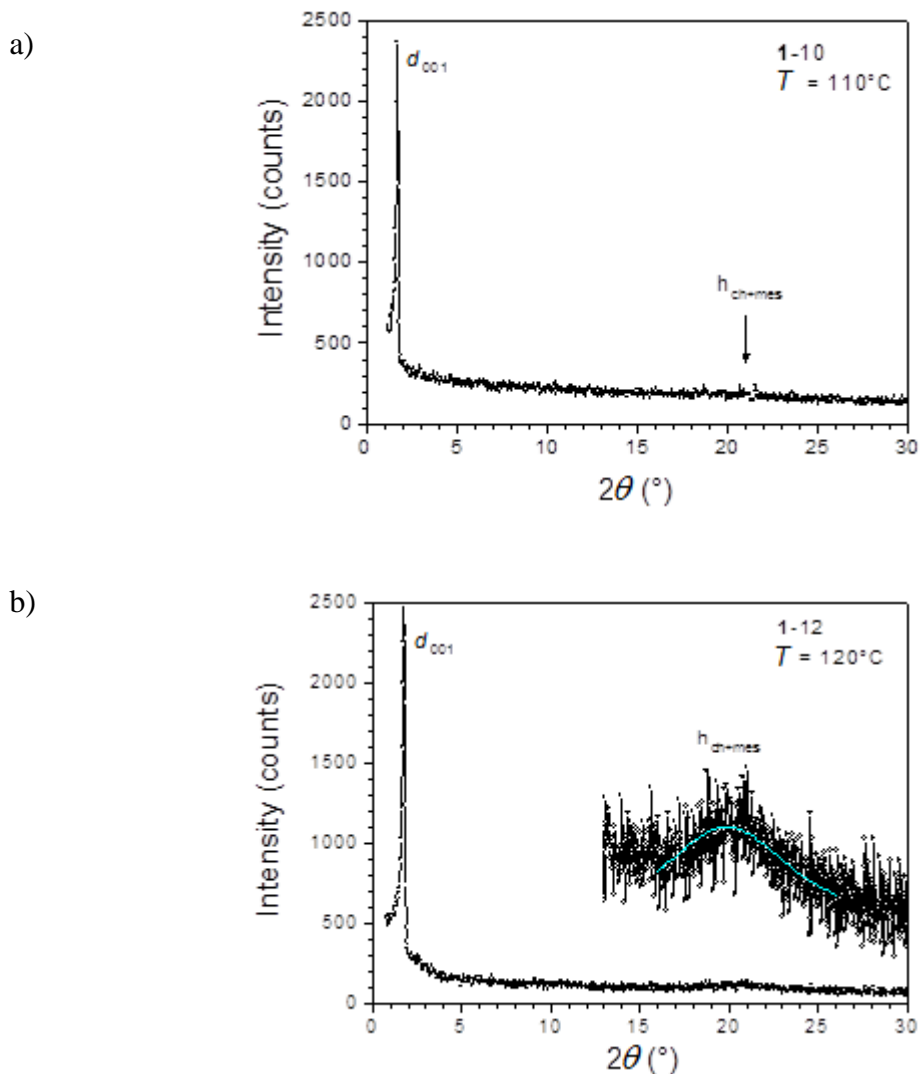


Figure 4-18: X-ray diffraction patterns in the SmC phase for a) **1-10** at 110 °C and b) **1-12** at 120 °C.

This small-angle reflection corresponds to the d -spacing in the SmC phase, which were measured to be 50.1 Å and 49.9 Å for **1-10** and **1-12**, respectively. The length of the monomeric 1:1 complex is 26.8 Å, which is significantly shorter than these d -spacings. This suggests that it is the 2:2 complex that is responsible for formation of the SmC phase and it is therefore possible that the weak I··I interaction plays an

^v Small-angle X-ray diffraction data collected by Dr Bertrand Donnio at the Université de Strasbourg.

important role in the liquid-crystalline properties of these complexes. The tilt angle, which is the angle between the molecule and the layer normal, could be determined to be approximately 30° , however, it was not possible to determine the I...I separation within the mesophase due to the flexibility of the molecule. The tilt angle of SmC phases typically decreases with increasing temperature, however, this temperature dependence could not be investigated for these complexes due to decomposition.¹⁹⁹ A second, broad single was observed at 4.5 \AA in the small angle X-ray diffraction pattern of 1-12 (Figure 4-18b), which corresponds to disordered alkyl chains and mesophases.

4.3.2 Electrophilic Bromination of Alkoxy stilbazoles

Having established that halogen-bonded complexes with molecular iodine have interesting liquid-crystalline properties, attempts to synthesise the analogous complexes with molecular bromine were carried out. Instead of forming a halogen-bonded complex, however, a stilbazolium bromide with a bromine atom replacing an ethylenic hydrogen was formed by adding bromine to a solution of the alkoxy stilbazole in THF and was identified by its crystal structure (Figure 4-19).^{vi} There is a hydrogen bond between the hydrogen bound to the pyridyl nitrogen and the bromide anion with a N...Br⁻ separation of $3.187(2) \text{ \AA}$ and an N-H...Br⁻ angle of $161(2)^\circ$, which is a significant deviation from linearity.

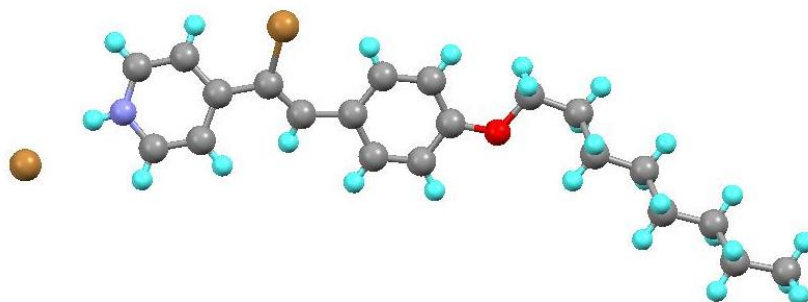


Figure 4-19: Molecular structure of 2.

^{vi} Initial synthesis carried out by and single crystal obtained by Joanna Wong.

The bromine atom bound to the ethylenic carbon in the stilbazolium bromide interacts with an oxygen atom in the alkoxy substituent of a neighbouring stilbazolium bromide (Figure 4-20). The Br...O separation is 3.263(1) Å, which is 97% of the sum of the van der Waals radii and the C–Br...O angle is 152.34(5)°, indicating that the interaction is weak and should only be considered a van der Waals interaction. There are also C–H...Br⁻ interactions between a pyridyl proton of a stilbazolium cation and a neighbouring bromide anion (Figure 4-20). This leads to a structure of interdigitated stilbazolium bromide molecules.

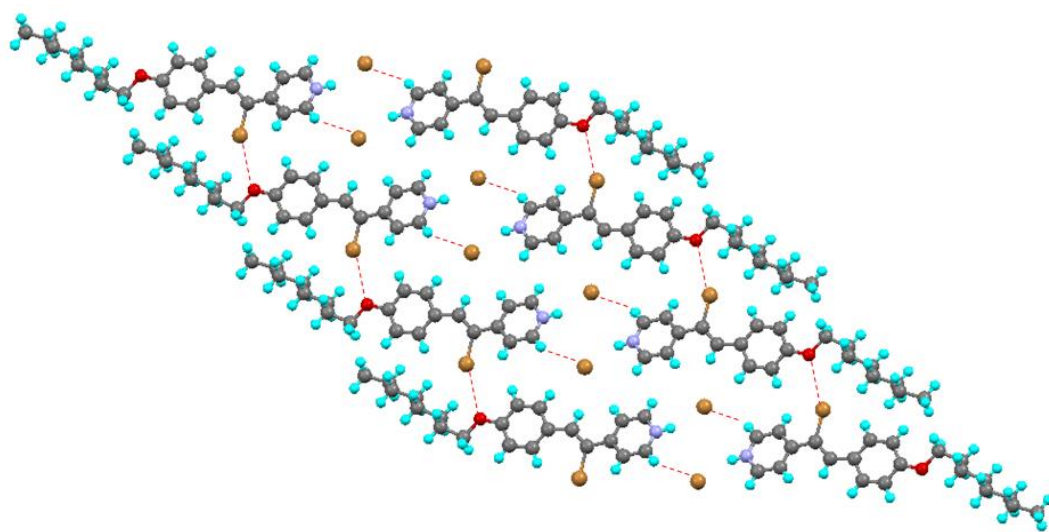


Figure 4-20: The Br...O and C–H...Br⁻ interactions (highlighted in red) in the molecular structure of **2**.

The stilbazolium bromide molecules stack along the *a*-axis in a slipped stacking arrangement with weak interactions between the ethylenic carbon atom and the pyridyl ring of a neighbouring ring (Figure 4-21). Furthermore, there are weak C–H...H–C interactions between the ends of the alkyl chains of neighbouring stilbazolium cations.

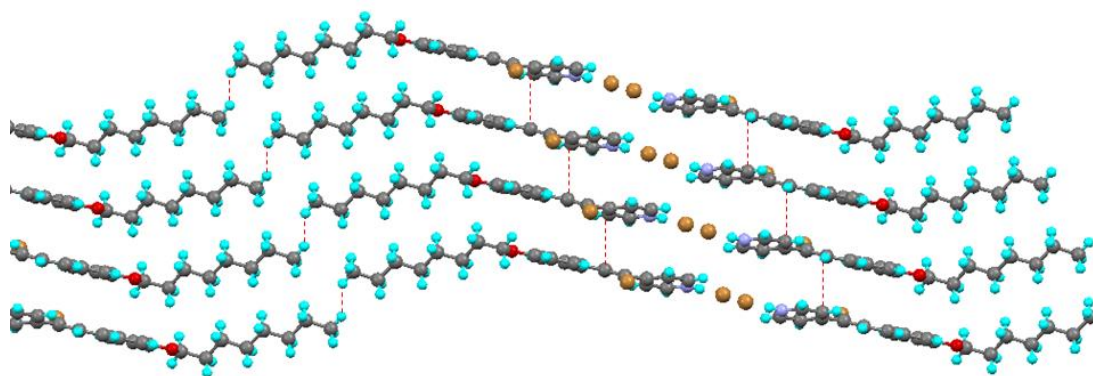


Figure 4-21: Stacking of the stilbazolium bromide molecules along the *a*-axis.

The aromatic region of the ^1H NMR spectrum of **2** is characterised by two AA'XX' systems corresponding to the two aromatic rings and a singlet at 7.7 ppm corresponding to the ethylenic hydrogen (Figure 4-22).

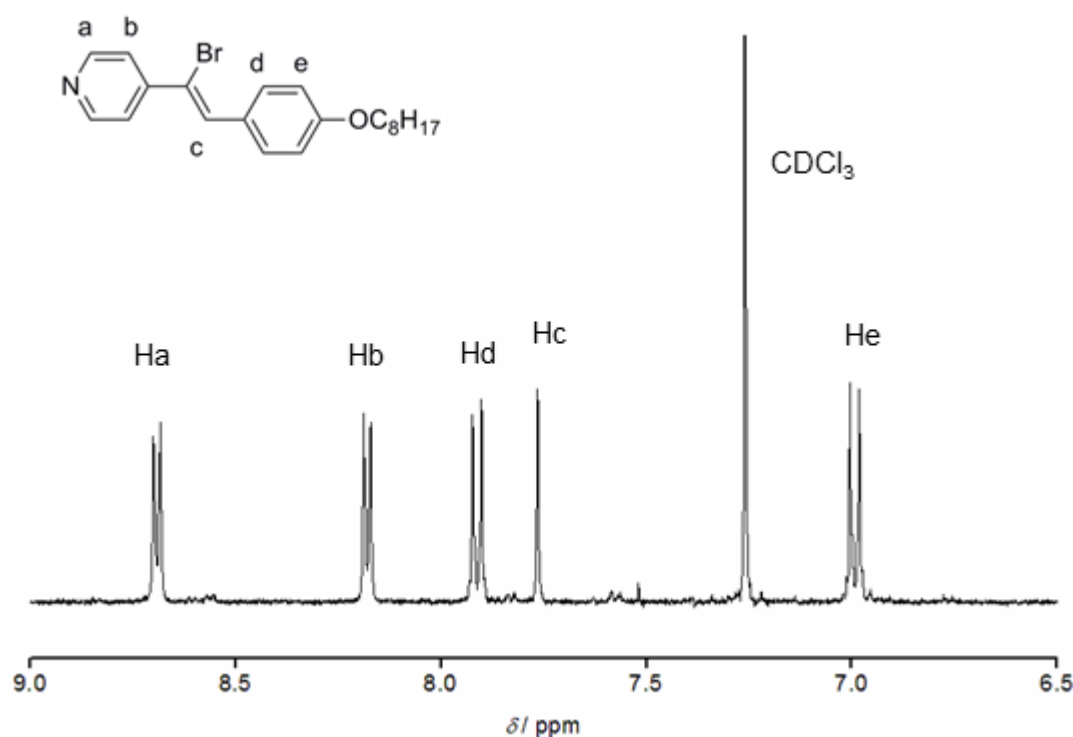


Figure 4-22: The aromatic region of the ^1H NMR spectrum of **2**.

In an attempt to produce larger quantities of **2** by allowing the solution of bromine and alkoxy stilbazole in THF to crystallise quickly at low temperatures, a mixture of two products was observed. The peaks corresponding to the isolated product **2** were

present, along with another pair of AA'XX' systems and an additional singlet (Figure 4-23). The ratio of these two sets of peaks was 10:1 in favour of the isolated product shown in Figure 4-19.

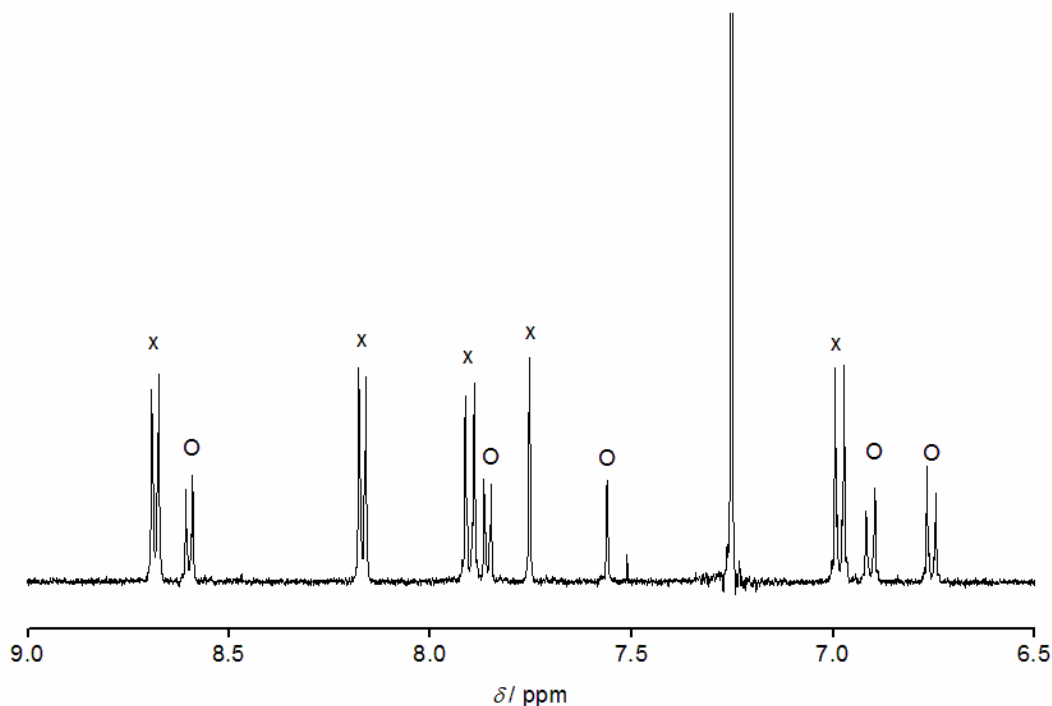


Figure 4-23: The aromatic region of the ¹H NMR spectrum of the *trans*(X) and *cis*(O) isomers of **2**.

Nuclear Overhauser Effect (NOE) experiments were carried out in order to identify the minor product. Thus, the two singlet peaks were each irradiated and the NOE spectra were examined. For the major product, irradiation of the singlet peak led to intensity enhancements at the hydrogen atoms in the pyridyl and phenyl rings (H₂ and H₃ in Figure 4-24b). This is consistent with the molecular structure of **2** found by X-ray crystallography (Figure 4-19) because both the pyridyl and phenyl protons are close in space to the ethylenic hydrogen atom. For the minor product, irradiation of the singlet peak led to only an enhancement corresponding to the hydrogen on the phenyl ring (H₃, Figure 4-24a), which is consistent with the stilbazole being in a *cis* conformation since the ethylenic proton would only be close in space to the phenyl protons.

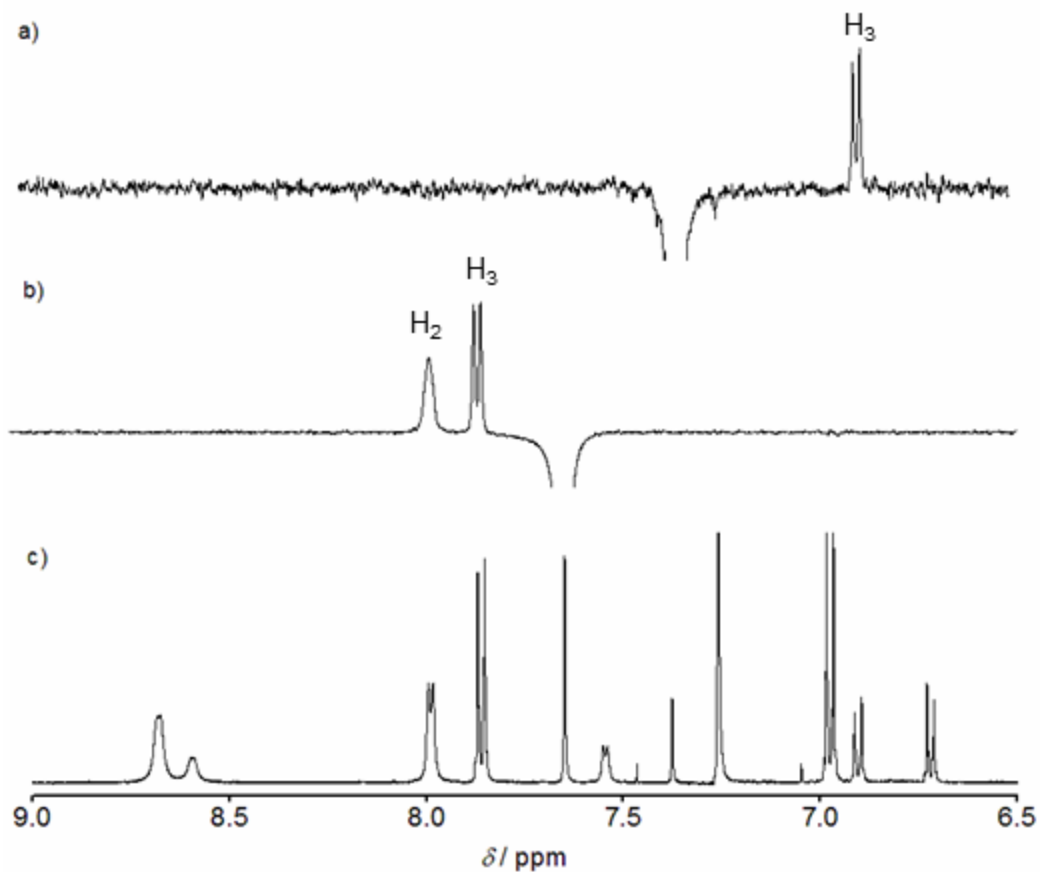
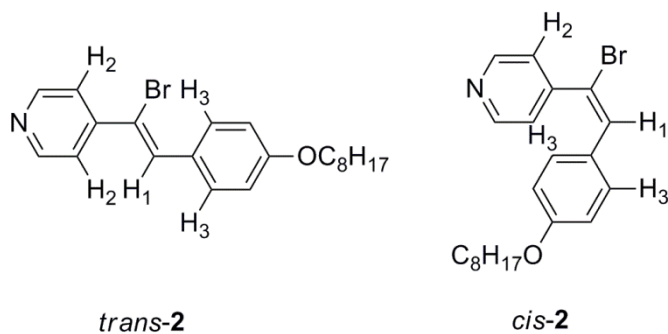


Figure 4-24: a) The NOE spectra observed upon irradiating the singlet of the minor product. b) The NOEs observed upon irradiating the singlet of the major product. c) The ^1H NMR spectrum of the mixture of *trans-2* and *cis-2*.

A mechanism for the formation of **2** was proposed and is shown in Figure 4-25. The first step of the reaction is an electrophilic bromination of the central alkene bond forming either a bromonium ion intermediate or a dibromoalkane. These two species could not be observed by NMR spectroscopy and attempts to isolate either species were unsuccessful. The second step of the mechanism involves cleavage of the C-Br

bond closest to the phenyl ring (Figure 4-25) leading to the formation of a carbocation intermediate that can be stabilised by resonance from the lone pair of the alkoxy oxygen. Rotation about the central C–C bond in this intermediate allows the formation of the *trans* and *cis* isomers of the product observed following elimination of HBr.

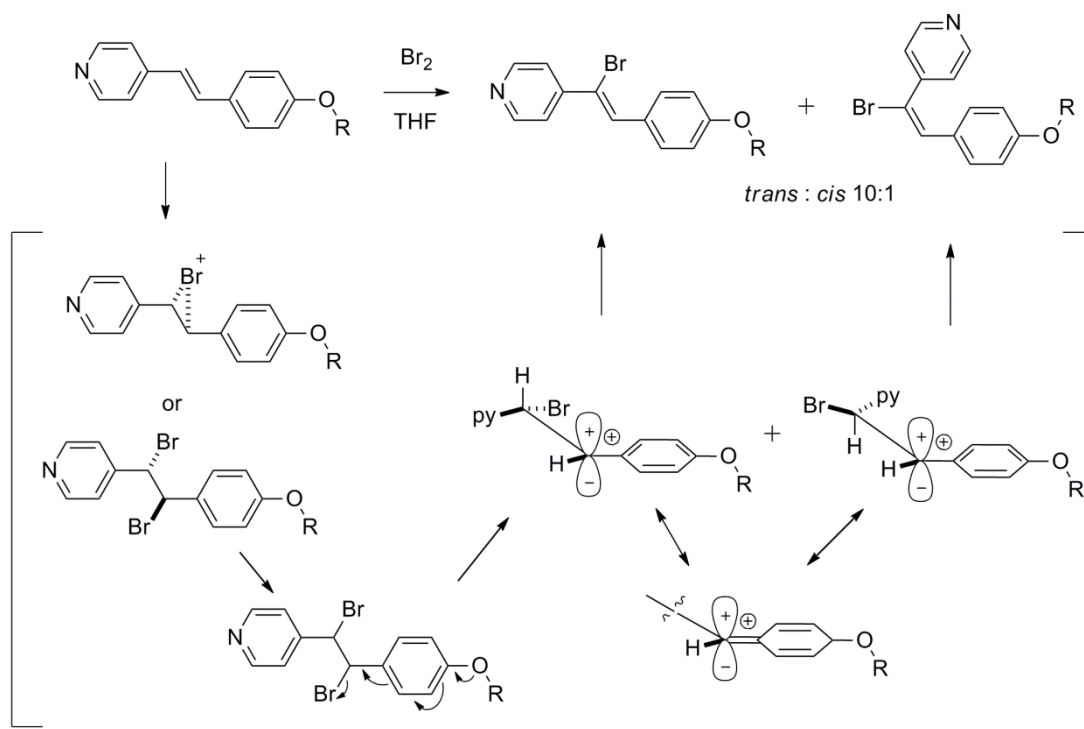


Figure 4-25: Proposed mechanism for the formation of 2.

Attempts to isolate the dibromoalkane intermediate were made by recrystallising the crude solid from the reaction using ethanol. These attempts were unsuccessful but it was observed that ethanolysis had taken place to produce compound 3, Figure 4-26.

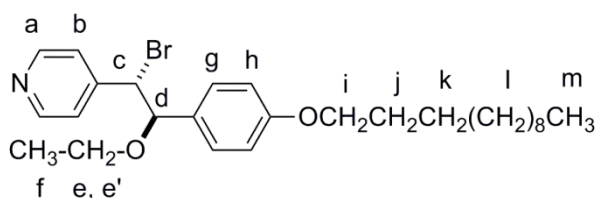


Figure 4-26: Ethanolysis product of alkoxy-stilbazoles (3).

It is well known that electrophilic bromination reactions carried out in protic solvents result in competition between the solvent and the bromide anion during the

nucleophilic addition step. The ^1H NMR spectrum of this ethanolysis product features an AB system corresponding to the protons bound to the central carbon atoms (Figure 4-27). The value of $^3J_{\text{AB}}$ is 5.3 Hz, consistent with the anti-addition product shown in Figure 4-26. The CH_2 protons in the EtO group bound to the ethylenic carbon are characterised by a quartet of an AB system at 3.42 ppm. This is observed because the two protons are diastereotopic and as well as coupling to the CH_3 protons in the EtO group with $^3J_{\text{HH}} = 6.9$ Hz, they also couple with one another with $^2J_{\text{HH}} = 7.1$ Hz.

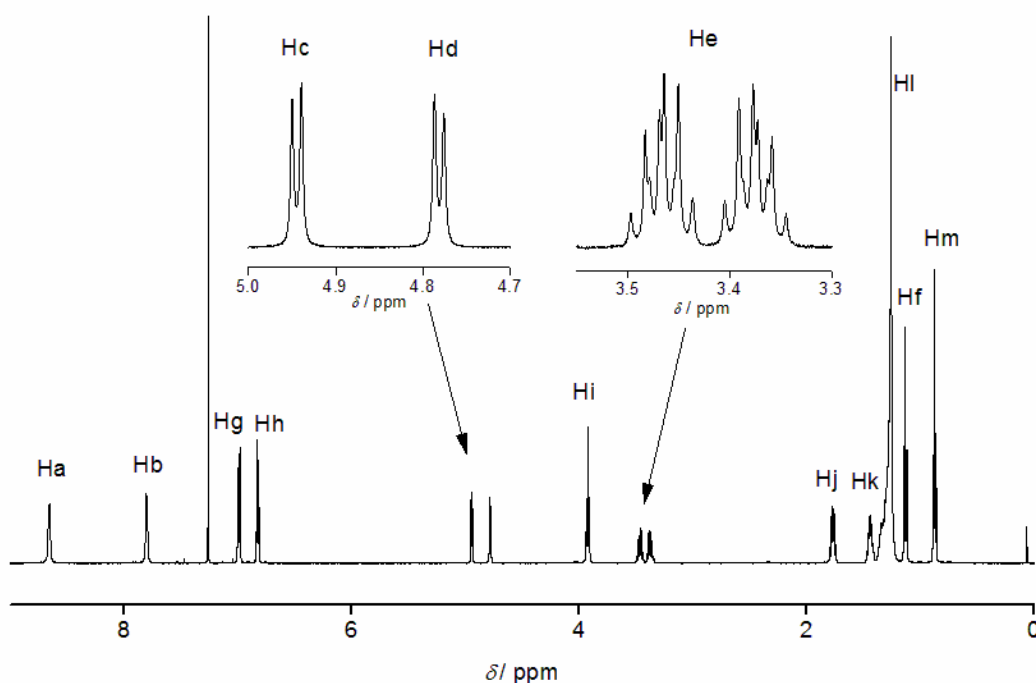


Figure 4-27: The ^1H NMR spectrum of the ethanolysis product of alkoxystilbazoles (3).

4.3.3 Electrophilic Bromination of Alkylstilbazoles

The elimination of HBr is driven by the alkoxy oxygen so it was believed that using a 4-alkylstilbazole would prevent this elimination and could allow the formation of a halogen-bonded complex with bromine. It was desirable to maintain the C–C double bond in the stilbazole because this causes the phenyl and pyridyl rings to be coplanar increasing the likelihood of the observation of liquid crystal behaviour.

Alkylstilbazoles were synthesised from the 4-alkylaniline *via* a Sandmeyer reaction.³²⁵ The 4-alkylaniline is treated with NaNO₂ and HCl, which forms nitrous acid, HNO₂, which can form the diazonium ion. This then undergoes a substitution reaction with potassium iodide to form the 4-alkyliodobenzene. This was then used in a Heck cross-coupling reaction^{326,327} with 4-vinylpyridine to form the alkylstilbazole, which is similar to the synthesis of alkoxy stilbazoles.³²⁸

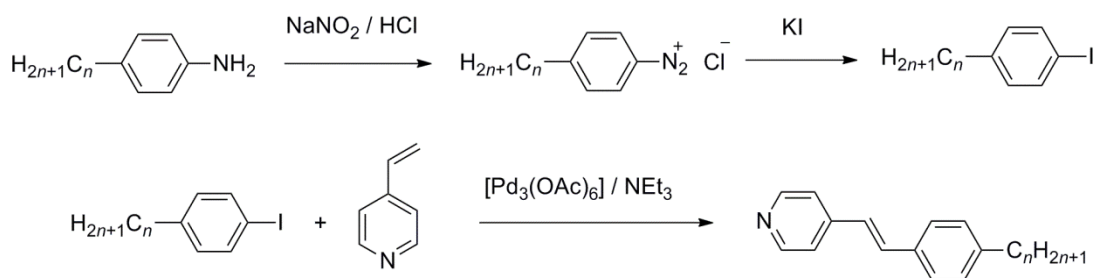


Figure 4-28: Synthesis of alkylstilbazoles *via* a Sandmeyer reaction³²⁵ followed by a Heck cross-coupling reaction.^{326,327}

Alkylstilbazoles were then mixed with bromine in THF in a similar manner to the reactions with alkoxy stilbazoles. Single crystals were obtained from the solution and X-ray crystallography revealed the formation of a dibromoalkane, **4**, Figure 4-29.

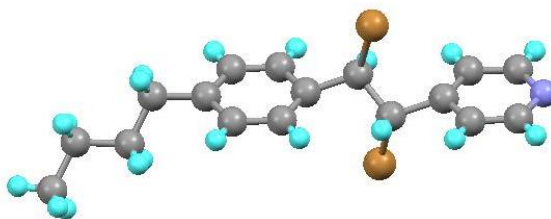


Figure 4-29: The molecular structure of **4**. Disorder has been removed for clarity and the 41.3% occupancy model is shown.

The crystal structure of **4** was found to be highly disordered particularly around the central C–C bond. This was characterised by the large thermal ellipsoids for the *ipso*-carbon atoms on the phenyl and pyridyl ring (Figure 4-30).

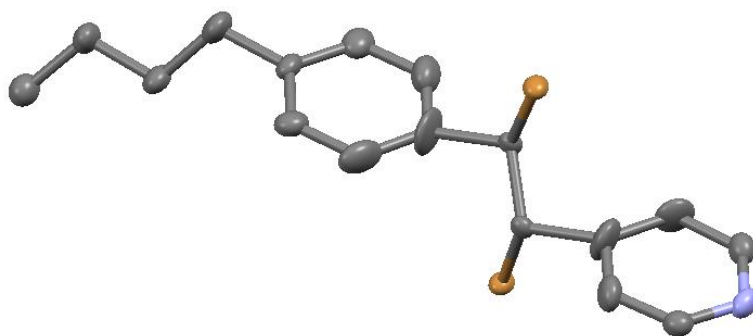


Figure 4-30: Ellipsoidal model of **4** showing the disorder in the carbon positions in the 41.3% occupancy model.

The disorder was modelled over four components with relative occupancies of 41.3%, 30%, 15% and 13.7%. The four models correspond to the central carbon atoms being above and below the plane of the pyridyl and phenyl rings and their mirror images. Initially, the structure was modelled as a bromonium ion with a bromide anion, Figure 4-31.

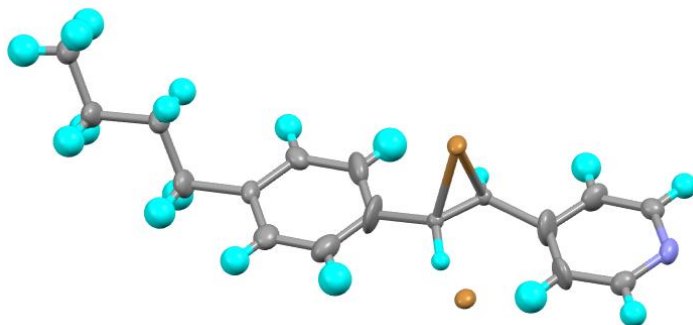


Figure 4-31: Ellipsoidal model of **4** modelled as a bromonium ion with an unbound bromide anion.

This model led us to believe that we had obtained the first example of a sterically unencumbered bromonium ion, however, reviewing the model revealed that 1,2-dibromo product, Figure 4-29, has a lower *R*-factor of 3.17% compared to 3.23% for the bromonium ion.

The molecules in the crystal structure of **4** pack in a herringbone pattern as shown in Figure 4-32. There are weak Br \cdots π interactions between the bromine atoms and the

pyridyl and phenyl rings in the neighbouring molecules. The distance between the Br atoms and the centroids of the phenyl and pyridine rings are 3.474 and 3.495 Å, respectively.

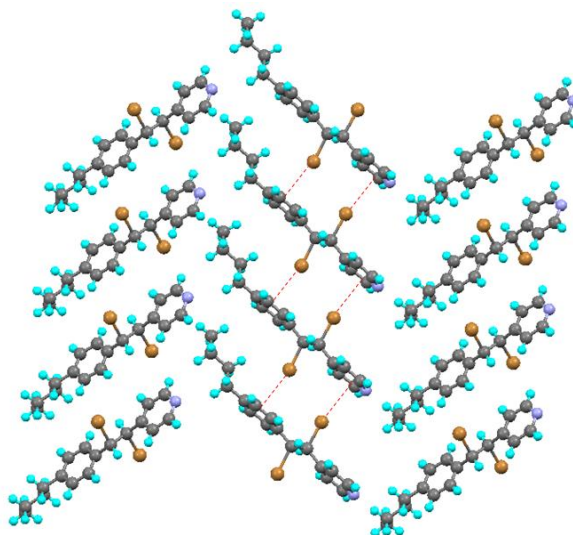


Figure 4-32: Herringbone packing in the crystal structure of **4**. Br... π interactions are highlighted in red.

The ^1H NMR spectrum of the dibromoalkane **4** shows an AB system corresponding to the protons on the central C–C bond that was centred on $\delta = 5.36$ with $J_{\text{AB}} = 11$ Hz (Figure 4-33). These values are consistent with *anti*-addition of bromine across the C–C double bond. In order to verify this, butylstilbazole was reacted with a mixture of Bu_4NBr and Bu_4NBr_3 , which has been shown to exclusively form the *anti*-brominated alkane.³²⁹ An AB system with $\delta = 5.37$ and $J_{\text{AB}} = 11$ Hz was observed indicating that *anti*-addition had been observed for **4**.

Even though electrophilic bromination of the alkylstilbazole was observed and a halogen-bonded complex was not formed, the synthesis of **4** shows that the proposal that the elimination of HBr in the formation of stilbazolium bromide, **2**, is driven by the oxygen atom of the alkoxy group of the alkoxystilbazole.

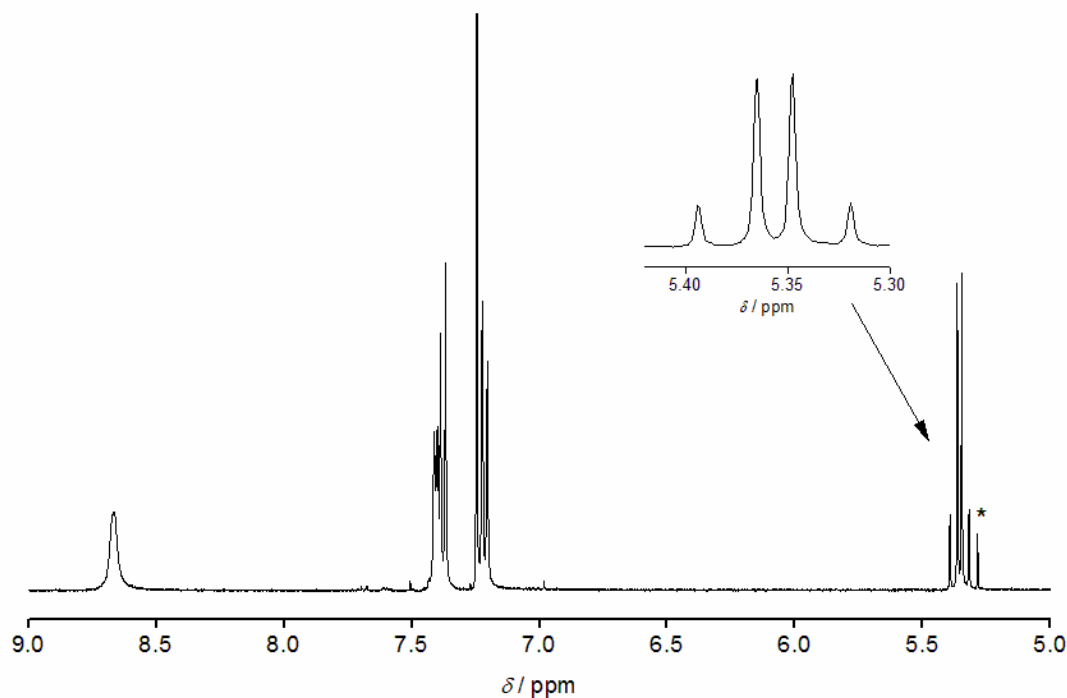


Figure 4-33: Section of the ^1H NMR spectrum of **4**. * indicates a small impurity in the sample.

4.3.4 Complexes between Alkoxyphenylpyridines and Dihalogens

In order to obtain a halogen-bonded complex with molecular bromine, it is necessary to prevent the electrophilic bromination reaction from taking place. In order to achieve this, alkoxyphenylpyridines, **5-*n***, were synthesised^{vii330} (Figure 4-34). First, 4-bromophenol was reacted with a bromoalkane *via* a Williamson ether reaction to form the 4-alkoxybromobenzene, which was then reacted with 4-pyridineboronic acid in a Suzuki-Miyaura cross-coupling reaction to form the alkoxyphenylpyridine (Figure 4-35). There were some difficulties purifying these compounds and it should be noted that the elemental analysis shows an impurity for hexyloxy and octyloxyphenylpyridine although this impurity has not been identified.

^{vii} Synthesis of alkoxyphenylpyridines was carried out by James Taylor, a MChem project student, whom I co-supervised.

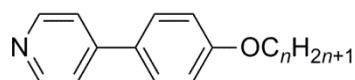


Figure 4-34: Structure of alkoxyphenylpyridines, **5-n**.

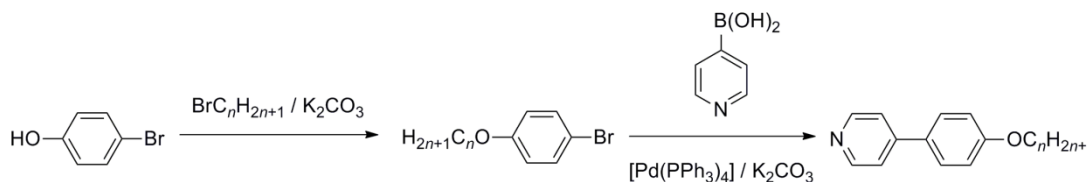


Figure 4-35: Synthesis of alkoxyphenylpyridines.

The alkoxyphenylpyridines are not mesomorphic, however, their *N*-oxides display SmA phases with increasing thermal stability as the alkyl chain length increases.³³¹ The presence of an oxygen atom increases the dipole moment of the molecule which leads to the observation of liquid-crystalline behaviour. The fact that the *N*-oxides form SmA phases rather than the nematic phase was rationalised by the formation of an interdigitated bilayer, similar to that observed in 4-cyanobiphenyls (Figure 4-36).

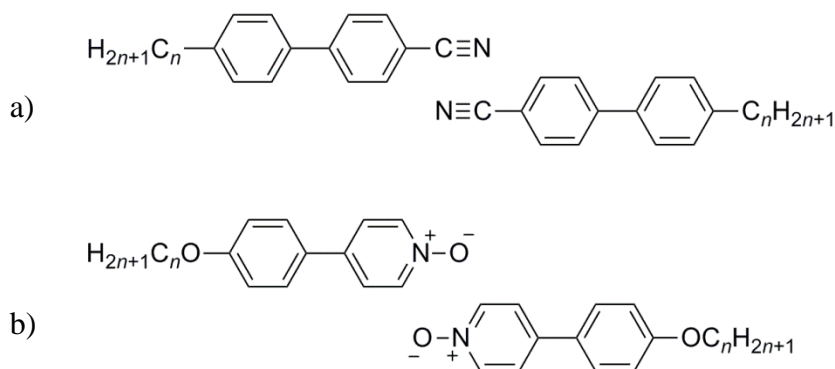


Figure 4-36: The interdigitated structures of a) 4'-alkyl-4-cyanobiphenyls and b) *N*-oxides of 4-(4'-alkoxyphenyl)pyridines.

The fact that increasing the dipole moment of the alkoxyphenylpyridine by forming the *N*-oxide leads to the formation of liquid crystal phases is promising because introducing a halogen bond should also increase the dipole moment. Therefore, complexes of alkoxyphenylpyridines and dihalogens (Figure 4-37) were synthesised and their liquid crystal properties were investigated.

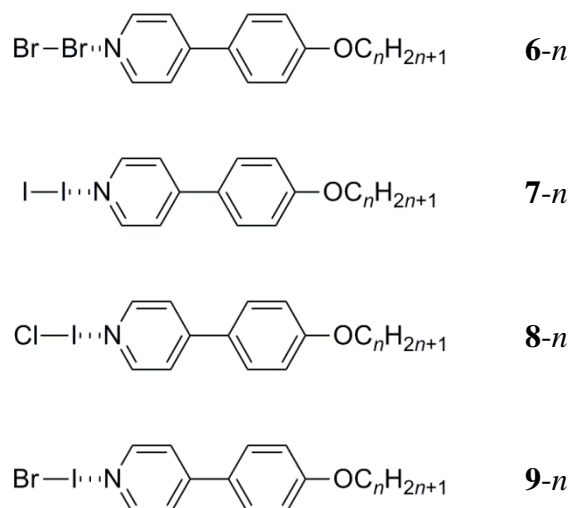


Figure 4-37: The complexes of alkoxyphenylpyridines with dihalogens investigated.

Attempts to crystallise the halogen-bonded complex between bromine and alkoxyphenylpyridines have been unsuccessful with the alkoxyphenylpyridine becoming protonated and being present as a bromide salt. An example of this crystal structure is shown in Figure 4-38.

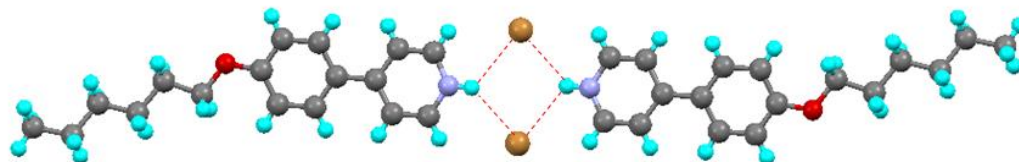


Figure 4-38: The molecular structure of hexyloxyphenylpyridinium bromide. $\text{H}\cdots\text{Br}$ interactions are highlighted in red.

The crystal structure contains hydrogen bonds between the protonated pyridine and the bromide anions. The $\text{H}\cdots\text{Br}$ distances at 2.66(2) and 2.83(3) Å, which is 87% and 93% of the sum of the van der Waals radii, respectively, are only just different from one another statistically. These hydrogen bonds deviate significantly from linearity with $\text{N}-\text{H}\cdots\text{Br}$ angles equal to 127(2)° and 133(2)°, respectively.

The structure propagates along the *b*-axis via $\text{Br}\cdots\text{H}$ interactions between a bromide anion and a pyridyl proton of a neighbouring hexyloxyphenylpyridinium molecule

(Figure 4-39). The Br \cdots H separation is 2.9015(3) Å, suggesting that the interaction is relatively weak compared to the Br \cdots H interactions shown in Figure 4-38. The C–H \cdots Br angle is 135.7(2)°, which is a significant deviation from linearity and further suggests that the interaction is weak.

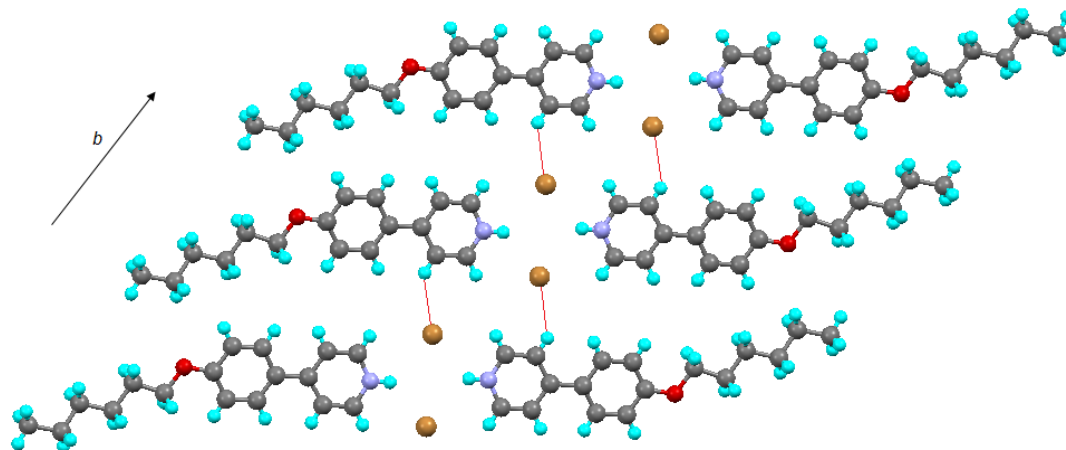


Figure 4-39: Propagation of the structure of hexyloxyphenylpyridinium bromide along the *b*-axis. Selected Br \cdots H interactions are shown in red.

The structure also propagates by stacking of the hexyloxyphenylpyridinium molecules. There are π - π stacking interactions between the pyridyl ring of one molecule and the phenyl ring of a neighbouring molecule leading to the slipped stacking motif shown in Figure 4-40.

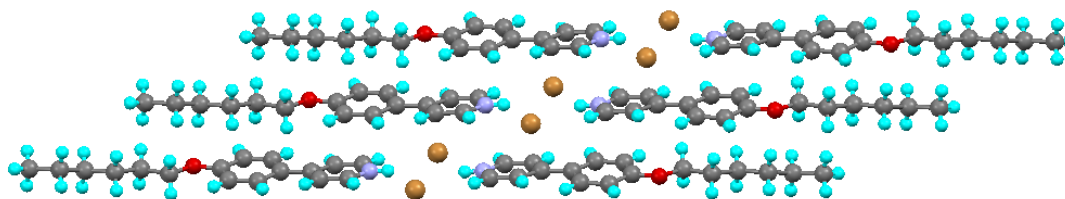


Figure 4-40: Stacking of the hexyloxyphenylpyridinium bromide.

Although a single crystal of a halogen-bonded complex between an alkoxyphenylpyridine and bromine could not be isolated, the complex could be formed as a precipitate. This was characterised by ^1H NMR spectroscopy, which maintained the two AA'XX' systems corresponding to the phenyl and pyridine rings

(Figure 4-41). Comparing this ^1H NMR spectrum with that of dodecyloxyphenylpyridine reveals that the chemical shifts of the pyridyl protons shift upfield by 0.09 ppm. A similar shift would be expected to be observed for the formation of dodecyloxypyridinium bromide, however, the elemental analysis is consistent with the halogen-bonded complex.

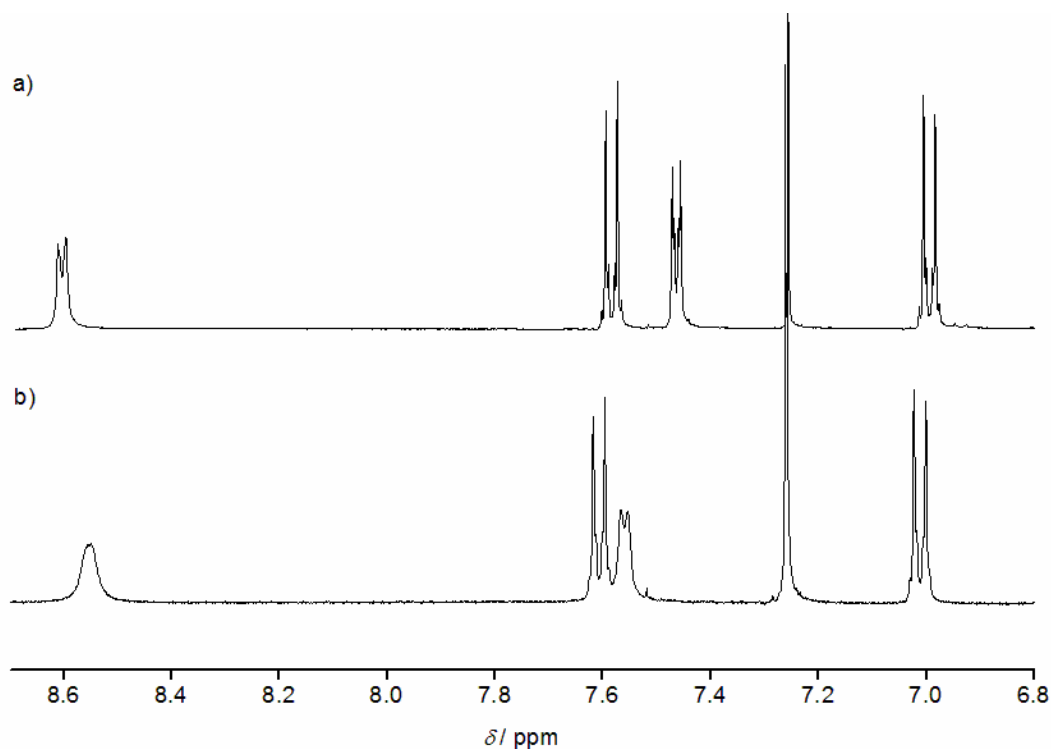


Figure 4-41: The aromatic region of the ^1H NMR spectrum of a) dodecyloxyphenylpyridine and b) its complex with bromine (6-12).

This complex was found to not be liquid-crystalline and decomposed upon heating releasing bromine. The fact that the complex with a relatively long chain length did not show liquid-crystalline behaviour suggests that none of the complexes will be liquid crystalline so complexes with shorter chain lengths were not synthesised.

Complexes between molecular iodine and alkoxyphenylpyridines were then prepared as precipitates by adding a solution of iodine in hexane to a solution of alkoxyphenylpyridine in chloroform. A single crystal of the complex was obtained

by slow evaporation from solution in toluene and the structure obtained by XRD is shown in Figure 4-42.

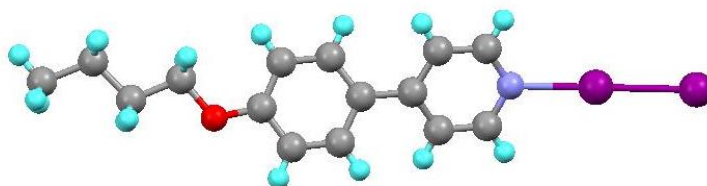


Figure 4-42: The molecular structure of the halogen bonded complex between iodine and butoxyphenylpyridine (7-4)

The I \cdots N separation is 2.398(3) Å, which is 68 % of the sum of the van der Waals radii of iodine and nitrogen. This is similar to that observed for the halogen bonded complex between iodine and octyloxystilbazole, Figure 4-13, showing that the alkoxytilbazole and alkoxyphenylpyridines are similar Lewis bases. The halogen bond is very close to linear with an N \cdots I–I angle equal to 176.92(7)°, as would be expected for a strong interaction. The length of the I–I bond is 2.8143(4) Å, which is significantly longer than in isolated molecular iodine where the bond length is 2.68 Å.³³² The pyridyl and phenyl rings are not co-planar and the torsion angle between the two rings is 24.2(6)°.

There is a secondary I \cdots I interaction between the iodine atom of one complex and an iodine atom of an adjacent complex, Figure 4-43. The I \cdots I separation is 3.6543(5) Å, which is 92% of twice the van der Waals radius of iodine. This is significantly shorter than the I \cdots I interaction observed for the halogen bonded complex between molecular iodine and octyloxystilbazole and can be considered an attractive interaction rather than a van der Waals interaction. The almost linear arrangement of the iodine atoms is surprising; the I \cdots I–I angle is 175.13(1)°. This angle is larger than would be expected for a Type I interaction similar to that observed for the complex with octyloxystilbazole. A search of the CSD carried out in 2006 reveals that although there are examples of C–X \cdots X–C contacts with C–X \cdots X angles in the range 170 – 180° when X = F, Cl or Br, there are no examples with X = I,³³³ showing that

this is a unique motif. The interaction is surprising because if the electrostatic surface potential of iodine is considered, then the positive regions of potential would be directed toward one another and any interaction would be expected to be repulsive in nature. The fact that the interaction is attractive suggests that in the halogen-bonded complex with butoxyphenylpyridine the iodine not involved in the I⋯N halogen bond no longer has a σ -hole. The electrostatic surface potential of the M06-2X/aug-cc-pVDZ optimised geometry of the halogen-bonded complex of iodine with pyridine was calculated and shows that the potential around the iodine atom not involved in the halogen bond is slightly negative (Figure 4-44). Therefore, the interaction observed in the complex of iodine with butoxyphenylpyridine is similar in nature to a Type I interaction and the unusual linear geometry observed could originate from crystal packing.

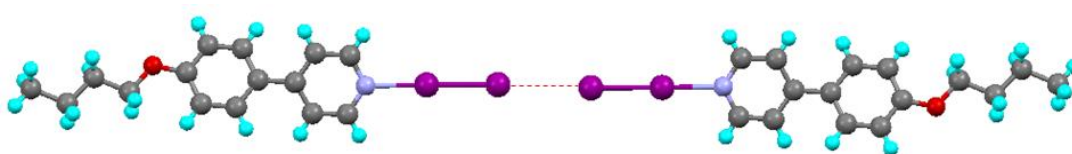


Figure 4-43: The 2:2 complex between molecular iodine and butoxyphenylpyridine (7-4).
The I⋯I interaction is highlighted in red.

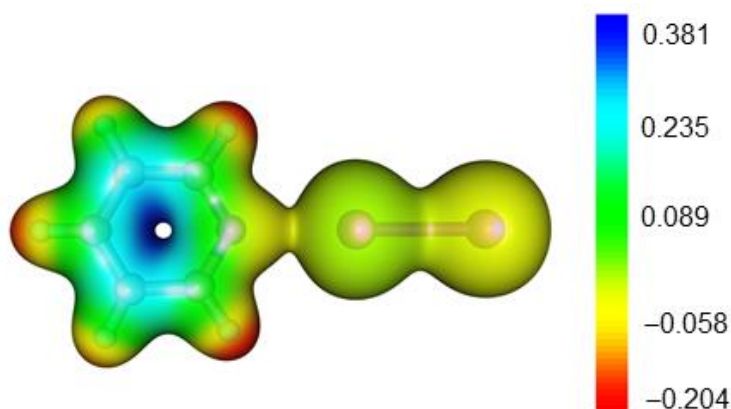


Figure 4-44: The electrostatic potential of the complex between pyridine and iodine mapped onto the $0.03 \text{ (e/bohr}^3)^{1/2}$ electronic density isosurface.

The structure propagates along the *c*-axis *via* I···H interactions between an iodine atom and a proton on the phenyl ring of a neighbouring butoxyphenylpyridine (Figure 4-45). The I···H separation is 3.1484(3) Å (99% of the sum of the van der Waals radii), which indicates a weak interaction that is predominantly dispersive in nature. The hydrogen atom interacts with the equatorial region of negative electrostatic surface potential on the iodine atom as shown by the I–I···H angle of 84.56(1)°. The C–H···I angle is 138.8(2)°, which is a significant deviation from linearity suggesting that this interaction should be classified as a van der Waals interaction rather than a hydrogen bond.

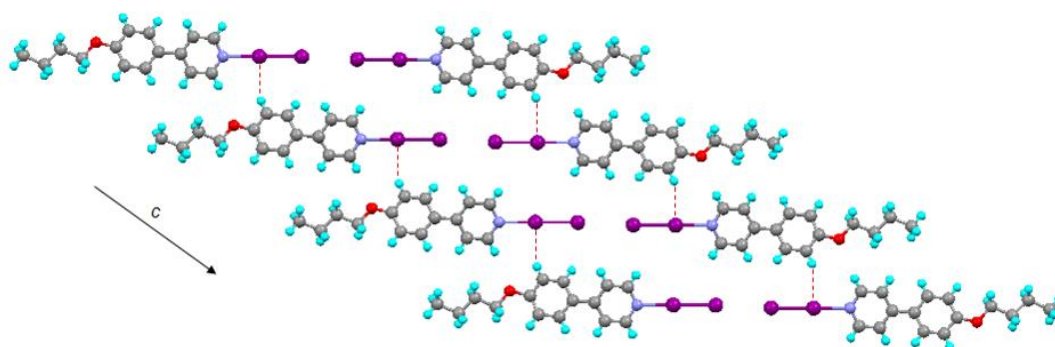


Figure 4-45: The propagation of the structure between iodine and butoxyphenylpyridine (7-4) along the *c*-axis. I···H interactions are highlighted in red.

The structure also propagates by the stacking of complexes through the *ab*-plane (Figure 4-46). The stacking proceed *via* weak H···H and C···H contacts between the protons in the alkyl chains and atoms in the pyridyl and phenyl rings of neighbouring butoxyphenylpyridine molecules.

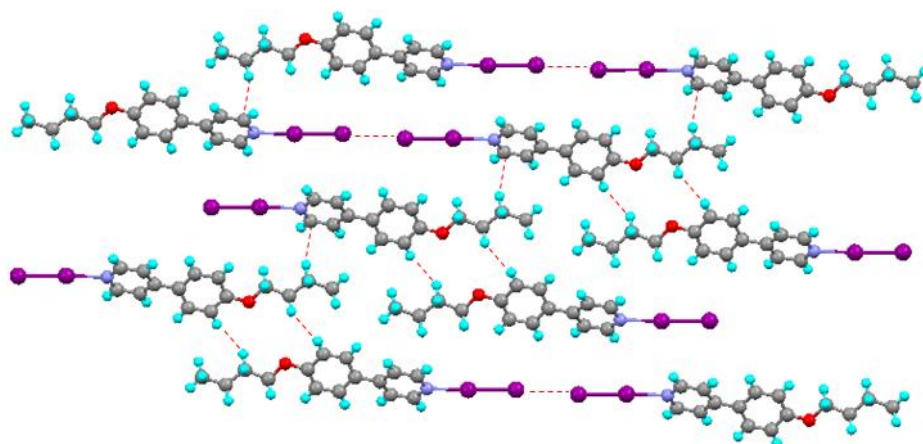


Figure 4-46: The stacking in the crystal structure of the complex between iodine and butoxyphenylpyridine (7-4). I...I, H...H and C...H interactions are highlighted in red.

This structure was disordered over two positions with a refined occupancy ratio of 0.9774: 0.0226. The major component has been discussed above, while the minor component consists of the complex rotated by 180 ° relative to the major component. During the refinement of the structure of the minor component, the pyridine and phenyl rings were constrained to be regular hexagons, the butoxy chain was constrained to be in the same plane as the phenyl ring, and bond distances and angles were constrained to be similar to those of the major product.

As the equivalent complexes with alkoxystilbazoles have liquid-crystalline properties,³³⁴ the thermal properties of the complexes with alkoxyphenylpyridines were investigated using the polarising optical microscope but these were found to not be liquid crystals and decomposed upon heating.

The lack of liquid crystal behaviour observed for complexes with iodine prompted the investigation of complexes with iodine monochloride and iodine monobromide. These dihalogens have larger dipole moments than iodine and it would be expected that the halogen-bonded complexes with these dihalogens would have larger dipole moments. Increasing the polarity of the complex increases the likelihood of the

formation of an interdigitated structure similar to that observed for the *N*-oxides of alkoxyphenylpyridines (Figure 4-36b) and the formation of smectic phases.

A single crystal of the halogen-bonded complex between iodine monochloride and butoxyphenylpyridine (**8-4**) was obtained by slow evaporation from a solution of dichloromethane. The structure was obtained using X-ray diffraction and is shown in Figure 4-47.

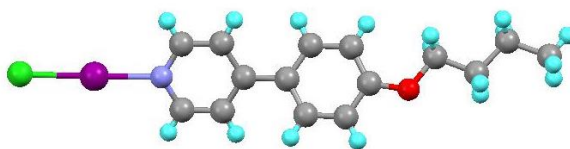


Figure 4-47: Molecular structure of the halogen-bonded complex between iodine monochloride and butoxyphenylpyridine (**8-4**).

The complex crystallised in space group $P\bar{1}$ with two complexes in the unit cell. The $N\cdots I$ separation is 2.276(2) Å, which at 64% of the sum of the van der Waals radii is remarkably short and the $Cl-I\cdots N$ angle is almost linear at 178.74(5)° indicating a strong interaction. This is consistent with Legon's observations that ICl a particularly strong halogen-bond donor.³² The $I-Cl$ bond length is 2.5174(7) Å, which is an elongation of the bond lengths in isolated ICl, which are 2.351 and 2.440 Å.³³⁵ Similar to the complex with iodine, the phenyl and pyridyl rings are not co-planar; the torsion angle between the two rings is 27.5(4)°.

The $N\cdots I$ separation is shorter than most examples of that in complexes between ICl and nitrogen bases and the only examples with shorter separations are complexes with DMAP³³⁶ (Figure 4-48a) and trimethylsilyl-trimethylphosphoranimine (Figure 4-48b),³³⁷ which have $I\cdots N$ separations of 2.246(2) and 2.228(8) Å, respectively.

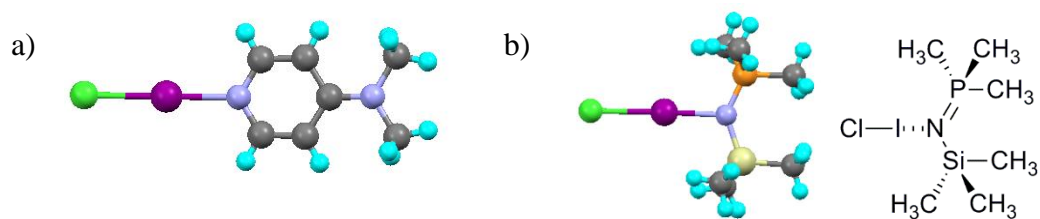


Figure 4-48: The molecular structures of complexes between ICl and a) DMAP³³⁶ and b) trimethylsilyl-trimethylphosphoranimine.³³⁷

Unlike the structure between iodine and butoxyphenylpyridine, the chlorine atom in this structure does not participate in any interactions. Figure 4-49 shows the anti-parallel arrangement of halogen-bonded complexes, which is similar to the interdigitated arrangement observed in the *N*-oxides of alkoxyphenylpyridines. This observation was promising since it indicates that these complexes have the potential to form liquid-crystalline smectic phases, although it should be noted that the arrangement of molecules in the crystal phase will not necessarily exist in the liquid crystal phase. The structure also propagates through the interlocking of the alkoxy chains and phenyl rings of neighbouring butoxyphenylpyridine molecules (Figure 4-50).

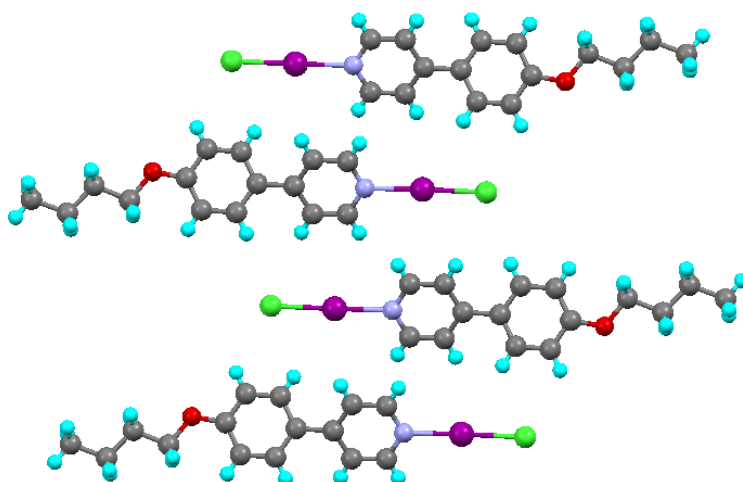


Figure 4-49: The interdigitated structure observed for the halogen-bonded complex of ICl with butoxyphenylpyridine (8-4).

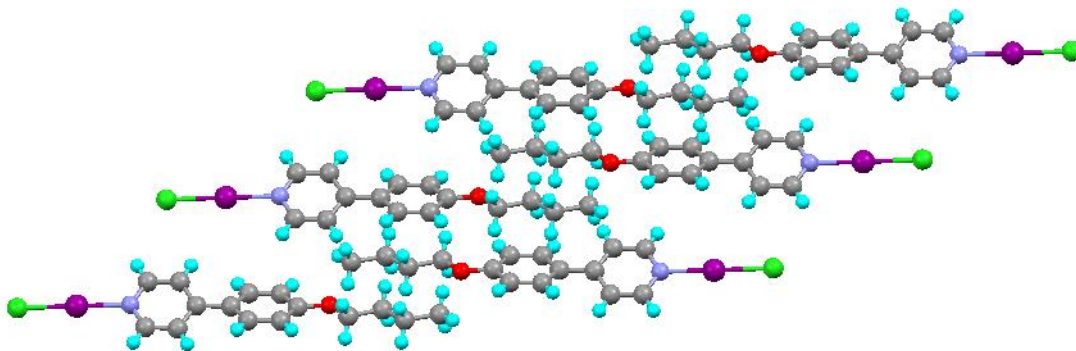


Figure 4-50: The stacking in the crystal structure of the complex between ICl and butoxyphenylpyridine (8-4).

A single crystal of the complex between iodine monobromide and butoxyphenylpyridine (9-4) was obtained by slow evaporation from solution in dichloromethane. The molecular structure obtained from XRD is shown in Figure 4-51.

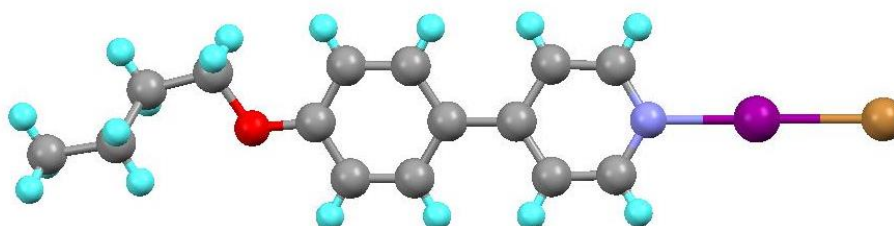


Figure 4-51: The molecular structure of the halogen bonded complex between iodine monobromide and butoxyphenylpyridine (9-4).

The I \cdots N separation is 2.289(3) Å, which is 65% of the sum of the van der Waals radii of iodine and nitrogen. This separation is slightly longer than that for the complex with iodine monochloride and shorter than for the complex with iodine, which is consistent with the strength of iodine monobromide as a halogen bond donor being in between I₂ and ICl. The halogen bond is approximately linear with an N \cdots I–Br angle of 178.58(7)°, consistent with a strong halogen bond. The I–Br bond length is 2.6716(4) Å, which is longer than the bond length in isolated IBr, which is 2.521(4) Å.³³⁸ Similar to the complex with iodine monochloride, the bromine atom

does not participate in any additional interactions in the structure. The torsion angle between the phenyl and pyridyl rings is $11.3(5)^\circ$, showing that the rings are closer to being planar than in the complexes with iodine and iodine monochloride. This angle is closer to that observed in octyloxystilbazole in its complex with iodine, which is promising in terms of liquid crystal properties.

There are only three other examples of complexes between IBr and nitrogen bases. The complex with pyridine, which was obtained by Hassel,²⁰ has an I \cdots N separation of $2.26(4)$ Å, which is shorter than that observed in the complex with butoxyphenylpyridine. The other two examples, which are complexes with 2,2'-bipyridine (Figure 4-52a)³³⁹ and tetra-2-pyridyl-pyrazine (Figure 4-52b),³⁴⁰ have I \cdots N separations of $2.4607(5)$ and $2.405(3)$ Å, respectively, which are longer than that observed for the complex with butoxyphenylpyridine. The short I \cdots N separation and lack of other structures of complexes between IBr and nitrogen bases highlights the significance of the structure between IBr and butoxyphenylpyridine.

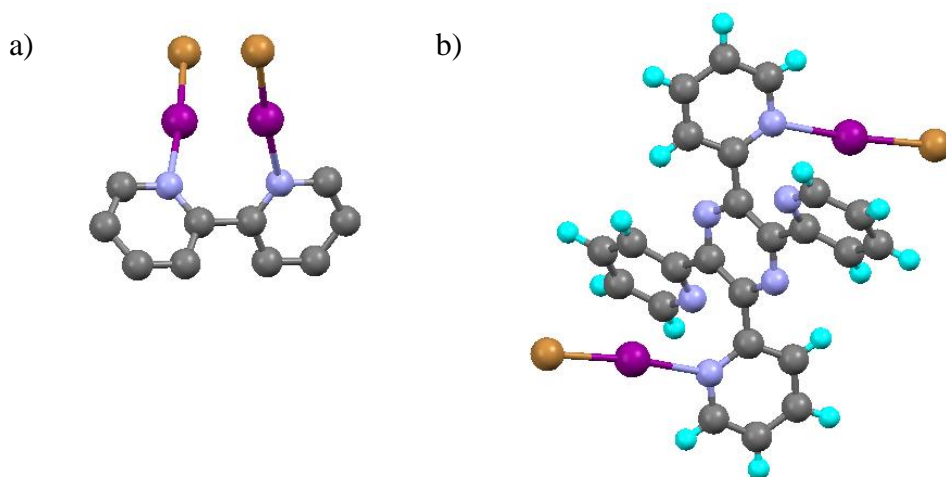


Figure 4-52: The molecular structures of complexes between IBr and a) 2,2'-bipyridine³³⁹ and b) tetra-2-pyridyl-pyrazine.³⁴⁰ Hydrogen atoms in the structure with 2,2'-bipyridine have not been included.

The structure propagates *via* weak I \cdots H contacts along the *a*-axis between the IBr and a pyridyl proton on a neighbouring butoxyphenylpyridine molecule (Figure

4-53). The I⋯H separation is 3.1306(3) Å suggesting that the interaction is dispersive in nature. The interaction can be classified as a weak hydrogen bond with the hydrogen atom interacting with the negative equatorial region of the iodine atom as shown by the Br–I⋯H angle of 84.92(1)°. The interaction deviates significantly from linearity with a C–H⋯I angle of 151.3(2)°. This packing is similar to that observed in the complexes with iodine monochloride with the complexes in an anti-parallel arrangement.

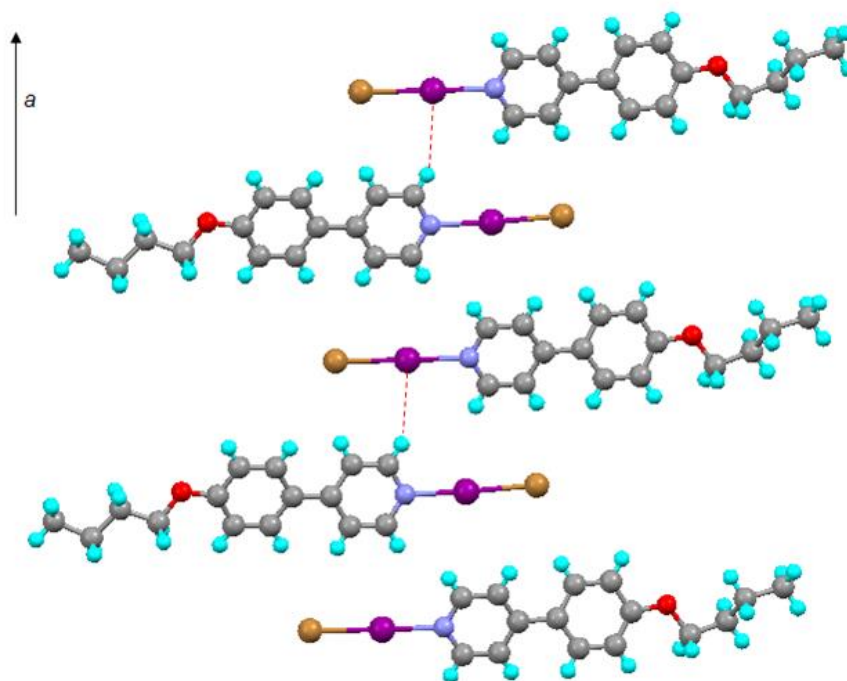


Figure 4-53: The packing of the complex between IBr and butoxyphenylpyridine (9-4) along the *a*-axis. I⋯H interactions are shown in red.

The structure also propagates through the *bc*-plane via Br⋯H interaction between the bromine atom of IBr and a proton of the alkoxychain of a neighbouring butoxyphenylpyridine (Figure 4-54). Similar to the I⋯H interaction, the Br⋯H interaction is weak and dispersive in nature as indicated by the Br⋯H separation of 2.9938(4) Å. The C–H⋯Br angle is 124.3(2)°, which is a significant deviation from linearity so this interaction should not be considered a hydrogen bond. The I–Br⋯H angle is 161.55(2)° suggesting that the proton is not interacting with the equatorial

negative electrostatic surface potential on the bromine atom. This suggests that the interaction is due to crystal packing and is insignificant.

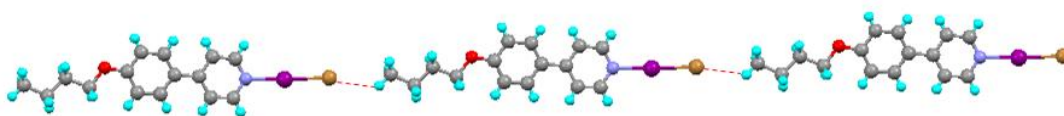


Figure 4-54: The propagation of the structure between IBr and butoxyphenylpyridine (**9-4**) across the *bc*-plane. Br...H interactions are highlighted in red.

The fact that the complexes with ICl and IBr are simple adducts is consistent with other complexes involving these halogen-bond donors.⁶

The elongation of the I–I, I–Cl and I–Br bond lengths in the halogen bonded complexes with butoxyphenylpyridine suggests that there is charge transfer from the lone pair of electrons on the pyridyl nitrogen to the σ^* anti-bonding orbital of the dihalogen bond.

4.3.5 Liquid Crystal Properties of Complexes with Alkoxyphenylpyridines

Complexes of iodine monochloride and iodine monobromide with alkoxyphenylpyridines were synthesised as precipitates using the same method as for the complexes with iodine and were studied using polarising optical microscopy. It should be noted that the complex of iodine monochloride with dodecyloxyphenylpyridine had a small impurity observed in the elemental analysis, which could affect the accuracy of transition temperatures observed.

The complex with dodecyloxyphenylpyridine (**8-12**) was found to melt into the SmA phase at 130 °C. This was characterised by the streaky texture shown in Figure 4-55a. Upon further heating, some decomposition of the complex was observed from approximately 165 °C, resulting in isotropic regions with the SmA phase as characterised by the appearance of bright filaments within an isotropic background

as shown in Figure 4-55b. The partly decomposed sample cleared into the isotropic phase at 196 °C. The phase behaviour observed upon heating could not be replicated upon cooling, confirming that the sample had decomposed.

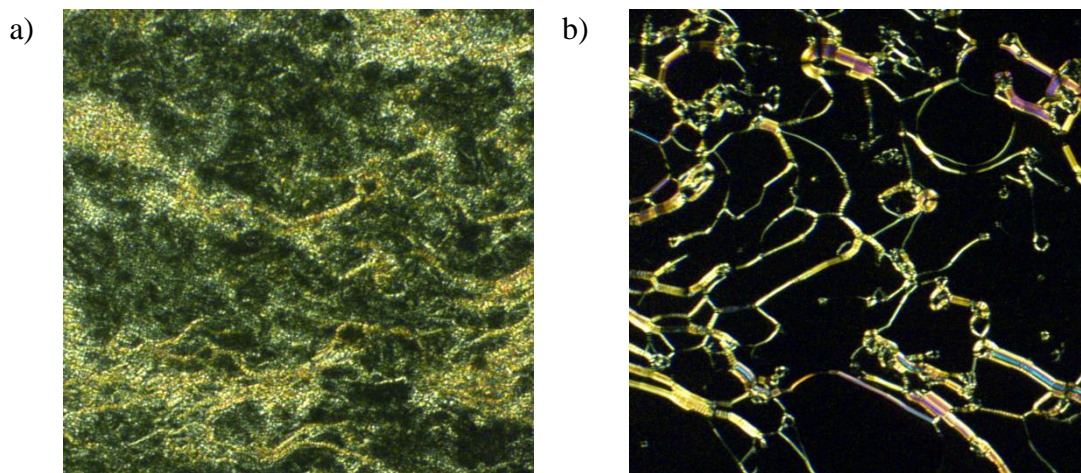


Figure 4-55: Optical micrographs of the textures observed for the halogen-bonded complex between iodine monochloride and dodecyloxyphenylpyridine (**8-12**) at a) 162 °C and b) 135 °C.

Similar behaviour was observed for complexes with shorter chain lengths and for complexes with iodine monobromide, however, the transition temperatures were slightly different. The melting temperatures into the SmA phase are shown in Table 4-2. The exception to the observation of liquid-crystalline phases in these complexes is the complex of iodine monochloride and butoxyphenylpyridine, which appeared to decompose before any liquid crystal phases were observed.

Table 4-2: The temperatures of the Cr – SmA transitions in the complexes of iodine monochloride and iodine monobromide with alkoxyphenylpyridines.

ICl Complexes	Cr – SmA / °C	IBr Complexes	Cr – SmA / °C
8-4	N/A	9-4	182
8-6	173	9-6	176
8-8	166	9-8	171
8-10	133	9-10	135
8-12	130	9-12	115

Unlike the complexes of iodine with alkoxy stilbazoles, which formed SmC phases, these complexes of ICl and IBr with alkoxyphenylpyridines only form SmA phases, which are typically observed for simple halogen- and hydrogen-bonded adducts. The fact that these SmA phases are observed shows that increasing the polarity of the alkoxyphenylpyridine allows the molecules form an interdigitated arrangement and for SmA phases to form. In order to confirm that this interdigitated arrangement is present in the mesophase, small angle X-ray diffraction measurements would need to be carried out. The SmA phases observed for complexes with alkoxyphenylpyridines are not as chemically stable as those observed previously for halogen-bonded complexes.^{67,197,198}

4.3.6 Quantum Chemical Calculations of Halogen-Bonded Complexes between Dihalogens and Alkoxyphenylpyridines

In order to gain an understanding into why complexes between iodine monochloride and iodine monobromide and alkoxyphenylpyridine are liquid crystalline, whereas complexes with iodine are not, the geometries of these complexes and the *N*-oxide of alkoxyphenylpyridine were optimised using quantum chemical methods and the dipole moments were calculated. Methoxyphenylpyridine was used to model the

alkoxyphenylpyridine to reduce computational cost as the length of the alkyl chain should have little effect on the electronic properties of the complex.

Table 4-3 shows the X...N separations, dihalogen bond lengths, binding energies and dipole moments of the complexes between the dihalogens and methoxyphenylpyridine. The complex with bromine is the weakest with the smallest binding energy. This is followed by the complexes with iodine, and then iodine monobromide and the complexes with iodine monochloride are the strongest. This is consistent with the Lewis acid strengths of the dihalogens which follows the trend $\text{Br}_2 < \text{I}_2 < \text{IBr} < \text{ICl}$.⁶ One surprising result is the increase in the X...N separation as a percentage of the sum of the van der Waals radii for the complex with iodine compared to that with bromine. This could be due to the potential energy surfaces for these complexes being relatively flat and therefore errors in the calculations are present.

Table 4-3: The X...N separation, X-X bond length, binding energy and dipole moment, μ , of the optimised geometries of the halogen-bonded complexes between dihalogens and methoxyphenylpyridine. Calculations were carried out at the level of theory indicated using the aug-cc-pVDZ basis set (a mixed aug-cc-pVDZ/cc-pVDZ basis set was used for MP2 calculations).

Dihalogen	Level of theory	$r(\text{X}\cdots\text{N}) / \text{\AA}$	$\Sigma\text{vdW radii} / \%$	$\Delta E / \text{kJ mol}^{-1}$	μ / D	$r(\text{X-X}) / \text{\AA}$		
						Monomer	Complex	% Difference
Br ₂	M06-2X	2.460	72.3	38.63	9.13	2.300	2.375	3.26
	MP2	2.410	70.9	45.28	9.42	2.324	2.422	4.22
I ₂	M06-2X	2.596	73.5	46.17	9.99	2.686	2.755	2.57
	MP2	2.580	73.1	51.58	10.17	2.720	2.803	3.05
IBr	M06-2X	2.497	70.7	61.84	11.53	2.492	2.582	3.61
	MP2	2.507	71.0	64.98	11.55	2.517	2.610	3.69
ICl	M06-2X	2.472	70.0	68.02	11.72	2.351	2.439	3.74
	MP2	2.471	70.0	73.24	12.05	2.369	2.464	4.01

The dipole moments of the complexes increase as the binding energy of the complex increases. The larger dipole moment for the complexes with IBr and ICl compared to the complex with I₂ could account for the presence of liquid crystal properties in the former. The larger dipole moment could suggest that an interdigitated arrangement of the molecules is more likely to form, which would lead to the formation of liquid-crystalline smectic phases. This interdigitated arrangement is observed in the *N*-oxides of alkoxyphenylpyridines³³¹ so the geometry of the *N*-oxide of methoxyphenylpyridine was optimised so that the dipole moment could be compared to those of halogen-bonded complexes of alkoxyphenylpyridines. In fact the dipole moment of the *N*-oxide of methoxyphenylpyridine (Table 4-4) is significantly smaller than those observed for the complexes with dihalogens. This suggests that perhaps the dipole moment does not have a significant effect on whether the interdigitated arrangement forms. The fact that there is not a significant difference between the dipole moments of the complexes of the interhalogens or the dihalogens agrees with this suggestion. Another explanation for the fact that the complexes with iodine do not form liquid crystal phases is that the I...I interaction observed in the crystal phase could also be formed in the liquid crystal phase and prevent the formation of an interdigitated arrangement.

Table 4-4: The N–O bond length and dipole moment of the *N*-oxide of methoxyphenylpyridine optimised at the M06-2X and MP2 level of theory using the aug-cc-pVDZ basis set.

Level of theory	$r(\text{N-O}) / \text{\AA}$	μ / D
M06-2X	1.273	5.95
MP2	1.268	6.78

The dihalogen bond in the complex can be compared to that in the monomer in order to establish if the bond is elongated upon complex formation (see Table 4-3), as observed in the crystal structures. There is a significant elongation of the dihalogen bond length upon complex formation suggesting that there is charge transfer into the

σ^* anti-bonding orbital of the dihalogen. With the exception of the complex with bromine, the percentage elongation of the dihalogen bond increases as the binding energy of complex increases.

NBO analysis has been carried out on the M06-2X/aug-cc-pVDZ optimised geometries of the complexes and the results are shown in Table 4-5.

Table 4-5: The occupancies of the lone pair of electrons on nitrogen, σ^* anti-bonding orbital of the dihalogen and the stabilisation energy for the complexes between dihalogens and methoxyphenylpyridine obtained from NBO analysis at the M06-2X/aug-cc-pVDZ level of theory.

Dihalogen	Occupancy LP(N)	Occupancy $\sigma^*(X-X)$	$E_{ij} / \text{kJ mol}^{-1}$
Br ₂	1.797	0.149	138.04
I ₂	1.812	0.134	130.00
IBr	1.784	0.166	184.26
ICl	1.781	0.167	191.84

The results in Table 4-5 corroborate the observations of the elongation of the X–X bond in the crystal structures; as the percentage elongation increases, the occupancy of the lone pair on the nitrogen decreases and the occupancy of the X–X anti-bonding orbital and the stabilisation energy increases.

The M06-2X and MP2 results are in reasonable agreement, which would suggest that the M06-2X functional is appropriate method for modelling these complexes. Comparing the I \cdots N separations and I–X bond lengths for the complexes with I₂, IBr and ICl to those in the crystal structures reveals that although values are not reproduced, the trends are correctly modelled by the calculations with the I \cdots N separation decreasing as the dipole moment of the halogen-bond donor increases.

4.4 Conclusions

New halogen-bonded complexes between dihalogens and pyridine bases have been synthesised. The majority of these complexes have remarkably short N...I separations and some of these complexes have interesting liquid-crystalline behaviour. Competition with the electrophilic bromination reaction has meant that in order to synthesise halogen-bonded complexes involving molecular bromine, no alkene bonds can be present in the Lewis base.

Halogen-bonded complexes between molecular iodine and alkoxy stilbazoles have interesting liquid-crystalline properties. Although complexes featuring stilbazoles with shorter alkoxy chains ($n = 4$ and 6) were found to show only monotropic SmA phases and decomposed upon heating, complexes with longer chains ($n = 10$ and 12) were found to have enantiotropic SmC and SmA phases. The formation of a SmC phase is unusual for complexes of this type and small-angle X-ray diffraction revealed that the complexes exist within the layers of the SmC phase as 2:2 complexes, with a weak I...I interaction between neighbouring 1:1 complexes.

Attempts to synthesise halogen-bonded complexes between bromine and alkoxy stilbazoles resulted in the formation of a stilbazolium bromide, where one ethylenic hydrogen atom had been replaced by a bromine atom. The mechanism for the formation of this product was believed to proceed *via* an electrophilic bromination reaction forming either a bromonium ion intermediate or a di bromoalkane, leading to a carbocation intermediate followed by elimination of HBr. The formation of both *trans* and *cis* isomers revealed that rotation about the central C-C bond in the intermediate was possible. The elimination of HBr is driven by the oxygen atom in the alkoxy substituent. Removal of this oxygen atom by synthesis of alkyl stilbazoles prevents the elimination step from taking place, however, the electrophilic bromination of the alkene bond still occurs.

Alkoxyphenylpyridines, which do not have an alkene bond that can undergo electrophilic bromination, can form halogen-bonded complexes with molecular bromine, however, attempts to form a single-crystal of these complexes has resulted in the formation of a pyridinium bromide salt.

Crystal structures have been obtained for complexes between iodine, iodine monochloride and iodine monobromide with butoxyphenylpyridine have been obtained. These structures have remarkably short I...N separations and the structure with iodine has an unusual I-I...I angle of 175.13(1)°. The structure with IBr is particularly important due to the lack of N...I-Br interactions in the literature.

The halogen-bonded complexes of alkoxyphenylpyridines with ICl and IBr have liquid-crystalline properties and form SmA phases. The complexes with iodine and bromine do not have any liquid crystal behaviour. Quantum chemical calculations of complexes of methoxyphenylpyridine with dihalogens and interhalogens and of the *N*-oxide reveal that although the dipole moment is larger than in the methoxyphenylpyridine, this cannot be used to predict whether mesophases will be formed.

4.5 Experimental

4.5.1 Crystallographic Parameters

The crystallographic parameters for the single crystal structures in this chapter are shown in Table 4-6.

Table 4-6: Crystallographic parameters of compounds **1 – 9**.

	1-8	2	4
CCDC Reference No.	905969	905970	905968
Molecular Formula	C ₂₁ H ₂₇ I ₂ NO	C ₂₁ H ₂₇ Br ₂ NO	C ₁₇ H ₁₉ Br ₂ N
Empirical formula	C ₂₁ H ₂₇ I ₂ NO	C ₂₁ H ₂₇ Br ₂ NO	C ₁₇ H ₁₉ Br ₂ N
Formula weight / g mol ⁻¹	563.24	469.26	397.15
<i>T</i> / K	110(2)	110(2)	110.00(10)
Wavelength (Å)	0.71073	0.71073	0.71073
Crystal system	Triclinic	Triclinic	Monoclinic
Space group	<i>P</i> $\bar{1}$	<i>P</i> $\bar{1}$	<i>Cc</i>
Colour	Yellow	Colourless	Colourless
Shape	block	plate	block
Unit cell dimensions / Å	<i>a</i> = 9.5988(17) <i>b</i> = 10.6104(19) <i>c</i> = 11.461(2)	<i>a</i> = 4.8844(6) <i>b</i> = 8.1363(9) <i>c</i> = 25.803(3)	<i>a</i> = 5.40904(18) <i>b</i> = 12.6594(4) <i>c</i> = 23.2463(8)
α / °	99.655(3)	93.248(2)	90
β / °	95.039(3)	92.730(3)	91.103(3)
γ / °	109.933(3)	90.372(3)	90
Volume / Å ³	1068.4(3)	1022.6(2)	1591.51(9)
<i>Z</i>	2	2	4
ρ_{calc} / Mg m ⁻³	1.751	1.524	1.658
Absorption coefficient / mm ⁻¹	2.952	3.972	5.084
<i>F</i> (000)	548	476	792
Crystal size / mm ³	0.12 x 0.10 x 0.09	0.38 x 0.19 x 0.04	0.15 x 0.13 x 0.11
θ range for data collection	1.82 to 28.32°	2.37 to 29.87°	3.22 to 32.20°
Index ranges	-12 ≤ <i>h</i> ≤ 12, -14 ≤ <i>k</i> ≤ 14, -15 ≤ <i>l</i> ≤ 15	-6 ≤ <i>h</i> ≤ 6, -11 ≤ <i>k</i> ≤ 11, -35 ≤ <i>l</i> ≤ 35	-7 ≤ <i>h</i> ≤ 7, -18 ≤ <i>k</i> ≤ 18, -28 ≤ <i>l</i> ≤ 32
Reflections collected	10215	15504	7949
Independent reflections	5208 [<i>R</i> _(int) = 0.0434]	5824 [<i>R</i> _(int) = 0.0228]	4415 [<i>R</i> _(int) = 0.0202]
Completeness to θ = 28.30°	97.5%	97.9%	99.7%
Max. and min. transmission	0.767 and 0.606	1.000 and 0.691	0.888 and 0.861
Data / restraints / parameters	5208 / 0 / 227	5824 / 0 / 231	4415 / 33 / 193
Goodness-of-fit on <i>F</i> ²	1.008	1.033	1.044
Final <i>R</i> indices [<i>I</i> > 2 σ (<i>I</i>)]	<i>R</i> ₁ = 0.0400, <i>wR</i> ₂ = 0.0728	<i>R</i> ₁ = 0.0264, <i>wR</i> ₂ = 0.0610	<i>R</i> ₁ = 0.0323, <i>wR</i> ₂ = 0.0736
<i>R</i> indices (all data)	<i>R</i> ₁ = 0.0772, <i>wR</i> ₂ = 0.0805	<i>R</i> ₁ = 0.0329, <i>wR</i> ₂ = 0.0641	<i>R</i> ₁ = 0.0341, <i>wR</i> ₂ = 0.0747
Largest diff. peak and hole	0.998 and -0.917	1.393 and -0.740	0.658 and -0.492

Table 4-6: (Continued)

	7-6	8-4	7-4
CCDC Reference No.	dwb1344	dwb1369	dwb1368
Molecular Formula	C ₁₇ H ₂₂ NOBr	C ₁₅ H ₁₇ NOICl	C ₁₅ H ₁₇ NOI ₂
Empirical formula	C ₁₇ H ₂₂ NOBr	C ₁₅ H ₁₇ NOICl	C ₁₅ H ₁₇ NOI ₂
Formula weight / g mol ⁻¹	336.27	389.65	481.09
<i>T</i> / K	110.05(10)	110.05(10)	110.05(10)
Wavelength (Å)	0.7107	0.7107	0.7107
Crystal system	Triclinic	Triclinic	Triclinic
Space group	<i>P</i> $\bar{1}$	<i>P</i> $\bar{1}$	<i>P</i> $\bar{1}$
Colour	Yellow	Colourless	Yellow
Shape	Plate	Plate	Plate
Unit cell dimensions / Å	<i>a</i> = 6.7843(3) <i>b</i> = 8.3585(3) <i>c</i> = 15.1607(7)	<i>a</i> = 7.8428(3) <i>b</i> = 8.7456(4) <i>c</i> = 11.7865(6)	<i>a</i> = 8.7375(3) <i>b</i> = 9.2799(4) <i>c</i> = 10.6024(7)
α / °	97.295(3)	81.274(4)	106.226(5)
β / °	93.314(4)	82.709(4)	98.182(4)
γ / °	111.978(4)	72.451(4)	100.729(4)
Volume / Å ³	785.58(6)	757.89(6)	793.61(7)
<i>Z</i>	2	2	2
ρ_{calc} / Mg m ⁻³	1.422	1.707	2.013
Absorption coefficient / mm ⁻¹	2.612	2.281	3.955
<i>F</i> (000)	348	384	456
Crystal size / mm ³	0.32 × 0.19 × 0.04	0.23 × 0.11 × 0.03	0.23 × 0.11 × 0.01
θ range for data collection	3.18 to 30.05°	3.11 to 27.83°	3.47 to 27.73°
Index ranges	-9 ≤ <i>h</i> ≤ 7, -11 ≤ <i>k</i> ≤ 11, -18 ≤ <i>l</i> ≤ 21	-10 ≤ <i>h</i> ≤ 10, -11 ≤ <i>k</i> ≤ 11, -15 ≤ <i>l</i> ≤ 14	-11 ≤ <i>h</i> ≤ 10, -12 ≤ <i>k</i> ≤ 11, -13 ≤ <i>l</i> ≤ 13
Reflections collected	6843	8707	9193
Independent reflections	4465	3180	3348 [<i>R</i> _{int}] = 0.0264]
Completeness (%) to (θ) =	96.90% (30.01°)	99.85% (25.01°)	97.38% (26.32°)
Max. and min. transmission	1.000 and 0.709	0.936 and 0.744	0.944 and 0.664
Data / restraints / parameters	4465 / 0 / 186	3180 / 0 / 173	3348 / 20 / 208
Goodness-of-fit on <i>F</i> ²	1.076	1.041	1.087
Final <i>R</i> indices [<i>I</i> > 2σ(<i>I</i>)]	<i>R</i> ₁ = 0.0366 and <i>wR</i> ₂ = 0.0832	<i>R</i> ₁ = 0.0235 and <i>wR</i> ₂ = 0.0434	<i>R</i> ₁ = 0.0242 and <i>wR</i> ₂ = 0.0489
<i>R</i> indices (all data)	<i>R</i> ₁ = 0.0460 and <i>wR</i> ₂ = 0.0890	<i>R</i> ₁ = 0.0280 and <i>wR</i> ₂ = 0.0456	<i>R</i> ₁ = 0.0355 and <i>wR</i> ₂ = 0.0429
Largest diff. peak and hole	0.798 and -1.181	0.451 and -0.455	0.689 and -0.678

Table 4-6: (Continued)

9-4	
CCDC Reference No.	dwb1416
Molecular Formula	C ₁₅ H ₁₇ NOIBr
Empirical formula	C ₁₅ H ₁₇ NOIBr
Formula weight / g mol ⁻¹	434.11
<i>T</i> / K	110.05(10)
Wavelength (Å)	0.7107
Crystal system	Triclinic
Space group	<i>P</i> $\bar{1}$
Colour	Colourless
Shape	Plate
Unit cell dimensions / Å	<i>a</i> = 10.0323(4) <i>b</i> = 11.3017(4) <i>c</i> = 15.5236(5)
α / °	106.418(3)
β / °	94.206(3)
γ / °	113.861(4)
Volume / Å ³	1508.27(11)
<i>Z</i>	4
ρ_{calc} / Mg m ⁻³	1.912
Absorption coefficient / mm ⁻¹	4.764
<i>F</i> (000)	840
Crystal size / mm ³	0.16 × 0.08 × 0.01
θ range for data collection	3.43 to 28.00°
Index ranges	-13 ≤ <i>h</i> ≤ 12, -10 ≤ <i>k</i> ≤ 14, -20 ≤ <i>l</i> ≤ 20
Reflections collected	11341
Independent reflections	6069
Completeness (%) to (θ) =	94.45% (26.32°)
Max. and min. transmission	0.933 and 0.620
Data / restraints / parameters	6069 / 0 / 345
Goodness-of-fit on <i>F</i> ²	1.046
Final <i>R</i> indices [<i>I</i> > 2σ(<i>I</i>)]	<i>R</i> ₁ = 0.0285 and <i>wR</i> ₂ = 0.0481
<i>R</i> indices (all data)	<i>R</i> ₁ = 0.0395 and <i>wR</i> ₂ = 0.0517
Largest diff. peak and hole	0.586 and -0.576

4.5.2 Materials

Alkoxytilbazoles were synthesized using literature procedures.³⁴¹ Bromine, iodine, iodine monobromide, 4-bromophenol, 1-bromoalkanes and 4-vinylpyridine were obtained from Sigma Aldrich. Alkylanilines were obtained from Alfa Aesar, TCI UK and Sigma Aldrich. Iodine monochloride was obtained from Alfa Aesar. 4-Pyridine boronic acid and tetrakis(triphenylphosphine)palladium(0) were purchased from Apollo Scientific. All solvents were HPLC grade and all materials were used without further purification.

4.5.3 NMR Spectroscopy

NMR spectra were obtained using either a Joel ECS400 400 MHz, which operates at 400 MHz for ^1H spectroscopy, 100 MHz for ^{13}C spectroscopy and 375 MHz for ^{19}F spectroscopy, or a Bruker AV500 500 MHz spectrometer, which operates at 500 MHz for ^1H spectroscopy, 126 MHz for ^{13}C spectroscopy and 470 MHz for ^{19}F spectroscopy. All spectra were obtained at ambient temperature using CDCl_3 as the solvent and as the internal standard for ^1H and ^{13}C spectra. All chemical shifts are given in ppm.

4.5.4 Single Crystal X-ray Diffraction

X-Ray diffraction data were collected at 110 K on a Bruker Smart Apex diffractometer with $\text{MoK}\alpha$ radiation ($\lambda = 0.71073 \text{ \AA}$) using a SMART CCD camera.

4.5.5 Low-Angle X-ray Diffraction

The XRD patterns were obtained with two different experimental set-ups at the Université de Strasbourg. In all cases, a linear monochromatic $\text{Cu-K}\alpha$ ($\lambda = 1.5405 \text{ \AA}$) was obtained using a sealed-tube generator (900 W) equipped with a bent quartz monochromator. In all cases, the crude powder was filled in Lindemann capillaries of 1 mm diameter and 10 μm wall thickness. An initial set of diffraction patterns was recorded with a curved Inel CPS 120 counter gas-filled detector linked to a data acquisition computer; periodicities up to 40 \AA can be measured, and the sample temperature controlled to within $\pm 0.01 \text{ }^\circ\text{C}$ from 20 to 200 $^\circ\text{C}$.

Patterns were also recorded on an image plate (scanned by STORM 820 from Molecular Dynamics with 50 μm resolution) where periodicities up to 70 \AA were measured. In each case, exposure times were varied from 1 to 4 h.

The tilt angle, ψ , was estimated using Equation 4-1 below.³⁴²

$$\psi = \arccos\left(\frac{d}{l}\right) \quad (4-1)$$

were d is the layer spacing and l is the length of the molecule, which was estimated from the crystal structure of the complex between iodine and octyloxystilbazole to be 57.5 Å.

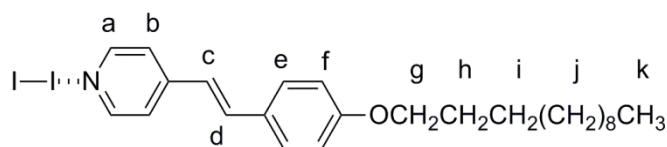
4.5.6 Polarising Optical Microscopy

Optical microscopy was performed using an Olympus BX50 microscope at X100 magnification. Temperature was controlled using a Linkam Scientific LTS 350 heating stage. Samples were held using VWR International borosilicate glass microscope cover slips with a thickness no. 1.

4.5.7 Preparation of Iodine Complexes of Alkoxytilbazoles (1)

Iodine (0.1269 g, 0.5 mmol) dissolved in hexane (25 cm³) was added to a solution of alkoxytilbazole (0.5 mmol) in chloroform (5 cm³). The contents were stirred for 2 h at room temperature. The orange precipitate was filtered and dried.

Iodine···Octyloxystilbazole (1-8)



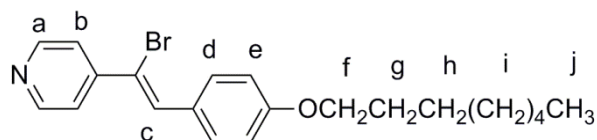
Yield: 88%. ¹H NMR: (400 MHz, CDCl₃) δ = 8.48 (2H, AA'XX', Ha, J = 6.3 Hz), 7.48 (2H, AA'XX', He, J = 8.8 Hz), 7.35 (2H, AA'XX', Hb, J = 6.3 Hz), 7.28 (1H, AB, Hc, J = 16.1 Hz), 6.91 (2H, AA'XX', Hf, J = 8.8 Hz), 6.86 (1H, AB, Hd, J = 16.3 Hz), 3.99 (2H, t, Hg, J = 6.6 Hz), 1.80 (2H, m, Hh), 1.46 (2H, m, Hi), 1.29 (8H, m, Hj), 0.89 (3H, t, Hk, J = 6.9 Hz). Spectra for other homologues were effectively identical save for the integration of the signal at δ = 1.29. Yields and elemental analysis are given in Table 4-7.

Table 4-7: Yields and elemental analysis of complexes of iodine with alkoxy stilbazoles.

Complex	Formula	Yield / %	Anal. Calcd. / %			Found / %		
			C	H	N	C	H	N
1-4	C ₁₇ H ₁₉ NOI ₂	35	40.3	3.8	3.2	40.3	3.7	2.8
1-6	C ₁₉ H ₂₃ NOI ₂	60	42.6	4.3	2.6	42.6	4.3	2.3
1-8	C ₂₁ H ₂₇ NOI ₂	88	44.8	4.8	2.5	44.7	4.7	2.3
1-10	C ₂₃ H ₃₁ NOI ₂	81	46.1	6.6	2.3	46.7	5.2	2.2
1-12	C ₂₅ H ₃₅ NOI ₂	87	48.3	6.1	2.3	48.5	5.7	2.1

4.5.8 Preparation of 2

Bromine (0.025 cm³, 0.5 mmol) was added to octyloxystilbazole (0.3095 g, 1 mmol) dissolved in THF (20 cm³) in a round-bottomed flask. The flask was flushed with nitrogen and once the bromine had decolourised, a second addition of bromine (0.025 cm³, 0.5 mmol) was added. The mixture was stirred for two hours at room temperature. Single crystals suitable for X-ray diffraction were obtained by dividing the solution into vials and placing in a fridge.

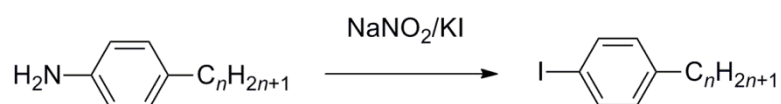


Yield: 23%. ¹H NMR (CDCl₃, 400 MHz): δ = 8.71 (2H, Ha, AA'XX', J = 7.0 Hz), 8.18 (2H, Hb, AA'XX', J = 7.0 Hz), 7.91 (2H, Hd, AA'XX', J = 8.9 Hz), 7.77 (1H, Hc, s), 6.99 (2H, He, AA'XX', J = 9.0 Hz), 4.03 (2H, Hf, t, J = 6.6 Hz), 1.82 (2H, Hg, m), 1.47 (2H, Hh, m), 1.29 (8H, Hi, m), 0.89 (3H, Hj, t, J = 6.9 Hz).

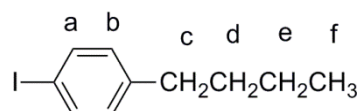
$^{13}\text{C}\{^1\text{H}\}$ NMR (CDCl_3 , 100 MHz): $\delta = 140.05, 139.40, 132.58, 128.56, 125.95, 124.00, 114.72, 113.00, 31.78, 29.29, 29.20, 29.07, 25.97, 22.63, 15.25, 14.09$.

Anal. Calcd. for $\text{C}_{21}\text{H}_{27}\text{NOBr}_2$: C, 53.8; H, 5.8; N, 3.0%. Found: C, 53.9; H, 5.8; N, 2.9%.

4.5.9 General Procedure for the Preparation of 4-Butyliodobenzene



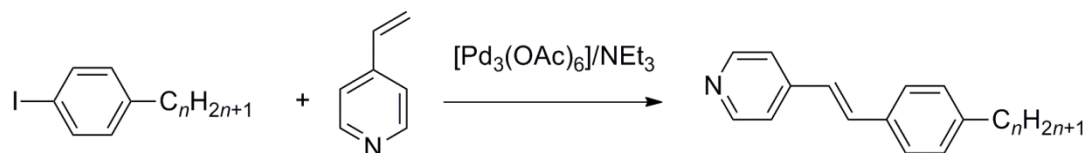
4-Butylaniline (20 mmol) was mixed with water (20 cm^3) in a round-bottomed flask and aqueous HCl (10 mol dm^{-3} , 2 cm^3) added at room temperature. The vessel was cooled to $0 \text{ }^\circ\text{C}$ and an HCl solution (10 mol dm^{-3} , 1.6 cm^3) was added, followed by the dropwise addition of a solution of NaNO_2 (1.38 g, 20 mmol) in water (10 cm^3). A solution of KI (3.32 g, 20 mmol) in water (10 cm^3) was then added dropwise to the solution. The reaction mixture was heated to $40 \text{ }^\circ\text{C}$ and stirred for 2 h until an oil separated from the solution. An aqueous solution of sodium thiosulfate (5 mol dm^{-3} , 100 cm^3) was added to the solution to remove excess iodine and the product was extracted with petroleum ether ($40 - 60 \text{ }^\circ\text{C}$). The organic layer was washed with water and brine and dried over anhydrous magnesium sulfate. The solvent was removed using a rotary evaporator and the resulting solid purified by column chromatography on silica gel eluting with hexane. The solvent was removed by rotary evaporator to give a colourless oil.



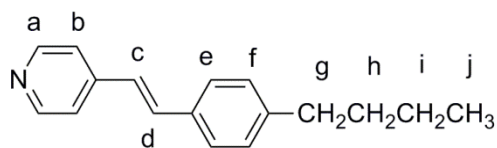
Yield: 64%. ^1H NMR: (400 MHz, CDCl_3) $\delta = 7.58$ (2H, AA'XX', Ha, $J = 8.2 \text{ Hz}$), 6.92 (2H, AA'XX', Hb, $J = 8.1 \text{ Hz}$), 2.55 (2H, t, Hc, $J = 7.7 \text{ Hz}$), 1.61 (2H, m, Hd), 1.31 (2H, m, He), 0.94 (3H, t, Hf, $J = 9.3 \text{ Hz}$).

$^{13}\text{C}\{^1\text{H}\}$ NMR: (100 MHz, CDCl_3) δ = 142.14, 136.89, 130.22, 90.16, 34.79, 33.09, 21.91, 13.57.

4.5.10 General Procedure for the Preparation of 4-Butylstilbazole



Palladium(II) acetate (0.0255 g, 0.1 mmol) and triethylamine (7 cm^3 , 50 mmol) were added to 4-alkyliodobenzene (10 mmol) in a Fischer-Porter vessel. To this 4-vinylpyridine (0.97 cm^3 , 9 mmol) and acetonitrile (20 cm^3) were added. The vessel was outgassed and then left under a nitrogen atmosphere at constant volume. The reaction vessel was heated to 100 $^\circ\text{C}$ with stirring for 96 h. The solvent was then removed using a rotary evaporator and the resulting solid dissolved in dichloromethane (20 cm^3) before being washed with water (3 x 15 cm^3). The organic layer was then dried over anhydrous sodium sulfate before being removed using a rotary evaporator. The solid was then extracted repeatedly with hexane using Soxhlet apparatus. The product was then filtered and dried after purification by crystallisation from hot hexane.



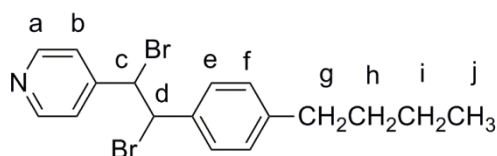
Yield: 42%. ^1H NMR: (400 MHz, CDCl_3) δ = 8.56 (2H, AA'XX', Ha, J = 6.1 Hz), 7.45 (2H, AA'XX', He, J = 8.1 Hz), 7.35 (2H, AA'XX', Hb, J = 6.1 Hz), 7.28 (1H, AB, Hc, J = 16.4 Hz), 7.20 (2H, AA'XX', Hf, J = 8.1 Hz), 6.97 (1H, AB, Hd, J = 16.3 Hz), 2.62 (2H, t, Hg, J = 7.7 Hz), 1.61 (2H, m, Hh), 1.36 (2H, m, Hi), 0.93 (3H, t, Hj, J = 7.3 Hz).

$^{13}\text{C}\{^1\text{H}\}$ NMR: (100 MHz, CDCl_3) $\delta = 150.25, 144.92, 144.06, 133.67, 133.23, 129.03, 127.06, 125.07, 120.86, 35.57, 33.60, 22.44, 14.05$

Anal. Calcd. for $\text{C}_{17}\text{H}_{19}\text{N}$: C, 86.0; H, 8.1; N, 5.9%. Found: C, 86.0; H, 8.1; N, 6.0%.

4.5.11 Preparation of the 1,2-Dibromo Adduct of Butylstilbazole (4)

4-Butylstilbazole (0.1187 g, 0.5 mmol) was dissolved in THF (20 cm^3) and held under an argon atmosphere. Bromine (13 μl , 0.25 mmol) was added to the solution whilst stirring. Once the solution had decolourised a second addition of bromine (13 μl , 0.25 mmol) was added to the solution. The reaction vessel was stirred at room temperature for 24 h. The yellow precipitate was filtered and dried. The filtrate was transferred into vials and placed in a fridge to crystallise. Crystals formed after 1 day and were analysed by X-ray diffraction.

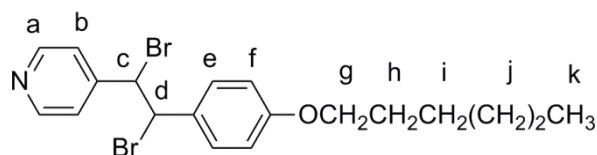


^1H NMR (400 MHz, CDCl_3): $\delta = 8.68$ (2H, Ha, AA'XX', $J = 3.4$ Hz), 7.42 (2H, Hb, AA'XX', $J = 5.6$ Hz), 7.39 (2H, He, AA'XX', $J = 8.2$ Hz), 7.23 (2H, Hf, AA'XX', $J = 8.1$ Hz), 5.39 (1H, Hc, AB, $J = 11.4$ Hz), 5.35 (1H, Hd, AB, $J = 11.4$ Hz), 2.64 (2H, Hg, t, $J = 7.7$ Hz), 1.62 (2H, Hh, m), 1.37 (2H, Hi, m), 0.94 (3H, Hj, t, $J = 7.3$ Hz).

4.5.12 Preparation of 1,2-Dibromo Adduct of Hexyloxystilbazole

4-Hexyloxystilbazole (0.1407 g, 0.5 mmol) was dissolved in 1,2-dichloroethane (20 cm^3). Tetrabutylammonium tribromide (0.4822 g, 1 mmol) was dissolved in 1,2-dichloroethane (20 cm^3). Tetrabutylammonium bromide (0.3224g, 1 mmol) was dissolved in 1,2-dichloroethane (20 cm^3). The three solutions were mixed in a round bottomed flask and stirred at room temperature for 24 h. The reaction mixture was washed with saturated sodium nitrite solution and water. The organic layer was dried

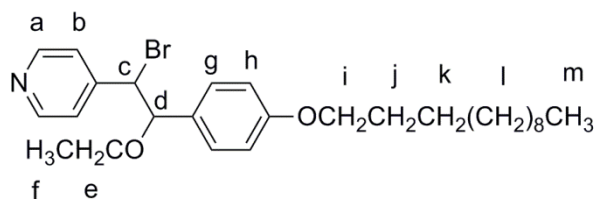
over anhydrous magnesium sulfate. The solvent was removed using a rotary evaporator to give the product.



¹H NMR (400 MHz, CDCl₃): δ = 8.65 (2H, Ha, AA'XX', J = 5.7 Hz), 7.37 (2H, Hb, AA'XX', J = 6.1 Hz), 7.35 (2H, He, AA'XX', J = 8.8 Hz), 6.92 (2H, Hf, AA'XX', J = 8.7 Hz), 5.29 (1H, Hc, AB, J = 10.2 Hz), 5.15 (1H, Hd, AB, J = 10.2 Hz), 3.98 (2H, Hg, t, J = 6.5 Hz), 1.79 (2H, Hh, m), 1.46 (2H, Hi, m), 1.33 (4H, Hj, m), 0.91 (3H, Hk, t, J = 7.0 Hz).

4.5.13 Preparation of Ethanolsis Product of Dodecyloxystilbazole (3)

4-Dodecyloxystilbazole (0.1830 g, 0.5 mmol) was dissolved in THF (5 cm³) in a round-bottomed flask. The flask was placed under an argon atmosphere. Bromine (13 μ l, 0.25 mmol) was added to the solution using a micropipette. Once the bromine had decolourised another addition of bromine (13 μ l, 0.25 mmol) was added to the flask. The solution was stirred at room temperature for 2 h. The solvent was removed by rotary evaporator and the solid was crystallised from hot ethanol. After each recrystallisation the sample was filtered and dried. The solvent in the filtrate was removed by rotary evaporator and the crystallisation process was repeated. The ethanolsis product was produced from a third recrystallisation step.

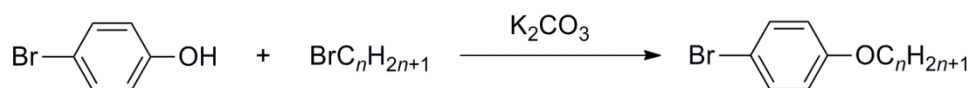


Yield: 26%. ^1H NMR: (500 MHz, CDCl_3) δ = 8.66 (2H, AA'XX', Ha, J = 5.3 Hz), 7.80 (2H, AA'XX', Hb, J = 5.2 Hz), 6.99 (2H, AA'XX', Hg, J = 8.5 Hz), 6.82 (2H, AA'XX', Hh, J = 8.6 Hz), 4.95 (1H, AB, Hc, J = 5.4 Hz), 4.78 (1H, AB, Hd, J = 5.4 Hz), 3.92 (2H, t, Hi, J = 6.6 Hz), 3.42 (2H, quartet of AB system, J_{AB} = 7.1 Hz, $^3J_{\text{HH}}$ = 6.9 Hz, He), 1.77 (2H, m, Hj), 1.44 (2H, m, Hk), 1.26 (16H, m, Hl), 1.13 (3H, t, Hf, J = 7.0 Hz), 0.88 (3H, t, Hm, J = 7.0 Hz).

$^{13}\text{C}\{^1\text{H}\}$ NMR (100 MHz, CDCl_3) δ = 150.13, 144.36, 136.22, 128.88, 127.73, 122.74, 54.77, 53.38, 35.41, 33.31, 22.38, 13.93.

Anal. Calcd. for $\text{C}_{27}\text{H}_{40}\text{NO}_2\text{Br}_2$: C, 56.9; H, 7.1; N, 2.5%. Found: C, 56.6; H, 7.1; N, 2.3%.

4.5.14 General Procedure for the Preparation of 4-Alkoxybromobenzene^{viii}

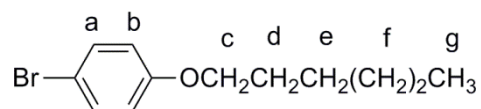


4-Bromophenol (3.46 g, 20 mmol) and potassium carbonate (13.82 g, 100 mmol) were added to acetone (160 cm^3) in a round-bottomed flask and the mixture was stirred for 10 min. A flow of nitrogen was passed through the equipment. The flask was heated under reflux at 60 $^\circ\text{C}$. Once reflux was achieved 1-bromoalkane (26 mmol) was added dropwise to the flask. The reaction mixture was heated under reflux for 16 h whilst stirring. The mixture was filtered and the filtrate was

^{viii} 4-Decyloxybromobenzene and 4-Dodecyloxybromobenzene were synthesised by James Taylor, an MChem project student whom I co-supervised.

concentrated *in vacuo*. The crude product was purified by column chromatography on silica gel eluted with 100:1 petroleum ether (40 – 60 °C): acetone.

4-Hexyloxybromobenzene

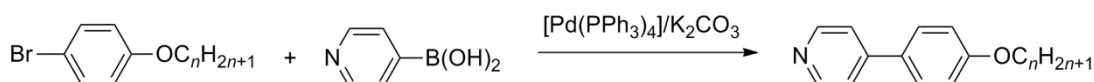


Yield: 71%. ^1H NMR (400 MHz, CDCl_3): δ = 7.35 (2H, Ha, AA'XX', J = 9.0 Hz), 6.77 (2H, Hb, AA'XX', J = 8.9 Hz), 3.91 (2H, Hc, t, J = 6.6 Hz), 1.76 (2H, Hd, m), 1.44 (2H, He, m), 1.33 (4H, Hf, m), 0.90 (3H, Hg, t, J = 7.1 Hz).

$^{13}\text{C}\{^1\text{H}\}$ NMR (100 MHz, CDCl_3): δ = 158.07, 132.00, 116.11, 112.36, 68.08, 31.39, 28.96, 25.50, 22.42, 13.86. Spectra for other homologues are essentially the same with a different integration in the ^1H NMR spectra for the peak at δ = 1.33 ppm and additional peaks in the high field region of the ^{13}C NMR spectra corresponding to the alkyl chain.

4.5.15 General Procedure for the Synthesis of 4-Alkoxyphenylpyridines

(5-*n*)^{ix}



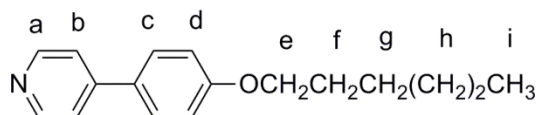
Potassium carbonate (7.7 g, 56 mmol) was dissolved in a mixture of water (20 cm³) and THF (40 cm³). This solution was added to 4-alkoxybromobenzene (14 mmol) in a round-bottomed flask under nitrogen. Tetrakis(triphenylphosphine)palladium(0) (0.485 g, 0.42 mmol) was added to the flask, which was then heated to 60 °C. A suspension of 4-pyridineboronic acid (2.46 g, 20 mmol) in THF (40 cm³) was added to the flask and the reaction mixture heated under reflux at 80 °C whilst stirring for 16 hours. The mixture was extracted with diethyl ether (100 cm³) and washed with

^{ix} 4-Decyloxyphenylpyridine and 4-Dodecyloxyphenylpyridine were synthesised by James Taylor, an MChem project student whom I co-supervised.

NaOH solution (10% w/v, 50 cm³) and water (100 cm³). The organic layer was dried over anhydrous magnesium sulfate and, after filtration, the solvent was removed using a rotary evaporator. The crude product was purified by column chromatography on silica gel, eluting with 1:1 petroleum ether (40 – 60 °C): acetone (1% triethylamine). The product was crystallised from hot petroleum ether (40 – 60 °C) to give a colourless solid.

There was some difficulty purifying these compounds as can be seen from the deviation between measured and calculated elemental analysis for carbon, Table 4-8, due to an unknown impurity. Attempts to purify further by column chromatography, recrystallisation and drying under vacuum were unsuccessful.

4-Hexyloxyphenylpyridine (5-6)



Yield: 28%. ¹H NMR (400 MHz, CDCl₃): δ = 8.61 (2H, Ha, AA'XX', J = 6.2 Hz), 7.59 (2H, Hc, AA'XX', J = 8.8 Hz), 7.47 (2H, Hb, AA'XX', J = 6.2 Hz), 7.00 (2H, Hd, AA'XX', J = 8.8 Hz), 4.01 (2H, He, t, J = 6.6 Hz), 1.81 (2H, Hf, m), 1.48 (2H, Hg, m), 1.35 (4H, Hh, m), 0.91 (3H, Hi, t, J = 7.0 Hz).

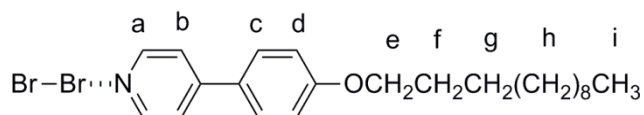
¹³C{¹H} NMR (100 MHz, CDCl₃): δ = 159.96, 150.02, 147.68, 129.92, 127.93, 120.85, 114.90, 68.00, 31.41, 29.02, 25.55, 22.44, 13.88. Spectra of other homologues are essentially identical with different integration for the peak at δ = 1.35 ppm in the ¹H NMR spectra and additional peaks in the high field region of the ¹³C NMR spectra corresponding to atoms in the alkoxy chain. Table 4-8 shows yields and elemental analysis for the alkoxyphenylpyridines (5-*n*).

Table 4-8: Yields and elemental analysis of alkoxyphenylpyridines (5-*n*)

Complex	Formula	Yield / %	Anal. Calcd. / %			Found / %		
			C	H	N	C	H	N
5-4	C ₁₅ H ₁₇ NO	23	79.3	7.5	6.2	78.9	7.5	6.0
5-6	C ₁₇ H ₂₁ NO	28	80.0	8.3	5.5	79.0	8.2	5.4
5-8	C ₁₉ H ₂₅ NO	24	80.5	8.9	4.9	79.5	8.9	4.7
5-10	C ₂₁ H ₂₉ NO	52	81.0	9.4	4.5	80.6	9.4	4.5
5-12	C ₂₃ H ₃₁ NO	59	81.4	9.8	4.1	81.3	9.8	4.0

4.5.16 Synthesis of Halogen-Bonded Complexes between 4-Dodecyloxyphenylpyridine and Bromine (6-12)

Bromine (0.0064 cm³, 0.125 mmol) was added to a solution of 4-dodecyloxyphenylpyridine (0.0425 g, 0.125 mmol) in hexane (20 cm³) in a round-bottomed flask. The reaction mixture was stirred at room temperature for 2 h. The precipitate was filtered, washed with hexane and dried under vacuum.



Yield: 52%

¹H NMR (CDCl₃, 400 MHz): δ = 8.55 (2H, Ha, AA'XX', *J* = 4.3 Hz), 7.61 (2H, Hc, AA'XX', *J* = 8.8 Hz), 7.56 (2H, Hb, AA'XX', *J* = 5.0 Hz), 7.01 (2H, Hd, AA'XX', *J* = 8.8 Hz), 4.02 (2H, He, t, *J* = 6.6 Hz), 1.81 (2H, Hf, m), 1.47 (2H, Hg, m), 1.26 (16H, Hh, m), 0.88 (3H, Hi, t, *J* = 6.8 Hz).

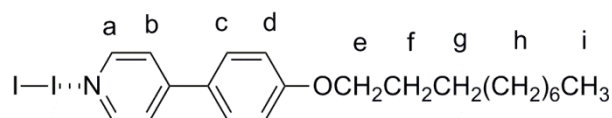
$^{13}\text{C}\{^1\text{H}\}$ NMR (CDCl_3 , 100 MHz): $\delta = 193.72, 164.45, 128.71, 115.63, 104.60, 101.22, 99.23, 68.58, 40.77, 32.22, 29.96, 29.94, 29.87, 29.68, 29.66, 29.46, 26.31, 23.00, 14.44$.

Anal. Calcd. For $\text{C}_{23}\text{H}_{33}\text{NOBr}_2$: C, 55.3; H, 6.7; N, 2.8%. Found: C, 55.5; H, 6.7; N, 2.8%.

4.5.17 Synthesis of Halogen-Bonded Complexes between 4-Alkoxyphenylpyridines and Iodine (7-*n*)

Iodine (0.0635 g, 0.25 mmol) in hexane (5 cm^3) was added to a solution of 4-alkoxyphenylpyridine (0.25 mmol) in chloroform (5 cm^3) in a round-bottomed flask. The reaction mixture was stirred at room temperature for 2 h. The precipitate was filtered, washed with hexane and dried under vacuum.

Iodine \cdots 4-Decyloxyphenylpyridine (7-10)



Yield: 30%. ^1H NMR (400 MHz, CDCl_3): $\delta = 8.57$ (2H, Ha, AA'XX', $J = 5.8$ Hz), 7.59 (2H, Hc, AA'XX', $J = 8.8$ Hz), 7.49 (2H, Hb, AA'XX', $J = 6.2$ Hz), 7.00 (2H, Hd, AA'XX', $J = 8.9$ Hz), 4.01 (2H, He, t, $J = 6.6$ Hz), 1.81 (2H, Hf, m), 1.47 (2H, Hg, m), 1.28 (12H, Hh, m), 0.88 (3H, Hi, t, $J = 6.8$ Hz). Spectra for other homologues were effectively identical save for the integration of the signal at $\delta = 1.28$. Table 4-9 shows yields and elemental analysis results for these complexes.

Table 4-9: Yields and elemental analysis for complexes of iodine with alkoxyphenylpyridines (7-*n*).

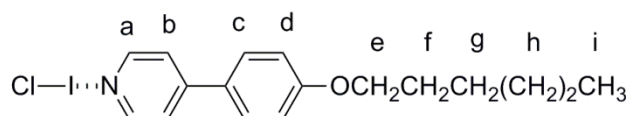
Complex	Formula	Yield / %	Anal. Calcd. / %			Found / %		
			C	H	N	C	H	N
7-4	C ₁₅ H ₁₇ NOI ₂	29	37.5	3.6	2.9	37.8	3.5	2.9
7-6	C ₁₇ H ₂₁ NOI ₂	46	40.1	4.2	2.8	39.8	4.3	2.8
7-8	C ₁₉ H ₂₅ NOI ₂	45	42.5	4.7	2.6	42.8	4.7	2.6
7-10	C ₂₁ H ₂₉ NOI ₂	30	44.6	5.2	2.5	44.0	5.1	2.4
7-12	C ₂₃ H ₃₁ NOI ₂	24	46.6	5.6	2.4	46.4	5.5	2.3

4.5.18 Synthesis of Halogen-Bonded Complexes between Alkoxyphenylpyridines and Iodine Monochloride (8-*n*)

Iodine monochloride (25 μ L, 0.5 mmol) in dry hexane (5 cm³) was added to a solution of alkoxyphenylpyridine (0.5 mmol) in chloroform (5 cm³) in a round-bottomed flask under a nitrogen atmosphere. The mixture was stirred at room temperature for 2 h. The precipitate was filtered, washed with dry hexane and dried under vacuum.

There was some difficulty when purifying the complex as can be seen by the elemental analysis in Table 4-10, due to an unknown impurity.

Iodine Monochloride...4-Hexyloxyphenylpyridine (8-6)



Yield: 79%. ^1H NMR (CDCl_3 , 400 MHz): δ = 8.57 (2H, Ha, AA'XX', J = 5.0 Hz), 7.59 (2H, Hc, AA'XX', J = 8.8 Hz), 7.56 (2H, Hb, AA'XX', J = 5.8 Hz), 7.01 (2H, Hd, AA'XX', J = 8.8 Hz), 4.01 (2H, He, t, J = 6.6 Hz), 1.80 (2H, Hf, m), 1.46 (2H, Hg, m), 1.34 (4H, Hh, m), 0.90 (3H, Hi, t, J = 7.1 Hz).

$^{13}\text{C}\{^1\text{H}\}$ NMR (CDCl_3 , 100 MHz): δ = 161.52, 148.28, 128.50, 123.22, 115.51, 100.89, 98.91, 68.34, 31.52, 29.06, 25.65, 22.58, 14.02. Spectra of other homologues are essentially identical with different integration of the peak at δ = 1.34 ppm in the ^1H NMR spectra and additional peaks in the high field region of the ^{13}C NMR spectra corresponding to carbons in the alkoxy chain. Table 4-10 shows the yields and results of elemental analysis for these complexes.

Table 4-10: Yields and elemental analysis for complexes of iodine monochloride with 4-alkoxyphenylpyridines (**8-*n***).

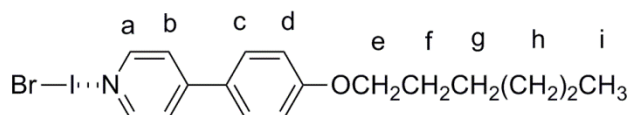
Complex	Formula	Yield / %	Anal. Calcd. / %			Found / %		
			C	H	N	C	H	N
8-4	$\text{C}_{15}\text{H}_{17}\text{NOICl}$	66	46.2	4.4	3.6	45.7	4.3	3.5
8-6	$\text{C}_{17}\text{H}_{21}\text{NOICl}$	79	48.9	5.1	3.4	48.6	4.9	3.2
8-8	$\text{C}_{19}\text{H}_{25}\text{NOICl}$	56	51.2	5.7	3.1	51.1	5.6	3.1
8-10	$\text{C}_{21}\text{H}_{29}\text{NOICl}$	64	53.2	6.2	3.0	52.9	6.0	2.8
8-12	$\text{C}_{23}\text{H}_{31}\text{NOICl}$	57	55.0	6.6	2.8	54.4	6.6	2.8

4.5.19 Synthesis of halogen bonded complexes between 4-alkoxyphenylpyridines and iodine monobromide (**9-*n***)

Iodine monobromide (0.1034 g, 0.5 mmol) in dry hexane (5 cm^3) was added to a solution of 4-alkoxyphenylpyridine (0.5 mmol) in chloroform (5 cm^3) in a round-bottomed flask under a nitrogen atmosphere. The reaction mixture was stirred at

room temperature for 2 h. The precipitate was filtered, washed with dry hexane and dried under vacuum.

Iodine Monobromide···4-Hexyloxyphenylpyridine (9-6)



Yield: 64%. ¹H NMR (400 MHz, CDCl₃): δ = 8.56 (2H, Ha, AA'XX', *J* = 6.5 Hz), 7.60 (2H, Hc, AA'XX', *J* = 8.8 Hz), 7.56 (2H, Hb, AA'XX', *J* = 6.5 Hz), 7.02 (2H, Hd, AA'XX', *J* = 8.8 Hz), 4.02 (2H, He, t, *J* = 6.6 Hz), 1.81 (2H, Hf, m), 1.48 (2H, Hg, m), 1.35 (4H, Hh, m), 0.91 (3H, Hi, t, *J* = 7.1 Hz).

¹³C {¹H} NMR (100 MHz, CDCl₃): δ = 161.35, 151.31, 147.93, 128.44, 123.07, 115.46, 106.05, 68.31, 31.52, 29.07, 25.65, 22.57, 14.02. Spectra for other homologues were essentially identical with different integration of the peak at δ = 1.35 ppm in the ¹H NMR spectra and additional peaks in the high field region of the ¹³C NMR spectra corresponding to carbon atoms in the alkoxy chain. Table 4-11 shows yields and results of elemental analysis for these complexes.

Table 4-11: Yields and elemental analysis for complexes of iodine monobromide with 4-alkoxyphenylpyridine (**9-n**).

Complex	Formula	Yield / %	Anal. Calcd. / %			Found / %		
			C	H	N	C	H	N
9-4	C ₁₅ H ₁₇ NOIBr	58	41.5	4.0	3.2	41.1	3.9	3.2
9-6	C ₁₇ H ₂₁ NOIBr	64	44.2	4.6	3.0	43.8	4.5	2.9
9-8	C ₁₉ H ₂₅ NOIBr	63	46.6	5.1	2.9	46.2	4.9	2.5
9-10	C ₂₁ H ₂₉ NOIBr	76	48.7	5.6	2.7	48.2	5.5	2.6
9-12	C ₂₃ H ₃₁ NOIBr	74	50.6	6.1	2.6	50.4	5.8	2.4

4.5.20 Computational Method

The geometries of the monomers and complexes between I₂, ICl, IBr and Br₂ and methoxyphenylpyridine were optimised at the MP2 and M06-2X levels of theory. The M06-2X calculations were carried out using the aug-cc-pVDZ basis set. The MP2 calculations were carried out using the aug-cc-pVDZ basis set to model the dihalogen and the pyridyl ring and the smaller cc-pVDZ basis set for the phenyl ring and the methoxy substituent, which are not directly involved in the interaction, in order to reduce the computational cost without losing accuracy. The aug-cc-pVDZ-PP basis set was used for iodine, which includes an effective core potential (ECP). The MP2(Full) keyword was employed to include correlation effects for all electrons. The M06-2X functional was chosen because it was found to be effective at modelling halogen-bonded complexes as described in Chapter 3.³⁴³

Vibrational frequencies were calculated to ensure that optimised geometries correspond to local minima on the potential energy surface. The M06-2X calculations were carried out using the pruned 'UltraFine' integration grid within

Gaussian09.²²⁶ The geometries of all complexes were optimised using the Boys-Bernardi counterpoise correction¹⁰⁶ of the basis set superposition error. Binding energies were calculated by taking the sum of the energies of the monomers from the energy of the complex.

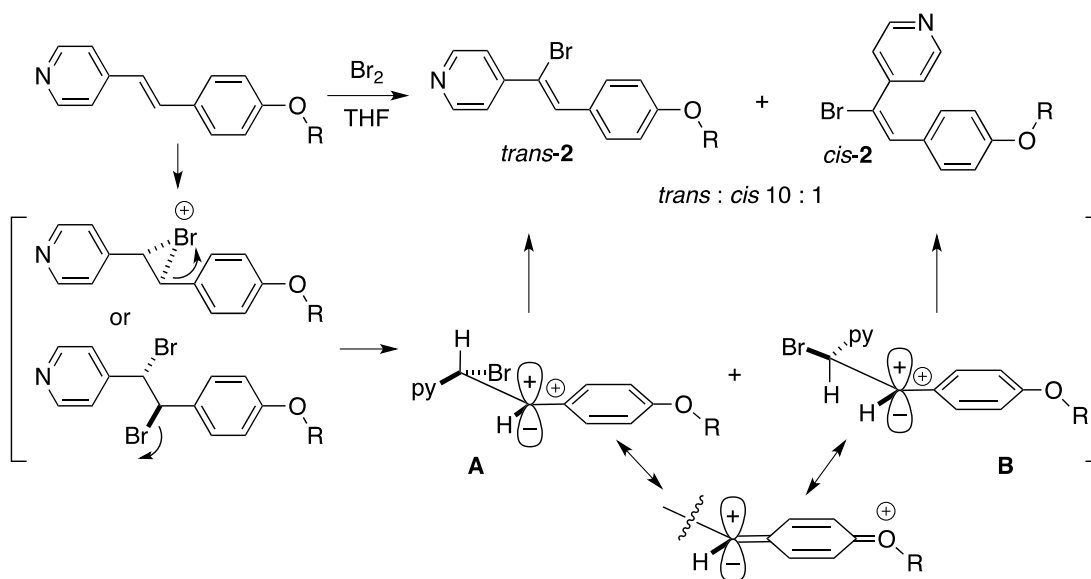


Figure 5-1: Proposed mechanism for the formation of compound 2.

5.1.1 The Electrophilic Bromination Reaction

The mechanism of electrophilic bromination in both protic and aprotic solvents has been studied extensively.³⁴⁵ The reaction starts with the formation of a charge-transfer complex (CreTC) between bromine and the alkene. In aprotic solvents the mechanism then proceeds *via* a cationic intermediate, followed by nucleophilic attack by a bromide ion, *via* an $\text{S}_{\text{N}}2$ mechanism, to form the 1,2-dibromo addition product. The intermediates in the electrophilic bromination of alkenes can exhibit one of three possible structures. Although the symmetrical bromonium ion, first proposed by Roberts and Kimball in 1937,³⁴⁶ is the most commonly postulated intermediate structure, it is also possible for the reaction to proceed *via* an open carbocation or an unsymmetrical bromonium ion intermediate where these are more stable. Yates and McDonald suggested that there is a spectrum of possible intermediate structures with the carbocation and bromonium ion as the extremes.³⁴⁷ In nucleophilic solvents such as methanol and water, the solvent molecules compete with the bromide ion to act as a nucleophile resulting in formation of a bromo ether product. The bromonium ion formed from reaction of adamantylidene adamantane with $\text{Br}_2/\text{Br}_3^-$ was isolated and characterised crystallographically; it is stable because

nucleophilic attack is hindered sterically.³⁴⁸⁻³⁵⁰ Isotopic perturbation of degenerate equilibrium shows that, in solution, the intermediate of the electrophilic chlorination and bromination of tetramethylethylene is a carbocation, due to the presence of equilibrium shifts in the ^{13}C NMR spectra.³⁵¹

The gas phase geometry of the CTC (or electron donor-acceptor complex) for the electrophilic bromination of ethene has been determined by rotational spectroscopy.³⁵² The Br–Br bond is oriented along the C_2 axis perpendicular to the molecular plane passing through the centre of the C–C double bond. The bromine closest to the double bond is 3.068(2) Å away from the centre of this bond and it is thought that the Br–Br bond lengthens by 0.02 Å upon approaching the ethene molecule. Comparing this complex to those of other dihalogens with ethene, it has been found that Br_2 achieves stronger binding than Cl_2 but weaker binding than the dipolar interhalogen compounds BrCl and ICl . The interaction between bromine and ethene can be considered as a halogen bond interaction between the region of positive electrostatic surface potential on bromine, known as the σ -hole,³⁸ and the π -electron cloud around the ethene double bond.

It is possible to establish the structure of the intermediate by comparing the electrophilic bromination of *cis* and *trans* isomers of substituted alkenes.³⁴⁷ An open carbocation intermediate can undergo free rotation about the central C–C bond, a process likely to occur during the electrophilic bromination of a *cis* alkene in order to relieve steric repulsions. In the case of a bromonium ion intermediate, this rotation is not feasible. By comparing the enthalpies of combustion of the alkenes and the enthalpies of activation for the electrophilic bromination of each isomer, it is possible to determine if rotation of the *cis* isomer has occurred and identify the structure of the intermediate. Electrophilic brominations of 1,2-dialkylethylenes were found to proceed *via* a symmetrical bromonium ion intermediate.

For stilbenes, it was established that electrophilic bromination could proceed *via* any of the three possible intermediates, which indicates that this reaction can follow a number of mechanistic pathways. According to analyses of experimental reactions rate constants performed by Ruasse and Dubois,³⁵³⁻³⁵⁵ the intermediate formed and the associated pathway depend on the substituents present on the stilbene; electron-donating substituents favour a carbocation intermediate, whereas electron-withdrawing substituents favour a symmetrical bromonium ion intermediate. The reaction pathway can be influenced significantly by the solvent.³⁵⁶

The understanding of the mechanism of electrophilic bromination of alkenes can be improved through quantum-chemical calculations. Teberekidis and Sigalas optimised the geometries and investigated the properties of the halonium ions of a series of methyl-substituted ethylenes at the MP2/6-311++G(d,p) and B3LYP/6-311++G(d,p) levels of theory.³⁵⁷ Their results indicate that, typically, bromine favours the bridged bromonium ion intermediate, whereas chlorine and fluorine are more likely to form a carbocation. Increasing the number of methyl substituents on the ethylene molecule appears to stabilise the bridged cation.

Islam and Poirier investigated the reaction mechanisms for the electrophilic bromination of ethene, propene, isobutene, fluoroethene, chloroethene, (*E*)-1,2-difluoroethene and (*E*)-1,2-dichloroethene at the HF, MP2 and B3LYP levels of theory with the 6-31G(d) basis set.³⁵⁸ The structure of the alkene was observed to have a minor effect on the results. It was suggested that the reaction between Br₂ and the alkene could proceed either *via* a perpendicular or a sideways attack, with the sideways attack leading to the desired *trans* product. All mechanisms were found to involve a bromonium ion intermediate.

5.2 Aim

The aim of the work presented in this chapter is to carry out geometry optimisations using quantum chemical methods on the intermediates of the electrophilic bromination reaction of a series of substituted stilbenes and stilbazoles, shown in Figure 5-2. The more electron-donating substituent is labelled as X_1 , while X_2 denotes the more electron-withdrawing substituent.

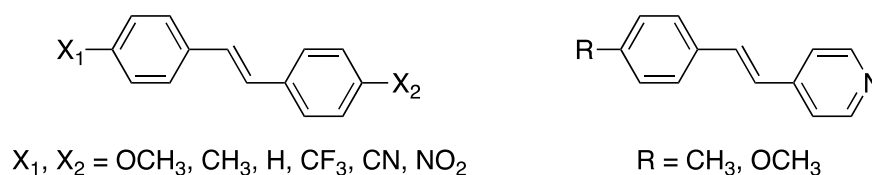


Figure 5-2: The substituted stilbenes and stilbazoles studied in this chapter.

This wide range of substituents allows us to present an in-depth analysis of the effect of their electron-withdrawing and electron-donating abilities on the structure of the intermediates. In order to identify a density functional theory (DFT) method which could be used as an alternative to the more computationally expensive MP2 approach, additional geometry optimisations on selected stilbene intermediates were performed with several popular density functional theory (DFT) exchange-correlation functionals. The most important features of the chemical bonding in the intermediates can be explained in detail using localised molecular orbitals (LMOs) and the natural bond orbital (NBO) method.¹²³

5.3 Method

Most of the geometry optimisations and single point calculations reported in this work were carried out on isolated gas phase molecules. The geometries of the intermediates of the electrophilic bromination of different substituted stilbenes and stilbazoles were optimised at the MP2/6-31G(d,p) level of theory using Gaussian 09.²²⁶ Vibrational frequencies were calculated to ensure that the optimised geometries corresponded to local minima on the respective potential energy surfaces.

The MP2 calculations were carried out using the MP2(Full) keyword to include correlation effects for all electrons.

The geometries of selected stilbene intermediates were also optimised using several DFT functionals (M06, M06-L, M06-2X, M06-HF, B3LYP and B97-D) and the same basis set, 6-31G(d,p), in order to identify a functional producing results which are in good agreement with their MP2/6-31G(d,p) counterparts. The closest agreement between MP2 and DFT results was observed for the M06-2X functional, and the M06-2X/6-31G(d,p) level of theory was employed to calculate a second set of optimised geometries for all intermediates. All DFT calculations were carried out using the Gaussian 'UltraFine' pruned integration grid.

In order to investigate the effect of the solvent on the structure of the intermediates, the geometries of the stilbazole intermediates were optimised in tetrahydrofuran using the polarizable continuum model (PCM), at the MP2/6-31G(d,p) and M06-2X/6-31G(d,p) levels of theory.

The Hartree-Fock (HF) molecular orbitals in the 6-31G(d,p) basis set were localised using the Edmiston-Ruedenberg localisation procedure in GAMESS-US.²⁸⁶ The outputs of the calculations were visualised using Molekel.²²⁸

NBO analyses were carried out at the MP2/6-31G(d,p) optimised geometries using NBO version 3 implemented in Gaussian 09.

The geometries of the CTCs were optimised using a total energy expression incorporating the Boys-Bernardi counterpoise (CP) correction for the basis set superposition error (BSSE).¹⁰⁶ The binding energies for these complexes were calculated using the expression $\Delta E = E_{\text{complex}} - \sum_{\text{all monomers}} E_{\text{monomer}}$ in which the CP correction for the BSSE was included in E_{complex} .

5.4 Results and Discussion

5.4.1 Structures of the Intermediates

The geometries of the stilbenes and the intermediates of the electrophilic bromination of the stilbenes optimised at the MP2/6-31G(d,p) and M06-2X/6-31G(d,p) levels of theory are provided, in terms of atomic Cartesian coordinates in the Appendix.

The type of intermediate observed (symmetrical bromonium ion, open carbocation or unsymmetrical bromonium ion) depends on the angle θ between the Br–C and central C–C bonds (see Figure 5-3).

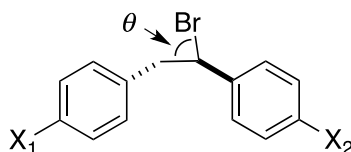


Figure 5-3: Definition of the angle θ between the Br–C and central C–C bonds used to classify intermediates.

The stilbenes studied can be arranged into five groups (see Table 5-1). Groups 1, 2 and 3 have $X_1 = \text{OCH}_3$, CH_3 and H , respectively, while groups 4 and 5 are symmetric or unsymmetric stilbenes in which both substituents X_1 and X_2 are electron withdrawing. The angles θ for the intermediates corresponding to these stilbenes, obtained through MP2/6-31G(d,p) geometry optimisations, are reported in the last column of Table 5-1.

All stilbenes in groups 1 to 3, for which a classical carbocation intermediate is observed, have at least one electron-donating substituent. The angle θ is obtuse and varies according to the electron-donating ability of the substituent in the X_1 position. The intermediates for the stilbenes with electron-withdrawing substituents included in group 4 exhibit angles θ of approximately 80° , consistent with an open

bromonium ion structure. The stilbenes with two identical electron-withdrawing substituents from group 5 give rise to bromonium ion intermediates with values of θ close to 70° . The observed wide range of values of the angle θ (*ca.* $70\text{--}109^\circ$) indicates that there is a spectrum of possible intermediates, which corroborates the proposal made by Yates and McDonald.³⁴⁷ Furthermore, the observation that electron-withdrawing substituents favour a bromonium ion intermediate while electron-donating groups favour a carbocation intermediate agrees with experimental evidence.³⁵³⁻³⁵⁵

Table 5-1: Types of intermediates observed for the electrophilic bromination of stilbenes **1** – **21** according to the magnitude of the angle θ measured for MP2/6-31G(d,p) optimised geometries.

Group	Compound	X ₁	X ₂	Type of Intermediate	$\theta / ^\circ$
1	1	OCH ₃	OCH ₃	Carbocation	108.97
	2	OCH ₃	CH ₃		103.62
	3	OCH ₃	H		102.22
	4	OCH ₃	CF ₃		101.95
	5	OCH ₃	NO ₂		101.79
	6	OCH ₃	CN		101.94
2	7	CH ₃	CH ₃	Carbocation	96.34
	8	CH ₃	H		96.14
	9	CH ₃	CF ₃		97.05
	10	CH ₃	NO ₂		97.33
	11	CH ₃	CN		96.95
3	12	H	H	Carbocation	88.40
	13	H	CF ₃		92.03
	14	H	NO ₂		92.96
	15	H	CN		91.74
4	16	CF ₃	NO ₂	Open Bromonium Ion	82.08
	17	CN	NO ₂		78.95
5	18	CF ₃	CF ₃	Bromonium Ion	70.13
	19	CF ₃	CN		70.70
	20	NO ₂	NO ₂		70.08
	21	CN	CN		70.06

The carbocation intermediates for the stilbazoles **22** and **23** exhibit angles θ similar to those in their stilbene counterparts with methoxy and methyl substituents, respectively (see Table 5-2).

Table 5-2: Types of intermediates observed for the electrophilic bromination of stilbazoles **22** and **23** according to the magnitude of θ measured for MP2/6-31G(d,p) optimised geometries.

Compound	R	Type of Intermediate	$\theta / ^\circ$
22	OCH ₃	Carbocation	101.79
23	CH ₃		97.21

5.4.2 Calculations using DFT

The geometries of selected stilbene intermediates, one representative from each group in Table 5-1, were optimised using the M06, M06-L, M06-2X, M06-HF, B3LYP and B97-D functionals and values of the most important parameters were compared to those calculated at the MP2 level of theory. The labels used for the bond distances that are compared are defined in Figure 5-4.

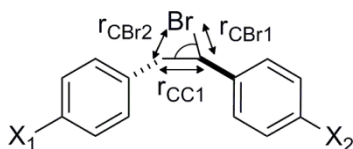


Figure 5-4: The bond distances used to compare DFT functionals to MP2 results.

Table 5-3: Comparison of key bond distances (in Å) and angles (in °) from the optimised geometries of selected stilbenes obtained using MP2 and different DFT methods, all within the 6-31G(d,p) basis.

Stilbene	Method	Intermediate Type	$r_{\text{CBr1}}/\text{Å}$	$r_{\text{CBr2}}/\text{Å}$	$r_{\text{CC1}}/\text{Å}$	$\theta/^\circ$
2	MP2	Carbocation	1.9775	2.7314	1.4751	103.62
	M06	Carbocation	1.9987	2.6394	1.4709	97.90
	M06-L	Carbocation	2.0031	2.6643	1.4680	99.01
	M06-2X	Carbocation	1.9787	2.6631	1.4803	99.69
	M06-HF	Carbocation	1.9720	2.6597	1.4919	99.39
	B3LYP	Carbocation	2.0333	2.6830	1.4792	98.48
	B97-D	Carbocation	2.0985	2.6485	1.4730	94.09
7	MP2	Carbocation	2.0051	2.6096	1.4692	96.34
	M06	Carbocation	2.0087	2.5719	1.4662	94.19
	M06-L	Carbocation	2.0267	2.5644	1.4640	93.14
	M06-2X	Carbocation	1.9974	2.5419	1.4732	92.94
	M06-HF	Bromonium Ion	2.1464	2.1464	1.4644	70.05
	B3LYP	Carbocation	2.0602	2.5836	1.4701	92.47
	B97-D	Bromonium Ion	2.3392	2.3392	1.4622	71.79
12	MP2	Carbocation	2.0249	2.4653	1.4639	88.40
	M06	Carbocation	2.0129	2.5039	1.4638	90.73
	M06-L	Carbocation	2.0471	2.4368	1.4628	86.25
	M06-2X	Bromonium Ion	2.1406	2.1406	1.4616	70.04
	M06-HF	Bromonium Ion	2.1337	2.1337	1.4643	69.93
	B3LYP	Carbocation	2.0880	2.4733	1.4667	86.31
	B97-D	Bromonium Ion	2.3014	2.3014	1.4648	71.44
16	MP2	Open Bromonium Ion	2.0433	2.3428	1.4617	82.08
	M06	Carbocation	2.0029	2.4879	1.4650	90.31
	M06L	Carbocation	2.0263	2.4358	1.4650	86.92
	M06-2X	Open Bromonium Ion	2.0541	2.2116	1.4640	75.84
	M06HF	Open Bromonium Ion	2.0897	2.1439	1.4651	71.76
	B3LYP	Carbocation	2.0547	2.4879	1.4702	88.17
	B97-D	Carbocation	2.1210	2.4565	1.4715	84.22

Table 5-3: (Continued).

	MP2	Bromonium Ion	2.1463	2.1463	1.4592	70.13
	M06	Carbocation	2.0126	2.4666	1.4632	88.96
	M06L	Carbocation	2.0455	2.4030	1.4630	84.73
18	M06-2X	Bromonium Ion	2.1251	2.1258	1.4622	69.86
	M06HF	Bromonium Ion	2.1194	2.1202	1.4645	69.82
	B3LYP	Carbocation	2.0887	2.4278	1.4663	84.20
	B97-D	Bromonium Ion	2.2782	2.2854	1.4660	71.53

Table 5-3 shows that the majority of the functionals perform reasonable well, however, there are instances where the type of intermediate predicted differs to that calculated at the MP2/6-31G(d,p) level of theory. The B3LYP functional fails to predict the bromonium ion and open bromonium ion intermediates for stilbenes **16** and **18** but performs well for carbocation intermediates. The M06-HF and B97-D functionals perform well for bromonium and open bromonium ion intermediates but fail to predict carbocation intermediates for stilbenes **7** and **12**.

The performances of the DFT functionals can be compared more effectively by calculating the errors in each parameter for each stilbene compared to MP2/6-31G(d,p) results and combining these to calculate a mean absolute error, Figure 5-5.

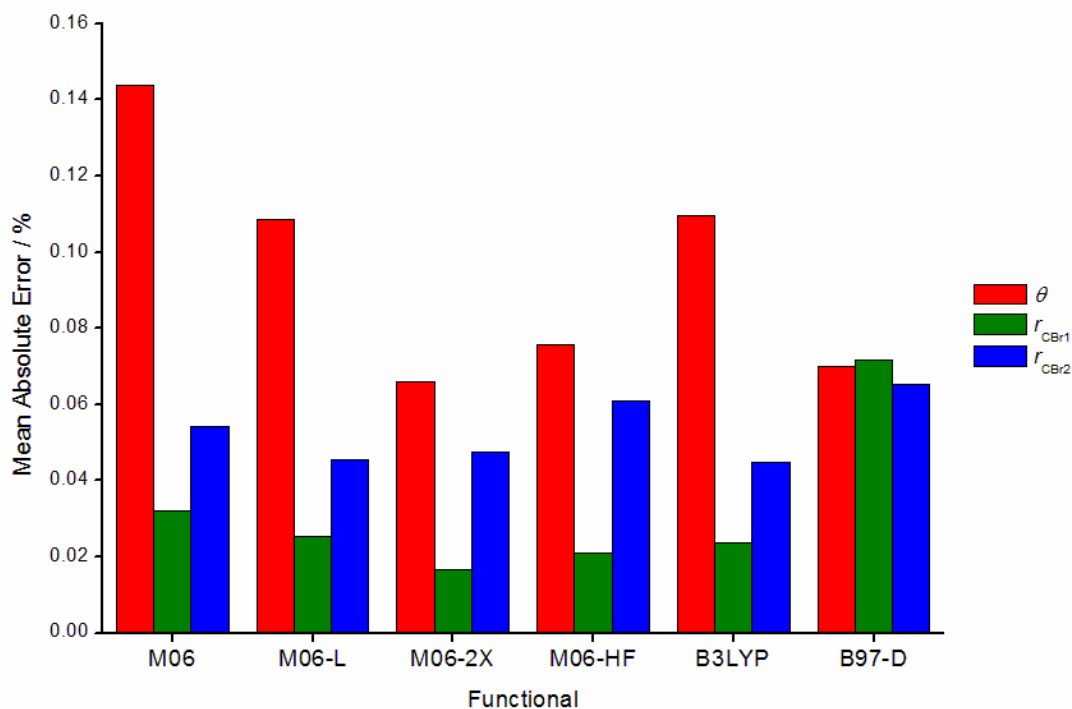


Figure 5-5: The mean absolute errors of key bond distances and angles calculated using different DFT functionals and the 6-31G(d,p) basis set compared to values calculated at the MP2/6-31G(d,p) level of theory.

Figure 5-5 shows that the M06-2X functional has the smallest mean absolute error and is the most appropriate density functional for studying these intermediates. It should be noted that these errors are calculated with respect to the MP2 level of theory, which will have some level of error. Ideally results would be compared to those calculated at the CCSD(T) level of theory extrapolated to the complete basis set limit, however, for these intermediates the calculations would be too computationally expensive.

Consequently, all MP2/6-31G(d,p) geometry optimisations of stilbene intermediates included in Table 5-1 were repeated at the M06-2X/6-31G(d,p) level of theory, see Table 5-4.

Table 5-4: The type of intermediates observed for the electrophilic bromination of stilbenes **1 – 21** grouped according to the magnitude of the angle θ calculated at the M06-2X/6-31G(d,p) level of theory.

Group	Compound	X ₁	X ₂	Type of Intermediate	$\theta / ^\circ$
1	1	OCH ₃	OCH ₃	Carbocation	105.83
	2	OCH ₃	CH ₃		99.69
	3	OCH ₃	H		99.53
	4	OCH ₃	CF ₃		100.08
	5	OCH ₃	NO ₂		100.49
	6	OCH ₃	CN		100.21
2	7	CH ₃	CH ₃	Carbocation	92.94
	8	CH ₃	H		94.07
	9	CH ₃	CF ₃		95.55
	10	CH ₃	NO ₂		96.34
	11	CH ₃	CN		96.09
3	12	H	H	Bromonium Ion	70.04
	13	H	CF ₃	Carbocation	80.91
	14	H	NO ₂		88.35
	15	H	CN		84.02
4	16	CF ₃	NO ₂		Open Bromonium Ion
	17	CN	NO ₂	75.06	
5	18	CF ₃	CF ₃	Bromonium Ion	69.86
	19	CF ₃	CN		71.90
	20	NO ₂	NO ₂		69.76
	21	CN	CN		69.88

On the whole, the MP2/6-31G(d,p) and M06-2X/6-31G(d,p) optimised geometries exhibit similar trends, but the angles θ are a few degrees smaller when measured at the M06-2X/6-31G(d,p) level of theory. One exception was the case of stilbene **12**, which was found to have a carbocation intermediate using the MP2/6-31G(d,p) level of theory and a bromonium ion intermediate at the M06-2X/6-31G(d,p) level of theory.

5.4.3 Solvent Effects

Solvent can play an important role in the electrophilic bromination reaction. The calculations were therefore repeated for the intermediates of stilbazoles **22** and **23** at the MP2/6-31G(d,p) level of theory using the PCM method to model THF solvent. The stilbazoles were selected because these have been investigated experimentally and THF was selected because this was the solvent used when the electrophilic bromination of alkoxy stilbazoles was observed. Table 5-5 compares the results of calculations carried out in the gas phase and using the PCM method to model solvent.

Table 5-5: Key bond distances and angles from the MP2/6-31G(d,p) optimised geometries of stilbazoles **22** and **23** carried out in the gas phase and in THF using the PCM method.

Stilbazole	<i>R</i>	Method	$r_{\text{CBr1}} / \text{\AA}$	$r_{\text{CBr2}} / \text{\AA}$	$r_{\text{CC1}} / \text{\AA}$	$\theta / ^\circ$
22	OCH ₃	Gas Phase	1.9813	2.7036	1.4786	101.79
		PCM (THF)	1.9799	2.7560	1.4822	104.59
23	CH ₃	Gas Phase	1.9901	2.6204	1.4731	97.21
		PCM (THF)	1.9801	2.7078	1.4783	102.09

Table 5-5 shows that there is very little difference between the geometry of the intermediate calculated in the gas phase and the geometry calculated in solvent using the PCM method. The angle θ is slightly larger in the PCM calculations, which could be an indication that the positive charge on the carbocation is partly stabilised by the dielectric medium.

The PCM method involves performing the calculation in a dielectric field that represents the solvent. This does not model the solvent effect particularly accurately and would not account for any specific interactions involving the solvent, however, modelling the solvent explicitly would be too computationally expensive.

5.4.4 Comparison of Intermediates

In order to determine the differences in energy between the observed carbocation intermediates and the related bromonium ions, bromonium ion geometries were calculated for stilbenes **1**, **7** and **12** (all of which feature $X_1 = X_2$), by imposing C_2 symmetry during the geometry optimisation. Each of these geometries with imposed C_2 symmetry was observed to exhibit a single imaginary vibrational frequency, which is an indication that the geometry corresponds to a transition state between two symmetry-equivalent carbocation intermediates existing in equilibrium. The geometries and the energies and Gibbs free energies of these transition states and the associated carbocation intermediates are compared in Table 5-6.

Table 5-6: Selected bond lengths, angles θ , energies E , activation energies ΔE^\ddagger , Gibbs free energies G and Gibbs free energies of activation ΔG^\ddagger for the bromonium ion transition states (C_2 symmetry) and the carbocation intermediates of stilbenes **1**, **7**, and **12**, optimised at the MP2/6-31G(d,p) level of theory. For further details, see text.

Stilbene	Intermediate	$r_{\text{CBr}} / \text{\AA}$	$r_{\text{CC1}} / \text{\AA}$	$r_{\text{CC2}} / \text{\AA}$	$r_{\text{CC3}} / \text{\AA}$	$\theta / ^\circ$	$E / \text{kJ mol}^{-1}$	$\Delta E^\ddagger / \text{kJ mol}^{-1}$	$G / \text{kJ mol}^{-1}$	$\Delta G^\ddagger / \text{kJ mol}^{-1}$
1	Bromonium	2.233	1.455	1.430	1.430	70.99	-8761739		-8761121	
	Ion							23.81		21.18
7	Carbocation	1.956	1.471	1.506	1.388	108.97	-8761763		-8761142	
	Bromonium	2.180	1.457	1.442	1.442	70.48	-8367803		-8367205	
	Ion							6.30		10.11
12	Carbocation	2.002	2.610	1.470	1.492	96.34	-8367810		-8367205	
	Bromonium	2.161	1.458	1.447	1.447	70.28	-8162014		-8161549	
	Ion							1.28		5.67
	Carbocation	2.025	1.464	1.484	1.405	88.40	-8162015		-8161554	

Table 5-6 shows that the magnitudes of the activation energies ΔE^\ddagger are fairly small, especially for stilbenes **7** and **12**, and decrease in parallel with the angle θ in the carbocation intermediate. The Gibbs free energies of activation ΔG^\ddagger are also small, which suggests that the interconversion between carbocation intermediates is facile, in agreement with experimental evidence indicating that these carbocation intermediates of symmetrical stilbenes exist in rapid equilibria.³⁵¹

5.4.5 Correlations with Hammett and Taft Parameters

Quantitative assessments of the extents to which intermediates are affected by substituents were obtained by correlating the angle θ with Hammett and Taft parameters.³⁵⁹ The effects of the two substituents were assumed to be non-additive since all stilbene intermediates have a central C-C single bond.

The effect of the X_1 substituent was investigated by examining a series of stilbenes in which the X_2 substituent was NO_2 .

As shown in Figure 5-6(a), there is a linear relationship between the angle θ and the σ_p parameter for the X_1 substituent for stilbenes with $X_2 = \text{NO}_2$. This is in agreement with the general observation that electron-donating substituents favour a classical carbocation intermediate while electron-withdrawing substituents favour a bromonium ion.

In order to establish whether it is the resonance or inductive effect of the substituent that affects the structure of the intermediate, the Taft parameters σ_R and σ_I for substituent X_1 were correlated with the angle θ for the series of stilbenes with $X_2 = \text{NO}_2$.

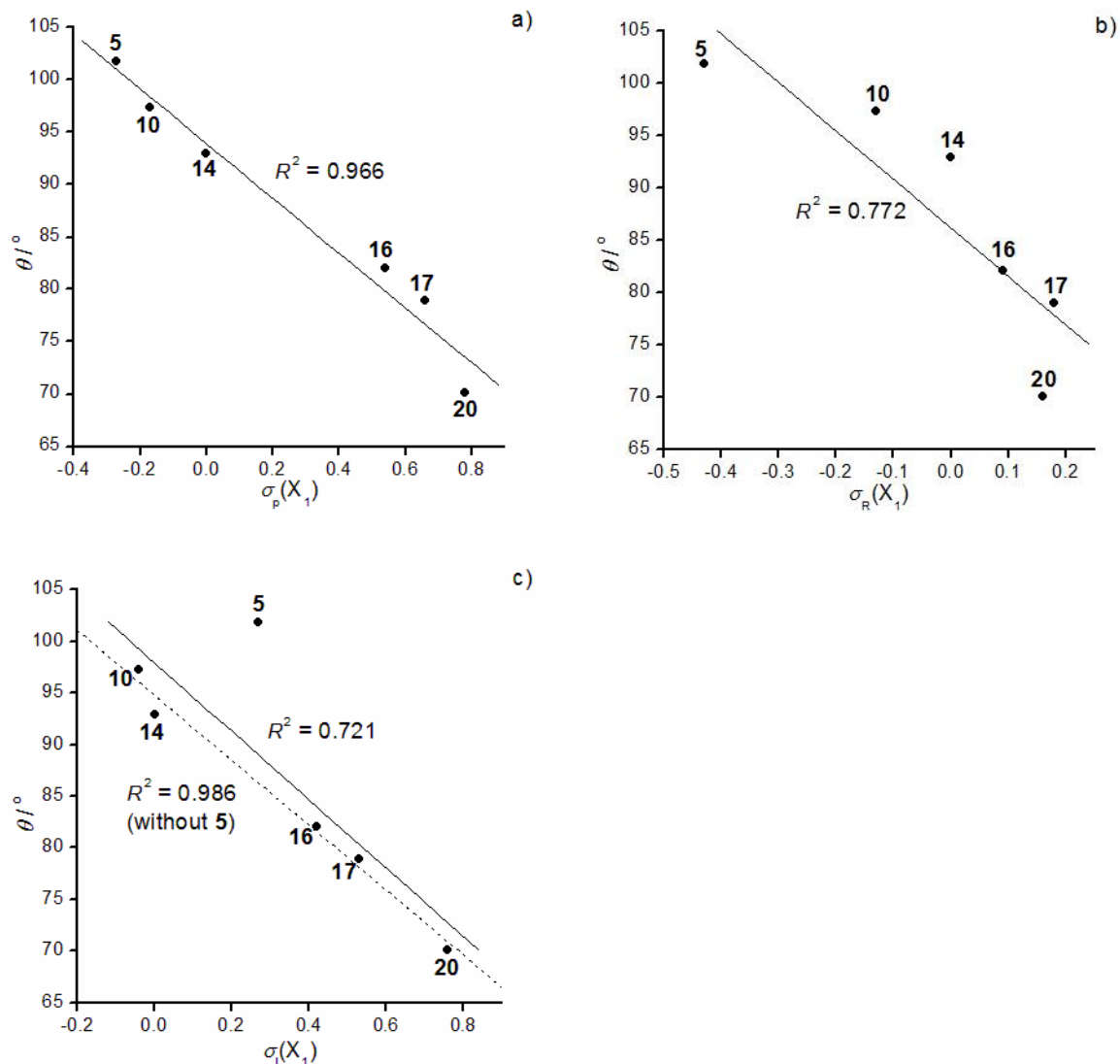


Figure 5-6: Relationship between the angle θ and (a) the Hammett parameter for para-substituted benzene derivatives σ_p , (b) the Taft parameter for resonance σ_R , (c) the Taft parameter for inductive effects σ_I of substituent X_1 for a series of stilbenes in which $X_2 = \text{NO}_2$.

The results [see Figure 5-6(b) and (c)] show that there is a tendency for the angle θ to decrease as each of the parameters σ_R and σ_I increases, which suggests that both inductive and resonance effects influence the structure of the intermediate. The poorer correlations observed in Figure 5-6(b) and (c) in comparison to that in Figure 5-6(a) suggest that the dependencies of the angle θ on σ_R and σ_I are more

complicated than simple linear models. Interestingly, exclusion of the outlier **5** ($X_1 = \text{OCH}_3$) makes the correlation between θ and σ_1 in Figure 5-6(c) much better.

The effect of the X_2 substituent can be investigated by looking at stilbenes featuring the same X_1 substituent, $X_1 = \text{OCH}_3$ (see group 1 in Table 5-1).

As shown in Figure 5-7, the angle θ does not change much with σ_p of substituent X_2 for the series of stilbenes with $X_1 = \text{OCH}_3$. This is an indication that the more electron-donating substituent X_1 plays a greater role in determining the type of intermediate formed during the electrophilic bromination of the stilbene. In addition to this, there is a linear relationship between the angle θ and σ_R of substituent X_2 , but no correlation between θ and σ_1 of substituent X_2 [see Figure 5-7(b) and (c), respectively]. This suggests that the resonance effect of substituent X_2 plays a greater role in determining the type of intermediate formed. Overall, the influence of substituent X_2 is much less significant than that of X_1 , as demonstrated by the narrow range of angle θ values for this series of intermediates (see Figure 5-7). This is due to the fact that substituent X_1 dominates the stabilisation of the carbocation whereas substituent X_2 is, to a large extent, electronically isolated from the carbocation (*vide infra*).

The intermediate of stilbene **1** is an obvious outlier in Figure 5-7(c). A possible reason for this behaviour is that both substituents in stilbene **1** are π -donors. In order to investigate this further, an additional geometry optimisation was carried out on the intermediate of the electrophilic bromination of a stilbene with another pair of identical π -donating substituents, $X_1 = X_2 = \text{NH}_2$ (see the data for stilbene **24** in Table 5-7).

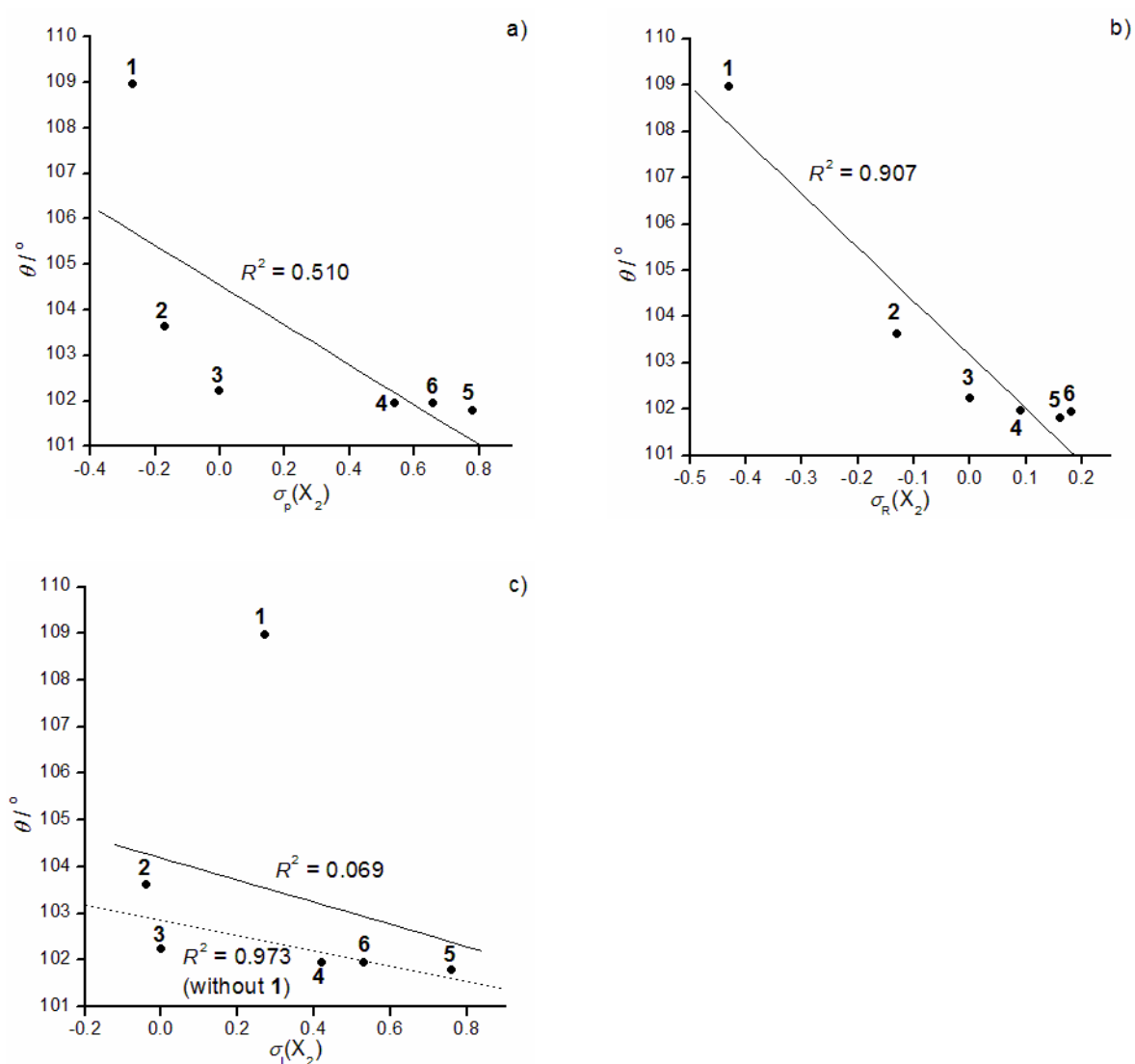


Figure 5-7: Relationship between the angle θ and (a) the σ_p parameter of substituent X_2 , (b) the Taft parameter for resonance σ_R , (c) the Taft parameter for inductive effects σ_I for substituent X_2 and for a series of stilbenes with $X_1 = \text{OCH}_3$.

Similar to stilbene **1**, this intermediate exhibits an exceptionally large angle θ . This suggests that the formation of intermediates of the electrophilic bromination of stilbenes with two π -donating substituents is dominated by resonance effects, leading to large angles θ .

Table 5-7: Type of intermediate observed for the electrophilic bromination of stilbene **24** according to the magnitude of the angle θ measured for the MP2/6-31G(d,p) optimised geometry.

Compound	X ₁	X ₂	Type of Intermediate	$\theta / ^\circ$
24	NH ₂	NH ₂	Carbocation	106.29

5.4.6 Localised Molecular Orbitals

In order to obtain a better understanding of the C–Br bond formation, localised molecular orbitals (LMOs) were calculated for all intermediates. The LMOs describing the C–Br bonds for selected intermediates are shown in Figure 5-8 together with the corresponding angles θ .

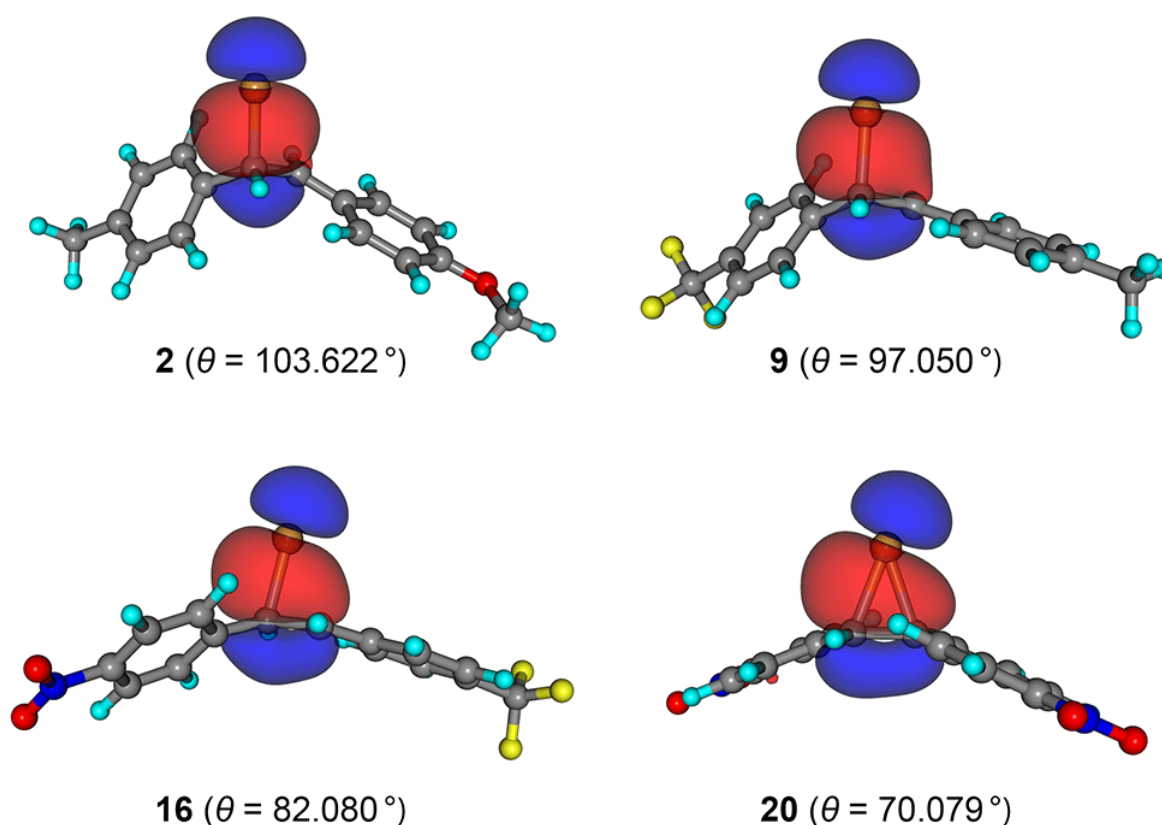


Figure 5-8: Localised molecular orbitals (LMOs) describing the C–Br bonds in selected intermediates of the electrophilic bromination of stilbenes. The orbitals are represented as isosurfaces at orbital values of ± 0.02 (e/bohr^3)^{1/2}.

The LMOs for the classical carbocation intermediates (**2** and **9**) have shapes that can be associated with a typical C–Br σ -bond. As the angle θ decreases, the LMOs develop a distortion towards the cationic carbon (**16**) and when a bromonium ion intermediate is formed (**20**), the shape of the LMO suggests the establishment of a 3-centre-2-electron bond encompassing the bromine and two carbons of the three-membered ring.

The overall contributions of the s basis functions on the carbon atoms in the C–Br bonds to the LMOs were found to correlate reasonably well with the angles θ (see Figure 5-9). These contributions range from approximately 21–22% in bromonium ion intermediates to about 33–35% in carbocation intermediates. The increase is an indication that the hybridisation state of the carbon atoms in the C–Br bonds changes from sp^3 to sp^2 as the angle θ increases.

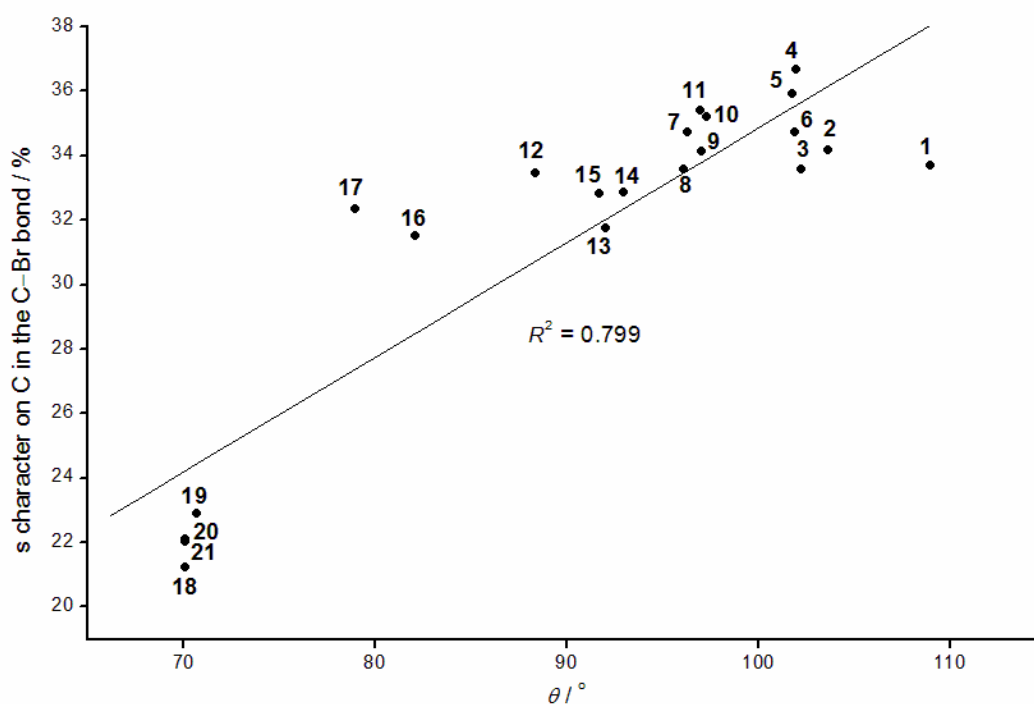


Figure 5-9: Correlation between the overall contribution of the s basis functions on the carbon atoms in the C–Br bonds to the LMOs and the angles θ .

5.4.7 Structural Correlations and NBO Analyses

In order to investigate possible interdependencies between the more important geometrical parameters from the optimised intermediate geometries, it is convenient to use the bond length definitions given in Figure 5-10. The bond lengths r_{CBr1} and $r_{\text{CC3}-r_{\text{CC5}}$ were plotted against the angle θ which yielded, in most cases, reasonably good linear correlations (see Figure 5-11).

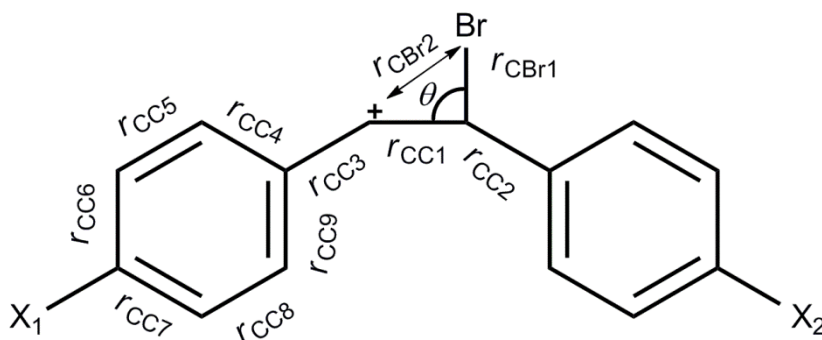


Figure 5-10: Bond length definitions in the intermediates of the electrophilic bromination of substituted stilbenes.

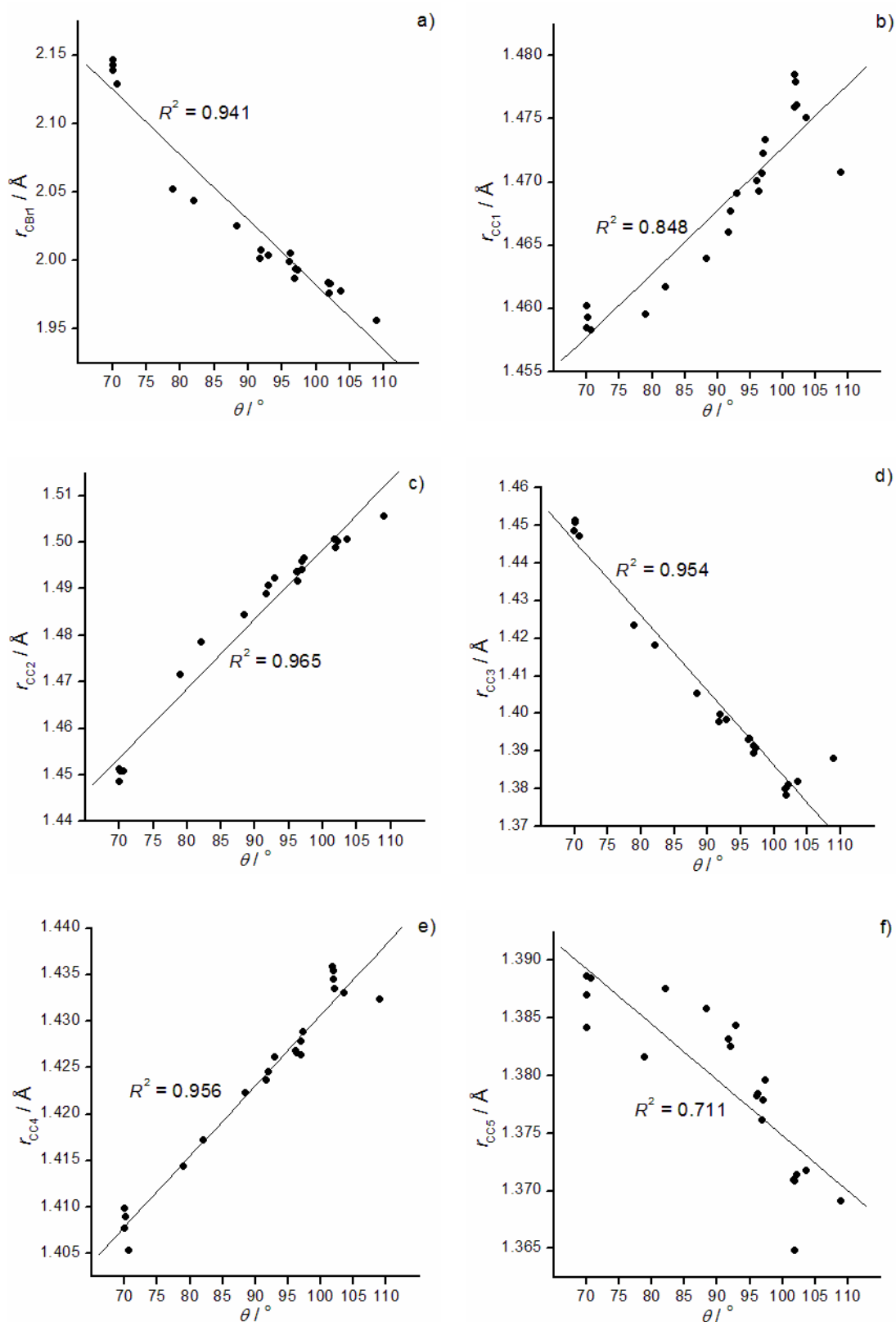


Figure 5-11: Relationships between bond lengths defined in Figure 5-10 and the angle θ for the geometries of the intermediates of the electrophilic bromination of stilbenes 1 – 21 optimised at the MP2/6-31G(d,p) level of theory.

As shown in Figure 5-11, the bond lengths r_{CC1} , r_{CC2} and r_{CC4} increase upon moving from a bromonium ion intermediate to a carbocation intermediate, whereas the bond lengths r_{CBr1} , r_{CC3} and r_{CC5} become shorter. These observations suggest that carbocations are stabilised by the resonance form drawn in Figure 5-12. Note, however, the compressed y-axis scale for r_{CC5} reflecting a total variation of <2% and indicative of the fact that in both the aromatic and quinoidal forms the corresponding bond retains multiple bond character.

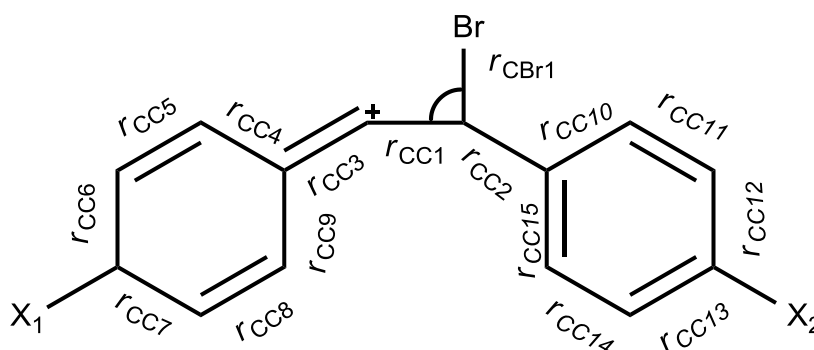


Figure 5-12: The resonance form expected to stabilise the classical carbocation intermediates of stilbenes **1** – **15**.

The intermediates in the electrophilic bromination of selected stilbenes were examined by means of natural bond order (NBO) analyses. These involved calculations of the π occupancies of the C–C bonds labelled through their bond lengths in Figure 5-12; the results are listed in Table 5-8.

The π occupancies of the C–C bonds show that, for all intermediates, the phenyl ring closest to the bromine atom (including bonds r_{CC10} – r_{CC15}) retains a Lewis structure with alternating single and double bonds. Carbocations with an angle θ exceeding 96° exhibit π occupancy in bond r_{CC3} . The second phenyl ring (including bonds r_{CC4} – r_{CC9}) displays the resonance pattern given in Figure 5-12, in which only bonds r_{CC5} and r_{CC8} have π occupancies. Carbocations with an angle θ under 93° also display the same resonance form in the second phenyl ring, but bond r_{CC3} no longer has any π occupancy. In bromonium ion intermediates, both phenyl rings exhibit Lewis structures with alternating single and double bonds.

For stilbenes with a π -donating substituent (*e.g.*, $X_1 = \text{OCH}_3$), it would be expected that the bond between X_1 and the carbon atom on the phenyl ring would have π occupancy. This was not observed, however, in the NBO analysis, although the carbon atom (C3) on the phenyl ring was found to have a positive charge in the natural population analysis (NPA) when the substituent X_1 was electron-donating (see Table 5-9). The effect is particularly pronounced in stilbenes with a methoxy substituent. Interestingly, calculating the LMOs on the methoxy oxygen shows two lone pair orbitals (Figure 5-13), the shapes of which suggest sp^3 hybridisation. This is consistent with the absence of double-bond character between the ring and the methoxy oxygen, and also with the presence of positive charge on C3. Our analyses do not provide further explanation for these chemically counterintuitive observations.

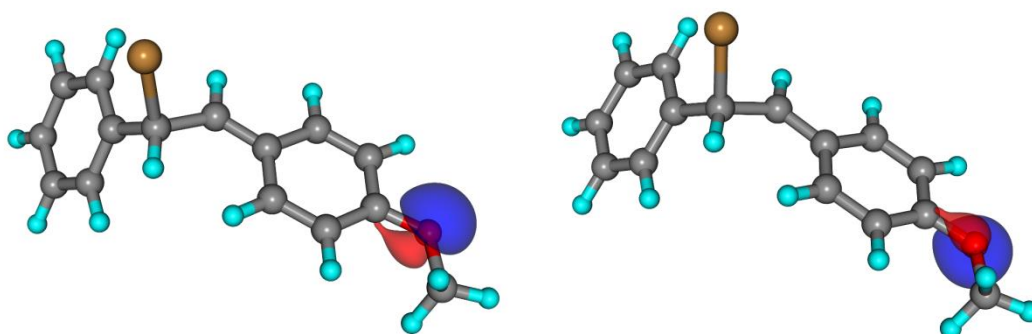


Figure 5-13: Localised Molecular Orbitals describing the lone pairs of electrons on the O atom of stilbene **3**, $X_1 = \text{OCH}_3$, $X_2 = \text{H}$.

Table 5-8: The π occupancies of the bonds in the intermediates of the electrophilic bromination of substituted stilbenes calculated using NBO analysis at the MP2/6-31G(d,p) level of theory.

Stilbene	X ₁	X ₂	$\theta / ^\circ$	π - Occupancy														
				r_{CC1}	r_{CC2}	r_{CC3}	r_{CC4}	r_{CC9}	r_{CC5}	r_{CC8}	r_{CC6}	r_{CC7}	r_{CC10}	r_{CC15}	r_{CC11}	r_{CC14}	r_{CC12}	r_{CC13}
3	OCH ₃	H	102.224	0	0	1.65	0	0	1.75	1.75	0	0	0	1.68	1.66	0	0	1.63
4	OCH ₃	CF ₃	101.952	0	0	1.66	0	0	1.75	1.76	0	0	0	1.67	1.64	0	0	1.65
7	CH ₃	CH ₃	96.343	0	0	1.57	0	0	1.67	1.70	0	0	0	1.69	1.67	0	0	1.61
13	H	CF ₃	92.964	0	0	0	0	0	1.64	1.67	0	0	0	1.68	1.65	0	0	1.65
16	CF ₃	NO ₂	82.080	0	0	0	0	0	1.65	1.60	0	0	0	1.67	1.64	0	0	1.64
18	CF ₃	CF ₃	70.127	0	0	0	0	1.65	1.65	0	0	1.63	0	1.65	1.65	0	0	1.63
20	NO ₂	NO ₂	70.079	0	0	0	0	1.64	1.64	0	0	1.63	0	1.64	1.64	0	0	1.63

The resonance form shown in Figure 5-12 rationalises the observation that substituent X_1 has a more pronounced effect on the form of the intermediate than substituent X_2 since the latter is, to a large extent, electronically isolated from the carbocation.

The results of the NPA analysis can also be used to rationalise the transition from carbocation intermediates to bromonium ion intermediates. The members of groups 1–3, which feature traditional carbocation intermediates, have small positive charges on carbon 1 (see Figure 5-14). It is interesting to note that these charges are slightly larger in group 2, in comparison to group 1, which is an indication that within the latter group the carbocation is stabilised by resonance from the π -donating methoxy substituent. In groups 4 and 5 it is the bromine atom that carries the small positive charge as would be expected for bromonium ion intermediates.

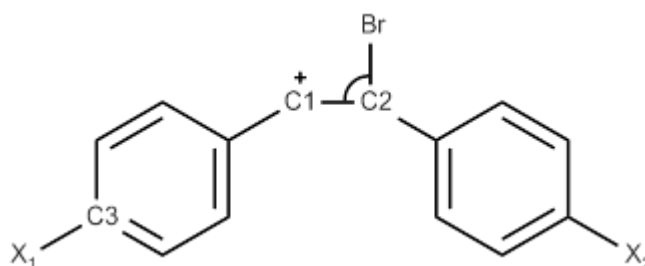


Figure 5-14: Atom numbering used in the natural population analysis (NPA).

Table 5-9: The natural charges of selected atoms in the intermediates of the electrophilic bromination of stilbenes **1** – **21** calculated using natural population analysis (NPA). The numbering used for the carbon atoms is shown in Figure 5-14.

Stilbene	X ₁	X ₂	Natural Charge			
			C1	C2	Br	C3
1	OCH ₃	OCH ₃	0.150	-0.330	0.054	0.584
2	OCH ₃	CH ₃	0.143	-0.315	0.046	0.600
3	OCH ₃	H	0.138	-0.312	0.049	0.605
4	OCH ₃	CF ₃	0.127	-0.315	0.058	0.610
5	OCH ₃	NO ₂	0.118	-0.231	0.065	0.613
6	OCH ₃	CN	0.122	-0.319	0.064	0.611
7	CH ₃	CH ₃	0.174	-0.294	0.057	0.186
8	CH ₃	H	0.171	-0.296	0.064	0.187
9	CH ₃	CF ₃	0.166	-0.306	0.074	0.195
10	CH ₃	NO ₂	0.160	-0.312	0.082	0.199
11	CH ₃	CN	0.163	-0.310	0.081	0.197
12	H	H	0.161	-0.256	0.091	-0.057
13	H	CF ₃	0.174	-0.286	0.094	-0.039
14	H	NO ₂	0.173	-0.296	0.100	-0.033
15	H	CN	0.171	-0.289	0.102	-0.038
16	CF ₃	NO ₂	0.114	-0.219	0.160	-0.039
17	CN	NO ₂	0.075	-0.188	0.187	-0.049
18	CF ₃	CF ₃	-0.053	-0.053	0.199	-0.172
19	CF ₃	CN	-0.044	-0.070	0.215	-0.100
20	NO ₂	NO ₂	-0.057	-0.057	0.225	0.120
21	CN	CN	-0.057	-0.057	0.213	-0.096

The occupancies of the σ bonding and σ^* antibonding orbitals associated with the C–Br bonds were also calculated within the NBO analyses; plots of the results against the angle θ are shown in Figure 5-15. For carbocation intermediates, the occupancy of the σ bonding orbital increases with the angle θ . The bromonium ion intermediates have similar occupancies that deviate from this trend. The occupancies of the σ^* antibonding orbital are very small for carbocation intermediates but increase for bromonium ions intermediates. This is an indication that the bonding in these bromonium ion intermediates involve a certain degree of hyperconjugation.¹³¹

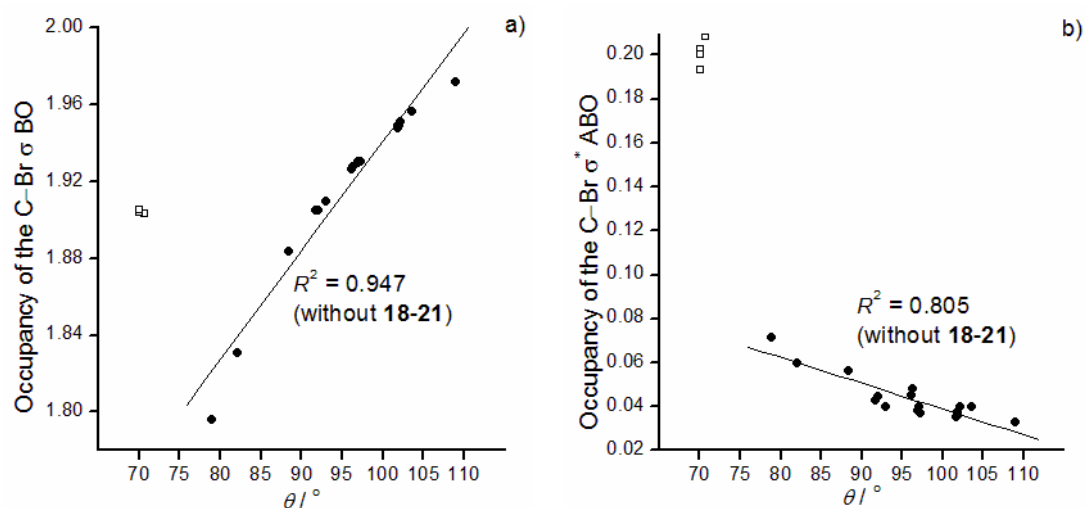


Figure 5-15: The relationships between (a) the occupancy of the C-Br σ bonding orbital and (b) the occupancy of the C-Br σ^* antibonding orbital and the angle θ for the intermediates of the electrophilic bromination of stilbenes **1** – **21**. Filled circles represent carbocation and open bromonium ion intermediates and open squares represent bromonium ion intermediates (**18** – **21**).

5.4.8 The Structure of Charge-Transfer Complexes

The geometries of selected CTCs between molecular bromine and stilbenes or stilbazoles were optimised at the MP2/6-31G(d,p) level of theory using a total energy expression including the Boys-Bernardi CP correction for the BSSE. An example of an optimised CTC geometry is shown in Figure 5-16.

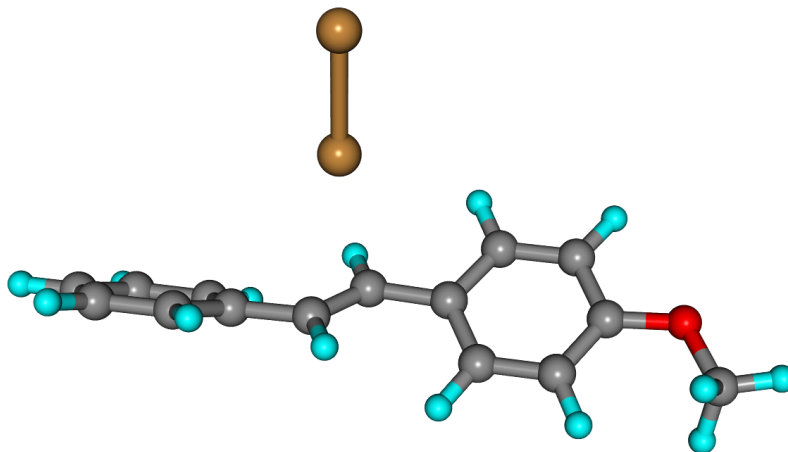


Figure 5-16: The charge-transfer complex of Br₂ and stilbene **3** (X₁ = OCH₃, X₂ = H) optimised at the MP2/6-31G(d,p) level of theory.

Typically, one of the bromines approaches the midpoint of the central C=C double bond in a stilbene remaining at very much the same distance from each of the two carbons. The C–Br separations in the CTCs can be correlated with the angles θ in the corresponding electrophilic bromination intermediates (see Figure 5-17). The C–Br separations in stilbenes which form bromonium ion intermediates are larger than those in stilbenes that form carbocation intermediates.

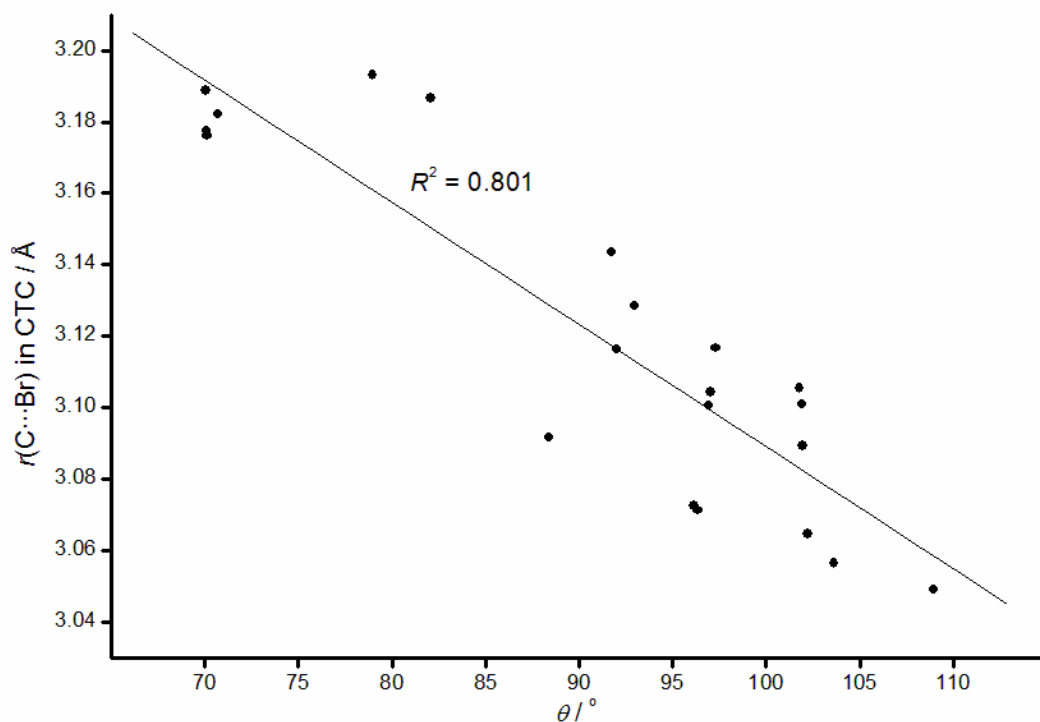


Figure 5-17: The relationship between the C-Br bond distances in the CTCs and the angle θ in the intermediates.

The r_{CC1} , r_{CC2} and r_{CC3} bond distances in the isolated stilbenes change very little upon CTC formation; r_{CC1} maintains a double bond character and r_{CC2} and r_{CC3} remain as single bonds.

The CTCs can also be viewed as halogen-bonded complexes between bromine and the π electrons of the stilbene C=C double bonds. The distances between the bromine atom and the midpoints of the stilbene C=C double bonds in the CTCs studied in this paper are reported in Table 5-10 together with the corresponding binding energies.

Table 5-10: The Br...C=C separations and binding energies of CTCs between bromine and substituted stilbenes

Stilbene	X ₁	X ₂	$r(\text{Br}\cdots\text{C}=\text{C})$ / Å	$r(\text{Br}-\text{Br})$ / Å	% Σ vdW radii	ΔE / kJ mol ⁻¹
1	OCH ₃	OCH ₃	2.972	2.343	81.43	-20.12
2	OCH ₃	CH ₃	2.984	2.341	81.74	-19.72
3	OCH ₃	H	2.994	2.340	82.03	-19.21
4	OCH ₃	CF ₃	3.027	2.336	82.92	-17.82
5	OCH ₃	NO ₂	3.056	2.334	83.72	-16.64
6	OCH ₃	CN	3.049	2.335	83.55	-16.91
7	CH ₃	CH ₃	2.995	2.340	82.06	-19.32
8	CH ₃	H	3.008	2.338	82.40	-18.65
9	CH ₃	CF ₃	3.039	2.334	83.25	-17.44
10	CH ₃	NO ₂	3.054	2.333	83.66	-16.86
11	CH ₃	CN	3.092	2.334	84.70	-17.01
12	H	H	3.016	2.337	82.63	-18.33
13	H	CF ₃	3.049	2.333	83.53	-16.98
14	H	NO ₂	3.064	2.332	83.94	-16.42
15	H	CN	3.078	2.332	84.34	-15.98
16	CF ₃	NO ₂	3.115	2.328	85.34	-14.72
17	CN	NO ₂	3.122	2.328	85.53	-14.53
18	CF ₃	CF ₃	3.104	2.330	85.03	-15.13
19	CF ₃	CN	3.109	2.329	85.17	-14.95
20	NO ₂	NO ₂	3.104	2.328	85.05	-14.90
21	CN	CN	3.116	2.328	85.36	-14.76

The data included in Table 5-10 indicate that the CTCs represent relatively strong halogen-bonded complexes. The $r(\text{Br}\cdots\text{C}=\text{C})$ distances in the CTCs are similar to the distance of 3.068 Å measured experimentally for the gas phase $\text{C}_2\text{H}_4\cdots\text{Br}_2$ complex.³⁵² Stilbenes that give rise to bromonium ion intermediates form weaker complexes than stilbenes that give rise to carbocation intermediates. Stilbenes from the second group include at least one electron-donating substituent capable of increasing the electron density along the central alkene bond. Stilbenes with electron-withdrawing substituents reduce the electron density at the central alkene bond leading to a weaker interaction with the σ -hole of the bromine atom. This can be illustrated quantitatively using the sum of the Hammett σ_p parameters of the two substituents, which can be assumed to be additive in these complexes since they are part of the same conjugated system (see Figure 5-18).

The explicit inclusion of a BSSE correction in the geometry optimisations and in the binding energy calculations is essential for a relatively small basis set such as 6-31G(d,p); this is highlighted by the fact that we observed BSSE energies for the CTC complexes ranging from 16.8 to 20.8 kJ mol^{-1} , which is very much the same as the range of binding energy magnitudes reported in Table 5-9.

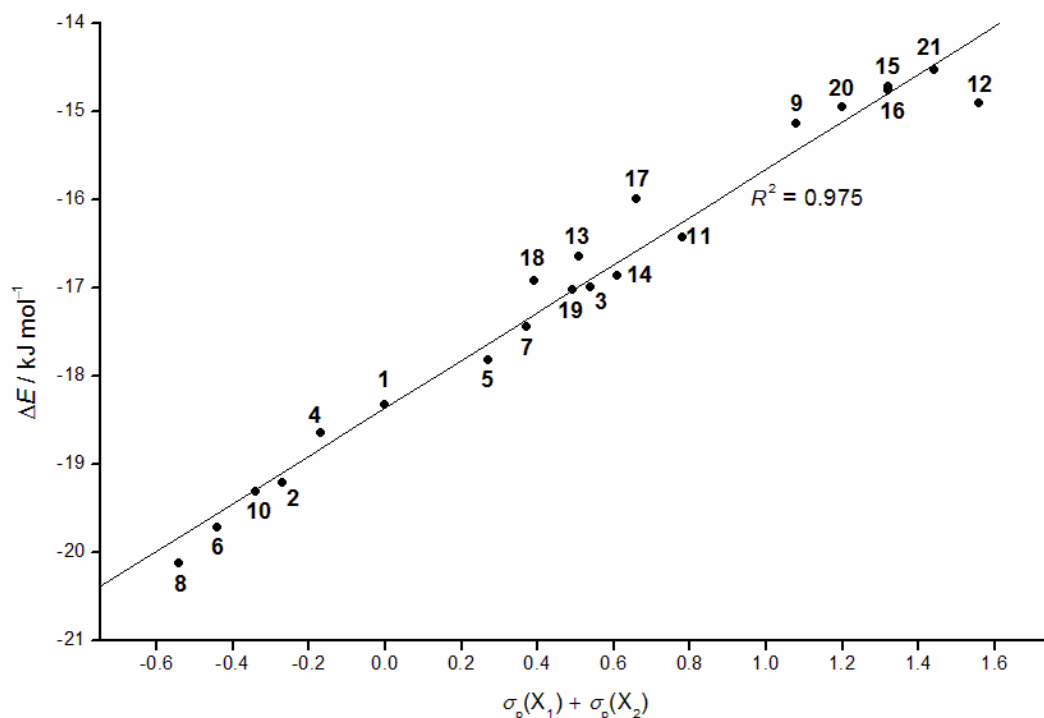


Figure 5-18: Relationship between the binding energy of the CTCs and the sum of the Hammett σ_p parameters of the two substituents of stilbenes **1** – **21**.

5.5 Conclusions

The effect of substituents on the electrophilic bromination of stilbenes and stilbazoles was studied by optimising the geometries of the reaction intermediates at the MP2/6-31G(d,p) and M06-2X/6-31G(d,p) levels of theory and performing an in-depth analysis of the most important structural and electronic features of these intermediates. The results indicate that stilbenes with two electron-withdrawing substituents favour a bromonium ion intermediate, whereas stilbenes with an electron-donating substituent give rise to a carbocation intermediate. This is consistent with the experimental observations of Ruasse and Dubois,³⁵³⁻³⁵⁵ and, in particular, with the findings of Ruasse *et al.* according to which the electrophilic bromination of *cis* and *trans*-stilbenes with a *para*-methoxy substituent in methanol and acetic acid was stereoconvergent, suggesting an open carbocation intermediate that would allow rotation about the C-C bond, whereas *cis* and *trans*-stilbenes with

para-trifluoromethyl substituents were stereospecific, indicating a bromonium ion intermediate.³⁵⁶

By comparing the geometries of selected stilbene intermediates optimised using DFT with the exchange-correlation functionals M06, M06-L, M06-2X, M06-HF, B3LYP and B97-D within the 6-31G(d,p) basis set to the corresponding MP2/6-31G(d,p) optimised geometries, we established that the closest agreement was observed for the M06-2X functional which can be recommended for further calculations (for example, of transition state geometries, reaction paths, rate constants, etc.) on these and other substituted stilbenes and stilbazoles.

Our calculations reveal a range of values for the BrCC angle θ , suggesting a spectrum of intermediates similar to the proposals made by Yates and MacDonald.³⁴⁷ Such a spectrum of intermediates has been observed experimentally for the electrophilic bromination of substituted *cis* and *trans*-stilbenes in acetic acid and trifluoroethanol, in which there was a progressive change from stereoconvergency to stereospecificity as the substituents became more electron withdrawing.

The calculations also showed that the structure of the intermediate was influenced to a greater extent by the nature of the more electron-donating substituent, X₁ (see Figure 5-2). This was confirmed by the strong correlation between the BrCC angle θ and the Hammett parameter σ_p for a series of stilbenes in which X₁ varied and X₂ was a nitro substituent. The effects of the two substituents were found not to be additive, which is consistent with kinetic studies of the electrophilic bromination of stilbenes with at least one electron-donating substituent, however, additivity *was* observed experimentally for stilbenes with two electron-withdrawing substituents,³⁵⁵ but this was not reproduced in the current calculations.

The very good qualitative agreement between our gas phase computational results and experimental observations for reactions in solution and the close similarity between the geometries of stilbazole intermediates optimised in the gas phase and in

tetrahydrofuran suggest that the solvent effects on the structures of the reaction intermediates in the electrophilic bromination of stilbenes and stilbazoles are relatively minor.

The shapes of the localised molecular orbitals over the Br and nearest C atoms show that the carbocation intermediates include C-Br σ bonds. As the angle θ decreases, the LMOs distort towards the cationic carbons, as a result of which the bromonium ion intermediates include 3-centre-2-electron bonds. These findings are corroborated by natural bond orbital analysis: The occupancy of the C-Br σ bonding orbital decreases and the occupancy of the C-Br σ^* anti-bonding orbital increases with the decrease of the angle θ , which is also an indication of a certain extent of hyperconjugation within the bromonium ion intermediates.

The π -occupancies of the C-C bonds in the phenyl rings in the intermediates calculated by NBO analysis have shown that carbocation intermediates are stabilised by a resonance form in which electron density is directed towards the cationic carbon. This is confirmed by the trends in the lengths of the C-C bonds observed upon varying the angle θ .

Our results for the charge-transfer complexes indicate that these can be viewed as halogen-bonded complexes with relatively strong binding energies ranging from 14.5 to 20.1 kJ mol⁻¹. Stilbenes with electron-withdrawing substituents form weaker complexes since these remove electron density from the alkene bond. Similarly, electron donating substituents give rise to stronger complexes, as illustrated by the strong correlation between the sum of the Hammett σ_p parameters of the two substituents and the binding energies of the complexes.

6 Halonium Ions as Halogen Bond Donors

6.1 Introduction

The investigation into the intermediates of the electrophilic bromination of stilbazoles and stilbenes (Chapter 5) revealed that for stilbenes with two electron-withdrawing groups, a bromonium ion intermediate is observed. These bromonium ions have a positive charge centred on the bromine atom, similar to the σ -hole in halogen bond donors,³⁸ which suggests that it could be possible for bromonium ions to form a halogen bond with Lewis bases.

The bromonium ion intermediate observed in the electrophilic bromination of alkenes is usually short-lived because it undergoes nucleophilic attack from a bromide ion to give the dibromoalkane product. Therefore, in order to observe interactions between halonium ions and Lewis bases, the halonium ion would need to be stable and isolable.

6.1.1 Stable Halonium Ions of Adamantylidene Adamantane [AdAdX]⁺

The bromonium ion of adamantylidene adamantane ([AdAdBr]⁺) is stable since nucleophilic attack is sterically hindered.^{348,350,360} Both the tribromide and triflate salts have been isolated and the crystal structures have been determined (Figure 6-1). In both structures the bromine bridges the central C–C bond, however, in the tribromide salt this is unsymmetrical with C–Br bond lengths of 2.116(7) and 2.194(7) Å and C–C–Br angles of 72.5(4) and 66.9(4)°, whereas in the triflate salt the C–Br distances are 2.09(1) and 2.11(1) Å leading to a symmetrical bromonium ion. The fact that the tribromide salt is unsymmetrical is attributed to a Br⋯Br interaction between the bromonium ion and the tribromide anion with a separation of 3.096(1) Å, which is 84% of the sum of the van der Waals radii. In the triflate salt the bromine atom forms a similar interaction with an oxygen atom on the triflate anion with a Br⋯O separation of 3.08(1) Å, which is 91% of the sum of the van der

Waals radii. This latter interaction is longer than the Br⋯Br interaction in the tribromide salt when considered as a percentage of the sum of the van der Waals radii, which could account for the fact that the tribromide salt is unsymmetrical but the triflate salt is symmetrical. The Br⋯O separation in the triflate salt is longer because there is a larger deviation from linearity. The Br⋯Br- π angle, where π is taken as the centre of the C-C bond, is 174.3(2)° in the tribromide salt, and the O⋯Br- π angle in the triflate salt is 149.8(4)°. This deviation from linearity in the triflate salt could be due to a second weaker interaction with another triflate anion with a Br⋯O separation of 3.367(8) Å, which at 99% of the sum of the van der Waals radii can only be considered as a van der Waals interaction. There are also water and dichloromethane in the structure which could affect the intermolecular interactions.

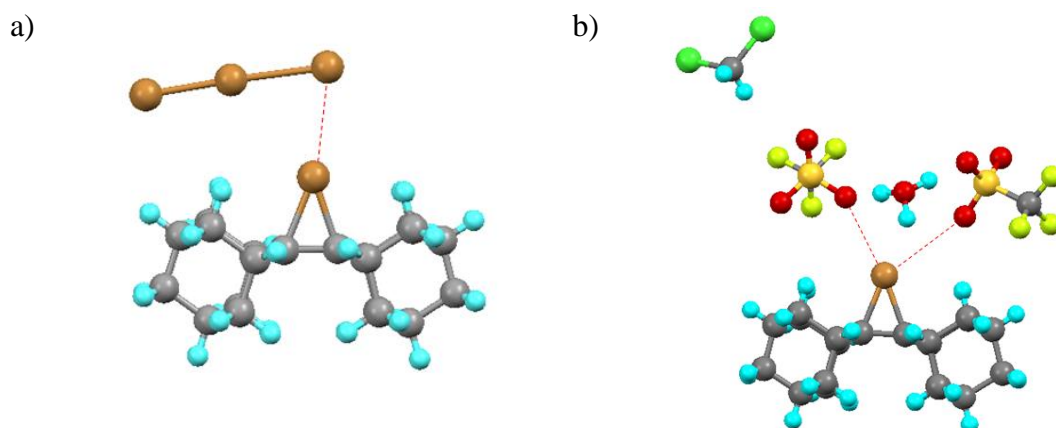


Figure 6-1: The molecular structures of a) [AdAdBr]⁺ Br₃⁻³⁴⁹ and b) [AdAdBr]⁺ OTf⁻.³⁵⁰

The Br⋯Br and Br⋯O interactions are highlighted in red.

Similarly, the iodonium ion of AdAd is stable and its X-ray crystal structure has been determined. The C-I bond distances are 2.338(5) and 2.362(3) Å, which once the esds are taken into account show that the iodonium ion is symmetrical. In this structure the iodine atom interacts with the oxygen atom of a crystallisation water, with an I⋯O separation of 2.630(4) Å, which is 75% of the sum of the van der Waals radii (Figure 6-2). The interaction is along the extension of the I- π axis, with the O⋯I- π angle of 176.9(2)°. The fact that this interaction is stronger than those of the

bromonium ions could indicate that the interactions increase in strength as the halogen becomes more polarisable and that interactions along the extension of the X- π axis are the strongest.

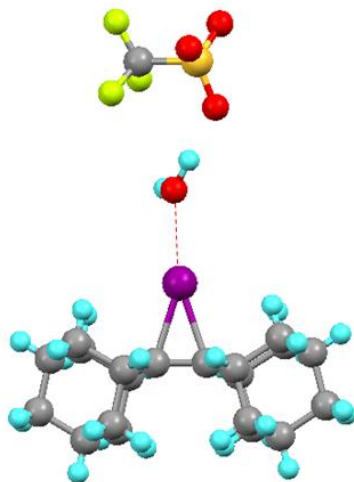


Figure 6-2: The molecular structure of AdAd iodonium triflate showing the I \cdots O interaction with a crystallisation water.³⁵⁰

The chloronium ion of AdAd was also isolated and is also not symmetrical; the C-Cl bond lengths are 1.924(4) and 2.075(4) Å.³⁶¹ It has been proposed that the chlorine atom is σ -bonded to a carbon atom and stabilises the charge on the other carbon atom through a lone electron pair. The lack of symmetry in this cation is thought by the authors to be due to a weak Cl \cdots Cl interaction (99% of the sum of the van der Waals radii) with the hexachloroantimonate anion, see Figure 6-3, since optimisation of the geometry of the chloronium ion using a semi empirical method (PM3) suggested that it should be symmetrical.³⁶² The Cl \cdots Cl- π angle is 164.0(2) $^\circ$ showing that the Cl \cdots Cl interaction deviates from the extension of the Cl- π axis, which could account for the chloronium ion being unsymmetrical.

The Cl \cdots Cl interaction, which should be classified as a van der Waals interaction, is considerably weaker than those observed in the bromonium and iodonium ions, which further suggests that the strengths of the interactions increase as the halogen becomes more polarisable.

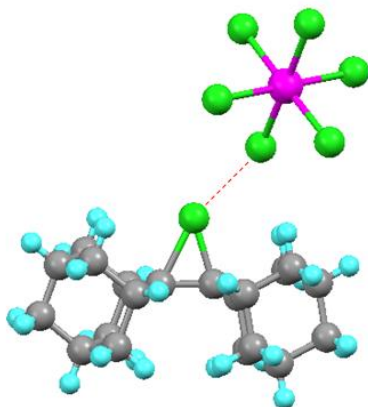


Figure 6-3: The molecular structure of $[\text{AdAdCl}]^+$ hexachloroantimonate.³⁶¹ The weak $\text{Cl}\cdots\text{Cl}$ interaction is shown in red.

The mechanism of the electrophilic bromination of AdAd has been studied using HF and B3LYP levels of theory.³⁶³ The reaction between AdAd and Br_2 was found to proceed *via* a single pathway with a bromonium ion bromide intermediate. The reaction between AdAd and 2Br_2 could proceed *via* three different pathways, all with a bromonium ion tribromide intermediate. The activation energy of the reaction with 2Br_2 is lower than that for Br_2 showing that the reaction is mediated by a second bromine molecule and explaining the fact that the crystal structure of adamantylidene adamantane bromonium ion exists as the tribromide salt.

This is one of only a few quantum chemical studies of the electrophilic bromination of AdAd.^{350,362,364} These calculations have been employing semi-empirical methods or low levels of theory using small basis sets, which lowers the accuracy of the calculation; the lack of studies using high-level calculations reflects the prohibitive computational cost. It is, therefore, necessary to use a smaller system to model the electrophilic bromination of AdAd, and the bromonium ion of 2,3-dimethyl-2-butene was found to be a suitable model.³⁵⁷ The halonium ions of ethenes would therefore be suitable model systems for the investigation of complexes between halonium ions and Lewis bases.

6.1.2 Halonium Ions of Ethenes

The electrophilic bromination of ethene proceeds *via* a bridged bromonium ion intermediate rather than a carbocation or open bromonium ion intermediate because it is a non-conjugated alkene. The geometry optimisations of the bridged halonium ions and cationic intermediates of ethene mentioned earlier reveal that while bromine favours a bridged bromonium ion intermediate, chlorine and fluorine favour a carbocation intermediate.^{357,365,366} The level of theory and the size of the basis set can affect the relative stabilities of the cationic intermediates although the general trend is unaffected.³⁶⁷ It is, therefore, necessary to include electron correlation in the calculation and polarisation functions in the basis set to model these intermediates.

The introduction of electron-donating methyl substituents was found to stabilise the bridged intermediate,³⁵⁷ so that the bridged chloronium ion of 2-methylpropene, 2-methyl-2-butene and 2,3-dimethyl-2-butene³⁶⁸ is very likely the global minimum on the potential energy surface. The carbocation remains the most stable intermediate in the case of fluorine. In the case of unsymmetrically substituted ethenes, the optimised geometry of the bridged halonium ion is unsymmetrical with C–X bonds of different lengths. Electron-withdrawing fluorine and trifluoromethyl groups typically reduce the stability of the bridged halonium ion leading to a carbocation intermediate becoming the most stable geometry on the potential energy surface.³⁶⁹

A quantum chemical investigation of the mechanism of the electrophilic bromination of ethene reveals that a sideways attack of bromine (Figure 6-4a) is favoured over a perpendicular approach (Figure 6-4b) leading to a bromonium ion bromide intermediate.³⁵⁸ Fluorine, chlorine and methyl substituents lead to a lowering of the activation barrier of the rate-determining step.

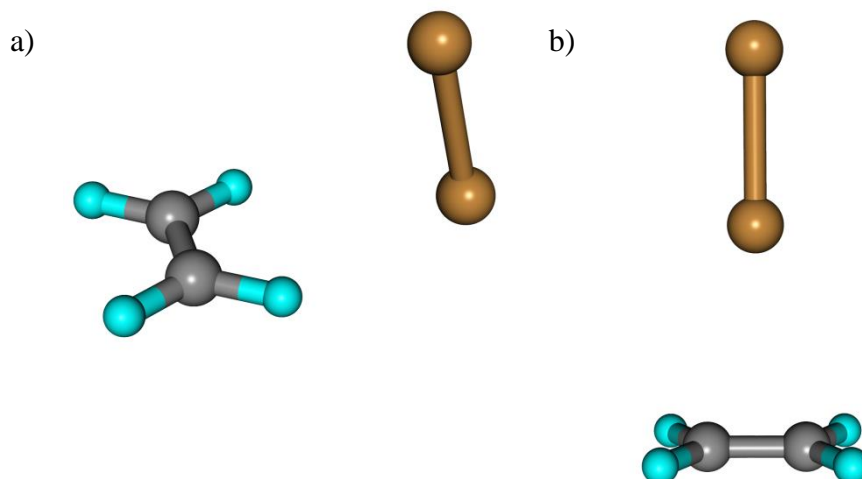


Figure 6-4: The pre-reactive complexes of the reaction between ethene and Br₂ via a) sideways and b) perpendicular attack of bromine.³⁵⁸

6.1.3 Dialkylhalonium Ions

Another class of halonium ions are acyclic or open-chain halonium ions, which include dialkyl and diarylhalonium ions.³⁷⁰ These acyclic halonium ions also carry a positive charge on the halogen atom, which could interact with regions of electron density.

Dialkylhalonium ions are typically synthesised by reacting alkyl halides with SbF₅-SO₂ and anhydrous fluoroantimonic acid in solution in SO₂ or by alkylating alkyl halides with methyl or ethyl fluoroantimonate in liquid SO₂ (examples are shown in Figure 6-5).³⁷⁰ These halonium ions increase in stability as the halogen becomes more polarisable but are generally quite reactive and are used as alkylating agents.

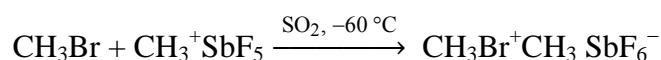
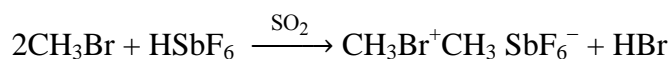
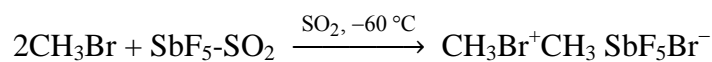


Figure 6-5: Different methods for synthesising dimethyl bromonium cations.

Stable dimethyl- and diethyl-chloronium ions have recently been synthesised by using a carborane anion, which is inert to the reactive cation and crystallises readily (Figure 6-6).³⁷¹ The structure reveals C–Cl bond lengths of 1.809(2) and 1.842(5) Å, respectively, and C–Cl–C angles of 101.55(7)° and 105.8(2)°, respectively. These values can be compared to those in the B3LYP/6-31G** optimised geometry of the dimethyl-chloronium cation, where the C–Cl bond length was 1.855 Å and the C–Cl–C angle was 105.0°.³⁷² This optimised geometry is in closer agreement with the diethyl- than the dimethyl-chloronium cation suggesting that this theoretical method does not accurately reproduce the results observed experimentally. The dimethyl-chloronium cation interacts with the carborane anion through weak C–H⋯Cl interactions, which could account for the disagreement between the experimental and theoretical results. The geometry of the diethyl-chloronium cation was not optimised so it is not possible to see if the B3LYP/6-31G** level of theory is capable of reproducing the trends observed in the C–Cl bond lengths and C–Cl–C bond angles.

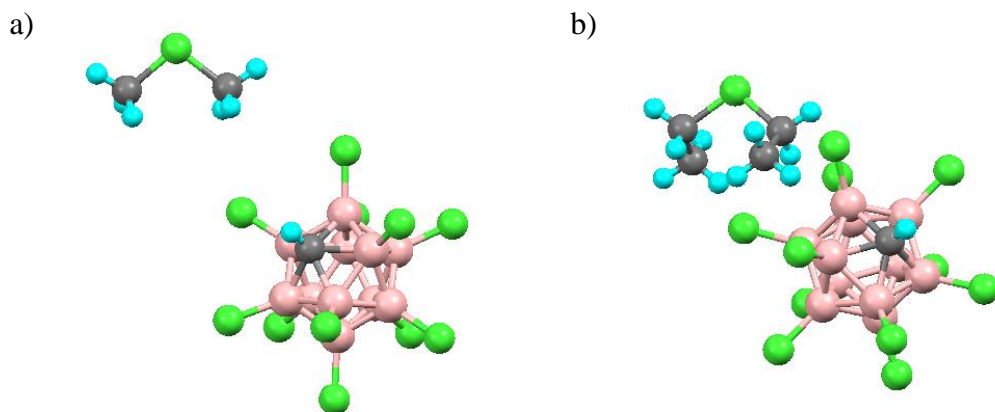


Figure 6-6: The molecular structure of a) dimethyl- and b) diethyl-chloronium carborane.³⁷²

Theoretical studies have shown that the C–X–C angle decreases as the halogen becomes more polarisable due to an increase in the *p*-character in the C–X bonding orbital, as observed by NBO analysis.³⁷³ These calculations were carried out using different basis sets for each of the halonium ions and although the basis set had little effect on the optimised C–Br–C angle of the dimethyl-bromonium cation, their

accuracy and reliability of the predicted trends should be questioned. A similar trend has also been observed in the crystal structures of $[\text{Me}_3\text{Si-X-SiMe}_3][\text{B}(\text{C}_6\text{F}_5)_4]$ salts, where there was also a significant increase in the C-X-C angle for the isolated fluoronium ion (Figure 6-7).³⁷⁴

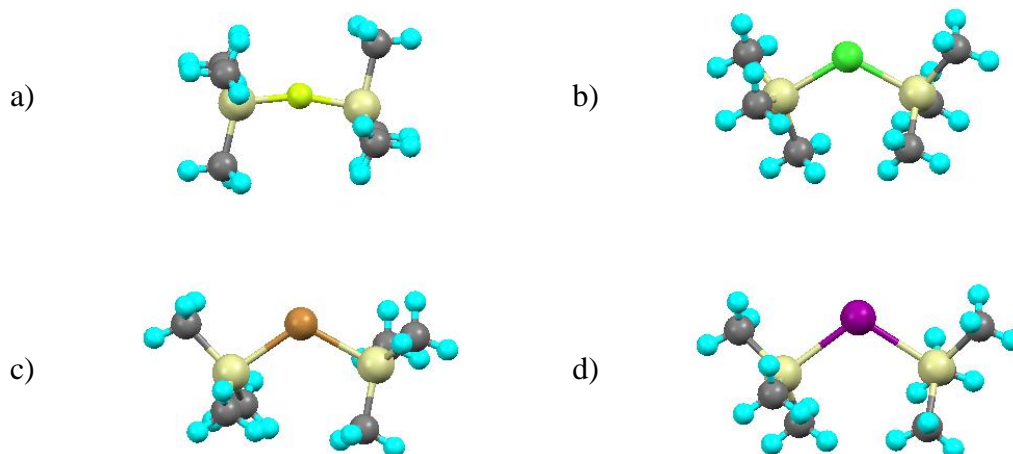


Figure 6-7: The crystal structures of bis(trimethylsilyl)halonium cations of a) fluorine, b) chlorine, c) bromine and d) iodine cations.³⁷⁴ The $[\text{B}(\text{C}_6\text{F}_5)_4]^-$ counteranion has been omitted for clarity and does not interact with the cation.

Although examples of stable dialkylhalonium ions do exist, the fact that their synthesis involves the use of superacidic media or the presence of very weakly coordinating anions makes this type of halonium ion unsuitable for use as a halogen bond donor.

6.1.4 Diaryliodonium Salts

Diaryliodonium salts are examples of stable halonium ions, which can be easily synthesised by oxidation of an aryl iodide to an iodine(III) complex, followed by ligand exchange with a second aryl ligand. The fact that they are stable makes them better potential candidates to act as halogen-bond donors.

Diaryliodonium salts (Figure 6-8a), which are also known as λ^3 -iodanes,³⁷⁵ have a hypervalent iodine (III) centre. The halide salts show a secondary interaction between the iodine atom and the halide anion leading to a pseudo trigonal bipyramid

geometry (Figure 6-8b), with one ligand in an equatorial position with respect to the lone pairs on iodine and another ligand in the axial position with the secondary interaction to the anion.³⁷⁶ Diaryliodonium salts, typically the triflate and tetrafluoroborate salts, which have improved solubility in organic solvents, are used in organic synthesis including the oxidation of alkenes and alcohols.^{375,377,378}

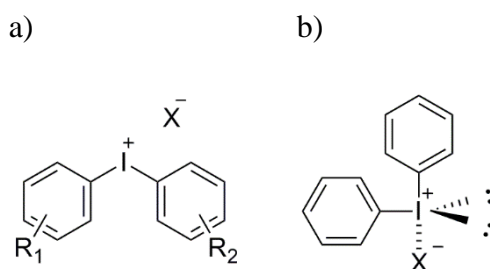


Figure 6-8: a) The general structure of diaryliodonium salts. b) The observed pseudo trigonal bipyramid geometry.

The secondary interaction between the I(III) centre and the halide anion has characteristics similar to those of a halogen bond and it was initially proposed to arise from the donation of electrons from a lone pair on the halide anion into the C–I σ^* anti-bonding orbital.³⁷⁶ The interaction is found to be dominated by the electrostatic term when an energy decomposition of the transition state is carried out.³⁷⁹

The presence of secondary interactions in diaryliodonium salts leads either to a tetra- or penta-coordinated iodine centre. In the case of tetra-coordinated centres, a square-planar geometry is adopted by the iodine as observed for the halide salts of diaryliodonium ions, whereas penta-coordinated centres have a pentagonal planar geometry.³⁸⁰

An investigation of the secondary bonding in structure of Bi(III) complexes, which are analogous to iodine(III) complexes, recognised the similarity to hydrogen bonding with Cl–Bi \cdots Cl interactions favouring a linear geometry.³⁸¹ It was proposed that in the [BiCl₂Ph₂]⁻ anion, the Cl⁻, which acts as a Lewis base, donates electrons into the Bi–Cl σ^* orbital leading to a 3-centre-4-electron Cl–Bi–Cl bond. Figure 6-9

shows the molecular structure of diphenylbismuth chloride and shows how the Cl–Bi...Cl interactions lead to the establishment of a polymeric structure.³⁸²

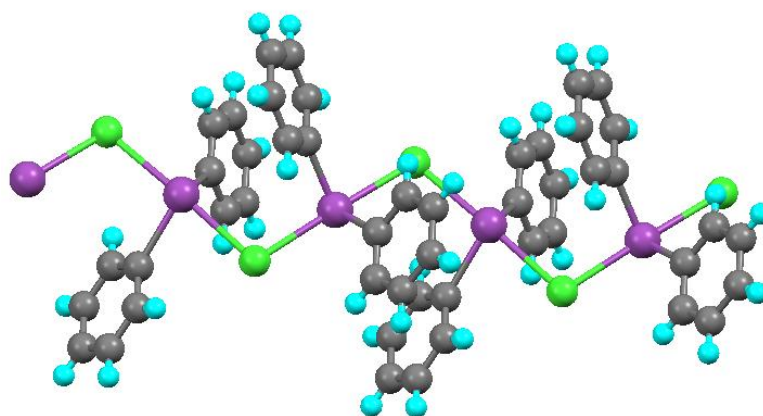


Figure 6-9: The molecular structure of diphenylbismuth chloride.³⁸²

Comparing the structure shown in Figure 6-9 with that of diphenyliodonium chloride³⁷⁶ (Figure 6-10) shows that there is a difference in the secondary interactions in bismuth(III) compounds and iodine(III) compounds. In the iodine(III) structure the I...Cl interaction is along the extension of the C–I bond with a C–I...Cl angle of 179.33°, whereas in the bismuth(III) structure the Bi...Cl interaction is along the extension of the Bi–Cl bond with a Cl–Bi...Cl angle of 175.6(3)° and is perpendicular to the C–Bi bonds. This leads to a square-planar geometry at the iodine atom, whereas the bismuth centre adopts a pseudo-trigonal bipyramid geometry. The interaction in the bismuth complex is significantly stronger with a Bi...Cl separation of 2.746(3) Å, which is 68% of the sum of the van der Waals radii, whereas the I...Cl separation in the diphenyliodonium chloride is 3.065(2) Å, 82% of the sum of the van der Waals radii.

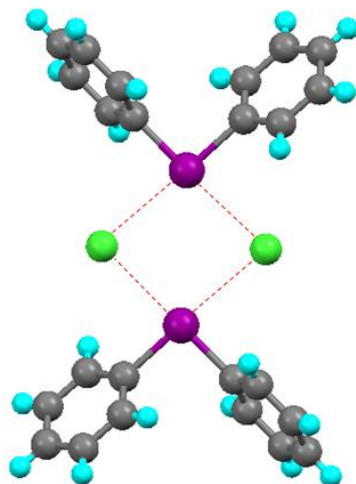


Figure 6-10: The molecular structure of diphenyliodonium chloride.³⁷⁶ I \cdots Cl $^-$ interactions are highlighted in red.

The structure of diphenyliodonium tetrafluoroborate is similar to that of the chloride salt with the iodine centre interacting with the fluorine atoms of two tetrafluoroborate anions with an I \cdots F separation of 2.947(4) Å (85% of the sum of the van der Waals radii), leading to a formally tetra-coordinated centre. The main difference between the two structures is the deviation of the C–I \cdots F angle at 152.5(8)° from linearity causing the geometry at iodine not to be square-planar (Figure 6-11).³⁸³ This is due to a weak I \cdots F contact with a second fluorine atom on the tetrafluoroborate anion with $r(\text{I}\cdots\text{F}) = 3.395(4)$ Å, which is 98% of the sum of the van der Waals radii for iodine and fluorine and a C–I \cdots F and of 150.9°.

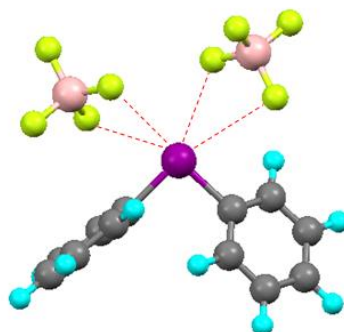


Figure 6-11: The molecular structure of diphenyliodonium tetrafluoroborate.³⁸³ One cation has been omitted for clarity. I \cdots F interactions are highlighted in red.

Deviations from the square-planar geometry have also been observed for a diphenyliodonium ion with a diethylaminocarbamate anion, Figure 6-12,³⁸⁴ and for a diphenyliodonium ion with intramolecular interactions, Figure 6-13.³⁸⁵

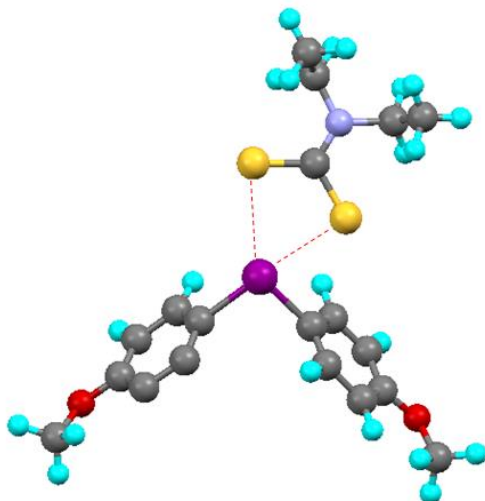


Figure 6-12: The molecular structure of [bis(p-methoxyphenyl)](diethylaminocarbamate)iodine(III).³⁸⁴ I...S interactions are shown in red.

Figure 6-12 shows that one sulfur atom of the diethylaminocarbamate anion interacts with the iodine of the diphenyliodonium ion with an I...S separation of 2.926(3) Å, 77.4% of the sum of the van der Waals radii and an almost linear C–I...S angle of 176.1(5)°. The second sulfur atom has an interaction that deviates substantially from linearity with a C–I...S angle of 125.7(5)° and is much longer at 3.286(4) Å, 86.9% of the sum of the van der Waals radii.

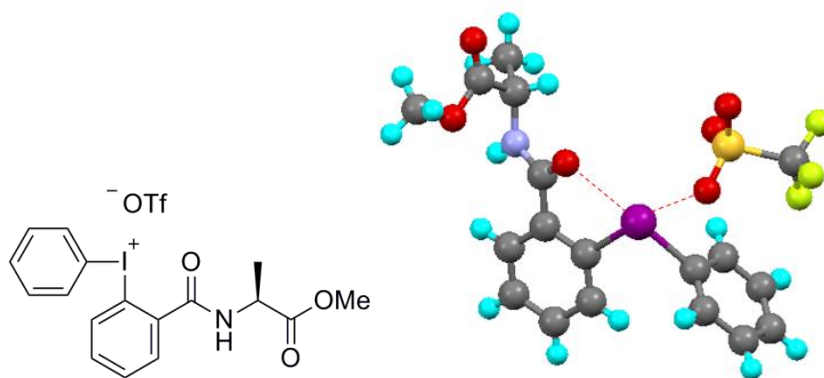


Figure 6-13: The molecular structure of phenyl(2-(1-(methoxycarbonyl)ethylaminocarbonyl)phenyl)iodonium trifluoromethanesulfonate.³⁸⁵ I...O interactions are shown in red.

The intramolecular separation between the iodine atom and the oxygen of the amide group in the structure shown in Figure 6-13 is 2.615(5) Å, 74.7% of the sum of the van der Waals radii and a C–I...O angle of 164.6(2)°, which is close to linearity. The triflate anion is also coordinated to the iodine atom with I...O separations of 3.008(7) and 3.320(5) Å, respectively, 85.9 and 94.9% of the sum of the van der Waals radii, respectively, and C–I...O angles of 162.9(2) and 151.3(2)°, respectively.

Interactions between diphenyliodonium ions with nitrogen bases have been observed in the molecular structures of complexes of diphenyliodonium tetrafluoroborate with 1,10-phenanthroline (Figure 6-14a)³⁸⁰ and pyridine (Figure 6-14b).³⁸⁶ The two I...N separations in the structure with 1,10-phenanthroline are 2.926(4) and 3.162(4) Å, which are 82.9 and 89.6% of the sum of the van der Waals radii, respectively. The I...N separation in the complex with pyridine is similar at 2.864(2) Å, which is 81.1% of the sum of the van der Waals radii. The iodine atom in the complex with pyridine has a square-planar geometry with a C–I...N angle of 175.74(8)°. The presence of two nitrogen atoms in 1,10-phenanthroline leads to a penta-coordinated iodine atom with C–I...N angles of 164.4(2) and 140.8(2)°, respectively. The difference in these angles highlights that one I...N interaction is slightly stronger and that the interaction with the 1,10-phenanthroline is not symmetrical.

The interaction with a fluorine atom of the tetrafluoroborate ion is similar in both structures. The I···F separations are 3.012(8) and 2.976(3) Å, (87.3% and 86.3% of the sum of the van der Waals radii, respectively), in the structures with 1,10-phenanthroline and pyridine, respectively. The C–I···F angles are 173.9(2)° and 167.72(7)°, respectively.

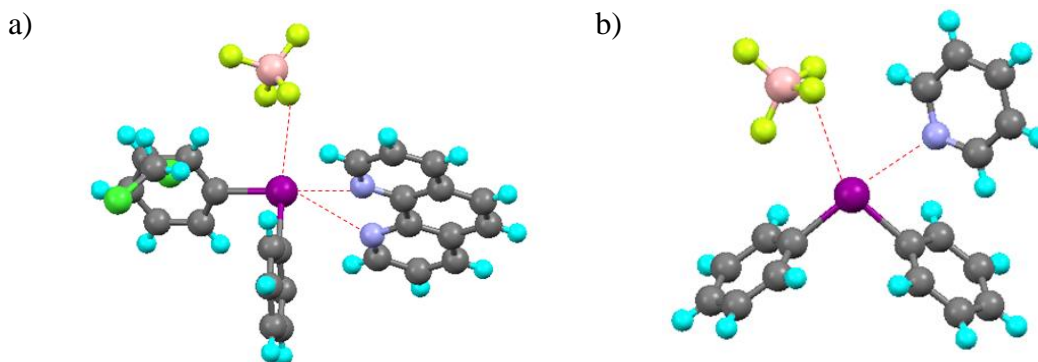


Figure 6-14: The molecular structure of a) diphenyliodonium tetrafluoroborate. 1,10-phenanthroline³⁸⁰ and b) diphenyliodonium tetrafluoroborate.pyridine.³⁸⁶ I···F and I···N interactions are shown in red.

In the majority of structures of diphenyliodonium salts, the iodine atom interacts with the counteranion and so, in order to form a structure with two nitrogen bases interacting with the iodine centre, the counteranion needs to be weakly coordinating. The tetraphenylborate salt of diphenyliodonium has a weakly coordinating anion. The crystal structure is shown in Figure 6-15.³⁸⁷

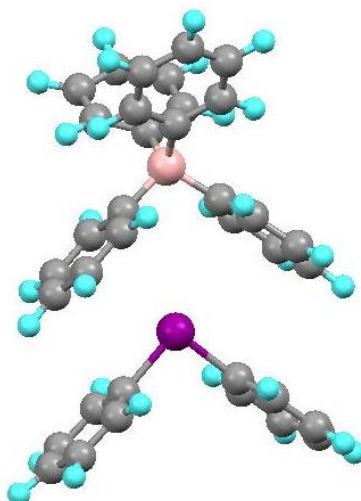


Figure 6-15: The molecular structure of diphenyliodonium tetraphenylborate.³⁸⁷

The plane of the phenyl ring of the diphenyliodonium cation is not quite parallel to the plane of the phenyl ring in the tetraphenylborate anion; the angle between the two planes is 1.46° . The distance between the centroids of the two rings is 4.777 \AA . The iodine atom in the diphenyliodonium cation interacts with the π electron density of the phenyl ring in the tetraphenylborate anion with the separation between the iodine atom and the ring centroid of the phenyl ring equal to 3.487 \AA , which is 95% of the sum of the van der Waals radii of iodine and carbon. The angle between the C–I bond and the centroid deviates from linearity at 164.87° , which suggests that the interaction is weaker than those observed in other examples, thus an interaction with a Lewis base would be expected to be favoured over an interaction with the tetraphenylborate anion.

6.1.5 Bis(pyridine)halonium Cations

Another example of a stable halonium ions are bis(pyridine) and bis(*sym*-collidine) halonium cations, which involve two pyridyl nitrogen atoms bonded to the halogen atom. The mechanism of halogen transfer from bis(*sym*-collidine) bromonium triflate to AdAd has been investigated and involves the formation of a complex between AdAd bromonium ion and *sym*-collidine (Figure 6-16).³⁸⁸ Within this complex the pyridyl nitrogen interacts with the bromine atom of the bromonium atom of AdAd in

a similar manner to that desired in this project. Although the complex has not been isolated in the solid state, kinetic measurements reveal an inverse first-order rate with [*sym*-collidine] suggesting the presence of one *sym*-collidine in the reactive species.

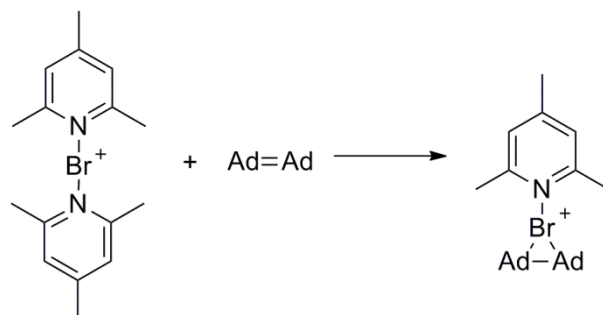


Figure 6-16: The bromine transfer reaction between bis(*sym*-collidine)bromonium triflate and AdAd.

A similar mechanism was postulated for bromine atom transfer from bis(pyridine)bromonium triflate to adamantylidene adamantane.³⁸⁹ Although the crystal structures of the proposed complexes with AdAd have not been obtained, those of bis(*sym*-collidine)bromonium perchlorate and bis(pyridine)bromonium triflate have and are shown in Figure 6-17.

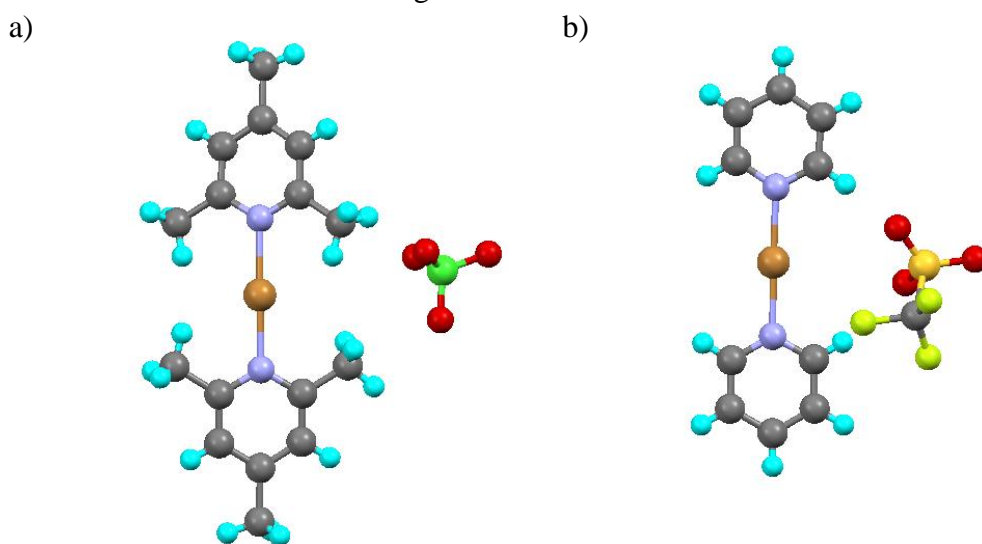


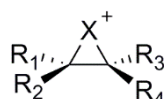
Figure 6-17: The crystal structures of a) bis(*sym*-collidine)bromonium perchlorate and b) bis(pyridine)bromonium triflate.

The Br–N separations in the two structures are similar; in the bis(*sym*-collidine)bromonium perchlorate they are 2.086(6) and 2.144(6) Å, and in the bis(pyridine)bromonium triflate they are 2.074(4) and 2.107(4) Å. These distances are significantly longer than the sum of the covalent radii, which is 1.84 Å, and significantly shorter than the sum of the van der Waals radii at 3.40 Å. The N–Br–N angles deviate slightly from linearity and are 176.2(2) and 178.4(2)°, respectively. This nearly linear arrangement is consistent with bromine being $sp^3d_z^2$ hybridised.³⁹⁰

The bonding in bis(pyridine)halonium cations has been investigated using quantum chemical methods.³⁹¹ Analysis of the thermochemistry of the dissociation of pyridine, energy decomposition analysis and molecular orbitals revealed that the N–I bonds in the bis(pyridine)iodonium cation can be viewed as N→I dative in nature. Wiberg bond indices (WBIs), which are calculated from the sum of the bond orders, serve as indicators of where along the bonding continuum, from a covalent bond to a weak interaction, a particular interaction between two atoms can be placed.³⁹² A covalent bond has a WBI equal to 1, the WBIs of dative bonds lie in the range of 0.3 – 0.8 dihalogen bonds have a WBI much smaller than 0.3.³⁹¹ The WBI for the I–N bond in the bis(pyridine)iodonium cation is 0.43, whereas the WBI in the I⋯N halogen bond in a complex between molecular iodine and 4,4'-bipyridine is 0.25, showing that these dative bonds are stronger than typical halogen bonds. Therefore the X–N bonds in the bromonium and chloronium ions can be considered as more covalent than dative. The fluoronium ion was found to have unsymmetrical F–N bonds; one, with an F–N length of 1.336 Å, which can be considered as a covalent bond and the second, with an F⋯N separation of 2.724 Å, corresponding to a weak dispersion interaction.

6.2 Aim

A series of halonium ions of substituted ethenes and their complexes with ammonia and pyridine, shown in Table 6-1, have been investigated using computational approaches. These were selected because the cyclic bridged halonium ion can be characterised experimentally³⁷⁰ and, in the case of the bromonium ion, has been shown to be the preferred intermediate of the electrophilic bromination reaction.³⁵⁷

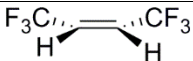
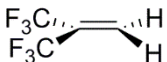
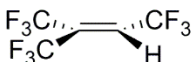
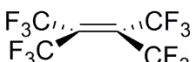
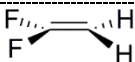
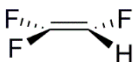
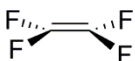


Scheme 6-1: The labelling of the halogen and substituents of the halonium ions.

Table 6-1: The variation of the halogen atom and the substituents of the halonium ions.

Halonium Ion	Ethene	X	R ₁	R ₂	R ₃	R ₄
1		Cl	H	H	H	H
2		Br	H	H	H	H
3		I	H	H	H	H
4		Br	CH ₃	H	H	H
5		Br	CH ₃	H	H	CH ₃
6		Br	CH ₃	H	CH ₃	H
7		Br	CH ₃	CH ₃	H	H
8		Br	CH ₃	CH ₃	CH ₃	H
9		Br	CH ₃	CH ₃	CH ₃	CH ₃
10		Br	CF ₃	H	H	H
11		Br	CF ₃	H	H	CF ₃

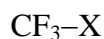
Table 6-1: (Continued).

12		Br	CF ₃	H	CF ₃	H
13		Br	CF ₃	CF ₃	H	H
14		Br	CF ₃	CF ₃	CF ₃	H
15		Br	CF ₃	CF ₃	CF ₃	CF ₃
<hr/>						
19		Br	F	F	H	H
20		Br	F	F	F	H
21		Br	F	F	F	F

Halonium ions **1** – **3** have been chosen to investigate the effect of the halogen atom on the interaction, while **4** – **9** were included to investigate the effect of electron-donating methyl substituents. The effect of the positions of the methyl substituents are investigated by comparing isomers **5** – **7**. The effect of electron-withdrawing trifluoromethyl and fluorine substituents on the interaction is investigated by comparing complexes with halonium ions **10** – **15** and **16** – **21**, respectively.

The bases chosen to form an interaction with the halonium ions used in this investigation are ammonia, **NH₃**, pyridine, **py**, and water, **H₂O**. The latter was chosen because a single crystal structure exists with an I⁺...O interaction.³⁵⁰

In order to make comparisons to conventional halogen bonds, complexes between trifluoromethylhalides and ammonia have also been investigated, which involve halogen-bond donors **22** – **24**, Scheme 6-2.



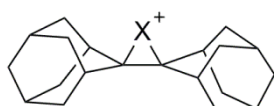
22: X = Cl

23: X = Br

24: X = I

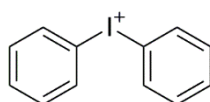
Scheme 6-2: The traditional halogen-bond donors, trimethylhalides.

Although ethylene halonium ions have been characterised in the gas phase, they have not been isolated in the solid state. It was therefore necessary to include complexes that include halonium ions that are isolable in the solid state such as the halonium ions of AdAd, **25** and **26**, and diphenyliodonium ions, **27**, Scheme 6-3.



25: X = Br

26: X = I



27

Scheme 6-3: The complexes between stable halonium ions and ammonia and pyridine, which were investigated.

Following geometry optimisations, structure and bonding in these complexes were analysed in detail using natural bond orbital (NBO) analysis and localised molecular orbitals (LMOs).

In order to try to compare theoretical with experimental results, diphenyliodonium salts and AdAd halonium ions, which are stable halonium ions, will be synthesised and attempts made to crystallise them with Lewis bases.

6.3 Computational Method

Monomer and complex geometries were optimised at the MP2/aug-cc-pVDZ level of theory. The aug-cc-pVDZ-PP basis set, which includes an effective core potential (ECP), was used for iodine. Vibrational frequencies were calculated to ensure that the optimised geometries corresponded to local minima on the respective potential

energy surfaces. The MP2 calculations were carried out using the MP2(Full) keyword to include correlation effects for all electrons. All geometry optimisation were carried out within Gaussian09.²²⁶

In order to be able to carry out reliable DFT calculations on complexes with the bromonium ion of AdAd and the diphenyliodonium ion, it is necessary to identify the DFT functional which is most appropriate for studying molecular systems of this type. In Chapters 3 and 5, the performances of different density functionals at modelling weak halogen-bonded complexes with rare gas atoms and the intermediates of the electrophilic bromination of stilbenes, respectively, were assessed. Generally the M06 suite of functionals are found to perform well³⁴³ and the M06-2X functional was found to perform best at modelling intermediates of electrophilic bromination of stilbenes.³⁴⁴ It could, therefore, be assumed that these functionals would perform best for modelling the complexes between halonium ions and Lewis bases. These complexes are significantly stronger, however, than other complexes investigated so the geometries of complexes **1**·NH₃, **2**·NH₃, **3**·NH₃ and **9**·NH₃ were optimised using the B3LYP, M06, M06L, M06-2X, M06HF, B97-D, X3LYP and PBE DFT functionals within the aug-cc-pVDZ basis set and compared to results at the MP2/aug-cc-pVDZ level of theory, see Figure 6-18. All DFT calculations were carried out using the Gaussian ‘UltraFine’ pruned integration grid. These complexes were chosen since they include all types of halogen and represent the stronger and weaker complexes in this study.

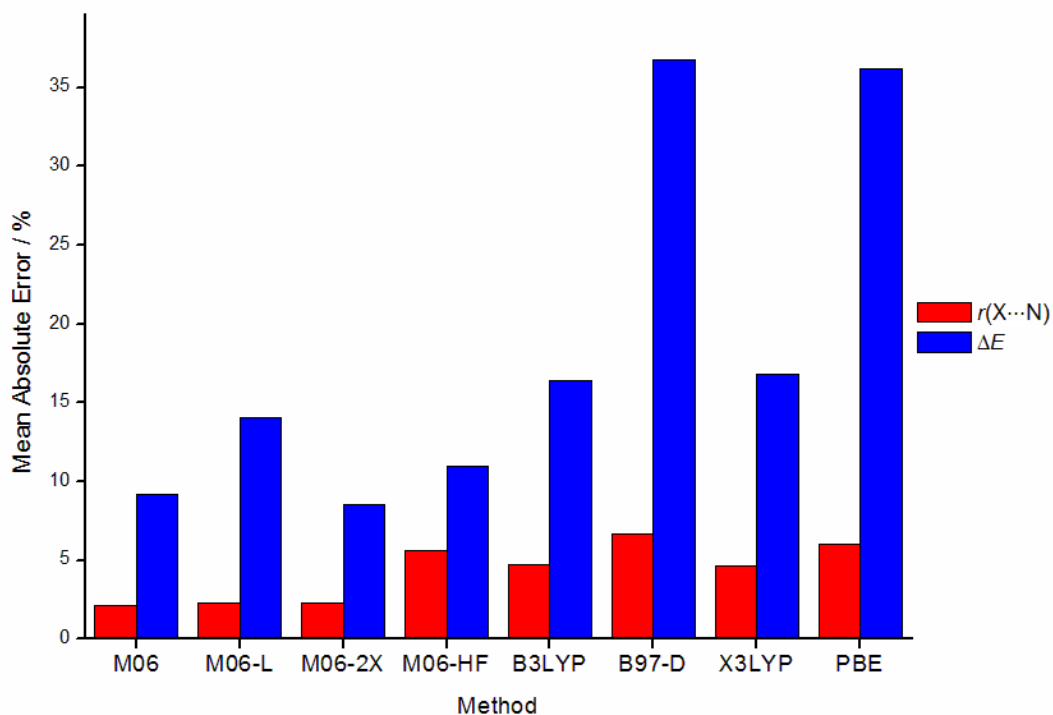


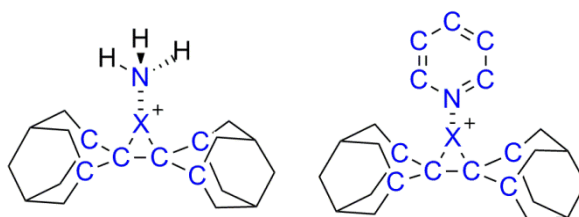
Figure 6-18: The mean absolute percentage errors in the $r(X\cdots N)$ separations as a percentage of the sum of the van der Waals radii and the binding energies for complexes of **1** – **3** and **9** with NH_3 calculated using different density functionals and the aug-cc-pVDZ basis set compared to results obtained at the MP2(Full)/aug-cc-pVDZ level of theory.

Figure 6-18 shows that the B3LYP, B97-D, X3LYP and PBE functionals perform poorly for these complexes in particular for the binding energy, which they were generally found to overestimate. The M06-HF functional performs better but the errors in the $X\cdots N$ separations are significantly larger than for the other M06 functionals. The M06-2X functional performs best when the binding energies are considered so this functional was used to study complexes with adamantylidene adamantane halonium ions and diphenyliodonium ions.

Geometries of the bromonium and iodonium ions of AdAd and their complexes with ammonia, pyridine and water (**25**· NH_3 , **26**· NH_3 , **25**·py, **26**·py and **26**· OH_2) were optimised at the M06-2X level of theory. The aug-cc-pVDZ basis set was used on the carbon atoms closest to the halonium ion, the nitrogen and carbon atoms in the base and the halogen atoms; the aug-cc-pVDZ-PP basis set was used for iodine. The

cc-pVDZ basis set was used for all remaining carbon atoms and all hydrogen atoms.

Scheme 6-4 shows the atoms described with the aug-cc-pVDZ basis set.



Scheme 6-4: The atoms in complexes of halonium ions **25** and **26** for which the aug-cc-pVDZ basis set was used (highlighted in blue). The basis set used for all other atoms was cc-pVDZ.

Scans of the potential energy surfaces were carried out by calculating single point energies, at the MP2(Full)/aug-cc-pVDZ level of theory whilst varying the angles θ and ϕ , as defined in Figure 6-19, with a step of 10° . These were rigid scans of the potential energy surface without geometry re-optimisation at each point. The position of the nitrogen atom of the ammonia was projected onto the xy -plane, which is the plane that passes through the halogen atom and is parallel to the C–C bond and the binding energies were plotted against the x and y coordinates to give three-dimensional plots.

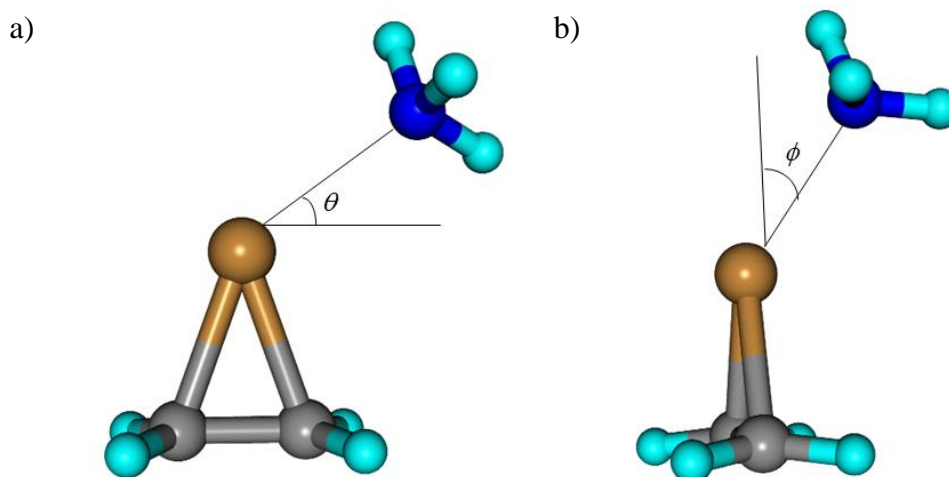


Figure 6-19: The definition of angles a) θ and b) ϕ .

The Hartree-Fock (HF) molecular orbitals in the aug-cc-pVDZ basis were localised using the Edmiston-Ruedenberg localisation procedure in GAMESS-US.²⁸⁶ The outputs of the calculations were visualised using Molekel.²²⁸

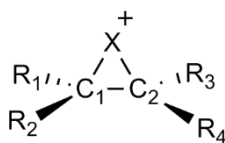
NBO analyses were carried out at the MP2/aug-cc-pVDZ optimised geometries using NBO version 3 implemented in Gaussian 09. The 3CBOND and RESONANCE keywords were used to help identify the 3-centre-2-electron bond in the halonium ion.

The geometries of all complexes were optimised using energy expressions including the Boys-Bernardi counterpoise (CP) correction for the basis set superposition error (BSSE).¹⁰⁶ The binding energies for these complexes were calculated by means of the equation $\Delta E = E_{\text{complex}} - \sum_{\text{all monomers}} E_{\text{monomer}}$.

6.4 Computational Results

6.4.1 Geometry Optimisation of Halonium Ion Monomers

The optimised geometries of the halonium ion monomers in complexes **1** – **21** were found to be bridged isomers. The C–C–X angles and C–X bond lengths, defined using the atom numbers shown in Scheme 6-5, are given in Table 6-2.

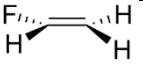
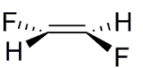
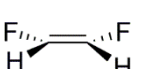
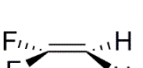

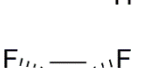


Scheme 6-5: The numbering of the atoms in the halonium ions intermediates.

Table 6-2: The C–X bonds and CCX angles in the MP2(Full)/aug-cc-pVDZ optimised geometries of the halonium ions **1** – **19**.

Halonium Ion	Ethene	X	$r(\text{C}_1\text{-X}) / \text{Å}$	$r(\text{C}_2\text{-X}) / \text{Å}$	$\alpha(\text{C}_1\text{C}_2\text{X}) / ^\circ$	$\alpha(\text{C}_2\text{C}_1\text{X}) / ^\circ$
1		Cl	1.881	1.881	67.07	67.07
2		Br	2.025	2.025	68.83	68.83
3		I	2.231	2.231	70.96	70.96
4		Br	2.084	2.018	71.54	66.70
5		Br	2.067	2.067	69.25	69.25
6		Br	2.069	2.069	69.21	69.21
7		Br	2.156	2.010	74.84	64.17
8		Br	2.126	2.055	72.00	66.83
9		Br	2.103	2.103	69.38	69.38
10		Br	2.007	2.030	67.93	69.58
11		Br	2.012	2.012	68.68	68.68
12		Br	2.014	2.014	68.55	68.55
13		Br	1.998	2.032	69.91	67.42
14		Br	2.005	2.015	68.87	68.15
15		Br	2.011	2.011	68.20	68.20

Table 6-2: (Continued)

16		Br	2.129	2.014	65.25	73.76
17		Br	2.075	2.075	69.31	69.31
18		Br	2.088	2.088	69.44	69.44
19		Br	2.444	1.981	89.41	54.15
20		Br	2.347	1.992	83.85	57.55
21		Br	2.116	2.116	69.51	69.51

The data in Table 6-2 show that halonium ions **1 – 3**, **5**, **6**, **9**, **11**, **12**, **15**, **17**, **18** and **21** are symmetrical with equal C₁-X and C₂-X bond lengths and C₁C₂X and C₂C₁X angles; this result may have been expected because the ethene is symmetrical. Halonium ions **19** and **20** are carbocation intermediates as characterised by the large differences in the C-X bond lengths and C₁-C₂-X angles approaching 90°. The remaining halonium ions are slightly unsymmetrical, although the optimised geometries correspond to bridged halonium ion intermediates. In **4**, **7** and **8**, the C-X bond closest to the larger number of methyl substituents, C₁-X, is slightly longer. In **10**, **13** and **14** it is the C-X bond furthest from the largest number of trifluoromethyl substituents, C₂-X, that is longer.

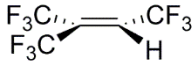
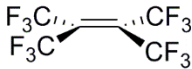
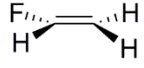
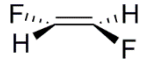
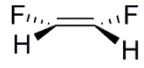
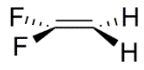


Natural population analysis (NPA) within the natural bond orbital analysis (NBO) was carried out on each of the halonium ions in order to investigate how the halogen and substituents affect the charges on the halogen atom and the C₁ and C₂ atoms (see Table 6-3). As the halogen becomes more polarisable (**1 – 3**) the positive charge on the halogen atom increases and the charge on the carbon atoms becomes more negative. The introduction of methyl substituents (**4 – 9**) reduces the positive charge on the halogen atom and the charge on the carbon atoms increases. The charge on the

halogen atom is greater than on the carbon atoms so the halonium ions can be classified as bridged halonium ions. The presence of trifluoromethyl substituents (**10** – **15**) causes the positive charge on the halogen atom to increase and the charges on the carbon atoms to become more negative.

Table 6-3: Charges on the halogen atoms of the halonium ions included in this study calculated using natural population analysis for geometries optimised at the MP2(Full)/aug-cc-pVDZ level of theory.

Halonium Ion	Ethene	X	Charge		
			C ₁	C ₂	X
1		Cl	-0.200	-0.200	0.269
2		Br	-0.273	-0.273	0.406
3		I	-0.351	-0.351	0.565
4		Br	-0.036	-0.300	0.349
5		Br	-0.070	-0.070	0.311
6		Br	-0.068	-0.068	0.308
7		Br	0.202	-0.332	0.296
8		Br	0.159	-0.104	0.271
9		Br	0.117	0.117	0.246
10		Br	-0.232	-0.250	0.466
11		Br	-0.211	-0.211	0.526
12		Br	-0.205	-0.205	0.527
13		Br	-0.192	-0.236	0.524

Table 6-3: (Continued)

14		Br	-0.165	-0.197	0.581
15		Br	-0.147	-0.147	0.636
16		Br	0.496	-0.381	0.349
17		Br	0.372	0.372	0.355
18		Br	0.380	0.380	0.334
19		Br	1.318	-0.569	0.239
20		Br	1.228	0.156	0.263
21		Br	0.959	0.959	0.339

Halonium ions with fluorine substituents (**16** – **21**) show a different behaviour. Thus, while it would be expected that the introduction of electron-withdrawing substituents would lead to an increase in the positive charge of the halogen atom, the charge is in fact lower than that for **2** and the carbon atoms have larger positive charges than the halogen atom. This observation is particularly pronounced in halonium ions **19** and **20**, which were found to have carbocation intermediates and feature a large positive charge on carbon atom, C_1 . This suggests that these halonium ions cannot be classified as bridged halonium ions and should not be considered further in this study. This is also supported by shapes of the localised molecular orbitals, see Figure 6-20. Rather than observing an LMO that is delocalised along the C_1 - C_2 -Br ring corresponding to a 3-centre-2-electron bond, there are two LMOs that are similar to C-Br σ -bonding orbitals. One explanation for this observation could be that although fluorine acts as an electron-withdrawing group through induction ($\sigma_I = 0.52$) it acts as an electron-donating group through resonance ($\sigma_R = -0.33$).³⁵⁹

Therefore the fluorine removes electron density from the carbon atoms leading to an increase in charge and donates electron density from its lone pair of electrons through resonance to the bromine atom causing its charge to decrease.

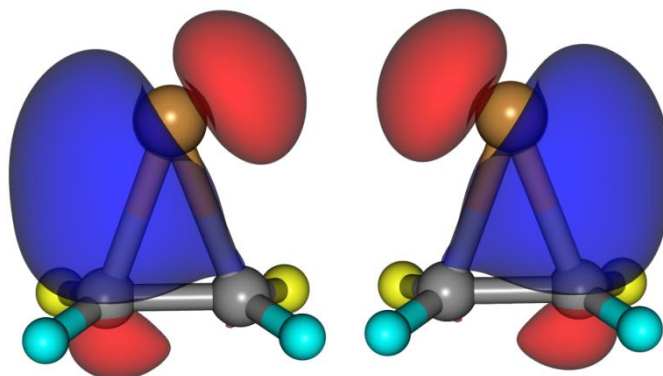


Figure 6-20: The localised molecular orbitals of halonium ion **18** (formed from Z-CHF=CHF) corresponding to the C–Br σ -bonding orbitals. Orbitals are represented as isosurfaces at orbital values of ± 0.05 (e/bohr⁻³)^{1/2}.

6.4.2 Geometry Optimisation of Complexes with Ammonia

The halogen...nitrogen separations and the binding energies of the MP2(Full)/aug-cc-pVDZ optimised geometries of complexes of **1** – **15** with NH₃ are shown in Table 6-4.

Table 6-4: The $r(X\cdots N)$ separations and binding energies of halonium ions **1** – **15** with NH_3 optimised at the MP2(Full)/aug-cc-pVDZ level of theory.

Halonium ion	Ethene	X	$r(X\cdots N) / \text{\AA}$	% Σ vdW radii	$\Delta E / \text{kJ mol}^{-1}$
1		Cl	2.555	77.4	54.96
2		Br	2.526	74.3	71.62
3		I	2.481	70.3	95.66
<hr/>					
4		Br	2.580	75.9	64.68
5		Br	2.635	77.5	58.41
6		Br	2.631	77.4	58.49
7		Br	2.610	76.8	59.30
8		Br	2.668	78.5	53.76
9		Br	2.708	79.7	49.59
<hr/>					
10		Br	2.334	68.7	81.40
11		Br	2.181	64.2	92.69
12		Br	2.169	63.8	90.90
13		Br	2.189	64.4	92.81
14		Br	2.054	60.4	101.96
15		Br	1.956	57.5	118.87

As the halogen atom becomes more polarisable in complexes **1** – **3** with NH_3 , the complexes become stronger, similar to conventional halogen bonds, due to the

increase in positive charge on the halogen atom (*vide infra*) as it becomes more polarisable.

Compared to conventional halogen bonds, see Table 6-5, the separations are noticeably shorter and the binding energies of complexes involving halonium ions are considerably larger.

Table 6-5: The halogen...nitrogen separations and binding energies of complexes $\text{CF}_3\text{X}\cdots\text{NH}_3$.

Complex	$r(\text{X}\cdots\text{N}) / \text{\AA}$	% ΣvdW radii	$\Delta E / \text{kJ mol}^{-1}$
$\text{CF}_3\text{Cl}\cdots\text{NH}_3$	3.128	94.8	10.17
$\text{CF}_3\text{Br}\cdots\text{NH}_3$	3.068	90.2	15.20
$\text{CF}_3\text{I}\cdots\text{NH}_3$	3.037	86.0	23.07

Introducing electron-donating methyl groups to the bromonium ion (**4 – 9**) weakens the interaction due to electron donation, which reduces the positive charge on the bromine atom as observed in the natural population analysis (NPA) (Table 6-3). This corroborates the observation that methyl substituents stabilise the bromonium ion intermediates of ethene.³⁵⁷ Comparison of complexes of **5 – 7** with NH_3 , all of which have two methyl substituents on the bromonium ion, shows that the relative disposition of these groups makes little difference to the strength of the complex with ammonia.

The introduction of electron-withdrawing groups to the bromonium ion (complexes of **11 – 15** with NH_3) strengthens the complex since this leads to an increase in the charge on the bromine atom (see Table 6-3). In the case of complexes of **14** and **15** with NH_3 , the bromine atom has transferred from the halonium ion to the nitrogen atom of the ammonia (*vide infra*). Furthermore, the charge on the halogen atom in the halonium ion exhibits a linear correlation with the binding energy of its complex with ammonia calculated at the MP2(Full)/aug-cc-pVDZ level of theory, see Figure 6-21, suggesting that the interaction is predominantly electrostatic in nature.

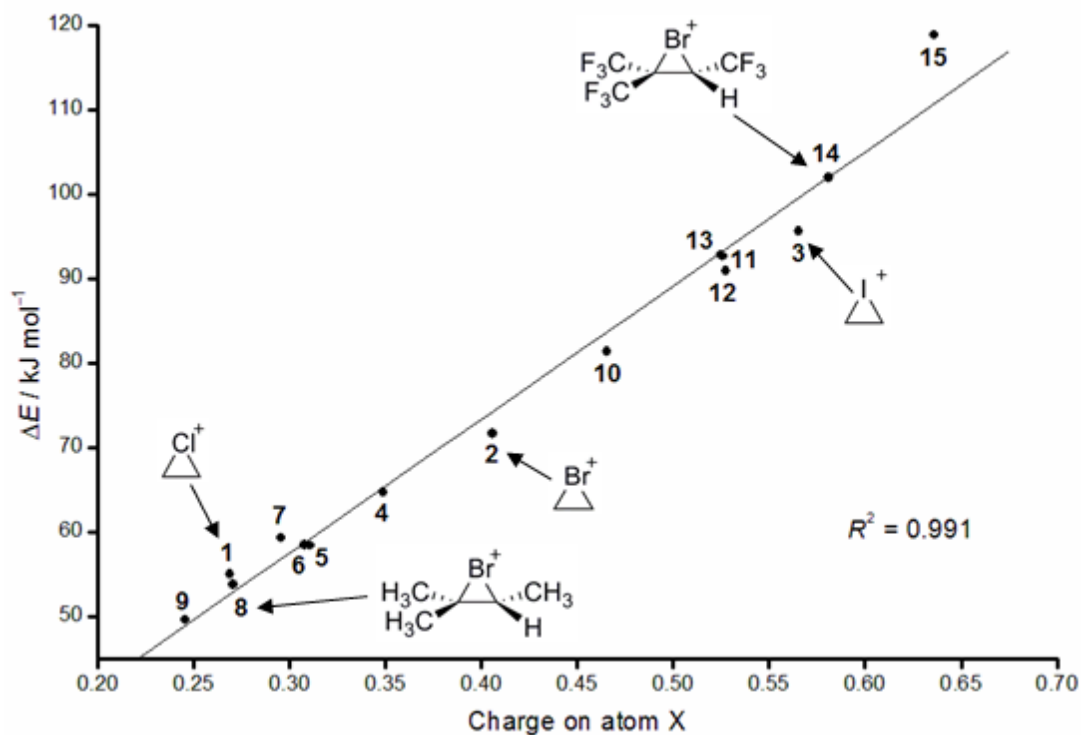


Figure 6-21: The relationship between the charge of the halogen atom in the halonium ion and the binding energy of the complex with ammonia calculated at the MP2(Full)/aug-cc-pVDZ level of theory.

The effect of electron-donating and electron-withdrawing substituents on the strength of the complexes with the halonium ions can also be observed clearly using the sum of the Hammett parameters, σ_p , of the substituents, which has a linear relationship with the binding energies of the complexes (Figure 6-22).

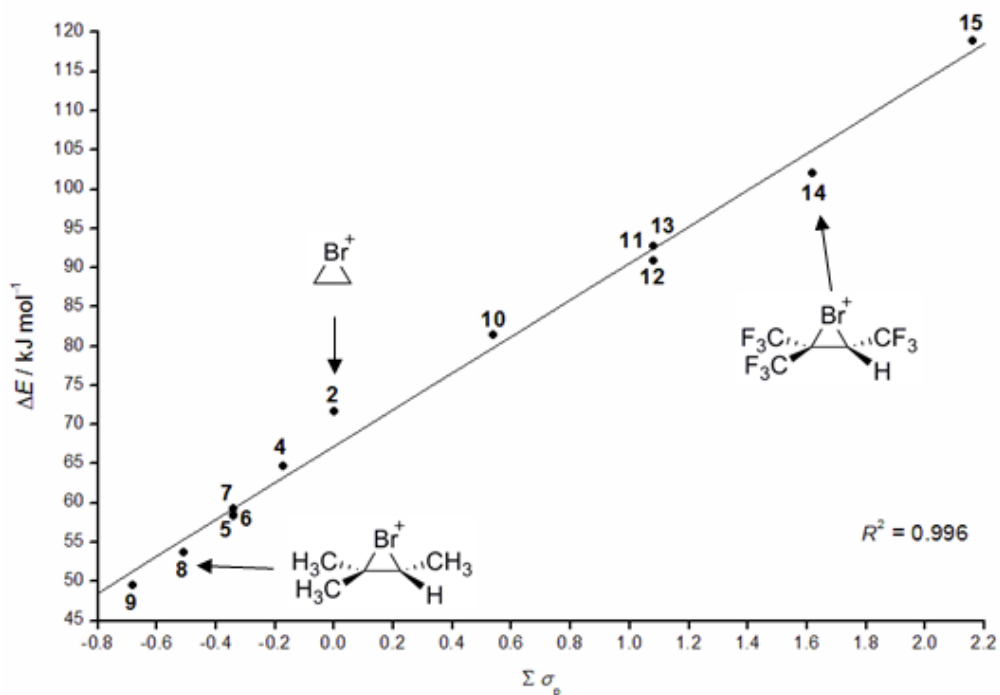


Figure 6-22: The relationship between the binding energy and the sum of the Hammett parameters of the substituents, σ_p , for complexes **2** and **4 – 15**.

6.4.3 Localised Molecular Orbitals

The molecular orbitals were localised using an Edmiston-Ruedenberg localisation procedure and two of the key orbitals for complex **2**·**NH**₃ are shown in Figure 6-23.

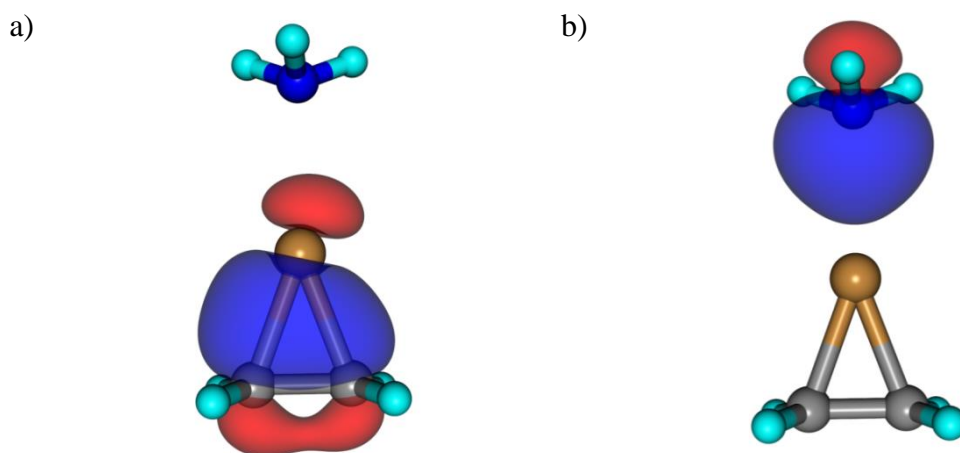


Figure 6-23: The localised molecular orbitals (LMO) for complex **2**·**NH**₃ representing the a) 3-centre-2-electron bond of the bromonium ion of ethene and b) the lone pair of electrons on the nitrogen atom of ammonia. Orbitals are represented as isosurfaces at orbital values of ± 0.05 (e/bohr⁻³)^{1/2}.

There is an orbital representing the 3-centre-2-electron bond of the bromonium ion of ethene, similar to those observed for the bromonium ion intermediates of stilbenes with two electron-withdrawing substituents (see Chapter 5). The observation that the orbital is not symmetrical is unexpected since the bromonium ion and its complex with ammonia are symmetrical. This was also observed when the Boys localisation procedure was used, showing that this result is not due to the choice of localisation procedure. In order to understand this further, the LMOs representing lone pairs of electrons on the bromine atom should be considered as shown in Figure 6-24.

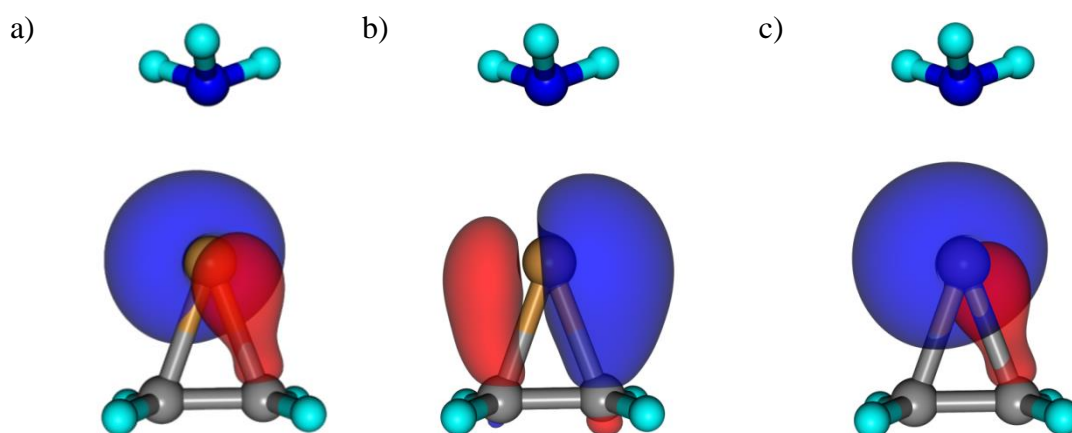


Figure 6-24: The LMOs corresponding to the lone pair of electrons on the bromine atom of the bromonium ion in complex $2 \cdot \text{NH}_3$. Orbitals are represented as isosurfaces at orbital values of ± 0.05 ($\text{e}/\text{bohr}^{-3}$)^{1/2}.

The LMOs show that there is a significant contribution from these orbitals to the C–Br bonds in the bromonium ion particularly for the LMO shown in Figure 6-24b, which could account for the lack of symmetry for the LMO representing the 3-centre-2-electron bond in Figure 6-23a.

The LMOs in Figures 6-23a and 6-24 were then calculated for a series of complexes where the Br– π distance was increased whilst the position of the ammonia was kept fixed with respect to the bromine atom, see Figure 6-25.

As the $r(\text{Br}-\pi)$ separation increases, the distortion of the LMO representing the lone pair of electrons on Br over the C–Br bonds decreases until it has a form typical for a

lone pair of electrons at $r(\text{Br}-\pi) = 2.30 \text{ \AA}$. The LMO representing the 3-centre-2-electron bond becomes more symmetrical as the $r(\text{Br}-\pi)$ separation increases, suggesting that the lack of symmetry at the optimised geometry is due to an interaction with the LMOs in Figure 6-24b. Increasing the $r(\text{Br}-\pi)$ separation further shows that the orbital corresponding 3-centre-2-electron bond transforms into the ethene π orbital, see Figure 6-25c.

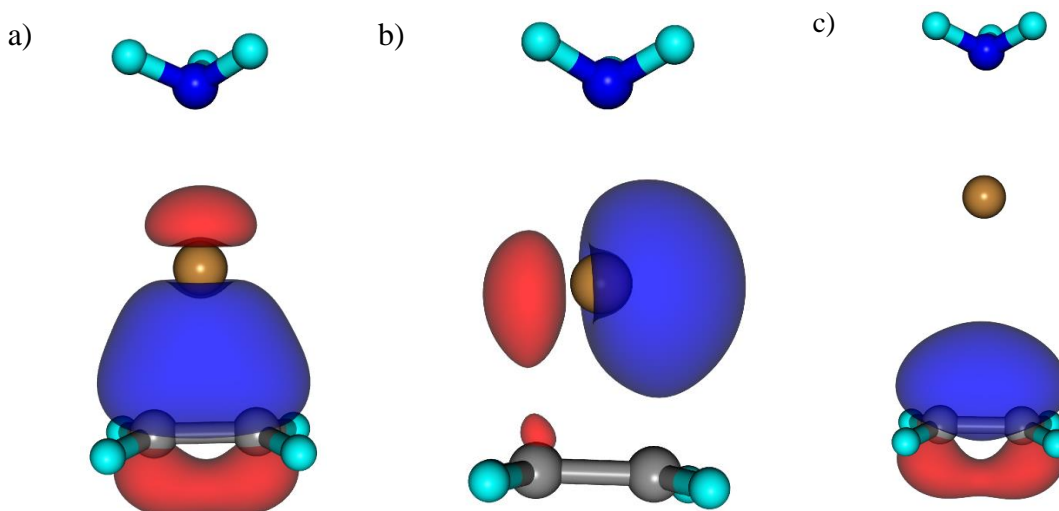


Figure 6-25: The LMOs corresponding to a) the 3-centre-2-electron bond of the bromonium ion of ethene, b) the lone pair of electrons on bromine at $r(\text{Br}-\pi) = 2.30 \text{ \AA}$ and c) the 3-centre-2-electron bond in the bromonium ion of ethene at $r(\text{Br}-\pi) = 4.0 \text{ \AA}$. Orbitals are represented as isosurfaces at orbital values of $\pm 0.05 (\text{e}/\text{bohr}^{-3})^{1/2}$.

The contribution from the bromine atom at $r(\text{Br}-\pi) = 4.00 \text{ \AA}$ is so small that it cannot be seen at the isosurface level chosen for Figure 6-25c. There is also an LMO representing the lone pair of electrons on the nitrogen of the ammonia that is directed towards the bromine atom in the bromonium ion, see Figure 6-23b. These electrons are able to interact with the positive charge on the bromine atom to form a halogen bond.

It is possible to compare a series of complexes, **1** – **3** with NH_3 , in order to investigate the effect of changing the halogen atom on the form of the LMO. Figures 6-23b and 6-26 show that as the halogen becomes larger and more polarisable, the

LMO representing the lone pair of electrons on the nitrogen atom of ammonia becomes distorted in the region approaching the halogen atom. This suggests that there is a degree of charge transfer as the complexes become stronger, which corroborates the results of the NBO analysis.

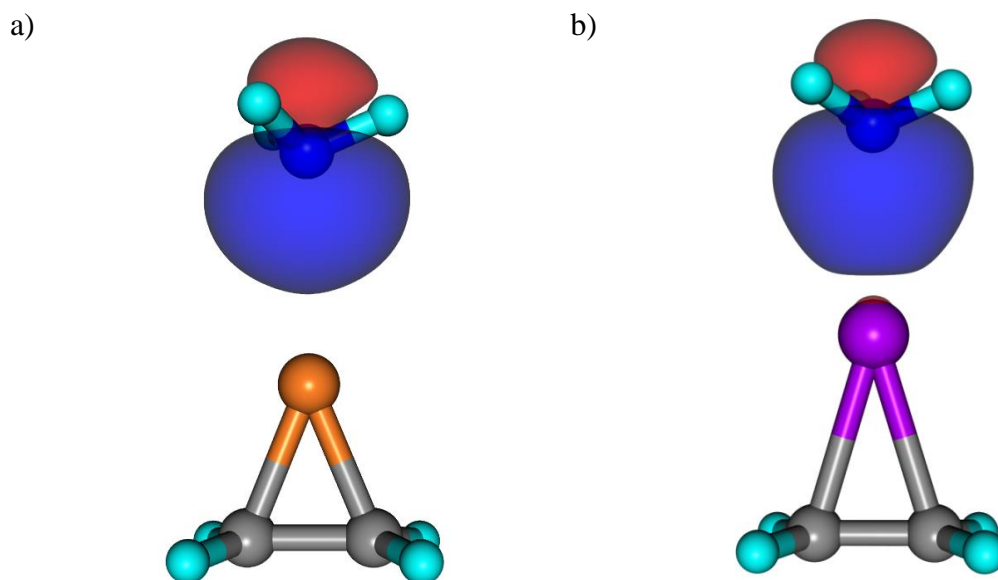


Figure 6-26: The localised molecular orbitals (LMOs) representing the lone pair of electrons on ammonia for a) complex **1·NH₃** and b) complex **3·NH₃**. Orbitals are represented as isosurfaces at orbital values of ± 0.05 (e/bohr^{-3})^{1/2}.

6.4.4 Complexes with Pyridine

Complexes of **1** – **10** with pyridine as the Lewis base are stronger than the corresponding complexes with ammonia. The halogen···nitrogen separations and binding energies for the MP2(Full)/aug-cc-pVDZ optimised geometries are shown in Table 6-6. Complexes of **11** – **15**, which have multiple electron withdrawing CF₃ groups, with pyridine have not been included due to the prohibitively large computational effort required.

Table 6-6: The $r(\text{X}\cdots\text{N})$ separations, distances between the halogen and the centres of the carbon-carbon bonds, $r(\text{X}\cdots\pi)$, and binding energies for MP2(Full)/aug-cc-pVDZ optimised geometries of complexes of **1** – **10** with pyridine.

Halonium Ion	X	$r(\text{X}\cdots\text{N}) / \text{\AA}$	% Σ vdW radii	$r(\text{X}\cdots\pi) / \text{\AA}$	$\Delta E / \text{kJ mol}^{-1}$
1	Cl	1.924	58.3	2.370	96.41
2	Br	2.007	59.0	2.520	134.37
3	I	2.295	65.0	2.481	143.79
4	Br	2.137	62.8	2.349	106.98
5	Br	2.178	64.0	2.264	93.75
6	Br	2.181	64.1	2.265	93.89
7	Br	2.167	63.7	2.224	96.52
8	Br	2.210	65.0	2.209	84.83
9	Br	2.252	66.2	2.202	76.35
10	Br	2.019	59.4	2.496	146.20

The strengths of the complexes follow the same trend as the equivalent complexes with ammonia as the base, becoming stronger as the halogen becomes more polarisable and with the introduction of electron-withdrawing substituents on the halonium ion. In these complexes the halogen – nitrogen separation is very short and the binding energy is large, so that in some cases (complexes of **1**, **2** and **10** with pyridine) the halogen atom could be considered to have transferred from the halonium ion to the pyridine similar to the observation made for the complexes of **14** and **15** with NH_3 .

6.4.5 NBO Analysis

In halogen bonding involving traditional halogen-bond donors such as $\text{CF}_3\text{-X}$, there is typically transfer of charge from the lone pair of electrons on the Lewis base to the C-X σ^* anti-bonding orbital, leading to a lengthening of the C-X bond upon complex formation.

NBO analyses of the complexes between the halonium ions and ammonia shows that there is similar charge transfer from the lone pair of electrons on the nitrogen atom of the ammonia to the anti-bonding, 3-centre orbital on the halogen and central carbon atoms. The occupancies of these two NBOs and the stabilisation energies calculated from perturbation theory energy analyses are shown in Table 6-7.

Table 6-7: Occupancies of the NBOs corresponding to the lone pair of electrons on the nitrogen atom of ammonia and the anti-bonding orbitals of the 3-centre Br-C-C orbital and the stabilisation energy ΔE_{ij} of the interaction between these orbitals for complexes of **1** – **13** with NH₃.

Halonium Ion	X	Occupancy LP(N)	Occupancy 3C*(XCC)	$\Delta E_{ij} / \text{kJ mol}^{-1}$
1	Cl	1.968	0.078	30.10
2	Br	1.904	0.091	126.36
3	I	1.824	0.170	275.11
4	Br	1.920	0.085	100.48
5	Br	1.935	0.090	81.94
6	Br	1.934	0.092	83.40
7	Br	1.928	0.080	85.62
8	Br	1.941	0.094	71.59
9	Br	1.949	0.106	62.89
10	Br	1.807	0.172	260.17
11	Br	1.668	0.318	602.23
12	Br	1.655	0.331	715.89
13	Br	1.676	0.311	577.57

The occupancies of the lone pair on the nitrogen atom and of the anti-bonding orbital of the 3-centre-2-electron bond should add up to two electrons, however, this is not always observed to be the case. The largest deviations are observed for the complexes of halonium ions **9** and **10**, where the occupancies of the two NBOs add

up to 2.055 and 1.979, respectively. The reasons for these deviations are associated with donation from the lone pair of electrons on the nitrogen into Rydberg orbitals of the bromine atom and donation of electrons from the N–H bonding orbitals on the ammonia into the anti-bonding orbital over the 3-centre bond on the halonium ion. These donor-acceptor interactions have a negligible stabilisation energy so it can be assumed that the main donor-acceptor interaction present in the complexes is that from the lone pair of electrons on the nitrogen into the anti-bonding orbital over the 3-centre bond on the halonium ion.

The stronger complexes (**3**·NH₃ and **10** – **13**·NH₃) have larger stabilisation energies indicating that there is a higher degree of charge transfer in these complexes. This is also characterised by the decrease in occupancy of the nitrogen lone pair NBO and the increase in occupancy of the anti-bonding orbital over the 3-centre bond on the halonium ion.

The charge transfer observed is likely to lead to an elongation of the C–X bonds due to the increase in occupancy in the 3-centre anti-bonding orbital. The elongation can be observed by comparing the distances between the halogen atom and the centre of the C–C bond, $r(X-\pi)$, in the halonium ion monomers and in the complexes with ammonia, see Table 6-8.

Table 6-8: The X- π separation in the halonium ions **1** – **13** and in complexes with NH₃.

Halonium ion	X	$r(X-\pi) / \text{\AA}$		
		Monomer	Complex	% Difference
1	Cl	1.732	1.769	2.14
2	Br	1.888	1.999	5.88
3	I	2.109	2.327	10.34
4	Br	1.914	1.947	1.72
5	Br	1.933	1.998	3.36
6	Br	1.934	2.003	3.57
7	Br	1.941	2.012	3.66
8	Br	1.955	2.009	2.76
9	Br	1.968	2.012	2.24
10	Br	1.881	2.106	11.96
11	Br	1.874	2.255	20.33
12	Br	1.874	2.280	21.66
13	Br	1.877	2.246	19.66

The data in Table 6-8 show that for all complexes there is a significant elongation of the X- π separation upon complex formation. This elongation increases as the complex becomes stronger.

NBO analyses show that in the complexes of **14** and **15** with NH₃, halogen transfer has taken place and the halogen atom is bonded to the nitrogen of the ammonia rather than to the carbon atoms in the halonium ion, which in these complexes are very much linked by a π bond as in an isolated ethene (see Table 6-9). There is an orbital interaction involving the C-C π -bond and the σ^* anti-bonding orbital of the Br-N bond. The stabilisation energy of this interaction is larger for **14**·NH₃ indicating that a greater degree of charge transfer to bromine transfer has occurred.

Table 6-9: The Occupancies of the NBOs corresponding to the C–C π bond and σ^* anti-bonding orbitals of the Br–N bond in the complexes of **14** and **15** with ammonia. Stabilisation energies for the interaction between these two orbitals are also provided.

Halonium ion	X	Occupancy π NBO (C–C)	Occupancy σ^* NBO (Br–N)	$\Delta E_{ij} / \text{kJ mol}^{-1}$
14	Br	1.764	0.181	251.21
15	Br	1.894	0.041	47.86

NBO analyses (Table 6-11) show that halogen transfer has taken place for complexes of **1**, **2** and **10** with pyridine. Complexes of **3** – **9** with pyridine are similar to the equivalent complex with ammonia as the base and have an interaction from the lone pair of electrons on the nitrogen and the anti-bonding orbital over the 3-centre bond between the halogen and two central carbon atoms, see Table 6-10.

Table 6-10: The occupancies of the NBOs corresponding to the lone pair of electrons on the nitrogen of pyridine and the antibond of the 3-centre XCC bond and stabilisation energies of the interaction between these two orbitals for complexes of **3** – **9** with pyridine.

Halonium ions	X	Occupancy LP(N)	Occupancy 3C*(XCC)	$\Delta E_{ij} / \text{kJ mol}^{-1}$
3	I	1.706	0.265	508.03
4	Br	1.650	0.327	641.96
5	Br	1.699	0.284	503.09
6	Br	1.696	0.285	510.16
7	Br	1.686	0.303	515.44
8	Br	1.730	0.264	406.75
9	Br	1.767	0.233	335.57

As the complexes become weaker with the introduction of electron-donating methyl substituents, the stabilisation energy decreases suggesting a decrease in charge transfer. This is also observed in the increase in occupancy of the lone pair on

nitrogen and a decrease in occupancy of the anti-bonding orbital over the 3-centre bond of the halonium ion.

Complexes where halogen transfer has taken place can be identified by the presence of a X–N σ NBO and a π NBO for the central C–C bond, and the absence of a 3-centre-2-electron bond in the halonium ion. In these complexes the predominant stabilising interaction is from the C–C π bond to the X–N σ^* NBO.

Table 6-11: The occupancies of the C–C π NBO, X–N σ^* NBO and stabilisation energies of the interaction between these two orbitals for complexes of **1**, **2** and **10** with pyridine.

Halonium ion	X	Occupancy π NBO (C–C)	Occupancy σ^* NBO (X–N)	$\Delta E_{ij} / \text{kJ mol}^{-1}$
1	Cl	1.737	0.260	320.38
2	Br	1.771	0.228	282.23
10	Br	1.779	0.204	256.86

The localised molecular orbitals involved in the interactions of these two types of complexes are shown in Figure 6-27.

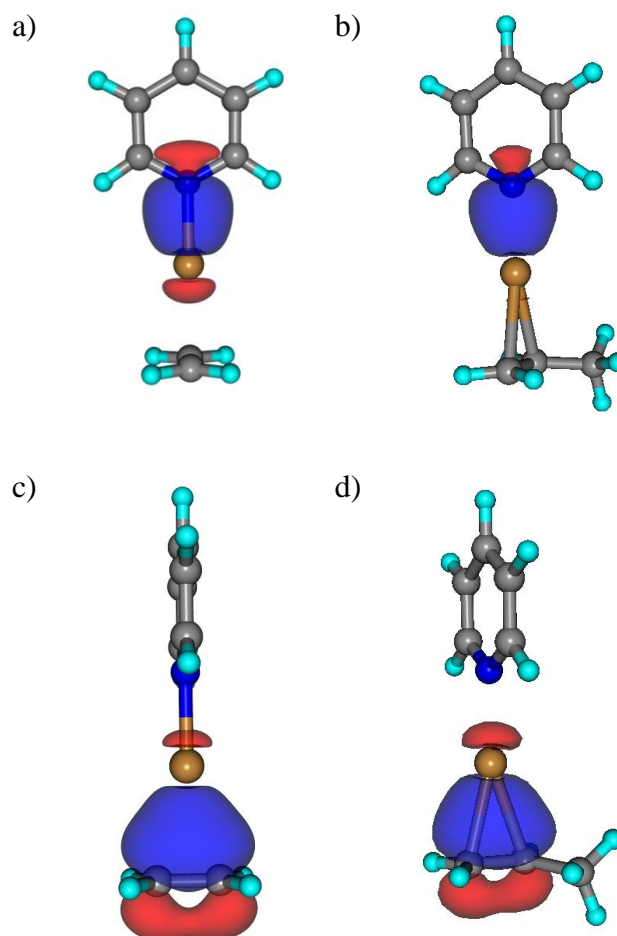


Figure 6-27: The localised molecular orbitals representing a) the Br-N σ -bond in complex **2.py**, b) the lone pair of electrons on N in complex **4.py**, c) the C-C π -bond of complex **2.py** and d) the 3-centre-2-electron bond in complex **4.py**. Orbitals are represented as isosurfaces at orbital values of ± 0.05 ($\text{e}/\text{bohr}^{-3}$)^{1/2}.

There is a similarity between the localised molecular orbitals in both types of complex irrespective of whether the halogen has transferred from the halonium ion to the pyridine. This suggests that although the NBO analysis optimises the structures as different Lewis structures, the bonding is very similar. The halogen atom should therefore not be described as bonded to the pyridine nitrogen atom or to the carbon atoms of the ethene but as intermediate between these two Lewis structures.

The Wiberg bond indices (WBI) of the halogen...nitrogen interaction and the C-X bonds in the complexes can be calculated within the NBO analysis in order to

determine the nature of the bonds. This approach has been used to distinguish between covalent bonds, dative bonds and halogen bonds.³⁹¹

Table 6-12 shows that the WBIs of the X...N interaction for complexes of **1** – **10** with NH₃, where the base is ammonia, are in the range 0.03 – 0.25, which is similar to the value observed for traditional halogen bonds.

Table 6-12: The WBI of the X...N interaction and C-X bonds in complexes of **1** – **15** with NH₃ and of **1** – **10** with pyridine.

Halonium Ion	X	Complexes with ammonia			Complexes with pyridine		
		WBI (X...N)	WBI (C ₁ -X)	WBI (C ₂ -X)	WBI (X...N)	WBI (C ₁ -X)	WBI (C ₂ -X)
1	Cl	0.034	0.768	0.0768	0.648	0.187	0.187
2	Br	0.116	0.661	0.661	0.608	0.178	0.178
3	I	0.242	0.463	0.463	0.377	0.310	0.310
4	Br	0.094	0.602	0.703	0.413	0.290	0.354
5	Br	0.076	0.651	0.651	0.344	0.368	0.368
6	Br	0.077	0.648	0.648	0.340	0.371	0.371
7	Br	0.084	0.524	0.732	0.360	0.284	0.418
8	Br	0.086	0.583	0.685	0.294	0.361	0.432
9	Br	0.057	0.630	0.630	0.234	0.434	0.434
10	Br	0.243	0.539	0.505	0.633	0.166	0.156
11	Br	0.435	0.341	0.341			
12	Br	0.453	0.326	0.326			
13	Br	0.424	0.373	0.326			
14	Br	0.647	0.161	0.163			
15	Br	0.809	0.035	0.035			

These WBIs are slightly larger in magnitude than those for complexes $\text{CF}_3\text{X}\cdots\text{NH}_3$, see Table 6-13, indicating that the interactions are stronger than in the complexes included in Table 6-12.

Table 6-13: The WBIs of the $\text{X}\cdots\text{N}$ interaction in complexes $\text{CF}_3\text{X}\cdots\text{NH}_3$.

Complex	WBI($\text{X}\cdots\text{N}$)
$\text{CF}_3\text{-Cl}\cdots\text{NH}_3$	0.0075
$\text{CF}_3\text{-Br}\cdots\text{NH}_3$	0.0165
$\text{CF}_3\text{-I}\cdots\text{NH}_3$	0.0372

The WBIs of the $\text{X}\cdots\text{N}$ interaction complexes of **1** – **10** with NH_3 are smaller than that for the $\text{I}\cdots\text{N}$ interaction in the complex between iodine and 4,4'-bipyridine, (0.253),³⁹¹ showing that these interactions are weaker than the strongest halogen bonds.

The WBIs of the C-X bonds of complexes of **1** – **10** with NH_3 are less than unity showing that the bonds are not covalent bonds. This is anticipated since the carbon and halogen atoms are involved in a 3-centre-2-electron bond, therefore the WBIs correspond to this type of bonding. The WBIs increase with the introduction of methyl substituents and decrease when an electron-withdrawing trifluoromethyl group is present. This shows that the WBIs and therefore the strengths of the C-X bonds decrease as the strength of the complex increases.

The WBIs of the $\text{X}\cdots\text{N}$ interaction complexes of **11** – **15** with NH_3 and of **1** – **10** with pyridine are significantly larger than those for the complexes of **1** – **10** with ammonia (Table 6-12). The WBIs of complexes of **8** and **9** with pyridine, which are weaker complexes due to the presence of electron-donating methyl substituents, are in the range of strong halogen bonds. The remaining complexes have WBIs in the range of 0.33 to 0.65, which is in the range of dative bonds and are similar to the value for the I-N bonds in the bis(pyridine)iodonium cation.³⁹¹ The general trend is

for the WBIs to increase as the complexes become stronger, see Figure 6-28, suggesting that the WBI of the X...N separation is a good indication of the strength of the interaction. There are exceptions to this trend including **1·py** and **3·py** and complexes of **11 – 15** with ammonia. The latter have binding energies that are lower than would be expected from the WBI of the X...N interaction, suggesting that the WBI fails for particularly strong complexes and when bromine transfer has occurred.

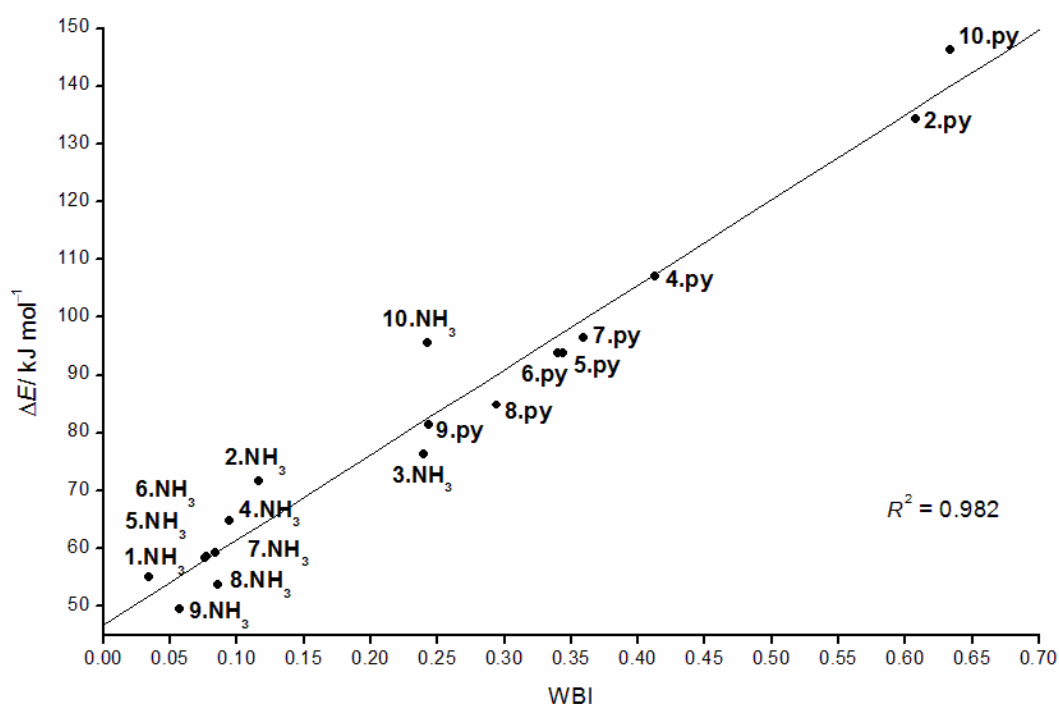


Figure 6-28: The variation of the binding energies of complexes of **1 – 10** with ammonia and pyridine with the WBI of the X...N interaction.

The WBIs of the C–X bonds in the complexes of **1 – 10** with pyridine are smaller than those in the complexes of **1 – 10** with ammonia. In the case of the strongest complexes (*e.g.* **10·py**) the WBI shows that the bonds correspond to non-covalent interactions between the bromine and the carbon atoms. Similar to the complexes with ammonia, the WBI decreases as the strength of the complex increases showing that the halogen atom moves away from the C–C bond as the complexes become stronger.

6.4.6 Application of the Steiner-Limbach Equation

The halogen atom in complexes of **1** – **10** with pyridine is observed to change from being bonded to the carbon atoms in the halonium ion to forming a bond with the pyridyl nitrogen. This is similar to the transfer of the chlorine atom from the halogen bond donor to the Lewis base in complexes between FCl and isocyanides as the base becomes stronger.²¹⁹ In the latter complexes, the Steiner-Limbach equation, Equation 2-1, which was discussed in Chapter 2, was found to provide a suitable model for the bonding.

$$(r_1 + r_2) = 2r_{02} + (r_1 - r_2) + 2b \ln \left[1 + \exp \left\{ \frac{(r_{01} - r_{02} - r_1 + r_2)}{b} \right\} \right] \quad (2-1)$$

It was therefore appropriate to apply the Steiner-Limbach equation to the complexes between bromonium ions and Lewis bases, (complexes involving the chloronium and iodonium ions were not included because the Steiner-Limbach equation only applies to systems where the atoms involved in the non-covalent interaction are identical for all complexes). The value of r_1 was taken to be the separation between the halogen and the centre of the carbon-carbon bond and r_2 was taken to be the Br...N separation.

The parameters of the Steiner-Limbach equation were optimised for the bromonium ion complexes and were used to produce a Steiner-Limbach plot for these complexes (Figure 6-29).

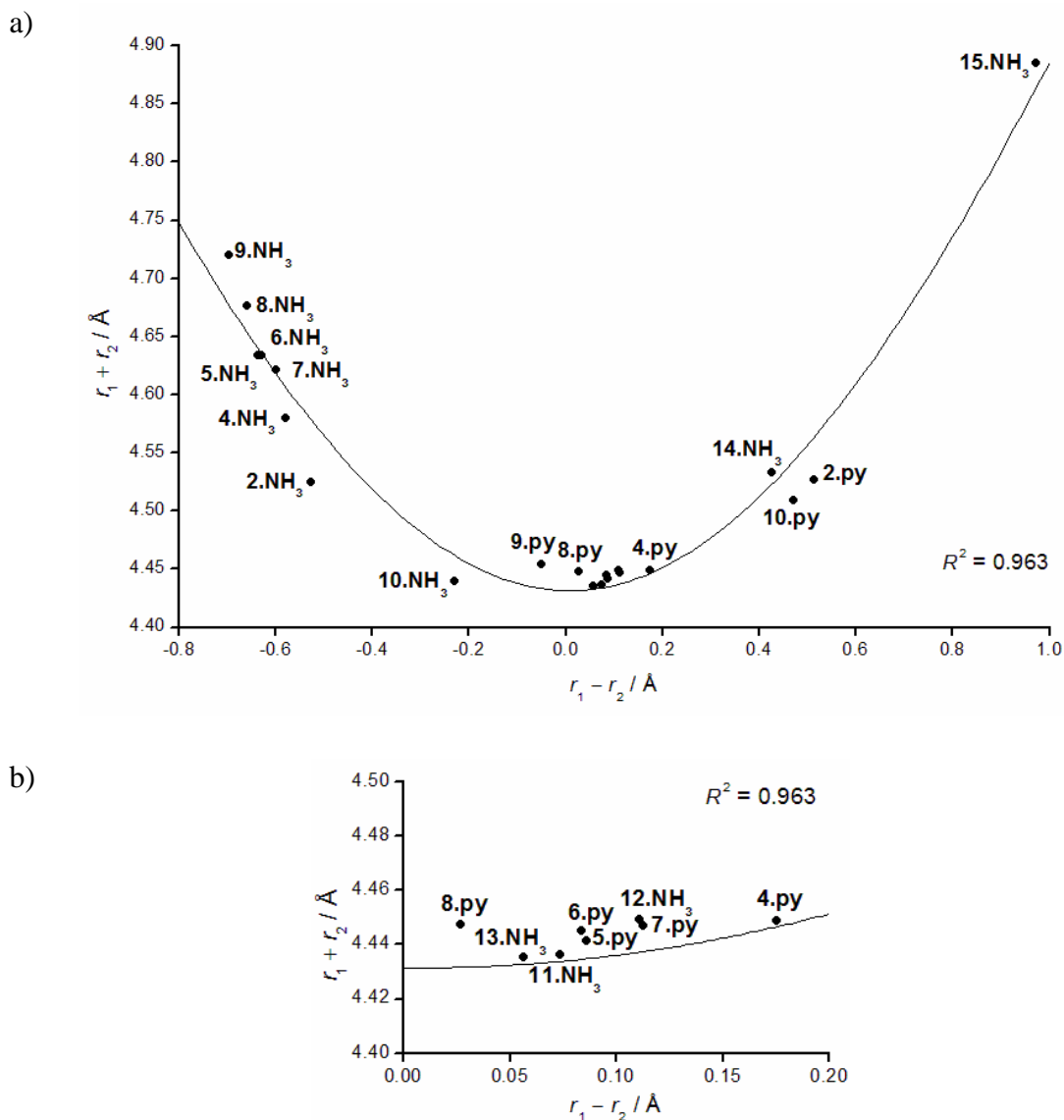


Figure 6-29: a) Steiner-Limbach plot for complexes of **2** and **4 – 15** with NH_3 and pyridine and b) expansion in the region $0.0 < r_1 - r_2 < 0.2$. The line represents the optimised Steiner-Limbach equation with $r_{01} = 1.899 \text{ \AA}$, $r_{02} = 1.892 \text{ \AA}$ and $b = 0.461$. The average and maximum residuals, e_{av} and e_{max} , are 0.0173 and 0.0532, respectively.

The fact that the bonding in these complexes can be modelled by the Steiner-Limbach equation shows that the interactions in these complexes are similar to traditional hydrogen and halogen bonds.

The optimised value of r_{01} is 1.899, which is similar to the $\text{Br} \cdots \pi$ separation in the bromonium ion of ethene (1.888 \AA), where π is the centre of the C–C bond. The

optimised value of r_{02} is 1.892 Å, which is between the Br–N bond in $[\text{C}_5\text{H}_5\text{NBr}]^+$, which is 1.879 Å and the Br–N bond in $[\text{H}_3\text{NBr}]^+$, which is 1.912 Å.

In Chapter 2, a new parameter was introduced to the Steiner-Limbach equation and was found to improve the goodness of fit for complexes between fluorohalides and isocyanides.³⁹³ The goodness-of-fit for hydrogen-bonded complexes, where the three-parameter Steiner-Limbach equation (in the form shown in Equation 2-7) gave a very good fit, could not be improved by the introduction of a new parameter.

$$r_2 = r_{02} - b \ln \left(1 - \exp \left(\frac{r_{01} - r_1}{b} \right) \right) \quad (2-7)$$

A similar conclusion is reached in the case of these complexes of halonium ions. Figure 6-30 shows the fit of the three-parameter Steiner-Limbach equation in its form in Equation 2-7 to these complexes. The goodness of fit is similar to that for the Steiner-Limbach equation in its original form in Equation 2-1. The optimised values of r_{01} and r_{02} are 1.875 and 1.862 Å, respectively, which are slightly smaller than those values obtained for the original Steiner-Limbach equation (Figure 6-29) making them slightly further from the Br $\cdots\pi$ separation in the bromonium ion of ethene and the Br–N distances in the $[\text{C}_5\text{H}_5\text{NBr}]^+$ and $[\text{H}_3\text{NBr}]^+$ cations, respectively. This highlights that, similar to hydrogen-bonded and halogen-bonded complexes, there are benefits to having the Steiner-Limbach equation in its original form.

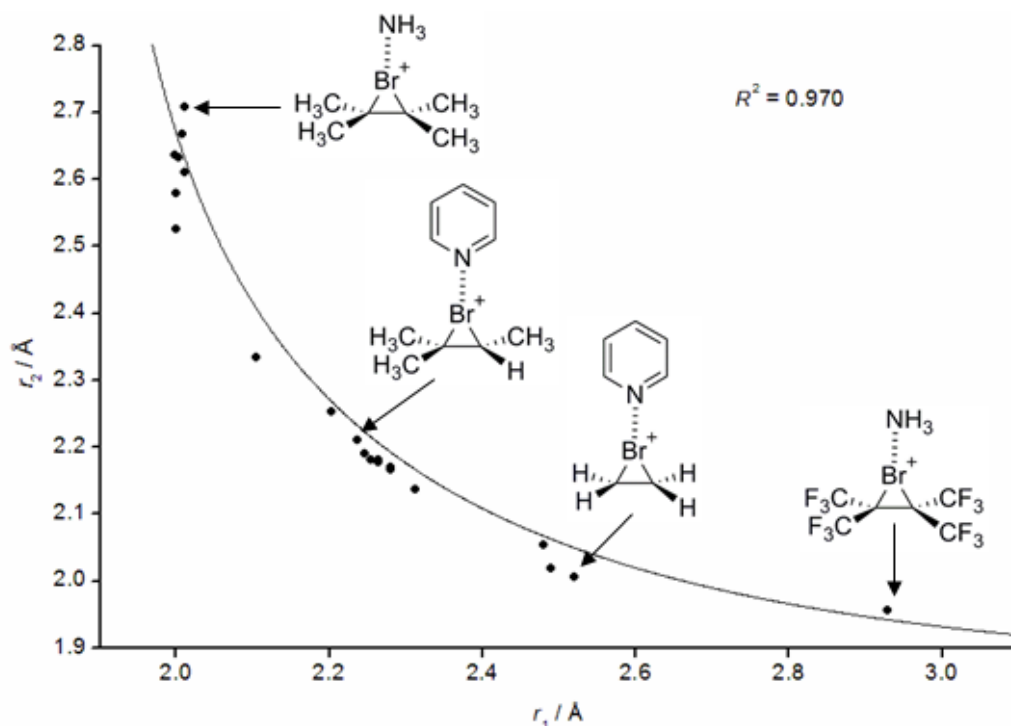


Figure 6-30: Plot showing the fit of the three-parameter Steiner-Limbach relationship in its r_2 vs. r_1 form (Equation 2-7) for complexes of **2** and **4-15** with NH_3 and pyridine. The curve represents the optimised 3-parameter Steiner-Limbach equation with $r_{01} = 1.875 \text{ \AA}$, $r_{02} = 1.862 \text{ \AA}$ and $b = 0.507244$. The average and maximum residuals, e_{av} and e_{max} , are 0.0253 and 0.1145, respectively.

Attempts to use the four-parameter Steiner-Limbach equation (Equation 2-10) to these complexes were unsuccessful because the optimised parameters were identical to those obtained with the three-parameter equation with b_1 equal to b_2 . This shows that these complexes behave similar to hydrogen-bonded complexes and three parameters are sufficient for describing the bonding.

$$r_2 = r_{02} - b_2 \ln \left(1 - \exp \left(\frac{r_{01} - r_1}{b_1} \right) \right) \quad (2-10)$$

6.4.7 Directionality of Interactions with Halonium Ions

The halogen-bond interaction is strongly directional, favouring a linear arrangement, which can be rationalised by the σ -hole on the halogen atom,³⁸ however, in halonium

ions, the positive charge is distributed more evenly around the halogen atom, which could affect the directionality.

Three-dimensional plots showing the variation of binding energy at different angles of approach of the ammonia were made by plotting the binding energy against the projection of the position of the nitrogen atom of ammonia onto the xy -plane, see Figure 6-31. The x -axis is defined as that pointing along the C–C bond in the halonium ion and the y -axis is perpendicular to the C–C bond. Plots were constructed for both traditional halogen bonds in the $\text{CF}_3\text{X}\cdots\text{NH}_3$ complexes and complexes of **1** – **3** with NH_3 , so that the effect of the halogen could be investigated.

Figures 6-31a, c and e show the binding energy plot for traditional halogen-bond donors, CF_3X , $\text{X} = \text{Cl}, \text{Br}$ or I , and it can be seen that the binding energy decreases as the angle of approach of the ammonia becomes closer to linear with respect to the C–I bond. The circular contours on the binding energy plots indicate that there is no variation of the binding energy as the $\text{N}\cdots\text{X}-\text{C}-\text{F}$ dihedral angle changes. By contrast, the binding energy plots for the halonium ion complexes, see Figure 6-31b, d and f, do show a variation of binding energy with the $\text{N}\cdots\text{X}-\text{C}-\text{H}$ dihedral angle, which is typically more pronounced along the axis of the C–C bond than perpendicular to it.

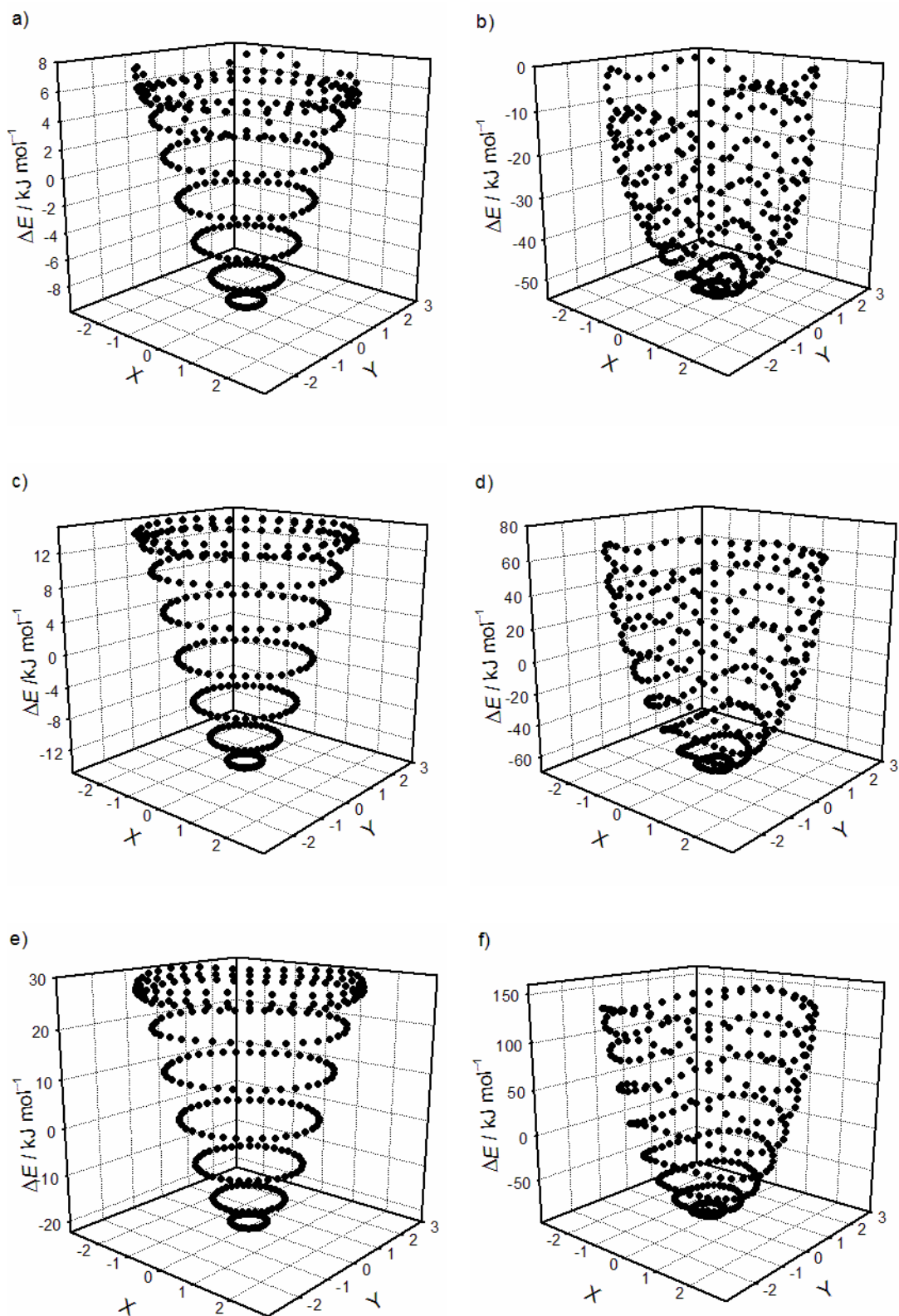


Figure 6-31: 3D plots showing the variation of binding energy of the complexes a) 22.NH₃, b) 1.NH₃, c) 23.NH₃ d) 2.NH₃ e) 24.NH₃ and f) 3.NH₃ with angle of approach of the ammonia.

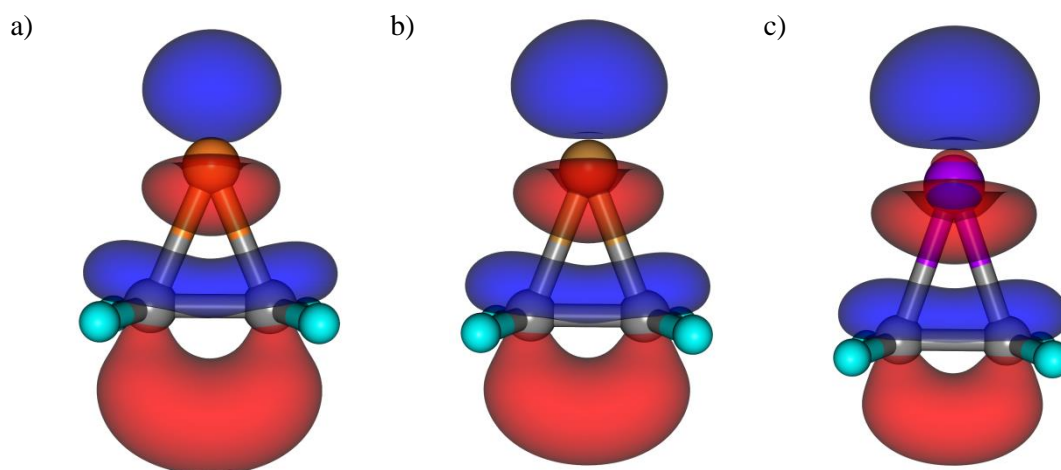


Figure 6-32: The LUMOs of halonium ions a) **1**, b) **2** and c) **3**. Orbitals are represented as isosurfaces at orbital values of ± 0.05 (e/bohr^{-3})^{1/2}

This variation of the binding energy with this dihedral angle can be accounted for by looking at the LUMO of the halonium ion, which corresponds to the anti-bonding orbital of the 3-centre-2-electron bond, see Figure 6-32. This anti-bonding orbital is oriented along the C–C bond of the halonium ion and NBO analysis shows that there is charge transfer from the lone pair of electrons on the nitrogen atom of the base into this anti-bonding orbital (*vide infra*). The overlap between the lone pair on the nitrogen and the anti-bonding orbital is higher along the C–C bond rather than perpendicular to it leading to an increase in binding energy along this C–C bond. The effect is more pronounced for **1**·NH₃ than for **2**·NH₃ and **3**·NH₃.

The binding energies for the halonium ion donors exceed those for the traditional halogen-bond donors. The repulsion in regions away from the optimised geometry are larger for **2**·NH₃ and **3**·NH₃, however for **1**·NH₃ which features a chloronium ion, the binding energy is always negative indicating an attractive interaction. These binding energy plots show that halonium ions are not as directional as traditional halogen-bond donors because the binding energy wells are broader. Nonetheless, the minimum corresponds to a linear geometry.

6.4.8 Complexes of Adamantylidene Adamantane Halonium Ions

In order for a halogen-bonded complex involving a halonium ion to be formed experimentally, it needs to be stable. AdAd has a stable bromonium ion since steric hindrance prevents nucleophilic attack. The geometries of complexes between AdAd bromonium and iodonium ions (**25** and **26**) and ammonia and pyridine were, therefore, optimised at the M06-2X level of theory using a combination of the aug-cc-pVDZ and cc-pVDZ basis sets explained earlier and key parameters are shown in Table 6-14.

Table 6-14: The halogen...nitrogen/oxygen separations and binding energies of the M06-2X/aug-cc-pVDZ/cc-pVDZ optimised geometries of complexes of **25** and **26** with NH₃ and pyridine and **26**·OH₂.

Halonium Ion	Base	$r(X\cdots N/O) / \text{\AA}$	% Σ vdW radii	$\Delta E / \text{kJ mol}^{-1}$
[AdAdBr] ⁺ (25)	NH ₃	2.819	82.9	45.9
	Pyridine	2.744	80.7	46.4
[AdAdI] ⁺ (26)	NH ₃	2.720	77.1	51.5
	Pyridine	2.520	71.4	64.4
	H ₂ O	2.881	82.3	35.8

Complexes of **25** and **26** with ammonia and pyridine are weaker than the other complexes studied in this investigation due to the electron-donating adamantyl groups, which lower the positive charge on the halogen atom. The binding energy is larger when compared to the traditionally halogen-bonded complexes CF₃X...NH₃ suggesting that it could be possible to form these complexes experimentally.

The geometry of the complex between AdAd iodonium ion and water, **26**·OH₂ was also optimised at the M06-2X/(aug-cc-pVDZ, cc-pVDZ) level of theory so that a comparison with the crystal structure, shown in Figure 6-2, can be made. The calculated I...O separation is 2.881 Å, which is significantly longer than that observed in the crystal structure, 2.630(4) Å, which suggests that the M06-2X level

of theory is underestimating the interaction in this complex. It should be noted that since the calculations are carried out in the gas phase, additional crystal packing forces present in the experimental structure are not included in the calculation. The binding energy for complex **26**·OH₂ is 35.77 kJ mol⁻¹, making this complex significantly weaker than the complexes between the AdAd iodonium ion and ammonia and pyridine. This is as expected because water is a weaker base and shows that although the level of theory fails to reproduce the experimental results, the trends observed are correct.

The bonding in these complexes is similar to that in complex **2**·NH₃; there is an LMO representing the 3-centre-2-electron bond of the bromonium ion and there is an LMO containing a lone pair of electrons on the nitrogen of the ammonia that is directed towards the bromine atom of the bromonium ion, see Figure 6-33.

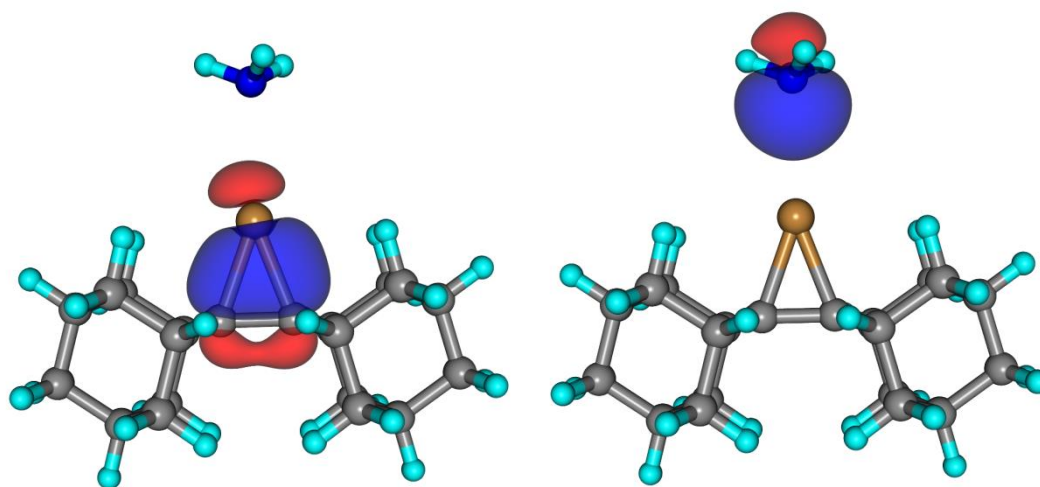


Figure 6-33: The LMOs of complex **25**·NH₃ corresponding to the 3-centre-2-electron bond on [AdAdBr]⁺ and the lone pair of electrons on ammonia. Orbitals are represented as isosurfaces at orbital values of $\pm 0.05 \text{ \AA}^{-3/2}$.

NBO analysis shows that, similar to the other complexes with ammonia, complexes of **1** – **10** with NH₃, this complex is stabilised by electron transfer from the lone pair of electrons on the nitrogen atom of ammonia into the anti-bonding orbital of the 3-centre-2-electron bond on the halonium ion (Table 6-15).

Table 6-15: The occupancies of the NBOs corresponding to the lone pair of electrons on the nitrogen of the base and the anti-bond of the 3-centre X–C–C bond and stabilisation energies for complexes of **25** and **26** with ammonia and pyridine and **26·OH₂**.

Halonium Ion	Base	Occupancy LP(N)	Occupancy 3C*(X–C–C)	$\Delta E_{ij} / \text{kJ mol}^{-1}$
[AdAdBr]⁺ (25)	NH ₃	1.93797	0.22028	18.09
	Pyridine	1.87544	0.22601	20.72
[AdAdI]⁺ (26)	NH ₃	1.87203	0.31873	108.27
	Pyridine	1.77196	0.28345	196.19
	H ₂ O	1.97343	0.10236	26.84

The WBIs of these complexes show that the halogen remains in a 3-centre-2-electron bond with the central carbon atoms of AdAd (Table 6-16). The WBI of the X···N interaction corresponds to a non-covalent interaction and is similar to those observed for halogen bonds. This shows that in these complexes the halogen has not transferred from the halonium ion to the base.

Table 6-16: The WBIs of the X···N interaction and C–X bonds of complexes of **25** and **26** with NH₃ and pyridine and **26·OH₂**.

Halonium Ion	Base	WBI(X···N/O)	WBI(C–X)
[AdAdBr]⁺ (25)	NH ₃	0.038	0.650
	Pyridine	0.076	0.644
[AdAdI]⁺ (26)	NH ₃	0.159	0.523
	Pyridine	0.229	0.458
	H ₂ O	0.036	0.614

6.4.9 Complexes with the Diphenyliodonium Ion

The geometry of the complex between the diphenyliodonium ion and ammonia, complex **27**·NH₃, was optimised at the M062X/aug-cc-pVDZ level of theory see Figure 6-34.

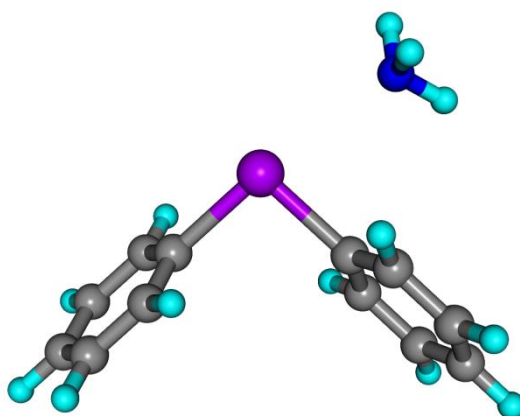


Figure 6-34: The M06-2X/aug-cc-pVDZ optimised geometry of the complex between the diphenyliodonium ion and ammonia.

The I···N separation is 2.9235 Å, which is 82% of the sum of the van der Waals radii of iodine and nitrogen, while the I···N–C angle is 174.13° and the two C–I bonds are 2.1228 and 2.1239 Å, respectively (the slightly shorter bond is the one opposite the ammonia). The binding energy was calculated to be 55.54 kJ mol⁻¹, much smaller than in complex **3**·NH₃ and the I···N separation is much longer than in **3**·NH₃ (see Table 6-3) which shows that the diphenyliodonium ion is a much weaker halogen-bond donor. The charge on the iodine atom in the diphenyliodonium ion is 0.949, which is significantly higher than the charge on the iodine in the halonium ion (0.565) suggesting that the difference in the binding energies is due to charge-transfer rather than electrostatics.

Diphenyliodonium ions have been shown to be capable of forming two interactions leading to a square planar arrangement at the iodine atom and so the complex

between the diphenyliodonium ion and two ammonia molecules ($27 \cdot 2\text{NH}_3$), was also optimised at the same level of theory (Figure 6-35).

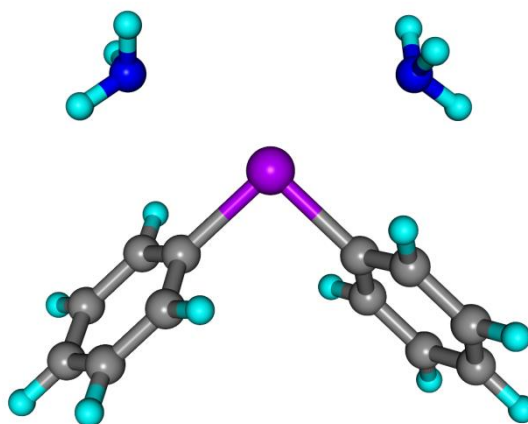


Figure 6-35: The M06-2X/aug-cc-pVDZ optimised geometry of the complex between the diphenyliodonium ion and two ammonia molecules.

The two $\text{I} \cdots \text{N}$ interactions are almost identical with $r(\text{I} \cdots \text{N}) = 2.965 \text{ \AA}$, which is 84% of the sum of the van der Waals radii and the $\text{C}-\text{I} \cdots \text{N}$ angle is equal to 170.6° for both. The $\text{C}-\text{I}$ bond lengths are 2.122 \AA and the overall binding energy is $105.43 \text{ kJ mol}^{-1}$. Since the $\text{I} \cdots \text{N}$ interactions are identical, the interaction energy for each of these is half the overall binding energy or $52.71 \text{ kJ mol}^{-1}$. Comparing these values to those for complex $27 \cdot \text{NH}_3$ ($\Delta E = 55.54 \text{ kJ mol}^{-1}$) shows that the introduction of additional interaction slightly reduces the strength of each individual interaction.

The $\text{I} \cdots \text{N}$ separation is similar to those observed in the crystal structures of complexes between diphenyliodonium ions and pyridine and 1,10-phenanthroline (see Figure 6-14), $2.864(2) \text{ \AA}$ and $2.926(4) \text{ \AA}$, respectively. It would be expected that the separation in complexes with ammonia would be longer than those involving pyridyl nitrogen atoms because ammonia is a weaker base. This suggests that the M06-2X functional is slightly overestimating the strengths of the complexes.

In complex $27 \cdot \text{NH}_3$ there is a localised molecular orbital corresponding to the lone pair of electrons on the nitrogen atom of ammonia that is directed towards the iodine

atom along the same axis as the C–I bond of the diphenyliodonium ion (see Figure 6-36). There are also two LMOs corresponding to the σ -bonding orbitals of the C–I bonds of the diphenyliodonium ion. The fact that there are two distinct LMOs representing these bonds shows that the bonding is very different from that in halonium ions of alkenes, where a 3-centre-2-electron bond exists.

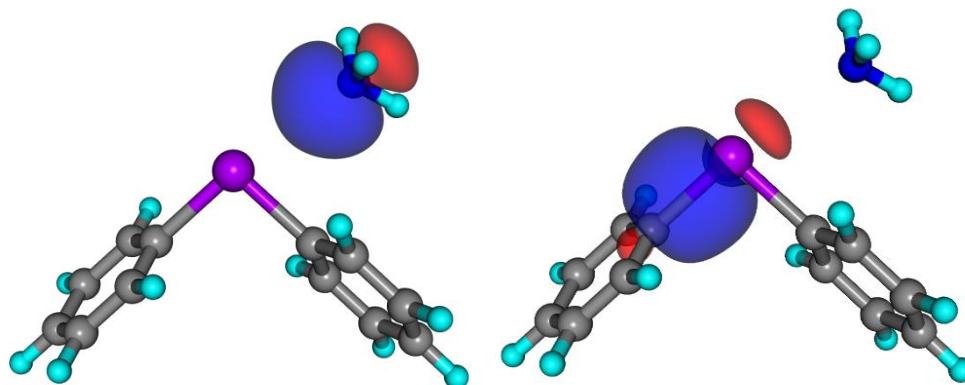


Figure 6-36: The localised molecular orbitals representing the lone pair of electrons on the nitrogen atom of ammonia and the σ bonding orbital of the C–I bond of the diphenyliodonium ion. Orbitals are represented as isosurfaces at orbital values of ± 0.05 $(e/\text{bohr}^{-3})^{1/2}$.

NBO analysis indicates that there is a small amount of charge transfer from the lone pair of electrons on the nitrogen to the σ^* anti-bonding orbital of the C–I bond opposite the ammonia. Table 6-17 shows the occupancies of the NBOs involved and the stabilisation energy.

Table 6-17: The occupancies of the NBO corresponding to the lone pair of electrons on nitrogen and the NBO corresponding to the σ^* C–I anti-bonding orbital and the stabilisation energy of the charge transfer for the complexes between the diphenyliodonium ion and ammonia.

Complex	Occupancy LP(N)	Occupancy σ^* NBO (C–I)	$\Delta E_{ij} / \text{kJ mol}^{-1}$
27·NH₃	1.94085	0.09606	37.89
27·2NH₃	1.94677	0.09320	34.33

The charge transfer into the C–I anti-bonding orbital can be confirmed by comparing the C–I bond lengths in the diphenyliodonium ion monomer and in the complex. In the monomer the C–I bond distance is 2.1255 Å, which is slightly longer than the C–I bond lengths in the optimised geometry of the complex. This indicates that the charge transfer is insignificant and the interaction is predominantly electrostatic.

The stabilisation energy is much smaller for this complex than for the complexes between halonium ions and ammonia, which suggests that there is less charge transfer and corroborates the idea that the interaction is predominantly electrostatic in nature. This is an indication that the diphenyliodonium ion resembles a traditional halogen-bond donor.

The LUMO of the diphenyliodonium ion was calculated and is shown in Figure 6-37. This MO corresponds to the two anti-bonding orbitals of the C–I bonds and consists of two lobes along the extension of the C–I bond that can accept electron density from the lone pair of electrons on the N atom in ammonia.

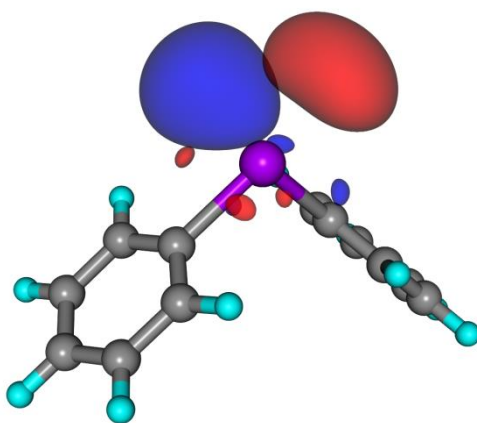


Figure 6-37: The LUMO of the diphenyliodonium ion represented as an isosurface at orbital values of ± 0.05 (e/bohr⁻³)^{1/2}.

The electrostatic surface potential (Figure 6-38) shows that there are two regions of more positive potential along the extension of the C–I bond in the same region as the lobes in the LUMO of the diphenyliodonium ions. These regions are similar in nature to the σ -hole observed for traditional halogen-bond donors suggesting that the

interactions involving diphenyliodonium ions can be considered as halogen bonds and will be directional.

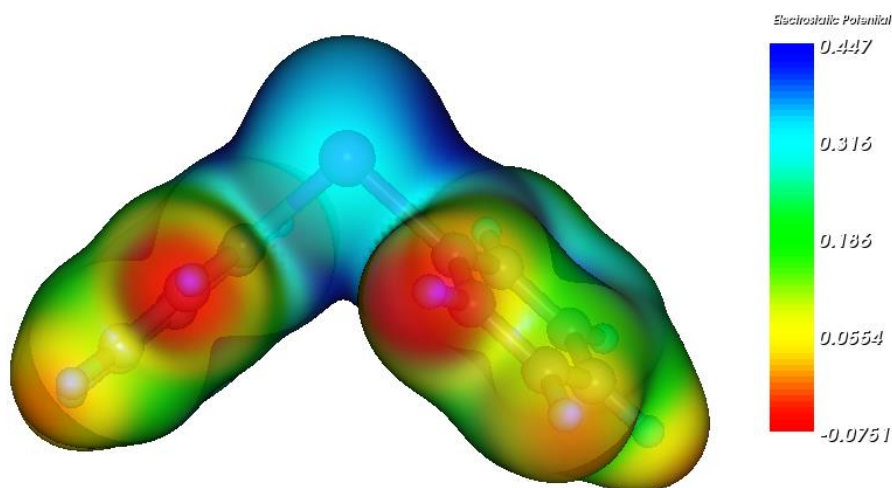


Figure 6-38: The electrostatic surface potential of the diphenyliodonium ion mapped on the $0.01 \text{ (e/bohr}^{-3})^{1/2}$ electronic density isosurface.

6.5 Experimental Results

Diphenyliodonium chloride is a commercially available diphenyliodonium salt, albeit with limited solubility in organic solvents. Therefore in order to make it more useable, the triflate salt was prepared by anion metathesis using AgOTf. Attempts were then made to co-crystallise this triflate salt with DMAP, 2,2'-bipyridine, 4,4'-bipyridine, thiophene and 2,2'-bithiophene with the aim of observing different supramolecular structures. Unfortunately, only the crystallisation with DMAP produced co-crystals suitable for single crystal X-ray diffraction. The molecular structure of this complex is given in Figure 6-39.

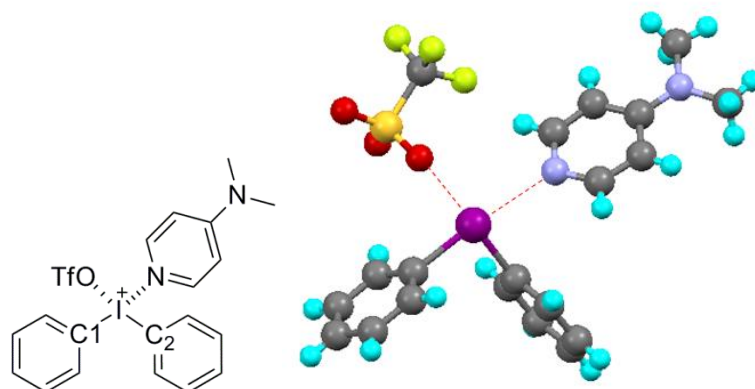


Figure 6-39: The molecular structure of the complex between diphenyliodonium triflate and DMAP

The iodine atom of the diphenyliodonium cation interacts with the nitrogen of the DMAP along the extension of the C1–I bond. The I···N separation is 2.733(3) Å, which is 77% of the sum of the van der Waals radii and the C1–I···N angle is almost linear at 173.93(10)°.

The iodine atom also interacts with an oxygen atom on the triflate anion along the extension of the other C2–I bond with a I···O separation of 2.923(2) Å, which is 84% of the sum of the van der Waals radii. The halogen bond angle deviates slightly from linearity with a C2–I···O angle of 170.42(9)°. The iodine also forms a weak interaction with a second oxygen atom in the triflate anion but with an I···O separation of 3.460(2) Å, which is 99% of the sum of the van der Waals radii, can only be considered a weak dispersion type interaction. This additional interaction could account for the deviation from linearity for the stronger I···O interaction. These two interactions result in an almost square planar arrangement at I; the C1–I–C2, C2–I···N, N···I···O and O···I–C1 angles are 93.59(11)°, 80.46(10)°, 101.75(7)° and 84.31(9)°, respectively (Figure 6-40).

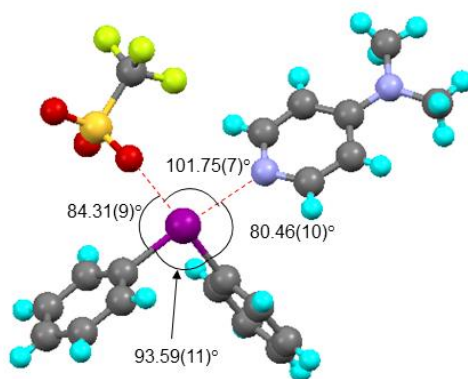


Figure 6-40: The angles about the square-planar iodine centre in the molecular structure of the complex between diphenyliodonium triflate and DMAP.

The I \cdots N separation present in the crystal structure is significantly shorter than those observed previously for structures involving diphenyliodonium ions; the I \cdots N separation in the crystal structure with pyridine is 2.864(2) Å and the I \cdots N separation in the crystal structure with 1,10-phenanthroline (Figure 6-14) are 2.926(4) and 3.162(4) Å. This is due to the fact that DMAP is a stronger base and has a greater nucleophilicity than pyridine or 1,10-phenanthroline. The I \cdots N separation is also shorter than in the calculated geometries of **27**·NH₃ and **27**·2NH₃. This is also likely to be due to the fact that DMAP is a stronger base than ammonia although the fact that the anion is not included in the calculations and that the calculations are in the gas phase and do not include crystal packing forces should also be taken into account when comparing these values..

The structure crystallised in the *C2/c* space group. The structure propagates *via* a 2-fold screw axis along the *b*-axis (Figure 6-41) with an additional I \cdots O interaction with a separation of 3.391(2) Å, 97% of the sum of the van der Waals interaction.

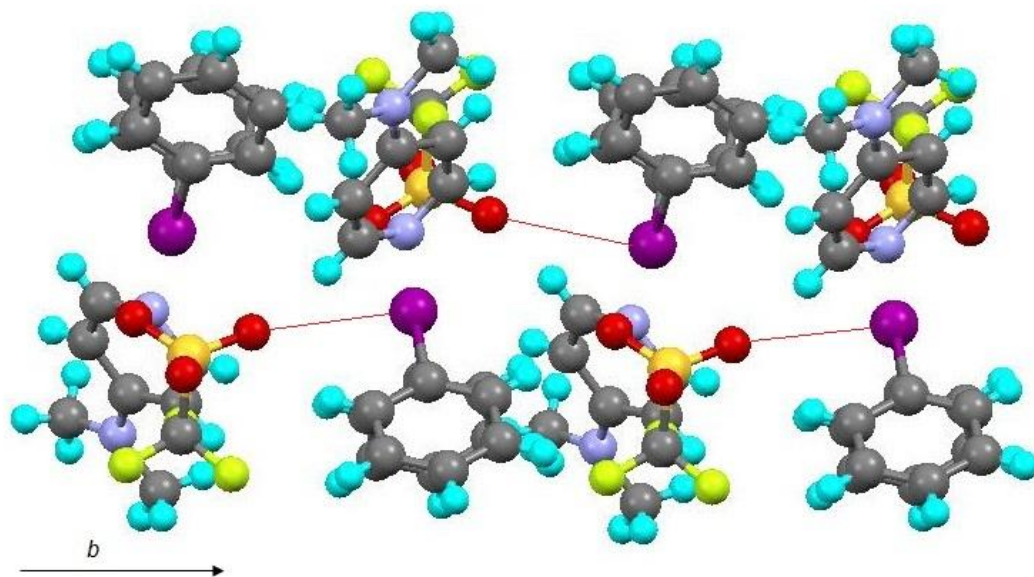


Figure 6-41: The 2-fold screw axis along the *b*-axis in the crystal structure of the complex between diphenyliodonium triflate and DMAP. I...O contacts are shown in red.

It was hoped that it would be possible to obtain a crystal structure of a complex with the iodine atom of the diphenyliodonium salt interacting with two Lewis bases in order to form a square planar arrangement without coordination of the anion. In order to achieve this, the tetraphenylborate salt of the diphenyliodonium cation was synthesised because the anion is very weakly coordinating and any halogen bond interactions will dominate over the π - π interactions between the anion and cation. Unfortunately crystallisations set up between this salt and Lewis bases were unsuccessful and did not produce crystals suitable for single crystal X-ray diffraction.

6.6 Conclusions

The geometries of a series of halonium ions of substituted ethenes and their complexes with ammonia and pyridine were optimised at the MP2(Full)/aug-cc-pVDZ and M06-2X/aug-cc-pVDZ levels of theory. The calculations have revealed a new type of halogen bond that involves a novel halogen-bond donor. These interactions have characteristics that are similar to halogen bonds involving traditional halogen-bond donors; the interaction becomes stronger as the halogen becomes more polarisable, favours a linear orientation and involves charge-transfer from the lone pair of the Lewis base into an anti-bonding orbital.

Similar to halogen bonding involving traditional halogen-bond donors, the interaction involving halonium ions are sensitive to substituent effects. The introduction of electron-donating methyl substituents were found to stabilise bromonium ions in agreement with previous investigations,³⁵⁷ as the electron-donating groups reduce the charge on the halogen atom the complexes with Lewis bases are weaker. Conversely, electron-withdrawing substituents increase the positive charge on the halogen atom and lead to stronger complexes. There was a linear correlation between the positive charge on the halogen atom and the binding energy of the complex suggesting that electrostatics make a significant contribution to the interaction. There was also a large degree of charge transfer from the lone pair of electrons on the nitrogen base to the anti-bonding orbital of the 3-centre-2-electron bond; the stabilisation energies from perturbation theory energy analysis are large.

The localised molecular orbitals of the complexes with ammonia showed an orbital representing the lone pair of electrons on nitrogen directed towards the halogen atom. As the complexes become stronger, this orbital became distorted and flattens on the edge closest to the halogen suggesting that charge transfer has taken place.

Complexes with pyridine were found to be significantly stronger than those with ammonia, consistent with the fact that pyridine has a higher pK_{B12} .¹¹ The halogen atom was observed to transfer from the halonium ion to the pyridyl nitrogen as the complex becomes stronger. Wiberg bond indices of the C–X and X···N bonds showed the change in the bonding; the X···N bond changes from a halogen bond to a dative bond and the C–X bonds change from dative bonds to non-covalent interactions as the strength of the complex increases. The change in the bonding as the strength of the complexes increases was similar to that observed for hydrogen and halogen-bonded complexes as demonstrated by the excellent fit of the Steiner-Limbach equation to the bond lengths in these complexes.

Similar to traditional halogen bonds, interactions with halonium ions were found to be directional with a linear geometry favoured, although scans of the potential energy surface varying the angle of approach of the Lewis base showed a broader range of favourable binding energies particularly along the axis of the C–C bond. This is due to the improved overlap and therefore larger charge transfer between the lone pair of electrons on the nitrogen base and the anti-bonding orbital of the 3-centre-2-electron bond along the axis of the C–C bond.

Geometry optimisations of complexes between the bromonium and iodonium ions of AdAd and ammonia and pyridine suggested that it should be possible to isolate a complex of this type. Although these complexes are weaker than those involving halonium ions of ethenes, the interaction is stronger than those observed for traditional halogen bonds. The geometry of the complex between the AdAd iodonium ion and water was optimised to allow comparison to an experimentally determined structure. The M06-2X/(aug-cc-pVDZ, cc-pVDZ) level of theory employed was found to underestimate the interaction strength, however the trends that iodonium ion complexes are stronger than bromonium ion complexes and that stronger bases form stronger complexes were as expected.

Complexes between the diphenyliodonium ion and ammonia were also optimised. The complex with a single ammonia molecule had a binding energy of 55.54 kJ mol⁻¹, which although weaker than the binding energies of complexes with halonium ions, was strong compared to other halogen-bond interactions. The complex with two ammonia molecules had a square planar geometry at the iodine centre. The interactions were found to be competitive because the introduction of a second I...N interaction leads to a reduction in the interaction energy. Analysis of the molecular orbitals, localised molecular orbitals and natural bonding orbitals showed that the interaction in these complexes is due to charge transfer from the lone pair of electrons on the ammonia and the LUMO of the diphenyliodonium ion, which is predominantly the σ^* anti-bonding orbitals of the C–I bonds. The stabilisation energy of the charge transfer interaction was fairly low compared to the other complexes. The electrostatic surface potential had two regions of positive potential along the extension of the C–I bond, which are similar to the σ -hole observed in typical halogen-bond donors.

The crystal structure of a complex between diphenyliodonium triflate and DMAP was obtained. The iodine centre had a square-planar geometry, similar to structures with secondary interactions involving diphenyliodonium ions previously obtained in the literature³⁸⁰ and the calculated structure with two ammonia molecules. The I...N separation was shorter than the examples in the literature and in the calculated structures with ammonia as the base because DMAP is a stronger base.

6.7 Experimental

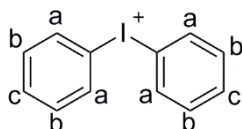
6.7.1 Crystallographic Parameters

	Diphenyliodonium triflate + DMAP
CCDC Reference No.	dwb1343
Molecular Formula	C ₂₀ H ₂₀ F ₃ IN ₃ O ₃ S
Empirical formula	C ₂₀ H ₂₀ F ₃ IN ₃ O ₃ S
Formula weight / g mol ⁻¹	552.34
<i>T</i> / K	110.05(10)
Wavelength (Å)	0.7107
Crystal system	Monoclinic
Space group	C2/c
Colour	Colourless
Shape	Plank
Unit cell dimensions / Å	<i>a</i> = 19.8123(7) <i>b</i> = 9.7935(2) <i>c</i> = 25.8006(9)
<i>α</i> / °	90.0
<i>β</i> / °	117.861(4)
<i>γ</i> / °	90.0
Volume / Å ³	4425.9
<i>Z</i>	8
ρ_{calc} / Mg m ⁻³	1.658
Absorption coefficient / mm ⁻¹	1.590
<i>F</i> (000)	2192
Crystal size / mm ³	0.21 × 0.06 × 0.02
θ range for data collection	3.52 to 27.834°
Index ranges	-23 ≤ <i>h</i> ≤ 26, -7 ≤ <i>k</i> ≤ 12, -33 ≤ <i>l</i> ≤ 25
Reflections collected	8519
Independent reflections	4479
Completeness (%) to (θ) =	99.71% (25.01°)
Max. and min. transmission	0.967 and 0.891
Data / restraints / parameters	4479 / 0 / 273
Goodness-of-fit on <i>F</i> ²	1.069
Final <i>R</i> indices [<i>I</i> > 2σ(<i>I</i>)]	<i>R</i> ₁ = 0.0328, <i>wR</i> ₂ = 0.0594
<i>R</i> indices (all data)	<i>R</i> ₁ = 0.0454, <i>wR</i> ₂ = 0.0649
Largest diff. peak and hole	0.753 and -0.544

6.7.2 Synthesis of Diphenyliodonium Triflate³⁹⁴



Diphenyliodonium chloride (1.26 g, 4.0 mmol) was dissolved in acetonitrile (200 cm³) in a round-bottomed flask by heating. After cooling the solution to room temperature, silver trifluoromethane sulfonate (0.98 g, 3.8 mmol) was added to the flask. The mixture was stirred at room temperature for 2 hours. Any precipitate formed was filtered and washed with acetonitrile (3 × 20 cm³). The solvent in the filtrate and washings was removed using a rotary evaporator. The residual solid was recrystallised from diethyl ether to give a white solid.



Yield = 61%. ¹H NMR (400 MHz, CDCl₃): δ = 7.97 (4H, Ha, d, *J* = 7.9 Hz), 7.63 (2H, Hc, t, *J* = 7.5 Hz), 7.48 (4H, Hb, t, *J* = 7.8 Hz).

¹⁹F NMR (400 MHz, CDCl₃): δ = -78.21.

¹³C {¹H} NMR (100 MHz, (CD₃)₂CO): δ = 207.20, 137.47, 134.51, 134.04, 116.46.

Anal. Calcd. for C₁₂H₁₀ICF₃O₃S: C, 36.3; H, 2.3%. Found: C, 36.5; H, 2.3%.

MS-ESI (*m/z*): [MH⁺] for [¹²C₁₂H₁₁I]⁺ found (expected) 280.9827 (280.9822).

MS-ESI (*m/z*): [M⁻] for [¹²CF₃O₃S]⁻ found (expected) 148.9532 (148.9526).

7 Competition and Cooperation between Halogen and Hydrogen Bonding^{395,396,xi}

7.1 Introduction

7.1.1 Halogen and Hydrogen Bonding in Supramolecular Architectures

In the design of supramolecular systems, it is beneficial to be able to predict the resulting structure and, in the case of building blocks with multiple donor and acceptor sites, is necessary to do so with any degree of confidence. Halogen bonding¹⁶⁴ is now becoming a well-established interaction used in supramolecular chemistry and has binding energies ranging from as little as 5 kJ mol⁻¹ to as much as 180 kJ mol⁻¹ when interactions with ions are involved, at which level it is easily comparable to hydrogen bonding. It is, therefore, necessary to understand the possibilities for competition and cooperation in systems where both halogen and hydrogen bonding are possible.

Instinctively, it would be expected that where there is simple competition then hydrogen bond formation would be preferred over the generally weaker and more labile halogen bond. For example, in studies of 2 : 1 and 1 : 1 co-crystals formed between 4-alkoxystilbazoles and 4-iodotetrafluorophenol, the 1 : 1 co-crystals showed N···H hydrogen bonding, although the strongly electrophilic nature of the iodine led to formation of intramolecular I···O contacts with the oxygen of the alkoxy chain to give a polymeric arrangement.⁶⁷

Examples exist of situations where halogen bonding is preferred over hydrogen bonding, as described by Corradi *et al.*³⁹⁷ who showed in a competition experiment that using 1,2-di(4-pyridyl)ethane, co-crystals formed with the very strong halogen bond donor, 1,4-diiodotetrafluorobenzene rather than with 1,4-hydroquinone, which

^{xi} This chapter is based on work published in two journal articles. I was a co-author of these articles and played a significant role in the editing process.

is perhaps not so strong a hydrogen bond donor. Indeed, some of the shortest pyridine...I halogen bonds have been found using 1,4-diiodotetrafluorobenzene.¹²² Turning the situation around, however, there are several examples where supramolecular structures have been formed using complementary and cooperative hydrogen and halogen bonding. For example, halogen and hydrogen bonding are observed cooperatively in the crystal structures of 4-iodopyridine with 4-nitrobenzoic acid and 3,5-dinitrobenzoic acid with hydrogen bonding between the pyridyl nitrogen and the carboxylic acid being favoured, leading to bifurcated halogen bonding between the iodine and nitro group (Figure 7-1).³⁹⁸

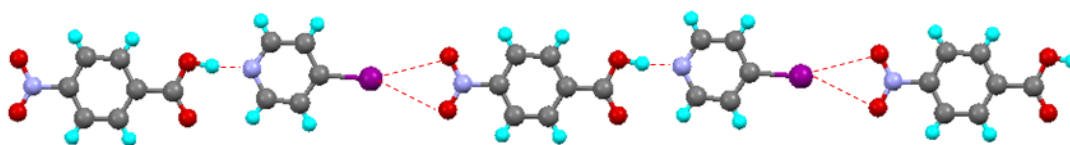


Figure 7-1: The molecular structure of the complex between 4-iodopyridine and 4-nitrobenzoic acid. O–H...N hydrogen bonds and bifurcated I...O halogen bonds are highlighted in red.

By far the most extensive study in this area has been conducted by Aakerøy and co-workers and some highlights are now described. Thus, halogen and hydrogen bonding have been combined in the formation of co-crystals between *iso*-nicotinamide and 1,4-diiodotetrafluorobenzene (Figure 7-2a).³⁹⁹ The *iso*-nicotinamide exists as a hydrogen-bonded dimer through the amide group and the pyridyl nitrogen forms a halogen bond with an iodine atom of the halogen bond donor. The amide group favours hydrogen bonding since it features a donor and an acceptor. Similarly, co-crystallisation of carboxylic acids with pyridine/aminopyrimidine synthons showed that the carboxylic acid binds preferentially to the aminopyrimidine site over the pyridyl site unless a sufficiently electrophilic halogen is present in which case a halogen bond is formed to the pyridyl nitrogen (Figure 7-2b).⁴⁰⁰ 2-Aminopyrazine also has two potential sites that

can accept hydrogen and halogen bonds and when co-crystallised with 1,4-diodotetrafluorobenzene, it is found to form a dimer with $N\cdots H-N$ hydrogen bonds leaving the single point pyrazine nitrogen to form a halogen bond with the iodine atom of the halogen-bond donor (Figure 7-2c).⁴⁰¹

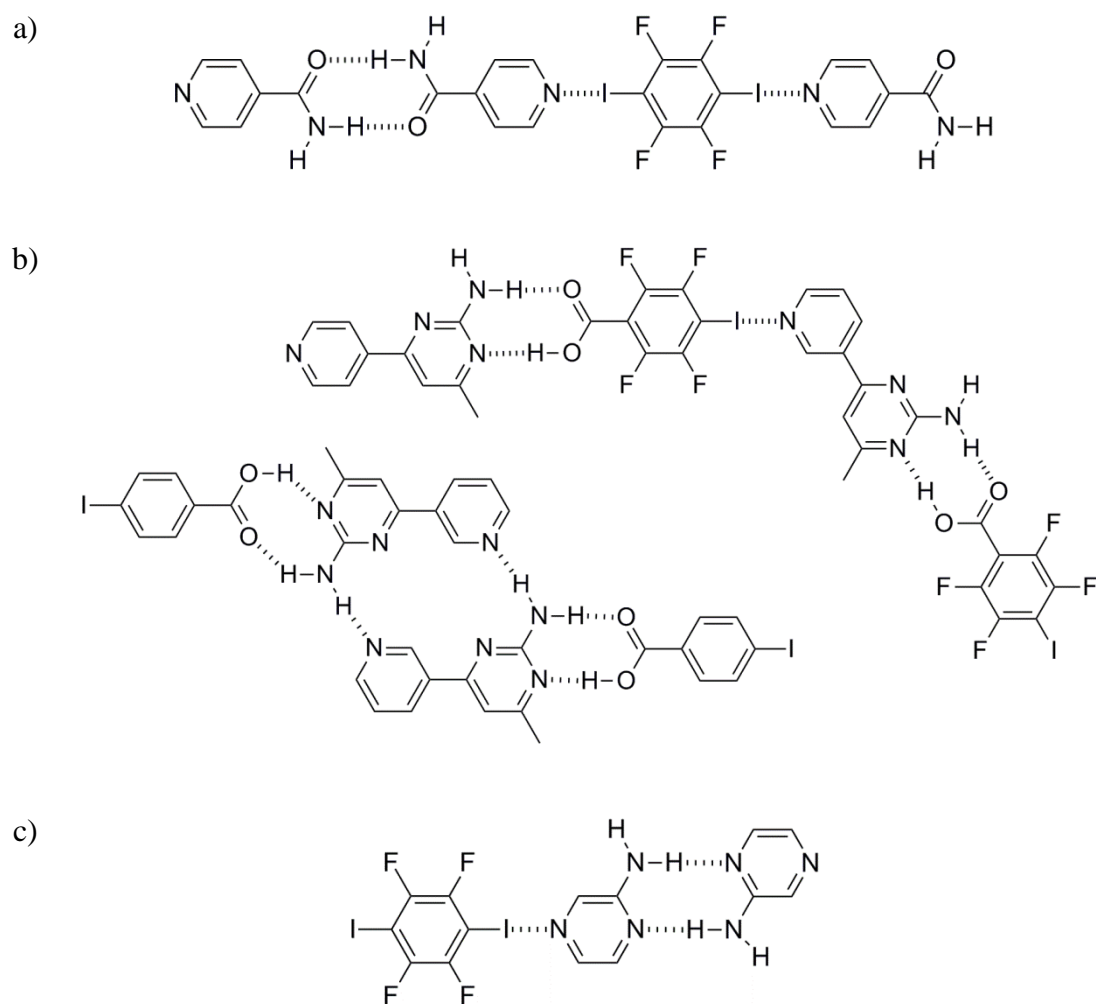


Figure 7-2: The halogen and hydrogen bonding motifs of the complex between a) 1,4-diodotetrafluorobenzene and isonicotinamide and b) 4-iodotetrafluorobenzoic acid and 4-iodobenzoic acid and 3-(2-amino-4-methylpyrimidin-6-yl)pyridine.

4-Halo-2,3,5,6-tetrafluorobenzoic acids are useful supramolecular building blocks since they feature both a halogen-bond donor, a hydrogen-bond donor and a halogen/hydrogen-bond acceptor. Co-crystallisation of these benzoic acids with aminopyrazines leads to the formation of a 1-dimensional chain with two hydrogen

bonds formed between the carboxyl group and the amino group and halogen bonds between the pyrazyl nitrogen and the halogen (Figure 7-3a).⁴⁰² Bromination of the base can reduce the basicity of the nitrogen atoms and prevent deprotonation of the carboxylic acid, as observed in the crystal structure with 2-aminopyrazine (Figure 7-3b).

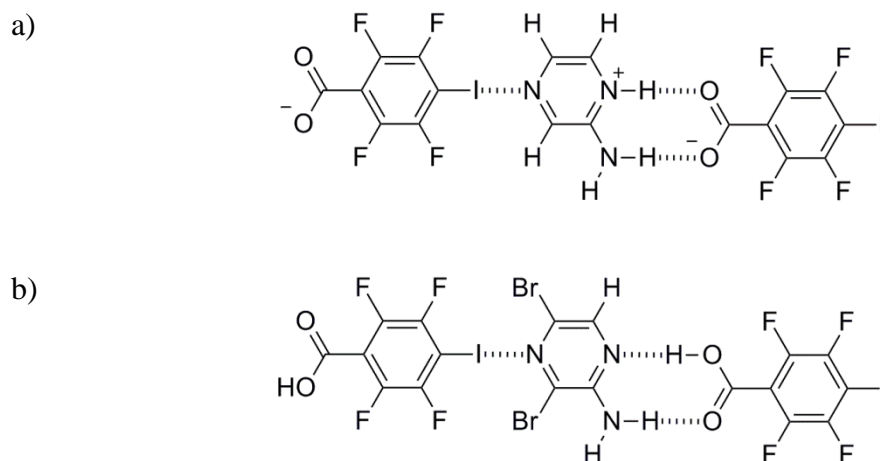


Figure 7-3: The halogen and hydrogen bonding motifs of a) 4-iodotetrafluorobenzoate and 2-aminopyrazinium and b) 4-iodotetrafluorobenzoic acid and 2-amino-3,5-dibromopyrazine.

Co-crystallisations between 4-halotetrafluorobenzoic acids, 4-halotetrafluorophenols and 4-halotetrafluoroaloximes, all of which have hydrogen- and halogen-bond donors, and 3,3'-azobipyridine and 4,4'-azobipyridine were set up to investigate the competition between hydrogen and halogen bonding to the pyridyl nitrogen atoms.⁴⁰³ In crystal structures with 4,4'-azobipyridine, where the pyridyl nitrogen atoms are in a co-linear arrangement, halogen and hydrogen bonding was found to be equally favourable with one interaction at each nitrogen (Figure 7-4a-c). The exception to this was the structure with 4-bromotetrafluoroaloximes, where hydrogen bonding to the pyridyl nitrogen atoms was preferential (Figure 7-4d). In this latter structure the bromine atoms were found to interact with the nitrogen atoms in the central double bond to form an unusual motif. With the exception of 4-iodotetrafluoroaloximes (Figure 7-5a), crystal structures with 3,3'-azopyridine,

where the pyridyl nitrogen atoms are antiparallel, hydrogen bonding was favoured over halogen bonding (Figure 7-5b and c).

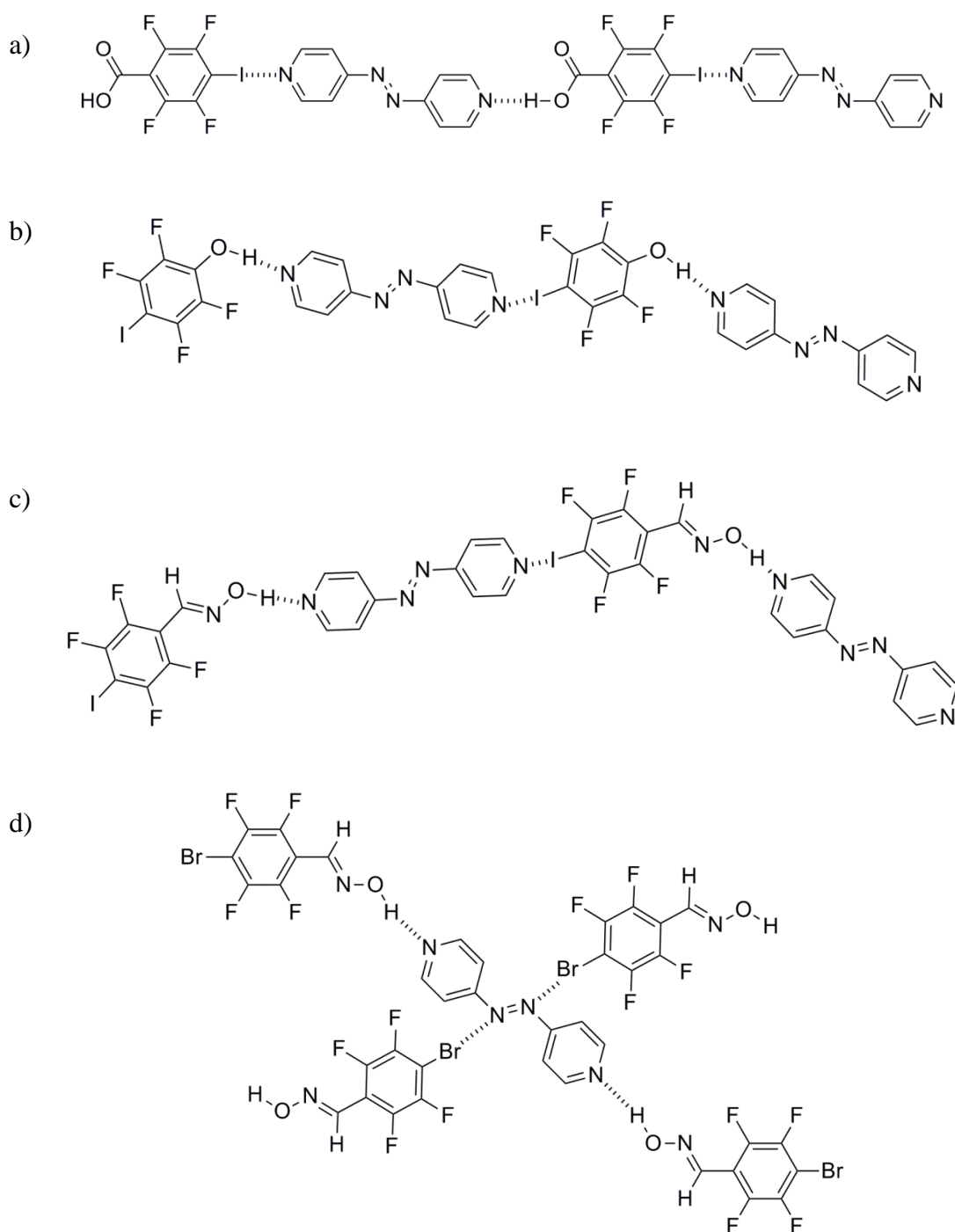


Figure 7-4: The halogen and hydrogen bonding motifs of a) 4-iodo-2,3,5,6-tetrafluorobenzoic acid, b) 4-iodo-2,3,5,6-tetrafluorophenol, c) 4-iodo-2,3,5,6-tetrafluoroaldoximide and d) 4-bromo-2,3,5,6-tetrafluoroaldoximide and 4,4'-azobipyridine.

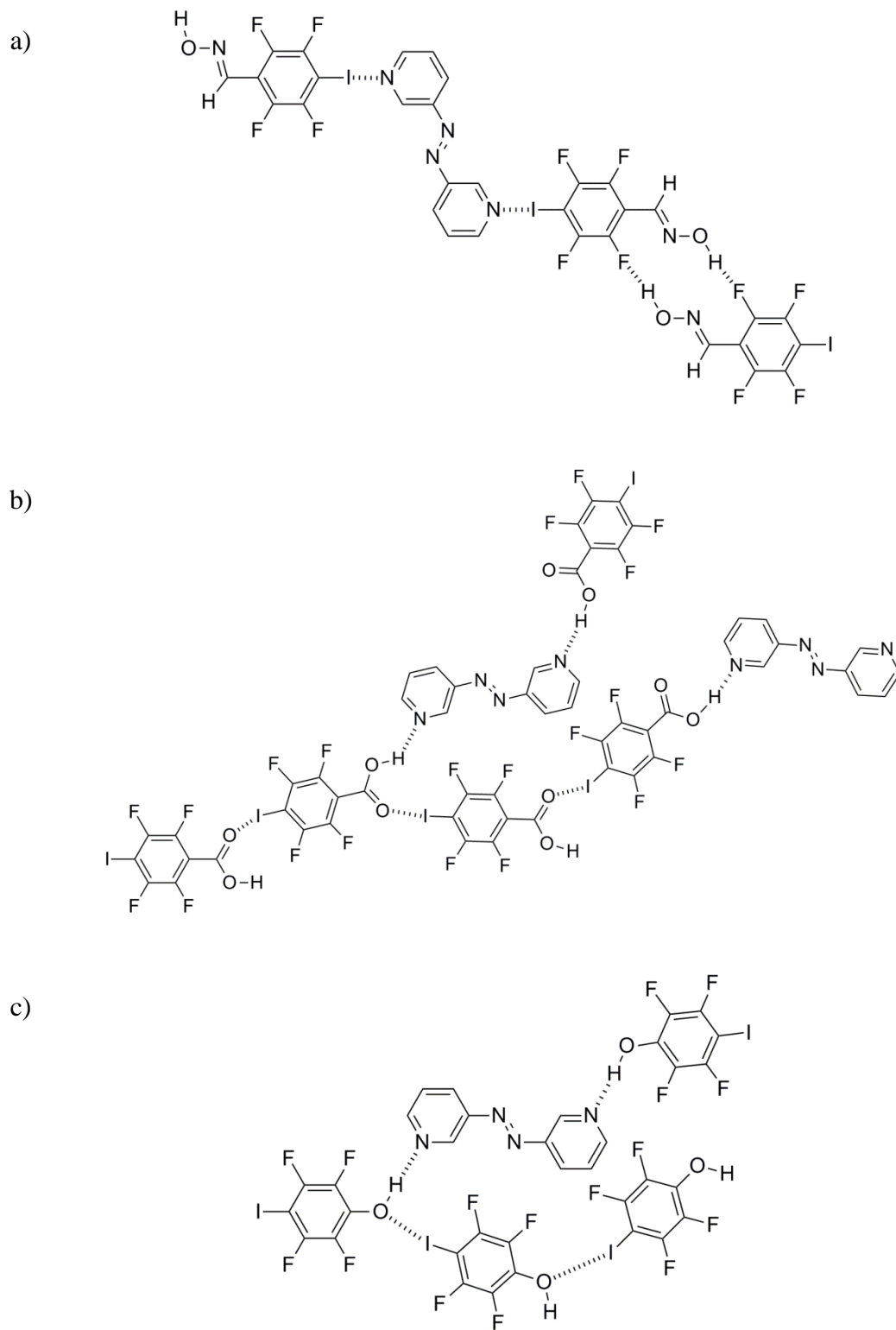


Figure 7-5: The halogen and hydrogen bonding motifs of a) 4-iodo-2,3,5,6-tetrafluoroaldoximide, b) 4-iodo-2,3,5,6-tetrafluorobenzoic acid and c) 4-iodo-2,3,5,6-tetrafluorophenol and 3,3'-azobipyridine.

7.2 Aim

Following on from the work of Aakeröy and co-workers, it was of interest to see what conditions might be necessary to favour halogen bonding over hydrogen bonding using the strong hydrogen-bond donor, 4-iodobenzoic acid and weak sulfur bases. The co-crystals that have been formed are shown in Figure 7-6.

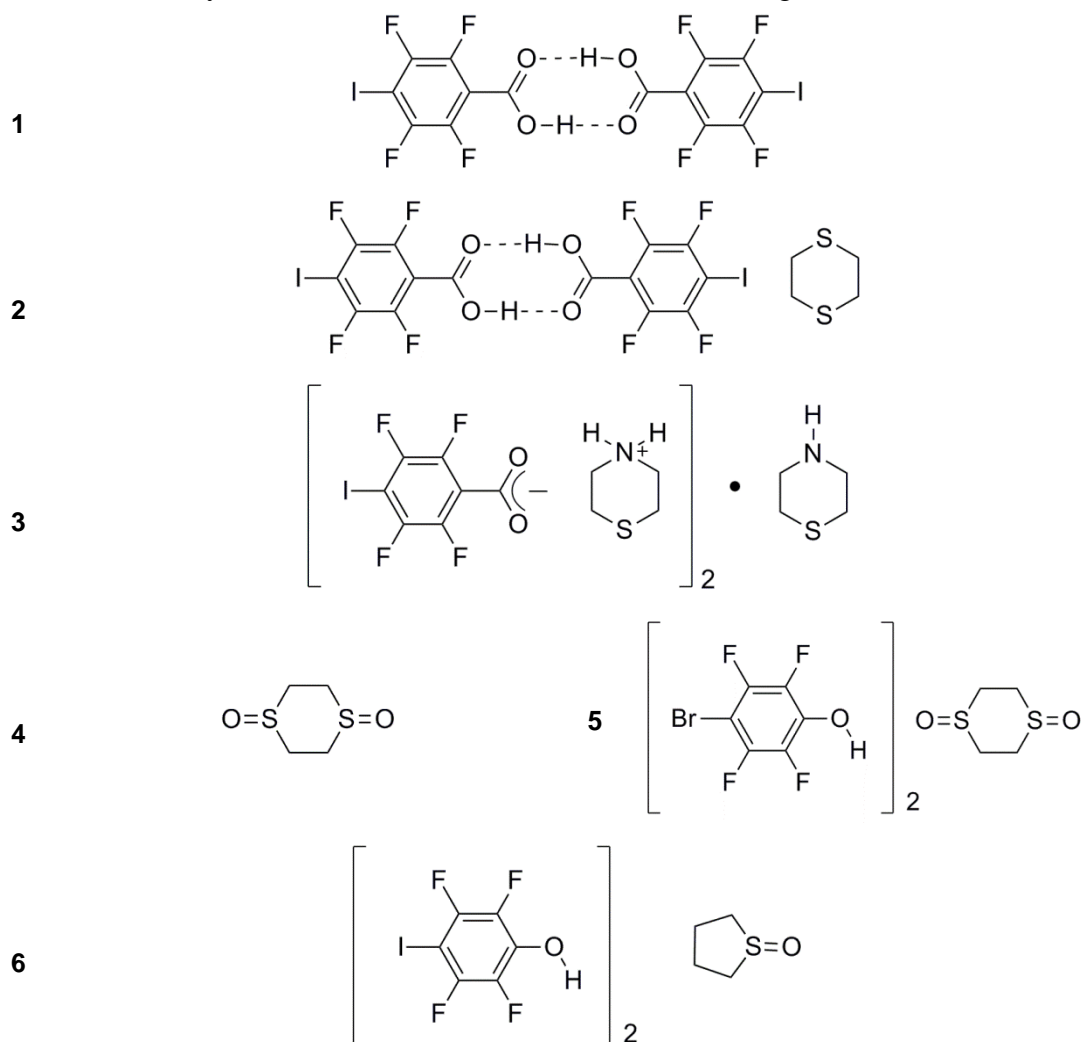


Figure 7-6: Co-crystals formed to investigate cooperativity between halogen and hydrogen bonding.

7.3 Results

7.3.1 4-Iodotetrafluorobenzoic Acid (1)

4-Iodotetrafluorobenzoic acid was chosen as the halogen-bond donor in this investigation because it forms a strongly bonded hydrogen-bonded dimer leaving the iodine available to form a halogen bond with an available Lewis base. The formation of the hydrogen-bonded dimer was confirmed in the crystal structure of 4-iodotetrafluorobenzoic acid (Figure 7-7a), which had two dimers in the unit cell. The two phenyl rings in each dimer are close to co-planar (inter-plane angles of 0.7° and 1.13°) while the carboxylate groups make angles to the phenyl rings of $12.3(8)^\circ$ and $-34.8(8)^\circ$, as seen clearly in an end-on view (Figure 7-7b); this twist is likely due to the steric effect of the fluorines *ortho* to the carboxylate function (Figure 7-7c). The oxygen...oxygen separation in the dimer is about 2.65 Å.

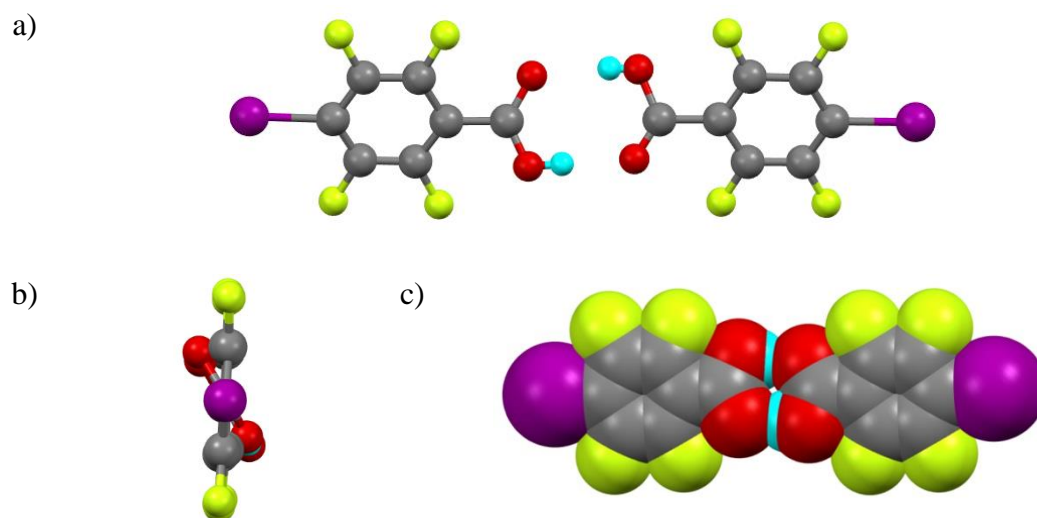


Figure 7-7: Molecular structure of the dimer of 4-iodotetrafluorobenzoic acid (a) seen from above and (b) in an end-on view, (c) space-filling representation of the 4-iodotetrafluorobenzoic acid dimer.

The dimers propagate through the structure in a slipped-stack (staircase) arrangement (Figure 7-8a) and the terminal iodines alternate their positions slightly

through the plane as shown in Figure 7-8a. The iodines are then close to the iodines of dimers in another such arrangement (Figure 7-8b) with I···I separations of 3.9502(5) Å (black lines, less than the sum of the van der Waals radii) and 4.1349(5) Å (red lines, greater than the sum of the van der Waals radii) depending on the position of alternation. With C–I···I angles at 166.5 and 97.4°, for those where there is some formal interaction (black lines) these interactions are geometrically Type II but are too long to be attractive in nature.

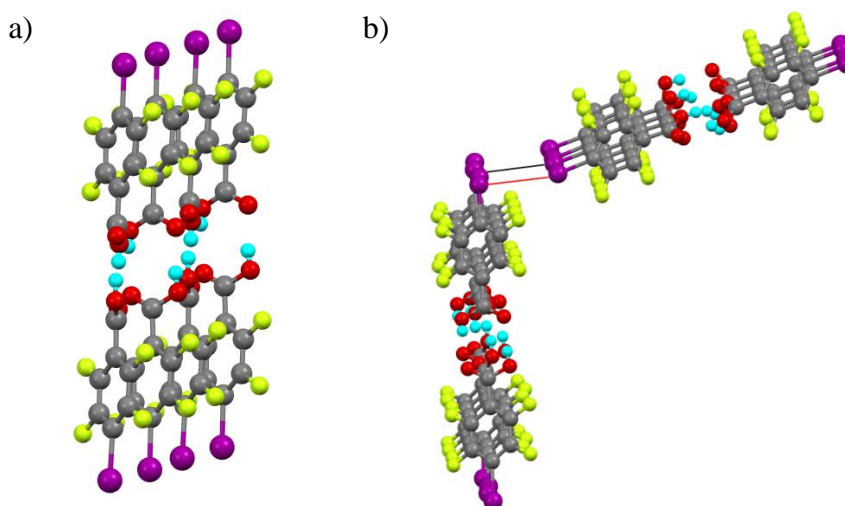


Figure 7-8: Packing of **1** in the solid state (a) showing the glide plane and (b) showing the shorter (black line) and longer (red line) I···I separations as two glide planes meet.

7.3.2 Co-crystal between 4-Iodotetrafluorobenzoic Acid and 1,4-Dithiane (**2**)

1,4-Dithiane was chosen as the Lewis base to form a halogen bond with 4-iodotetrafluorobenzoic acid because it is weak base and therefore will not disrupt the hydrogen-bonded dimer. This was observed to be the case and the complex was found as a polymer, which contains the dimer of 4-iodotetrafluorobenzoic acid with each iodine being bound to one sulfur of a dithiane; the polymer propagates as the other sulfur forms a halogen bond to the iodine of another benzoic acid dimer, as illustrated in Figure 7-9. The halogen bond length (all are symmetry equivalent) is

3.2644(7) Å representing 86.4% of the sum of the van der Waals radii of the two elements, while the C–I⋯S angle is 171.01(7)°.

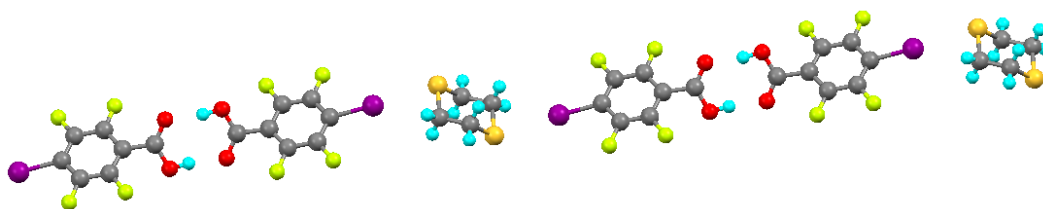


Figure 7-9: Structure of the polymeric unit of **2**.

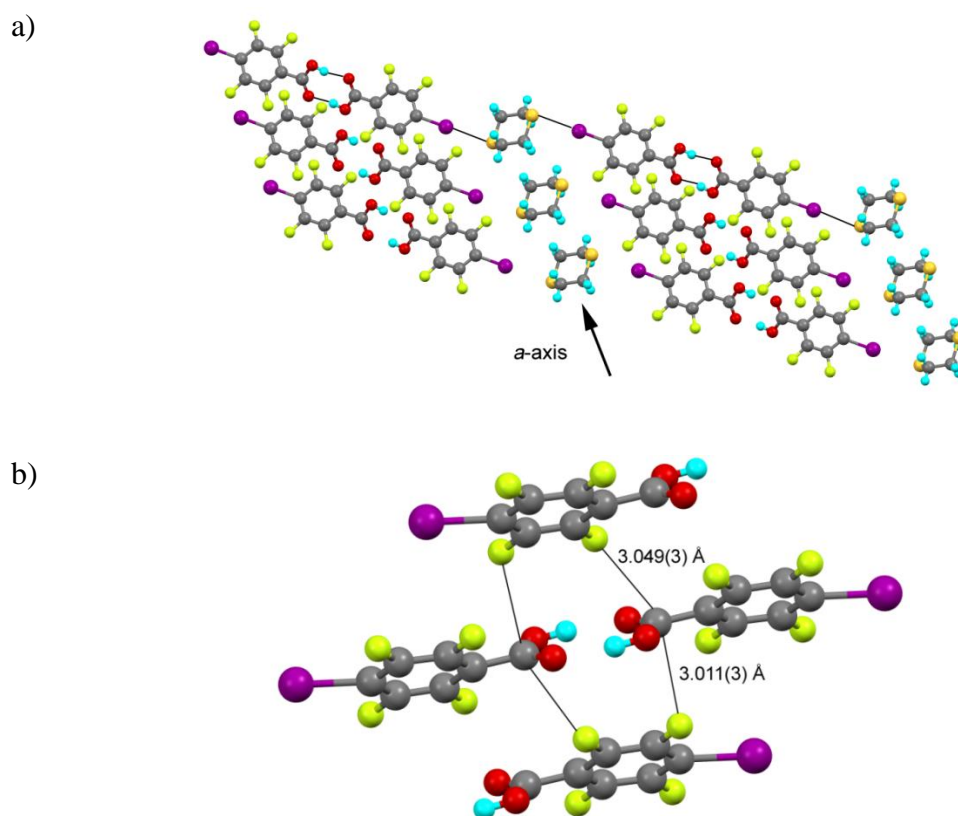


Figure 7-10: (a) Structure and packing of complex **2** with the direction of the *a*-axis shown, (b) **2** showing intermolecular interactions between the carboxylate carbon and neighbouring fluorine atoms.

The structure extends in a 'staircase' manner along the *a*-axis and an off-axis view is shown as Figure 7-10a. The only intermolecular interactions found in this direction are between the carboxylate carbons and fluorines from neighbouring molecules, whose lengths are 3.011(3) and 3.046(3) Å representing 95% and 96%, respectively,

of the sum of the van der Waals radii; the respective C–F...C angles are 117.5(1)° and 137.0(2)°. Thus, each carboxylate carbon has one of these fluorines above the plane and the other below (Figure 7-10b) and strictly they represent an electrostatically attractive interaction between δ^- fluorine and δ^+ carbon, but the extent to which these are truly structure-directing is perhaps open to debate.

The structure propagates in the *ab* plane as shown in Figure 7-11 and the only contacts shorter than the sum of the respective van der Waals radii are the indicated F...F interactions at 2.809(2) Å and arise due to the close packing of the molecules.

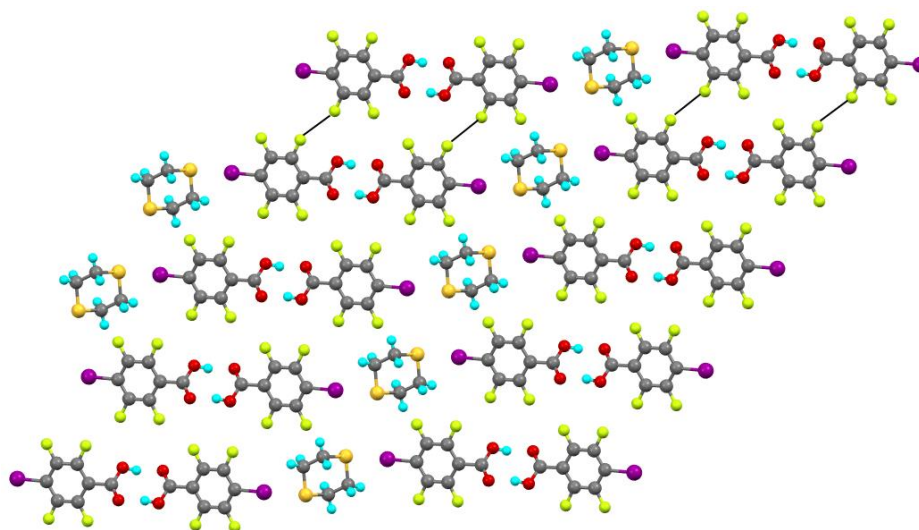


Figure 7-11: Structure and packing of co-crystal 2 in the *ab*-plane.

7.3.3 Salt/Co-Crystal between 4-Iodotetrafluorobenzoic Acid and Thiomorpholine (3)

In an attempt to produce a second example of halogen bonding being favoured over hydrogen bonding, thiomorpholine was selected as the Lewis base. The presence of a stronger nitrogen base causes the hydrogen bonds in the dimer to fall apart and the morpholinium nitrogen atom becomes protonated. The complex crystallises as $([\text{C}_4\text{H}_{10}\text{NS}][\text{IC}_6\text{F}_4\text{COO}])_2 \cdot \text{C}_4\text{H}_9\text{NS}$ – that is to say the molecular formula contains two equivalents of thiomorpholinium iodotetrafluorobenzoate, which co-crystallise with one equivalent of a neutral thiomorpholine. Within the structure, which is

represented in Figure 7-12a, the thiomorpholinium cations are not disordered, but the neutral thiomorpholine is because it sits on an inversion centre, so that while the carbons of the ring do not appear disordered, the S and N–H are indistinguishable (there is some disorder of the ring hydrogens). The iodotetrafluorobenzoic acid dimer breaks up on account of deprotonation by the thiomorpholinium nitrogen and the two carbonyl oxygens form hydrogen bonds – one to an N–H hydrogen that terminates the unit shown in Figure 7-12b ($d_{(O\cdots H)} = 1.933(4) \text{ \AA}$) and the other to a neighbouring N–H hydrogen ($d_{(O\cdots H)} = 1.800(4) \text{ \AA}$), which acts to propagate the structure in the *a*-direction. The iodine at the other end of the ring forms a halogen bond to the neutral thiomorpholine and the formula unit is shown in Figure 7-12a, while the propagation is shown in Figure 7-12b, which shows both the hydrogen and halogen bonds ($d_{(I\cdots S)} = 3.064(5) \text{ \AA}$ and $d_{(I\cdots N)} = 3.37(2) \text{ \AA}$, with the C–I \cdots S angle = $170.3(2)^\circ$ and the C–I \cdots N angle = $172.5(3)^\circ$). The halogen bonds are found at 81% (I \cdots S) and 95% (I \cdots N) of the sum of the respective van der Waals distances. Note that there are no short contacts to the two sulfur atoms at the end of each formula unit.

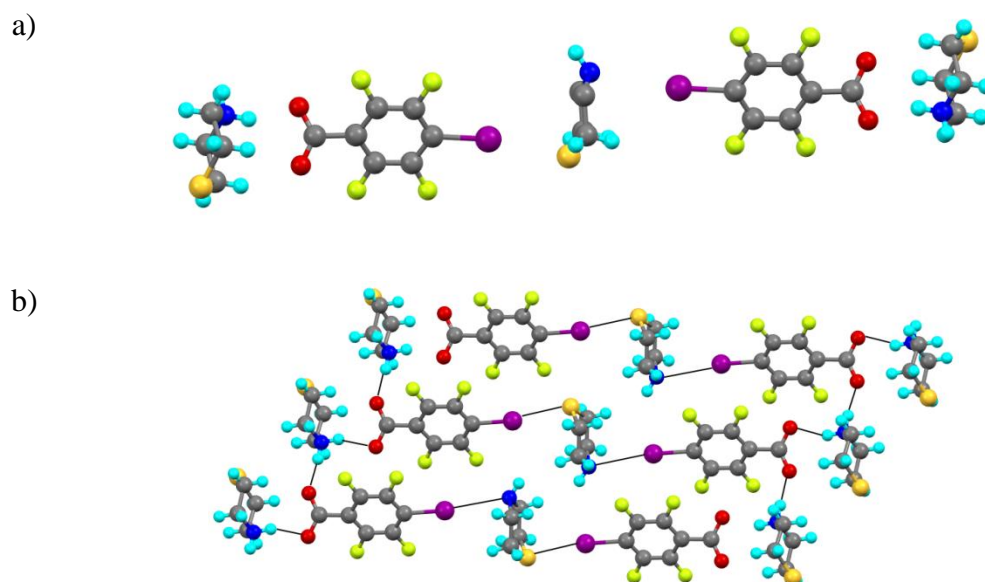


Figure 7-12: The structure of **3** showing (a) the formula unit and (b) propagation of the formula unit. Note that in (b), the distinction between S and N–H in the neutral thiomorpholine is an artefact of the program (Mercury) used to create the figure.

7.3.4 1,4-Dithiane-S,S'-dioxide (4)

Using the much weaker acid, 4-iodotetrafluorophenol, in an attempt to form co-crystals with sulfur donors, colourless crystals were obtained that turned out to be of 1,4-dithiane-S,S'-dioxide. The six-membered ring formed a perfect chair conformation with an *anti* arrangement of the S=O bonds; the S=O bond length was 1.505(1) Å. The molecular structure is shown as Figure 7-13. While the Cambridge database shows seven structural determinations of **4**, only one⁴⁰⁴ reports the same space group and in this earlier determination, the S=O bond length is reported as 1.4764 Å.

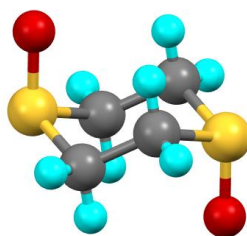


Figure 7-13: Molecular structure of **4**.

7.3.5 Co-crystal between 4-Bromotetrafluorophenol and 1,4-Dithiane-S,S'-dioxide (5)

Co-crystallisation of 4-bromotetrafluorophenol and 1,4-dithiane also led to the formation of the *S,S'*-dioxide, but this time two molar equivalents of 4-bromotetrafluorophenol were also found in the structure with the one phenolic hydrogen forming a hydrogen bond to an oxide oxygen at each end of the dithiane with $d_{\text{H-O}} = 1.88(4)$ Å. The structure then extends into a sort of linear polymer by virtue of an intermolecular Br \cdots F contact at 3.171(2) Å with a C–Br \cdots F angle of 155.98(8)°, representing a shortening of *ca.* 4% over the sum of the van der Waals radii (Figure 7-14).

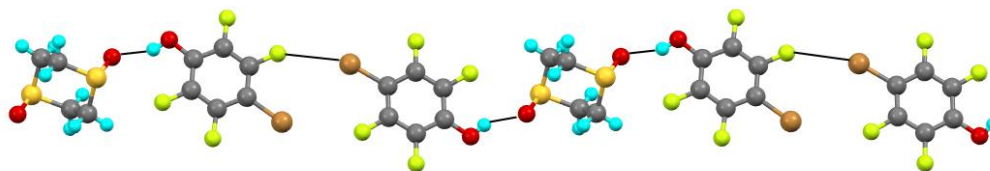


Figure 7-14: Polymeric arrangement in **5** showing the linking hydrogen bonds and Br...F interactions.

7.3.6 Co-crystal between 4-Iodotetrafluorophenol and Thiophene-S-oxide (**6**)

A similar co-crystallisation of 4-iodotetrafluorophenol with thiophene also led to oxidation to thiophene-S-oxide, but in this case the oxide co-crystallised with 4-iodotetrafluorophenol to give a crystal with a 2 : 1 ratio of phenol to oxide. The 2 : 1 ratio gives rise to a basic structural motif in which the oxygen of the thiophene-S-oxide forms hydrogen bonds to two phenol molecules in an unsymmetric fashion (Figure 7-15). Thus, $d_{(H1-O3)}$ is 1.81(4) Å, while $d_{(H2-O3)}$ is 1.97(3) Å, with the two making an angle at O3 of 137(2)°. Examination of other close contacts in the structure shows that both phenolic oxygen atoms (O1 and O2) are also halogen bonded, each to an iodine of another iodotetrafluorophenol (Figure 7-15), with I...O separations of 3.079(2) Å (I2...O1) and 3.156(2) Å (I1...O2), halogen-bond angles (C-I...O) of 172(4)° (I2) and 159(4)° (I1) and with H-O...I angles of 112(3)° at O1 and 104(3)° at O2.

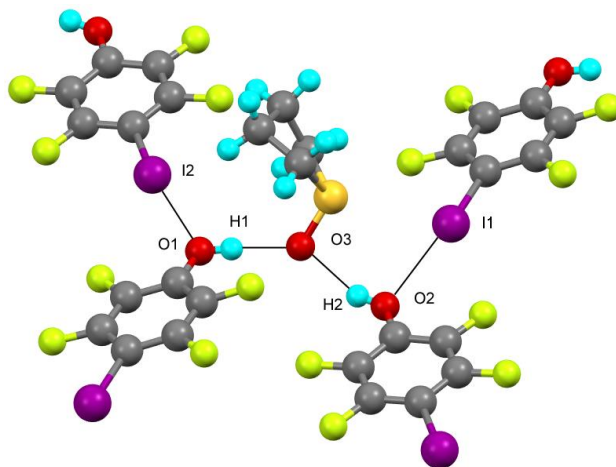


Figure 7-15: Molecular structure of **6** showing the two hydrogen bonds to the oxygen of the thiophene oxide. Atom numbering is from the cif file.

7.3.7 Cooperation between Halogen and Hydrogen Bonding

As noted in the introduction, there has been interest both in the competition between hydrogen and halogen bonding and their cooperative co-existence, which extends from work on small-molecule co-crystals and salts, through to the proposals of orthogonality of hydrogen and halogen bonding made by Voth *et al.* following their analysis of non-bonded contacts to amide oxygens in peptide chains.⁴⁰⁵

In this regard, Aakeröy has shown consistently that where there is a good hydrogen-bond acceptor, then the dimeric nature of 4-iodotetrafluorobenzoic acid will be disrupted to allow the carboxylate function to participate in hydrogen bonding; the iodine may then go on to form a halogen bond.³⁹⁹⁻⁴⁰³ In this work, 4-iodotetrafluorobenzoic acid was mixed with a rather weak hydrogen-bond acceptor in 1,4-dithiane, which has allowed the acid to maintain its dimeric arrangement while the iodine forms halogen bonds to the sulfur atoms of the heterocycle leading to a polymeric structure. Iodine...sulfur halogen bonds are well documented in the literature and indeed there are examples from Blake *et al.* of co-crystals formed between I₂ or IBr and various thioether crowns,^{406,407} although these were not labelled as being halogen-bonded interactions at that time. In these co-crystals with molecular iodine, S...I distances vary from the rather short (*e.g.* 2.747 Å – 75% of

the sum of the van der Waals radii – in $18[\text{ane}]S_6 \cdot I_2$, Figure 7-16a)⁴⁰⁸ to the appreciably longer (3.22 \AA – 85% of the sum of the van der Waals radii in $12[\text{ane}]S_4$, Figure 7-16b).⁴⁰⁶ In co-crystals with, for example, diiodoacetylene or 1,4-diiodotetrafluorobenzene with 1,4-dithiane, I...S distances are typically at the longer end of this range at 3.268 \AA ⁴⁰⁹ and 3.384 \AA ,⁴¹⁰ respectively. At 3.06 \AA and 81% of the sum of the van der Waals radii, the I...S separation in **3** is slightly shorter than some of these examples, whereas in **2** ($d_{\text{I}\cdots\text{S}} = 3.26 \text{ \AA}$) the distance is consistent with these other data.

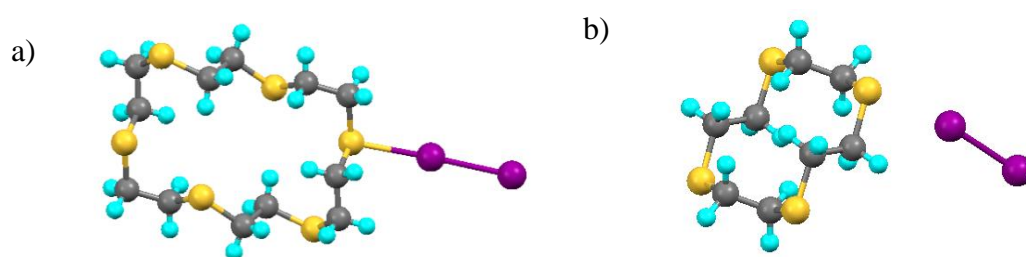


Figure 7-16: The crystal structures of a) $18[\text{ane}]S_6 \cdot I_2$ and b) $12[\text{ane}]S_4 \cdot I_2$.

Then, consistent with Aakeröy's work: replacing 1,4-dithiane with thiomorpholine, which contains a good hydrogen-bond acceptor (secondary N–H), breaks up the benzoic acid dimer deprotonating the acid and forming a thiomorpholinium salt of the iodobenzoate, with the electrophilic iodine of two such salts forming a halogen bond to both the sulfur and the nitrogen of a neutral (disordered) thiomorpholine that also co-crystallises in the lattice. Thus, it seems that under most circumstances, hydrogen bonding will prevail where it can, but if the odds are stacked a little, for example the use here of 1,4-dithiane (**2**) or in the work of Corradi *et al.*,³⁹⁷ then halogen bonding can be seen in preference.

Considering then that the 4-iodotetrafluorobenzoic acid dimer broke up on co-crystallisation with a nitrogen base, it was of interest to use instead the weaker hydrogen-bond donors, 4-iodo- and 4-bromo-tetrafluorophenol. A slightly surprising observation, however, was that co-crystallisation of the phenols, with 1,4-dithiane or

with thiophene led to the related *S,S'*-dioxide (**4**, **5**) or *S*-oxide (**6**), with 4-iodotetrafluorophenol and 4-bromotetrafluorophenol, respectively. Further investigation of this oxidation is beyond the scope of this study and the driving force is not evident as conditions for crystallisation were no different to those employed in the rest of this work. Of interest here, however, was that thiophene-*S*-oxide co-crystallised with two molar equivalents of 4-iodotetrafluorophenol (**6**). Here, the phenolic oxygen bound covalently to a hydrogen and, in addition, formed a hydrogen bond to the oxide oxygen and a halogen bond to the iodine of a neighbouring iodotetrafluorophenol. This can be thought of as an example of the orthogonal halogen and hydrogen bonding proposed by Voth *et al.*⁴⁰⁵ on the basis of an exploration of the PDB.

Table 7-1: pK_{BI2} and pK_{BHX} values of selected bases.¹¹

Base	Atomic site	solvent	pK_{BI2}	pK_{BHX}	pK_b
1,4-Dithiane	S	CCl ₄	1.64	-0.14	n/a
Piperazine	N- <i>sp</i> ³	heptane	3.74	2.11	4.17
Ethanethiol	S	hexane	1.37	-0.16	n/a
Ethylamine	N- <i>sp</i> ³	heptane	2.75	2.17	3.30

It is then of interest to interpret these results in terms of the iodine basicity scale discussed by Laurence *et al.*¹¹ The pK_{BI2} and pK_{BHX} scales they report are defined in such a way that larger values correspond to stronger halogen- and hydrogen-bond acceptors, respectively.^{11,411} Some pK_{BI2} and pK_{BHX} values of *S*- and *N*-containing bases are shown in Table 7-1, where it can be seen that while nitrogen analogues are indeed stronger halogen- and hydrogen-bond acceptors, they can, at the same time, be strong bases that will lead to deprotonation, promoting the formation of salts. On the other hand, although sulfur analogues are much weaker halogen- and hydrogen-bond acceptors, they are less likely to be strong bases, thus promoting formation of co-crystals instead of salts. In fact, the negative pK_{BHX} values for the sulfur analogues mean that, for the formation of hydrogen-bonded complexes of these

acceptors, the equilibrium lies towards the uncomplexed components. Thus, given the choice, these sulfur-containing acceptors are more likely to be involved in halogen bonding than hydrogen bonding, which was the case in **2**. The nitrogen atom in one of the thiomorpholinium cations in **3**, however, behaved as suggested above, which led to deprotonation and crystallisation of the salt.

The results are also consistent with Pearson's classification of Hard and Soft Acids and Bases (HSAB),¹⁰ which predicts successfully the preference for I \cdots S over I \cdots O interactions in **2** and **3** and the fact that, expressed as the sum of the van der Waals radii, the I \cdots S interaction is shorter than the I \cdots N interaction in **3** (*vide infra*).

The crystallographic disorder observed in **3** then provides interesting insights into the geometries of halogen bonding. The structures of 1,4-diiodotetrafluorobenzene and 1,4-dibromotetrafluorobenzene co-crystallised with thiomorpholine, thioxane, 1,4-dithiane, piperazine, morpholine and 1,4-dioxane have been reported in an extensive study by Cinčić *et al.*⁴¹² where the isostructurality of several of the halogen-bond acceptors was investigated. Although a direct analogy is inappropriate as the number of structures reported here is insufficient to identify structural equivalence, Cinčić *et al.* noted that the disorder of thio with imino or oxo groups suggests that all three groups may exhibit structural equivalence.^{413,414} In **3**, however, only one of the thiomorpholine molecules was found to be disordered, and the other two were involved only in hydrogen bonding. Here, therefore, two of the thiomorpholines acted as a base deprotonating the acid, while the third acted only to form halogen bonds and so the thio and imino groups could indeed be considered equivalent from the point of view of halogen bonding. That the halogen-bonded iodine atom is found on the axial positions (Figure 7-17) infers that the covalently bonded imine hydrogen atom is a sterically more demanding substituent as suggested by Cinčić *et al.* The halogen contact distances in these two structures are given in Table 7-2.

A further, interesting comparison can then be made in considering the non-covalent interactions found in **5** and **6**, in which the potential sulfur donor has been oxidised to the *S*-oxide. Here, the axial position at sulfur is now taken by the oxide oxygen, which acts as a pretty effective hydrogen-bond acceptor and now prevents the formation of a halogen bond at this position. This result is of interest as it shows clearly how the introduction of a good hydrogen-bond acceptor can generate alternative molecular arrangements and so provides a nice example of competition between halogen and hydrogen bonds.

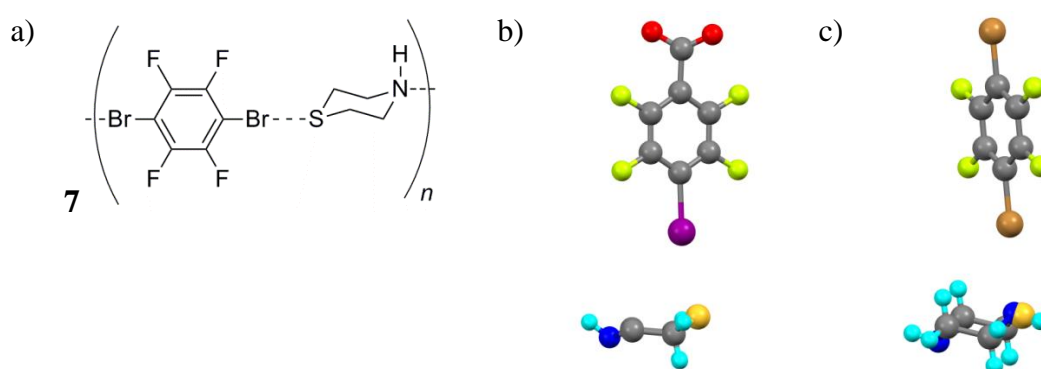


Figure 7-17: (a) Dibromodotetrafluorobenzene • thiomorpholine co-crystal (b) Axial arrangement of the halogen bond in **3** (disorder removed); (c) axial arrangement of the halogen bond in **7** reported by Cinčić *et al.*⁴¹²

Table 7-2: List of short halogen contacts in **2** and **7**.

Structure	Space group	Contacts		
		Halogen contacts	Length / Å	% of Σ vdW radii
3	<i>P</i> -1	I...S	3.064(5)	81%
		I...N	3.37(2)	95%
7 ⁴¹²	<i>P</i> -1	I...S	3.171(3)	84%
		I...N	2.989(9)	85%

It is clear from Table 7-2 that, while in **7** the I...S and I...N interactions show comparable degrees of contraction (16% and 15%), in **3** the contraction in I...S

(19%) is much more significant than that in I \cdots N (5%). It is also interesting that the I \cdots S halogen bonding in **3** is shorter than these in **2** and in the co-crystal between 1,4-diiodotetrafluorobenzene and thiomorpholine, however it is difficult to state conclusively that the I \cdots S halogen bond in **2** is stronger just by comparing the intermolecular distances. Based on the melting points of the co-crystals measured by differential scanning calorimetry, Cinčić *et al.* suggested that the I \cdots O and I \cdots S interactions are of similar strengths, while the I \cdots N bond is considerably stronger, although it is noted that the proposed equivalence of O and S would not necessarily agree with the iodine basicity scale.¹¹ That only one of the thiomorpholine molecules in **3** was involved in either, but not simultaneously, hydrogen bonding and halogen bonding represents an interesting balance between these two interactions. The crystallographic disorder observed in **2**, however, prevents a definitive classification of the I \cdots N and I \cdots S interactions in the hierarchy of intermolecular interactions.

7.4 Orthogonal and Non-Orthogonal Halogen and Hydrogen Bonding

The structure between iodotetrafluorophenol and thiophene S-oxide reveals halogen and hydrogen bonding that are almost orthogonal. This orthogonality has been observed in the area of biology by Ho and co-workers.⁴⁰⁵

In an attempt to produce small molecule analogues of the orthogonal halogen and hydrogen bond interactions observed in biological systems and to further understand the balance between the two interactions co-crystallisations between pentafluorophenol, 4-bromo-2,3,5,6-tetrafluorophenol and 4-iodo-2,3,5,6-tetrafluorophenol and different cyclic secondary and tertiary amines were set up (Figure 7-18).

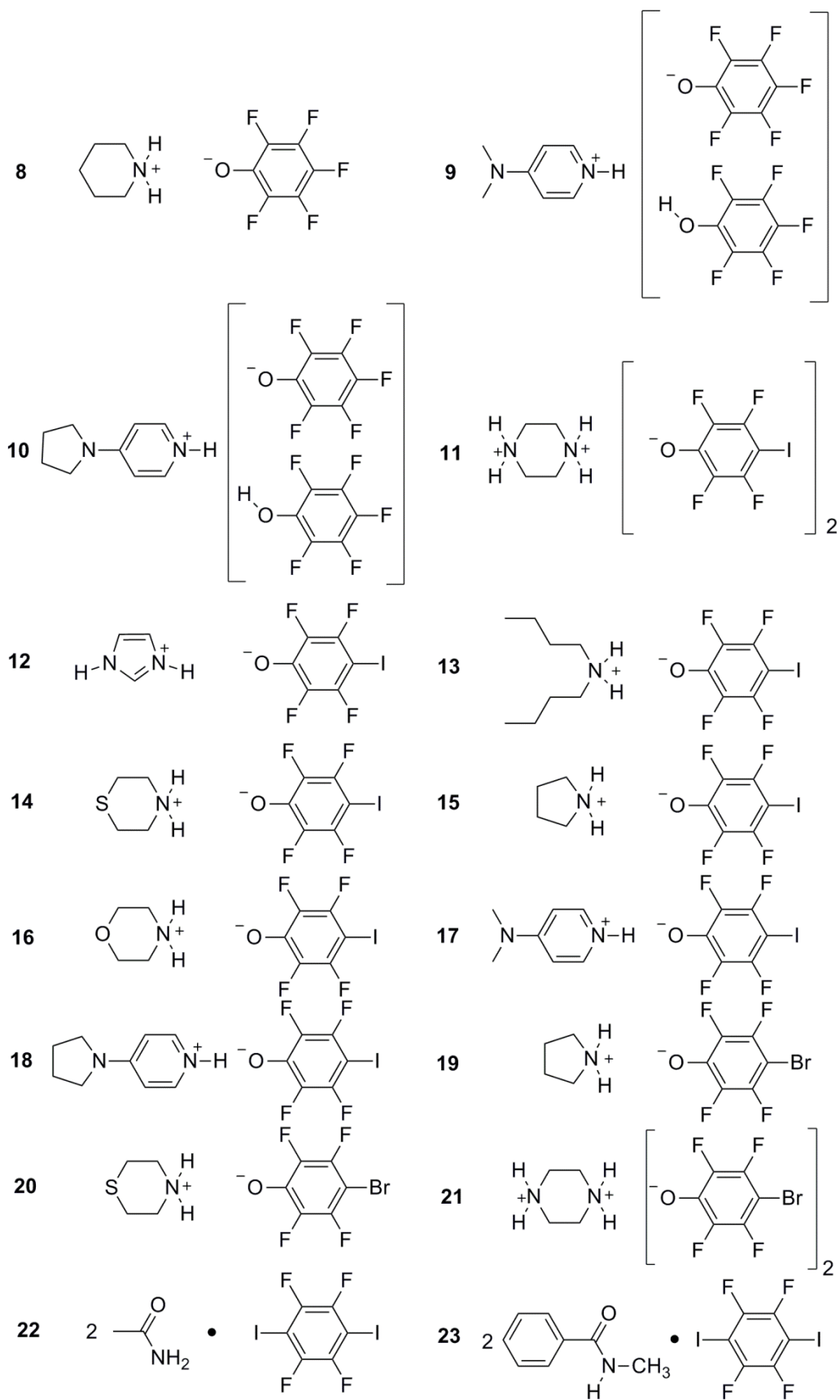


Figure 7-18: The co-crystals studied in this chapter.

7.5 Salts of Pentafluorophenol

7.5.1 Piperidinium Pentafluorophenate (8)

The complex crystallised with the expected 1 : 1 stoichiometry and the positions of the hydrogens on the nitrogen were confirmed by difference mapping, whereas all the positions of all other hydrogens were calculated and refined using a riding model. The piperidine deprotonated the pentafluorophenol (in contrast to the co-crystal with aniline where both components were neutral)⁴¹⁵ and the crystallised salt exists as a 2 : 2 dimer in which two of the phenate anions are held together by hydrogen bonding to the two N–H hydrogen atoms on each of the secondary ammonium cations (Figure 7-19a). This gives a bifurcated motif at oxygen and leads to the formation of a hydrogen-bonded, eight-membered ring arrangement involving two nitrogen atoms, two oxygen atoms and four hydrogen atoms, in which all atoms are close to being co-planar. The two oxygen atoms are not opposed directly and the C–O...O angle is found at 173.95°. The N–H distances are equivalent at about 1.8 Å and the two hydrogen atoms binding to oxygen make an angle of 96.32°.

The structure propagates in the direction perpendicular to the fluorophenyl rings which stack upon one another with a plane-to-plane separation of 3.310 Å to give the motif shown in Figure 7-19b. The apparent 'voids' to either side of the main stack are occupied by neighbouring stacks that are out of register.

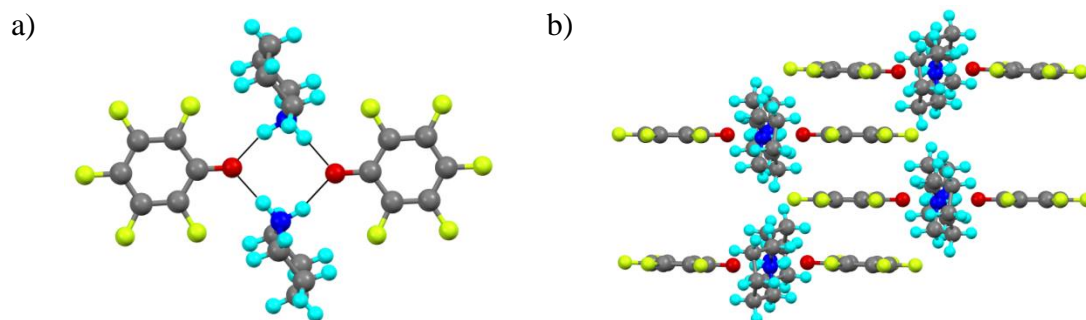


Figure 7-19: (a) Hydrogen-bonded 2 + 2 dimer of salt **8** (hydrogen bonds drawn in black);
(b) Packing motif in **8**.

7.5.2 4-(N,N-Dimethylamino)pyridinium Pentafluorophenate • Pentafluorophenol (9) and 4-(Pyrrolidino)pyridinium Pentafluorophenate • Pentafluorophenol (10)

As expected, in **9** the phenol is deprotonated by the DMAP and the N–H hydrogen atom forms a hydrogen bond to the phenate oxygen atom at a distance of 1.84(2) Å. Examination of the structure reveals that it crystallises with an additional molecule of pentafluorophenol and that this phenolic hydrogen atom forms a hydrogen bond to the oxygen of the phenate anion, a hydrogen bond that, at 1.68(3) Å, is just shorter statistically than that to the pyridinium hydrogen atom (Figure 7-20a). The dihedral angle between the aromatic ring and the phenolic hydrogen is 9(1)°, whereas it is 25.4(8)° when the N–H hydrogen is considered; the angle made at the phenate oxygen by the two hydrogen-bonded hydrogen atoms is 119(1)°. Also of note is that the angle made between the planes of the two phenolic rings makes them close to co-planar (8.5°), whereas the [DMAPH]⁺ ring makes an angle of 68.03° to the phenate ring (Figure 7-21a).

In **10**, the phenol is again deprotonated by the tertiary amine and, in common with the structure of **9**, the cation-anion pair co-crystallise with a molecule of pentafluorophenol (Figure 7-20b). The O–H···O hydrogen bond at 1.56(3) Å is again shorter than the N–H···O hydrogen bond at 1.79(2) Å. In this structure, the cation ring is now closer to the plane of the phenate ring with the two intersecting with an angle of 17.85° with the two phenolic rings making a larger angle of 46.94° (Figure 7-21b).

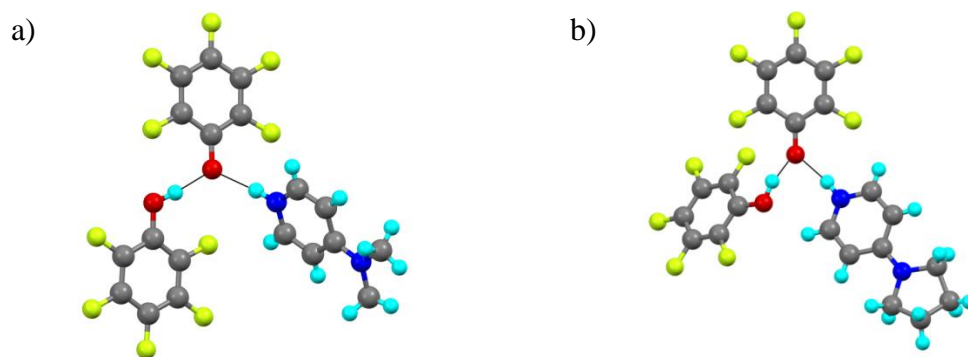


Figure 7-20: Molecular structure of (a) **9** and (b) **10**.

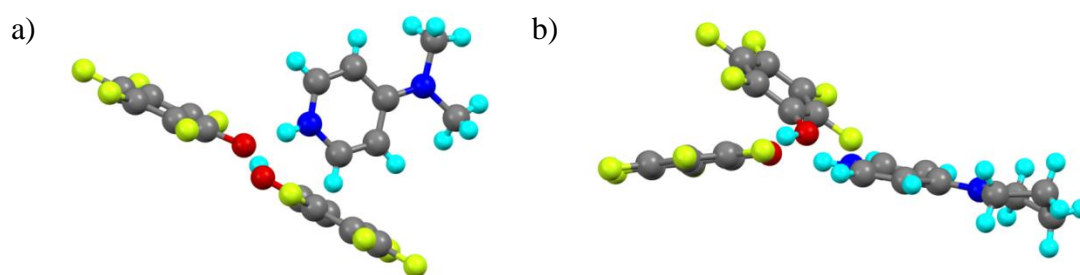


Figure 7-21: (a) View showing the relative disposition of the two fluorinated rings in (a) **9** and (b) **10**.

7.6 Salts of 4-Iodo-2,3,5,6-tetrafluorophenol

7.6.1 Piperazine-1,4-dium 4-Iodotetrafluorophenate (**11**)

The complex crystallised as a 2 : 1 (anion/cation) salt as both nitrogen atoms of the piperazine were protonated to give a dication. The basic motif is described by a polymeric arrangement in which two 'opposing' phenates are held together by two piperazine dications with a cationic NH_2^+ group hydrogen bonding to the two oxygen atoms ($d_{\text{O}\cdots\text{H}} = 1.774(1)$ and $1.863(1)$ Å – there is a formal inversion centre) giving an eight-membered ring embracing two dications and two phenates with the $\text{H}\cdots\text{O}\cdots\text{H}$ angle as $107.37(7)^\circ$. Note that the two aromatic rings are not coplanar (Figure 7-22a). The other end of each dication participates in an identical bonding pattern, leading to the basic polymeric unit (Figure 7-22b) and it can be seen that the

aromatic rings form a staircase-like arrangement. Other details of the crystal packing in **11** are shown in Figure 7-23.

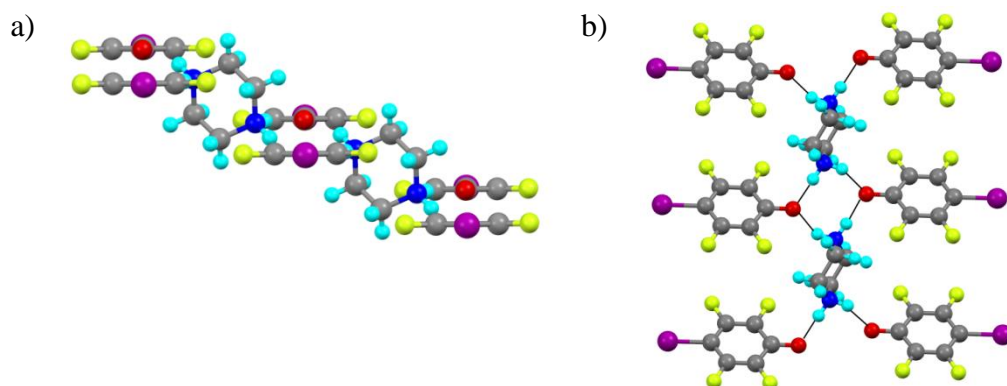


Figure 7-22: Two views of the polymeric motif of complex **11**: (a) Side view and (b) top view.

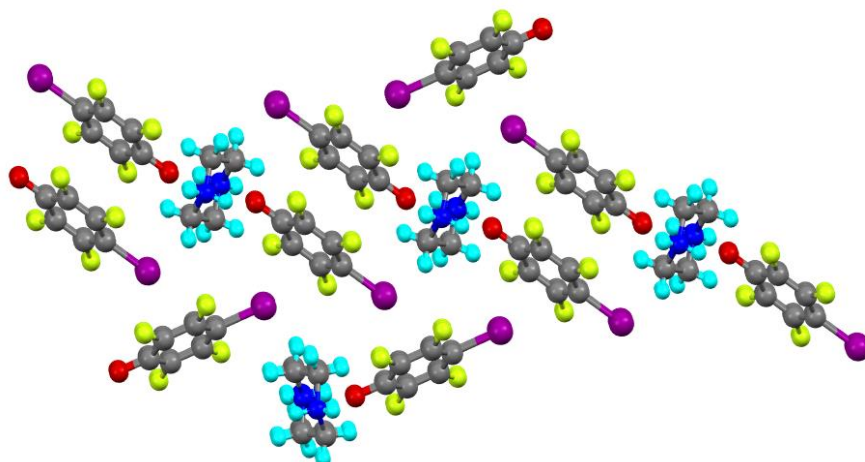


Figure 7-23: Crystal packing in **11**. The 4-iodotetrafluorophenol rings are antiparallel. They do not sit directly upon one another, but their planes are strictly co-parallel, being separated by 3.257 Å. Note that there are no short contacts to iodine.

7.6.2 Imidazolium Iodotetrafluorophenate (**12**)

The asymmetric unit contained two pairs of molecules, which were related symmetrically by a 180° rotation, although the axis of rotation did not correspond to a crystallographic axis. C–H hydrogen atoms were placed using a riding model, with acidic hydrogen atoms being located by difference mapping after all other atoms were located and refined.

The structure propagates as a hydrogen-bonded polymer with the hydrogen bonding describing a bifurcated motif at each phenate oxygen, which are of two types. Thus in Figure 7-24, all of the hydrogen bonds shown are statistically the same length (approximately 1.8 Å), but the torsion angles with respect to the six-membered ring differ. Thus, the torsions described by C11-C10-O2-H4 and by C15-C10-O2-H2 are 10(3)° and 3(3)°, respectively, whereas those described by C1-C2-O1-H1 and by C6-C1-O1-H3 are 16(3)° and 44(3)°, respectively. The less planar arrangement at O1 is understood as there is a long contact (2.434(3) Å) to the C–H (on the C4 carbon) of a neighbouring imidazole (Figure 7-25), which sits with a torsion angle of 53.3(4)° with respect to C6-C1-O1. There is no such interaction at O2. The two H···O···H angles are also different, with that at O2 being 104(3)° whereas that at O1 is larger at 116(3)°.

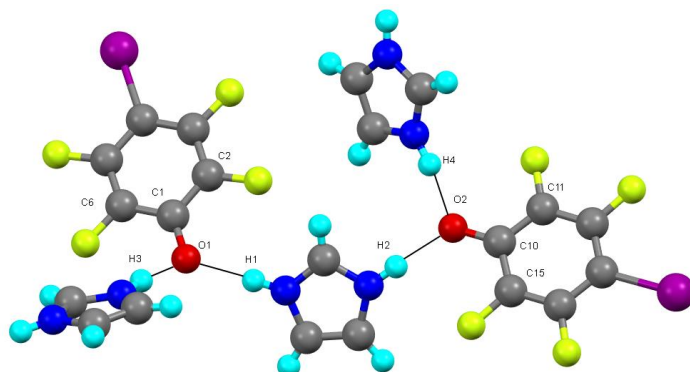


Figure 7-24: The basic polymeric repeat unit in **12**.

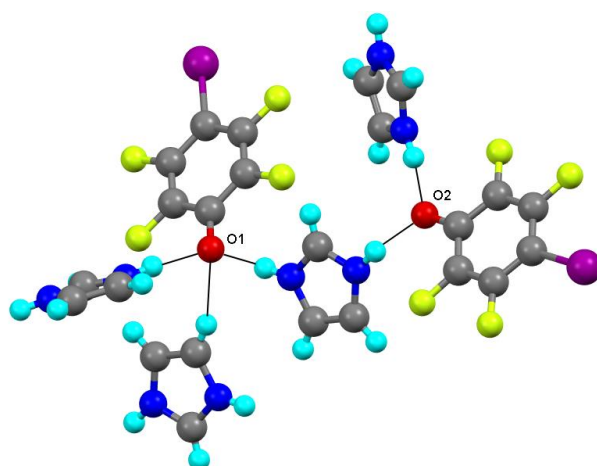


Figure 7-25: Illustration of the different hydrogen bonding interactions at O1 and O2 in **12**.

The hydrogen-bonding propagates in a sort of sigmoidal fashion (Figure 7-26a) linking together crystallographically related cations and anions. The other independent cation–anion pair propagates similarly and the interaction between the two chains comes in the form of I⋯F interactions (Figure 7-26b) with an I⋯F separation of 3.133(2) Å – about 90% of the sum of the two van der Waals radii. These have the geometric appearance of Type I interactions but, given that F is δ^- and I is δ^+ along the extension of the C–I axis, then it is likely that this is an attractive interaction, not least because the angle at iodine is not so far from linear. Thus, the angle of interaction measured at iodine is 167.3(1)°, while measured at fluorine it is 157.0(2)°. Examination of Figure 7-26b suggests also the possibility of a Type I I⋯I interaction, but with a separation of 3.8725(4) Å, it is almost exactly twice the van der Waals radius of iodine and so is considered unimportant.

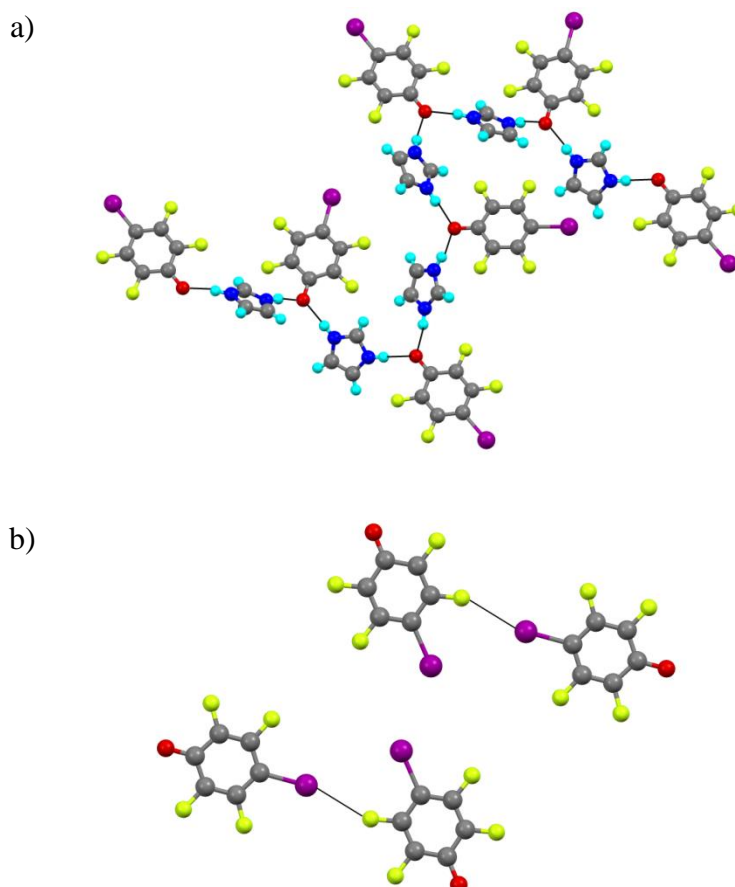


Figure 7-26: (a) The extended polymeric motif in **12** and (b) illustration of the short I⋯F interactions.

7.6.3 Dibutylammonium Iodotetrafluorophenate (13)

Dibutylammonium iodotetrafluorophenate crystallised in the space group I_2/m as a simple 1 : 1 salt in which two cations and two anions hydrogen bond together to form an eight-membered ring. Two views are shown as Figure 7-27, with Figure 7-27a showing the antiperiplanar arrangement in the dibutylammonium cation which is, perhaps, better viewed as a 4-azanonane. The packing arrangement is shown in Figure 7-28.

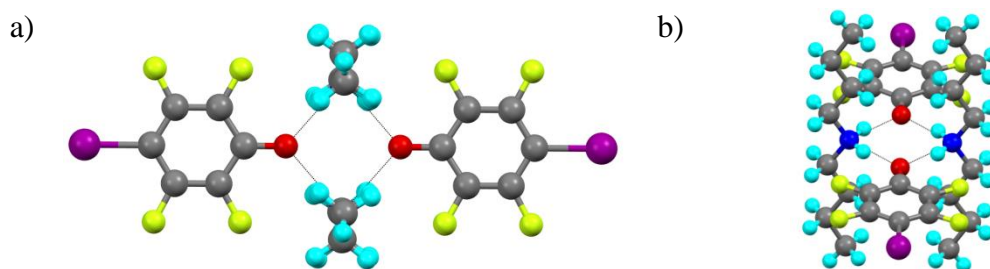


Figure 7-27: Two views of the hydrogen-bonded unit: (a) viewed looking down the 'axis' of the dibutylammonium chains and (b) at an angle to show the N–H...O hydrogen bonds.

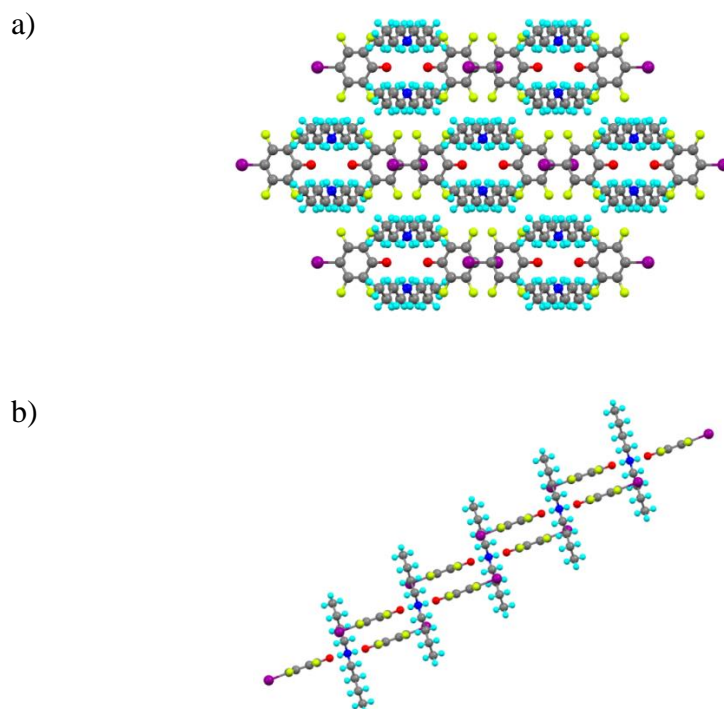


Figure 7-28: Views of the crystal packing in **13** (a) viewed down the *a*-axis and (b) viewed down the *b*-axis.

7.6.4 Thiomorpholinium Iodotetrafluorophenate (14)

The material crystallised as a 1 : 1 salt and, in common with the structures of the imidazolium and piperazine-1,4-dium salts of iodotetrafluorophenol, the basic structural motif showed a bifurcated motif for the hydrogen bonding at the oxygen atoms. Also in common with the salt of piperazine, the second hydrogen atom of the secondary ammonium cation took part in a similar interaction to give a hydrogen-bonded, eight-membered ring (Figure 7-29). Although not different statistically, the hydrogen-bond lengths are noted as 1.85(2) and 1.71(3) Å and the H···O···H angle is 106(1)°.

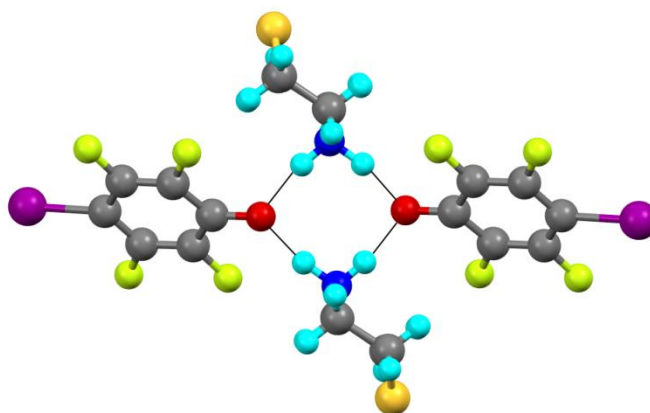


Figure 7-29: The hydrogen-bonded motif in **14**.

Assembly of this dimeric arrangement into a polymeric structure now brings halogen bonding into play, so that the iodine atoms interact with the thiomorpholinium sulfurs of neighbouring dimers to give the arrangement shown in Figure 7-30. The S···I separation is 3.3085(6) Å (87.5% of the sum of the two van der Waals radii) and the halogen bond angle at iodine is 172.19(5)°. The directionality of the interaction with sulfur is consistent with a classical view of the position of non-bonded (lone) pairs of electrons on the sulfur atoms, although it should be noted that the C–S···I angles are unsymmetric, being found at 87.81(7)° and 107.79(7)°. The polymer propagates in the *ac* plane and there are no structurally significant interactions to neighbouring chains in either the *a* or *b* directions.

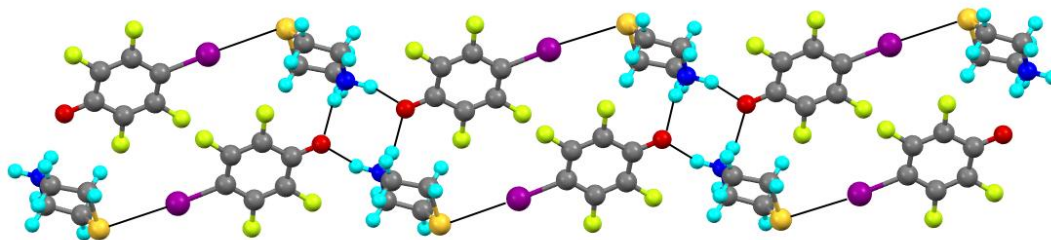


Figure 7-30: Polymeric arrangement in **14** viewed down the *b*-axis and showing the I...S halogen bonds.

7.6.5 Pyrrolidinium Iodotetrafluorophenate (**15**)

Being the salt of a secondary amine, this material forms the expected dimer supported by hydrogen bonding (Figure 7-31a) between the ammonium hydrogen atoms and two phenate oxygens with $d_{\text{H}\cdots\text{O}} = 1.79 \text{ \AA}$ and the H...O...H angle being 94° . What is totally unexpected, however, is that each oxygen also forms a halogen bond with iodine perpendicular to the plane of the phenate anion and, as shown in Figure 7-31b, one of these halogen bonds is above the plane of the dimer and the other below it. In each case, the halogen-bond length is $3.043(1) \text{ \AA}$ – 87% of the sum of the van der Waals radii.

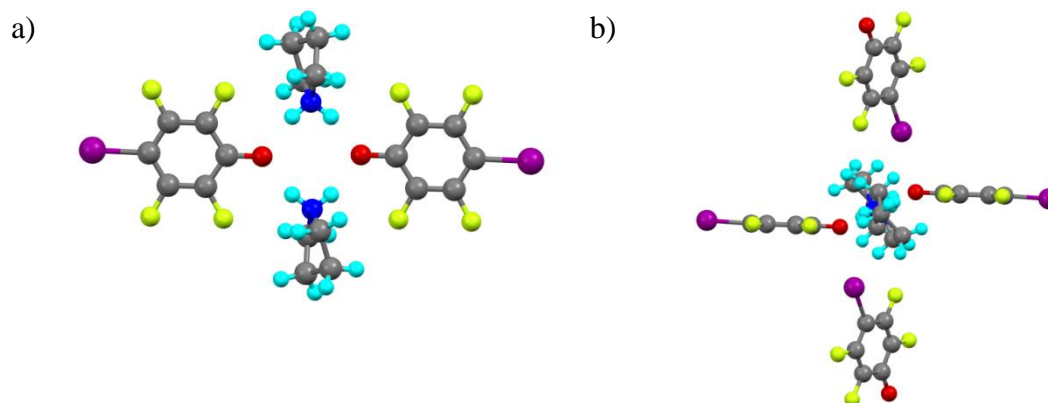


Figure 7-31: (a) The hydrogen-bonded dimer in **15** and (b) side view of the dimer showing the I...O halogen bonds.

The directionality of the halogen bond is shown in Figure 7-32, where the two torsion angles made with respect to the plane of the anion ring can be seen. The

torsion angle illustrated by Figure 7-32a and measured with respect to the normal to the ring is found to be 16.5° , while the $\text{C}-\text{O}\cdots\text{I}$ angle (Figure 7-32b) is $105.2(1)^\circ$.

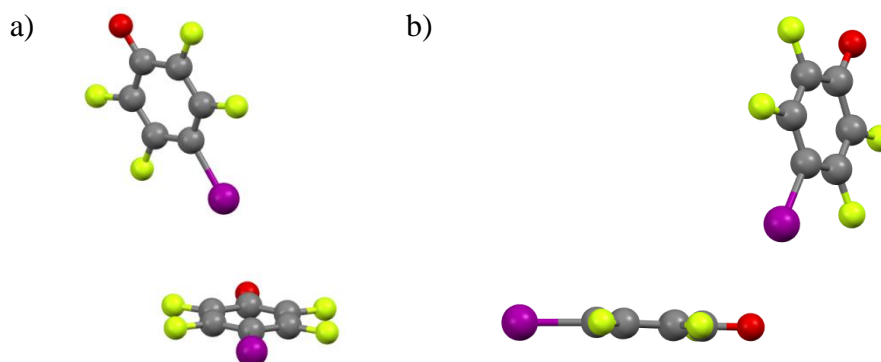


Figure 7-32: Two views illustrating the directionality of the $\text{I}\cdots\text{O}$ halogen bond in **15**.

If the crystal structure is grown by developing only $\text{I}\cdots\text{O}$ contacts, then a grid structure is formed as shown in Figure 7-33a, containing 'boxes' whose volume is estimated at about 740 \AA^3 based on the separation between iodophenate rings (10.092 \AA in one direction and 9.449 \AA in the other). With anions alone, however, this motif extends only in the b -direction and it is necessary to bring the cations into play in order to extend fully into the bc plane, as indicated in Figure 7-33b.

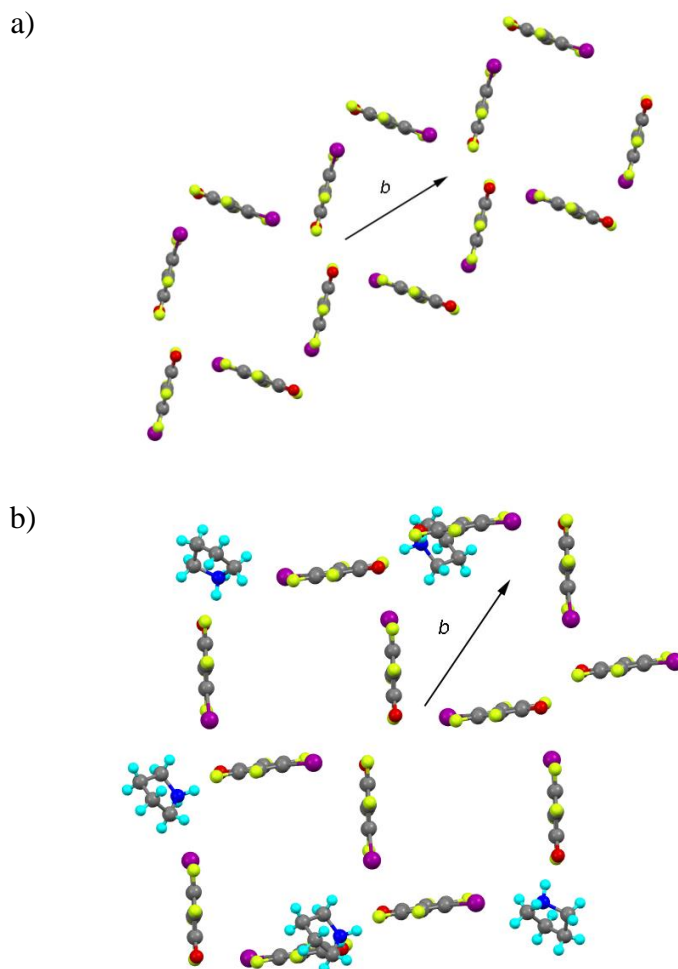


Figure 7-33: Two views of the crystal packing of **15** looking down the *a* axis:
 (a) 'boxes' described by the arrangement of the iodotetrafluorophenate anions and
 (b) showing the interaction with the pyrrolidinium cations.

Of course, these grids are not empty and closer examination of the crystal structure then shows a second motif. Thus, not all iodine atoms are involved in halogen bonding, rather arranging as shown in Figure 7-34 where there is a hydrogen-bonded dimeric unit in which neither of the phenate oxygens is halogen bonded to iodine and where the terminal iodines of the dimer show an I...F contact at 3.2476 Å (94% of the sum of the van der Waals radii) with a C-I...F angle of 156.4°. Two of these units then occupy the vacancies created by the grid structure and are arranged effectively orthogonal to the sides of the grid as illustrated in Figure 7-35.

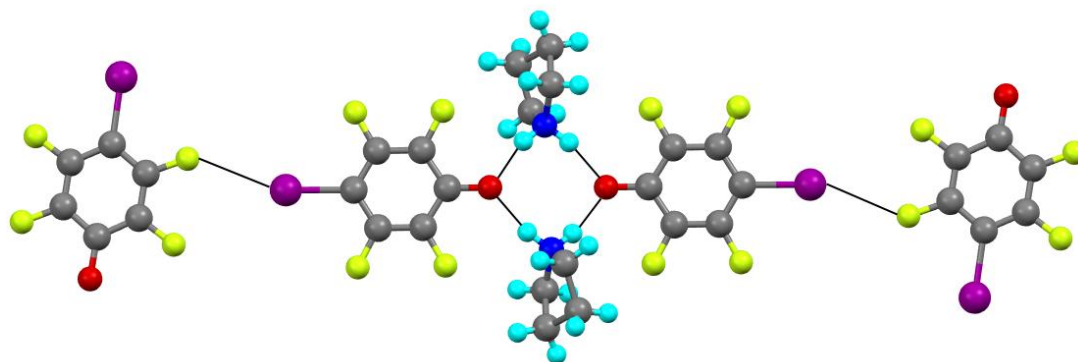


Figure 7-34: Part of the structure of **15** showing iodotetrafluorophenols not involved in halogen bonding.

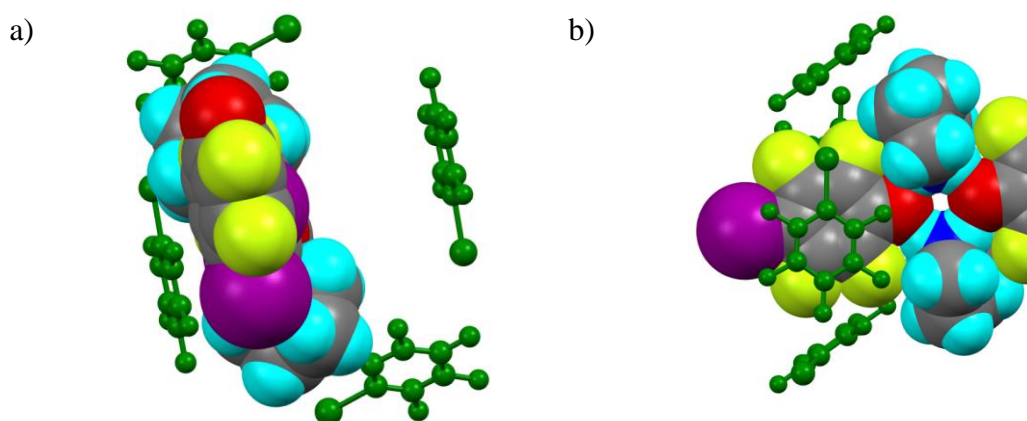


Figure 7-35: One of the two chains that occupy the vacancies generated by the grid (shown in green) described by interactions of phenate anions *via* O...I halogen bonding (a) end-on view and (b) side-on view.

7.6.6 Morpholinium Iodotetrafluorophenate (**16**)

In common with the above structures, a hydrogen-bonded dimer is formed involving two cations and two anions except that in **16** there dimers are distinct. In each case there are hydrogen-bond lengths of 1.93(3) and 1.77(3) Å; the hydrogen bonds are equal statistically, but differ in the H...O...H angles, which take the values 93° and 103°. In common with the structure of the pyrrolidinium salt **15**, I...O halogen bonds are found (Figure 7-36) and it was found that halogen bonding involves only the cation-anion rings that have the more acute angle. Thus, it is in these dimers that the phenate oxygen atoms interact to form halogen bonds and it is the iodine atoms of

the same phenate anion that interact with subsequent dimers forming halogen bonds. There are no close contacts involving the other, distinct cation-anion dimer. The I...O halogen bonds are found to be 3.053(1) Å in length (87% of the sum of the van der Waals radii) and the C-I...O angle is 164.06(5)°.

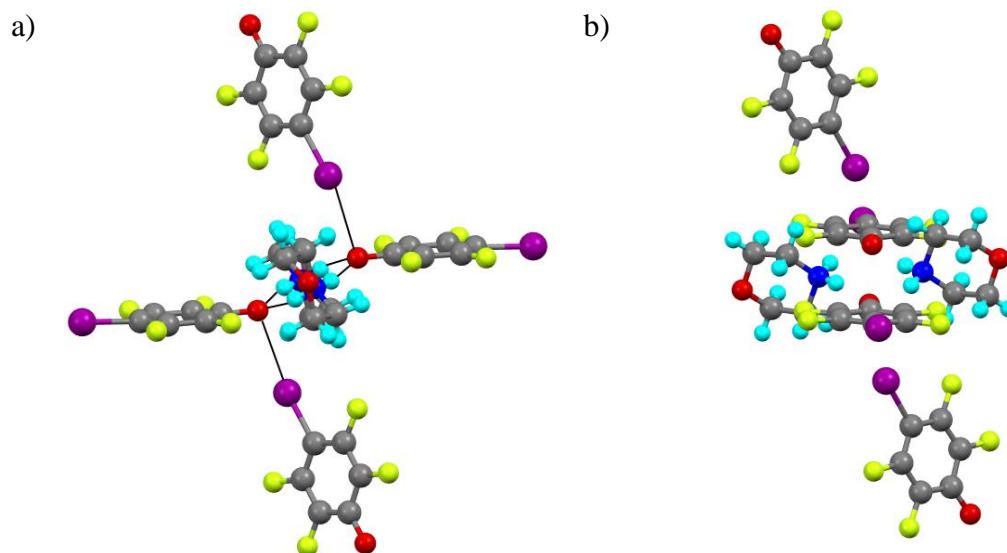


Figure 7-36: Two views on the halogen-bonding interactions into the hydrogen-bonded cation-anion dimers in **16**. The two views relate to one another through a 90° rotation.

Once more, the iodotetrafluorophenate anions define a grid structure (Figure 7-37), although this is not quite the same as that in **15** and has a larger volume at about 920 Å³. The grids are again filled by chains of the type seen in **15** (Figure 7-33).

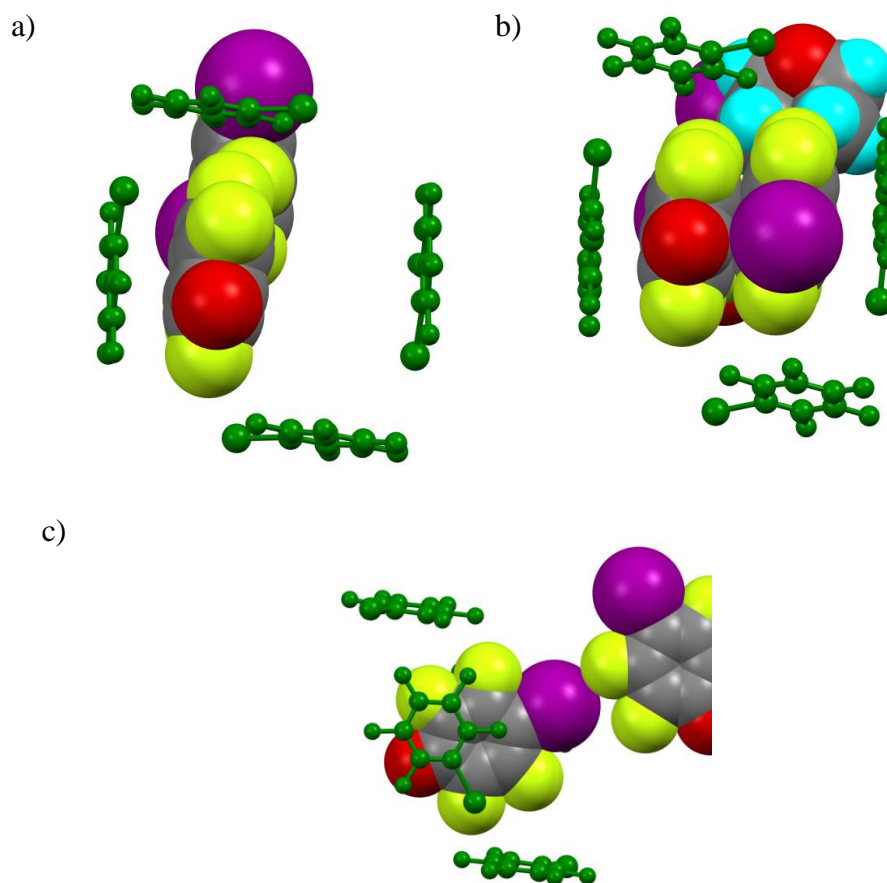


Figure 7-37: Three views of aspects of the crystal packing of **16**. (a) End-on view of a half-full anion box (b) end-on view of a full anion box and (c) half-full, end-on box from the side.

7.6.7 4-(N,N-Dimethylamino)pyridinium Iodotetrafluorophenate (**17**) and 4-(Pyrrolidino)pyridinium Iodotetrafluorophenate (**18**)

Being a tertiary amine, protonated DMAP offers only one hydrogen atom for hydrogen bonding, which binds to the phenate oxygen in the plane of the iodotetrafluorophenate ring. As found earlier with salts **9** and **10**, the phenate oxygen atom clearly prefers to bind to two electrophilic entities and so in the absence of another hydrogen atom, this role is fulfilled by the iodine atom of a neighbouring phenate anion to give the arrangement shown in Figure 7-38a, where $d_{I\cdots O} = 2.993(1)$ Å (85% of the sum of the van der Waals radii) and $d_{O\cdots H} = 1.76(2)$ Å; the $I\cdots O\cdots H$ angle is $100.1(8)^\circ$. Figure 7-38b shows the planarity of the arrangement in **17**. In

fact, there are two complexes in the unit cell and whereas the hydrogen-bond lengths are the same in each case, the other halogen bond is slightly shorter at 2.973(1) Å, although the I···O···H angle remains unchanged at 100.1(8)°. The 2D packing is shown as Figure 7-39.

A topologically similar motif has been reported recently by Aakeröy *et al.*⁴⁰³ in co-crystals of 4-iodotetrafluorophenol with 3,3'-azobipyridine, although in this case the phenol remains protonated and the I···O distance is longer at 3.091(10) Å, no doubt owing to its interaction with the neutral phenol rather than the anionic phenate ligand.

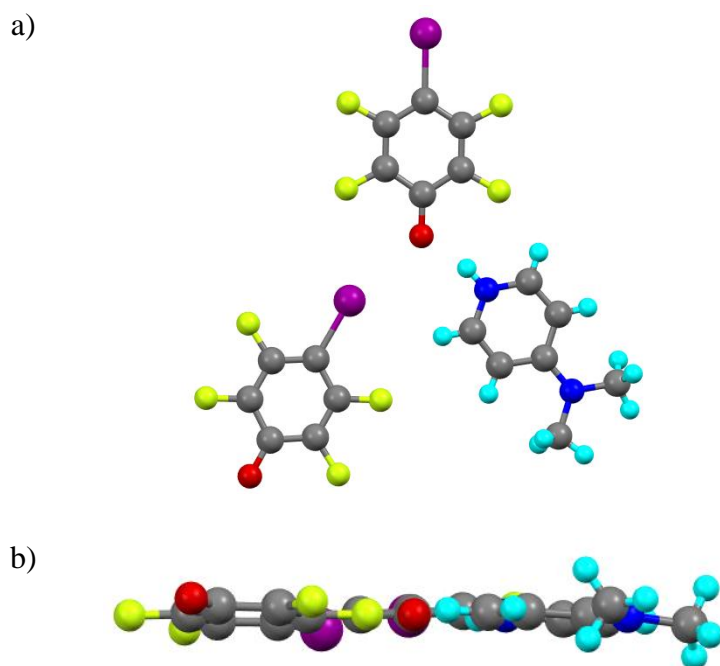


Figure 7-38: (a) View of complex **17** showing the O···H hydrogen bond and I···O halogen bond and (b) the same unit viewed from the side showing its planarity.

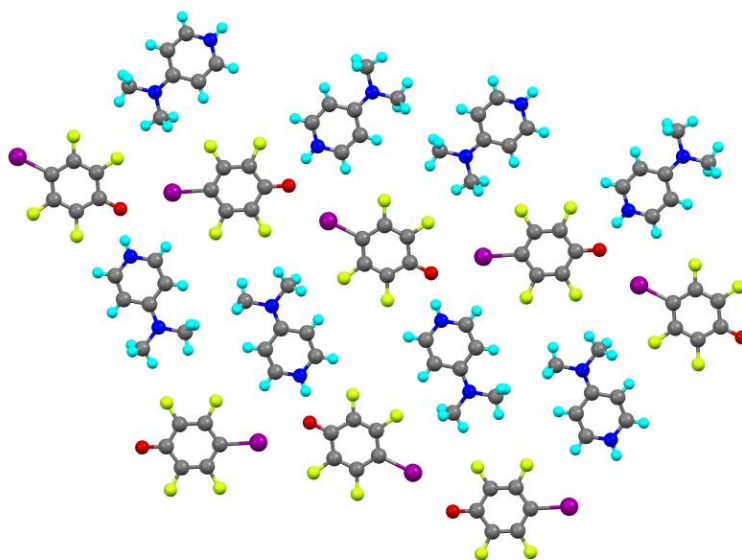


Figure 7-39: 2D packing in **17**.

Containing the 4-(pyrrolidino)pyridinium cation, **18** crystallised in a manner similar to that of **17** (Figure 7-40); the N \cdots H hydrogen bond is 1.79(4) Å long, whereas the O \cdots I halogen bond is found at 2.884(2) Å. This latter distance is 82% of the sum of the van der Waal's radii and so slightly shorter than that in **18**; the I \cdots O \cdots H angle is 100(1)°. The packing is also similar to that in **18** and is shown in Figure 7-41.

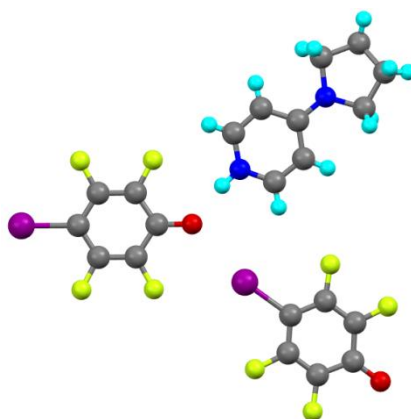


Figure 7-40: Partial structure of **18** showing both the hydrogen- and halogen-bonding interaction.

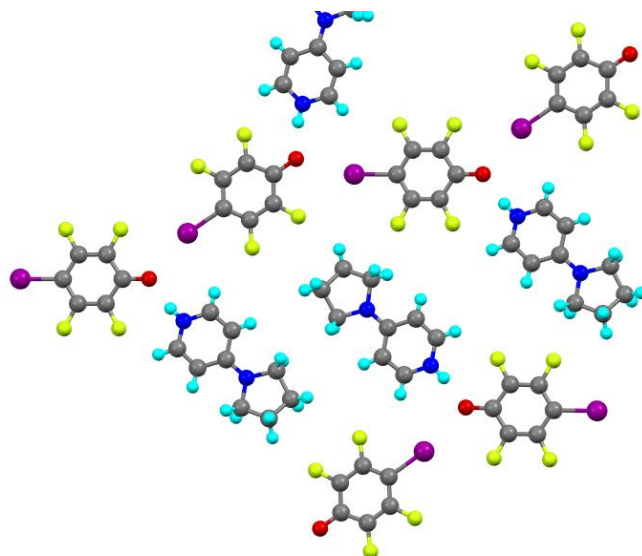


Figure 7-41: 2D packing in **18**.

7.7 Salts of 4-Bromo-2,3,5,6-tetrafluorophenol

7.7.1 Pyrrolidinium Bromotetrafluorophenate (**19**)

The material crystallised as a 1 : 1 salt and shows the now-familiar eight-membered, hydrogen-bonded ring with a bifurcated hydrogen bonding motif at the phenate oxygen atoms (Figure 7-42); the hydrogen bond distance is about 1.87 Å with the H···O···H angle being 105(1)°.

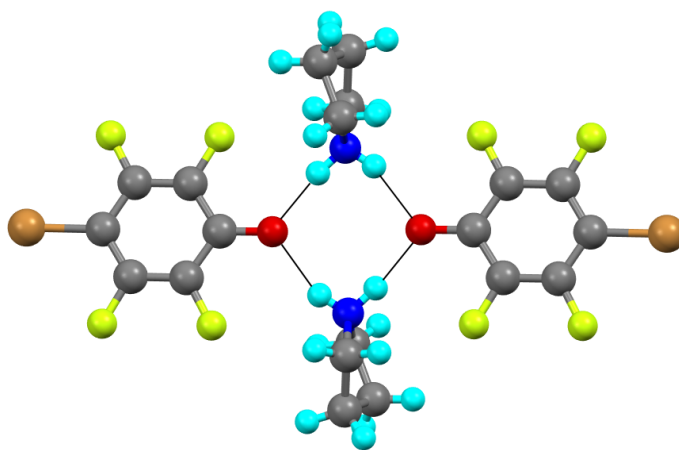


Figure 7-42: Arrangement of the hydrogen-bonded dimer of **19**.

The propagation of the structure is shown in Figure 7-43 and it is noted that there are no significant, intermolecular, structure-directing interactions and no short contacts to bromine.

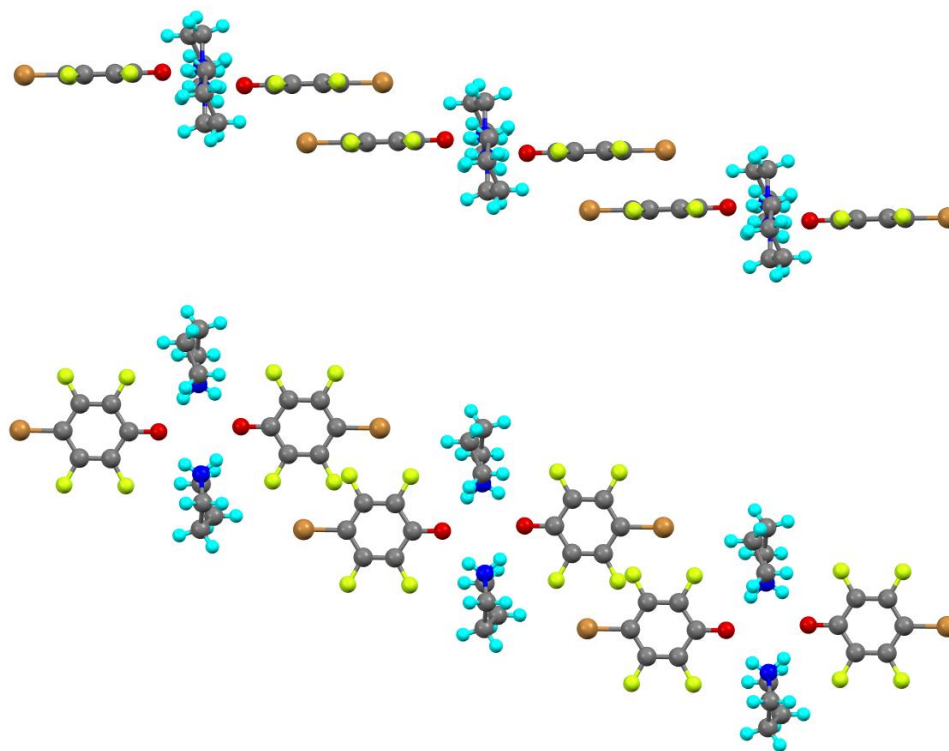


Figure 7-43: Crystal packing in **19**.

7.7.2 Thiomorpholinium Bromotetrafluorophenate (**20**)

This material crystallises as the 1 : 1 salt, but although it shows the same topological pattern of hydrogen bonding at the phenate oxygen atom, this leads to formation of a linear polymer and the eight-membered ring observed in all of the other structures of salts of secondary amines is absent (Figure 7-44). More than that, the angle made at the oxygen atom by the two ammonium hydrogen atoms is $136(1)^\circ$, whereas in the structure of thiomorpholinium iodotetrafluorophenate (**14**) it is $106(1)^\circ$ and for pyrrolidinium bromotetrafluorophenate (**19**) it is $105(1)^\circ$.

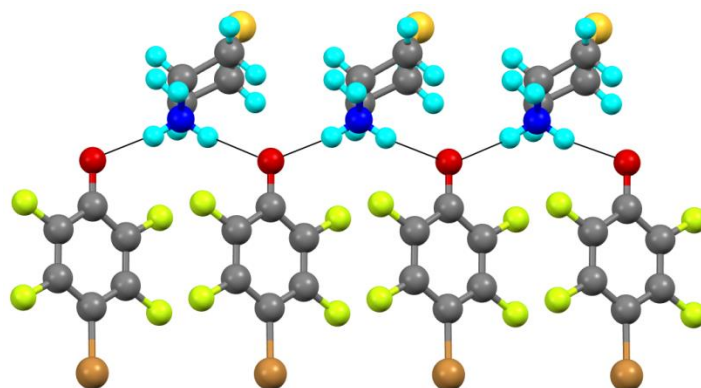
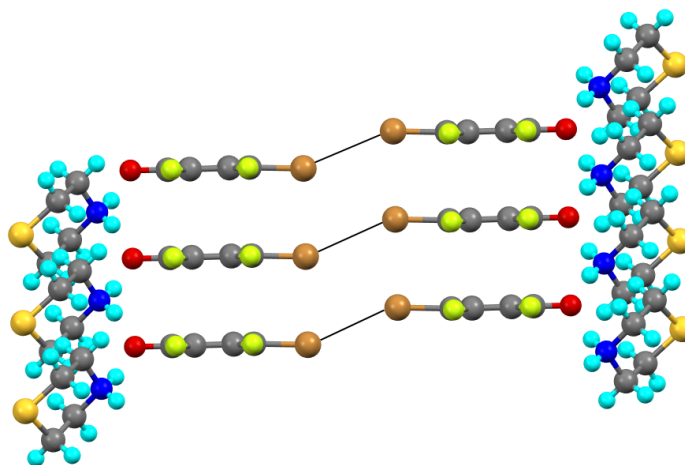


Figure 7-44: Linear, hydrogen-bonded polymeric arrangement in **20**.

The structure propagates as shown in Figure 7-45a, whereby there are Br...Br interactions with a Type I geometry, with the Br...Br distance being found at 3.3967(4) Å (92% of twice the van der Waals radius) and with an interaction angle at bromine of 155.83(6)°. Figure 7-45a is slightly misleading as it is not the case that the different bromotetrafluorophenate rings are stacked one upon the other, rather they are slipped with respect to one another, which is illustrated in Figure 7-45b. The distance between the planes described by the anion rings is 3.039 Å.

a)



b)

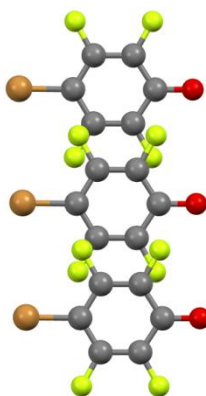


Figure 7-45: (a) Side-on view of the extended structure showing the Type I Br...Br interactions and (b) Top view showing only the relative positions of the bromotetrafluorophenate anions.

7.7.3 Piperazine-1,4-dium 4-Bromotetrafluorophenate (21)

This salt is all but isomorphous and isostructural with its iodo analogue (**10**) and is not discussed further save to say that there are no short contacts to bromine. Illustrative diagrams are shown in Figure 7-46.

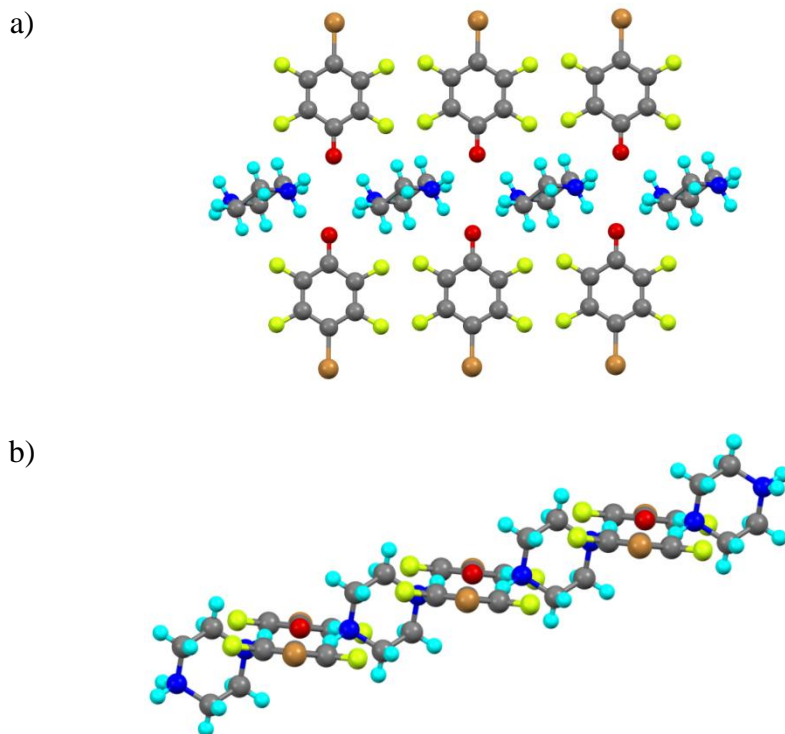


Figure 7-46: View of the polymeric structure of **21** (a) from above and (b) from the side.

7.8 Co-crystals of 1,4-Diiodotetrafluorobenzene with Amides

7.8.1 Acetamide : 1,4-Diiodotetrafluorobenzene (**22**)

The crystallisation was set up with *N*-methylacetamide and 1,4-diiodotetrafluorobenzene, but adventitious water caused hydrolysis to acetamide, which crystallised as a 2 : 1 co-crystal (amide/diiodotetrafluorobenzene). As seen in Figure 7-47a, the amide forms hydrogen-bonded sheets with the N–H hydrogen atoms and the carbonyl oxygen atoms, constituting the now topologically familiar eight-membered ring structure that arises from the arrangement of hydrogen-bonded, dimeric acetamide units. This arrangement is distinct from those found in the two crystal polymorphs of acetamide itself.^{416,417} The N⋯H separations are 2.06(3) and 2.16(3) Å with the H⋯O⋯H angle = 76(1)°. These sheets are then held together through halogen bonding as shown in Figure 7-47b, with the detail of the interaction of an iodine with the amide oxygen shown in Figure 7-47c. The I⋯O halogen bond

distance is 2.973(2) Å (84.9% of the sum of the van der Waals radii) with the C–I⋯O angle being 176.54(8)°. There are two H⋯O⋯I angles of 90.9(8)° and 86.5(9)°, whereas the C–O⋯I angle is 111.3(1)°. The packing of the 1,4-diiodobenzene units is shown in Figure 7-47d, viewed as looking down the *c*-axis. The separation of the planes defined by the aromatic rings is 3.294 Å although there are no short, inter-planar interactions.

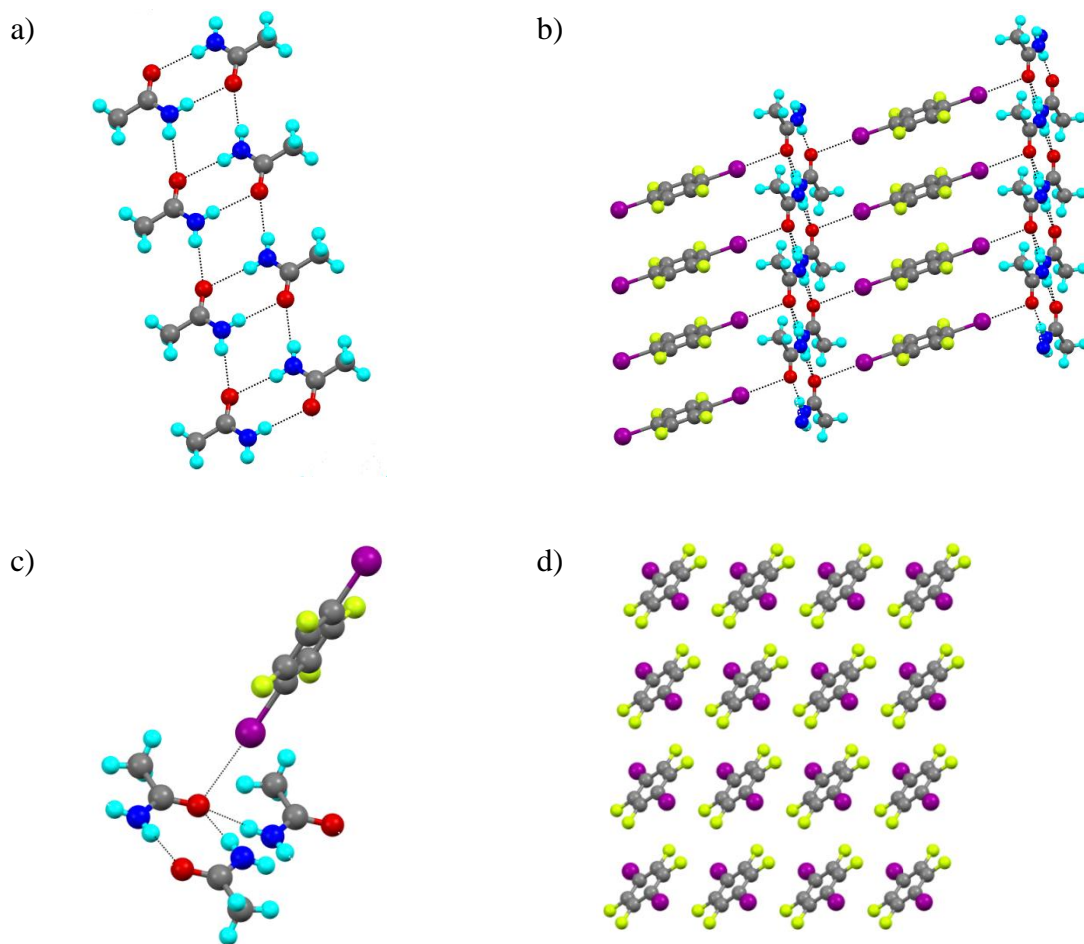


Figure 7-47: Aspects of the structure of **22**: (a) hydrogen-bonded sheet formed by acetamide; (b) linking of the hydrogen-bonded acetamide sheets by halogen bonding to 1,4-diiodotetrafluorobenzene; (c) 'close-up' showing the hydrogen and halogen bonding at the amide oxygen; (d) packing of 1,4-diiodotetrafluorobenzene viewed down the *c*-axis.

7.8.2 N-Methylbenzamide : 1,4-Diiodotetrafluorobenzene (23)

The co-crystals formed also have a 2 : 1 *N*-methylbenzamide/diiodotetrafluorobenzene stoichiometry, but with one proton less than **22**; it forms a one-dimensional chain through hydrogen bonding between the amide hydrogen and the carbonyl group of an adjacent amide. The aromatic rings do not sit one upon another, rather they propagate through the crystal in a stepped arrangement, with the rings being formally co-parallel every second molecule with a measured separation of 6.348 Å. This differs from the structure of *N*-methylbenzamide itself, where the aromatic rings alternate from one side of the hydrogen-bonded chain to the other.⁴¹⁸ Pairs of these chains are then bridged by molecules of 1,4-diiodotetrafluorobenzene (Figure 7-48a) which form an I···O halogen bond in which the I···O separation is 2.884(3) Å (82.4% of the sum of the van der Waals radii) with a C–I···O angle of 169.54(9)° and an I···O···H angle of 83.0(9)°. Note that in this case, the reduced number of hydrogen atoms available for hydrogen bonding means that each oxygen interacts with only one hydrogen and one iodine (Figure 7-48b), whereas in **22** there are two interactions with hydrogen. The crystal packing in **23** is illustrated in Figure 7-49.

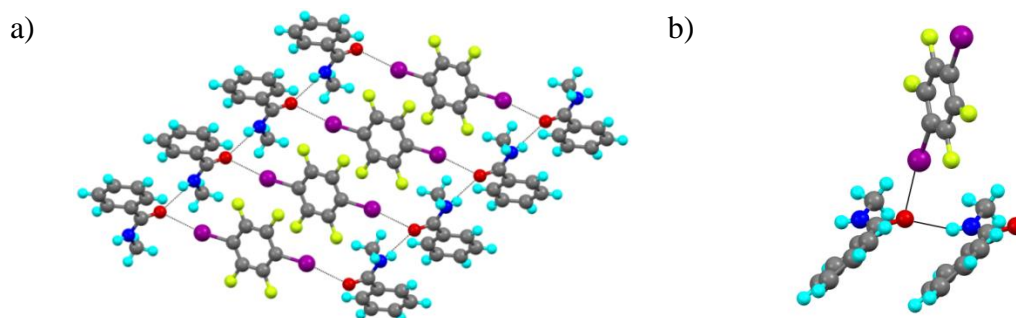


Figure 7-48: Structure of **23** showing (a) the linear, hydrogen-bonded motif of the methylbenzamide linked by 1,4-diiodotetrafluorobenzene and (b) detail of the hydrogen and halogen bonding at the amide carbonyl oxygen.

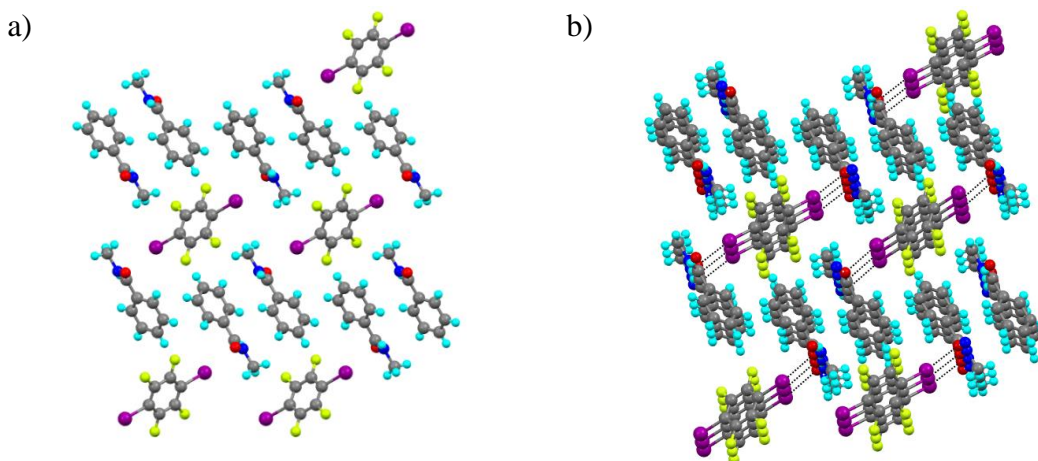


Figure 7-49: Crystal packing in **23** (a) viewed down the *b*-axis and (b) viewed just off the *b*-axis (halogen bonds indicated).

7.9 Discussion

7.9.1 Bonding in the Phenate Anions

When analysing the structures of the various salts described, it quickly became apparent that in almost every case, the C–O bond of the phenate was shorter than might otherwise be expected, being found between 1.291(2) and 1.312(3) Å. The only exception was in the neutral pentafluorophenols in **9** and **10**, not discussed further, where the distances were 1.3391(17) and 1.335(2) Å, respectively. The C–O length in pentafluorophenol itself is around 1.37 Å (data exist for >1 polymorph).

The contraction is consistent with the development of C=O π -bond character and prompted examination of the C–C bond lengths in the ring (Figure 7-50). Thus, in all cases but **8** and **11**, there was evidence for changes in the C–C bond lengths to a structure that could be described as either fully delocalised (Figure 7-50a: **9** (phenate ring), **10**, **13**, **14**, **15**, **20**) or partially delocalised (Figure 7-50b: **12**, **16**, **17**, **18**, **19**, **21**). 'Full delocalisation' means that the C1–C2 bond was statistically longer than both C2–C3 and C3–C4, while 'partial delocalisation' means that the C2–C3 bond

was statistically shorter than C1–C2 and C3–C4.^{xii} The distinction between the two classes takes the values of the estimated standard deviation (esd) into account, which in turn depend on the *R*-factor. That said, it is felt that, in reality, probably all of the structures fall into the 'fully delocalised' category. Interrogation of the Cambridge Crystallographic Database shows rather few structures of the free pentafluorophenate anion where such delocalisation is observed, although the papers tend to contain no comments, however, the Database also shows that such delocalisation is quite common in phenate anions.

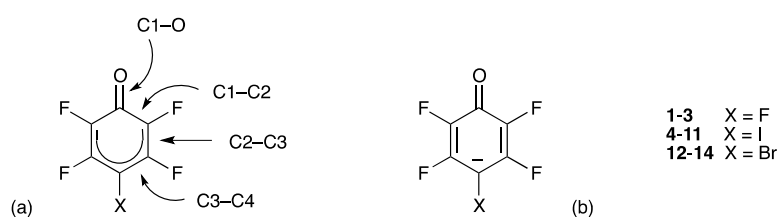


Figure 7-50: (a) The 'fully' delocalised and (b) the 'partially' delocalised bonding motifs found in the various phenate anions.

To probe this further, the geometries of pentafluorophenol, 4-halotetrafluorophenols and their anions were optimised at the MP2(Full) level of theory and their electronic structures were subjected to natural bond orbital (NBO) analyses. Thus, computational results (Figure 7-51) show the shortening of the C–O bond on ionisation and are also consistent with a 'fully' delocalised structure.

^{xii} Note that C1, C2 *etc.* are generic labels and that the actual atom numbers will vary from structure to structure.

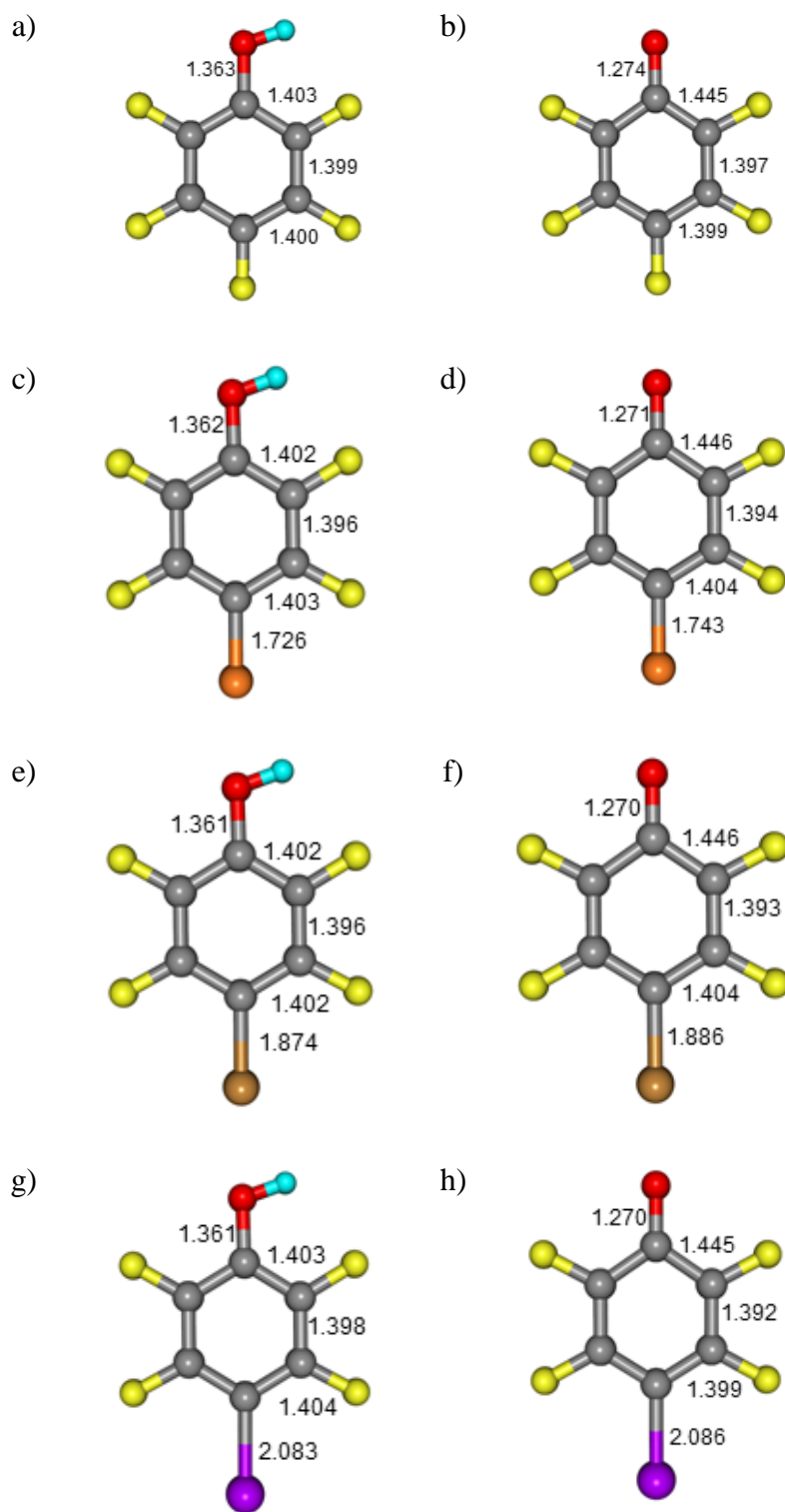


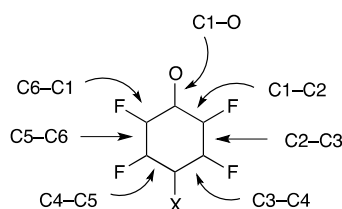
Figure 7-51: MP2(Full)-optimised geometries: C–C and C–O bond lengths (in Å) of a) pentafluorophenol, b) the pentafluorophenate anion, c) 4-chlorotetrafluorophenol, d) the 4-chlorotetrafluorophenate anion, e) 4-bromotetrafluorophenol f) the 4-bromotetrafluorophenate anion, g) 4-iodotetrafluorophenol and g) the 4-iodotetrafluorophenate anion.

Table 7-3: Key phenate bond lengths in complexes studied.

	8	9 (phenol)	9 (phenate)	10 (phenol)	10 (phenate)	11	12	13	14
$d(\text{C1}=\text{O}) / \text{\AA}$	1.311(3)	1.3391(17)	1.3116(16)	1.335(2)	1.301(2)	1.306(2)	1.304(5)	1.297(5)	1.297(2)
$d(\text{C1}-\text{C2}) / \text{\AA}$	1.400(3) / 1.404(3)	1.390(2) / 1.400(2)	1.406(2) / 1.414(2)	1.392(2) / 1.384(2)	1.402(2) / 1.404(2)	1.412(5) / 1.409(5)	1.412(5) / 1.409(5)	1.404(4)	1.406(3) / 1.408(3)
$d(\text{C2}-\text{C3}) / \text{\AA}$	1.384(3) / 1.373(3)	1.385(2) / 1.3874(19)	1.3866(19) / 1.3833(19)	1.376(2) / 1.384(2)	1.377(2) / 1.373(2)	1.376(3) / 1.379(3)	1.380(6) / 1.382(5)	1.371(5)	1.376(3) / 1.370(3)
$d(\text{C3}-\text{C4}) / \text{\AA}$	1.377(4) / 1.376(3)	1.383(2) / 1.378(2)	1.377(2) / 1.384(2)	1.370(2) / 1.374(2)	1.377(2) / 1.372(2)	1.385(3) / 1.390(3)	1.388(5) / 1.395(6)	1.379(4)	1.387(3) / 1.389(3)
Angle Type	H...O...H	H...O...H	H...O...H	H...O...H	H...O...H	H...O...H	H...O...H	H...O...H	H...O...H
Angle /°	96	119	96	107	104 116	110	106		
	15*	16*	17	18	19	20	21	22	23
$d(\text{C1}=\text{O}) / \text{\AA}$	1.298(2)	1.3079(18)	1.291(2)	1.292(3)	1.298(2)	1.301(2)	1.301(5)	1.242(3)	1.240(2)
$d(\text{C1}-\text{C2}) / \text{\AA}$	1.405(3) / 1.403(3)	1.406(2) / 1.402(2)	1.406(2) / 1.412(2)	1.409(3) / 1.413(4)	1.417(3) / 1.407(3)	1.404(3) / 1.406(3)	1.413(6) / 1.406(6)	—	—
$d(\text{C2}-\text{C3}) / \text{\AA}$	1.376(3) / 1.374(3)	1.376(2) / 1.382(2)	1.378(2) / 1.375(2)	1.370(4) / 1.368(4)	1.367(3) / 1.376(3)	1.374(3) / 1.376(3)	1.367(6) / 1.370(6)	—	—
$d(\text{C3}-\text{C4}) / \text{\AA}$	1.382(3) / 1.383(3)	1.385(2) / 1.381(2)	1.395(2) / 1.375(2)	1.386(3) / 1.390(4)	1.385(3) / 1.393(3)	1.382(3) / 1.378(3)	1.400(6) / 1.385(5)	—	—
Angle Type	H...O...H	H...O...H	H...O...I	H...O...I	H...O...H	H...O...H	H...O...H	H...O...H	H...O...I
Angle /°	94 104	93 103	100	100	105	136	103	76	83

* For **15** and **16** there are two H...O...H angles as there are two, independent dimers in the asymmetric unit. In each case, the smaller value refers to the hydrogen-bonded dimer where there is, in addition, a halogen bond to iodine. In addition, each structure has two H...O...I angles: **15**: 84° and 114° and **16**: 106° and 128°.

The results of the NBO analyses were utilised to probe further the quinoidal type structure. In the case of the phenol, the π -occupancies of the ring C–C bonds were observed to be between 1.67 and 1.71, which is consistent with a fully delocalised structure with no π -occupancy of the C–O bond. In the phenate anion, however, the π -occupancy of the C–O bond became 1.99, whereas that for C2–C3 was found to be 1.79 and C1–C2 and C3–C4 were found not to have π -occupancy, consistent with the quinoidal arrangement. A table containing calculated NBO values for each phenol/phenate pair can be found in Table 7-4. Scheme 6 shows the numbering system used in the table.



Scheme 6: Skeletal numbering system used in Table 7-4.

Table 7-4: The π -occupancies of the C–C bonds and C–O bond in the phenols and phenate (NBO results)

Phenol/Phenate	π -Occupancy									
	C1–O	C1–C2	C2–C3	C3–C4	C4–C5	C5–C6	C6–C1			
Pentafluorophenol	0	1.67	0	1.69	0	1.69	0	1.69	0	0
Pentafluorophenate	1.99	0	1.79	0	0	1.79	0	1.79	0	0
4–Chlorotetrafluorophenol	0	1.68	0	1.71	0	1.68	0	1.68	0	0
4–Chlorotetrafluorophenate	1.99	0	1.79	0	0	1.79	0	1.79	0	0
4–Bromotetrafluorophenol	0	1.67	0	1.71	0	1.68	0	1.68	0	0
4–Bromotetrafluorophenate	1.99	0	1.79	0	0	1.79	0	1.79	0	0
4–Iodotetrafluorophenol	0	1.66	0	1.71	0	1.68	0	1.68	0	0
4–Iodotetrafluorophenate	1.99	0	1.79	0	0	1.79	0	1.79	0	0

Examination of the electrostatic surface potentials (ESPs) of the phenols and phenates provides further insights into their electronic structures and are given in Figure 7-52. Deprotonation of the phenols to give the corresponding phenate leads to a more negative potential around the oxygen atom and, as the halogen in the para position becomes more polarisable, the potential around the halogen becomes more positive in the phenol. In the phenate, however, the positive electrostatic potential around the halogen decreases and, in the cases of F and Cl, becomes negative.

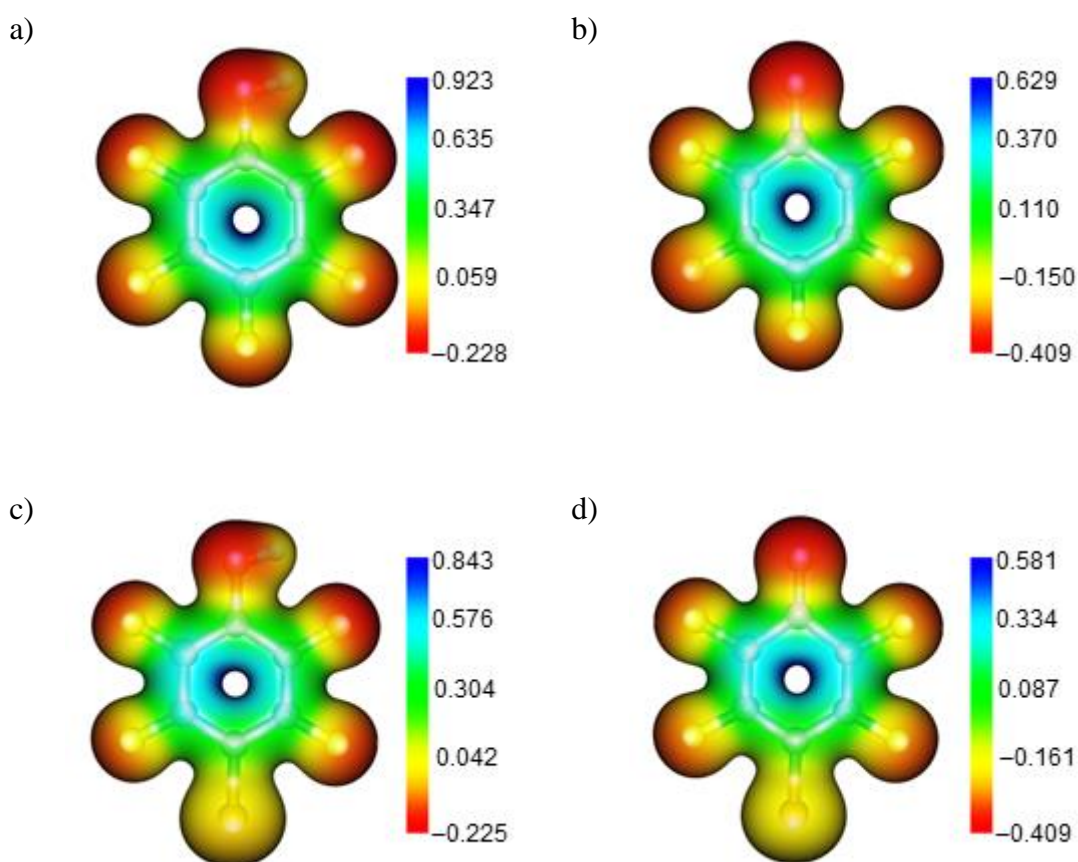


Figure 7-52: Electrostatic surface potentials for (a) pentafluorophenol, b) the pentafluorophenate anion, c) 4-chlorotetrafluorophenol, d) the 4-chlorotetrafluorophenate anion, e) 4-bromotetrafluorophenol, f) the 4-bromotetrafluorophenate anions, g) 4-iodotetrafluorophenol and h) the 4-iodotetrafluorophenate anion mapped on the respective 0.03 HF total electronic density isosurfaces.

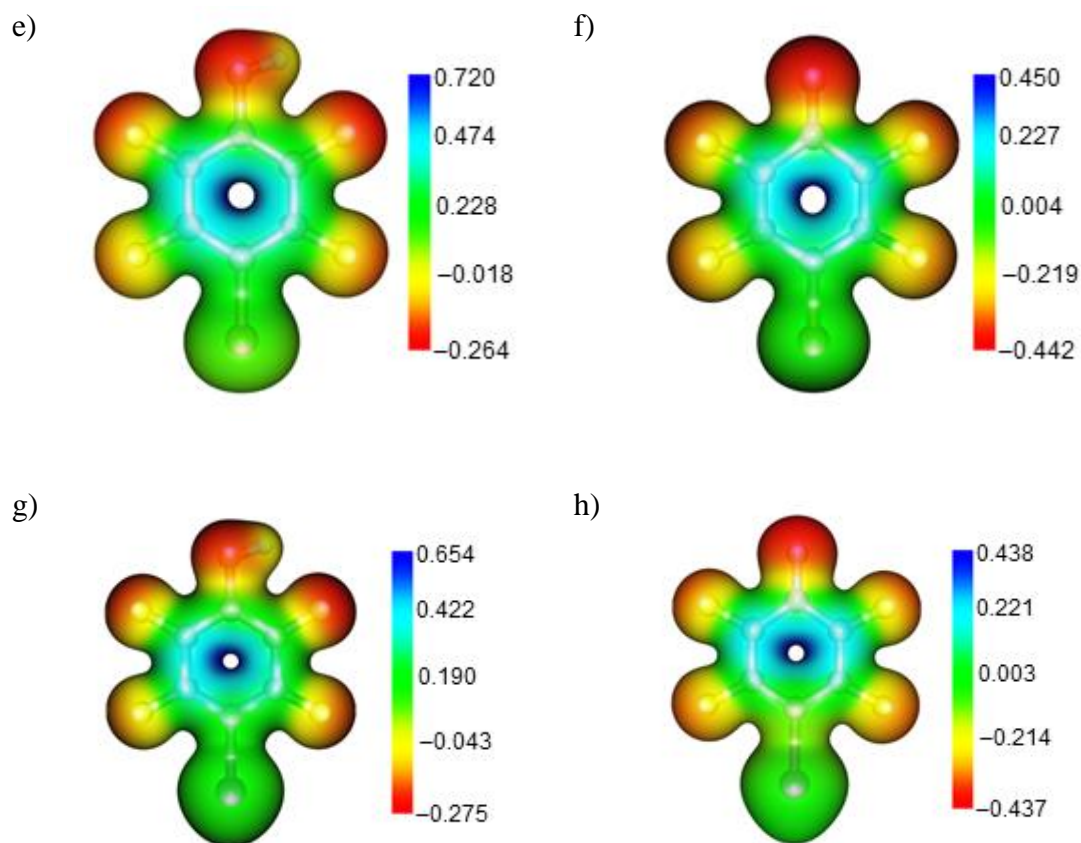


Figure 7-52: (Continued).

The negative potential around the oxygen atom in the ESPs of the phenate anion is very similar to that of the carbonyl oxygen atoms in *N*-methylacetamide and formaldehyde (Figure 7-53). This corroborates the C=O π -bond character observed in the phenate anions.

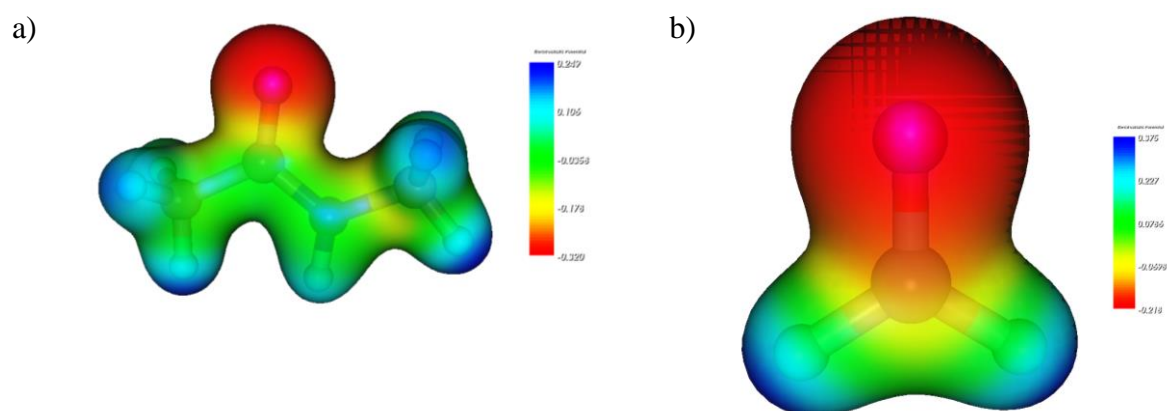


Figure 7-53: The electrostatic surface potentials of a) *N*-methylacetamide and b) formaldehyde mapped on the 0.03 HF/aug-cc-pVDZ total electronic density isosurface.

7.9.2 Halogen Bonding to Carbonyl Oxygen Atoms

The interactions between halogens and phenate oxygen atoms observed in this investigation are similar to those of halogens with carbonyl oxygen atoms, whose study goes back to the work of Hassel and Strømme who, in 1959, described¹⁶ the formation of a polymer between Br₂ and acetone, where bromine bridged between two acetone molecules to form the repeating motif (Figure 7-54a). The angle at the oxygen atom was reported as 110°, whereas the Br–Br···O angles were strictly linear. The motif would suggest that the oxygen uses *sp*² orbitals in the bonding, although a recent theoretical study questions this.⁴¹⁹ A similar polymeric motif is described when the ketone is found in 4,4'-bis(*N,N*-dimethylamino)benzophenone and the dihalogen is 1,4-diiidotetrafluorobenzene (Figure 7-54b).⁴²⁰ The interaction was a little weaker than that observed for the bromine-acetone complex with an I···O separation of 3.097(4) Å, 88% of the sum of the van der Waals radii. The C–I···O angle was 163.29(9)° which is a significant deviation from linearity. The C=O···I angle at 138.5(4)° also deviates from the optimum angle for interaction with the *sp*² orbitals on oxygen.

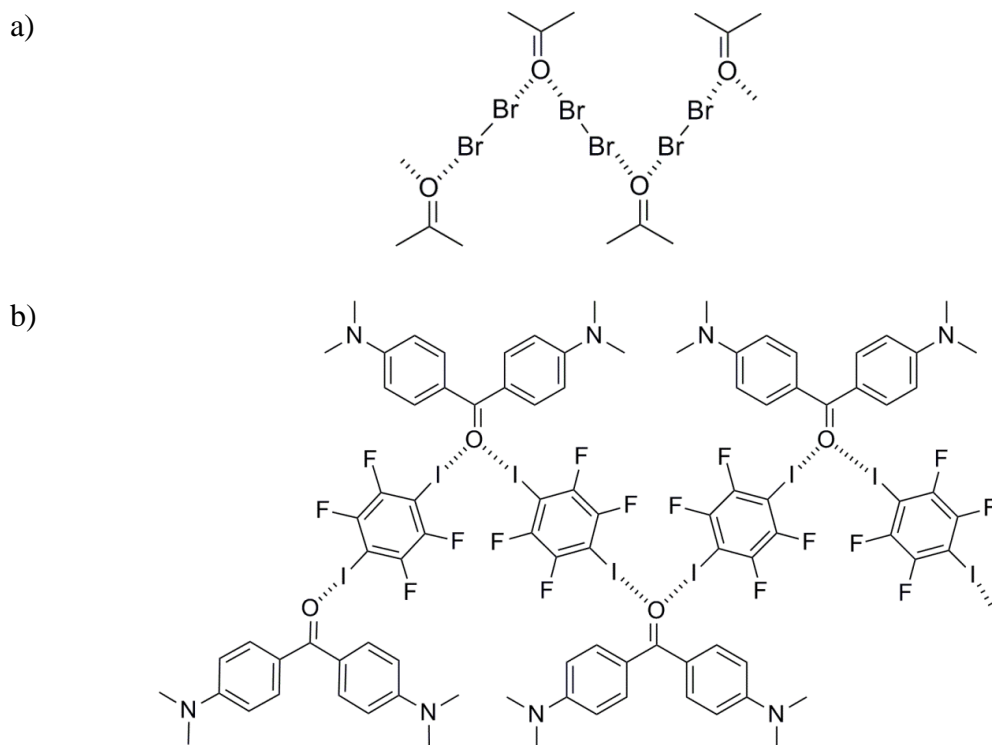


Figure 7-54: Halogen bonded interactions with ketones. The interaction motif found in (a) acetone : I₂ and (b) 1,4-diodotetrafluorobenzene with a bis-4-(*N,N*-dimethylamino)benzophenone.

More recently, intermolecular C=O \cdots Br interactions were found to direct the crystal structures of *o*-bromoaromatic aldehydes (Figure 7-55),⁴²¹ whereas halogen bonding between carbonyl oxygen atoms and bromine has been found to induce phosphorescence in organic compounds, namely with 2,5-dihexyloxy-4-bromobenzaldehyde (Figure 7-56)⁴²² and a Boc- and *N,N*-dicyclohexylurea-capped γ -amino acid with a bromo substituent (Figure 7-57).⁴²³ In the former example, the Br \cdots O interaction is strong with a separation of 2.857(1) Å and is reasonably linear with a C–Br \cdots O angle of 175.05(5)°; the Br \cdots O=C angle was 125.99(9)°, consistent with interaction with the *sp*² orbitals on oxygen. In the latter, the interaction is significantly weaker with a Br \cdots O separation of 3.152(2) Å, 94% of the sum of the van der Waals radii, while the Br \cdots O=C angle is 159.3(2)°, which is a significant deviation from alignment with the *sp*² orbitals on oxygen due to a secondary weak C–H \cdots O hydrogen bond with a neighbouring cyclohexyl group.

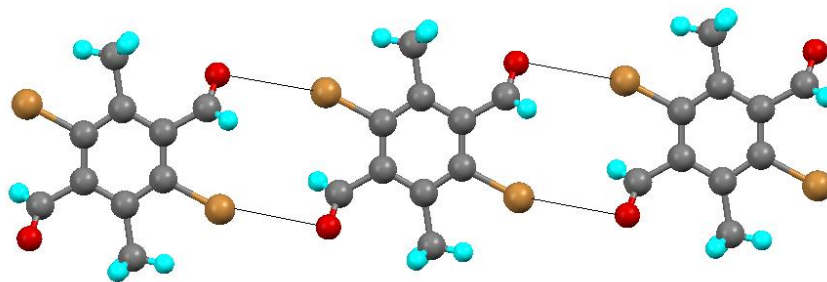


Figure 7-55: The crystal structure of 3,6-dibromo-2,5-dimethylterephthalaldehyde. Br \cdots O=C contacts are shown in black.

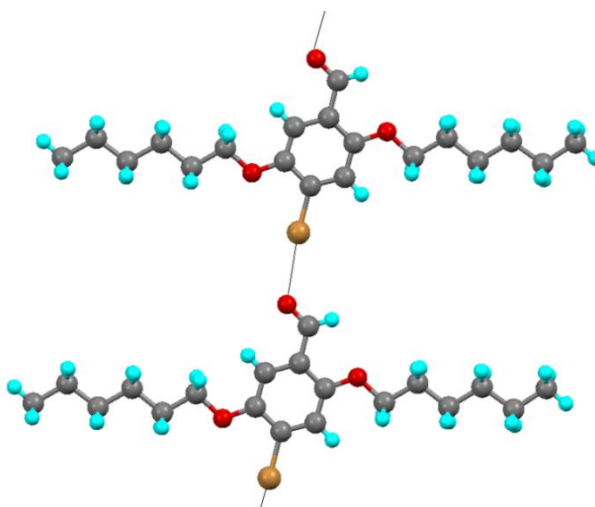


Figure 7-56: The crystal structure of 2,5-dihexyloxy-4-bromobenzaldehyde. The Br \cdots O=C interaction is shown in black.

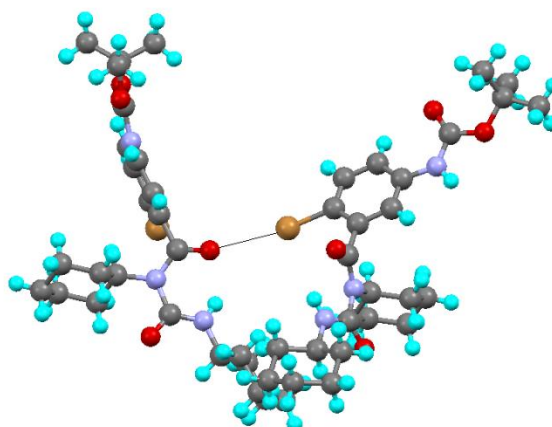


Figure 7-57: The crystal structure of the bromine substituted, Boc- and *N,N*-dicyclohexylurea-capped γ -amino acid foldamer. The Br \cdots O=C interaction is shown in black.

The examples above show that strong halogen-bond interactions with carboxyl oxygen atoms favour a C=O...X angle of approximately 125° corresponding to interaction with the sp^2 orbitals on the oxygen atom. As the interaction becomes weaker, this angle changes due to additional interactions present in the structure and interaction with the π electron density of the carbonyl bond.

Described as a 'small molecule analogue' of the orthogonal interactions observed in biological systems, El-Sheshtawy *et al.* reported the structures of a cucurbit[6]uril containing either Br₂ or I₂ inside the cavity (Figure 7-58).⁴²⁴ Examination of the lengths of the I...O and Br...O separations (99% of the sum of the van der Waals radii), the magnitudes of the I-I...O and Br-Br...O angles (major deviations from linearity) and the space-filling model rather suggest a simple inclusion complex stabilised by weak dispersion forces.

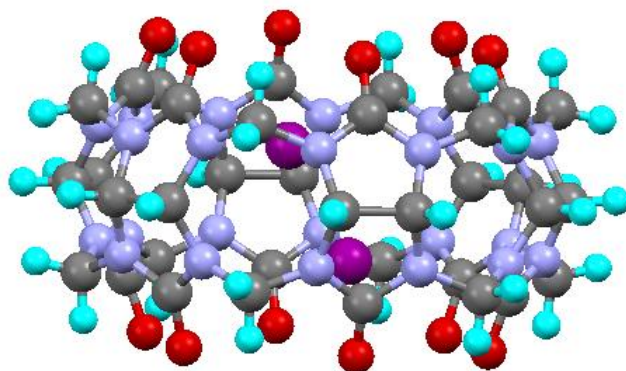


Figure 7-58: Molecular structure of molecular iodine enclosed in cucurbit[6]uril

7.9.3 Bonding Motifs in the Structures and Comparison to Halogen Bonding in Biology

Halogen bonding to carbonyl oxygen atoms has also been observed in biological systems, most notably in the approach of the halogen to the π -system of the carboxyl oxygen of an amide link.⁴²⁵ It was shown that hydrogen and halogen bonds to such carbonyl oxygen atoms could be regarded as orthogonal, providing examples where

both were found simultaneously.⁴⁰⁵ These important, original studies have then led to wider interest.⁴²⁶⁻⁴²⁹

In the discussion that follows, the ketonic nature of the C–O bond is important as it allows comparison with the interactions between the amide carbonyl of a protein chain and bromo compounds as discussed by Ho and co-workers.^{405,425}

The structures of all complexes with the exception of **17** and **18**, reveal a strong preference for the phenate oxygen to accommodate two hydrogen-bond donors in the plane of the ring, so much so that in **9** and **10** a neutral pentafluorophenol co-crystallises to take up the second of these positions in the absence of a second ammonium hydrogen. This is consistent with the phenate anion having developed C=O bond character, which would lead to the presence of two sp^2 orbitals in the plane of the ring. This shows a parallel with the co-crystal structures in Figure 7-54 where there are two halogen bonds into lone-pair sp^2 orbitals on a carbonyl oxygen atom and is consistent with experiments in the gas phase, which showed that FCl will form a halogen bond with the lone pairs of electrons of the carbonyl oxygen atom of formaldehyde with a C=O...Cl angle of 110.9°. ³² Interaction with the lone pairs of electrons was found to take precedence over interactions with the π electrons.

In order to probe this further, the HF molecular orbitals at the MP2(Full) optimised geometries were localised using the Edmiston-Ruedenberg localisation procedure. The results are illustrated for the iodotetrafluorophenate anion. Figure 7-59a and Figure 7-59b show the presence of sp^2 orbitals on oxygen, clearly consistent with the strong preference shown in the crystal structures for two hydrogen-bond donors bound to oxygen in the plane of the ring.

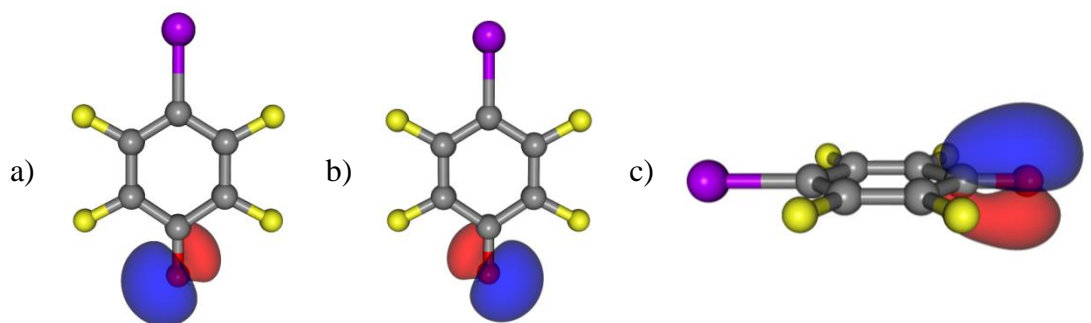


Figure 7-59: a) and b) the LMOs corresponding to the lone electron pairs on O and c) the π orbital on the C=O bond. The orbitals are represented as blue/red isosurfaces at orbital values of ± 0.05 (e/bohr³)^{-1/2}.

The majority of cations used were secondary amines, meaning that there were two N–H hydrogens at the cationic centre and so formation of the [2 + 2], hydrogen-bonded dimer is readily rationalised. Use of a tertiary amine means that there is only one such hydrogen available and so in **17** and **18**, in-plane hydrogen and halogen bonds are formed (Figures 7-43 and 7-45), while in the case of **12**, there is a second N–H hydrogen available and so a linear polymer is seen (Figures 7-29 and 7-31), which also provides for two hydrogen bonds at oxygen.

Then, considering **13** and **14**, the presence of a secondary ammonium cation allows for the formation of the [2 + 2] hydrogen-bonded dimer, but in the case of **14**, the thiomorpholinium cation also contains a sulfur atom that then forms a halogen bond to the phenate iodine atom leading to a polymeric structure as shown in Figure 7-30.

In the case of **15** (pyrrolidinium cation) and **16** (morpholinium cation), although the expected [2 + 2] dimer is indeed observed, examination of the structure shows that there is also an intermolecular I \cdots O halogen bond. This forms between the iodine of a neighbouring iodotetrafluorophenate anion (itself part of a [2 + 2] dimer) and a phenate oxygen atom of the hydrogen-bonded dimer, with the iodine atom approaching out of the plane of the phenate ring (Figures 7-36b, 7-37 and 7-41). Interaction of the iodine atom with the oxygen atom uses the π -system of the C=O

bond as illustrated in Figure 7-59c. So far as we are aware, such a combined hydrogen- and halogen-bonding motif is without precedent in the literature of synthetic co-crystals.

Comparison with the motifs described by Ho and co-workers is then instructive. They first described systems mined from the Protein Data Bank (PDB) in which there was halogen bonding by Cl, Br or I to carbonyl oxygen atoms, almost all of which were associated with amide links in the peptide chain (Figure 7-60). In these cases and considering only the halogen...oxygen interaction, iodine showed a very strong preference for binding to the π -system of the C=O bond, whereas for bromine the preference in favour of binding to the π -system over binding to the lone pairs on oxygen was appreciably smaller, albeit over a smaller data set.⁴²⁵

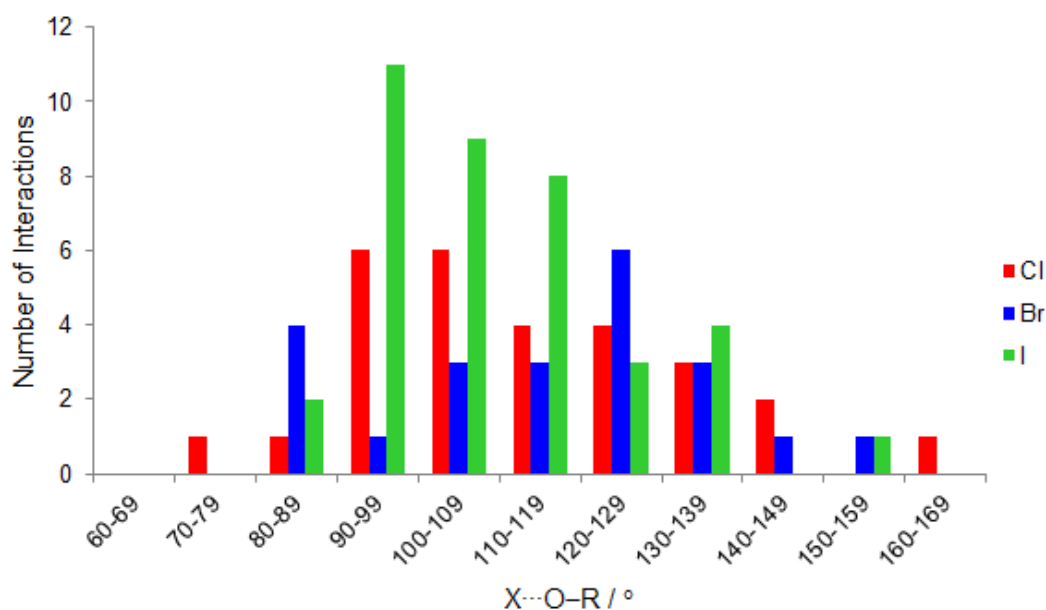


Figure 7-60: Histogram showing the distribution of X...O-R angles in halogen bonds to oxygen atoms in the PDB. Adapted from Auffinger and co-workers.⁴²⁵

They then went on to mine data from the PDB for a series of protein-ligand combinations containing short X...O interactions.⁴⁰⁵ This study showed that when only hydrogen bonding was present, the hydrogen bond formed preferentially directly opposite to the C=O bond and, as such, in the plane of the amide bond. In

cases where there was both hydrogen and halogen bonding to the oxygen atom, however, then either the halogen would approach from the plane above the amide bond and the hydrogen bond would be found below the same plane (Figure 7-61a), or both the halogen and hydrogen bond would be found bound to the oxygen in the plane of the amide bond (Figure 7-61b). In the majority of cases, the angle, α , was found to be between 75 and 90° leading them to propose that the hydrogen and halogen bonds, when both present, should be regarded as orthogonal. Indeed, this idea was supported further by calculations, which showed that the energy of a hydrogen bond between two amide units was unaffected by the approach of the Br of bromobenzene to the hydrogen-bond acceptor (oxygen), and, similarly, the energy of interaction between the hydrogen-bond acceptor (oxygen) and a halogen-bonded bromine atom was unaffected by the length of the hydrogen bond to oxygen. For comparison, the strength of one hydrogen bond to oxygen was affected appreciably by the presence of a second hydrogen bond.

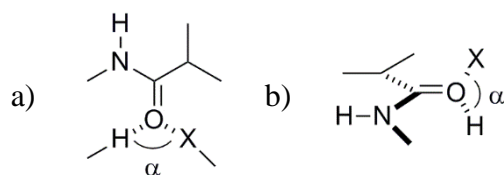


Figure 7-61: Possible arrangements of hydrogen and halogen bonding at amide oxygens showing (a) both in plane and (b) both out of plane with respect the amide link. After Ho and co-workers.⁴⁰⁵

To make an even more direct comparison between the biological and synthetic systems, this study allowed the amides *N*-methylacetamide and *N*-methylbenzamide to co-crystallise with 1,4-diiodotetrafluorobenzene. The *N*-methylacetamide hydrolysed during crystallisation to give acetamide and the structure of the resulting co-crystal (**22**) showed sheets made up of hydrogen-bonded acetamides (Figure 7-47a) linked by the aromatic diiodide through I \cdots O halogen bonding into the π -system of the amide carbonyl group (Figure 7-47b). *N*-Methylbenzamide did not hydrolyse during crystallisation and the structure also showed a one-dimensional,

sheet-like arrangement but with one hydrogen fewer available for hydrogen bonding. Again, I \cdots O halogen bonding into the π -system of the amide carbonyl held the sheets together.

These structures provide an excellent link between the biological systems and the co-crystal salts of the amine/phenol combinations as now described. Thus the *N*-methylbenzamide structure **23** mirrors the behaviour described by Voth *et al.* in having effectively orthogonal halogen and hydrogen bonding with an H \cdots O \cdots I angle of 83.0° (arrangement as Figure 7-61b), which agrees well with the modal angle they report in such cases. Then there are the cases of **17** and **18**, where in each there is also a single hydrogen atom available for hydrogen bonding and so both a hydrogen and halogen bond are seen with the H \cdots O \cdots I angle = 100(1)° in each case. These can also be regarded as orthogonal, but in this case they exist in the plane of the phenate ring, which would not be possible in **23** on steric grounds.

In **22**, however, although there is also an I \cdots O halogen bond into the C=O π -system, there are, in addition, two hydrogen bonds that bind into the lone-pair sp^2 orbitals on the amide oxygen atom, a motif that is not found in the biological systems as the amide link contains a single hydrogen available for hydrogen bonding and the close approach of two hydrogen atoms is likely disfavoured sterically. As noted already, this motif is also found in **15** and **16**. In these three structures, the H \cdots O \cdots H angle in the [2 + 2] dimer is 76° (**22**) and 93.5° (**15** and **16**), whereas in structures of 4-halotetrafluorophenates where there is a [2 + 2] dimer and no halogen bonding (**11-14** and **19-21**), then the same angle is in the range 100 to 107°. ^{xiii} Thus, in contrast to the calculations reported by Voth *et al.*, in this case the hydrogen and halogen bonding are not orthogonal as it is evident that the H \cdots O \cdots H angle is appreciably smaller where there is additional I \cdots O halogen bonding. This is shown elegantly in the structures of **15** and **16**, where in each case there are two, independent [2 + 2]

^{xiii} The exception is the angle of 136° in **20** where the hydrogen bonding describes a polymeric arrangement.

dimers and, in the dimer where there is no halogen bond the HOH angle is 103.5°, whereas in the other (which is halogen bonded) the angle is 93.5°. ^{xiv}

In the original paper by Auffinger *et al.* ⁴²⁵ and to an extent in the study by Voth *et al.*, ⁴⁰⁵ significant emphasis was placed on biological Br···O halogen bonds, whereas this synthetic study has concentrated on iodo materials. To this end, salts **19** to **21** were obtained and it is noteworthy that, save for the Type I Br···Br interactions in **20** (Figure 7-45a), no other short contacts to Br are seen. In general terms, halogen bonds to bromine are expected to be weaker than iodine analogues and one very simple illustration of this is in the comparison between the 2 : 1 complexes formed between 4-alkoxystilbazoles and 1,4-diiodo- and 1,4-dibromo-tetrafluorobenzene. Thus, in both cases 2 : 1 co-crystals are obtained, but only the complex of the diiodotetrafluorobenzene showed liquid crystal properties as the analogous dibromotetrafluorobenzene complex fell apart on heating suggesting weaker halogen bonding. ²⁰⁷

While it is recognised that there are many factors that can affect the intermolecular interactions observed in a co-crystal system, it is interesting that analogous halogen-bonding motifs are not seen in any of **19** to **21**. What this may point to is the fact that in protein systems, interactions that form can be a result of a range of steric and allosteric factors related to secondary and tertiary structure, and indeed Voth *et al.* draw attention to α -helices and β -sheets in their discussions. ⁴⁰⁵ Therefore, although the structures reported here offer synthetic analogues that can help in the interpretation and understanding of the halogen bonds found in proteins, it is clear that the analogy cannot be taken too far given the structural complexity in proteins at the secondary and tertiary level.

Of course, one might then go further and argue that in the solid-state structures of molecular species, the importance or not of any given intermolecular, interatomic

^{xiv} The two angles are recorded by Mercury as 94(1)° for **15** and 93(1)° for **16** so given the esds, a simple average is quoted.

contact(s) may be a delicate function of the enthalpic contribution made to the lattice energy when compared to the general driving force for efficient molecular packing, which may lead to such interactions by accident rather than design.

7.10 Conclusion

This study contributes to the body of work on co-existence of, and possible competition between, hydrogen and halogen bonding in co-crystals where one component has the possibility to participate in both binding modes. The molecular structure of the co-crystal between 4-iodo-2,3,5,6-tetrafluorobenzoic acid and 1,4-dithiane shows that the benzoic acid maintains its dimer motif allowing the iodine atom to form a halogen bond with the sulfur atom of 1,4-dithiane. This demonstrated that by choosing units carefully, halogen bonding between unlike components can be favoured over hydrogen bonding and that such results are consistent with both the iodine basicity scale and the long-established HSAB concept. Furthermore, the results also show some consistency with the proposal for the structural equivalence of thio with imino or oxo functions.

Co-crystallisation of 4-iodo- and 4-bromo-2,3,5,6-tetrafluorophenol with sulfur bases caused oxidation to form either the *S,S'*-dioxide or *S'*-oxide. In the molecular structure of the co-crystal between 4-iodo-2,3,5,6-tetrafluorophenol and thiophene-*S*-oxide, halogen and hydrogen bonds are observed to be orthogonal in the structure. This led to an extensive and systematic study of salts and co-crystals formed mainly between 4-halotetrafluorophenols and cyclic amines, and it is noted that in all cases the phenate ion formed adopted a delocalised, Meissenheimer-like structure in which double-bond character developed in the C–O bond. This was supported by calculations at the MP2 level of theory and then explained the observation that the hydrogen bonding motifs of these phenates was dominated by interaction with the lone-pair sp^2 orbitals on the oxygen. Where there were insufficient hydrogens to

allow formation of two hydrogen bonds per oxygen, then both hydrogen *and* halogen bonding into the sp^2 orbitals is observed.

In some cases where there are already two hydrogen bonds to oxygen, an additional I...O halogen bond formed representing an interaction between the electrophilic iodine of the 4-iodotetrafluorophenolate and the π -bonding orbital of the carbonyl group. The broader significance of this observation is that not only is the motif without precedent in studies of halogen-bonded materials, but it also presents a synthetic analogy with observations of halogen bonding in the structures of proteins as described by Ho and co-workers.^{405,425,430} Moreover, while the synthetic studies can reproduce the orthogonality of hydrogen and halogen bonding proposed by Ho and supported by calculation, they also show that this orthogonality breaks down where there are simultaneously two hydrogen bonds and a halogen bond to oxygen.

Finally, structures obtained using 4-bromotetrafluorophenol do not reproduce these motifs, which may point to the greater importance of steric and allosteric factors in determining intermolecular arrangements in protein systems.

7.11 Experimental

7.11.1 Crystallographic Tables

Table 7-5 shows the crystallographic parameters for the co-crystals and salts included in this chapter.

4-Iodo-2,3,5,6-tetrafluorophenol¹⁹⁷ and 4-Iodo-2,3,5,6-tetrafluorobenzoic acid⁴⁰² were prepared using literature methods.

Table 7-5: Crystallographic Properties for the salts and co-crystals studied.

	1	2	3	4	5
CCDC Reference No	985842	985843	985844	985845	985846
Empirical formula	C ₇ HF ₄ IO ₂	C ₉ H ₅ F ₄ IO ₂ S	C ₁₁ H ₁₀ F ₄ INOS	C ₄ H ₈ O ₂ S ₂	C ₁₆ H ₁₀ Br ₂ F ₈ O ₄ S ₂
Formula weight / g mol ⁻¹	319.98	380.09	949.50	152.22	642.18
T / K	110.00(10)	110.00(10)	110.00(10)	110.00(10)	110.05(10)
Wavelength / Å	0.7107	0.7107	0.7107	0.7107	0.7107
Crystal system	Monoclinic	Triclinic	Triclinic	Monoclinic	Monoclinic
Space group	P2 ₁	P $\bar{1}$	P $\bar{1}$	P2 ₁ /h	P2 ₁ /c
Unit cell dimensions / Å	a = 6.7596(2) b = 31.6474(8) c = 7.9922(3)	a = 6.2546(4) b = 7.8761(4) c = 11.5781(6)	a = 5.7209(7) b = 10.3273(13) c = 14.4539(17)	a = 6.2950(3) b = 6.3948(5) c = 8.090(3)	a = 5.89886(16) b = 21.0112(5) c = 16.1143(4)
α / °	90	78.743(5)	107.044(11)	90.00	90.00
β / °	108.548(3)	75.347(5)	99.741(10)	104.161(13)	95.557(3)
γ / °	90	83.455(5)	92.149(10)	90.00	90.00
Volume / Å ³	1620.92(9)	539.94(5)	801.23(17)	315.78(11)	1987.85(9)
Z	8	2	1	2	4
$\rho_{\text{calc}} / \text{Mg m}^{-3}$	2.6222	2.338	1.968	1.601	2.146
Absorption coefficient / mm ⁻¹	3.989	3.200	2.243	0.747	4.386
F(000)	1181.7	360	464	160.0	1248.0
Crystal size / mm ³	0.266 x 0.1624 x 0.0939	0.22 x 0.17 x 0.11	0.20 x 0.06 x 0.02	0.294 x 0.2065 x 0.1504	0.3096 x 0.0734 x 0.0333
\square range for data collection	3.98 to 30.08°	2.94 to 30.01°	3.00 to 29.77°	3.69 to 31.88°	3.17 to 27.95°
Index ranges	-8 ≤ h ≤ 9, -44 ≤ k ≤ 44, -11 ≤ l ≤ 10	-8 ≤ h ≤ 8, -11 ≤ k ≤ 11, -16 ≤ l ≤ 16	-6 ≤ h ≤ 7, -12 ≤ k ≤ 13, -19 ≤ l ≤ 10	-8 ≤ h ≤ 9, -9 ≤ k ≤ 8, -9 ≤ l ≤ 11	-7 ≤ h ≤ 6, -27 ≤ k ≤ 25, -21 ≤ l ≤ 21
Reflections collected	15874	6552	6397	1632	11592
Independent reflections	8789 [R(int) = 0.0206]	6552 [R(int) = 0.000]	4026 [R(int) = 0.0311]	973 [R(int) = 0.0181]	4103 [R(int) = 0.0290]
Completeness (%) to \square	99.10 (30.01)	99.70 (30.18°)	99.01% (27.50°)	97.52 (30.01)	99.56% (25.01°)
Data / restraints / parameters	8789/144/517	6552 / 0 / 159	4026 / 14 / 211	973/0/37	4103 / 0 / 297
Goodness-of-fit on F ²	1.046	1.097	1.066	1.139	1.032
Final R indices [$> 2\sigma(I)$]	R ₁ = 0.0341, wR ₂ = 0.0808	R ₁ = 0.0346, wR ₂ = 0.1000	R ₁ = 0.0494, wR ₂ = 0.1024	R ₁ = 0.0292, wR ₂ = 0.0759	R ₁ = 0.0292, wR ₂ = 0.0612
R indices (all data)	R ₁ = 0.0359, wR ₂ = 0.0848	R ₁ = 0.0393, wR ₂ = 0.1025	R ₁ = 0.0695, wR ₂ = 0.1123	R ₁ = 0.0337, wR ₂ = 0.0827	R ₁ = 0.0395, wR ₂ = 0.0651
Largest diff. peak and hole	0.98/-1.50	1.066/-0.679	3.307/-1.378	0.35/-0.37	0.53/ -0.39

Table 7-5: (Continued)

	8	9	10	11
CCDC Reference No	985847	984767	984768	984769
Empirical formula	C ₁₀ H ₉ F ₄ OIS	C ₁₉ H ₁₂ F ₁₀ N ₂ O ₂	C ₂₁ H ₁₄ F ₁₀ N ₂ O	C ₈ H ₆ F ₄ INO
Formula weight / g mol ⁻¹	688.10	490.31	516.34	335.04
T / K	110.00(10)	110.00(10)	110.05(10)	110.00(10)
Wavelength / Å	0.7107	0.7107	0.7107	0.7107
Crystal system	Triclinic	Monoclinic	Monoclinic	Monoclinic
Space group	P $\bar{1}$	P2 ₁	P2 ₁ /c	P2 ₁ /n
Unit cell dimensions / Å	a = 9.1682(14) b = 9.4618(16) c = 12.3168(16)	a = 9.4894(6) b = 7.8420(5) c = 12.4570(4)	a = 16.2450(5) b = 14.4578(3) c = 8.8748(2)	a = 6.69911(10) b = 9.33898(11) c = 16.2139(2)
α / °	75.183(14)	90.00	90.00	90.00
β / °	74.084(13)	97.414(4)	102.335(3)	101.4762(15)
γ / °	79.202(14)	90.00	90.00	90.00
Volume / Å ³	985.6(3)	2296.61(16)	2036.28(9)	994.11(2)
Z	2	2	4	4
$\rho_{\text{calc}} / \text{Mg m}^{-3}$	2.319	1.771	1.684	2.239
Absorption coefficient / mm ⁻¹	3.387	0.184	0.171	3.253
F(000)	648	492	1040	632
Crystal size / mm ³	0.14 × 0.09 × 0.06	0.26 × 0.19 × 0.10	0.27 × 0.15 × 0.06	0.24 × 0.14 × 0.10
□ range for data collection	2.93 to 32.08°	3.34 to 27.11°	3.23 to 31.84°	3.10 to 32.29°
Index ranges	-12 ≤ h ≤ 12, -14 ≤ k ≤ 14, -12 ≤ l ≤ 18	-14 ≤ h ≤ 17, -23 ≤ k ≤ 22 -17 ≤ l ≤ 17	-23 ≤ h ≤ 23, -21 ≤ k ≤ 17 -12 ≤ l ≤ 12	-9 ≤ h ≤ 9, -13 ≤ k ≤ 13 -17 ≤ l ≤ 23
Reflections collected	10138	9127	13670	10476
Independent reflections	6120 [R _{int} = 0.0239]	5423 [R _{int} = 0.0226]	6489 [R _{int} = 0.0298]	3292 [R _{int} = 0.0224]
Completeness (%) to (□)	99.20% (30.01°)	99.83% (30.01°)	99.84% to (30.01°)	99.87% (30.30°)
Data / restraints / parameters	6120 / 0 / 279	5423 / 1 / 309	6489 / 0 / 324	3292 / 0 / 136
Goodness-of-fit on F ²	1.044	1.061	1.037	1.034
Final R indices [I > 2σ(I)]	R ₁ = 0.0254, wR ₂ = 0.0517	R ₁ = 0.0343, wR ₂ = 0.0877	R ₁ = 0.0482, wR ₂ = 0.1095	R ₁ = 0.0240, wR ₂ = 0.0526
R indices (all data)	R ₁ = 0.0317, wR ₂ = 0.0556	R ₁ = 0.0374, wR ₂ = 0.0910	R ₁ = 0.0723, wR ₂ = 0.1236	R ₁ = 0.0275, wR ₂ = 0.0545
Largest diff. peak and hole	0.871 / -0.733	0.374 and -0.284	0.471 and -0.259	1.951 and -1.721

Table 7-5: (Continued)

	12	13	14	15	16
CCDC Reference No	984770	984771	984772	984773	984774
Empirical formula	C ₉ H ₆ F ₄ IN ₂ O	C ₁₄ H ₂₀ F ₄ INO	C ₁₀ H ₁₀ F ₄ INOS	C ₁₀ H ₁₀ F ₄ INO	C ₁₀ H ₁₀ F ₄ INO ₂
Formula weight / g mol ⁻¹	360.05	421.21	395.15	363.10	379.09
T / K	110.00(10)	110.00(14)	110.00(10)	110.00(10)	110.00(10)
Wavelength / Å	0.7107	0.7107	0.7107	0.7107	0.7107
Crystal system	Monoclinic	Monoclinic	Monoclinic	Monoclinic	Monoclinic
Space group	P2 ₁ /c	I2/m	P2 ₁ /n	P2 ₁ /c	P2 ₁ /c
Unit cell dimensions / Å	a = 10.4977(4) b = 16.7524(5) c = 13.5611(6)	a = 9.38708(18) b = 15.3050(6) c = 12.0334(2)	a = 9.178(5) b = 10.1094(4) c = 13.6592(3)	a = 9.2414(4) b = 17.0242(11) c = 14.7830(7)	a = 9.3549(6) b = 17.1719(9) c = 14.8240(7)
α / °	90.00	90	90.00	90.00	90.00
β / °	107.709(4)	99.4186(18)	93.161(9)	92.746(4)	94.680(6)
γ / °	90.00	90	90.00	90.00	90.00
Volume / Å ³	2271.86(16)	1705.53(9)	1265.4(7)	2323.1(2)	2373.4(2)
Z	8	4	4	8	8
ρ _{calc} / Mg m ⁻³	2.105	1.640	2.074	2.076	2.122
Absorption coefficient / mm ⁻¹	2.857	1.914	2.732	2.792	2.744
F(000)	1360	832.0	760	1390	1456
Crystal size / mm ³	0.23 × 0.13 × 0.11	0.1064 × 0.08 × 0.0167	0.25 × 0.09 × 0.06	0.16 × 0.10 × 0.08	0.33 × 0.29 × 0.20
□ range for data collection	2.90 to 32.07°	3.00 to 28.102°	2.98 to 32.11°	2.81 to 30.01°	2.92 to 32.15°
Index ranges	-12 ≤ h ≤ 15, -23 ≤ k ≤ 21 -20 ≤ l ≤ 14	-12 ≤ h ≤ 11, -18 ≤ k ≤ 19 -15 ≤ l ≤ 15	-5 ≤ h ≤ 13, -12 ≤ k ≤ 14 -19 ≤ l ≤ 20	-6 ≤ h ≤ 13, -24 ≤ k ≤ 23 -20 ≤ l ≤ 20	-14 ≤ h ≤ 13, -25 ≤ k ≤ 25 -21 ≤ l ≤ 22
Reflections collected	13044	8663	6888	13176	37198
Independent reflections	7149 [R _{int} = 0.0319]	1915 [R _{int} = 0.0354]	4000 [R _{int} = 0.0190]	6782 [R _{int} = 0.0227]	7799 [R _{int} = 0.0280]
Completeness (%) to (□)	99.88% (30.01°)	97.95% (26.32°)	99.75% (30.01°)	99.35% (30.01°)	99.85% (30.01°)
Data / restraints / parameters	7149 / 0 / 323	1915 / 0 / 107	4000 / 0 / 171	6782 / 0 / 322	7799 / 0 / 341
Goodness-of-fit on F ²	1.193	1.103	1.042	1.030	1.019
Final R indices [I > 2σ(I)]	R ₁ = 0.0443, wR ₂ = 0.0994	R ₁ = 0.0356, wR ₂ = 0.0683	R ₁ = 0.0251, wR ₂ = 0.0527	R ₁ = 0.0228, wR ₂ = 0.0480	R ₁ = 0.0215, wR ₂ = 0.0474
R indices (all data)	R ₁ = 0.0608, wR ₂ = 0.1085	R ₁ = 0.0528, wR ₂ = 0.0756	R ₁ = 0.0298, wR ₂ = 0.0554	R ₁ = 0.0275, wR ₂ = 0.0507	R ₁ = 0.0252, wR ₂ = 0.0492
Largest diff. peak and hole	1.603/-1.262	0.76/-1.64	0.676/-0.825	0.597/-0.533	1.134/-1.101

Table 7-5: (Continued)

	17	18	19	20	21
CCDC Reference No	984775	984776	984777	984778	984779
Empirical formula	$C_{13}H_{11}F_4IN_2O$	$C_{15}H_{13}F_4IN_2O$	$C_{10}H_{10}F_4BrNO$	$C_{10}H_{10}BrF_4NOS$	$C_8H_6BrF_4NO$
Formula weight / g mol ⁻¹	414.14	440.17	316.10	348.16	288.05
T / K	110.00(10)	110.00(10)	110.00(10)	110.05(10)	109.9(4)
Wavelength / Å	0.7107	0.7107	0.7107	0.7107	0.7107
Crystal system	Monoclinic	Monoclinic	Triclinic	Triclinic	Monoclinic
Space group	$P2_1/c$	$P2_1/c$	$P\bar{1}$	$P\bar{1}$	$P2_1/c$
Unit cell dimensions / Å	$a = 13.6933(12)$ $b = 17.119(3)$ $c = 12.5567(11)$	$a = 13.5613(5)$ $b = 16.8209(3)$ $c = 14.2920(3)$	$a = 7.6424(4)$ $b = 9.0687(8)$ $c = 9.2891(7)$	$a = 4.9948(4)$ $b = 10.4598(10)$ $c = 11.4729(7)$	$a = 6.7736(3)$ $b = 9.0512(3)$ $c = 15.7194(8)$
$\alpha / ^\circ$	90.00	90.00	112.071(8)	88.147(6)	90.00
$\beta / ^\circ$	107.061(11)	107.619(3)	104.481(6)	83.401(6)	101.833(5)
$\gamma / ^\circ$	90.00	90.00	98.633(6)	79.578(7)	90.00
Volume / Å ³	2814.0(6)	3107.27(14)	555.88(7)	585.56(8)	943.26(7)
Z	8	8	2	2	4
$\rho_{\text{calc}} / \text{Mg m}^{-3}$	1.955	1.882	1.889	1.975	2.028
Absorption coefficient / mm ⁻¹	2.321	2.108	3.734	3.727	4.391
$F(000)$	1600	1712	312	344	560.0
Crystal size / mm ³	$0.18 \times 0.11 \times 0.08$	$0.12 \times 0.06 \times 0.05$	$0.29 \times 0.09 \times 0.07$	$0.89 \times 0.06 \times 0.05$	$0.3187 \times 0.0783 \times 0.0756$
\square range for data collection	2.84 to 32.10°	2.84 to 32.10°	3.80 to 31.55°	3.96 to 31.77°	3.07 to 31.01°
Index ranges	$-20 \leq h \leq 20$, $-25 \leq k \leq 25$ $-17 \leq l \leq 18$	$-15 \leq h \leq 20$, $-24 \leq k \leq 21$ $-20 \leq l \leq 14$	$-10 \leq h \leq 10$, $-12 \leq k \leq 11$ $-13 \leq l \leq 12$	$-7 \leq h \leq 7$, $-14 \leq k \leq 13$ $-17 \leq l \leq 13$	$-9 \leq h \leq 8$, $-13 \leq k \leq 13$ $-22 \leq l \leq 18$
Reflections collected	34791	18292	4975	5262	5677
Independent reflections	9145 [$R_{\text{int}} = 0.0271$]	9781 [$R_{\text{int}} = 0.0275$]	3249 [$R_{\text{int}} = 0.0217$]	3626 [$R_{\text{int}} = 0.0227$]	2977 [$R_{\text{int}} = 0.0547$]
Completeness (%) to (\square)	99.88% (30.01°)	99.69% (30.01°)	99.48% (30.01°)	98.57% to (30.01°)	99.46% to (30.01°)
Data / restraints / parameters	9145 / 0 / 391	9781 / 0 / 423	3249 / 0 / 162	3626 / 0 / 171	2977 / 0 / 144
Goodness-of-fit on F^2	1.076	1.065	1.041	1.074	1.048
Final R indices [$I > 2\sigma(I)$]	$R_1 = 0.0227$, $wR_2 = 0.0475$	$R_1 = 0.0360$, $wR_2 = 0.0765$	$R_1 = 0.0324$, $wR_2 = 0.0716$	$R_1 = 0.0319$, $wR_2 = 0.0621$	$R_1 = 0.0610$, $wR_2 = 0.1226$
R indices (all data)	$R_1 = 0.0313$, $wR_2 = 0.0515$	$R_1 = 0.0465$, $wR_2 = 0.0823$	$R_1 = 0.0389$, $wR_2 = 0.0742$	$R_1 = 0.0417$, $wR_2 = 0.0665$	$R_1 = 0.1125$, $wR_2 = 0.1461$
Largest diff. peak and hole	1.078/-0.474	3.221/-1.188	0.690/-0.506	0.674/-0.406	1.60/-1.31

Table 7-5: (Continued).

	22	23
CCDC Reference No	984780	984781
Empirical formula	C ₁₀ H ₁₀ F ₄ N ₂ O	C ₂₂ H ₁₈ F ₄ N ₂ O ₂
Formula weight / g mol ⁻¹	520.00	672.18
T / K	110.05(10)	110.05(10)
Wavelength / Å	0.7107	0.7107
Crystal system	Triclinic	Monoclinic
Space group	<i>P</i> $\bar{1}$	<i>C</i> 2/c
Unit cell dimensions / Å	<i>a</i> = 4.93832(20) <i>b</i> = 5.7442(4) <i>c</i> = 13.5949(5)	<i>a</i> = 33.521(4) <i>b</i> = 4.96250(16) <i>c</i> = 19.466(2)
α / °	101.851(4)	90.00
β / °	90.864(3)	135.083(19)
γ / °	93.542(4)	90.00
Volume / Å ³	376.55(3)	2286.4(6)
Z	1	4
$\rho_{\text{calc}} / \text{Mg m}^{-3}$	2.293	1.953
Absorption coefficient / mm ⁻¹	4.220	2.805
<i>F</i> (000)	242	1288
Crystal size / mm ³	0.17 × 0.11 × 0.05	0.17 × 0.09 × 0.04
□ range for data collection	3.63 to 31.52°	3.43 to 32.09°
Index ranges	-6 ≤ <i>h</i> ≤ 6, -8 ≤ <i>k</i> ≤ 8 -19 ≤ <i>l</i> ≤ 9	-41 ≤ <i>h</i> ≤ 46, -6 ≤ <i>k</i> ≤ 6 -27 ≤ <i>l</i> ≤ 27
Reflections collected	3269	5598
Independent reflections	2135 [<i>R</i> _(int) = 0.0199]	3312 [<i>R</i> _(int) = 0.0218]
Completeness (%) to (□)	97.49% to (29.97°)	99.16% to (29.97°)
Data / restraints / parameters	2135 / 0 / 100	3312 / 0 / 150
Goodness-of-fit on <i>F</i> ²	1.023	1.043
Final <i>R</i> indices [<i>I</i> > 2σ(<i>I</i>)]	<i>R</i> ₁ = 0.0238, <i>wR</i> ₂ = 0.0482	<i>R</i> ₁ = 0.0248, <i>wR</i> ₂ = 0.0501
<i>R</i> indices (all data)	<i>R</i> ₁ = 0.0275, <i>wR</i> ₂ = 0.0498	<i>R</i> ₁ = 0.0309, <i>wR</i> ₂ = 0.0534
Largest diff. peak and hole	0.706/-0.500	0.459/-0.464

7.11.2 Co-crystal Formation

In a typical co-crystallisation experiment, vapour diffusion techniques were used. The components were dissolved in a small volume of common solvent and placed inside a tablet tube inside a vial and the tablet tube was then covered with aluminium foil, which was punctured by using a needle. The anti-solvent (ca 2 cm³) was added to the vial, which was then sealed with a cap and covered in parafilm to prevent evaporation of the solvents. Solvents and anti-solvents are given in Table 7-6.

Table 7-6: Solvents and Anti-solvents used in the co-crystallisations.

	Solvent	Anit-solvent		Solvent	Anti-solvent
1	Chloroform	Cyclohexane	13	THF	Cyclohexane
2	Diisopropylether	Cyclohexane	14	Methanol	Diisopropylether
3	THF	Cyclohexane	15	Chloroform	Cyclohexane
4	Diisopropylether	Cyclohexane	16	THF	Cyclohexane
5	THF	None	17	THF	Diethyl ether
6	Hexane	None	18	Chloroform	Cyclohexane
8	Dichloromethane	Cyclohexane	19	Acetonitrile	None
9	THF	Cyclohexane	20	Acetonitrile	None
10	THF	None	21	THF	None
11	Methanol	Toluene	22	Dichloromethane	None
12	THF	Hexane	23	Dichloromethane	None

7.11.3 Computational Procedure

The geometries of 4-halotetrafluorophenols and their phenate anions were optimised at the MP2(Full)/aug-cc-pVDZ level of theory using Gaussian09.²²⁶ The aug-cc-pVDZ-PP basis set was used for iodine with an effective core potential (ECP) to take into account relativistic effects. Vibrational frequency calculations were carried out to ensure that optimised geometries corresponded to global minima on the potential energy surface.

NBO analysis was carried out using NBO version 3 implemented in Gaussian09 using the RESONANCE keyword.

8 Conclusions

This investigation has involved the study of a variety of halogen-bonded complexes that have ranged from the very weak complexes with rare gas atoms to strong complexes involving halonium ions acting as halogen-bond donors. Although the complexes investigated have such different strengths, many of the properties observed are similar. A linear geometry is preferred in all cases unless there are secondary interactions involved. The interaction predominantly arises from an electrostatic interaction, however hyperconjugation from the lone pair of electrons on the halogen-bond acceptor into an anti-bonding orbital on the halogen-bond donor also makes a significant contribution. The relative contributions of these interactions differ with the strength of the complexes, with dispersion interactions also playing a significant role in the weak complexes with rare gas atoms.

The halogen bond has been shown to be analogous to the hydrogen bond and the work presented in this thesis corroborates this observation. The Steiner-Limbach equation, which relates the A–H and H···B bond lengths in A–H···B hydrogen bonds, was shown to also apply to halogen-bonded systems, although improvements of fit can be made in some cases with the introduction of a new parameter. The ability of the equation to describe both interactions highlights their similarity and, since the equation also describes the changes in the bond lengths during proton transfer reactions, also shows that halogen-bonding plays a role in halogen transfer mechanisms.

The ability to predict the formation of interactions is necessary in the design of new supramolecular architectures. Typically, hydrogen bonding is predicted to be favoured over halogen bonding, however there have been examples of halogen bonding being preferred. A new example of halogen bonding being favoured over hydrogen bonding has been presented in the co-crystal of 4-iodo-2,3,5,6-tetrafluoroiodobenzene and 1,4-dithiane. The base is sufficiently weak for the

hydrogen-bonded dimer of the benzoic acid to be maintained in accordance to the iodine basicity scale¹¹ and Pearson's classification of Hard and Soft Acids and Bases,¹⁰ which have been shown to be useful tools to predict hydrogen and halogen bond formation in co-crystals.

Other examples of hydrogen and halogen bonding being combined in motifs have been observed in the co-crystals of 4-halo-2,3,5,6-tetrafluorophenols with cyclic amines. In some of these examples, the base deprotonated the phenol to produce a phenate anion, which exists in a Meissenheimer-like structure with double bond character in the C–O bond. The oxygen atom interacts with hydrogen- and halogen-bond donors through its sp^2 lone pairs of electrons and in situations where there are two hydrogen-bond donors available to interact with the oxygen atom, halogen bonding forms orthogonally to the hydrogen bonds. This is a small molecule analogue of the orthogonal halogen and hydrogen bonding observed in biological systems.⁴⁰⁵

Halogen bonding has also been observed to induce liquid crystal behaviour in components that are not themselves mesomorphic. Additional examples of halogen-bonded liquid crystals have been observed in the complexes of iodine with alkoxystilbazoles and of ICl and IBr with alkoxyphenylpyridines. In the former unusual mesomorphic behaviour was observed; SmC phases formed and small-angle X-ray diffraction revealed that the complexes existed in a 2:2 ratio with a weak I...I interaction present.

Analogous complexes of molecular bromine with alkoxystilbazoles could not be formed, rather an electrophilic bromination reaction took place followed by elimination of HBr. This reaction likely proceeded *via* a carbocation intermediate stabilised by resonance, as observed in calculations of the intermediates of stilbenes with electron-donating substituents. Stilbenes with two electron-withdrawing substituents were observed to form bromonium ion intermediates, which feature a

halogen atom with a positive charge. Calculations have revealed that such intermediates can act as halogen-bond donors and form strong interactions with Lewis bases that have properties similar to traditional halogen bonds.

Both experiment and quantum chemical calculations have been used together in order to study the different halogen bonds in this investigation. Calculations have proven to be useful for explaining observations made experimentally and increase understanding of bonding in complexes. It has been found that when using quantum chemistry to investigate the halogen bond there are some considerations that need to be made. It is important to use methods that include electron correlation because this plays a role in the interaction. Calculations using DFT need to use functionals that can account for the dispersion interactions particularly if the halogen bond being investigated is relatively weak. The M06 suite of functionals, particularly M06-2X, and Grimme's DFT-D3 correction were found to be appropriate for the complexes investigated. The density of the integration grid should also be considered when carrying out DFT calculations of halogen-bonded complexes because oscillations observed in the potential energy surfaces can cause erroneous results. The use of counterpoise (CP) correction of the basis set superposition (BSSE) is also recommended in calculations of halogen-bonded complexes.

There are a few areas where the work presented in this thesis could be taken forwards. It would be of interest to see whether the rare gas complexes investigated in Chapter 3 can be observed experimentally. Molecular dynamics calculations using the shielding tensor functions determined during this project could be used to estimate the ^{129}Xe chemical shift of xenon dissolved in halogen-bond donors. The refractive index of the halogen-bond donor solvent could also be used to predict the change in chemical shift if the interaction was due to only dispersion forces. ^{129}Xe NMR experiments could then be carried out to evaluate the extent of the interaction and if the change in chemical shift deviates from that anticipated from the refractive index of the halogen-bond donor solvent, then an electrostatic interaction is present.

Attempts to carry out these NMR experiments were made during the course of this project but were unsuccessful. Collaboration with experts in ^{129}Xe NMR spectroscopy could ensure more success in this research.

The work on halogen-bonded liquid crystals with dihalogens could be extended further. Complexes of iodine monochloride and iodine monobromide with alkoxy stilbazoles could be synthesised and their liquid crystal properties investigated. The complexes should be stronger than those with iodine due to the larger dipole moment of these dihalogens and therefore greater thermal stability of any liquid crystal phases should be observed. A single crystal of a halogen-bonded complex between bromine and an alkoxyphenylpyridine should be possible to obtain by taking care to avoid protonation of the pyridine base. It would then be of interest to investigate whether a complex with molecular bromine can be liquid crystalline. The complexes of iodine monochloride and iodine monobromide with alkoxyphenylpyridines could be investigated using small angle X-ray diffraction to determine the arrangement of the molecules in the liquid crystal phase and verify the theory that an interdigitated bilayer is formed.

Another area of further work would be to show the formation of a halogen-bonded complex between a halonium ion and a Lewis base experimentally. The most likely way to achieve this would be to synthesise the halonium ion of adamantylidene adamantane, which is stable and can be isolated, and make attempts to form single crystals with Lewis bases. A crystal structure of a complex of this type could be compared to the results of the calculations presented in this thesis and validate the level of theory used. One of the challenges of this would be to select an anion that is weakly coordinating and will not affect the interaction.

The fact that halonium ions can form interactions with Lewis bases has implications in the electrophilic bromination reaction because the halonium ion should interact with free bromide ions. Although such an interaction is unlikely to be sufficiently

strong to have a significant effect on the reaction, it would be of interest to perform calculations of complexes of halonium ions with halide anions.

9 Abbreviations

°	Degrees
°C	Degrees Celcius
Å	Ångström
AdAd	Adamantylidene Adamantane
AIM	Atoms in Molecules
B3LYP	Becke three-parameter hybrid functional with Lee, Yang and Parr correlation functional
B97-D	Becke's 1997 functional with Grimme's dispersion correction
bcp	Bond Critical Point
BJ	Becke-Johnson
BSIE	Basis Set Incompleteness Error
BSSE	Basis Set Superposition Error
CBS	Complete basis set
CCD	Charged-Coupled Device
CCSD	Coupled Cluster Singles and Doubles
cif	Crystallographic Information Framework
CP	Counterpoise
Cr	Crystal Phase
CSD	Crystallographic Structural Database
CTC	Charge-Transfer Complex
d	Doublet
D	Debye
DCP	Dispersion Correcting Potential
DFT	Density Functional Theory
DMAP	Dimethylaminopyridine
DNA	Deoxyribonucleic Acid

DSC	Differential Scanning Calorimetry
E	Energy
ECP	Effective core potential
ESP	Electrostatic Surface Potential
FC	Frozen Core
FTIR	Fourier Transform Infrared
GGA	Generalised Gradient Approximation
GIAO	Gauge-Independent Atomic Orbital
HC	Hydrocarbon
HF	Hartree-Fock
HSAB	Hard and Soft Acids and Bases
Hz	Hertz
Iso	Isotropic Phase
IUPAC	International Union of Pure and Applied Chemistry
K	Kelvin
LCAO	Linear Combination of Atomic Orbitals
LDA	Local-density Approximation
LMO	Localised Molecular Orbital
LUMO	Lowest Unoccupied Molecular Orbital
m	Multiplet
MD	Molecular Dynamics
MP2	Second Order Møller-Plesset Perturbation theory
N	Nematic Phase
N*	Chiral Nematic Phase
NAO	Natural Atomic Orbital
NBO	Natural Bonding Orbital
NHO	Natural Hybrid Orbital
NLMO	Natural Localised Molecular Orbital
NMDA	<i>N</i> -methyl- <i>D</i> -aspartate

NMR	Nuclear Magnetic Resonance
NOE	Nuclear Overhauser Effect
NPA	Natural Population Analysis
OTf	Trifluoromethylsulfonate
PBE	The correlation functional of Perdew, Burke and Ernzerhof
PCM	Polarisable Continuum Model
PDB	Protein Data Bank
PFC	Perfluorocarbon
POM	Polarising Optical Microscopy
PP	Pseudo-potential
ppm	parts per million
s	Singlet
SAPT	Symmetry Adapted Perturbation Theory
SmA	Smectic A Phase
SmC	Smectic C Phase
S _N 2	Bimolecular Nucleophilic Substitution
STO-3G	Slater Type Orbital with 3 Gaussian type functions
SVWN	Slater exchange with Vosko, Wilk and Nusair correlation
t	Triplet
THF	Tetrahydrofuran
UV	UltraViolet
WBI	Wiberg bond index
X3LYP	Xu's extended hybrid functional with Lee, Yang and Parr correlation functional
XDM	Exchange Dipole Moment
XRD	X-ray diffraction

10 References

1. G. R. Desiraju, P. S. Ho, L. Kloo, A. C. Legon, R. Marquardt, P. Metrangolo, P. Politzer, G. Resnati and K. Rissanen, *Pure Appl. Chem.*, 2013, **85**, 1711-1713.
2. F. Guthrie, *J. Chem. Soc.*, 1863, **16**, 239-244.
3. I. Remsen and J. F. Norris, *Am. Chem. J.*, 1896, **18**, 90-95.
4. R. S. Mulliken, *J. Am. Chem. Soc.*, 1950, **72**, 600-608.
5. O. Hassel and J. Hvoslef, *Acta. Chem. Scand.*, 1954, **8**, 873-873.
6. W. T. Pennington, T. W. Hanks and H. D. Arman, in *Halogen Bonding Fundamentals and Applications*, eds. P. Metrangolo and G. Resnati, Springer, Berlin. 2008, vol. 126, pp. 65 - 104.
7. O. Hassel, *Science*, 1970, **170**, 497-502.
8. G. Y. Chao and J. D. McCullough, *Acta Crystallogr.*, 1960, **13**, 727-732.
9. J. D. McCullough, Y. Chao and D. E. Zuccaro, *Acta Crystallogr.*, 1959, **12**, 815-816.
10. R. G. Pearson, *J. Am. Chem. Soc.*, 1963, **85**, 3533-3539.
11. C. Laurence, J. Graton, M. Berthelot and M. J. El Ghomari, *Chem. Eur. J.*, 2011, **17**, 10431-10444.
12. J.-Y. Le Questel, C. Laurence and J. Graton, *CrystEngComm*, 2013, **15**, 3212-3221.
13. O. Hassel and K. O. Strømme, *Acta Chem. Scand.*, 1959, **13**, 1775-1780.
14. O. Hassel, *Acta Chem. Scand.*, 1965, **19**, 2259-2259.
15. O. Hassel and J. Hvoslef, *Acta Chem. Scand.*, 1956, **10**, 138-139.
16. O. Hassel and K. O. Strømme, *Acta. Chem. Scand.*, 1959, **13**, 275-280.
17. P. Groth and O. Hassel, *Acta Chem. Scand.*, 1964, **18**, 402-408.
18. O. Hassel, C. H. R. Rømming and T. Tufte, *Acta. Chem. Scand.*, 1961, **15**, 967 - 974.

19. O. Hassel and C. Rømming, *Acta Chem. Scand.*, 1956, **10**, 696-698.
20. T. Dahl, O. Hassel and K. Sky, *Acta Chem. Scand.*, 1967, **21**, 592-593.
21. K. O. Strømme, *Acta Chem. Scand.*, 1959, **13**, 268-274.
22. O. Hassel and H. Hope, *Acta Chem. Scand.*, 1960, **14**, 391-397.
23. C. Rømming, *Acta Chem. Scand.*, 1960, **14**, 2145-2151.
24. O. Hassel and C. Rømming, *Acta Chem. Scand.*, 1967, **21**, 2659-2662.
25. O. Hassel and C. Rømming, *Acta Chem. Scand.*, 1960, **14**, 398-406.
26. T. Bjorvatten and O. Hassel, *Acta Chem. Scand.*, 1961, **15**, 1429-1436.
27. T. Dahl and O. Hassel, *Acta Chem. Scand.*, 1971, **25**, 2168-2174.
28. H. A. Bent, *Chem. Rev.*, 1968, **68**, 587-648.
29. F. J. Strieter and D. H. Templeton, *J. Chem. Phys.*, 1962, **37**, 161-164.
30. T. Sakurai, M. Sundaralingam and G. A. Jeffrey, *Acta Crystallogr.*, 1963, **16**, 354-363.
31. T. Sakurai, *Acta Crystallogr.*, 1962, **15**, 1164-1173.
32. A. C. Legon, in *Halogen Bonding: Fundamentals and Applications*, eds. P. Metrangolo and G. Resnati. 2008, vol. 126, pp. 17-64.
33. P. Metrangolo, H. Neukirch, T. Pilati and G. Resnati, *Acc. Chem. Res.*, 2005, **38**, 386-395.
34. A. Priimagi, G. Cavallo, P. Metrangolo and G. Resnati, *Acc. Chem. Res.*, 2013, **46**, 2686-2695.
35. K. Rissanen, *CrystEngComm*, 2008, **10**, 1107-1113.
36. G. R. Desiraju, *Angew. Chem. Int. Ed.*, 2011, **50**, 52-59.
37. T. Brinck, J. S. Murray and P. Politzer, *Int. J. Quantum Chem.*, 1992, **44**, 57-64.
38. T. Clark, M. Hennemann, J. S. Murray and P. Politzer, *J. Mol. Model*, 2007, **13**, 291-296.

39. P. Politzer, J. S. Murray and M. C. Concha, *J. Mol. Model.*, 2007, **13**, 643-650.
40. K. Riley, J. Murray, J. Fanfrlík, J. Řezáč, R. Solá, M. Concha, F. Ramos and P. Politzer, *J. Mol. Model.*, 2011, **17**, 3309-3318.
41. K. E. Riley, J. S. Murray, P. Politzer, M. C. Concha and P. Hobza, *J. Chem. Theor. Comput.*, 2009, **5**, 155-163.
42. P. Metrangolo, J. S. Murray, T. Pilati, P. Politzer, G. Resnati and G. Terraneo, *Cryst. Growth Des.*, 2011, **11**, 4238-4246.
43. P. Metrangolo, J. S. Murray, T. Pilati, P. Politzer, G. Resnati and G. Terraneo, *CrystEngComm*, 2011, **13**, 6593-6596.
44. P. Politzer, J. S. Murray and T. Clark, *Phys. Chem. Chem. Phys.*, 2013, **15**, 11178-11189.
45. U. Adhikari and S. Scheiner, *Chem. Phys. Lett.*, 2012, **532**, 31-35.
46. S. Zahn, R. Frank, E. Hey-Hawkins and B. Kirchner, *Chem. Eur. J.*, 2011, **17**, 6034-6038.
47. U. Adhikari and S. Scheiner, *J. Phys. Chem. A*, 2014.
48. S. Scheiner, *CrystEngComm*, 2013, **15**, 3119-3124.
49. A. Frontera, A. Bauza, D. Quinonero and P. M. Deya Serra, *CrystEngComm*, 2013, **15**, 3137-3144.
50. D. Britton, V. G. Young and E. O. Schlemper, *Acta. Crystallogr. Sect. C*, 2002, **58**, m307-m309.
51. N. A. Barnes, S. M. Godfrey, R. T. A. Halton, I. Mushtaq, S. Parsons, R. G. Pritchard and M. Sadler, *Polyhedron*, 2007, **26**, 1053-1060.
52. F. Carré, C. Chuit, R. J. P. Corriu, P. Monforte, N. K. Nayyar and C. Reyé, *J. Organomet. Chem.*, 1995, **499**, 147-154.
53. M. M. Chowdhry, D. M. P. Mingos, A. J. P. White and D. J. Williams, *J. Chem. Soc., Perkin Trans. 1*, 2000, 3495-3504.
54. P. G. Taylor, A. R. Bassindale, Y. El Aziz, M. Pourny, R. Stevenson, M. B. Hursthouse and S. J. Coles, *Dalton Trans.*, 2012, **41**, 2048-2059.

55. A. Bauzá, T. J. Mooibroek and A. Frontera, *Angew. Chem. Int. Ed.*, 2013, **52**, 12317-12321.
56. M. F. Roll, J. W. Kampf and R. M. Laine, *Cryst. Growth Des.*, 2011, **11**, 4360-4367.
57. D. Mani and E. Arunan, *Phys. Chem. Chem. Phys.*, 2013, **15**, 14377-14383.
58. S. J. Grabowski, *Phys. Chem. Chem. Phys.*, 2014, **16**, 1824-1834.
59. S. P. Thomas, M. S. Pavan and T. N. Guru Row, *Chem. Commun.*, 2014, **50**, 49-51.
60. S. P. Thomas, K. Nagarajan and T. N. G. Row, *Chem. Commun.*, 2012, **48**, 10559-10561.
61. E. Arunan, G. R. Desiraju, R. A. Klein, J. Sadlej, S. Scheiner, I. Alkorta, D. C. Clary, R. H. Crabtree, J. J. Dannenberg, P. Hobza, H. G. Kjaergaard, A. C. Legon, B. Mennucci and D. J. Nesbitt, *Pure. Appl. Chem.*, 2011, **83**, 1637-1641.
62. Z. P. Shields, J. S. Murray and P. Politzer, *Int. J. Quantum Chem.*, 2010, **110**, 2823-2832.
63. A. C. Legon, *Chem. Eur. J.*, 1998, **4**, 1890-1897.
64. S. A. Cooke, G. Cotti, C. M. Evans, J. H. Holloway, Z. Kisiel, A. C. Legon and J. M. A. Thumwood, *Chem. Eur. J.*, 2001, **7**, 2295-2305.
65. A. C. Legon, *Angew. Chem. Int. Ed.*, 1999, **38**, 2687-2714.
66. A. C. Legon, *Phys. Chem. Chem. Phys.*, 2010, **12**, 7736-7747.
67. C. Präsang, H. L. Nguyen, P. N. Horton, A. C. Whitwood and D. W. Bruce, *Chem. Commun.*, 2008, 6164-6166.
68. E. Corradi, S. V. Meille, M. T. Messina, P. Metrangolo and G. Resnati, *Angew. Chem. Int. Ed.*, 2000, **39**, 1782-1786.
69. P. Metrangolo and G. Resnati, *Science*, 2008, **321**, 918-919.
70. M. Carter and P. S. Ho, *Cryst. Growth Des.*, 2011, **11**, 5087-5095.
71. C. B. Aakeröy, P. D. Chopade, C. Ganser, M. Fasulo, N. C. Schultheiss and J. Desper, The Balance Between Hydrogen Bonds and Halogen Bonds, IUCr

- 2011 Satellite Workshop: Categorizing Halogen Bonding and Other Noncovalent Interactions Involving Halogen Atoms, Sigüenza, Spain,
72. C. B. Aakeröy, M. Fasulo, N. Schultheiss, J. Desper and C. Moore, *J. Am. Chem. Soc.*, 2007, **129**, 13772-13773.
 73. W. Clegg, *Crystal Structure Determination*, Oxford University Press, Oxford, 1998.
 74. P. W. Atkins and J. De Paula, *Atkins' Physical Chemistry*, 8th Ed. edn., Oxford University Press, Oxford, 2006.
 75. C. Präsang, A. C. Whitwood and D. W. Bruce, *Cryst. Growth Des.*, 2009, **9**, 5319-5326.
 76. C. B. Aakeröy, M. Baldrighi, J. Desper, P. Metrangolo and G. Resnati, *Chem. Eur. J.*, 2013, **19**, 16240-16247.
 77. M. T. Messina, P. Metrangolo, W. Panzeri, E. Ragg and G. Resnati, *Tetrahedron Lett.*, 1998, **39**, 9069-9072.
 78. P. Metrangolo, W. Panzeri, F. Recupero and G. Resnati, *J. Fluorine Chem.*, 2002, **114**, 27-33.
 79. S. Libri, N. A. Jasim, R. N. Perutz and L. Brammer, *J. Am. Chem. Soc.*, 2008, **130**, 7842-7844.
 80. T. Beweries, L. Brammer, N. A. Jasim, J. E. McGrady, R. N. Perutz and A. C. Whitwood, *J. Am. Chem. Soc.*, 2011, **133**, 14338-14348.
 81. D. A. Smith, L. Brammer, C. A. Hunter and R. N. Perutz, *J. Am. Chem. Soc.*, 2014, **136**, 1288-1291.
 82. M. G. Sarwar, B. Dragisic, L. J. Salsberg, C. Gouliaras and M. S. Taylor, *J. Am. Chem. Soc.*, 2010, **132**, 1646-1653.
 83. C. M. Widdifield, G. Cavallo, G. A. Facey, T. Pilati, J. Lin, P. Metrangolo, G. Resnati and D. L. Bryce, *Chem. Eur. J.*, 2013, **19**, 11949-11962.
 84. J. Viger-Gravel, I. Korobkov and D. L. Bryce, *Cryst. Growth Des.*, 2011, **11**, 4984-4995.
 85. R. J. Attrell, C. M. Widdifield, I. Korobkov and D. L. Bryce, *Cryst. Growth Des.*, 2012, **12**, 1641-1653.

86. A. Szabo and N. S. Ostlund, *Modern Quantum Chemistry: Introduction to Advanced Electronic Structure Theory*, Dover Publications, INC., New York, 1996.
87. G. H. Grant and W. G. Richards, *Computational Chemistry*, Oxford University Press, Oxford, 1995.
88. C. C. J. Roothaan, *Rev. Mod. Phys.*, 1951, **23**, 69-89.
89. J. S. Binkley and J. A. Pople, *Int. J. Quantum Chem.*, 1975, **9**, 229-236.
90. G. E. Scuseria, C. L. Janssen and H. F. Schaefer, *J. Chem. Phys.*, 1988, **89**, 7382-7387.
91. J. Řezáč and P. Hobza, *J. Chem. Theor. Comput.*, 2013, **9**, 2151-2155.
92. R. Ditchfield, W. J. Hehre and J. A. Pople, *J. Chem. Phys.*, 1971, **54**, 724-728.
93. T. H. Dunning, *J. Chem. Phys.*, 1989, **90**, 1007-1023.
94. D. E. Woon and T. H. Dunning, *J. Chem. Phys.*, 1993, **98**, 1358-1371.
95. R. A. Kendall, T. H. Dunning and R. J. Harrison, *J. Chem. Phys.*, 1992, **96**, 6796-6806.
96. J. Autschbach, *J. Chem. Phys.*, 2012, **136**, 150902.
97. W. R. Wadt and P. J. Hay, *J. Chem. Phys.*, 1985, **82**, 284-298.
98. P. Hohenberg and W. Kohn, *Phys. Rev.*, 1964, **136**, B864-B871.
99. W. Kohn and L. J. Sham, *Phys. Rev.*, 1965, **140**, A1133-A1138.
100. W. Koch and M. C. Holthausen, *A Chemist's Guide to Density Functional Theory*, 2nd Ed. edn., Wiley-VCH, Weinheim, 2001.
101. K. Burke and L. O. Wagner, *Int. J. Quantum Chem.*, 2013, **113**, 96-101.
102. S. F. Sousa, P. A. Fernandes and M. J. Ramos, *J. Phys. Chem. A*, 2007, **111**, 10439-10452.
103. W. Kohn, A. D. Becke and R. G. Parr, *J. Phys. Chem.*, 1996, **100**, 12974-12980.
104. Y. Zhao and D. G. Truhlar, *Theor. Chem. Acc.*, 2008, **120**, 215-241.

105. S. Grimme, J. Antony, S. Ehrlich and H. Krieg, *J. Chem. Phys.*, 2010, **132**, 154104.
106. S. F. Boys and F. Bernardi, *Mol. Phys.*, 1970, **19**, 553-566.
107. F. B. van Duijneveldt, J. G. C. M. van Duijneveldt-van de Rijdt and J. H. van Lenthe, *Chem. Rev.*, 1994, **94**, 1873-1885.
108. D. W. Schwenke and D. G. Truhlar, *J. Chem. Phys.*, 1985, **82**, 2418-2426.
109. X. W. Sheng, L. Mentel, O. V. Gritsenko and E. J. Baerends, *J. Comput. Chem.*, 2011, **32**, 2896-2901.
110. M. J. Frisch, J. E. Del Bene, J. S. Binkley and H. F. Schaefer III, *J. Chem. Phys.*, 1986, **84**, 2279-2289.
111. K. R. Liedl, *J. Chem. Phys.*, 1998, **108**, 3199-3204.
112. A. Roztoczyńska, A. Kaczmarek-Kędziera, R. W. Góra and W. Bartkowiak, *Chem. Phys. Lett.*, 2013, **571**, 28-33.
113. T. H. Dunning, *J. Phys. Chem. A*, 2000, **104**, 9062-9080.
114. A. Halkier, W. Klopper, T. Helgaker, P. Jørgensen and P. R. Taylor, *J. Chem. Phys.*, 1999, **111**, 9157-9167.
115. N. Kobko and J. J. Dannenberg, *J. Phys. Chem. A*, 2001, **105**, 1944-1950.
116. P. Salvador, M. Duran and J. J. Dannenberg, *J. Phys. Chem. A*, 2002, **106**, 6883-6889.
117. S. Simon, M. Duran and J. J. Dannenberg, *J. Chem. Phys.*, 1996, **105**, 11024-11031.
118. A. Ebrahimi, M. Habibi and H. R. Masoodi, *Mol. Phys.*, 2007, **105**, 2259-2268.
119. C. Edmiston and K. Ruedenberg, *Rev. Mod. Phys.*, 1963, **35**, 457-465.
120. J. M. Foster and S. F. Boys, *Rev. Mod. Phys.*, 1960, **32**, 300-302.
121. D. A. Kleier, T. A. Halgren, J. H. Hall and W. N. Lipscomb, *J. Chem. Phys.*, 1974, **61**, 3905-3919.
122. L. C. Roper, C. Präsang, V. N. Kozhevnikov, A. C. Whitwood, P. B. Karadakov and D. W. Bruce, *Cryst. Growth Des.*, 2010, **10**, 3710-3720.

123. A. E. Reed, L. A. Curtiss and F. Weinhold, *Chem. Rev.*, 1988, **88**, 899-926.
124. A. E. Reed, F. Weinhold, L. A. Curtiss and D. J. Pochatko, *J. Chem. Phys.*, 1986, **84**, 5687-5705.
125. L. A. Curtiss, D. J. Pochatko, A. E. Reed and F. Weinhold, *J. Chem. Phys.*, 1985, **82**, 2679-2687.
126. Y.-X. Lu, J.-W. Zou, Y.-H. Wang, Y.-J. Jiang and Q.-S. Yu, *J. Phys. Chem. A*, 2007, **111**, 10781-10788.
127. A. Mohajeri, M. Alipour and M. Mousaee, *J. Phys. Chem. A.*, 2011, **115**, 4457-4466.
128. J. G. Hill and X. Hu, *Chem. Eur. J.*, 2013, **19**, 3620-3628.
129. S. V. Rosokha, C. L. Stern and J. T. Ritzert, *Chem. Eur. J.*, 2013, **19**, 8774-8788.
130. Y. Chen, *J. Phys. Chem. A*, 2013, **117**, 8081-8090.
131. P. P. Zhou, W. Y. Qiu, S. Liu and N. Z. Jin, *Phys. Chem. Chem. Phys.*, 2011, **13**, 7408-7418.
132. H. Zhuo, Q. Li, W. Li and J. Cheng, *Phys. Chem. Chem. Phys.*, 2014.
133. H. A. Bent, *Chem. Rev.*, 1961, **61**, 275-311.
134. H. A. Bent, *J. Chem. Phys.*, 1960, **33**, 1258-1259.
135. S. J. Grabowski, *J. Phys. Chem. A*, 2011, **115**, 12340-12347.
136. S. Tsuzuki, A. Wakisaka, T. Ono and T. Sonoda, *Chem. Eur. J.*, 2012, **18**, 951-960.
137. Y. Zeng, X. Zhang, X. Li, S. Zheng and L. Meng, *Int. J. Quantum Chem.*, 2011, **111**, 3725-3740.
138. I. Alkorta, I. Rozas and J. Elguero, *J. Phys. Chem. A.*, 1998, **102**, 9278-9285.
139. A. Karpfen, in *Halogen Bonding Fundamentals and Applications*, eds. P. Metrangolo and G. Resnati, Springer, Berlin. 2008, vol. 126, pp. 1-15.
140. E. Arunan, G. R. Desiraju, R. A. Klein, J. Sadlej, S. Scheiner, I. Alkorta, D. C. Clary, R. H. Crabtree, J. J. Dannenberg, P. Hobza, H. G. Kjaergaard, A. C.

- Legon, B. Mennucci and D. J. Nesbitt, *Pure. Appl. Chem.*, 2011, **83**, 1619-1636.
141. J. P. M. Lommerse, A. J. Stone, R. Taylor and F. H. Allen, *J. Am. Chem. Soc.*, 1996, **118**, 3108-3116.
142. P. Politzer, K. E. Riley, F. A. Bulat and J. S. Murray, *Comp. Theor. Chem.*, 2012, **998**, 2-8.
143. T. Clark, *WIREs Comput. Mol. Sci.*, 2013, **3**, 13-20.
144. K. Riley, J. Murray, J. Fanfrlík, J. Řezáč, R. Solá, M. Concha, F. Ramos and P. Politzer, *J. Mol. Model.*, 2012, 1-9.
145. A. J. Stone, *J. Am. Chem. Soc.*, 2013, **135**, 7005-7009.
146. Q. Zhao, D. Feng and J. Hao, *J. Mol. Model.*, 2011, **17**, 2817-2823.
147. Q. Li, R. Li, Z. Liu, W. Li and J. Cheng, *J. Comput. Chem.*, 2011, **32**, 3296-3303.
148. Y. Lu, Y. Liu, H. Li, X. Zhu, H. Liu and W. Zhu, *J. Phys. Chem. A*, 2012, **116**, 2591-2597.
149. W. Wang, Y. Zhang and Y.-B. Wang, *J. Phys. Chem. A*, 2012, **116**, 12486-12491.
150. B. Ji, W. Wang, D. Deng, Y. Zhang, L. Cao, L. Zhou, C. Ruan and T. Li, *CrystEngComm*, 2013, **15**, 769-774.
151. M. Solimannejad, M. Malekani and I. Alkorta, *J. Phys. Chem. A*, 2013, **117**, 5551-5557.
152. A. Bauzá, D. Quiñonero, A. Frontera and P. M. Deyà, *Phys. Chem. Chem. Phys.*, 2011, **13**, 20371-20379.
153. S. Tsuzuki, T. Uchimaru, A. Wakisaka, T. Ono and T. Sonoda, *Phys. Chem. Chem. Phys.*, 2013, **15**, 6088-6096.
154. I. Alkorta, G. Sanchez-Sanz and J. Elguero, *CrystEngComm*, 2013, **15**, 3178-3186.
155. Q. Z. Li, B. Jing, R. Li, Z. B. Liu, W. Z. Li, F. Luan, J. B. Cheng, B. A. Gong and J. Z. Sun, *Phys. Chem. Chem. Phys.*, 2011, **13**, 2266-2271.

156. J. B. Cheng, R. Li, Q. Z. Li, B. Jing, Z. B. Liu, W. Z. Li, B. A. Gong and J. Z. Sun, *J. Phys. Chem. A.*, 2010, **114**, 10320-10325.
157. Q. Z. Li, B. Jing, Z. B. Liu, W. Z. Li, J. B. Cheng, B. A. Gong and J. Z. Sun, *J. Chem. Phys.*, 2010, **133**, 114303.
158. J. W. Steed and J. L. Atwood, *Supramolecular Chemistry*, Wiley, Chichester, 2000.
159. G. R. Desiraju, *J. Chem. Sci.*, 2010, **122**, 667-675.
160. L. Brammer, G. M. Espallargas and S. Libri, *CrystEngComm*, 2008, **10**, 1712-1727.
161. M. Fourmigué, *Curr. Opin. Solid. St. M.*, 2009, **13**, 36-45.
162. P. Metrangolo, T. Pilati, G. Resnati and A. Stevanazzi, *Curr. Opin. Colloid Interface Sci.*, 2003, **8**, 215-222.
163. P. Metrangolo, G. Resnati, T. Pilati, R. Liantonio and F. Meyer, *J. Polym. Sci., Part. A: Polym. Chem.*, 2007, **45**, 1-15.
164. P. Metrangolo, G. Resnati, T. Pilati and S. Biella, in *Halogen Bonding Fundamentals and Applications*, eds. P. Metrangolo and G. Resnati, Springer, Berlin. 2008, vol. 126, pp. 105-136.
165. V. Amico, S. V. Meille, E. Corradi, M. T. Mesina and G. Resnati, *J. Am. Chem. Soc.*, 1998, **120**, 8261-8262.
166. P. Metrangolo, F. Meyer, T. Pilati, G. Resnati and G. Terraneo, *Angew. Chem. Int. Ed.*, 2008, **47**, 6114-6127.
167. A. De Santis, A. Forni, R. Liantonio, P. Metrangolo, T. Pilati and G. Resnati, *Chem. Eur. J.*, 2003, **9**, 3974-3983.
168. R. Thaimattam, C. V. K. Sharma, A. Clearfield and G. R. Desiraju, *Cryst. Growth Des.*, 2001, **1**, 103-106.
169. P. Metrangolo, T. Pilati, G. Terraneo, S. Biella and G. Resnati, *CrystEngComm*, 2009, **11**, 1187-1196.
170. J. Grebe, G. Geiseler, K. Harms and K. Dehnicke, *Z. Naturforsch., B: Chem. Sci.*, 1999, **54**, 77-86.

171. P. Metrangolo, Y. Carcenac, M. Lahtinen, T. Pilati, K. Rissanen, A. Vij and G. Resnati, *Science*, 2009, **323**, 1461-1464.
172. A. Mele, P. Metrangolo, H. Neukirch, T. Pilati and G. Resnati, *J. Am. Chem. Soc.*, 2005, **127**, 14972-14973.
173. M. G. Sarwar, B. Dragisić, E. Dimitrijević and M. S. Taylor, *Chem. Eur. J.*, 2013, **19**, 2050-2058.
174. M. G. Sarwar, B. Dragisic, S. Sahoo and M. S. Taylor, *Angew. Chem. Int. Ed.*, 2010, **49**, 1674-1677.
175. E. Dimitrijević, O. Kvak and M. S. Taylor, *Chem. Commun.*, 2010, **46**, 9025-9027.
176. T. M. Beale, M. G. Chudzinski, M. G. Sarwar and M. S. Taylor, *Chem. Soc. Rev.*, 2013, **42**, 1667-1680.
177. M. G. Chudzinski, C. A. McClary and M. S. Taylor, *J. Am. Chem. Soc.*, 2011, **133**, 10559-10567.
178. L. C. Gilday, N. G. White and P. D. Beer, *Dalton Trans.*, 2013, **42**, 15766-15773.
179. N. G. White, A. Caballero and P. D. Beer, *CrystEngComm*, 2014, **16**, 3722-3729.
180. A. Caballero, N. G. White and P. D. Beer, *Angew. Chem. Int. Ed.*, 2011, **50**, 1845-1848.
181. N. H. Evans and P. D. Beer, *Chem. Soc. Rev.*, 2014.
182. C. J. Serpell, N. L. Kilah, P. J. Costa, V. Félix and P. D. Beer, *Angew. Chem. Int. Ed.*, 2010, **49**, 5322-5326.
183. A. Caballero, S. Bennett, C. J. Serpell and P. D. Beer, *CrystEngComm*, 2013, **15**, 3076-3081.
184. N. L. Kilah, M. D. Wise, C. J. Serpell, A. L. Thompson, N. G. White, K. E. Christensen and P. D. Beer, *J. Am. Chem. Soc.*, 2010, **132**, 11893-11895.
185. N. L. Kilah, M. D. Wise and P. D. Beer, *Cryst. Growth Des.*, 2011, **11**, 4565-4571.

186. A. Caballero, F. Zapata, N. G. White, P. J. Costa, V. Félix and P. D. Beer, *Angew. Chem. Int. Ed.*, 2012, **51**, 1876-1880.
187. L. C. Gilday, T. Lang, A. Caballero, P. J. Costa, V. Félix and P. D. Beer, *Angew. Chem. Int. Ed.*, 2013, **52**, 4356-4360.
188. P. G. De Gennes, *The Physics of Liquid Crystals*, Oxford University Press, Oxford, 1974.
189. P. J. Collings and M. Hird, *Introduction to Liquid Crystals*, Taylor & Francis, London, 1997.
190. M. Schadt, 1997, **27**, 305-379.
191. G. Meier, E. Sackmann and J. G. Grabmaier, *Applications of Liquid Crystals*, Springer-Verlag, Berlin, 1975.
192. Y. N. Xia, P. D. Yang, Y. G. Sun, Y. Y. Wu, B. Mayers, B. Gates, Y. D. Yin, F. Kim and Y. Q. Yan, *Adv. Mater.*, 2003, **15**, 353-389.
193. C. Tschierske, *J. Mater. Chem.*, 1998, **8**, 1485-1508.
194. D. W. Bruce, in *Halogen Bonding Fundamentals and Applications*, eds. P. Metrangolo and G. Resnati, Springer, Berlin. 2008, vol. 126, pp. 161-180.
195. C. Tschierske, *Chem. Soc. Rev.*, 2007, **36**, 1930-1970.
196. J. Nehring and A. Saupe, *J. Chem. Soc., Faraday Trans. 2*, 1972, **68**, 1-15.
197. D. W. Bruce, P. Metrangolo, F. Meyer, T. Pilati, C. Präsang, G. Resnati, G. Terraneo, S. G. Wainwright and A. C. Whitwood, *Chem. Eur. J.*, 2010, **16**, 9511-9524.
198. H. L. Nguyen, P. N. Horton, M. B. Hursthouse, A. C. Legon and D. W. Bruce, *J. Am. Chem. Soc.*, 2004, **126**, 16-17
199. G. W. Gray and J. W. G. Goodby, *Smectic Liquid Crystals Textures and Structures*, Leonard Hill, Glasgow, 1984.
200. T. Kato and J. M. J. Frechet, *J. Am. Chem. Soc.*, 1989, **111**, 8533-8534.
201. J. P. W. Wong, A. C. Whitwood and D. W. Bruce, *Chem. Eur. J.*, 2012, **18**, 16073-16089.

202. B. Friot, D. Boyd, K. Willis, B. Donnio, G. Ungar and D. W. Bruce, *Liq. Cryst.*, 2000, **27**, 605-611.
203. D. J. Price, H. Adams and D. W. Bruce, *Mol. Cryst. Liq. Cryst.*, 1996, **289**, 127-140.
204. P. J. Martin and D. W. Bruce, *Liq. Cryst.*, 2007, **34**, 767-774.
205. K. Willis, D. J. Price, H. Adams, G. Ungar and D. W. Bruce, *J. Mater. Chem.*, 1995, **5**, 2195-2199.
206. D. J. Price, K. Willis, T. Richardson, G. Ungar and D. W. Bruce, *J. Mater. Chem.*, 1997, **7**, 883-891.
207. D. W. Bruce, P. Metrangolo, F. Meyer, C. Präsang, G. Resnati, G. Terraneo and A. C. Whitwood, *New J. Chem.*, 2008, **32**, 477-482.
208. A. Abate, M. Brischetto, G. Cavallo, M. Lahtinen, P. Metrangolo, T. Pilati, S. Radice, G. Resnati, K. Rissanen and G. Terraneo, 2010, **46**.
209. T. Steiner and W. Saenger, *Acta Crystallogr., Sect. B. Struct. Sci.*, 1994, **50**, 348-357.
210. I. D. Brown, *Acta Crystallogr., Sect. B. Struct. Sci.*, 1992, **48**, 553-572.
211. H. Benedict, H.-H. Limbach, M. Wehlan, W.-P. Fehlhammer, N. S. Golubev and R. Janoschek, *J. Am. Chem. Soc.*, 1998, **120**, 2939-2950.
212. A. D. Buckingham, J. E. Del Bene and S. A. C. McDowell, *Chem. Phys. Lett.*, 2008, **463**, 1-10.
213. M. Sánchez, P. F. Provasi, G. A. Aucar, I. Alkorta and J. Elguero, *J. Phys. Chem. B*, 2005, **109**, 18189-18194.
214. I. Alkorta, O. Picazo and J. Elguero, *Tetrahedron: Asymmetry*, 2004, **15**, 1391-1399.
215. M. Ramos, I. Alkorta, J. Elguero, N. S. Golubev, G. S. Denisov, H. Benedict and H. H. Limbach, *J. Phys. Chem. A.*, 1997, **101**, 9791-9800.
216. I. Alkorta, J. Elguero, H.-H. Limbach, I. G. Shenderovich and T. Winkler, *Magn. Reson. Chem.*, 2009, **47**, 585-592.
217. O. Picazo, I. Alkorta and J. Elguero, *J. Org. Chem.*, 2003, **68**, 7485-7489.

218. O. Picazo, I. Alkorta and J. Elguero, *Struct. Chem.*, 2005, **16**, 339-345.
219. J. E. Del Bene, I. Alkorta and J. Elguero, *J. Phys. Chem. A.*, 2010, **114**, 12958-12962.
220. J. E. Del Bene, I. Alkorta and J. Elguero, *Chem. Phys. Lett.*, 2011, **508**, 6-9.
221. I. Alkorta, G. Sanchez-Sanz, J. Elguero and J. E. Del Bene, *J. Phys. Chem. A*, 2012, **116**, 2300-2308.
222. J. E. Del Bene, I. Alkorta and J. Elguero, *Chem. Phys. Lett.*, 2006, **429**, 23-26.
223. Q. Li, S. Ma, X. Liu, W. Li and J. Cheng, *J. Chem. Phys.*, 2012, **137**, 084314.
224. J. Alvarez-Idaboy and A. Galano, *Theor. Chem. Acc.*, 2010, **126**, 75-85.
225. Gaussian03, Revision C.02, M. J. Frisch, G. W. Trucks, H. B. Schlegel, G. E. Scuseria, M. A. Robb, J. R. Cheeseman, J. J. A. Montgomery, T. Vreven, K. N. Kudin, J. C. Burant, J. M. Millam, S. S. Iyengar, J. Tomasi, V. Barone, B. Mennucci, M. Cossi, G. Scalmani, N. Rega, G. A. Petersson, H. Nakatsuji, M. Hada, M. Ehara, K. Toyota, R. Fukuda, J. Hasegawa, M. Ishida, T. Nakajima, Y. Honda, O. Kitao, H. Nakai, M. Klene, X. Li, J. E. Knox, H. P. Hratchian, J. B. Cross, V. Bakken, C. Adamo, J. Jaramillo, R. Gomperts, R. E. Stratmann, O. Yazyev, A. J. Austin, R. Cammi, C. Pomelli, J. W. Ochterski, P. Y. Ayala, K. Morokuma, G. A. Voth, P. Salvador, J. J. Dannenberg, V. G. Zakrzewski, S. Dapprich, A. D. Daniels, M. C. Strain, O. Farkas, D. K. Malick, A. D. Rabuck, K. Raghavachari, J. B. Foresman, J. V. Ortiz, Q. Cui, A. G. Baboul, S. Clifford, J. Cioslowski, B. B. Stefanov, G. Liu, A. Liashenko, P. Piskorz, I. Komaromi, R. L. Martin, D. J. Fox, T. Keith, M. A. Al-Laham, C. Y. Peng, A. Nanayakkara, M. Challacombe, P. M. W. Gill, B. Johnson, W. Chen, M. W. Wong, C. Gonzalez and J. A. Pople, Gaussian, Inc., Wallingford CT, 2004, <http://www.gaussian.com/>.
226. Gaussian09, Revision A.1, M. J. Frisch, G. W. Trucks, H. B. Schlegel, G. E. Scuseria, M. A. Robb, J. R. Cheeseman, G. Scalmani, V. Barone, B. Mennucci, G. A. Petersson, H. Nakatsuji, M. Caricato, X. Li, H. P. Hratchian, A. F. Izmaylov, J. Bloino, G. Zheng, J. L. Sonnenberg, M. Hada, M. Ehara, K. Toyota, R. Fukuda, J. Hasegawa, M. Ishida, T. Nakajima, Y. Honda, O. Kitao, H. Nakai, T. Vreven, J. A. M. Jr., J. E. Peralta, F. Ogliaro, M. Bearpark, J. J. Heyd, E. Brothers, K. N. Kudin, V. N. Staroverov, R. Kobayashi, J. Normand, K. Raghavachari, A. Rendell, J. C. Burant, S. S.

- Iyengar, J. Tomasi, M. Cossi, N. Rega, J. M. Millam, M. Klene, J. E. Knox, J. B. Cross, V. Bakken, C. Adamo, J. Jaramillo, R. Gomperts, R. E. Stratmann, O. Yazyev, A. J. Austin, R. Cammi, C. Pomelli, J. W. Ochterski, R. L. Martin, K. Morokuma, V. G. Zakrzewski, G. A. Voth, P. Salvador, J. J. Dannenberg, S. Dapprich, A. D. Daniels, Ö. Farkas, J. B. Foresman, J. V. Ortiz, J. Cioslowski and D. J. Fox, Gaussian, Inc., Wallingford CT, 2009, <http://www.gaussian.com/>.
227. G. Schaftenaar and J. H. Noordik, *J. Comput.-Aided Mol. Des.*, 2000, **14**, 123-134.
228. Molekel 5.4.0.8, U. Varetto, Swiss National Supercomputing Centre, Manno (Switzerland), 2009, <http://molekel.cscs.ch/wiki/pmwiki.php>.
229. Mathematica, 8, Wolfram, 2011, <http://www.wolfram.com/mathematica/>.
230. S. W. Hunt and K. R. Leopold, *J. Phys. Chem. A*, 2001, **105**, 5498-5506.
231. S. N. Eustis, D. Radisic, K. H. Bowen, R. A. Bachorz, M. Haranczyk, G. K. Schenter and M. Gutowski, *Science*, 2008, **319**, 936-939.
232. N. W. Howard and A. C. Legon, *J. Chem. Phys.*, 1988, **88**, 4694-4701.
233. A. C. Legon and D. Stephenson, *J. Chem. Soc., Faraday Trans.*, 1992, **88**, 761-762.
234. N. W. Howard and A. C. Legon, *J. Chem. Phys.*, 1987, **86**, 6722-6730.
235. G. M. Chaban, R. B. Gerber and K. C. Janda, *J. Phys. Chem. A*, 2001, **105**, 8323-8332.
236. A. J. Barnes and A. C. Legon, *J. Mol. Struct.*, 1998, **448**, 101-106.
237. I. Alkorta, I. Rozas, O. Mó, M. Yáñez and J. Elguero, *J. Phys. Chem. A*, 2001, **105**, 7481-7485.
238. A. C. Legon, *Chem. Soc. Rev.*, 1993, **22**, 153-163.
239. K. Xu, D. M. Ho and R. A. Pascal, *J. Am. Chem. Soc.*, 1994, **116**, 105-110.
240. K. Raatikainen, M. Cametti and K. Rissanen, *Beilstein J. Org. Chem.*, 2010, **6**, 4.
241. S. C. Cullen and E. G. Gross, *Science*, 1951, **113**, 580-582.

242. N. P. Franks, R. Dickinson, S. L. M. de Sousa, A. C. Hall and W. R. Lieb, *Nature*, 1998, **396**, 324-324.
243. L. T. Liu, Y. Xu and P. Tang, *J. Phys. Chem. B*, 2010, **114**, 9010-9016.
244. V. Aquilanti, E. Cornicchi, M. Moix Teixidor, N. Saendig, F. Pirani and D. Cappelletti, *Angew. Chem. Int. Ed.*, 2005, **44**, 2356-2360.
245. M. Rozenberg, A. Loewenschuss and C. J. Nielsen, *Phys. Chem. Chem. Phys.*, 2010, **12**, 4024-4031.
246. P. Wawrzyniak, J. Panek, J. Lundell and Z. Latajka, *J. Mol. Model.*, 2005, **11**, 351-361.
247. Q. Cao, M. Melavuori, J. Lundell, M. Räsänen and L. Khriachtchev, *J. Mol. Struct.*, 2012, **1025**, 132-139.
248. J. J. Panek, P. K. Wawrzyniak, Z. Latajka and J. Lundell, *Chem. Phys. Lett.*, 2006, **417**, 100-104.
249. G. O. Ildiz, C. M. Nunes, N. Kuş and R. Fausto, *J. Chem. Phys.*, 2012, **137**, 064309.
250. D. Gąszowski and M. Ilczyszyn, *Chem. Phys. Lett.*, 2012, **538**, 29-34.
251. D. Gąszowski and M. Ilczyszyn, *Chem. Phys. Lett.*, 2013, **556**, 59-64.
252. A. Rohrbacher, J. Williams and K. C. Janda, *Phys. Chem. Chem. Phys.*, 1999, **1**, 5263-5276.
253. M. D. Bradke and R. A. Loomis, *J. Chem. Phys.*, 2003, **118**, 7233-7244.
254. K. Higgins, F. M. Tao and W. Klemperer, *J. Chem. Phys.*, 1998, **109**, 3048-3061.
255. J. B. Davey, A. C. Legon and E. R. Waclawik, *Chem. Phys. Lett.*, 2001, **346**, 103-111.
256. J. B. Davey, A. C. Legon and E. R. Waclawik, *Chem. Phys. Lett.*, 1999, **306**, 133-144.
257. S. J. Harris, S. E. Novick, W. Klemperer and W. E. Falconer, *J. Chem. Phys.*, 1974, **61**, 193-197.

258. S. L. Stephens, N. R. Walker and A. C. Legon, *J. Chem. Phys.*, 2011, **135**, 224309.
259. G. Cavallo, S. Biella, J. A. Lu, P. Metrangolo, T. Pilati, G. Resnati and G. Terraneo, *J. Fluorine Chem.*, 2010, **131**, 1165-1172.
260. A. Abate, S. Biella, G. Cavallo, F. Meyer, H. Neukirch, P. Metrangolo, T. Pilati, G. Resnati and G. Terraneo, *J. Fluorine Chem.*, 2009, **130**, 1171-1177.
261. Q. Jin Shen and W. Jun Jin, *Phys. Chem. Chem. Phys.*, 2011, **13**, 13721-13729.
262. R. Liantonio, P. Metrangolo, T. Pilati and G. Resnati, *Cryst. Growth Des.*, 2003, **3**, 355-361.
263. P. Metrangolo, C. Präsang, G. Resnati, R. Liantonio, A. C. Whitwood and D. W. Bruce, *Chem. Commun.*, 2006, 3290-3292.
264. P. W. Atkins and R. S. Friedman, *Molecular Quantum Mechanics*, 3rd edn., Oxford University Press, Oxford, 1997.
265. A. D. Becke and E. R. Johnson, *J. Chem. Phys.*, 2005, **122**, 154104-154105.
266. M. Swart, M. Solà and F. M. Bickelhaupt, *J. Comput. Chem.*, 2011, **32**, 1117-1127.
267. K. E. Riley, M. Pitoňák, P. Jurečka and P. Hobza, *Chem. Rev.*, 2010, **110**, 5023-5063.
268. S. Grimme, *J. Comput. Chem.*, 2006, **27**, 1787-1799.
269. X. Xu and W. A. Goddard, *Proc. Natl. Acad. Sci. USA*, 2004, **101**, 2673-2677.
270. M. Swart, M. Solà and F. M. Bickelhaupt, *J. Chem. Phys.*, 2009, **131**, -.
271. L. Goerigk and S. Grimme, *Phys. Chem. Chem. Phys.*, 2011, **13**, 6670-6688.
272. Y. Zhao and D. G. Truhlar, *J. Chem. Phys.*, 2006, **125**, 194101.
273. Y. Zhao and D. G. Truhlar, *J. Phys. Chem. A*, 2006, **110**, 13126-13130.
274. G. A. DiLabio, *Chem. Phys. Lett.*, 2008, **455**, 348-353.
275. E. Torres and G. A. DiLabio, *J. Phys. Chem. Lett.*, 2012, **3**, 1738-1744.

276. I. D. Mackie and G. A. DiLabio, *J. Phys. Chem. A*, 2008, **112**, 10968-10976.
277. G. A. DiLabio, E. R. Johnson and A. Otero-de-la-Roza, *Phys. Chem. Chem. Phys.*, 2013, **15**, 12821-12828.
278. P. Hobza, *Acc. Chem. Res.*, 2012, **45**, 663-672.
279. K. E. Riley, J. Řezáč and P. Hobza, *Phys. Chem. Chem. Phys.*, 2011, **13**, 21121-21125.
280. J. A. Plumley and J. J. Dannenberg, *J. Comput. Chem.*, 2011, **32**, 1519-1527.
281. Y. Zhao and D. G. Truhlar, *J. Chem. Theory Comput.*, 2005, **1**, 415-432.
282. W. Hujo and S. Grimme, *Phys. Chem. Chem. Phys.*, 2011, **13**, 13942-13950.
283. M. G. Chudzinski and M. S. Taylor, *J. Org. Chem.*, 2012, **77**, 3483-3491.
284. DFT-D3, V2.1 Rev. 6, <http://toc.uni-muenster.de/DFTD3/index.html>.
285. S. Grimme, S. Ehrlich and L. Goerigk, *J. Comput. Chem.*, 2011, **32**, 1456-1465.
286. GAMESS, 21 Nov, M. W. Schmidt, K. K. Baldrige, J. A. Boatz, S. T. Elbert, M. S. Gordon, J. J. Jensen, S. Koseki, N. Matsunaga, K. A. Nguyen, S. Su, T. L. Windus, M. Dupuis and J. A. Montgomery, 1995, <http://www.msg.ameslab.gov/gamess/gamess.html>.
287. T. van der Wijst, C. F. Guerra, M. Swart and F. M. Bickelhaupt, *Chem. Phys. Lett.*, 2006, **426**, 415-421.
288. J. P. Perdew, K. Burke and M. Ernzerhof, *Phys. Rev. Lett.*, 1996, **77**, 3865-3868.
289. E. R. Johnson, R. A. Wolkow and G. A. DiLabio, *Chem. Phys. Lett.*, 2004, **394**, 334-338.
290. E. R. Johnson, A. D. Becke, C. D. Sherrill and G. A. DiLabio, *J. Chem. Phys.*, 2009, **131**, 034111.
291. S. E. Wheeler and K. N. Houk, *J. Chem. Theory Comput.*, 2010, **6**, 395-404.
292. J. Gräfenstein, D. Izotov and D. Cremer, *J. Chem. Phys.*, 2007, **127**, 214103.
293. P. Politzer, J. S. Murray and T. Clark, *Phys. Chem. Chem. Phys.*, 2010, **12**, 7748-7757.

294. G. Valerio, G. Raos, S. V. Meille, P. Metrangolo and G. Resnati, *J. Phys. Chem. A*, 2000, **104**, 1617-1620.
295. D. Cappelletti, P. Candori, F. Pirani, L. Belpassi and F. Tarantelli, *Cryst. Growth Des.*, 2011, **11**, 4279-4283.
296. K. Bartik, M. Luhmer, J.-P. Dutasta, A. Collet and J. Reisse, *J. Am. Chem. Soc.*, 1998, **120**, 784-791.
297. T. Brotin, A. Lesage, L. Emsley and A. Collet, *J. Am. Chem. Soc.*, 2000, **122**, 1171-1174.
298. M. M. Spence, S. M. Rubin, I. E. Dimitrov, E. J. Ruiz, D. E. Wemmer, A. Pines, S. Q. Yao, F. Tian and P. G. Schultz, *Proc. Natl. Acad. Sci.*, 2001, **98**, 10654-10657.
299. G. Huber, L. Beguin, H. Desvaux, T. Brotin, H. A. Fogarty, J.-P. Dutasta and P. Berthault, *J. Phys. Chem. A*, 2008, **112**, 11363-11372.
300. M. S. Syamala, R. J. Cross and M. Saunders, *J. Am. Chem. Soc.*, 2002, **124**, 6216-6219.
301. M. Ilczyszyn, M. Selent and M. M. Ilczyszyn, *J. Phys. Chem. A*, 2012, **116**, 3206-3214.
302. K. W. Miller, N. V. Reo, A. J. Schoot Uiterkamp, D. P. Stengle, T. R. Stengle and K. L. Williamson, *Proc. Natl. Acad. Sci.*, 1981, **78**, 4946-4949.
303. N. S. Bayliss, *J. Chem. Phys.*, 1950, **18**, 292-296.
304. E. M. Arnett and P. C. Wernett, *J. Am. Chem. Soc.*, 1993, **115**, 12187-12188.
305. P. Diehl, R. Ugolini, N. Suryaprakash and J. Jokisaari, *Magn. Reson. Chem.*, 1991, **29**, 1163-1164.
306. Y. H. Lim and A. D. King, *J. Phys. Chem.*, 1993, **97**, 12173-12177.
307. M. Luhmer and K. Bartik, *J. Phys. Chem. A*, 1997, **101**, 5278-5283.
308. H. Yuan, S. Murad, C. J. Jameson and J. D. Olson, *J. Phys. Chem. C*, 2007, **111**, 15771-15783.
309. Y. H. Lim, A. R. Calhoun and A. D. King, *Appl. Magn. Reson.*, 1997, **12**, 555-574.

310. C. J. Jameson, D. N. Sears and A. C. de Dios, *J. Chem. Phys.*, 2003, **118**, 2575-2580.
311. M. Bühl, M. Kaupp, O. L. Malkina and V. G. Malkin, *J. Comput. Chem.*, 1999, **20**, 91-105.
312. D. N. Sears and C. J. Jameson, *J. Chem. Phys.*, 2004, **121**, 2151-2157.
313. C. J. Jameson, D. N. Sears and S. Murad, *J. Chem. Phys.*, 2004, **121**, 9581-9592.
314. T. Kato, *Struct. Bond.*, 2000, **96**, 95-146.
315. C. Präsang, A. C. Whitwood and D. W. Bruce, *Chem. Commun.*, 2008, 2137-2139.
316. R. A. Reddy and C. Tschierske, *J. Mater. Chem.*, 2006, **16**, 907-961.
317. R. D. Bailey, G. W. Drake, M. Grabarczyk, T. W. Hanks, L. L. Hook and W. T. Pennington, *J. Chem. Soc., Perkin Trans. 2*, 1997, 2773-2780.
318. R. B. Walsh, C. W. Padgett, P. Metrangolo, G. Resnati, T. W. Hanks and W. T. Pennington, *Cryst. Growth Des.*, 2001, **1**, 165-175.
319. T. Uchida and K. Kimura, *Acta. Crystallogr. Sect. C*, 1984, **40**, 139-140.
320. E. L. Rimmer, R. D. Bailey, T. W. Hanks and W. T. Pennington, *Chem. Eur. J.*, 2000, **6**, 4071-4081.
321. F. Cristiani, F. A. Devillanova, F. Isaia, V. Lippolis, G. Verani and F. Demartin, *Polyhedron*, 1995, **14**, 2937-2943.
322. L. Lee, D. J. Crouch, S. P. Wright, R. Berridge, P. J. Skabara, N. Bricklebank, S. J. Coles, M. E. Light and M. B. Hursthouse, *CrystEngComm*, 2004, **6**, 612-617.
323. F. Cristiani, F. Demartin, F. A. Devillanova, F. Isaia, V. Lippolis and G. Verani, *Inorg. Chem.*, 1994, **33**, 6315-6324.
324. R. H. Jones, K. S. Knight, W. G. Marshall, J. Clews, R. J. Darton, D. Pyatt, S. J. Coles and P. N. Horton, *CrystEngComm*, 2014, **16**, 237-243.
325. H. H. Hodgson, *Chem. Rev.*, 1947, **40**, 251-277.
326. R. F. Heck and J. P. Nolley, *J. Org. Chem.*, 1972, **37**, 2320-2322.

327. I. P. Beletskaya and A. V. Cheprakov, *Chem. Rev.*, 2000, **100**, 3009-3066.
328. D. M. Huck, H. Loc Nguyen, S. J. Coles, M. B. Hursthouse, B. Donnio and D. W. Bruce, *J. Mater. Chem.*, 2002, **12**, 2879-2886.
329. G. Bellucci, R. Bianchini, C. Chiappe, R. S. Brown and H. Slebocka-Tilk, *J. Am. Chem. Soc.*, 1991, **113**, 8012-8016.
330. J. Taylor, MChem Project, 2013
331. D. J. Byron, D. Lacey and R. C. Wilson, *Mol. Cryst. Liq. Cryst.*, 1981, **76**, 253-260.
332. P. H. Svensson and L. Kloo, *Chem. Rev.*, 2003, **103**, 1649-1684.
333. F. F. Awwadi, R. D. Willett, K. A. Peterson and B. Twamley, *Chem. Eur. J.*, 2006, **12**, 8952-8960.
334. L. J. McAllister, C. Prasang, J. P. W. Wong, R. J. Thatcher, A. C. Whitwood, B. Donnio, P. O'Brien, P. B. Karadakov and D. W. Bruce, *Chem. Commun.*, 2013, **49**, 3946-3948.
335. G. B. Carpenter and S. M. Richards, *Acta Crystallogr.*, 1962, **15**, 360-364.
336. A. S. Batsanov, J. A. K. Howard, A. P. Lightfoot, S. J. R. Twiddle and A. Whiting, *Eur. J. Org. Chem.*, 2005, **2005**, 1876-1883.
337. J. Grebe, K. Harms, F. Weller and K. Dehnicke, *Z. Annorg. Allg. Chem.*, 1995, **621**, 1489-1495.
338. L. N. Swink and G. B. Carpenter, *Acta Crystallogr., Sect. B*, 1968, **24**, 429-433.
339. S. Soled and G. B. Carpenter, *Acta Crystallogr. Sect. B*, 1974, **30**, 910-914.
340. M. C. Aragoni, M. Arca, F. A. Devillanova, M. B. Hursthouse, S. L. Huth, F. Isaia, V. Lippolis, A. Mancini, H. R. Ogilvie and G. Verani, *J. Organomet. Chem.*, 2005, **690**, 1923-1934.
341. D. W. Bruce, D. A. Dunmur, E. Lalinde, P. M. Maitlis and P. Styring, *Liq. Cryst.*, 1988, **3**, 385-395.
342. Z. T. Nagy, B. Heinrich, D. Guillon, J. Tomczyk, J. Stumpe and B. Donnio, *J. Mater. Chem.*, 2012, **22**, 18614-18622.

343. L. J. McAllister, D. W. Bruce and P. B. Karadakov, *J. Phys. Chem. A*, 2012, **116**, 10621-10628.
344. L. J. McAllister, D. W. Bruce and P. B. Karadakov, *Phys. Chem. Chem. Phys.*, 2014, **16**, 2576-2587.
345. D. Lenoir and C. Chiappe, *Chem. Eur. J.*, 2003, **9**, 1036-1044.
346. I. Roberts and G. E. Kimball, *J. Am. Chem. Soc.*, 1937, **59**, 947-948.
347. K. Yates and R. S. McDonald, *J. Org. Chem.*, 1973, **38**, 2465-2478.
348. J. Strating, J. H. Wieringa and H. Wynberg, *J. Chem. Soc. Chem. Commun.*, 1969, 907-908.
349. H. Slebocka-Tilk, R. G. Ball and R. S. Brown, *J. Am. Chem. Soc.*, 1985, **107**, 4504-4508.
350. R. S. Brown, R. W. Nagorski, A. J. Bennet, R. E. D. McClung, G. H. M. Aarts, M. Klobukowski, R. McDonald and B. D. Santarsiero, *J. Am. Chem. Soc.*, 1994, **116**, 2448-2456.
351. B. K. Ohta, R. E. Hough and J. W. Schubert, *Org. Lett.*, 2007, **9**, 2317-2320.
352. A. C. Legon and J. M. A. Thumwood, *Phys. Chem. Chem. Phys.*, 2001, **3**, 1397-1402.
353. M.-F. Ruasse and J.-E. Dubois, *Tetrahedron Lett.*, 1970, **11**, 1163-1166.
354. M. F. Ruasse and J. E. Dubois, *J. Org. Chem.*, 1972, **37**, 1770-1778.
355. M.-F. Ruasse, *Acc. Chem. Res.*, 1990, **23**, 87-93.
356. M.-F. Ruasse, G. Lo Moro, B. Galland, R. Bianchini, C. Chiappe and G. Bellucci, *J. Am. Chem. Soc.*, 1997, **119**, 12492-12502.
357. V. I. Teberekidis and M. P. Sigalas, *Tetrahedron*, 2005, **61**, 3967-3976.
358. S. M. Islam and R. A. Poirier, *J. Phys. Chem. A*, 2007, **111**, 13218-13232.
359. C. Hansch, A. Leo and R. W. Taft, *Chem. Rev.*, 1991, **91**, 165-195.
360. R. S. Brown, *Acc. Chem. Res.*, 1997, **30**, 131-137.
361. T. Mori and R. Rathore, *Chem. Commun.*, 1998, 927-928.
362. F. Pichierri, *J. Mol. Struct. Theochem*, 2004, **668**, 179-187.

363. S. M. Islam and R. A. Poirier, *J. Phys. Chem. A*, 2007, **112**, 152-159.
364. C. Chiappe, A. D. Rubertis, A. Jaber, D. Lenoir, C. Wattenbach and C. S. Pomelli, *J. Org. Chem.*, 2002, **67**, 7066-7074.
365. C. H. Reynolds, *J. Am. Chem. Soc.*, 1992, **114**, 8676-8682.
366. V. I. Teberekidis and M. P. Sigalas, *Tetrahedron*, 2002, **58**, 6171-6178.
367. R. Damrauer, M. D. Leavell and C. M. Hadad, *J. Org. Chem.*, 1998, **63**, 9476-9485.
368. G. A. Olah, G. K. S. Prakash and G. Rasul, *Proc. Natl. Acad. Sci., U. S. A.*, 2013, **110**, 8427-8430.
369. D. F. Shellhamer, D. C. Gleason, S. J. Rodriguez, V. L. Heasley, J. A. Boatz and J. J. Lehman, *Tetrahedron*, 2006, **62**, 11608-11617.
370. G. A. Olah, *Halonium Ions*, Wiley, New York, 1975.
371. E. S. Stoyanov, I. V. Stoyanova, F. S. Tham and C. A. Reed, *J. Am. Chem. Soc.*, 2010, **132**, 4062-4063.
372. G. A. Olah, G. Rasul, M. Hachoumy, A. Burcher and G. K. Surya Prakash, *J. Am. Chem. Soc.*, 2000, **122**, 2737-2741.
373. L. A. Noronha, T. J. L. Judson, J. F. Dias, L. S. Santos, M. N. Eberlin and C. J. A. Mota, *J. Org. Chem.*, 2006, **71**, 2625-2629.
374. M. Lehmann, A. Schulz and A. Villinger, *Angew. Chem. Int. Ed.*, 2009, **48**, 7444-7447.
375. E. A. Merritt and B. Olofsson, *Angew. Chem. Int. Ed.*, 2009, **48**, 9052-9070.
376. N. W. Alcock and R. M. Countryman, *J. Chem. Soc. Dalton Trans.*, 1977, 217-219.
377. V. V. Zhdankin and P. J. Stang, *Chem. Rev.*, 2002, **102**, 2523-2584.
378. V. V. Zhdankin and P. J. Stang, *Chem. Rev.*, 2008, **108**, 5299-5358.
379. G. A. Landrum, N. Goldberg, R. Hoffmann and R. M. Minyaev, *New J. Chem.*, 1998, **22**, 883-890.
380. M. Ochiai, T. Suefuji, K. Miyamoto and M. Shiro, *Chem. Commun.*, 2003, 1438-1439.

381. J. Starbuck, N. C. Norman and A. G. Orpen, *New. J. Chem.*, 1999, **23**, 969-972.
382. R. Hillwig, F. Kunkel, K. Harms, B. Neumuller and K. Dehnicke, *Z. Naturforsch., B: J. Chem. Sci.*, 1997, **52**, 149-152.
383. J. T. Struchkov and T. L. Khotsyanova, *Acta Crystallogr.*, 1960, **13**, 1140-1140.
384. A. P. Bozopoulos and P. J. Rentzeperis, *Acta. Cryst.*, 1987, **43**, 914-916.
385. V. V. Zhdankin, A. Y. Kuposov, L. Su, V. V. Boyarskikh, B. C. Netzel and V. G. Young, *Org. Lett.*, 2003, **5**, 1583-1586.
386. T. Suefuji, M. Shiro, K. Yamaguchi and M. Ochiai, *Heterocycles*, 2006, **67**, 391-397.
387. O. Knop, T. S. Cameron, P. K. Bakshi, A. Linden and S. P. Roe, *Can. J. Chem.*, 1994, **72**, 1870-1881.
388. A. A. Neverov and R. S. Brown, *J. Org. Chem.*, 1998, **63**, 5977-5982.
389. A. A. Neverov, H. X. Feng, K. Hamilton and R. S. Brown, *J. Org. Chem.*, 2003, **68**, 3802-3810.
390. N. W. Alcock and G. B. Robertson, *J. Chem. Soc., Dalton Trans.*, 1975, 2483-2486.
391. D. C. Georgiou, P. Butler, E. C. Browne, D. J. D. Wilson and J. L. Dutton, *Aust. J. Chem.*, 2013, **66**, 1179-1188.
392. K. B. Wiberg, *Tetrahedron*, 1968, **24**, 1083-1096.
393. L. J. McAllister, D. W. Bruce and P. B. Karadakov, *J. Phys. Chem. A.*, 2011.
394. S. I. Watanabe, K. Yamamoto, Y. Itagaki, T. Iwamura, T. Iwama and T. Kataoka, *Tetrahedron*, 2000, **56**, 855-863.
395. A. Takemura, L. J. McAllister, P. B. Karadakov, N. E. Pridmore, A. C. Whitwood and D. W. Bruce, *CrystEngComm*, 2014, **16**, 4254-4264.
396. A. Takemura, L. J. McAllister, S. Hart, N. E. Pridmore, P. B. Karadakov, A. C. Whitwood and D. W. Bruce, *Chem. Eur. J.*, 2014, **20**, 6721-6732.

397. E. Corradi, S. V. Meille, M. T. Messina, P. Metrangolo and G. Resnati, *Angew. Chem. Int. Ed.*, 2000, **39**, 1782-1786.
398. B. K. Saha, A. Nangia and M. Jaskolski, *CrystEngComm*, 2005, **7**, 355-358.
399. C. B. Aakeröy, J. Desper, B. A. Helfrich, P. Metrangolo, T. Pilati, G. Resnati and A. Stevenazzi, *Chem. Commun.*, 2007, 4236-4238.
400. C. B. Aakeröy, N. C. Schultheiss, A. Rajbanshi, J. Desper and C. Moore, *Cryst. Growth Des.*, 2009, **9**, 432-441.
401. C. B. Aakeröy, P. D. Chopade and J. Desper, *Cryst. Growth Des.*, 2011, **11**, 5333-5336.
402. C. B. Aakeröy, P. D. Chopade, C. Ganser and J. Desper, *Chem. Commun.*, 2011, **47**, 4688-4690.
403. C. B. Aakeroy, S. Panikkattu, P. D. Chopade and J. Desper, *CrystEngComm*, 2013, **15**, 3125-3136.
404. H. M. M. Shearer, *J. Chem. Soc.*, 1959, 1394-1397.
405. A. R. Voth, P. Khuu, K. Oishi and P. S. Ho, *Nat. Chem.*, 2009, **1**, 74-79.
406. A. J. Blake, F. Cristiani, F. A. Devillanova, A. Garau, L. M. Gilby, R. O. Gould, F. Isaia, V. Lippolis, S. Parsons, C. Radek and M. Schroder, *J. Chem. Soc., Dalton. Trans.*, 1997, 1337-1346.
407. A. J. Blake, F. A. Devillanova, A. Garau, F. Isaia, V. Lippolis, S. Parsons and M. Schroder, *J. Chem. Soc., Dalton Trans.*, 1999, 525-532.
408. H. Bock, N. Nagel and A. Seibel, *Liebigs Ann.*, 1997, **1997**, 2151-2159.
409. O. Holmesland and C. H. R. Rømming, *Acta Chem. Scand.*, 1966, **20**, 2601-2610.
410. D. Cinčić, T. Friščić and W. Jones, *CrystEngComm*, 2011, **13**, 3224-3231.
411. C. Laurence, K. A. Brameld, J. r. m. Graton, J.-Y. Le Questel and E. Renault, *J. Med. Chem.*, 2009, **52**, 4073-4086.
412. D. Cinčić, T. Friščić and W. Jones, *Chem. Eur. J.*, 2008, **14**, 747-753.
413. D. Cinčić, T. Friščić and W. Jones, 2008, **14**, 747-753.
414. A. Dey and G. R. Desiraju, *CrystEngComm*, 2004, **6**, 642-646.

415. M. Gdaniec, *CrystEngComm*, 2007, **9**, 286-288.
416. D. Zobel, P. Luger, W. Dreissig and T. Koritsanszky, *Acta Crystallogr., Sect. B: Struct. Sci.*, 1992, **48**, 837-848.
417. J. W. Bats, M. C. Haberecht and M. Wagner, *Acta Crystallogr., Sect. E: Struct. Rep. Online*, 2003, **59**, o1483-o1485.
418. L. Leiserowitz and M. Tuval, *Acta Crystallogr., Sect. B: Struct. Sci., Cryst. Eng. Mater.*, 1978, **34**, 1230-1247.
419. R. Lo, A. Ballabh, A. Singh, P. Dastidar and B. Ganguly, *CrystEngComm*, 2012, **14**, 1833-1841.
420. J.-L. Syssa-Magalé, K. Boubekeur and B. Schöllhorn, *J. Mol. Struct.*, 2005, **737**, 103-107.
421. J. N. Moorthy, P. Venkatakrishnan, P. Mal, S. Dixit and P. Venugopalan, *Cryst. Growth Des.*, 2003, **3**, 581-585.
422. O. Bolton, K. Lee, H.-J. Kim, K. Y. Lin and J. Kim, *Nat. Chem.*, 2011, **3**, 205-210.
423. S. K. Maity, S. Bera, A. Paikar, A. Pramanik and D. Haldar, *Chem. Commun.*, 2013, **49**, 9051-9053.
424. H. S. El-Sheshtawy, B. S. Bassil, K. I. Assaf, U. Kortz and W. M. Nau, *J. Am. Chem. Soc.*, 2012, **134**, 19935-19941.
425. P. Auffinger, F. A. Hays, E. Westhof and P. S. Ho, *Proc. Natl. Acad. Sci. U. S. A.*, 2004, **101**, 16789-16794.
426. R. Wilcken, M. O. Zimmermann, A. Lange, A. C. Joerger and F. M. Boeckler, *J. Med. Chem.*, 2013, **56**, 1363-1388.
427. L. A. Hardegger, B. Kuhn, B. Spinnler, L. Anselm, R. Ecabert, M. Stihle, B. Gsell, R. Thoma, J. Diez, J. Benz, J. M. Plancher, G. Hartmann, D. W. Banner, W. Haap and F. Diederich, *Angew. Chem. Int. Ed.*, 2011, **50**, 314-318.
428. A. R. Voth, F. A. Hays and P. S. Ho, *Proc. Natl. Acad. Sci. U. S. A.*, 2007, **104**, 6188-6193.

429. M. Carter, A. R. Voth, M. R. Scholfield, B. Rummel, L. C. Sowers and P. S. Ho, *Biochemistry*, 2013, **52**, 4891-4903.
430. M. R. Scholfield, C. M. V. Zanden, M. Carter and P. S. Ho, *Protein Sci.*, 2013, **22**, 139-152.